Department of Mechanical Engineering

Technical published papers

Nima Geran Malek

- An open-source framework for the FE modeling and optimal design of fiber-steered variable-stiffness composite cylinders using water strider algorithm (Mechanics Based Design of Structures and Machines - 2020)
- Highly stretchable and sensitive strain sensors based on carbon nanotube–elastomer nanocomposites: the effect of environmental factors on strain sensing performance (Journal of Materials Chemistry C - 2020)
- Machine learning regression approaches for predicting the ultimate buckling load of variable-stiffness composite cylinders (Acta Mechanica - 2021)
- An open-source computational framework for optimization of laminated composite plates (Acta Mechanica - 2020)
- Electrical properties of stretchable and skin–mountable PDMS/MWCNT hybrid composite films for flexible strain sensors (Journal of Composite Materials - 2019)
- Comprehensive Optimization of Friction Stir Weld Parameters of Lap Joint AA1100 Plates using Artificial Neural Networks and modified NSGA-II (Materials Research Express - 2018)
- Effects of the impactor geometrical shape on the non-linear low-velocity impact response of sandwich plate with CNTRC face sheets (Journal of Sandwich Structures & Materials - 2018)
- Buckling load of laminated composite plates using three variants of the biogeography-based optimization algorithm (Acta Mechanica - 2018)
- Robust design optimization of laminated plates under uncertain bounded buckling loads (Structural and Multidisciplinary Optimization - 2018)
- Optimum stacking sequence design of composite laminates for maximum buckling load capacity using parameter-less optimization algorithms (Engineering with Computers - 2018)
- Evaluation of non-linear Effects in Piezoresistive PDMS/MWCNT Sensing Elements (The Biennial International Conference on Experimental Solid Mechanics (X-Mech 2018))
- Piezoresistive Behavior of PDMS/CNT Nanocomposites Made by Vacuum Filtration Method (1st Iran Congress on Industrial Applications of Advanced Materials and Manufacturing - 2017)
- Investigation on the Size of reinforcement in AZ31/Al2O3 Nanocomposite with Array Distribution (1st Iran Congress on Industrial Applications of Advanced Materials and Manufacturing - 2017)
- Evaluation of The Mechanical Properties of Carbon Nanotube Nanocomposites and The Effect of The Number of Interphase Layers Using the Representative Volume Element (RVE) (Iran industrial applications of composite structures - 2016)

An open-source framework for the FE modeling and optimal design of fiber-steered variable-stiffness composite cylinders using water strider algorithm.pdf

Highly stretchable and sensitive strain sensors based on carbon nanotube–elastomer nanocomposites the effect of environmental factors on strain sensing performance.pdf

Robust design optimization of laminated plates under uncertain bounded buckling loads.pdf

Effects of the impactor geometrical shape on the non-linear low-velocity impact response of sandwich plate with CNTRC face sheets.pdf

Electrical properties of stretchable and skin–mountable PDMSMWCNT hybrid composite films for flexible strain sensors.pdf

Buckling load of laminated composite plates using three variants of the biogeography-based optimization algorithm.pdf

Comprehensive optimization of friction stir weld parameters of lap joint AA1100 plates using artificial neural networks and modified NSGA-II.pdf

An open-source computational framework for optimization of laminated composite plates. Acta Mechanica.pdf

Machine learning regression approaches for predicting the ultimate buckling load of variable-stiffness composite cylinders.pdf

Optimum stacking sequence design of composite laminates for maximum buckling load capacity using parameter-less optimization algorithms.pdf

Investigation on the Size of reinforcement in AZ31Al2O3 Nanocomposite with Array Distribution.pdf

National Conference.pdf

Piezoresistive Behavior of PDMSCNT Nanocomposites Made by Vacuum Filtration Method.pdf

Evaluation of non-linear Effects in Piezoresistive PDMSMWCNT Sensing Elements.pdf

Mechanics Based Design of Structures and Machines
An International Journal

ISSN: (Print) (Online) Journal homepage: https://www.tandfonline.com/loi/lmbd20

An open-source framework for the FE modeling and optimal design of fiber-steered variable-stiffness composite cylinders using water strider algorithm

A. Kaveh , N. Geran Malek , A. Dadras Eslamlou & M. Azimi

To cite this article: A. Kaveh , N. Geran Malek , A. Dadras Eslamlou & M. Azimi (2020): An open-source framework for the FE modeling and optimal design of fiber-steered variable-stiffness composite cylinders using water strider algorithm, Mechanics Based Design of Structures and Machines, DOI: 10.1080/15397734.2020.1835489

To link to this article: https://doi.org/10.1080/15397734.2020.1835489

View supplementary material

Published online: 22 Oct 2020.

Submit your article to this journal

Article views: 8

View related articles

View Crossmark data

Full Terms & Conditions of access and use can be found at
https://www.tandfonline.com/action/journalInformation?journalCode=lmbd20

MECHANICS BASED DESIGN OF STRUCTURES AND MACHINES
https://doi.org/10.1080/15397734.2020.1835489

An open-source framework for the FE modeling and optimal design of fiber-steered variable-stiffness composite cylinders using water strider algorithm

A. Kaveh[a], N. Geran Malek[a], A. Dadras Eslamlou[a], and M. Azimi[b]

[a]Centre of Excellence for Fundamental Studies in Structural Engineering, Iran University of Science and Technology, Tehran, Iran; [b]Department of Civil Engineering, University of British Columbia, Vancouver, BC, Canada

ABSTRACT

As the automated fiber placement (AFP) manufacturing technology is developed, curvilinear fiber path composite structures received extensive attention. Therefore, developing a design framework capable of optimizing such structures is a significant challenge for researchers and engineers in this domain. In this article, an open-source ABAQUS/MATLAB-based framework is developed for the bending-induced buckling design of variable-stiffness (VS) composite cylinders made using the AFP method. The framework is based on an interface between ABAQUS FE packages with MATLAB environment using Python scripting language. In this framework, the optimized fiber angle distribution of steered plies and associated bending-induced buckling load of its FE model is obtained by applying a meta-heuristic optimization algorithm. The developed Python script submits dimensions, angle distributions, as well as loading and boundary conditions to ABAQUS/CAE. This framework can be customized to meet industrial demands. To show such flexibility, different types of metaheuristic optimization algorithms and aspect ratios are applied, and the associated problems are optimized separately. In addition to the simplicity and versatility of the proposed framework, the results indicate the higher performance of a novel metaheuristic, the so-called Water Strider Algorithm (WSA). Moreover, this framework can be used for finite element modeling and analysis in the metamodeling step for composite cylinders with higher aspect ratios.

ARTICLE HISTORY
Received 23 June 2020
Accepted 7 October 2020

KEYWORDS
Design optimization; fiber placement; variable-stiffness composite cylinder; water strider algorithm; computational framework

1. Introduction

Composite structures are widely used as the load-carrying components of automotive structures because these components possess excellent mechanical properties as well as weight efficiency. Their functionality is related to a diverse range of features and parameters involved in designing these structures. Due to numerous advantages over isotropic materials, such as high stiffness, superior features in strength, lightweight, and directional properties, laminated composites are used in several industrial structures (Paris 2009; Shahgholian-Ghahfarokhi et al. 2020).

There are two main strategies for designing laminated structures. First, composite structures are designed as a permutation of several straight-fiber plies called constant-stiffness (CS) composite design. In this kind of problem, there is just one variable in every lamina of the structure, i.e.

CONTACT A. Kaveh alikaveh@iust.ac.ir Centre of Excellence for Fundamental Studies in Structural Engineering, Iran University of Science and Technology, Tehran 16844, Iran.
Communicated by Corina Sandu.
Supplemental data for this article can be accessed at publisher's website.
© 2020 Taylor & Francis Group, LLC

the constant angle of the fiber. Second, composite structures might be designed for each of the plies as a matrix embracing fibers positioned in the curvilinear paths known as variable-stiffness (VS) design. Each ply could be designed separately in this type of problem since each fiber path could be estimated by multiple numbers of variables (Ghiasi, Pasini, and Lessard 2009; Ghiasi et al. 2010). Along with the above-mentioned variation of fiber angles in CSs structures or fiber paths in VSs, composite laminates may be designed based on other parameters, such as the number of plies and dimensions (Kaveh, Dadras, and Geran Malek 2019a, 2019b). These parameters bring about potential capability in such and other similar composite structures to be tailored and meet the practitioners' and scientists' specific needs.

Due to the advent of automated fiber placement technology (AFP), the uses of VS composites are increased. Accordingly, improving the load-carrying capacity of variable-stiffness structures by optimizing the fiber path has been in the center of attention. In this regard, various continuous path functions have been introduced, such as the linear function that has already been used widely. As the most practical and straightforward fiber path variation, linear variation was proposed in the early stages by Gürdal, Tatting, and Wu (2008). Afterward, other fiber path functions, including trigonometric functions (Blom et al. 2009), cubical and quadratic functions (Muc and Ulatowska 2010), Lagrangian polynomials (Wu et al. 2012), and cubic Bezier curves (Parnas, Oral, and Ceyhan 2003) were also used in the design of VS structures.

AFP is a hybrid manufacturing method with both advantages of automated tape laying and filament winding technologies (Oromiehie et al. 2019). Both plate and cylindrical structures could be fiber-placed using AFP technology. For plate structures, pioneering investigations were conducted by Hyer and Lee (1991) and Gurdal and Olmedo (1993). After that, various experimental, analytical, and numerical methods were adopted for VS panels, most of which are reviewed by Ribeiro et al. (2014). Setoodeh, Abdalla, and Gürdal (2006) demonstrated a substantial increase in the buckling load of variable-stiffness composite plates compared with constant-stiffness design, using lamination parameters methodologies.

White, Weaver, and Wu (2015) studied the buckling and post-buckling behavior of VS cylindrical structures under axial compression. Li (2017) implemented the variable-stiffness properties of the composite cylinders using a user-written subroutine capable of assigning location-based features to every element. In each layer of VS composite structures, the fiber path is a continuous curve, which can be designed in response to the local load-bearing stiffness demand. A multi-step radial basis function (RBF) metamodel-based design approach for maximizing the buckling load of VS cylinders subjected to pure bending was proposed by Rouhi et al. (2017). In their works, at the neighborhood of the optimum points resulted from the previous optimization steps, the side constraints of the design variables are narrowed down. Additionally, sampling, metamodeling, and optimization steps are repeated until convergence is reached. A similar design approach was used to tailor the buckling behavior of laminated composite elliptical cylinders subjected to compressive axial (Rouhi et al. 2016) and bending (Ghayoor et al. 2017) loads. Rouhi et al. (2015) developed a multi-objective optimization to investigate the effect of the variation in bending load direction on the buckling performance of composite cylinders.

Developing straightforward approaches for the efficient design of structures would be a worthwhile effort. In this regard, for instance, Zuo (2013) developed a GA-based optimization software and object-oriented graphics interface design for the cross-sectional shape of thin-walled beams in the automobile body. Tauzowski, Blachowski, and Lógó (2019) proposed a new approach to finite element classes implementation benefiting smaller hierarchy. As another example, an object-oriented MATLAB toolbox, based on the transfer stiffness matrix method, was developed by Qin et al. (2017) to promote automotive body-in-white structure design. This study continues the current authors' previous research on a framework developed for the optimization of laminated composite plates (Kaveh et al. 2020). Taking into account that there is not available any convenient, user-friendly approach for numerical modeling and optimization of VS cylindrical

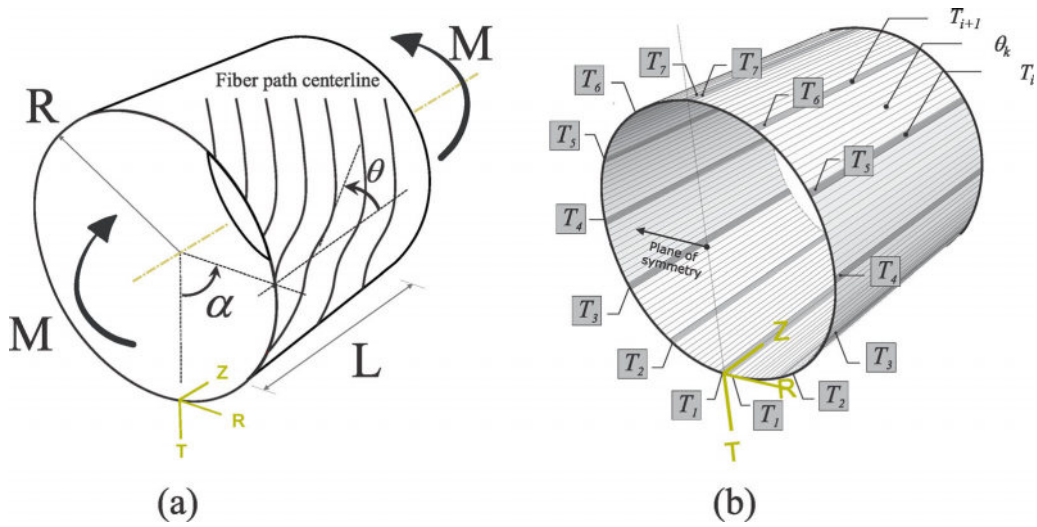

Figure 1. Bending-induced buckling of variable-stiffness composite cylinder: (a) Configuration of the composite cylinder with the coordinate system and dimensions, subjected to pure bending loads, (b) piece-wise constant orientation angle narrow section.

composites, the main goal of this study is to develop such a framework. Additionally, this procedure is equipped with a novel metaheuristic for optimizing the orientation distribution of the steered plies. This optimization algorithm encompasses ABAQUS solver, capable of solving nonlinear mechanical problems (Geng, Zhao, and Zhou 2020; Hosseini et al. 2020; Qablan et al. 2020), the result of which is considered as the outcome of the objective function for optimization. After verifying the framework based on the available data from the literature, it is used for the buckling design of cylinders with various aspect ratios. Interfacing this algorithm with ABAQUS/CAE is conducted through a Python-script.

This article is organized into five sections. Numerical simulation of the variable-stiffness cylinder FE model is provided in Section 2. The description of the FEM design framework is presented in Section 3. This section represents the MATLAB/Python interface by summarizing the Python code fundamental blocks, followed by a review of two well-known and one novel optimization algorithms. Section 4 aims to show the suitability of the proposed framework by employing it in the problem of cylindrical variable-stiffness composites having various study cases. Eventually, concluding remarks are provided in Section 5.

2. Numerical analysis using the finite element method

In this study, the numerical simulations are carried out using ABAQUS software (Systèmes 2010). Figure 1(a) shows the configuration, loading, and coordinate system of the cylinder model with the length and radius of L and R. Here, the diameter to thickness ratio of the cylinders is low, and so the thin-walls hypothesis can be used. It should be noted that the cylinders with moderate and thick walls behave differently from the thin wall cylinders because of the influence of shear stresses and lower stiffness. The linear buckling model is utilized here. However, in thick cylinders, reinforcing layers are prone to delamination failures that cannot be captured with the linear, geometric warping model (Ehsani and Rezaeepazhand 2016; Alidoost and Rezaeepazhand 2017).

To apply the concept of the variability of stiffness to cylindrical composite, it must be partitioned into a certain number of narrow sections (see Fig. 1(b)). $[0^\circ,\ \theta^\circ,\ 90^\circ,\ -\theta^\circ,\ -\theta^\circ,\ 90^\circ,\ \theta^\circ,\ 0^\circ]s$ (symmetric 16-ply laminate) is the laminate layups of each of these narrow sections, where θ plies are the plies whose direction needs to be steered. The values of design variables T_i s and therefore θ_k

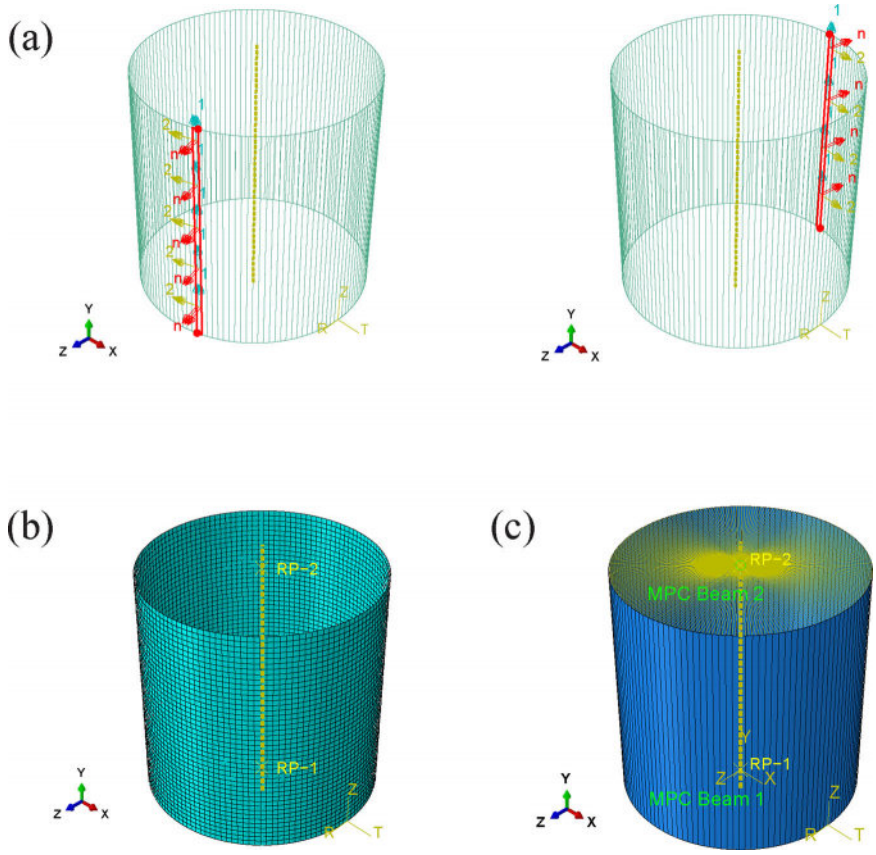

Figure 2. Finite element modeling: (a) material orientation, (b) meshing, and (c) MPC constraint.

are assumed to be continuously varied between 0° and 90°. The angle α determines the spatial location of the narrow sections to which θ is assigned. The composite cylinder is symmetrical with respect to the ZT-plane of the coordinate system, as shown in Fig. 1(b). The angles of the fibers are the same in any two narrow sections that are symmetrical about this plane, but with the opposite sign, i.e. $(\theta = -\theta)$. T_i s $(i = 1,\ 2,\ \ldots,\ 7)$ are the narrow sections whose fiber angles, in one of their plies, constitute seven design variables of the optimization problem, which is discussed further in the following section. The changes in the fiber angles of the rest of the sections are considered as linear.

Moreover, the buckling behavior of the composite cylinder is analyzed. Critical buckling moments of the present optimization problem are calculated via ABAQUS/CAE, by which Lanczos eigensolver is employed to obtain the critical buckling loads and mode shapes.

For each of the narrow sections, the orientation of the material must be defined separately (Fig. 2(a)). The material orientation of each narrow section should be defined in reference to the RTZ datum cylindrical coordinate system. In this figure, the direction of axis 2 remains the same when rotating around the cylinder's circumference. "S8R5" element type, as shown in Fig. 2(b), is used to execute the finite element analyses, in which each element has 8-node of five degrees of freedom. Material characteristics and meshing are assigned according to the modeling procedure studied by Rouhi et al. (2017). Five thousand seven hundred and sixty-two number of quadratic quadrilateral elements of type S8R5 are generated with the approximate global size of 10.6, in which on every top and bottom edges of the 134 sections, only one seed is assigned. To ensure that the circular geometry of the upper and lower edges is preserved during deformation, beam-

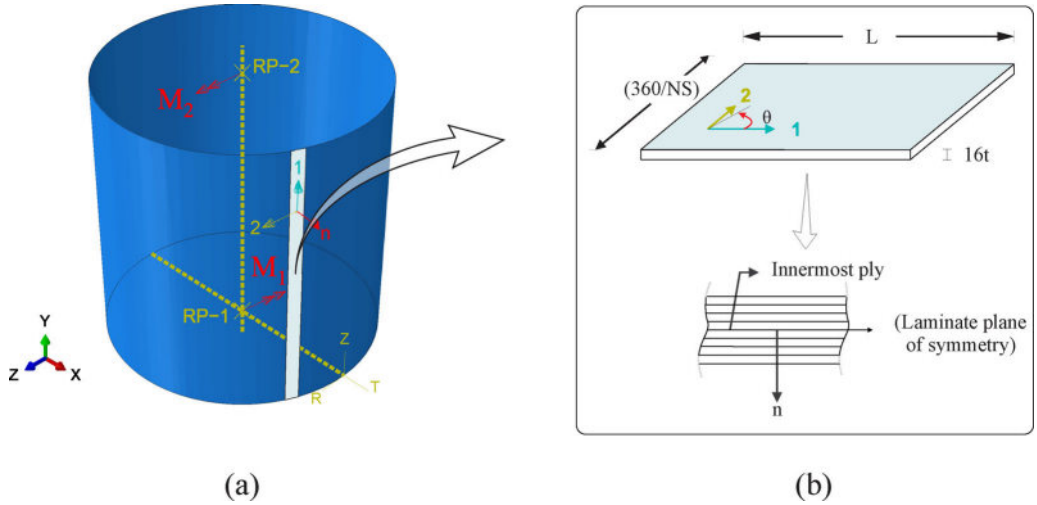

Figure 3. Configuration of the variable-stiffness composite cylinders: (a) piece-wise constant model of the variable-stiffness cylinder, (b) laminate fiber path direction and plane of symmetry.

type multipoint constraint (MPC) constraint, as shown in Fig. 2(c), is applied on the top and bottom edges of the cylinder. These constraints tied the circular edge to the central points of their associated endings. The loading in the form of pure bending is applied on both sides of the cylinder.

3. Finite element framework

The main goal of the current framework is to interface an optimization algorithm implemented in MATLAB with a Python-script that is connected to the ABAQUS FE solver. The optimization problem is to find the optimum orientation angle distribution T_i s that result in the maximum possible buckling load capacity. A Python-script does finite element modeling and analysis, and optimization is executed by MATLAB code. Herein, the Water Strider Algorithm (WSA) as a novel population-based and nature-inspired optimization algorithm and two well-known optimization algorithms, namely PSO and GA, are applied to the current problem. From the framework implementation perspective, these optimization strategies could be replaced with other algorithms easily. The entire code of this framework, for a typical verified case, is available in the supplemental online material. Not only the optimization algorithm, but loadings, dimensions, and boundary conditions can be customized to meet the researchers' needs.

3.1. Python-script

The need for a Python-script arises from the automated procedure required for the finite element numerical analysis and iteration-based mechanism of the optimization. For the finite element analysis of the continuity of change in the fiber angles of the steered plies, the circumference of the cylinder must be divided into a limited number of narrow sections. Such simplification is as if the structure is made by connecting a multitude of constant-stiffness laminated composite plates (134, in this study). That results in a number of variables equal to the number of these laminated composite plates. If θ_k is the steered ply angle of each of these constant-stiffness plates, the number of variables is reduced by half due to the symmetry of the cylinder relative to the ZT-plane ($\theta_k = -\theta_k$). Doing that is similar to the case where the continuous fiber path is being replaced with a discrete piece-wise constant one having a limited number of design variables.

Table 1. Implementation of Python code fundamental blocks.

1.	`NS = 134 # Number of narrow sections`
	`L=457.200012 # Length of the cylinder (L=D=18 in)`
	`D=L # Diameter of the cylinder`
	`ThicknessOfEachPly = 0.127 # Thickness of each ply`
	`MyModel=mdb.Model(name='VS_Cylinder')`
		# Create model with arbitrary dimension

2.	`mdb.models['Model-1'].Material(name='Material_1'))`
	`mdb.models['Model-1'].materials['Material_1'].`
	`Elastic(type=ENGINEERING_CONSTANTS,table=((134000.0, 7710.0, 7710.0,`
	`0.301, 0.301, 0.396, 4310, 4310, 2760), ))`
		# Import material (all properties are given in N, and mm)

3.	`mdb.models['VS_Cylinder'].BuckleStep(name='Step-1',`
	`previous='Initial',numEigen = 1,eigensolver=LANCZOS, minEigen =`
	`0.0,blockSize=DEFAULT,maxBlocks=DEFAULT)`
		# Import step (Buckling with zero as the minimum interested Eigen)

4.	`mdb.models['VS_Cylinder'].MultipointConstraint(name='Constraint-1',`
	`controlPoint=Region1RefPointBottom, surface=BottomEdge,`
	`mpcType=BEAM_MPC, userMode=DOF_MODE_MPC, userType = 0, csys=None)`
		# Create MPC Constraint for the bottom and top circular Edges

5.	`d=p.datums`
	`p.DatumCsysByOffset(datumCoordSys=d[Datume_Keys[-1]],`
	`Datume_Keys=d.keys()`
	`name='MySecond_CSYS', coordSysType=CYLINDRICAL, vector=(D/2,`
	`0.0, 0.0))`
		# Create cylindrical coordinate system

6.	`for i in range(NS):`
	`region=p.sets['NarrowSegment_%d'%(i+1)]`
	`orientation=mdb.models['Model-1'].parts['Part-`
	`1'].datums[Datume_Keys[-1]]`
	`mdb.models['Model-1'].parts['Part-`
	`1'].MaterialOrientation(region=region, orientationType=SYSTEM ,`
	`axis=AXIS_2, localCsys=orientation, fieldName='',`
	`additionalRotationType=ROTATION_ANGLE, additionalRotationField = '',`
	`angle = 0.0)`
		# Assign material orientation for each narrow sections (NS)

7.
```
# Top reference point
a=mdb.models['VS_Cylinder'].rootAssembly
region=a.sets['RefPointSet_TOP']
mdb.models['VS_Cylinder'].DisplacementBC(name='BC-RefPointSet_Top',
  createStepName='Step-1', region=region, u1=0.0, u2=UNSET, u3=0.0,
  ur1=0.0, ur2=0.0, ur3=UNSET,amplitude=UNSET,
  buckleCase=PERTURBATION_AND_BUCKLING, fixed=OFF,
  distributionType=UNIFORM, fieldName='', localCsys=None)
# Bottom reference point
a=mdb.models['VS_Cylinder'].rootAssembly
region=a.sets['RefPointSet_Bottom']
mdb.models['VS_Cylinder'].DisplacementBC(name='BC-
  RefPointSet_Bottom', createStepName='Step-1', region=region,
  u1=0.0, u2=0.0, u3=0.0, ur1=0.0, ur2=0.0, ur3=UNSET,
  amplitude=UNSET, buckleCase=PERTURBATION_AND_BUCKLING,
  fixed=OFF,distributionType=UNIFORM, fieldName='', localCsys=None)
```
 # Create boundary condition

8.
```
# on bottom RP
mdb.models['VS_Cylinder'].Moment(name='Load-1', createStepName='Step-
  1', region=Region1RefPointBottom,cm3=-1, distributionType=UNIFORM,
  field='',localCsys=None)
# on top RP
  mdb.models['VS_Cylinder'].Moment(name='Load-2',
  createStepName='Step-1',region=Region1RefPointTop,cm3=1,
  distributionType=UNIFORM,field='',localCsys=None)
```
 # Import load

Further simplification could be applied if these θ_k variables were reduced to T_i $(i = 1,\ 2,\ \ldots,\ 7)$ variables whose narrow sections are placed equally-spaced apart from each other on the circumference of the cylinder. Here, for the rest of the narrow sections between each of the two subsequent T_i s, fiber angles are also assumed to vary linearly according to Eq. (1):

$$\theta_k = T_i + \frac{\alpha_k - \alpha_i}{\alpha_{i+1} - \alpha_i}(T_{i+1} - T_i);\ \ i = 1,\ \ldots, m,\ \text{and}\ k = 1,\ \ldots,\ n \tag{1}$$

where m and n are the number of design variables ($m = 7,$ in this study) and the number of narrow sections between two subsequent sections having T_i as their fiber path angle. In the presented codes, the reader can choose either the mentioned linear or spline fit through the seven design points. It should be pointed out that in this study, $n = 10,$ given that the circumference of the cylinders is divided into 134 number of narrow sections. Overall, the problem of modeling the geometry of the variable-stiffness composite cylinder can be considered similar to the modeling of several constant-stiffness laminated composites that are arranged one after the other, and their fiber angles follow a specific relationship. One such laminated composite, along with its material orientation, is shown schematically in Fig. 3. Material orientation in each laminated composite is implemented by creating the *1-2-n* datum coordinate system relative to the previously defined RTZ cylindrical coordinate system. The fiber angle is measured relative to the *1*-axis of this local coordinate system (see Fig. 3(b)).

Besides implementing the piece-wise constant concept, Python-script introduces other parameters to the ABAQUS/CAE: dimensions, material properties, boundary condition, material orientation, and applied loads. Bending-induced buckling occurs through applying moment M_1 on a bottom and M_2 on a top reference point as $M_1 = M_2 = 1$ (N.mm). Moments should be applied such that compression will be exerted on the part of the cylinder located at 180°, given the RTZ coordinate system. Thus, considering the XYZ coordinate system of Fig. 3, the moment applied on the top edge's central point (reference point 1) must be in the $+z$-direction, and the moment on the bottom reference point should be in the reversed direction. Pure bending loads were applied at the top and bottom center points of the cylinder, where they tied to their associated circular base edges using beam-type Multipoint constraint (MPC beam). MPC constraint preserves the upper and lower edges of the cylinder circular during any arbitrary deformations. It is to be noted that negative buckling loads were exempt from the analyses (`minEigen = 0.0`).

Code customizability is further understood by considering lines 1–8 in Table 1. Some fundamental blocks of the Python-script are given in this table, while the entire code can be accessed from the supplemental online material. Lines 1 to 8 show how to model the main parts of the finite element analysis from assigning the dimensions of the cylinder to apply loadings and boundary conditions. After setting the length, diameter, and the number of narrow sections of the cylinder in line 1, material properties of the composite plies are imported in line 2. Then, in lines 3 and 4, the number of desired critical buckling load is asked, and beam-type MPC constraint on the top and bottom edges of the cylinder are defined. RTZ datum coordinate system is specified by offsetting the primary coordinate system located at the center point of the bottom ending (line 5). The orientation of the material, which must be defined separately for each section, is implemented by a `for` loop, as given in line 6. For each node, there are three degrees of freedom for displacements and three for rotations. As mentioned in row 7 of Table 1, simply supported-simply supported (SS) boundary condition is applied by allowing the top reference point to move along the centerline of the cylinder ($U1 = U3 = UR1 = UR2 = 0$) and fixing the bottom reference point ($U1 = U2 = U3 = UR1 = UR2 = 0$). Here, Ui denotes the translational and URi is the rotational degree of freedom in reference to the i axis. Besides, 1, 2, and 3 represents the direction along the x-axis, y-axis, and z-axis, respectively. In simple terms, for implementing the SS boundary condition, all the rotational and translational degrees of freedoms at the bottom reference point are fixed except for the rotation in the z-direction. Also, the

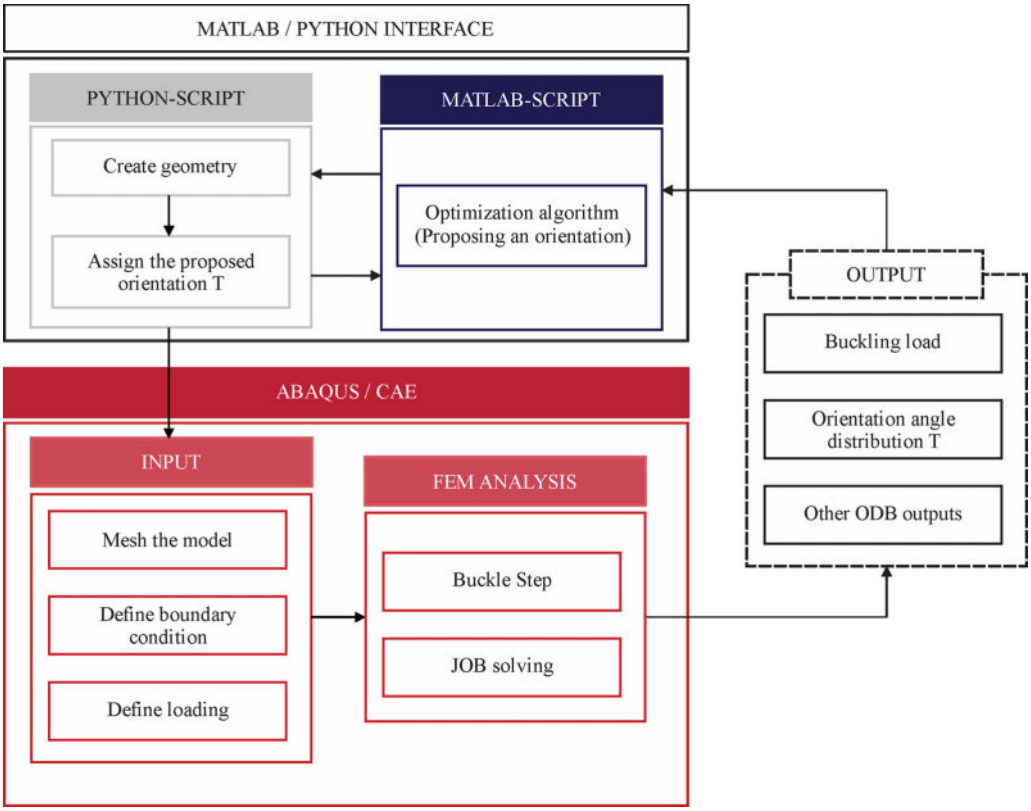

Figure 4. Flowchart of the FE-based framework.

translation of the top reference point in the y-direction and rotation around the z-direction is allowed. This boundary condition can also be changed to other types of boundary conditions, such as simply supported-fixed, fixed-simply supported, and fixed-fixed, in case they are the desired boundary conditions (Hu and Chen 2018). Moreover, loadings could be changed into a desirable one such as concentrated force, thermal, displacements, and pressure, by replacing them with line 8.

As shown in the MATLAB/ABAQUS interface flowchart of Fig. 4, the framework acts such that ABAQUS is the solver for every single analysis of the objective function. Once the framework starts running, for every single execution of the objective function, Python-script creates a folder with the same name in which it stores the associated model and its produced outputs (as shown in ABAQUS/CAE block of Fig. 4). When a FE function evaluation, three text files are generated to store the information for the proposed orientation angle distribution T, critical buckling moment, and overall layup angles. Then, the objective function, i.e. the critical buckling load value, is read by MATLAB, and according to its essence of the optimization algorithm, a new orientation angle distribution T is proposed. These recursive processes, which are shown in Fig. 4 using cyclic arrows, continues until the termination condition of the optimization algorithm is satisfied.

3.2. Optimization strategies

Limitations of gradient-based methods, such as convergence to localized minima or high dependency on the initial solution, have led to the increasing use of metaheuristic algorithms. Due to

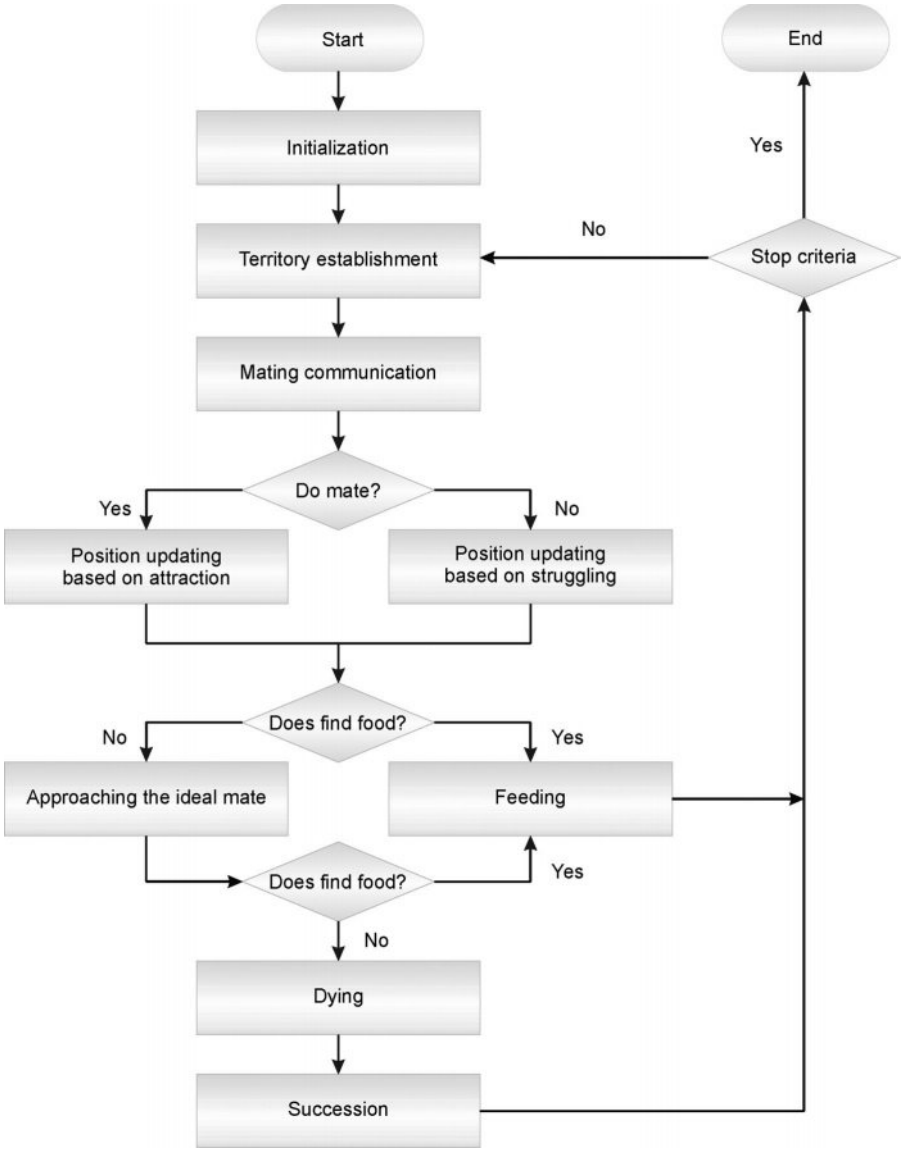

Figure 5. Flowchart of the WSA algorithm.

their capability to find and explore the promising regions with reasonable computational effort, metaheuristic algorithms are suitable for global searches over the entire search space. Some of the applications of these algorithms and their implementations can be found in the literature (Kaveh and Dadras Eslamlou 2020a, 2020b).

3.2.1. A brief overview of the WSA algorithm

Water strider algorithm (WSA) is a novel population-based swarm intelligent optimization algorithm inspired by water striders' life cycle. WSA mimics intelligent ripple communication, territorial behavior, mating style, succession, and water striders' feeding mechanisms. These strategies were implemented with an attempt to utilize mathematically simple formulations representing the life cycle of water striders by Kaveh and Dadras Eslamlou (2020a, 2020b).

Due to the hydrophobic legs of WSs and surface tension of the water, this family of animals has achieved a natural ability to live on top of the water. For female water striders, defending from food resources, and for male striders, protecting from their mating partners is the reason why the striders establish a territory for themselves. Each territory is usually inhabited by a couple of female striders and one male so-called '*keystone*' strider. By oscillating their legs on the top surface of the water, the striders produce ripples with different frequencies, durations, and amplitudes, by which they could convey different types of information with one another. Depending on the features that each signal possesses, a different type of information is sent out, such as repelling the invader, positioning the pray, and courtship. Incoming signals are received through a sensory receptor organ on their legs. This organ can also distinguish signals that are being produced by prey insects trapped on the surface of the water. The pre-copulatory calling signal transmitted by a male insect will be responded by a negative or positive message from the female insect. Based on that feedback, the striders will update their positions as given in Eq. (2):

$$\begin{aligned} WS_i^{t+1} &= WS_i^t + R.\ rand\ ;\ \ Positive\ response \\ WS_i^{t+1} &= WS_i^t + R.\ (1 + rand);\ \ negative\ response \end{aligned} \tag{2}$$

where WS_i^t is the position of *ith* WS in the *t*th cycle, and *rand* is a random number between 0 and 1. Also, $R = WS_F^{t-1} - WS_i^{t-1}$.

The exploitative, exploratory, convergence, local optima avoidance, and other proposed algorithm features were studied by applying it on a large number of multimodal unimodal, shifted, biased, and composite functions. Besides, the WSA is employed successfully in numerous continuous, constrained, discrete, and unconstrained engineering design problems (Kaveh and Dadras Eslamlou 2020a, 2020b). The flowchart of the WSA is illustrated in Fig. 5. A comprehensive description of the WSA is provided in Kaveh and Dadras Eslamlou (2020a, 2020b).

3.2.2. A brief overview of genetic algorithm (GA)

The genetic algorithm (GA), which is derived from the theory of Darwin, is first developed by Holland (1992). As the most common optimization method used in the broad range of engineering problems (Khalkhali, Ebrahimi-Nejad, and Malek 2018), GA is inspired by the evolution of biological individuals. Crossover, mutation, survivor selection, and parent selection are the leading operators (Sivanandam and Deepa 2008).

GA comprises two essential steps, including initialization and the main loop of the algorithm. The critical task that GA undertakes is to produce a highly evolved version of the population from a random initial solution with its operators and selection mechanisms. In the initialization phase, random chromosomes for the first generation are produced (*nPop*). This part of the code runs outside the main loop. However, in the main loop, crossover and mutation operations are performed as large as the population designated based on the crossover and mutation probability ($nc + nm$). All of these populations ($nPop + nc + nm$) are then sorted according to the value of their objective functions. The function evaluation of these populations is conducted using the ABAQUS FE Package. Every time the objective function is called, it executes the Python code. This step is carried out through what was described in Section 3.1 on interfacing MATLAB environment with ABAQUS FEA software using Python-script.

After sorting, populations should be truncated; therefore, *nPop* number or populations being remained. To randomly select two parents among the *nPop* available parents tournament selection is utilized to produce offspring.

In this article, 80% of the populations are selected for the *crossover* operation. Besides, to keep the biological diversity that is an essential feature of the genetic algorithm, in a step called *mutation*, 20% of the populations are being mutated. In contrast to crossover that results in producing two offspring from two random parents, in mutation, a random parent is being mutated,

Table 2. Material properties of unidirectional carbon/epoxy composite ply (Barbero 2013).

Property	AS4D/9310
E_1	134 GPa
$E_2 = E_3$	7.71 GPa
$G_{12} = G_{13}$	4.31 GPa
G_{23}	2.76 GPa
$\nu_{12} = \nu_{13}$	0.301
ν_{23}	0.396
Thickness of each ply (t)	0.127 mm

resulting in one child. The total number of parents is not going to be considered as it needs to sort and truncate them to have *nPop* number of populations.

3.2.3. A brief overview of PSO algorithm

Developed by Kennedy and Eberhart (1995), PSO is a swarm intelligence optimization technique that is inspired by the social behavior of animal packs, such as fish schools or bird flocks. It starts with random initialization of a swarm (population) of particles (individuals) in a search space of n-dimension, which is the problem's dimension. Position $x_i = (x_1, x_2, ..., x_n)$ and velocity $v_i = (v_1, v_2, ..., v_n)$ are the two features by which every particle i is characterized. Besides these features, each particle holds the memories of its best personal experience P_i and the best group experience P_g. In other words, P_i and P_g represent the best previous position of each individual as well as all of them, respectively. Here, the best position means the location at which the objective function reached the maximum (optimum) value. The value of the objective function associated with these positions are called P_{best} and g_{best}, respectively. These particles are moved from the position x_i^t with velocity v_i^t to a new position x_i^{t+1} whose velocity is v_i^{t+1}, according to the following relationships:

$$\begin{aligned} v_i^{t+1} &= \omega v_i^t + c_1 r_1 \left(p_i^t - x_i^t\right) + c_2 r_2 \left(p_g^t - x_i^t\right) \\ x_i^{t+1} &= x_i^t + v_i^{t+1} \end{aligned} \tag{3}$$

where r_1 and r_2 are uniformly distributed random numbers in the interval $[-1, 1]$. Also, c_1 and c_2 are acceleration constants changing the velocity of a particle toward the best individual experience and the best group's experience, respectively. In other words, these coefficients determine how much a particle follows cognitive and social components, respectively. Delving further into that, when the value of c_2 decreases, particle i tends to move more toward p_i^t than p_g^t, and vice versa. Besides the direction to which the particles should move, it must be available a factor that controls how much this movement should be. This factor, which controls the amount of exploitation and exploration of the search space, is called inertia weight factor ω. The higher amount of this factor results in more new areas to be searched by the particles, and vice versa (Moussavian and Jafari 2017).

4. Verification of the framework

The performance of the presented FE approach is verified by comparing the obtained buckling load capacity of the QI and VS cylinders with their counterparts in Rouhi et al. (2014, 2017). The validity of the numerical FE simulation and the proposed optimization framework is shown with the QI and VS cases, respectively. The cylinders have simply supported-simply supported boundary conditions, and constant length L as well as diameter D, where $L = D = 457.2$ mm. A 16-ply symmetric, balanced having stacking sequence of $[0°, \theta°, 90°, -\theta°, -\theta°, 90°, \theta°, 0°]_s$ is considered as the layup of VS composite cylinder. Plies with an angle of θ are regarded as the

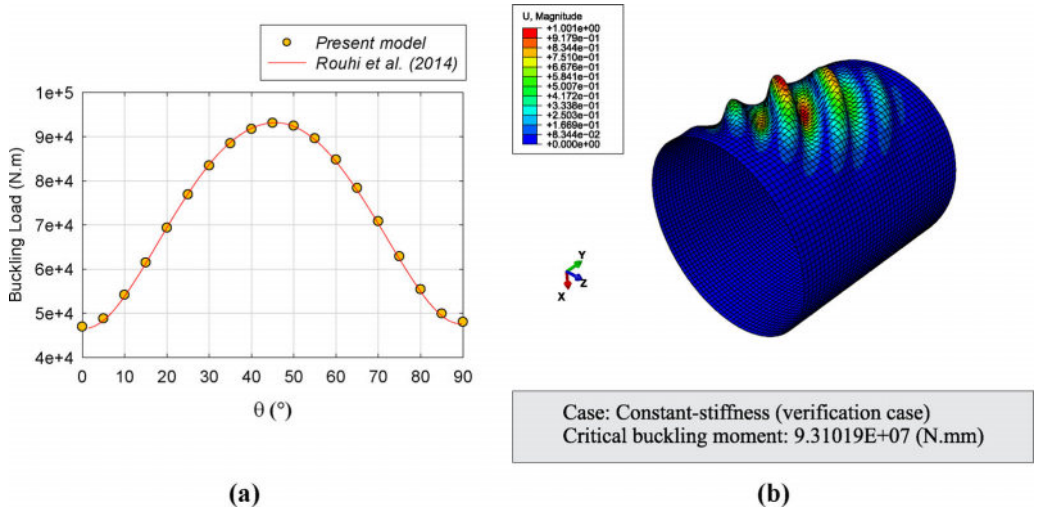

Figure 6. Verification of presented FE approach for QI composite cylinder ($\frac{L}{R} = 2$): (a) buckling loads at different values of θ (for every 5° angle), (b) mode shape of the verified case for $\theta = 45°$.

candidate plies that need to be fiber-steered such that the bending-induced buckling reaches its maximum value. Buckling is induced by the pure bending load of $M_1 = M_2 = 1\text{N mm}$ applied to the reference points at the top and bottom of the cylinder. Mechanical properties of AS4D/9310 lamina are taken as the material properties (Table 2).

The same layup is considered for the constant-stiffness composite cylinder. Constant-stiffness cylinder comprises of several narrow sections whose θ values are the same. For the case of a constant-stiffness composite, the buckling moment is verified for several constant values of θ between 0 and 90. As can be seen from Fig. 6(a), θ is changed in every 5° interval from 0° to 90°. As shown in this figure, the maximum bending moment that the cylinder could withstand is achieved when all narrow sections have a fixed steered ply angle of 45°. Moreover, as the θ angle of these sections deviates from 45°, the cylinder buckles at lower loads. Therefore, $[0°,\ 45°,\ 90°,\ -45°,\ -45°,\ 90°,\ 45°,\ 0°]_s$ is the optimum stacking sequence of all the narrow sections comprising the QI cylinder. The mode shape associated with this layup is presented in Fig. 6(b).

After the verification of the FE analysis for the QI case, to verify the optimization performance of the framework, the VS design is carried out as well. Boundary conditions, dimensions, and loading are the same as the case of the QI cylinder. However, as α varies between 0° and 180°, around the circumference of the cylinder, θ is not constant, and it undergoes seven discontinuous changes. These changes in the value of θ occur at seven, specific narrow sections whose θ values are identified by T_1 to T_7. Once again, to show the validity of the FE modeling, this time for the VS case, for the same values of the T_i reported in Rouhi et al. (2017), buckling load is obtained, which shows a good agreement, as given in Table 3.

As shown in Fig. 7, with a population size of 10 and 600 number of eigenvalue analyses (NEA), buckling load is optimized. The optimum verified orientation angle distribution of the steered plies and the buckling mode shape of the converged composite cylinder are shown in Figs. 7(b) and 7(c), respectively. The distinct difference between the values of T_3 appears from the better buckling load that the framework is converged to. It is noteworthy that, for both of the QI and VS cylinders, there is a line in the Python-script through which other desirable stacking sequences could be implemented by modifying it as follows:

```
myOrientationsList[i].extend([0,tetta[i],90,-tetta[i],-
tetta[i],90,tetta[i],0])
```

Table 3. Buckling load of the QI and VS composite cylinders ($D = L = 457.2$ mm).

Composite cylinder	Buckling load (N mm)	
	Rouhi et al. (2017) ($\times 10^7$)	Present study ($\times 10^7$)
QI	9.32	9.31
VS	11.64	11.641

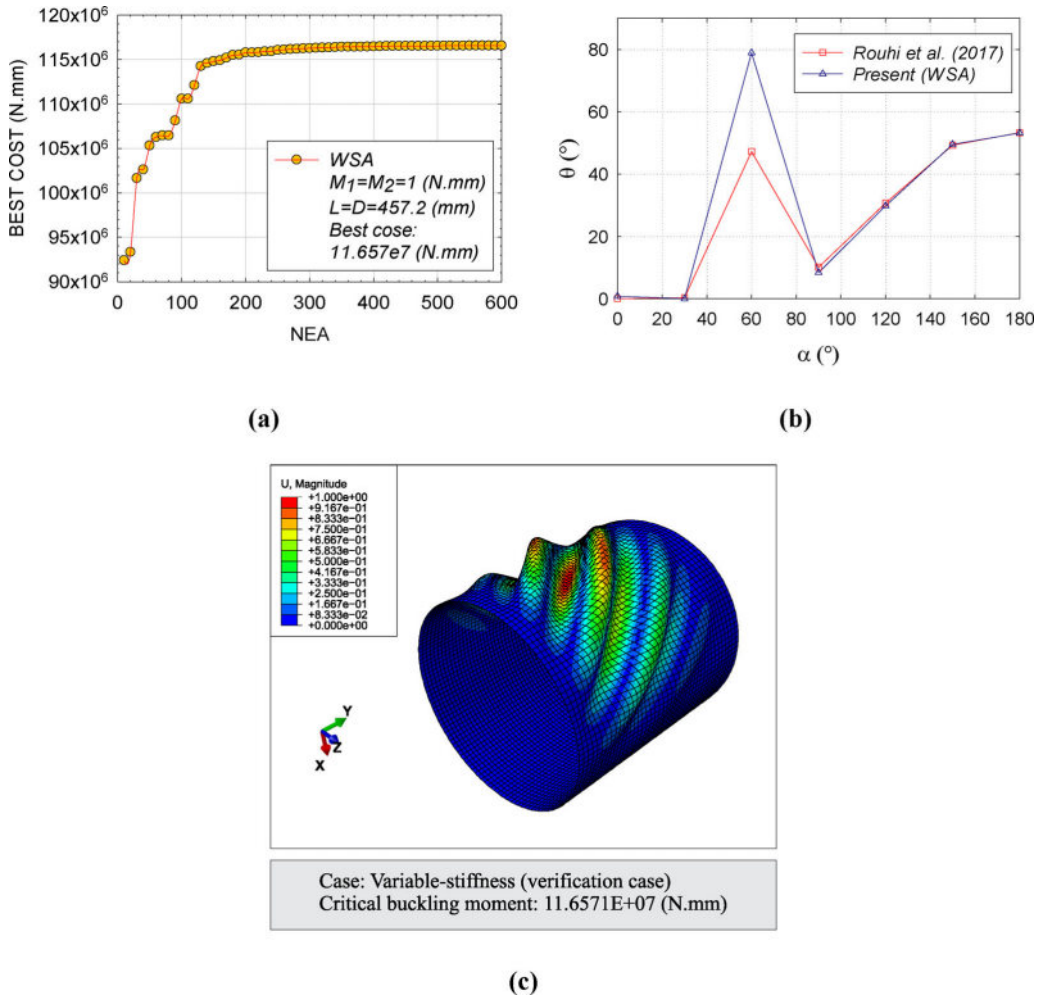

Figure 7. Verification of presented FE framework for VS composite cylinder ($\frac{L}{R} = 2$): (a) converged buckling load after 60 number of iterations and population size of 10, (b) optimum orientation angle distribution of the steered plies, (c) mode shape of the optimized model.

5. Numerical results and discussions

For a thin structure, structural performance may be influenced by the length to radius aspect ratio (L/R). To examine the effect of aspect ratio, the length of the cylinder is changed while the radius and thickness of the cylinder are kept constant. The current section studies the impact of different aspect ratios of the cylinder on the optimized orientation angle distribution and critical buckling load of the VS composite cylinders. Simply supported-simply supported boundary condition is considered as the boundary conditions of the cylinders. These composite cylinders are subjected to pure bending moments of M_1 and M_2 at both sides, where $M_1 = M_2 = 1$ N mm. The radius of the cylinder at the top and bottom ends are equal to 457.2 mm. However, the

Table 4. Optimized buckling load (N.mm) of variable-stiffness cylinders for different optimization algorithms along with QI cylinders at different aspect ratios ($R = 457.2$ mm).

Case	L/R	QI ($\times 10^7$)	Rouhi et al. (2014) ($\times 10^7$)	PSO ($\times 10^7$)	GA ($\times 10^7$)	WSA ($\times 10^7$)
1	0.1	41.160	50.169	56.706	54.842	**56.881**
2	0.2	16.743	22.254	22.963	22.923	**22.971**
3	0.3	12.325	15.844	**16.129**	15.454	16.061
4	0.4	11.235	14.169	14.333	13.816	**14.411**
5	0.5	10.542	13.308	13.273	13.378	**13.407**
6	0.6	10.073	12.844	12.480	12.319	**12.867**
7	0.7	9.807	12.346	12.516	12.259	**12.518**
8	0.8	9.642	12.187	12.028	12.135	**12.322**
9	0.9	9.534	12.026	12.120	11.894	**12.145**
10	1	9.464	11.864	11.995	11.649	**12.008**
11	2	9.310	11.64	11.601	11.522	**11.657**
12	3	9.295	11.506	11.520	11.062	**11.597**

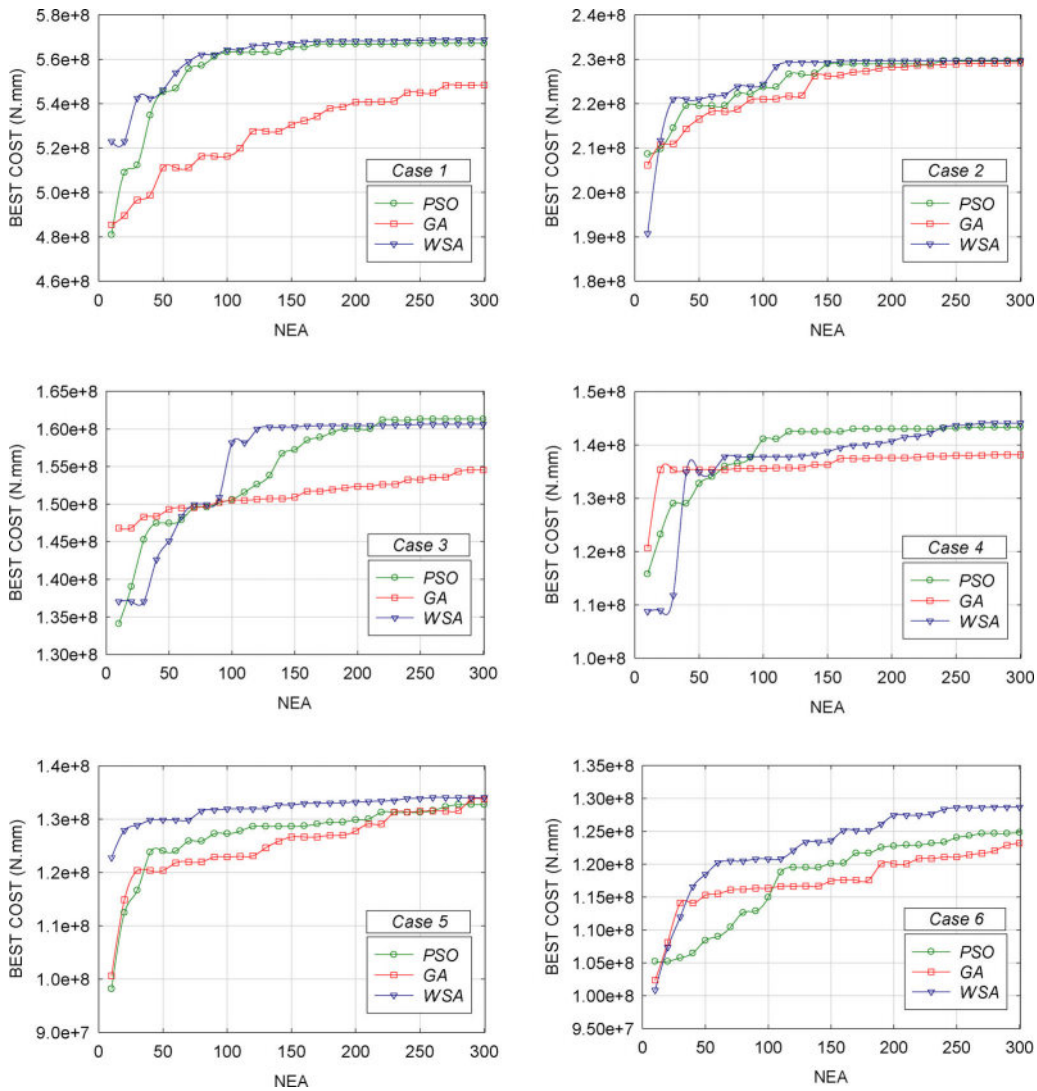

Figure 8. Convergence curves of the algorithms.

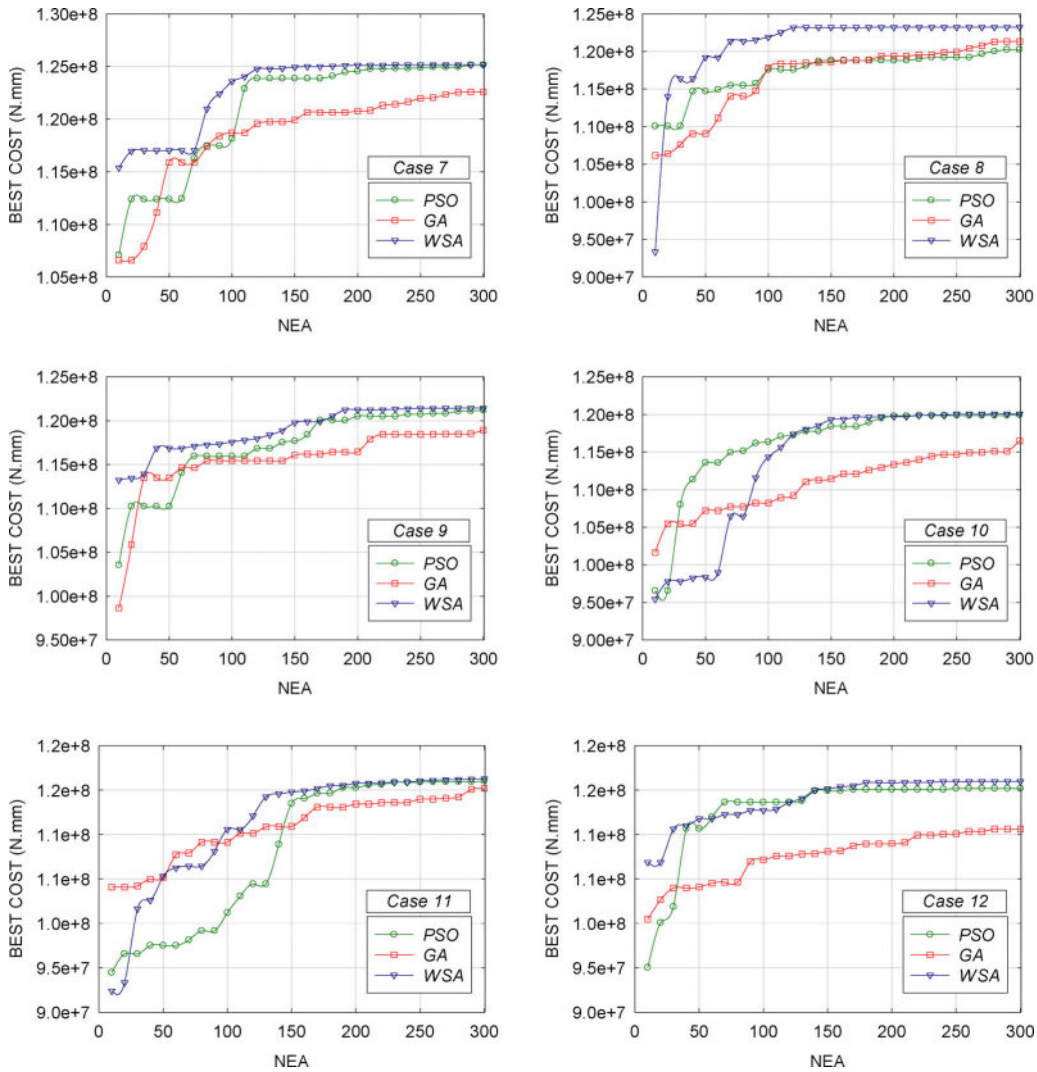

Figure 8. Convergence curves of the algorithms.

length of the cylinder L varies between 1.8 in and 54 in. Here, 12 cases associated with these aspect ratios (L/R) are considered. These cases are listed in Table 4, where the best result for each case is written in boldface.

$[0^\circ,\ \theta^\circ,\ 90^\circ,\ -\theta^\circ,\ -\theta^\circ,\ 90^\circ,\ \theta^\circ,\ 0^\circ]s$ are the laminate layups of the composite cylinders, where θ plies are the plies whose direction needs to be optimized. Seven design variables are considered for the optimization of the fiber path. Moreover, the thickness of each ply is 0.127 mm, and the total thickness of the laminate is 2.032mm. The laminae are assumed to be bonded together perfectly. Also, material constitutive properties of the carbon/epoxy lamina are given in Table 2.

The framework could be equipped with various optimization strategies. In this article, for demonstrating this notable feature, three different optimization algorithms are implemented and introduced to the main code. One novel optimization algorithm, WSA, and GA and PSO, as the most common optimization algorithms, are selected. The settings of GA, PSO, and WSA are the same as those set in Refs. (Simon 2008; Kaveh and Dadras Eslamlou 2020a, 2020b). Accordingly, for the GA, a mutation probability of 0.01, a crossover probability of 1, and roulette wheel

Table 5. Optimized orientation angle distribution obtained by each algorithm.

Case	Algorithm	T_1 (°)	T_2 (°)	T_3 (°)	T_4 (°)	T_5 (°)	T_6 (°)	T_7 (°)
1	PSO	11.113	0.590	24.555	3.938	0.000	36.178	47.958
	GA	0.577	13.427	47.683	7.002	0.000	21.148	36.259
	WSA	0.107	0.000	71.641	27.332	0.503	38.742	50.494
2	PSO	0.000	1.637	50.523	3.276	0.000	38.935	49.295
	GA	0.142	0.600	79.873	5.467	0.000	40.450	52.137
	WSA	0.000	0.000	70.137	0.000	0.000	41.559	50.265
3	PSO	2.006	0.000	84.209	5.773	18.543	48.337	53.319
	GA	20.207	1.119	53.798	28.427	6.755	41.597	41.271
	WSA	0.221	4.470	0.000	0.000	20.644	47.993	53.633
4	PSO	3.050	6.831	24.294	3.286	25.879	49.827	55.890
	GA	2.989	0.000	76.347	15.564	14.285	46.535	41.948
	WSA	0.000	0.024	37.659	0.000	28.133	49.115	56.707
5	PSO	6.460	0.000	41.471	38.887	22.262	49.183	50.951
	GA	25.125	0.845	55.877	13.773	23.407	49.543	53.588
	WSA	0.000	4.642	49.525	29.922	23.255	48.898	52.796
6	PSO	6.328	4.940	47.242	50.955	22.053	49.017	52.630
	GA	11.639	17.210	37.274	53.313	23.346	45.960	53.888
	WSA	6.001	0.029	41.422	9.920	25.553	53.658	53.384
7	PSO	0.808	0.000	28.542	4.889	29.423	49.877	52.955
	GA	2.077	3.635	80.700	28.218	29.314	43.983	57.424
	WSA	0.000	0.000	2.432	1.092	29.693	48.830	54.263
8	PSO	3.707	1.408	70.353	37.954	27.728	48.565	53.275
	GA	2.645	5.825	54.882	24.478	28.116	46.326	56.338
	WSA	0.000	0.800	58.881	0.520	29.632	47.804	55.169
9	PSO	0.451	0.000	73.788	12.458	26.910	49.027	52.775
	GA	0.163	24.755	68.924	11.850	27.263	49.964	50.844
	WSA	0.870	0.696	90.000	3.426	28.247	49.182	52.683
10	PSO	8.712	0.000	88.026	4.259	27.838	48.148	53.890
	GA	13.279	2.142	39.176	29.492	24.585	48.219	57.147
	WSA	0.000	1.025	65.134	0.174	30.702	48.451	56.842
11	PSO	8.417	1.187	41.436	2.221	32.088	48.282	51.825
	GA	3.498	1.831	50.425	23.064	25.589	52.141	50.289
	WSA	0.764	0.000	78.905	8.362	29.772	49.515	53.180
12	PSO	0.000	9.457	21.278	6.196	32.233	48.224	53.104
	GA	8.902	2.671	55.086	67.097	20.995	51.578	47.925
	WSA	0.127	0.000	60.915	3.979	31.992	46.930	54.008

selection are used. For PSO, a social constant for swarm interaction equal to 1, a cognitive constant of 1, and an inertial constant equal to 0.3 are set.

Furthermore, in WSA, the number of territories is considered 2, according to the original article (Kaveh and Dadras Eslamlou 2020a, 2020b). In all algorithms, the number of populations and the maximum NEA is set to 10 and 300. Buckling performance design using PSO, GA, and WSA optimization algorithms are carried out by the FEM optimization framework on variable-stiffness cylindrical composites having different aspect ratios, separately.

Table 4 provides the optimized buckling load with respect to the aspect ratio L/R for each algorithm. From Table 4, it can be seen that the optimal buckling load increases significantly as the aspect ratio decreases from 3 to 0.1. That means it is harder to force the shorter cylinders to buckle in comparison with the longer ones. For $\frac{L}{R} > 1$, the buckling load reduces to an asymptotic value. The convergence curves of the algorithms for each case are presented in Fig. 8, where the best so far obtained buckling moments (in N mm) are plotted against NEA.

Optimization of the buckling load resulted in an improved FE model with better orientation angle distribution $T = [T_1,\ T_2,\ T_3,\ T_4,\ T_5,\ T_6,\ T_7]$ for the steered plies. Table 5 gives these orientation angle distributions for the optimized models of each algorithm for all the cases, separately. It could be found that for the part of the cylinder close to the narrow section with $\theta = T_1$ degree, where is under tension, lower fiber angles (with a median of 1°) are required to bear the tensile load. On the other hand, the opposite side of the cylinder, where it is close to the narrow section having $\theta = T_7$, which is under compression, demands higher values of the orientation

angle (with a median of 53°). As a result, the distribution of the compressive load in the T_7 side is taking place more appropriately and is transferred more effectively from the T_7 to T_1 section. That leads to higher load-carrying capacity in VS cylinders in comparison to QI cylinders. Also, it can be concluded that the buckling moment has a lower sensitivity to the fiber angles assigned to the middle sections than those assigned to the upper and lower sections.

To compare the maximum buckling loads of VS cylinders with QI cylinders, a column for the QI cases is also provided in Table 4. With a simple comparison between the maximum optimized values obtained by the optimization algorithms and the refereed article, which appears in bold font, and the constant-stiffness ones, which have $\theta = 45°$ in all their narrow sections, it reveals that the buckling performance of the cylinders has been improved considerably. The improvement percentage in critical load for each case is equal to: 27.64%, 27.11%, 23.58%, 22.04%, 21.37%, 21.71%, 21.66%, 21.75%, 21.50%, 21.19%, 20.13%, 19.85%, respectively.

13The values optimized by this framework, in approximately all cases, reported better results than Rouhi et al. (2014). In the present study, optimization was conducted by performing approximately 300 number of function evaluations, while in the referred article, there are several sampling stages, each of which requires 550 structural analyses. After the sampling phase, optimization on the surrogate model was also performed with a population size of 1000 and 10 number of generations. It is also noteworthy that in the metamodeling approach, the results are always accompanied by some errors.

6. Conclusion

In summary, we developed and utilized an ABAQUS/MATLAB interface for the analysis and optimal design of VS cylindrical composites subjected to bending-induced buckling moments. Different cases for the length to radius aspect ratios are considered for the VS composite cylinder in order to show the applicability of the framework. The radius of the cylinder at the top and bottom ends are equal to 457.2 mm. However, the length of the cylinder L varies between 45.72 and 1371.6 mm. Also, $\left[0°,\ \theta°,\ 90°,\ -\theta^{\circ},\ -\theta^{\circ},\ 90°,\ \theta°,\ 0°\right]s$ are the laminate layups of the composite cylinders, where θ plies are the plies whose direction needs to be optimized. For this purpose, seven design variables for the path function were considered. It is shown that nearly all of the parameters involved in the finite element modeling phase of the script could be easily customized to meet the researchers' needs. In this study, a recently developed algorithm – the so-called Water Strider Algorithm (WSA) – is applied as one of the novel optimization metaheuristics to show the versatility of the framework in the optimization stage. Buckling loads are maximized for all of the aspect ratios, separately. Commercial finite element analysis (FEA) software ABAQUS was used for the buckling analysis of the cylindrical composites for the mechanical properties given in Table 2.

The following blocks of the python-script could be readily customized to meet the researchers' needs:

- Dimensions of the cylinder (length `L` and diameter `D`)
- The number of design variables `m`. The values of narrow sections `NS` and `n` might need to be changed accordingly. `m` represents the number of design variables, and `n` is the number of narrow sections between each of the two subsequent T_i s. Also, `NS` is the total number of narrow sections.
- Material properties
- Number of desired critical buckling loads (`numEigen`)
- Loading
- Boundary condition

In comparison to the results provided in the literature, it is observed that this framework not only does reach better results but also reduces the computational cost significantly. The sensitivity of the load-bearing capacity of optimally designed cylinders to middle section angles is examined. The results show that the buckling load is highly sensitive to the top and bottom angles rather than side angles. This mechanical interpretation of the results, in addition to its applicability in industry sectors, can be put into practice in the development of new optimization methods for VS cylinders. For example, an intelligent new method can adaptively distribute the computational cost to update the fiber angles considering their sensitivity.

This framework can perform optimization task satisfactorily, more specifically, for lower aspect ratios ($\frac{L}{R} < 2$). The applicability of the approach can be extended to data generation for high-fidelity surrogate models such as deep neural networks (DNN).

Disclosure statement

The author(s) declared no potential conflicts of interest with respect to the research, authorship, and/or publication of this article.

Funding

The author(s) received no financial support for the research, authorship, and/or publication of this article.

ORCID

M. Azimi http://orcid.org/0000-0001-7406-6721

References

Alidoost, H., and J. Rezaeepazhand. 2017. Instability of a delaminated composite beam subjected to a concentrated follower force. *Thin-Walled Structures* 120:191–202. doi:10.1016/j.tws.2017.08.032.

Barbero, E. J. 2013. *Finite element analysis of composite materials using AbaqusTM*. Boca Raton, FL: CRC Press.

Blom, A. W., B. F. Tatting, J. M. A. M. Hol, and Z. Gürdal. 2009. Fiber path definitions for elastically tailored conical shells. *Composites Part B: Engineering* 40 (1):77–84. doi:10.1016/j.compositesb.2008.03.011.

Ehsani, A., and J. Rezaeepazhand. 2016. Stacking sequence optimization of laminated composite grid plates for maximum buckling load using genetic algorithm. *International Journal of Mechanical Sciences* 119:97–106. doi:10.1016/j.ijmecsci.2016.09.028.

Geng, X., L. Zhao, and W. Zhou. 2020. Finite-element buckling analysis of functionally graded GPL-reinforced composite plates with a circular hole. *Mechanics Based Design of Structures and Machines* 1–17.doi:10.1080/15397734.2019.1707688.

Ghayoor, H., M. Rouhi, S. V. Hoa, and M. Hojjati. 2017. Use of curvilinear fibers for improved bending-induced buckling capacity of elliptical composite cylinders. *International Journal of Solids and Structures* 109:112–22. doi:10.1016/j.ijsolstr.2017.01.012.

Ghiasi, H., K. Fayazbakhsh, D. Pasini, and L. Lessard. 2010. Optimum stacking sequence design of composite materials. Part II: Variable stiffness design. *Composite Structures* 93 (1):1–13. doi:10.1016/j.compstruct.2010.06.001.

Ghiasi, H., D. Pasini, and L. Lessard. 2009. Optimum stacking sequence design of composite materials. Part I: Constant stiffness design. *Composite Structures* 90 (1):1–11. doi:10.1016/j.compstruct.2009.01.006.

Gurdal, Z., and R. Olmedo. 1993. In-plane response of laminates with spatially varying fiber orientations-variable stiffness concept. *AIAA Journal* 31 (4):751–8. doi:10.2514/3.11613.

Gürdal, Z., B. F. Tatting, and C. K. Wu. 2008. Variable stiffness composite panels: Effects of stiffness variation on the in-plane and buckling response. *Composites Part A: Applied Science and Manufacturing* 39 (5):911–22. doi:10.1016/j.compositesa.2007.11.015.

Holland, J. H. 1992. *Adaptation in natural and artificial systems: An introductory analysis with applications to biology, control, and artificial intelligence*. Cambridge, MA: MIT Press.

Hosseini, K., M. Safarabadi, M. Ganjiani, E. Mohammadi, and A. Hosseini. 2020. Experimental and numerical fatigue life study of cracked AL plates reinforced by glass/epoxy composite patches in different stress ratios. *Mechanics Based Design of Structures and Machines* 1–17. doi:10.1080/15397734.2020.1714448.

Hu, H.-T., and H.-C. Chen. 2018. Buckling optimization of laminated truncated conical shells subjected to external hydrostatic compression. *Composites Part B: Engineering* 135:95–109. doi:10.1016/j.compositesb.2017.09.065.

Hyer, M. W., and H. H. Lee. 1991. The use of curvilinear fiber format to improve buckling resistance of composite plates with central circular holes. *Composite Structures* 18 (3):239–61. doi:10.1016/0263-8223(91)90035-W.

Kaveh, A., A. Dadras, and N. Geran Malek. 2019a. Optimum stacking sequence design of composite laminates for maximum buckling load capacity using parameter-less optimization algorithms. *Engineering with Computers* 35 (3):813–32. doi:10.1007/s00366-018-0634-2.

Kaveh, A., A. Dadras, and N. Geran Malek. 2019b. Robust design optimization of laminated plates under uncertain bounded buckling loads. *Structural and Multidisciplinary Optimization* 59 (3):877–91. doi:10.1007/s00158-018-2106-0.

Kaveh, A., and A. Dadras Eslamlou. 2020a. Water strider algorithm: A new metaheuristic and applications. *Structures* 25:520–41. doi:10.1016/j.istruc.2020.03.033.

Kaveh, A., and A. Dadras Eslamlou. 2020b. *Metaheuristic optimization algorithms in civil engineering: New applications*. Switzerland: Springer.

Kaveh, A., A. Dadras Eslamlou, N. Geran Malek, and R. Ansari. 2020. An open-source computational framework for optimization of laminated composite plates. *Acta Mechanica* 231 (6):2629–50. doi:10.1007/s00707-020-02648-0.

Kennedy, J., and R. Eberhart. 1995. Particle swarm optimization. Paper presented at Proceedings of ICNN'95 – International Conference on Neural Networks, Perth, WA, Australia, Australia, November 27 to December 1.

Khalkhali, A., S. Ebrahimi-Nejad, and N. G. Malek. 2018. Comprehensive optimization of friction stir weld parameters of lap joint AA1100 plates using artificial neural networks and modified NSGA-II. *Materials Research Express* 5 (6):066508. doi:10.1088/2053-1591/aac6f6.

Li, E. 2017. Fast cylinder variable-stiffness design by using Kriging-based hybrid aggressive space mapping method. *Advances in Engineering Software* 114:215–26. doi:10.1016/j.advengsoft.2017.07.004.

Moussavian, H., and M. Jafari. 2017. Optimum design of laminated composite plates containing a quasi-square cutout. *Structural and Multidisciplinary Optimization* 55 (1):141–54. doi:10.1007/s00158-016-1481-7.

Muc, A., and A. Ulatowska. 2010. Design of plates with curved fibre format. *Composite Structures* 92 (7):1728–33. doi:10.1016/j.compstruct.2009.12.015.

Oromiehie, E., B. G. Prusty, P. Compston, and G. Rajan. 2019. Automated fibre placement based composite structures: Review on the defects, impacts and inspections techniques. *Composite Structures* 224:110987. doi:10.1016/j.compstruct.2019.110987.

Paris, A. J. 2009. Bending of two-ply cord composite cylindrical shells. *Mechanics Based Design of Structures and Machines* 37 (3):283–98. doi:10.1080/15397730902845057.

Parnas, L., S. Oral, and Ü. Ceyhan 2003. Optimum design of composite structures with curved fiber courses. *Composites Science and Technology* 63 (7):1071–82. doi:10.1016/S0266-3538(02)00312-3.

Qablan, H. A., S. Rabab'ah, B. A. Alfoul, and O. A. Hattamleh. 2020. Semi-empirical buckling analysis of perforated composite panel. *Mechanics Based Design of Structures and Machines* 1–18. doi:10.1080/15397734.2020.1784198.

Qin, H., Z. Liu, Y. Liu, and H. Zhong. 2017. An object-oriented MATLAB toolbox for automotive body conceptual design using distributed parallel optimization. *Advances in Engineering Software* 106:19–32. doi:10.1016/j.advengsoft.2017.01.003.

Ribeiro, P., H. Akhavan, A. Teter, and J. Warmiński. 2014. A review on the mechanical behaviour of curvilinear fibre composite laminated panels. *Journal of Composite Materials* 48 (22):2761–77. doi:10.1177/0021998313502066.

Rouhi, M., H. Ghayoor, S. V. Hoa, and M. Hojjati. 2014. Effect of structural parameters on design of variable-stiffness composite cylinders made by fiber steering. *Composite Structures* 118:472–81. doi:10.1016/j.compstruct.2014.08.021.

Rouhi, M., H. Ghayoor, S. V. Hoa, and M. Hojjati. 2015. Multi-objective design optimization of variable stiffness composite cylinders. *Composites Part B: Engineering* 69:249–55. doi:10.1016/j.compositesb.2014.10.011.

Rouhi, M., H. Ghayoor, S. V. Hoa, and M. Hojjati. 2017. Computational efficiency and accuracy of multi-step design optimization method for variable stiffness composite structures. *Thin-Walled Structures* 113:136–43. doi:10.1016/j.tws.2017.01.019.

Rouhi, M., H. Ghayoor, S. V. Hoa, M. Hojjati, and P. M. Weaver. 2016. Stiffness tailoring of elliptical composite cylinders for axial buckling performance. *Composite Structures* 150:115–23. doi:10.1016/j.compstruct.2016.05.007.

Setoodeh, S., M. M. Abdalla, and Z. Gürdal. 2006. Design of variable–stiffness laminates using lamination parameters. *Composites Part B: Engineering* 37 (4-5):301–9. doi:10.1016/j.compositesb.2005.12.001.

Shahgholian-Ghahfarokhi, D., G. Rahimi, M. Zarei, and H. Salehipour. 2020. Free vibration analyses of composite sandwich cylindrical shells with grid cores: Experimental study and numerical simulation. *Mechanics Based Design of Structures and Machines* 1–20. doi:10.1080/15397734.2020.1725565.

Simon, D. 2008. Biogeography-based optimization. *IEEE Transactions on Evolutionary Computation* 12 (6):702–13. doi:10.1109/TEVC.2008.919004.

Sivanandam, S., and S. Deepa. 2008. *Genetic algorithms. Introduction to genetic algorithms*, 15–37. Berlin-Heidelberg: Springer.

Systèmes, D. 2010. *Abaqus 6.10: Analysis user's manual*. Providence, RI: Dassault Systèmes Simulia Corp.

Tauzowski, P., B. Blachowski, and J. Lógó. 2019. Functor-oriented topology optimization of elasto-plastic structures. *Advances in Engineering Software* 135:102690. doi:10.1016/j.advengsoft.2019.102690.

White, S. C., P. M. Weaver, and K. C. Wu. 2015. Post-buckling analyses of variable-stiffness composite cylinders in axial compression. *Composite Structures* 123:190–203. doi:10.1016/j.compstruct.2014.12.013.

Wu, Z., P. M. Weaver, G. Raju, and B. Chul Kim. 2012. Buckling analysis and optimisation of variable angle tow composite plates. *Thin-Walled Structures* 60:163–72. doi:10.1016/j.tws.2012.07.008.

Zuo, W. 2013. An object-oriented graphics interface design and optimization software for cross-sectional shape of automobile body. *Advances in Engineering Software* 64:1–10. doi:10.1016/j.advengsoft.2013.04.003.

Journal of Materials Chemistry C

ROYAL SOCIETY OF CHEMISTRY

PAPER

View Article Online
View Journal

Check for updates

Cite this: DOI: 10.1039/d0tc00373e

Highly stretchable and sensitive strain sensors based on carbon nanotube–elastomer nanocomposites: the effect of environmental factors on strain sensing performance†

Mohammad Nankali,[a] Norouz Mohammad Nouri,*[a] Mahdi Navidbakhsh,[a] Nima Geran Malek,[a] Mohammad Amin Amindehghan,[a] Abdolsamad Montazeri Shahtoori,[a] Marita Karimi[a] and Morteza Amjadi *[b]

There is an increasing demand for stretchable and wearable strain sensors because of their potential in human motion detection, healthcare monitoring, and soft robotics. Besides their high stretchability and high sensitivity, the durability of wearable strain sensors under variations in atmospheric conditions is another important consideration for their practical use. To date, however, little attention has been given to the impact of environmental factors on the sensing performance of stretchable strain sensors. Herein, we present highly stretchable and sensitive strain sensors based on carbon nanotube–polydimethylsiloxane nanocomposite films and systematically investigate the effect of environmental parameters (*i.e.*, changes in temperature and relative humidity) on their strain sensing characteristics. The strain sensors possess a maximum gauge factor of around 10, stretchability of up to 60%, and response time of 204 ms with good reliability and low hysteresis. Our detailed study on the long-term exposure of strain sensors to controlled temperature and relative humidity levels reveals their significant influence on the strain sensing behavior, particularly temperature fluctuations. As application demonstrations, the stretchable strain sensors are utilized to track the deformation state of an air-inflated balloon and human body movements for healthcare monitoring.

Received 20th January 2020,
Accepted 20th March 2020

DOI: 10.1039/d0tc00373e

rsc.li/materials-c

Published on 20 March 2020. Downloaded by Ontario Tech Library on 4/8/2020 7:22:30 PM.

Introduction

Strain sensors transduce mechanical deformations into electrical signals such as changes in resistance, capacitance, and voltage.[1] In recent years, stretchable and wearable strain sensors have been actively explored owing to their potential applications in personalized healthcare, facial expression recognition, sport performance monitoring, soft robotics, human–machine interfaces, and beyond.[2–4] Among the different types of stretchable strain sensors,[5–7] resistive-type sensors comprise conductive sensing films incorporated into stretchable polymers.[1,8,9] When stretched, geometrical changes together with microstructural interactions in the sensing layer lead to alteration of the electrical resistance as a function of the applied strain. Metallic nanomaterials (*e.g.*, nanowires[10] and nanoparticles[11]), intrinsically conductive polymers (*e.g.*, polypyrrole,[12] polyaniline,[13] and poly(3,4-ethylenedioxythiophene):polystyrene sulfonate (PEDOT:PSS)[14]), and carbonaceous materials (*e.g.*, carbon black,[15,16] carbon nanotubes (CNTs),[17,18] carbon fibers,[19,20] graphite,[21,22] and graphene[23,24]) have been widely investigated for the fabrication of strain-sensitive films. On the other hand, Ecoflex,[25] polydimethylsiloxane (PDMS),[20,24] Dragon Skin,[6] and natural rubber[26] are the most commonly used stretchable supporting materials. Recent advances in materials science and nanotechnology have led to resistive-type strain sensors with tunable sensitivities or gauge factors (GFs) of 1–10[6] and stretchability of over 800% (GF defined as GF = $\Delta R/\varepsilon R_0$, where $\Delta R/R_0$ and ε are the relative change of the resistance and applied strain, respectively).[1,2]

The CNT–elastomer nanocomposites have been extensively studied for wearable strain sensing applications.[1] Wearable strain sensors based on CNT nanocomposites often possess high stretchability due to the robust percolation network of overlapped CNTs, while they suffer from poor GFs.[1] For instance, researchers, including us, have reported strain sensors based on CNT–Ecoflex nanocomposites with ultra-stretchability ($\varepsilon \geq 500\%$) and relatively low GFs of around 1–2.5.[25] Recently, considerable efforts have been devoted to boosting the sensitivity

[a] School of Mechanical Engineering, Iran University of Science and Technology, Tehran, Iran. E-mail: mnouri@iust.ac.ir

[b] Institute of Mechanical, Process and Energy Engineering, Heriot-Watt University, Edinburgh, UK. E-mail: m.amjadi@hw.ac.uk

† Electronic supplementary information (ESI) available. See DOI: 10.1039/d0tc00373e

Published on 20 March 2020. Downloaded by Ontario Tech Library on 4/8/2020 7:22:30 PM.

of CNT nanocomposite-based stretchable strain sensors through microstructural design and novel material formulation.[7,27–29] Pu *et al.* have presented high-performance strain sensors (GF ∼ 248 and stretchability of 300%) by developing 2D end-to-end contact networks of CNTs in an ethylene-α-octene block copolymer matrix.[7] Zhang *et al.* reported a highly sensitive strain sensor with tunable GFs of 3–18 and a broad sensing range (from 1% to 500%) based on vertically grown CNTs wrapped by Ecoflex.[27] Gao *et al.* developed high-performance strain sensors using fragmentized CNT–PDMS nanocomposites with GFs of over 200 and stretchability of up to 80%.[28] In another example, strain sensors based on network cracks in CNT film–PDMS nanocomposites exhibited a high sensitivity of 87 coupled with a wide sensing range up to 100%.[29] Zhang *et al.* enhanced the dispersion of CNTs in waterborne polyurethane to improve the sensing performance of stretchable strain sensors.[30]

The strain sensing performance of wearable strain sensors is vulnerable to atmospheric conditions such as variations in temperature and relative humidity (RH). To date, several strategies have been pursued to eliminate these unwanted interferences. For example, piezoresistive films have been sandwiched between two layers of elastomers to protect them from direct exposure to the environment.[25,31,32] Superhydrophobic coatings have been utilized to prevent the penetration of water molecules into the strain sensing films.[33–36] High-temperature resistant polymeric matrices were utilized to increase the robustness of sensors against harsh temperature environments.[37] Most recently, we have proposed a temperature self-compensated hybrid film to decouple the effect of the temperature change on the sensing behavior of strain sensors.[38] Despite these efforts in recent years, the major research focus has so far been directed toward the sensitivity or stretchability enhancement of stretchable strain sensors.[1,27,39,40] In fact, there is still little in-depth study on the prolonged impact of the environment on the dynamic sensing properties of wearable strain sensors.[41,42]

Herein, we report highly stretchable and sensitive strain sensors made of CNT–PDMS nanocomposites for wearable and soft robotic applications. The fabrication process involves the vacuum-assisted formation of thin CNT networks on nanofiltration membranes, followed by their transfer to the top surface of the PDMS film. The strain sensors possess GFs of 6–10 and stretchability of up to 60% with good durability and low hysteresis behavior under both small and large strains. The key contribution of this work is that we systematically tested the dynamic sensing performance of strain sensors under controlled environmental conditions by varying the temperature and RH levels. Finally, we demonstrate the potential applications of our strain sensors in human body motion detection and deformation monitoring of an air-inflated balloon.

Results and discussion

Fig. 1a schematically illustrates the fabrication process of the CNT–PDMS nanocomposite based stretchable strain sensors (see Experimental section for details). Briefly, a CNT thin film was first formed on a nanofiltration membrane by drop-casting the CNT suspension and a subsequent vacuuming process.[43] The liquid PDMS was next coated over the CNT film and cured at 70 °C for 2 hours. The PDMS elastomer with the embedded CNT film was then peeled off from the membrane. Finally, the

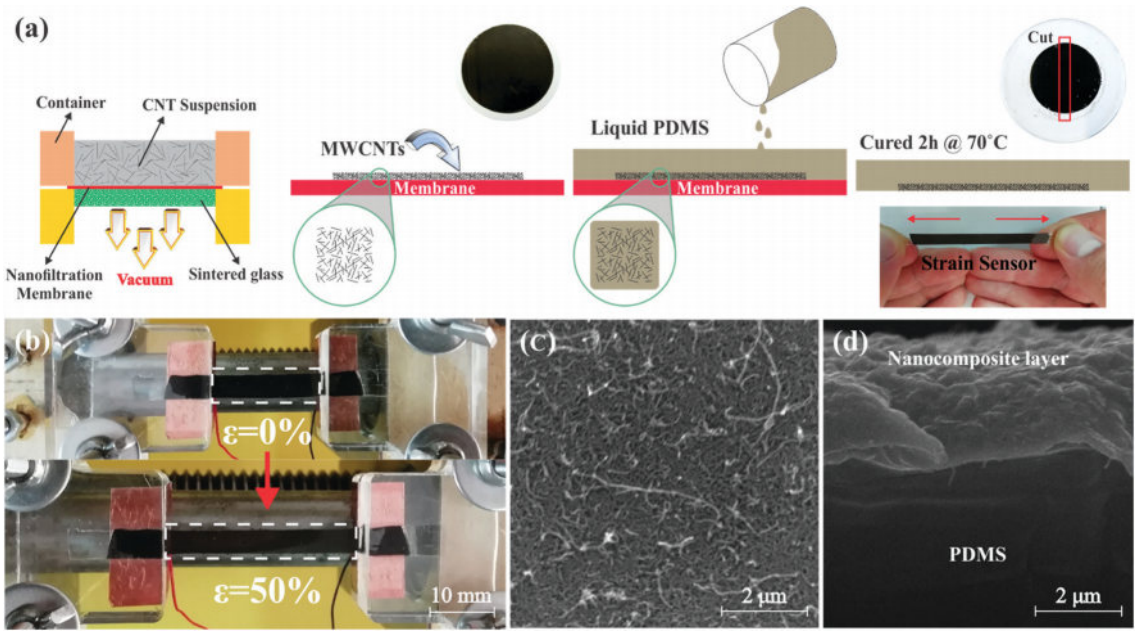

Fig. 1 (a) Fabrication process of the CNT–PDMS nanocomposite strain sensors. (b) Photographs of a strain sensor at the initial length and under 50% strain. (c) SEM image of the CNT thin film deposited on the nanofiltration membrane. (d) Cross-sectional SEM image of a strain sensor showing complete penetration of the liquid PDMS into the porous CNT network.

 This journal is © The Royal Society of Chemistry 2020

Published on 20 March 2020. Downloaded by Ontario Tech Library on 4/8/2020 7:22:30 PM.

nanocomposite film was trimmed into rectangle-shaped strain sensors with length × width dimensions of 35 × 6 mm^2. The entire fabrication process of the strain sensors is simple, scalable, and cost-effective. The resultant strain sensors are highly stretchable and can be directly mounted onto the human skin for wearable and skin-mountable sensing applications (Fig. 1a and b).

Fig. 1c shows a scanning electron microscopy (SEM) image of the CNT thin film-coated nanofiltration membrane, revealing that all CNTs are uniformly distributed in the form of a 3D porous microstructure, and a percolation network is effectively established between the self-assembled CNTs. The homogeneity of the CNT film is guaranteed during the vacuum filtration process since the local permeation rate of the membrane decreases with the accumulation of CNTs; thus, the deposition rate is tuned automatically (Fig. S1, ESI†). Additionally, the electrical conductivity of the processed film is maximized under vacuum because CNTs tend to lie down and adhere well to the filtration membrane, which in turn strengthens the linkage of overlapped CNTs and thereby reduces the contact resistance among them. Fig. 1d depicts the cross-sectional SEM image of the CNT-embedded PDMS film, showing that the low-viscous liquid PDMS evenly filled the gaps among CNTs and formed a robust nanocomposite layer (thickness ∼ 1.5 μm) on the top surface of the PDMS film. Therefore, the high porosity of the CNT films is crucial for their complete transfer to the PDMS elastomer.

We initially investigated the mechanical properties of the CNT–PDMS nanocomposite strain sensors under both static and dynamic loading conditions. Fig. 2a shows the quasi-static tensile testing data for PDMS specimens cured at 30, 70, 100, and 150 °C. The elastic modulus and ultimate stress of PDMS increased as the curing temperature rose, while its linear stress–strain relationship deteriorated. The sample cured at 30 °C (ambient temperature) exhibited the greatest linear behavior for strains up to 50%, though its curing time was extremely long (around 48 hours). On the other hand, the linear stress–strain region decreased to 30% strain for the PDMS film cured at 150 °C for 10 min. We found that samples cured at 70 °C for 2 hours offer acceptable curing duration and linearity for around 40% strain. Hence, hereafter, we maintained this curing condition for the fabrication of strain sensors. The nonlinear behavior of PDMS samples cured at higher temperatures can be explained by the degree of crosslinking. The cured PDMS elastomer consists of many wrinkled and wavy chains of siloxane oligomer that are chemically bonded to each other by a network of siloxane cross-linker.[44] When stretched, the polymeric chains start to align themselves in the direction of stretching. Above a specific stress, cross-linkers prevent polymeric chains from straightening themselves anymore, thus inducing nonlinear mechanical properties. The PDMS samples cured at higher temperatures have a higher density of cross-linking, which impedes the effective alignment of polymeric chains, leading to the nonlinear behavior at high strain levels.[45] It is important to broaden the linear stress–strain range of sensing materials as it may influence the linear response of strain sensors.[46]

To further study the dynamic mechanical properties of the strain sensor (*i.e.*, a PDMS layer with the embedded CNT film) and pure PDMS film, we calculated their loss tangent as follows:[47]

$$\tan\delta = \frac{E''}{E'} \tag{1}$$

where E', E'', and $\tan\delta$ are storage modulus, loss modulus, and loss tangent (or damping factor) of the samples, respectively. The loss tangent is typically used to determine the elastic and viscoelastic behavior of materials and indicates how efficiently materials dissipate energy due to molecular rearrangements and internal friction.[48] An elastomer exhibits more viscoelasticity when its $\tan\delta$ is higher. The measured $\tan\delta$ values of the sensor and pure PDMS for temperatures ranging from −20 to 100 °C are compared in Fig. 2b. The loss tangent continuously decreased for both samples when the temperature increased. For the pure PDMS film, free volume increases for temperatures higher than the glass transition temperature, providing more space

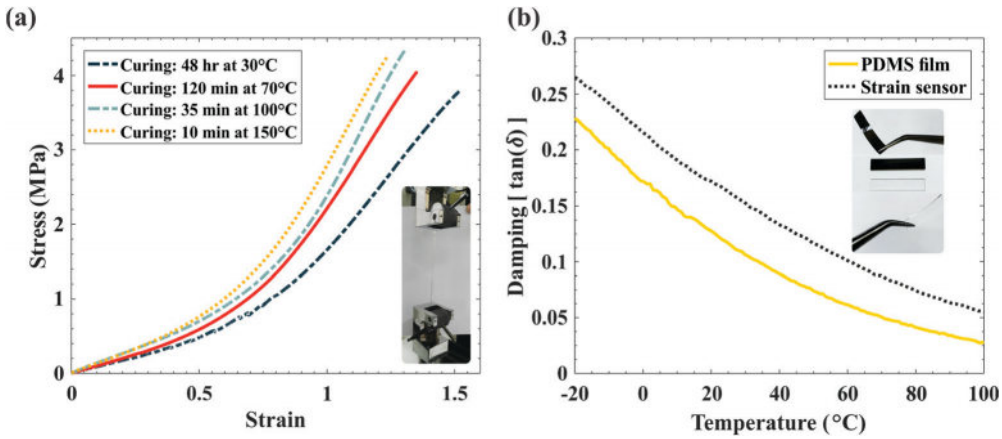

Fig. 2 (a) Stress–strain curves of PDMS strips cured at different temperatures; inset, photograph of a PDMS specimen under stretching. (b) Loss tangent of the pure PDMS film and strain sensor *versus* temperature; inset, photographs of the pure PDMS and strain sensor samples.

Published on 20 March 2020. Downloaded by Ontario Tech Library on 4/8/2020 7:22:30 PM.

for elastomeric chains to move and thereby continuously decreasing the damping factor (see Fig. S2 and S3, ESI†). According to Fig. 2b, the tan δ value for the strain sensor always remained higher than that of the pure PDMS sample within the tested temperature range, demonstrating its more viscoelastic behavior. This can be explained by the interaction between CNTs and PDMS matrix upon dynamic loading.[47–49] In areas with agglomerated CNTs or CNT bundles, the liquid PDMS may partially cover the CNTs, leading to a weak interfacial force between CNTs and PDMS matrix. When the strain sensor is subjected to an external load, the mismatch in the elastic properties of CNTs and PDMS matrix generates shear stresses between the CNT walls and the surrounding matrix, resulting in the sliding and debonding of several CNTs from the matrix.[50] The energy dissipated during this slippage event further augments the damping factor of the strain sensor sample. Additionally, unlike conventional fiber-reinforced composites, CNT-based polymer composites have fillers with a large surface area, which is on the same scale as the polymer molecules. Therefore, the polymer molecule segments may interact strongly with the CNTs and consume significant energy. These strong molecule interactions between CNTs and polymer molecules could be another reason for the higher values of tan δ observed for the sensor sample.[50–52] A similar trend has been observed by Wu *et al.* in the CNT–PDMS nanocomposite containing 2 wt% CNTs.[53] In contrast, the storage modulus of the strain sensor remained higher than that of the pure PDMS sample, although the nanocomposite layer is very thin (thickness $\sim$ 1.5 μm) compared to the overall thickness of the sensor (thickness $\sim$ 500 μm) (Fig. S2a, ESI†). This implies that there is an effective load transfer between CNT fillers and PDMS matrix. Therefore, we believe that the interfacial force between CNTs and PDMS is very local. The interfacial adhesion of CNTs fully infiltrated by the liquid PDMS is strong due to the mechanical interlocking effect and van der Waals forces.[54] These types of CNTs greatly contribute to load sharing and enhance the stiffness of the nanocomposite material. On the other hand, the interfacial adhesion between PDMS and partially infiltrated CNTs is poor, leading to an increase in the damping factor.[50]

In order to assess the strain sensing behavior of the CNT–PDMS nanocomposite strain sensors, they were clamped to a motorized moving stage. The sensors were then subjected to various cyclic loading conditions while their resistance change was measured simultaneously. Fig. 3a illustrates a typical curve of the relative change in resistance against the applied strain for a strain sensor in both loading and unloading cycles. The strain sensor linearly ($R^2 > 0.98$) responded to strains up to 15% with the corresponding GF of around 10. The response of the sensor became nonlinear for higher strains, and the GF slowly declined to 7.5 at 40% strain. As shown in the figure, the resistance of the sensor was partially recovered after releasing it from 40%. This can be explained by the sliding of some CNTs upon stretching due to their poor interaction with the PDMS matrix, leading to the permanent disconnection of several overlapped CNTs, which in turn irreversibly increases the electrical resistance. It is noted that this behavior was observed only in the first few stretching–releasing cycles. The response of the sensor became highly reversible afterward. In addition to the sliding effect, possible plastic deformation of the PDMS matrix at high strains, and sliding of the strain sensors from fixing jigs are other reasons for their irreversible response in the initial cycles.[25]

The change of the electrical conductance within the percolation network is the main reason for the resistance–strain dependency of the CNT–PDMS nanocomposites.[55,56] Furthermore, CNTs are separated apart upon stretching, leading to the increase of the tunneling resistance between adjacent CNTs and consequently reduction of the electrical conductance.[25] We calculated the conductivity of the nanocomposites as a function of the applied strain using percolation theory and found a good agreement between our experimental and theoretical data (see "Percolation theory" section and Fig. S4 in the ESI† for details).[57,58] Compared to previously reported CNT nanocomposite strain sensors,[25,59] the sensitivity improvement of our sensors could be due to the process of vacuum filtration, providing a larger number of adjacent CNTs for the tunneling effect under stretching. As shown in Fig. 3a, the hysteresis of the sensor was almost negligible for strains smaller than 20%, while it became apparent for larger values. We further derived the hysteresis loops of a strain sensor at 15% strain under different strain rates from 4.5 to 18% s^{-1} (Fig. 3b). The maximum values of $\Delta R/R_0$ remained nearly identical regardless of the strain rate. However, the hysteresis of the sensor gradually increased as the strain rate elevated. The hysteresis behavior of strain sensors is attributed to the strain rate dependent viscoelastic nature of PDMS elastomer and the damping effect of the CNT–PDMS nanocomposite films upon dynamic loading–unloading.[60,61]

Fig. 3c and d show the electromechanical response of a strain sensor to repeated stretching–releasing cycles. The strain sensor retained its sensing characteristics under both small ($\sim$2%) and large ($\sim$60%) deformations in a reversible manner. Notably, the strain sensor could detect 100 μm elongation corresponding to only 0.5% strain with high sensitivity (Fig. S5, ESI†). The strain sensors were able to detect even smaller strains by eliminating their sliding from clamps of the motorized moving stage. We carried out additional tests to evaluate the long-term durability and response time of the strain sensors. The strain sensor exhibited good stability and reliability when subjected to over 1000 cycles of repeated loading–unloading (from 0% to 15%) with a constant strain rate of 14% s^{-1} (Fig. 3e). We could observe a small downward drift in the value of $\Delta R/R_0$ ($\sim$15%) for the first 30 cycles, possibly due to the sliding of the strain sensor from the clamps and plastic deformation of the PDMS matrix.[31]

To calculate the response time, a strain sensor was subjected to a ramp strain from 0% to 15% with a high strain rate of 44% s^{-1} (see inset of Fig. 3f). The resistance change of the sensor indicates that the dynamic response of the sensor could be assumed to be a first-order dynamic system. The error fraction function of a first-order dynamic system is expressed as:

$$\Gamma(t) = \frac{R(t) - R_{\max}}{R_0 - R_{\max}} = e^{-t/\tau} \quad (2)$$

 This journal is © The Royal Society of Chemistry 2020

Published on 20 March 2020. Downloaded by Ontario Tech Library on 4/8/2020 7:22:30 PM.

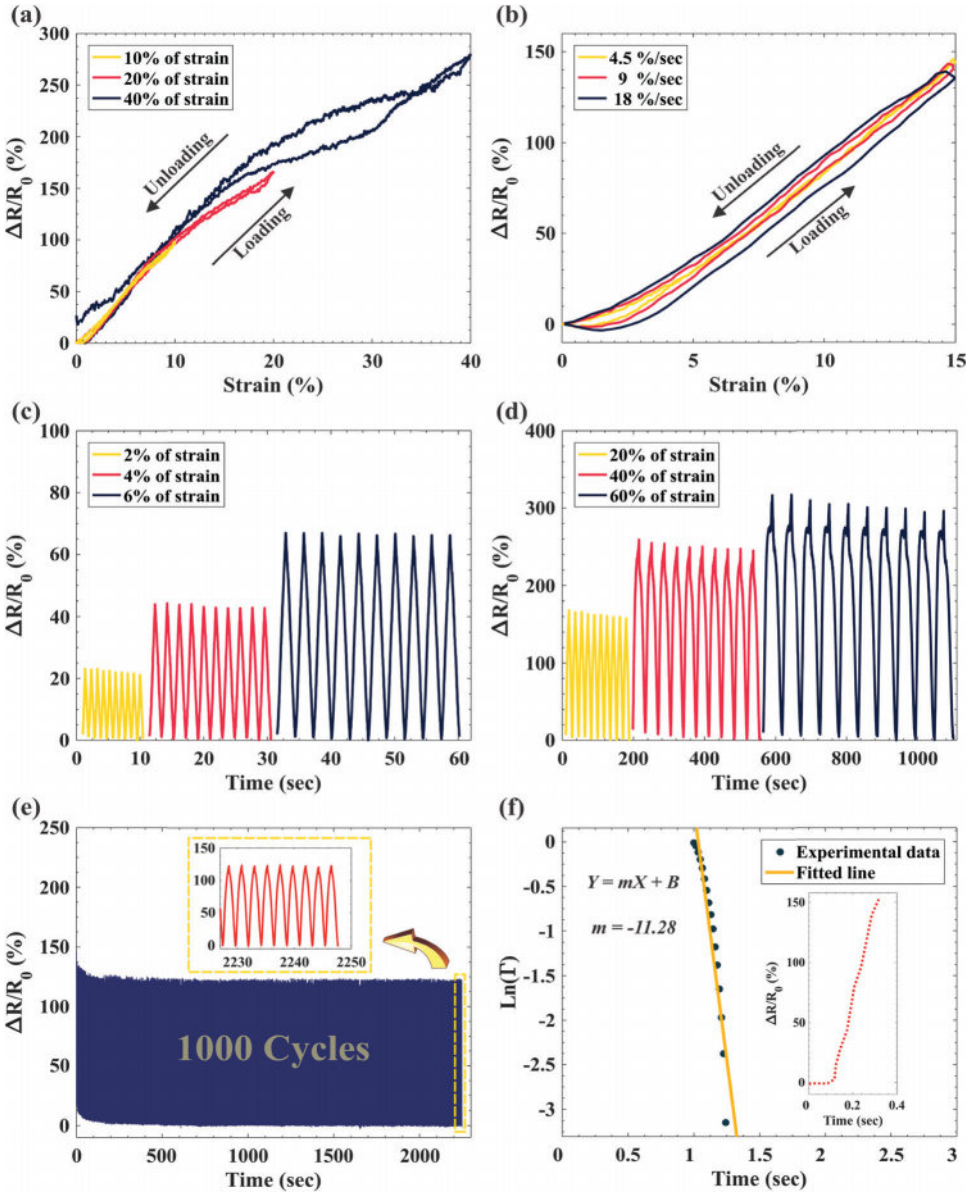

Fig. 3 Strain sensing performance of the CNT–PDMS nanocomposite-based strain sensors. (a) Relative change of the resistance *versus* the applied strain upon loading and unloading. (b) Hysteresis loop of a strain sensor at different strain rates. (c and d) Dynamic response of a strain sensor to small and large stretching cycles, respectively. (e) Durability test of a strain sensor under 1000 stretching–releasing cycles (from 0 to 15%). (f) Error fraction function of a strain sensor subjected to a ramp strain profile; inset, the electromechanical response of the strain sensor to the ramp strain.

where $\Gamma(t)$ is the error fraction and τ is the time constant of the system. $R(t)$ and R_{max} are the time-dependent and maximum resistance values during the ramp input, respectively. The equation is equivalent to the transformation $\ln \Gamma = -(1/\tau)t$, which is of the linear form $Y = mX + B$ (where $Y = \ln \Gamma$, $m = -(1/\tau)$, $X = t$, and $B = 0$) (see "System time constant" in the ESI† for details). By linear curve fitting of $\ln \Gamma$ *versus* time in Fig. 3f, the time constant of the strain sensor is calculated to be 0.088. Therefore, the 90% time constant ($\tau_{90\%}$) or response time of the sensor is ~204 ms, in good agreement with that of our strain sensors based on silver nanowire–PDMS nanocomposites (~200 ms).[31]

In practical applications, wearable sensors are constantly subjected to daily changes in atmospheric conditions. Thus, it is crucial to evaluate the prolonged influence of the environment on the dynamic sensing performance of wearable strain sensors. To address this, we built a custom-made test setup capable of synchronized monitoring of the applied dynamic strain, resistance change, surrounding temperature, and RH level (Fig. S6, ESI†). The response of the sensors was measured in two different scenarios: steady-state, where the resistance of the strain sensors was recorded under constant and stable levels of temperature and RH; a transient mode, in which the dynamic sensing performance was monitored upon continuously increasing values of temperature and RH. The latter one resembles the natural condition where both temperature and RH change over time. Fig. 4a shows the response of a sensor to

Published on 20 March 2020. Downloaded by Ontario Tech Library on 4/8/2020 7:22:30 PM.

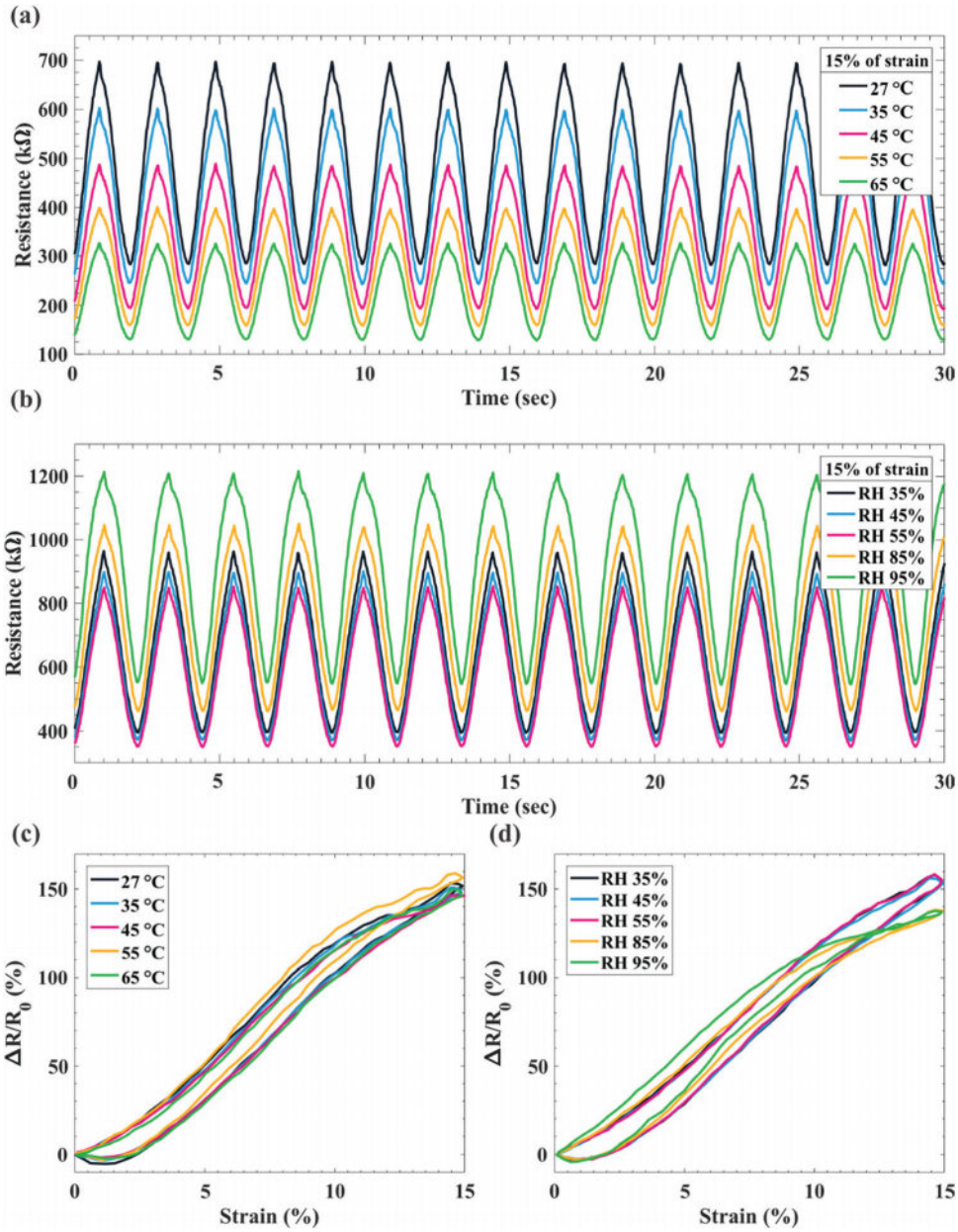

Fig. 4 Steady-state response of a strain sensor to different levels of (a) temperature and (b) RH. Hysteresis loops of the strain sensor at different levels of (c) temperature and (d) RH.

repeated loading–unloading cycles (from 0 to 15%) at a steady temperature. The base resistance of the sensor decreased by 43% (from 470 to 270 kΩ) when the temperature was incrementally increased from 27 to 65 °C, showing the negative thermoresistivity of the nanocomposite (see Fig. S7a, ESI†). The overall resistance of the nanocomposite depends on the summation of intrinsic resistance of individual CNTs, contact resistance of overlapped CNTs, and tunneling effect between adjacent CNTs. The intrinsic resistance of CNTs is known to decrease with increasing temperature due to various hopping mechanisms.[38] On the other hand, the elevated temperature alters the potential barrier height, leading to a decrease of tunneling resistance. These two mechanisms lead to a decrease in the electrical resistance of the CNT nanocomposites.[62] In contrast, the large thermal expansion of the PDMS matrix induces strain on the nanocomposites with increasing temperature and thus leads to an increase of the electrical resistance. Based on our experiments, the changes in the intrinsic resistance of CNTs and tunneling resistance dominate the overall resistance of the nanocomposite and cancel the effect of the thermal expansion. Although the base resistance shifted dramatically, the amplitude of $\Delta R/R_0$ stayed constant regardless of the temperature variations because ΔR values also proportionally declined at elevated temperatures (see Fig. 4c).

The relative resistance change of a sensor exposed to different levels of RH is depicted in Fig. 4b. The base resistance of the

 This journal is © The Royal Society of Chemistry 2020

Published on 20 March 2020. Downloaded by Ontario Tech Library on 4/8/2020 7:22:30 PM.

sensor gently dropped when RH increased from 35 to 55%, and it conversely increased for RH values higher than 55% (Fig. S7b, ESI†). In the first regime (RH ∼ 35–55%), the water molecules are adsorbed on the surface of the nanocomposite layer, producing hydronium ions when an electrostatic field is applied to the sensor.[63] The hydronium ions act as charge carriers and enhance the electron transfer between electrodes, thus decreasing the resistance between the two electrodes. For RH over 55%, water molecules start to penetrate the nanocomposite layer, causing the CNT–PDMS nanocomposites to swell.[63] This swelling affects the CNT junctions by inducing strain on the nanocomposites, which increases the resistance of the sensors. As shown in Fig. 4d, the strain sensing performance of the sensor was mostly stable up to 55% RH, while both sensitivity and linearity were slightly destroyed at higher RH levels. We also observed an irreversible and permanent effect of RH on the base resistance and strain sensing behavior of the strain sensor after humidity experiments (Fig. S7c, ESI†).

We next examined the dynamic sensing properties of the strain sensors under transient environmental conditions. Fig. 5a illustrates the response of a sensor to the long-term loading cycles when the temperature was gradually increased from ambient temperature (∼26.5 °C) to 65 °C with a constant rate of 2.6 °C min^{-1}. The $\Delta R/R_0$ value of the strain sensor was continuously narrowed by the temperature rise. We further derived the base resistance of the sensor in each cycle and normalized it against the initial resistance value. As depicted in Fig. 5c, the normalized base resistance of the sensor was

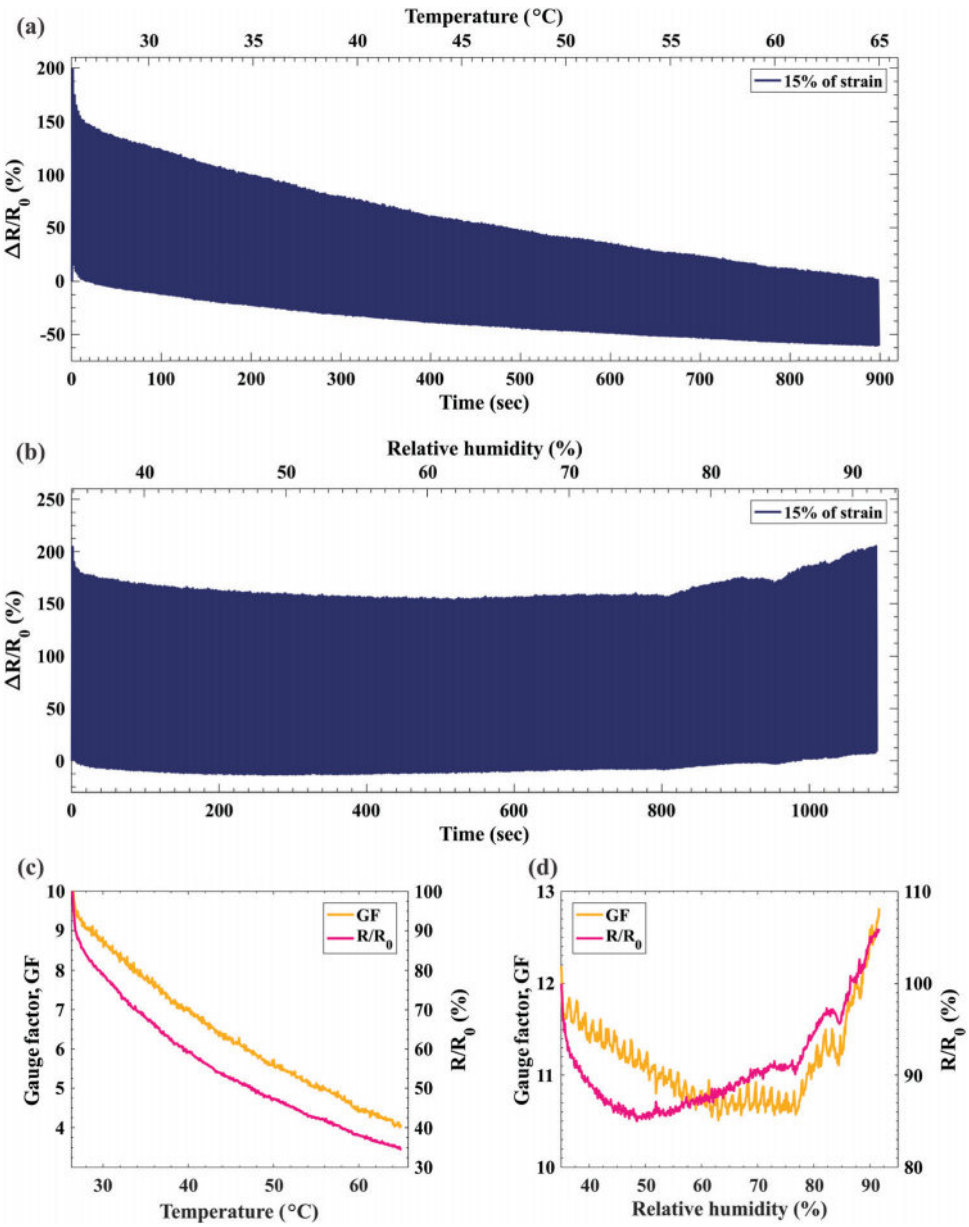

Fig. 5 Response of a strain sensor to transient (a) temperature and (b) RH changes. (c and d) Variations of GF and normalized base resistance of the strain sensor due to (c) temperature and (d) RH changes.

Published on 20 March 2020. Downloaded by Ontario Tech Library on 4/8/2020 7:22:30 PM.

reduced by 65% when the temperature reached 65 °C. As a result, the GF of the sensor declined from 10 to about 4, showing a tangible impact of the temperature change on the strain sensing performance of the CNT–PDMS nanocomposite films (Fig. 5c).

Fig. 5b depicts the response of a strain sensor to the transient humidity changes from 35% to 92% RH. Compared to the temperature change, the RH variations are less destructive toward the strain sensing behavior. Furthermore, the peak value of $\Delta R/R_0$ fluctuated between 150 and 210%. The GF and normalized base resistance of the sensor upon RH changes are presented in Fig. 5d. The base resistance initially decreased upon RH increase and then gradually increased for RH over 50%. Similarly, the GF declined from 12 to 10.6 when the RH reached 77% and then shifted to 12.8 at 92% RH. Unlike the steady-state experiments conducted by us and others,[25,27,38] our results reveal that the effect of the transient changes of the environmental parameters on the strain sensing performance of stretchable strain sensors can be significant. Based on our observation, in practical applications, it is inadequate to simply monitor mechanical deformations by measuring the resistance change across wearable strain sensors because environmental parameters can alter their output signal in a complicated manner. Therefore, new material compositions and advanced packaging strategies are needed to eliminate these unwanted environmental effects, which are out of the main focus of the present work.

As our electromechanical experiments verified, the CNT–PDMS nanocomposite strain sensors offer high stretchability and sensitivity, making them suitable for shape-change monitoring of soft robots and full-range human motion detection ranging from large bending movements of joints to minute deformation during respiration. As an example of the soft robotic application, we implemented a strain sensor on an air-inflated balloon to monitor its body deformation. The balloon was pressurized in a stepwise manner while the output signal of the sensor was recorded at the same time (see Movie S1, ESI†). As illustrated in Fig. 6a, the resistance of the sensor increased in each step with a distinguished signal shift, highlighting that the sensor experienced tensile strain. In contrast, the resistance of the sensor decreased when the applied strain was released by depressurizing the balloon. Therefore, the integrated sensor could successfully monitor the inflation state with high sensitivity. The sensory information could be utilized for the feedback control of soft robots and sensory skin, enabling soft robots to sense their environment and interactive objects.[64]

To illustrate the applicability of our strain sensors as wearable electronic devices for human activity recognition, a sensor

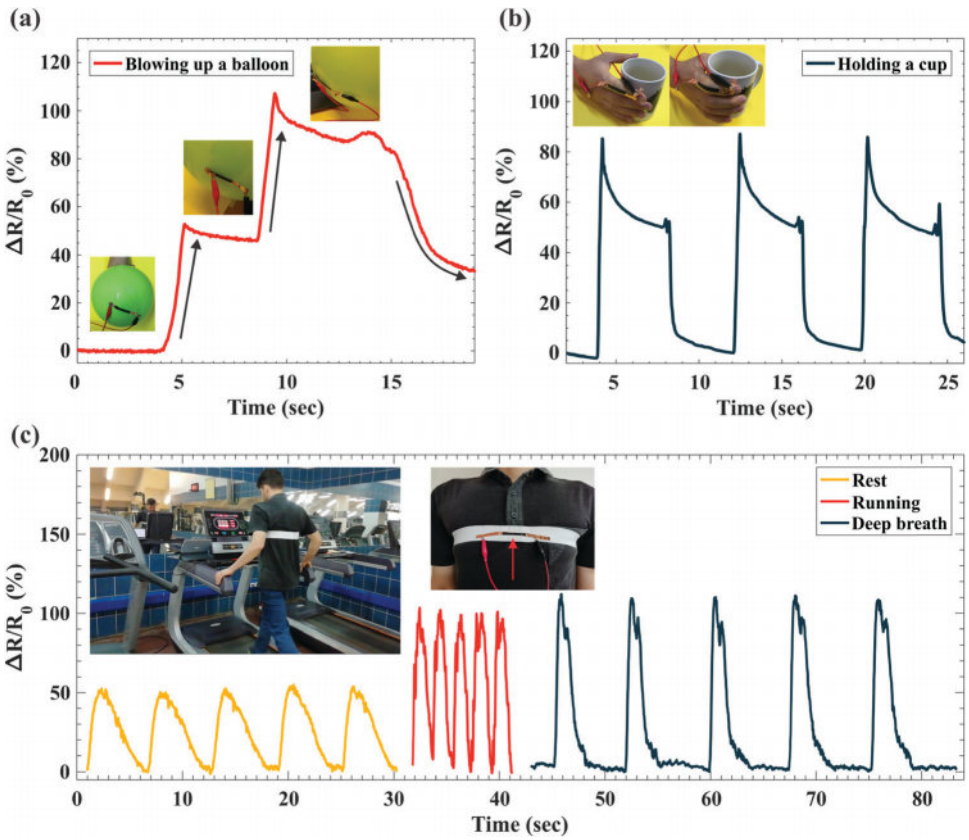

Fig. 6 Application demonstration of CNT–PDMS nanocomposite strain sensors. (a) Response of a sensor to the deformation of an air-inflated balloon; inset, photographs of the strain sensor at each inflation stage. (b) Response of a strain sensor attached to the index finger when holding–releasing a cup; inset, photographs of the sensor attached to the finger. (c) Respiration monitoring by wearing the smart belt at the chest area; insets, photographs of the smart belt worn by a volunteer.

 This journal is © The Royal Society of Chemistry 2020

Published on 20 March 2020. Downloaded by Ontario Tech Library on 4/8/2020 7:22:30 PM.

was mounted onto the index finger by using medical tape. We then measured the resistance change of the sensor under different conditions, including natural bending–straightening, clicking a mouse, and holding a cup (see Movie S2 (ESI†), Fig. 6b, and Fig. S8, ESI†). The strain sensor responded to all strain conditions with high sensitivity, fast response, and good dynamic performance. As a healthcare monitoring application, we constructed a smart belt by attaching a strain sensor to a stretchable bandage (see inset of Fig. 6c). Fig. 6c shows the response of the sensor when a volunteer wore the belt in the chest area for respiration monitoring. Peaks and valleys represent the loading and unloading of the strain sensor induced by the extension and shrinkage of the chest area during respiration, respectively. The strain sensor could distinguish the breathing pattern and frequency in rest, running, and deep respiration modes with a considerable signal difference (see Movie S3, ESI†). As expected, the signal of the strain sensor increased during deep breathing since larger strains were applied to the sensor. Real-time detection of abnormal respiration rate and temporal patterns can help early diagnosis of several diseases such as asthma, heart failure, embolism, and so forth.[65] These experiments highlight the potential of the CNT–PDMS nanocomposite strain sensors for wearable and soft robotic applications. It should be noted that we conducted these experiments under ambient conditions, assuming that the environmental parameters remained stable for the measurement periods. For prolonged healthcare monitoring, accurate strain measurements would be challenging, given noticeable changes in environmental conditions.

The key advancement of this work is that the dynamic strain sensing characteristics of the CNTs–PDMS nanocomposite-based stretchable strain sensors have been systematically investigated under various environmental conditions. We found that the impact of transient changes in temperature and RH on the strain sensing behavior of sensors is substantial, making accurate and noise-free strain monitoring more complex in practical applications. As our future plan, we aim to investigate different methodologies to fully decouple the effect of environmental variations. For instance, the effect of the temperature changes can be compensated by the hybridization of semiconducting CNTs with metallic nanomaterials like graphite particles with the optimal mass ratio.[38] Zhang *et al.* have reported that sandwiching CNT–Ecoflex nanocomposite strain sensors between two layers of Ecoflex can greatly enhance their endurance upon RH variations.[27] In another work, a temperature self-compensated pressure sensor made of dimethylsulfoxide-treated PEDO:PSS aerogel could precisely read the pressure level at different temperatures (20–45 °C).[66] In terms of the strain sensing performance of our strain sensors, the sensitivity can be further improved by generating controllable microcracks in the CNT–PDMS nanocomposite layers or creating fragmentized CNT–PDMS nanocomposite films.[28,64,67] On the other hand, the stretchability of sensors can be greatly extended by replacing the PDMS matrix with a more stretchable material like Ecoflex.[25]

Conclusion

In summary, we presented a simple, cost-effective, and scalable approach for the fabrication of highly stretchable and sensitive strain sensors based on CNT–elastomer nanocomposites. The strain sensors offer a stable, reliable, low hysteresis, and fast response to both small and large strains. The electromechanical response of the strain sensors to long-term loading cycles under controlled temperature and RH profiles revealed the significant dependence of strain sensing performance on environmental variations, particularly temperature fluctuations. Therefore, further research activities are required to explore the possible elimination of these effects through advanced packaging or novel material formulation. As application demonstrations, the stretchable strain sensors were utilized to track the deformation state of an air-inflated balloon, as well as human body movements for healthcare monitoring. We anticipate that our findings will provide new insights into the design of stretchable and wearable strain sensors for wearable applications.

Experimental section

Materials

Sylgard 184 (Dow Corning, USA) was used as the PDMS elastomer for the fabrication of strain sensors. Multiwall CNTs with average diameter × length dimensions of 50 nm × 5 μm were purchased from Sigma-Aldrich. Isopropyl alcohol (IPA) from Sigma-Aldrich was used to disperse CNTs. Hydrophilic polyethersulfone (PES) nanofiltration membrane with a pore size of 220 nm was purchased from Membrane Solutions. A self-adhesive film from HARTMANN Hydrofilm was used as an intermediate adhesive layer to attach strain sensors to the skin and balloon. For all experiments involving human subjects, informed consent was obtained.

Preparation of the CNT suspension

The CNT suspension was prepared by adding CNTs to IPA with a concentration of 0.1 mg ml^{-1}. In order to obtain a well-dispersed suspension, the CNT solution was first stirred for 15 minutes. Then, the mixture was sonicated by an ultrasonic disperser (Bandelin HD 3200) for 30 minutes and subsequently centrifuged at 4000 rpm for 15 minutes (Universal-320 centrifuge machine) to sediment large agglomerated CNT bundles. The resultant CNT suspension was stored for further experiments.

Fabrication of strain sensors

4 ml of the CNT suspension was drop-cast into a filtration funnel equipped with a PES membrane with the surface area of 1385 mm^2. The funnel was kept under vacuum to create a differential pressure across the membrane, accelerating the filtration of the CNT solution. After vacuum filtration, an ultrathin film of randomly oriented CNTs was formed on the membrane. In the next step, the PDMS prepolymer and curing agent were mixed at a 10 : 1 weight ratio and then degassed for 1 hour to remove micro-bubbles. Afterward, about 1 g of the mixture was cast on the CNT-coated membrane and cured at

Published on 20 March 2020. Downloaded by Ontario Tech Library on 4/8/2020 7:22:30 PM.

70 °C for 2 hours to achieve a 500 μm thick PDMS layer on the membrane. The PDMS film with the embedded CNT network was peeled off from the membrane. The sample was finally cut into rectangular shapes with dimensions of 35 mm × 6 mm to complete the fabrication of the strain sensors. A copper adhesive film was attached to the two ends of the film to establish the electrical connection.

Material characterization

The SEM images and EDS data were obtained using a scanning electron microscope (TESCAN VEGA II). Quasi-static tensile tests were conducted on rectangle-shaped samples with dimensions of 100 × 4 mm^2 using a universal tensile tester (SANTAM STM-50) under a constant strain rate of 0.5 mm s^{-1} according to the ASTM-D412a standard for vulcanized rubber and thermoplastic elastomers. The dynamic-mechanical thermal analysis (DMTA) was performed using a Mettler-Toledo thermal analyzer (DMA1-Star^e system, Switzerland) in tension mode. Rectangle-shaped samples with dimensions of 30 × 5 mm^2 were subjected to 50 μm sinusoidal displacement with a frequency of 1 Hz at different temperatures ranging from −150 to 170 °C.

Electromechanical tests

The strain sensing performance of the strain sensors was tested by clamping them on a custom-made motorized moving stage. Their electrical resistance was simultaneously measured by a custom-made data acquisition unit.

Environmental tests

Strain sensors were subjected to different temperatures and RH levels while their strain sensing behavior was evaluated. For temperature experiments, the motorized moving stage with mounted sensors was placed inside a temperature programmable oven (ParsAzma KM55 with slight modifications). A modified insulated styrofoam cooler box (770 × 470 × 480 mm^3) with air circulation was used as a closed chamber for humidity tests. A cold mist humidifier with flow control (FreshLife GO-2011F) was connected to the chamber to adjust the RH level. An integrated digital temperature and humidity sensor (SHT31 from SENSIRION) was used to record the data for temperature and RH (see Fig. S6 for details, ESI†). For each steady temperature experiment, strain sensors were kept in the oven for 20 min to ensure that their surrounding temperature was fully stabilized. The same settings were applied for the humidity tests.

Conflicts of interest

There are no conflicts to declare.

Acknowledgements

This work was partially supported by the Iran Nanotechnology Initiative Council (INIC). Additionally, the authors would like to thank the members of the Soft Sensors and Actuators Laboratory (SSA Lab) of Iran University of Science and Technology and Iran Polymer and Petrochemical Institute.

References

1 M. Amjadi, K.-U. Kyung, I. Park and M. Sitti, *Adv. Funct. Mater.*, 2016, **26**, 1678–1698.
2 T. Q. Trung and N.-E. Lee, *Adv. Mater.*, 2016, **28**, 4338–4372.
3 H.-R. Lim, H. S. Kim, R. Qazi, Y.-T. Kwon, J.-W. Jeong and W.-H. Yeo, *Adv. Mater.*, 2019, 1901924.
4 W. A. D. M. Jayathilaka, K. Qi, Y. Qin, A. Chinnappan, W. Serrano-García, C. Baskar, H. Wang, J. He, S. Cui, S. W. Thomas and S. Ramakrishna, *Adv. Mater.*, 2019, **31**, 1805921.
5 J. M. Wu, C.-Y. Chen, Y. Zhang, K.-H. Chen, Y. Yang, Y. Hu, J.-H. He and Z. L. Wang, *ACS Nano*, 2012, **6**, 4369–4374.
6 L. Cai, L. Song, P. Luan, Q. Zhang, N. Zhang, Q. Gao, D. Zhao, X. Zhang, M. Tu, F. Yang, W. Zhou, Q. Fan, J. Luo, W. Zhou, P. M. Ajayan and S. Xie, *Sci. Rep.*, 2013, **3**, 3048.
7 J.-H. Pu, X.-J. Zha, M. Zhao, S. Li, R.-Y. Bao, Z.-Y. Liu, B.-H. Xie, M.-B. Yang, Z. Guo and W. Yang, *Nanoscale*, 2018, **10**, 2191–2198.
8 J. Chen, Q. Yu, X. Cui, M. Dong, J. Zhang, C. Wang, J. Fan, Y. Zhu and Z. Guo, *J. Mater. Chem. C*, 2019, **7**, 11710–11730.
9 H. Liu, Q. Li, S. Zhang, R. Yin, X. Liu, Y. He, K. Dai, C. Shan, J. Guo, C. Liu, C. Shen, X. Wang, N. Wang, Z. Wang, R. Wei and Z. Guo, *J. Mater. Chem. C*, 2018, **6**, 12121–12141.
10 S. Zhang, H. Liu, S. Yang, X. Shi, D. Zhang, C. Shan, L. Mi, C. Liu, C. Shen and Z. Guo, *ACS Appl. Mater. Interfaces*, 2019, **11**, 10922–10932.
11 I. You, B. Kim, J. Park, K. Koh, S. Shin, S. Jung and U. Jeong, *Adv. Mater.*, 2016, **28**, 6359–6364.
12 Y. Liu and M. Liu, *Compos. Sci. Technol.*, 2017, **143**, 56–66.
13 S. Zheng, X. Wu, Y. Huang, Z. Xu, W. Yang, Z. Liu, S. Huang, B. Xie and M. Yang, *Composites, Part A*, 2019, **121**, 510–516.
14 H. Wu, Q. Liu, H. Chen, G. Shi and C. Li, *Nanoscale*, 2018, **10**, 17512–17519.
15 N. Lu, C. Lu, S. Yang and J. Rogers, *Adv. Funct. Mater.*, 2012, **22**, 4044–4050.
16 P. Zhan, W. Zhai, N. Wang, X. Wei, G. Zheng, K. Dai, C. Liu and C. Shen, *Mater. Lett.*, 2019, **236**, 60–63.
17 H. Zhu, X. Wang, J. Liang, H. Lv, H. Tong, L. Ma, Y. Hu, G. Zhu, T. Zhang, Z. Tie, Z. Liu, Q. Li, L. Chen, J. Liu and Z. Jin, *Adv. Funct. Mater.*, 2017, **27**, 1606604.
18 K. Suzuki, K. Yataka, Y. Okumiya, S. Sakakibara, K. Sako, H. Mimura and Y. Inoue, *ACS Sens.*, 2016, **1**, 817–825.
19 F. Zhang, S. Wu, S. Peng and C. H. Wang, *Compos. Sci. Technol.*, 2018, **165**, 131–139.
20 S. Wu, J. Zhang, R. B. Ladani, A. R. Ravindran, A. P. Mouritz, A. J. Kinloch and C. H. Wang, *ACS Appl. Mater. Interfaces*, 2017, **9**, 14207–14215.
21 J. Wu, H. Wang, Z. Su, M. Zhang, X. Hu, Y. Wang, Z. Wang, B. Zhong, W. Zhou, J. Liu and S. G. Xing, *ACS Appl. Mater. Interfaces*, 2017, **9**, 38745–38754.

 This journal is © The Royal Society of Chemistry 2020

Published on 20 March 2020. Downloaded by Ontario Tech Library on 4/8/2020 7:22:30 PM.

22 Q.-J. Sun, J. Zhuang, S. Venkatesh, Y. Zhou, S.-T. Han, W. Wu, K.-W. Kong, W.-J. Li, X. Chen, R. K. Y. Li and V. A. L. Roy, *ACS Appl. Mater. Interfaces*, 2018, **10**, 4086–4094.
23 Y. Qin, Q. Peng, Y. Ding, Z. Lin, C. Wang, Y. Li, F. Xu, J. Li, Y. Yuan, X. He and Y. Li, *ACS Nano*, 2015, **9**, 8933–8941.
24 D.-Y. Wang, L.-Q. Tao, Y. Liu, T.-Y. Zhang, Y. Pang, Q. Wang, S. Jiang, Y. Yang and T.-L. Ren, *Nanoscale*, 2016, **8**, 20090–20095.
25 M. Amjadi, Y. J. Yoon and I. Park, *Nanotechnology*, 2015, **26**, 375501.
26 C. S. Boland, U. Khan, C. Backes, A. O'Neill, J. McCauley, S. Duane, R. Shanker, Y. Liu, I. Jurewicz, A. B. Dalton and J. N. Coleman, *ACS Nano*, 2014, **8**, 8819–8830.
27 S. Zhang, L. Wen, H. Wang, K. Zhu and M. Zhang, *J. Mater. Chem. C*, 2018, **6**, 5132–5139.
28 Y. Gao, X. Fang, J. Tan, T. Lu, L. Pan and F. Xuan, *Nanotechnology*, 2018, **29**, 235501.
29 S. Wang, P. Xiao, Y. Liang, J. Zhang, Y. Huang, S. Wu, S.-W. Kuo and T. Chen, *J. Mater. Chem. C*, 2018, **6**, 5140–5147.
30 S. Zhang, K. Sun, H. Liu, X. Chen, Y. Zheng, X. Shi, D. Zhang, L. Mi, C. Liu and C. Shen, *Chem. Eng. J.*, 2020, **387**, 124045.
31 M. Amjadi, A. Pichitpajongkit, S. Lee, S. Ryu and I. Park, *ACS Nano*, 2014, **8**, 5154–5163.
32 Z. Gao, K. Jiang, Z. Lou, W. Han and G. Shen, *J. Mater. Chem. C*, 2019, **7**, 9648–9654.
33 X. Su, H. Li, X. Lai, Z. Chen and X. Zeng, *ACS Appl. Mater. Interfaces*, 2018, **10**, 10587–10597.
34 M. Amjadi, S. Sheykhansari, B. J. Nelson and M. Sitti, *Adv. Mater.*, 2018, **30**, 1704530.
35 P. Ahuja, S. Akiyama, S. K. Ujjain, R. Kukobat, F. Vallejos-Burgos, R. Futamura, T. Hayashi, M. Kimura, D. Tomanek and K. Kaneko, *J. Mater. Chem. A*, 2019, **7**, 19996–20005.
36 Q. Li, H. Liu, S. Zhang, D. Zhang, X. Liu, Y. He, L. Mi, J. Zhang, C. Liu, C. Shen and Z. Guo, *ACS Appl. Mater. Interfaces*, 2019, **11**, 21904–21914.
37 X. Chen, H. Liu, Y. Zheng, Y. Zhai, X. Liu, C. Liu, L. Mi, Z. Guo and C. Shen, *ACS Appl. Mater. Interfaces*, 2019, **11**, 42594–42606.
38 M. Amjadi and M. Sitti, *Adv. Sci.*, 2018, **5**, 1800239.
39 Y. Jiang, Z. Liu, N. Matsuhisa, D. Qi, W. R. Leow, H. Yang, J. Yu, G. Chen, Y. Liu, C. Wan, Z. Liu and X. Chen, *Adv. Mater.*, 2018, **30**, 1706589.
40 C. Deng, P. Gao, L. Lan, P. He, X. Zhao, W. Zheng, W. Chen, X. Zhong, Y. Wu, L. Liu, J. Peng and Y. Cao, *Adv. Funct. Mater.*, 2019, 1907151.
41 A. Lekawa-Raus, K. K. K. Koziol and A. H. Windle, *ACS Nano*, 2014, **8**, 11214–11224.
42 S. Luo and T. Liu, *Adv. Mater.*, 2013, **25**, 5650–5657.
43 X. He, W. Gao, L. Xie, B. Li, Q. Zhang, S. Lei, J. M. Robinson, E. H. Hároz, S. K. Doorn, W. Wang, R. Vajtai, P. M. Ajayan, W. W. Adams, R. H. Hauge and J. Kono, *Nat. Nanotechnol.*, 2016, **11**, 633.
44 S. H. Jeong, S. Zhang, K. Hjort, J. Hilborn and Z. Wu, *Adv. Mater.*, 2016, **28**, 5830–5836.
45 A. Mata, A. J. Fleischman and S. Roy, *Biomed. Microdevices*, 2005, **7**, 281–293.
46 C.-X. Liu and J.-W. Choi, *Microelectron. Eng.*, 2014, **117**, 1–7.
47 J. Suhr and N. A. Koratkar, *J. Mater. Sci.*, 2008, **43**, 4370–4382.
48 P.-C. Ma, N. A. Siddiqui, G. Marom and J.-K. Kim, *Composites, Part A*, 2010, **41**, 1345–1367.
49 J. Suhr, W. Zhang, P. M. Ajayan and N. A. Koratkar, *Nano Lett.*, 2006, **6**, 219–223.
50 X. Zhou, E. Shin, K. W. Wang and C. E. Bakis, *Compos. Sci. Technol.*, 2004, **64**, 2425–2437.
51 J. Gou, *Polym. Int.*, 2006, **55**, 1283–1288.
52 M. D. Frogley, D. Ravich and H. D. Wagner, *Compos. Sci. Technol.*, 2003, **63**, 1647–1654.
53 C.-L. Wu, H.-C. Lin, J.-S. Hsu, M.-C. Yip and W. Fang, *Thin Solid Films*, 2009, **517**, 4895–4901.
54 S. Gong and Z. H. Zhu, *Polymer*, 2014, **55**, 4136–4149.
55 M. Haghgoo, R. Ansari, M. K. Hassanzadeh-Aghdam and M. Nankali, *Composites, Part A*, 2019, **126**, 105616.
56 M. Nankali, N. M. Nouri, N. Geran Malek and M. A. Sanjari Shahrezaei, *J. Compos. Mater.*, 2019, **53**, 3047–3060.
57 M. Park, J. Im, M. Shin, Y. Min, J. Park, H. Cho, S. Park, M.-B. Shim, S. Jeon, D.-Y. Chung, J. Bae, J. Park, U. Jeong and K. Kim, *Nat. Nanotechnol.*, 2012, **7**, 803–809.
58 M. Park, J. Park and U. Jeong, *Nano Today*, 2014, **9**, 244–260.
59 B. Liang, Z. Lin, W. Chen, Z. He, J. Zhong, H. Zhu, Z. Tang and X. Gui, *Nanoscale*, 2018, **10**, 13599–13606.
60 L. Ci, J. Suhr, V. Pushparaj, X. Zhang and P. M. Ajayan, *Nano Lett.*, 2008, **8**, 2762–2766.
61 T. Ogasawara, T. Tsuda and N. Takeda, *Compos. Sci. Technol.*, 2011, **71**, 73–78.
62 S. Gong, Z. H. Zhu and Z. Li, *Phys. Chem. Chem. Phys.*, 2017, **19**, 5113–5120.
63 L. Miao, J. Wan, Y. Song, H. Guo, H. Chen, X. Cheng and H. Zhang, *ACS Appl. Mater. Interfaces*, 2019, **11**, 39219–39227.
64 M. Amjadi, M. Turan, C. P. Clementson and M. Sitti, *ACS Appl. Mater. Interfaces*, 2016, **8**, 5618–5626.
65 D.-M. Drotlef, M. Amjadi, M. Yunusa and M. Sitti, *Adv. Mater.*, 2017, **29**, 1701353.
66 S. Han, F. Jiao, Z. U. Khan, J. Edberg, S. Fabiano and X. Crispin, *Adv. Funct. Mater.*, 2017, **27**, 1703549.
67 H. Liu, Q. Li, Y. Bu, N. Zhang, C. Wang, C. Pan, L. Mi, Z. Guo, C. Liu and C. Shen, *Nano Energy*, 2019, **66**, 104143.

Robust design optimization of laminated plates under uncertain bounded buckling loads

A. Kaveh, A. Dadras & N. Geran Malek

Structural and Multidisciplinary Optimization

ISSN 1615-147X
Volume 59
Number 3

Struct Multidisc Optim (2019)
59:877-891
DOI 10.1007/s00158-018-2106-0

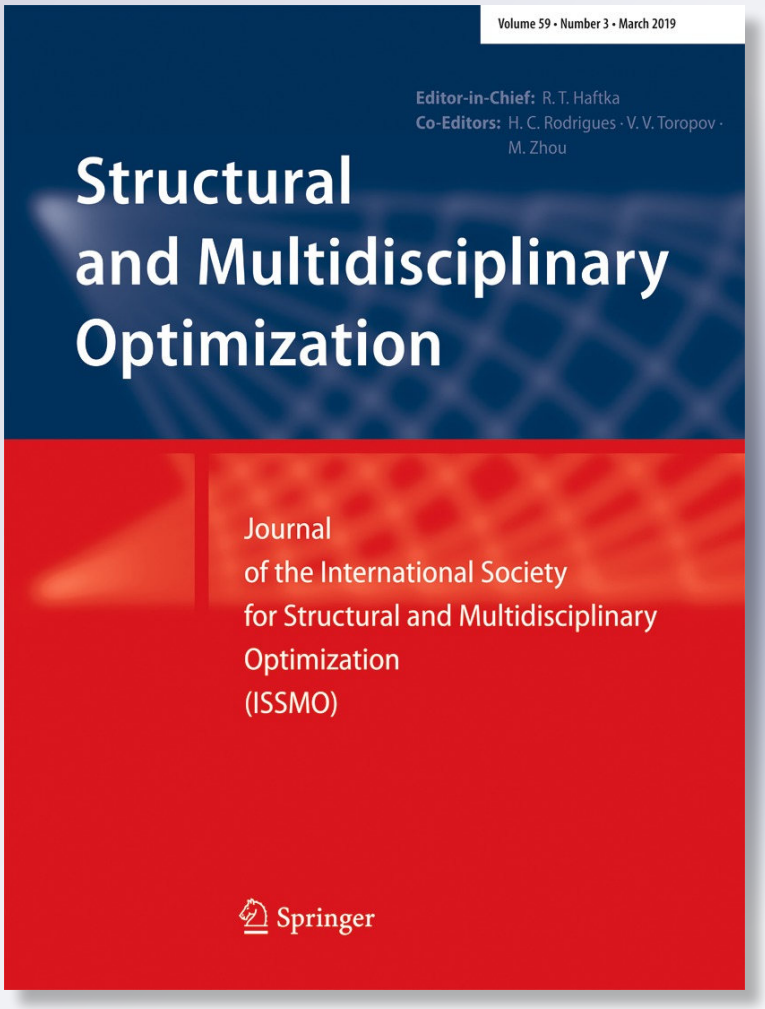

Springer

Your article is protected by copyright and all rights are held exclusively by Springer-Verlag GmbH Germany, part of Springer Nature. This e-offprint is for personal use only and shall not be self-archived in electronic repositories. If you wish to self-archive your article, please use the accepted manuscript version for posting on your own website. You may further deposit the accepted manuscript version in any repository, provided it is only made publicly available 12 months after official publication or later and provided acknowledgement is given to the original source of publication and a link is inserted to the published article on Springer's website. The link must be accompanied by the following text: "The final publication is available at link.springer.com”.

Springer

Author's personal copy

Structural and Multidisciplinary Optimization (2019) 59:877–891
https://doi.org/10.1007/s00158-018-2106-0

RESEARCH PAPER

Robust design optimization of laminated plates under uncertain bounded buckling loads

A. Kaveh[1] · A. Dadras[1] · N. Geran Malek[2]

Received: 31 May 2018 / Revised: 29 July 2018 / Accepted: 19 September 2018 / Published online: 3 October 2018
© Springer-Verlag GmbH Germany, part of Springer Nature 2018

Abstract

In this paper, a new systematic approach is suggested for better exploration of given uncertain buckling loads in the problem of optimal designs of hybrid symmetric laminated composites. Laminated composites are made up of 16-layered carbon-epoxy, glass-epoxy, and hybrid carbon-glass plies with discrete ply angles as design variables. In the analysis, the ply angles and the type of constituents in the laminates are varied, and one source of uncertainty, namely, uncertainty in buckling load is incorporated. In order to form nested optimization, a new improved rank-based version of Quantum-inspired Evolutionary Algorithm (QEA) is proposed and different versions of QEA and Genetic Algorithm (GA) are utilized. Using anti-optimization approach, the worst case biaxial compressive loading is obtained by Golden Section Search (GSS) method and the buckling load capacity is maximized. Numerical results of the optimal configurations are obtained under several bi-axial loading cases, panel aspect ratios, and materials. The results are investigated from different perspectives and sensitivity analyses are performed.

Keywords Hybrid laminated composite · Quantum-inspired evolutionary algorithm (QEA) · Load uncertainty · Anti-optimization · Robust design optimization (RDO)

1 Introduction

In recent decades, laminated composites received considerable attention from many scientists as potentially promising alternatives to traditional structures, owing to their remarkable characteristics such as high stiffness, specific strength, and light weight. The design of laminated composites deals with different parameters, like dimension, fiber orientation, number of plies, stacking sequence, and the type of constituents in hybrid laminates; and optimal selection of these parameters to achieve the desired mechanical performance.

Responsible Editor: Emilio Carlos Nelli Silva

Electronic supplementary material The online version of this article (https://doi.org/10.1007/s00158-018-2106-0) contains supplementary material, which is available to authorized users.

✉ A. Kaveh
alikaveh@iust.ac.ir

[1] Centre of Excellence for Fundamental Studies in Structural Engineering, Iran University of Science and Technology, Narmak, P.O. Box 16846-13114, Tehran, Iran

[2] Department of Automotive Engineering, Iran University of Science and Technology, Narmak, P.O. Box 16846-13114, Tehran, Iran

In the past few decades, significant research has been conducted to examine the design problem of composite structures. Fukunaga et al. (1995) presented an approach for optimal configurations of symmetrically laminated plates to maximize buckling loads. In this paper, the Automated Design Synthesis (ADS) method had been used as the optimizer and four lamination parameters were considered as the design variables. Based on the flexural lamination parameter technique, Liu et al. (2004) investigated a continuous variable optimization approach for maximization of the buckling loads of unstiffened composite panels. The results obtained from a combinatorial design of the stacking sequence via a Genetic Algorithm had been compared in relation with the solutions of the flexural lamination parameter method. In another study, Liu et al. (2015) have addressed a lamination parameter-based approach seeking the weight and mechanical performance optimization of blended composite panels. Comprehensive reviews on the classification and comparison of optimization methods for the problem of lay-up selection of the laminated composite structures have been presented in Ghiasi et al. (2010, 2009). Among the various classifications described in these reviews, four of them are outlined as follows: (1) an approach proposed by Venkataraman and Haftka (1999), in which the procedure was categorized into two single laminate

Author's personal copy

and stiffened plate design; (2) Abrate (1994), in which the problems were classified according to their objective functions; (3) Fang and Springer (1993), that used four categories for the designing approach, i.e., analytical approaches, enumeration procedures, heuristic methods, and nonlinear programming; and (4) Setoodeh et al. (2006) that considered two approaches for the design of composite structures, namely constant stiffness with the aim of obtaining optimum stacking sequence for material distribution and variable stiffness over the domain of the structure.

The term "hybrid" encompasses all laminated composites with more than one type of constituent as the matrix and reinforcement phases. Development of hybrid laminated composites led to improvements in terms of principal features, for example, improvements in performance, flexibility, weight, and cost (Reis et al. 2007). Several studies can be found on the optimal design of hybrid laminated composites in the literature. Huang and Haftka (2005) optimized the fiber orientations near a hole in a single layer of a multilayered composite laminate for increased strength using gradient-based and genetic algorithms. Lee et al. (2013) incorporated variable critical load cases (bending, shear and torsion) within the design optimization problem of hybrid (fiber–metal) composite structures (HCS). Kalantari et al. (2017) investigated the design problem of carbon-glass/epoxy hybrid composite laminates in the presence of three different uncertainty sources, including uncertainties in lamina thickness, fiber orientation, and matrix voids. In their work, the conflicting objectives were considered as material cost and density, where minimum flexural strength was chosen as a constraint. Adali et al. (2003) compared the optimal stacking configuration of constant thickness symmetric hybrid laminates for both robust and deterministic buckling load cases. They observed that the stacking sequence designed for a deterministic load case differs considerably from that of a robust laminate designed by taking the load uncertainties into account. Recently, Akmar et al. (2017)discussed the probabilistic optimization of hybrid laminated composites from two different points of view. Firstly, in the fine scale, weave pattern was considered as the design variable of single-ply Representative Volume Element (RVE), in the presence of four uncertain microscopic parameters, namely, yarn spacing, yarn width, yarn height, and misalignment in yarn angle. In the second problem, Ant Colony Optimization (ACO) was utilized in the problem of stacking sequence design of hybrid laminated composites. Al_2O_3/Al was considered as the inner laminate plies while (SiC/Al) was used for the outer plies.

The present study is a continuation of the previous work (Kaveh et al. 2018), in which the Biogeography-Based Optimization (BBO) algorithm has been utilized to determine the optimal stacking sequence of hybrid laminates under deterministic conditions. The objective of the present paper is finding the optimum designs of hybrid symmetrically laminated composites to maximize the biaxial buckling load when they are subjected to a domain of bounded uncertain loading. As suggested in Elishakoff et al. (1994), a two-level design approach using anti-optimization is conducted to deal with the uncertain loads. Thus the critical buckling load factor λ_{cb} is maximized under the worst condition of loading.

In the past, the stacking sequence optimization problem was solved by classical gradient-based methods. The deficiencies of the methods in dealing with non-convex spaces and discrete variables led to their limited success (Soremekun et al. 2001). During the recent decades, different metaheuristic algorithms have been established as the most promising and effective tools for dealing with optimal design problems (Çarbaş and Saka 2012; Saka and Erdal 2009; Tejani et al. 2016; Kaveh 2017a,b). These iterative algorithms are commonly inspired by natural phenomena including biology, ethology, or even physical processes (Hussain et al. 2018). Evolutionary algorithms (EAs) are the most well-known metaheuristics that mimic the evolutionary process in nature to improve the initial solutions over consecutive generations. For example, the Genetic Algorithm (GA) (Goldberg and Holland 1988) that is inspired by the "natural selection theory" of Darwin, utilizes the selection and mutation as the search operators, or Quantum-inspired Evolutionary Algorithm (QEA) (Han and Kim 2002) which follows concepts from quantum computing such as Q-bits, superposition, quantum gates, and quantum measurement. Their outstanding features including simplicity of implementation, being gradient-free, compatibility with discrete variables, and finding near global optimal solutions have made them popular tools for optimization. It should be noted that one of the challenges in the implementation of evolutionary algorithms is the difficulty in determination of algorithm-specific parameters, such as crossover and mutation rates of GA. Finding the ideal parameters is a time-consuming task, and the inappropriate parameter setting may damage the performance of the algorithms. For instance, de Almeida (2016) demonstrated that the harmony memory size (HMS), harmony memory consideration rate (HMCR), and pitch adjusting rate (PAR) have an apparent effect on the reliability of the Harmony Search Algorithm (HSA) for optimizing the laminated composites. From this point of view, the parameter-less algorithms like QEA are at an advantage, which needs only the general parameters. Moreover, QEA is a binary-coded algorithm which makes it suitable for studying the stacking sequence problem with discrete variables. So here, an improved version of Quantum-Inspired Evolutionary Algorithm (QEA) is proposed and along with two other versions, are applied for solving the optimal design problem of hybrid laminated composites, for the first time in literature. Furthermore, two versions of a Genetic Algorithm (GA) are implemented for comparison. The Golden-Section Search (GSS) method is employed as the anti-optimizer for comparison of the results with those of Adali et al. (2003).

Author's personal copy

The rest of the paper is elucidated through the following sections. In Section 2, a description of the optimization and anti-optimization procedures are presented. In Section 3, the theoretical framework of the problem is provided. Section 4 defines the objective function of the problem, the numerical results, and investigations. Finally, Section 5 contains some concluding remarks.

2 Optimization and anti-optimization methods

Since the laminated composites experience varying loads, they must be designed in such a way to withstand and meet the design requirements. Here, the aim of the optimal robust design is maximizing the capacity of laminated composites when they are encountered with the worst case of aforementioned uncertain condition (Adali et al. 2003). Therefore, here the stacking sequence is optimized by a metaheuristic algorithm and the worst loading condition is found by an anti-optimizer. In the following, the utilized algorithms are reviewed.

2.1 Quantum-inspired evolutionary algorithm (QEA)

Quantum-inspired evolutionary algorithm (QEA) is a well-known quantum computing-inspired optimization algorithm, proposed by Han and Kim (2002). The basic information and concepts about quantum computing, steps of QEA, and its different versions are given in following.

2.1.1 The basics of quantum computing

The common classical computers require the data to be encoded into bits, where they always represent one of two definite states "0" or "1". While quantum computers use Q-bits as unit of quantum information, which can be in the "0" state, "1"state, or in superposition of these states (Hey 1999). Thus, the state of a Q-bit is represented as follows:

$$|\Psi\rangle = \alpha|0\rangle + \beta|1\rangle \tag{1}$$

where α and β are complex numbers, and $|\,.\,\rangle$ stands for state of the system. The values of $|\alpha|^2$ and $|\beta|^2$ represent the probability of "0" and "1" states, respectively. It is clear that according to the probability axioms, the following equation holds:

$$\alpha^2 + \beta^2 = 1 \tag{2}$$

In QEA, the information unit is Q-bit which is shown in the following equation:

$$q = \begin{bmatrix} \alpha \\ \beta \end{bmatrix} \tag{3}$$

In order to transfer more quantum information, the Q-bits join together and create an individual. A string of m Q-bit contains the information of 2^m states, which shows the efficiency of this representation. A two-Q-bit individual is defined as:

$$q = \begin{bmatrix} \alpha_1 & \alpha_2 \\ \beta_1 & \beta_2 \end{bmatrix} \tag{4}$$

This individual represents the state of the system as:

$$|\Psi\rangle = |\alpha_1|^2.|\alpha_2|^2|00\rangle + |\alpha_1|^2.|\beta_2|^2|01\rangle + |\beta_1|^2.|\alpha_2|^2|10\rangle + |\beta_1|^2.|\beta_2|^2|11\rangle \tag{5}$$

(5) means that, for instance, the probability of $|\,10\,\rangle$ state is $|\beta_1|^2.\,|\alpha_2|^2$.

2.1.2 Steps of the QEA

QEA as an evolutionary algorithm having population of individuals. The population of n individuals at generation t is defined as:

$$Q(t) = \{q_1{}^t, q_2{}^t, \ldots, q_n{}^t\} \tag{6}$$

where q_i^t is the ith individual in the tth generation. The steps of QEA are provided in the subsequent sections.

Initialization At the first step, with the assumption that the probabilities of all the solutions are equal, $Q(t)$ is initialized. Hence, both α^2 and β^2 are equal to $^1/_2$ resulting in $^{\sqrt{2}/2}$ for α and β.

Observation Since QEA is working on a classical computer, so the quantum states do not collapse into a single state. The binary solutions ($P(t)$) are made by observing the states of $Q(t)$ and using a probabilistic approach. For this purpose, a uniform random parameter within (0, 1) is generated for each Q-bit. If the random number is less than α^2, the corresponding binary bit is 0, otherwise it is 1.

Evaluation Considering the binary solutions which are created for each individual, they are evaluated using the objective function. The obtained values are associated to the corresponding solutions.

Saving The solutions, which have higher quality, can help the algorithm by searching their neighborhood and increase the convergence rate of the algorithm (Kaveh and Dadras 2017). In this regard, the best solutions among $B(t-1)$ and $P(t)$ are selected and stored into $B(t)$.

Author's personal copy

Migration Two main models of migration are suggested, local migration and global migration. In local migration, the b_j^t, which is the better one of two neighboring solutions is copied in $B(t)$, while in global migration b is copied to all solutions in $B(t)$.

Updating In iterative optimization algorithms, the new solutions are usually generated according to the previous ones. In QEA, the Q-gate is defined as the updating operator. The Q-bits can be represented as the components of a point on unit circle as illustrated in Fig. 1. A suitable tool for updating the points on the circle to new position is rotation around the center by a definite degree, as given in (7). Hence, the rotation gate is utilized as the basic Q-gate:

$$U(\Delta\theta_i) = \begin{bmatrix} cos(\Delta\theta_i) & -sin(\Delta\theta_i) \\ sin(\Delta\theta_i) & cos(\Delta\theta_i) \end{bmatrix} \tag{7}$$

where Δθ is the rotation angle of each Q-bit, which are defined according to Table 1. (In Fig. 1 the θs are replaced by the radian and; if q is not located in the first/third quadrant, negative values will be used for θs).

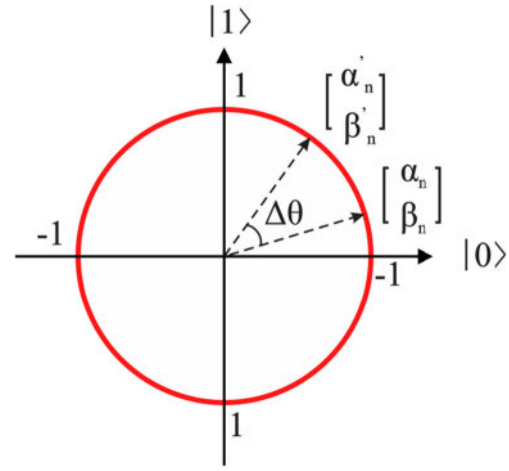

Fig. 1 Quantum rotation gate (Q-gate).

Termination Different criteria can be considered as the termination condition. Here, when the number of generations reaches a predefined maximum number, the algorithm breaks and reports the best solution found so far.

To clarify the structure of QEA, it is schematically demonstrated in Fig. 2 and the pseudo code of the QEA follows.

The pseudo code of QEA

begin

$t \leftarrow 0$

Initialize $Q(t)$

Make $P(t)$ *by observing the states of* $Q(t)$

Evaluate $P(t)$

Store the best solutions among $P(t)$ *into* $B(t)$ *and the best solution* ***b*** *among* $B(t)$

while *(termination condition is unsatisfied)* ***do***

$t \leftarrow t + 1$

Make $P(t)$ *by observing the states of* $Q(t-1)$

Evaluate $P(t)$

Update $Q(t)$ *using Q-gates*

Store the best solutions among $P(t)$ *and* $B(t-1)$ *into* $B(t)$ *and the best solution* ***b*** *among* $B(t)$

if *(migration condition)*

Migrate ***b*** *or* b_j^t *to* $B(t)$ *globally or locally, respectively*

end

end

end

Author's personal copy

Table 1 $\Delta\theta_i$ look-up table for maximization

x_i	b_i	$f(\mathbf{x}) \geq f(\mathbf{b})$	Rotation gate $\Delta\theta_i$	Improved rotation gate $\Delta\theta_i$
0	0	False	0	0
0	0	True	0	0
0	1	False	0.01π	d
0	1	True	0	0
1	0	False	-0.01π	$-d$
1	0	True	0	0
1	1	False	0	0
1	1	True	0	0

2.1.3 QEA-H_ϵ gate

This version of QEA follows the procedure mentioned above, excluding the updating step. In QEA-H_ϵ gate, an extended version of Rotation gate is utilized which is called H_ϵ. This gate is defined as follows:

$$[\alpha', \beta']^T = H_\varepsilon(\alpha, \beta, \Delta\theta), \text{ where for } \left[\alpha_i'' \ \beta_i''\right] = R(\alpha, \beta, \Delta\theta):$$

$$\text{if } \left|\alpha_i''\right|^2 \leq \varepsilon \text{ and } \left|\beta_i''\right|^2 \geq 1-\varepsilon \rightarrow \left[\alpha_i' \ \beta_i'\right]^T = \left[\sqrt{\epsilon} \ \sqrt{1-\epsilon}\right]^T$$

$$\text{if } \left|\alpha_i''\right|^2 \geq 1-\varepsilon \text{ and } \left|\beta_i''\right|^2 \geq \varepsilon \rightarrow \left[\alpha_i' \ \beta_i'\right]^T = \left[\sqrt{1-\epsilon} \ \sqrt{\epsilon}\right]^T$$

$$\text{otherwise } \left[\alpha_i' \ \beta_i'\right]^T = \left[\alpha_i'' \ \beta_i''\right]^T$$

where $0 < \varepsilon \ll 1$, here ε is assumed as 0.0075; R stands for rotation gate which was defind in (7). This gate is depicted in Fig. 3.

2.1.4 QEA-iRotation gate

In the basic version of QEA, a constant value (0.01π) is utilized as the step size. In this paper, a rank-based dynamic mechanism is proposed. As given in Table 1, the new version utilizes the rank of individuals to update Q-bits. The parameter d is calculated as follows:

$$d_i = dmin + \frac{dmax - dmin}{nPop - 1}(r_i - 1) \tag{8}$$

where r_i and $nPop$ stand for the rank of ith particle and the number of populations, respectively. $dmax$ and $dmin$ are respectively assumed as 0.05π and 0.001π. According to this equation, around the better populations are exploited slightly, while the updating of inferior individuals is performed by larger steps. This improved QEA is called as "QEA-iRotation gate".

2.2 The genetic algorithm

GA is one of the most commonly used evolutionary optimization algorithm which is inspired by theory of Darwin from biological evolutions and survival of the fittest. The GA developed by Holland (1992), involves a selection mechanism, such as Roulette wheel selection or Tournament selection (Sivanandam and Deepa 2007) and genetic operators such as crossover and mutation (Kaveh and Ilchi Ghazaan 2015). The main goal of the Genetic Algorithm is to produce a new population (child or offspring), that has been improved with reference to the previous population (parents), through the use of genetic operators and selection mechanisms. The Genetic Algorithm can be categorized into two major binary (or integer)

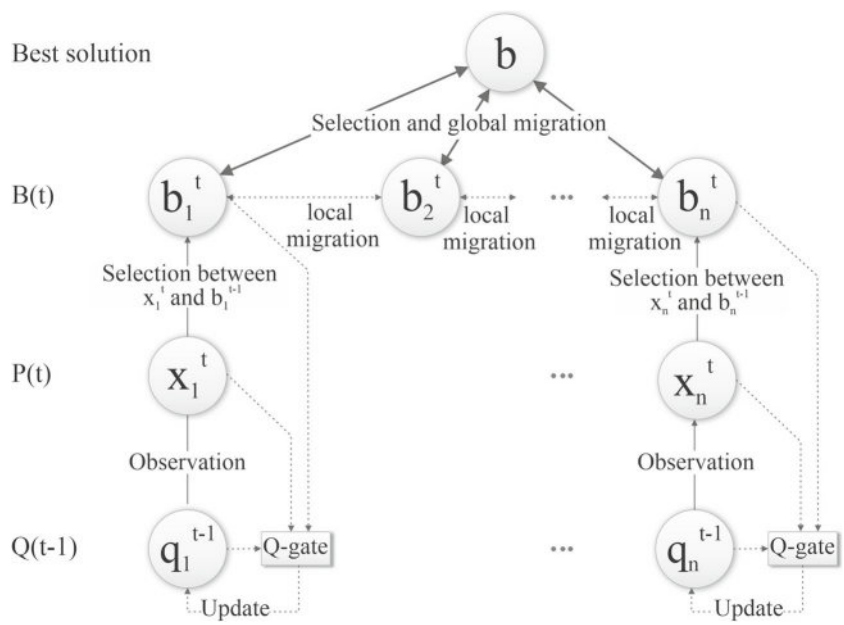

Fig. 2 Overall configuration for the QEA algorithm

Author's personal copy

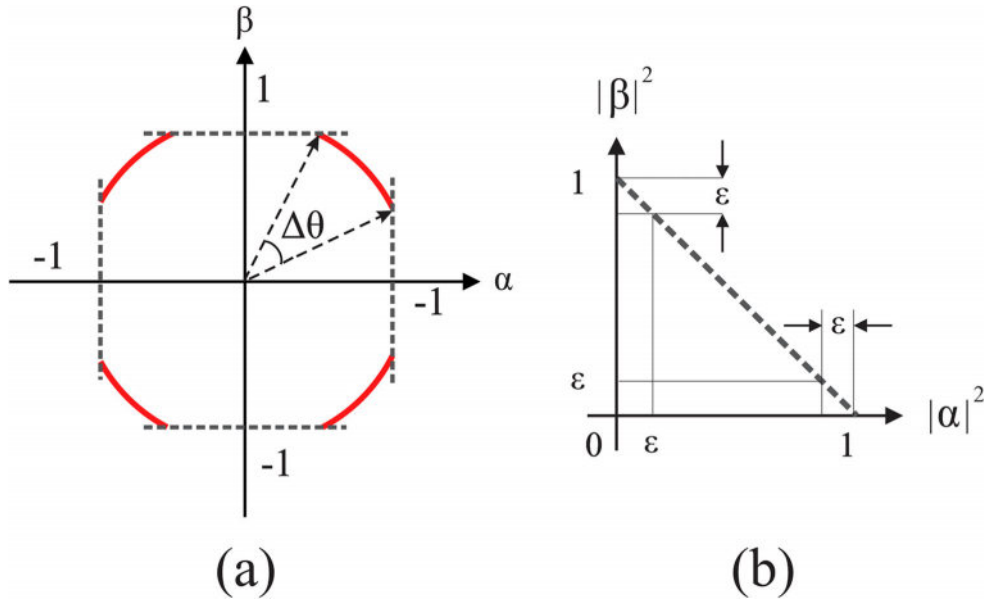

Fig. 3 H_ϵ gate for **a** condition iii and **b** conditions i and ii

GA and real (or continuous) GA types. In this paper, the discrete stacking sequence problem is studied, therefore the binary version is employed and in the following sections, steps of the Binary Genetic Algorithm (Arora 2017) are outlined.

2.2.1 Initialization

In the first step, primary population (chromosomes) is randomly generated. Each chromosome comprises of a set of genes (variables) and each gene can contain one or more genomes with digits of 0 or 1. The components of population in GA method are illustrated in Fig. 4. In this paper, four states (ply angles) are considered for each design variable, due to binary encoding, thus the variables contain two genomes.

2.2.2 Evaluation

The fitness values of the chromosomes are determined using the objective function, which is defined in the next sections.

2.2.3 Selection

Different selection methods have been proposed to determine the parents for the next generation. Here, Roulette wheel selection and Tournament selection techniques are employed. In Roulette wheel, the chromosomes are selected with a probability proportional to their fitness value, while in Tournament selection, a few groups are made randomly, and their best chromosomes are selected. For more details, the

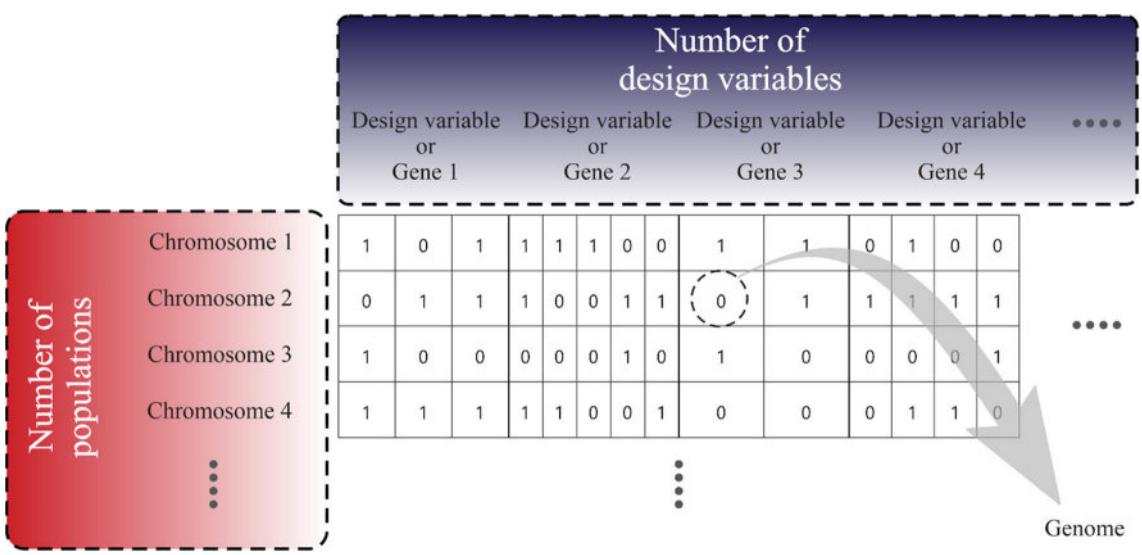

Fig. 4 Components of population in the GA method

Author's personal copy

reader may refer to Goldberg and Deb (1991) and Sivanandam and Deepa (2008).

2.2.4 Crossover

Each pair selected in the previous step, reproduces two children. Here, three most well-known crossover operators, including one point, two point, and uniform random crossover are utilized to reproduce the children. It should be mentioned that 80% of the GA's population is generated by crossover.

2.2.5 Mutation

This step mimics the biological mutation and tries to maintain genetic diversity. Up to this stage, a few numbers of individuals are randomly selected and some of their genes are replaced by a random value. Here, 20% of the population is mutated and only one gene of each chromosome is exposed to mutation. These values are determined based on a trial and error process to get the best performance.

2.2.6 Elitism

In order to survive, the best chromosomes are evaluated and *nPop* number of the best elite chromosomes are considered as the next generation.

2.2.7 Termination

The procedure mentioned in the previous steps continues in succession until the employed stopping criterion is met. Here, the number of objective function evaluations (NFE) are limited to a predefined number.

The flowchart of the GA is illustrated in Fig. 5.

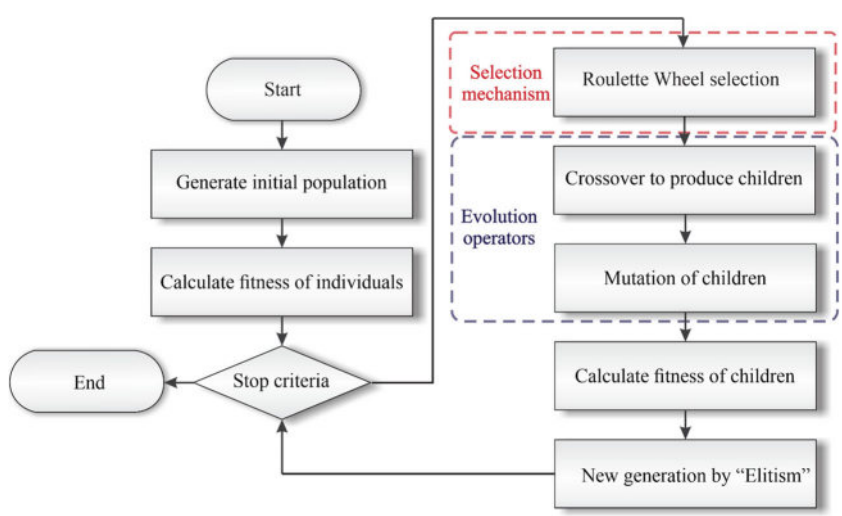

Fig. 5 Flowchart of a general GA algorithm

2.3 Anti-optimization problem

Elishakoff et al. (1994) conducted one of the earliest works on the robust design of structures under bounded uncertainty in loads. Lombardi and Haftka (1998) applied the anti-optimization technique to the problem of structural optimization in the presence of uncertainty in loading conditions. Anti-optimization is about exploring an uncertain domain for the worst case. The GSS algorithm is a simple and real-coded optimization algorithm. As explained in the following, it is very fast and suitable for single-variable problems (Arora 2017), so the worst case values of the continuous uncertain domains can be easily obtained in the searching interval with this algorithm. It is used to find the extremum by reducing the width of the search intervals, consecutively.

2.3.1 Golden section search (GSS)

This scheme is one of the numerical optimization techniques in the class of variable interval-reducing methods (Arora 2017). Unlike equal-interval search method, in the variable interval-reducing methods, the uncertain increment reduces systematically according to the associated technique. In the GSS method, the increment is varied in each step. The increment of the previous step (δ) is multiplied by a constant value known as the Golden Ratio (φ) which is defined in (9).

$$\varphi = \left(1 + \sqrt{5}\right)/2 \tag{9}$$

Once the new uncertainty interval is less than a certain amount, the termination condition is satisfied. The steps of this method for a minimization one-dimensional (single-variable) problem are provided in the following:

Author's personal copy

Step 1: For an interval of $[a, b]$, evaluate the objective function for

$$c = a + \frac{b-a}{\varphi} \tag{10}$$

and

$$d = d - \frac{b-a}{\varphi} \tag{11}$$

Step 2: If $f(c) > f(d)$, move the interval to $[c, b]$, otherwise, move the interval to $[a, c]$.

Step 3: If the stopping criteria is satisfied, stop, and report the solution, otherwise, come back to step 1 for a new round of minimization.

3 Theoretical framework and problem formulation

3.1 Theoretical framework

Based on the classical laminated plate theory (CLPT), the governing equation of buckling for a symmetric N layer laminate can be expressed as (Reddy 2004):

$$D_{11}\frac{\partial^4 w}{\partial x^4} + 4D_{16}\frac{\partial^4 w}{\partial x^3 \partial y} + 2(D_{12} + 2D_{66})\frac{\partial^4 w}{\partial x^2 \partial y^2} + 4D_{26}\frac{\partial^4 w}{\partial x \partial y^3} + D_{22}\frac{\partial^4 w}{\partial y^4} + \lambda\left(N_x\frac{\partial^2 w}{\partial x^2} + N_y\frac{\partial^2 w}{\partial y^2}\right) = 0 \tag{12}$$

In (12), w is the deflection in the z direction, and h is the total thickness of the laminate. In addition, D_{ij} stands for the bending stiffness coefficients, and can be expressed by (13)

$$D_{ij} = \int_{-\frac{h}{2}}^{\frac{h}{2}} \overline{Q}_{ij}(z^2)dz = \sum_{k=1}^{N} \int_{z_k}^{z_{k+1}} \overline{Q}_{ij}^{(k)}(z^2)dz = \frac{1}{3}\sum_{K=1}^{N} \overline{Q}_{ij}^{(k)}\left(z_{k+1}^3 - z_k^3\right) \tag{13}$$

where $\overline{Q}_{ij}^{(k)}$ represents the transformed reduced stiffness of this layer, which is expressed by:

$$\overline{Q}_{ij}^{(k)} = [T]^{-1}[Q]\left([T]^{-1}\right)^T. \tag{14}$$

The coefficients of the reduced stiffness matrix ($[Q]$) can be stated as the following equation:

$$[Q] = \begin{bmatrix} Q_{11} & Q_{12} & 0 \\ Q_{12} & Q_{22} & 0 \\ 0 & 0 & Q_{66} \end{bmatrix}; = \frac{E_1}{1-\upsilon_{12}\upsilon_{21}}, Q_{12} = \frac{\upsilon_{12}E_2}{1-\upsilon_{12}\upsilon_{21}} = \frac{\upsilon_{21}E_1}{1-\upsilon_{12}\upsilon_{21}}, Q_{22} = \frac{E_2}{1-\upsilon_{12}\upsilon_{21}}, Q_{66} = G_{12}. \tag{15}$$

In the above equation, E_1, E_2, and $G_{12}$are longitudinal Young's modulus, transverse Young's modulus, and shear modulus, respectively and υ_{12} and υ_{21} are Poisson's ratios. Further, the transformation matrix $[T]$ can be calculated by:

$$[T] = \begin{bmatrix} C^2 & S^2 & 2CS \\ S^2 & C^2 & -2CS \\ -CS & CS & C^2 - S^2 \end{bmatrix}; C = Cos(\theta), S = Sin(\theta). \tag{16}$$

For simply supported edges, the boundary conditions are stated as:

$$w = 0, M_x = 0 \quad \text{at} x = 0, a \tag{17}$$

$$w = 0, M_y = 0 \quad \text{at} y = 0, b \tag{18}$$

Considering the governing equation expressed in (12) and the boundary conditions in (17) and (18), the following value of the critical buckling load multiplier λ_{cb} of biaxial compression case is obtained (Haftka and Gürdal 2012; Reddy 2004):

$$\lambda_b(m,n) = \pi^2\left[\frac{m^4 D_{11} + 2(D_{12} + D_{66})(rmn)^2 + (rn)^4 D_{22}}{(am)^2 N_x + (ran)^2 N_y}\right] \tag{19}$$

where length and width of the plate are denoted by a and b, respectively. $r = a/b$ is the aspect ratio, and bending stiffness matrix coefficients are indicated by D_{ij}. Different mode shapes can be obtained by inserting different values of m and n associated with the transverse displacement patterns. Here, the smallest of $\lambda_b(1,1)$, $\lambda_b(1,2)$, $\lambda_b(2,1)$, and $\lambda_b(2,2)$ is taken as the critical buckling load. The results given by Nemeth (1986) indicate that when the following constraints are satisfied, D_{16} and D_{26} terms are insignificant

$$\delta = \frac{D_{16}}{\left(D_{11}{}^3 D_{22}\right)^{-\frac{1}{4}}} \leq 0.2, \tag{20}$$

$$\gamma = \frac{D_{26}}{\left(D_{11} D_{22}{}^3\right)^{-\frac{1}{4}}} \leq 0.2 \tag{21}$$

Author's personal copy

In computations, the satisfaction of the above constraints is ensured. Therefore the mentioned terms do not arise in (19).

4 Problem definition and numerical results

Studying the performance of laminated composite under buckling loads, as one of the most frequent causes of failure in laminated composites, is fairly crucial. In the presence of unavoidable uncertainty in buckling loads, mitigating the influences of such uncertainty is the only existing choice.

In Fig. 6, the schematic illustration of the geometry of this simply supported composite plate, subjected to an in-plane compressive load, is demonstrated. In order to compare and verify the validity of the results, the problem conditions are in accordance with those of Adali et al. (2003). It is assumed that the plate is symmetric, balanced, and comprised of 16 layers, made of hybrid carbon-glass, carbon-epoxy, and glass-epoxy plies. Due to the symmetry of the plates, the number of design variables is reduced from 16 to 8. Material properties of carbon–glass/epoxy laminates are given in Table 2. The optimization problem can be defined as the maximization of the critical buckling load factor λ_{cb} as the objective function, which can be formulated as follows (Adali et al. 2003):

$$\text{Maximize}: \lambda_{cb}(\theta) = \pi^2 \left[\frac{m^4 D_{11} + 2(D_{12} + D_{66})(rmn)^2 + (rn)^4 D_{22}}{(am)^2 N_x + (ran)^2 N_y} \right] \tag{22}$$

where θ is the vector of design variables, containing the fiber ply angle of laminates. Besides, λ_{cb} can be found using combinations of m and n that yield the lowest buckling load. In binary implementation for discrete ply angles, stacks with $\theta = 0^\circ, +45^\circ, -45^\circ$, and 90° are converted to binary numbers 00, 01, 10, and 11, respectively. It should be noted that, the achieved optimal sequences are in the standard order of outermost lamina to innermost one (see Fig. 6b).

Table 2 Material properties of carbon–glass/epoxy laminates

	E_1	E_2	G_{12}	υ_{12}
Carbon–epoxy (T300/280)	181	10.3	7.17	0.28
Glass–epoxy (Scotch-ply 1002)	38.6	8.27	4.14	0.26

In many conditions, precise probabilistic data on uncertainty in buckling loads of laminated composites are not available a priori; however, these can be bounded to a defined set. These bounded domains that are denoted by U_p; ($p = 1, 2, \ldots, \infty$), can be defined by:

$$U_p = \left\{ (N_x, N_y) | N_x \geq 0, N_y \geq 0, N_x^p + N_y^p \leq 1 \right\} \tag{23}$$

Based on the value of exponent p, distinct shapes for uncertain domains are obtained. As illustrated in Fig. 7, $p = 1$ and $p = 2$ stand for triangular and circular domains, respectively. For a given p, the minimum value of buckling load factor is determined by solving the following anti-optimization problem:

$$\lambda(\theta_K; N^*) = \min_{N \epsilon U_p} \lambda(\theta_K; N) \tag{24}$$

In the level of anti-optimization, $N = (N_x, N_y) \in U_p$ are considered as the design variables corresponding to the lowest buckling capacity (worst case).

The results are presented for both triangular domain U_1, and circular domain U_2. As illustrated in Fig. 6, in the case of hybrid carbon–glass/epoxy laminate, glass–epoxy layers are considered as the inner plies of the plate, and carbon–epoxy layers are the outer plies. Moreover, an equal number of plies are assumed for both of them. It is assumed that the plate has the original width of $b = 1$ m ($a = br$), and total

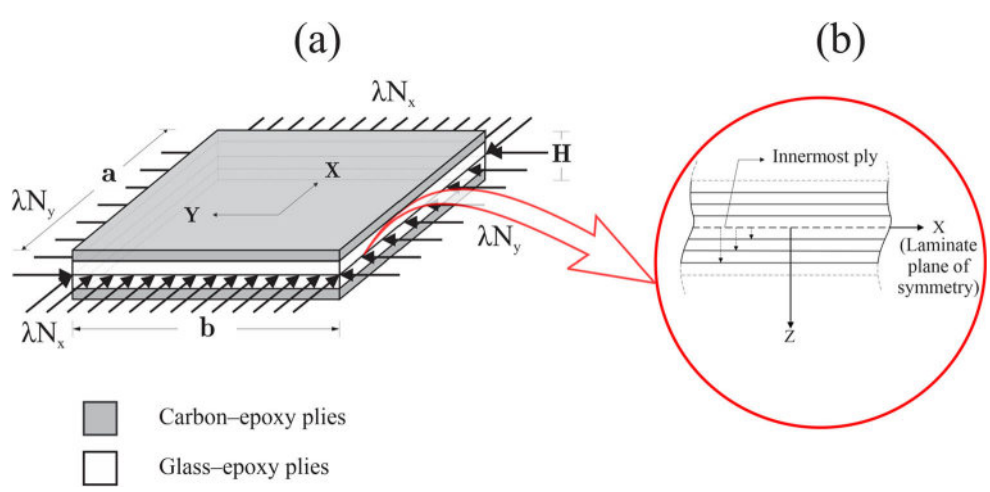

Fig. 6 Schematic configuration of a multilayered sandwich panel: **a** Geometry of the laminated plate and applied loads, **b** sequence of plies

Author's personal copy

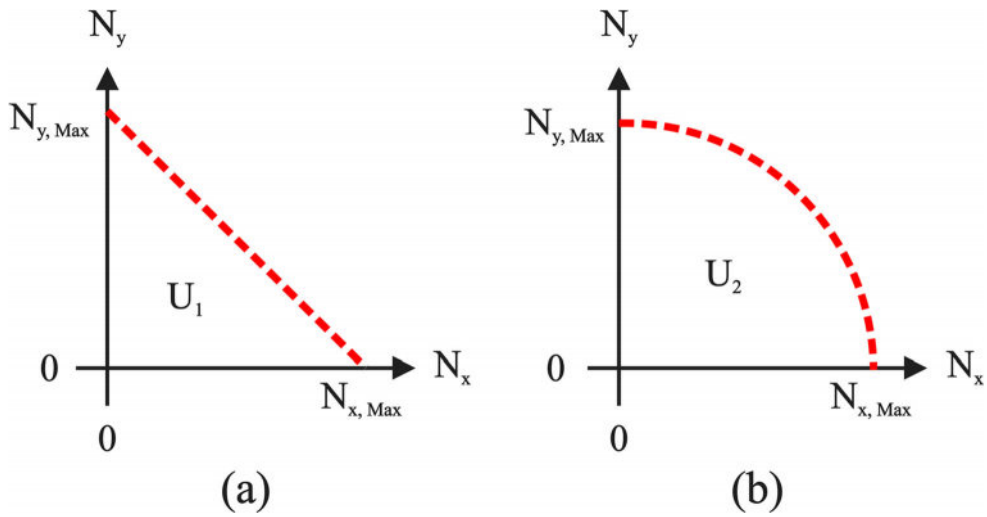

Fig. 7 Domains of uncertainty: **a** triangular, **b** circular

thickness of $H = 0.1\ m$. It should be noted that, N_x and N_y are in kN/m.

Considering different materials and loading domains, six cases are examined, where each set includes ten experiments for different panel aspect ratios. The introduced optimization algorithms are independently run 30 times for each of the problems, and the number of objective function evaluations (NFE) is limited to 5000 as the stopping criteria (Kaveh et al. 2018). The optimal buckling loads obtained for the examples along with the results of Adali et al. (2003) are presented in Tables 3, 4 and 5. For the sake of brevity, the optimal orientations are provided in Tables 6–11 of the online Appendix. The results are investigated from different aspects in the following sections.

4.1 A comparison of the effect of different materials

For comparison, the bar chart of the values of optimal buckling factors is illustrated in Figs. 8 and 9. As it can be seen, in both types of the loading domains (U_1 and U_2), the carbon-epoxy plate has maximum robust buckling load capacity among the examined materials and glass-epoxy plate has the minimum buckling load. The ratios of buckling capacity of plates constructed with different materials are shown in Fig. 10. As it can be seen in Fig. 10, the capacity ratio of carbon/glass to carbon-epoxy is almost constant and equal to 90%, while this ratio for carbon/glass to glass-epoxy varies from 361 to 431%. The effect of aspect ratios is investigated in the next section.

4.2 An investigation on the effect of aspect ratio

As provided in Tables 3, 4 and 5 and illustrated in Figs. 8 and 9, by increasing the aspect ratio, the buckling capacity of plates decrease. Moreover, it is observed that the more the aspect ratios increase, the capacity reduction rates decrease. For instance, by increasing the aspect ratio from 0.2 to 0.4, the carbon-epoxy plate has a capacity reduction of 74%, while by changing the aspect ratio from 1.8 to 0.4, this ratio is fallen by only 1%. According to Fig. 10, the capacity ratio of carbon/glass to glass/epoxy, rises in side aspect ratios and it is sensitive to the type of loading domain.

Table 3 Buckling loads obtained for the glass-epoxy plate exposed to uncertain loads

r	U_1 Examined algorithms and Adali et al. (2003)	U_2 Examined algorithms and Adali et al. (2003)
0.2	822.8	822.2
0.4	219.6	216.9
0.6	109.2	102.7
0.8	81.1	68.3
1	78.2	55.3
1.2	55.6	45.7
1.4	43.3	38.6
1.6	40.0	37.2
1.8	38.2	36.5
2	37.0	35.9

Author's personal copy

Table 4 Buckling loads obtained for the carbon-epoxy plate exposed to uncertain loads

	U_1		U_2	
r	Examined algorithms	Adali et al. (2003)	Examined algorithms	Adali et al. (2003)
0.2	3767.0	3446.7	3764.0	3393.0
0.4	964.3	895.8	931.6	878.1
0.6	446.8	431.9	428.7	406.4
0.8	325.5	325.5	274.2	274.2
1	316.1	316.1	223.5	223.5
1.2	223.9	223.9	183.9	183.9
1.4	172.5	172.5	153.6	153.6
1.6	161.9	157.9	147.7	146.9
1.8	159.1	151.6	146.2	144.8
2	157.2	149.0	144.6	142.9

Table 5 Buckling loads obtained for the carbon-glass/epoxy plate exposed to uncertain loads

	U_1		U_2	
r	Examined algorithms	Adali et al. (2003)	Examined algorithms	Adali et al. (2003)
0.2	3399.0	3115.8	3399.0	3092.1
0.4	871.2	818.3	844.7	796.0
0.6	404.6	385.8	383.4	367.7
0.8	295.0	295.0	248.6	248.6
1	286.4	286.4	202.5	202.5
1.2	202.8	202.8	166.6	166.6
1.4	156.3	156.3	139.3	139.3
1.6	146.7	140.4	134.1	133.2
1.8	144.0	137.0	132.6	130.9
2	142.1	135.3	131.8	129.0

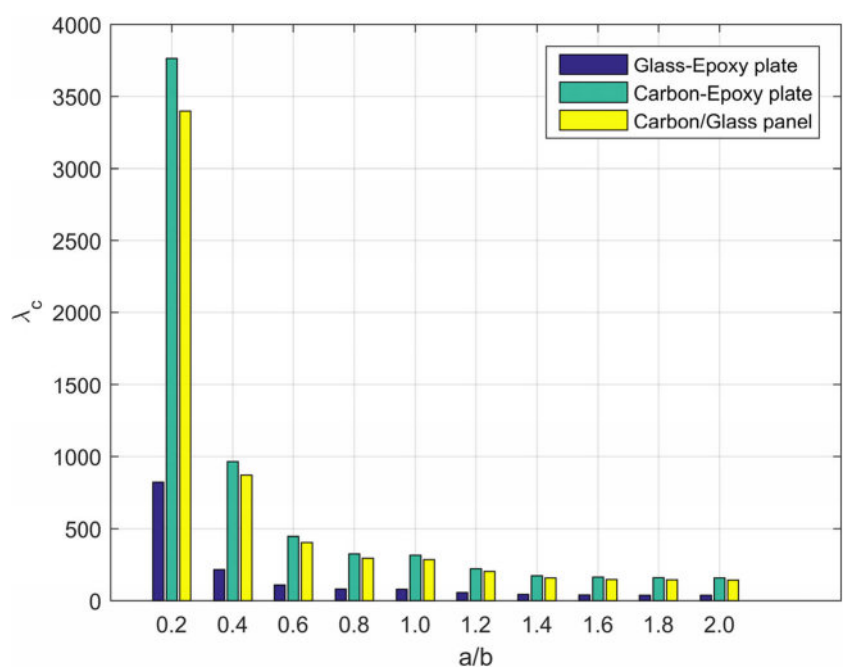

Fig. 8 Optimal values of the buckling factors for the case of U_1 loading domain

Author's personal copy

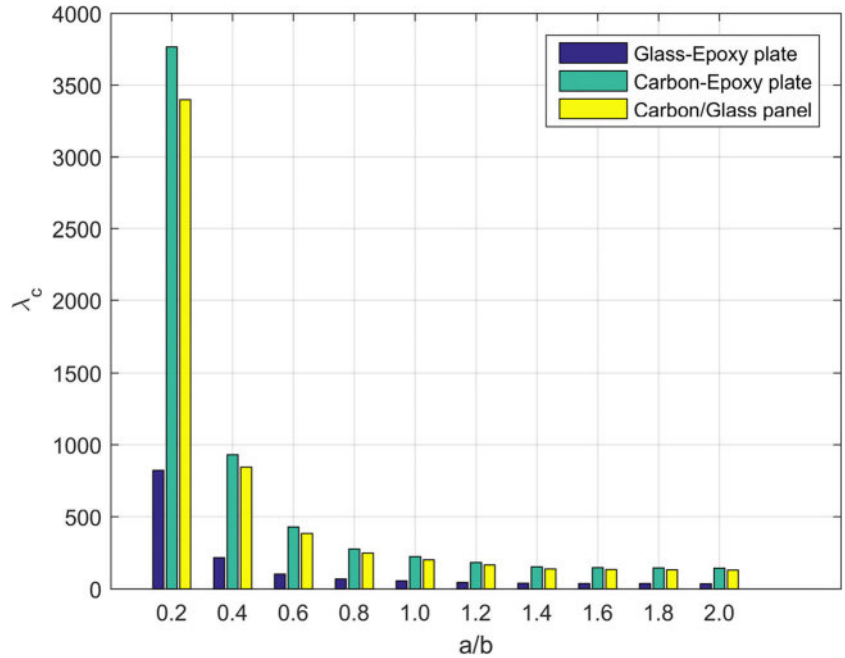

Fig. 9 Optimal values of buckling factors for the case of U_2 loading domain

4.3 An investigation on the effect of loading domain

Ratios of the buckling capacity subjected to circular domain (U_2) to those of subjected to triangular domain (U_1), are plotted in Fig. 11. This figure shows a V-shape behavior. In case that $\frac{a}{b} = 0.2$, the capacities of all materials for both loading domains are almost equal, while in other cases, the capacities corresponding to U_1 are higher than those of U_2.

When $\frac{a}{b} = 0.8, 1, 1.2,$ and 1.4, the ratios for different materials are almost equal. The minimum ratio is 70.7% which corresponds to $\frac{a}{b} = 1$ (square plate), and by moving away from this particular aspect ratio, the capacity ratios are increased.

4.4 A comparison among performance of the different optimization algorithms

Examining the primary statistical results showed that there is no meaningful difference between the utilized algorithms, and all the meta-heuristics strongly have found the global optima (see Tables 3, 4 and 5; 6–11). In order to find the algorithms which converged to the solution faster than the rest, their

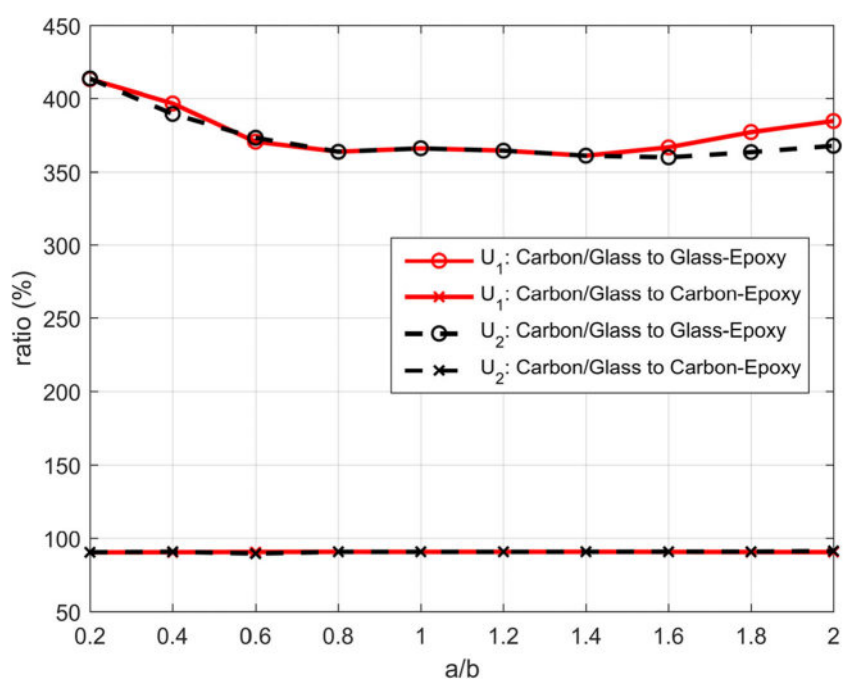

Fig. 10 The ratios of buckling capacity of the plates for both loading domains

Author's personal copy

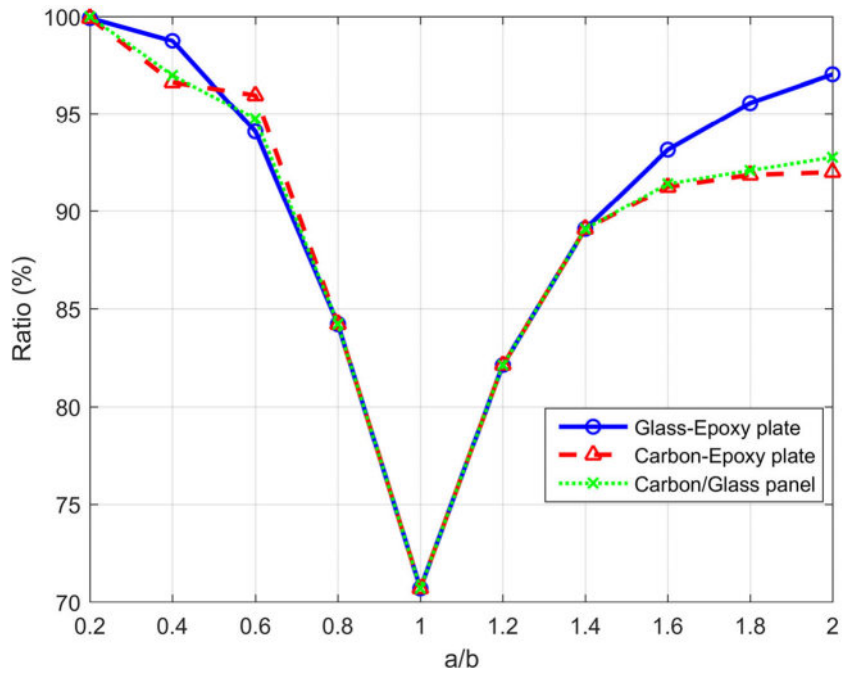

Fig. 11 The ratios of the results of U_2 loading domain to U_1

status were studied, when they have passed half of the path (2500 *NFE*). The average percent of independent runs which converged to the global optima are given in Table 6, and the best results are written in bold font. As indicated in Table 6, the optimum result can be found by all of the algorithms in this *NFE*, when $\frac{a}{b} = 0.8, 1, 1.2,$ and 1.4. This event may imply that the global optima in the mentioned aspect ratios are more accessible than others. This point can be confirmed by the results of Adali et al. (2003), in which, the Golden Section Search method has obtained the same buckling capacity of the present paper, while in other ratios it is trapped to local optima. It can be also seen from Table 6, that the proposed improved QEA algorithm obtained the best performance for lower aspect ratios ($\frac{a}{b} = 0.2, 0.4,$ and 0.6), while

Table 6 The average percent of convergence to global optima in half of the optimization procedure for different cases

Material	Loading domain	Aspect ratios	GA-Roulette wheel	GA-Tournament	QEA-Rotation gate	QEA-H_ϵ gate	QEA-iRotation gate
Glass-epoxy	U_1	0.2, 0.4, 0.6	**100**	88.89	97.78	97.78	**100**
		0.8, 1, 1.2, 1.4	**100**	**100**	**100**	**100**	**100**
		1.6, 1.8, 2	**98.89**	90	96.67	97.78	97.78
	U_2	0.2, 0.4, 0.6	**100**	88.89	97.78	97.78	**100**
		0.8, 1, 1.2, 1.4	**100**	**100**	**100**	**100**	**100**
		1.6, 1.8, 2	98.89	90	96.67	97.78	**100**
Carbon-epoxy	U_1	0.2, 0.4, 0.6	88.89	64.44	85.56	83.33	**90**
		0.8, 1, 1.2, 1.4	**100**	**100**	**100**	**100**	**100**
		1.6, 1.8, 2	94.44	60	97.78	**95.56**	82.22
	U_2	0.2, 0.4, 0.6	70	60	83.33	84.44	**86.67**
		0.8, 1, 1.2, 1.4	100	100	100	100	100
		1.6, 1.8, 2	94.44	55.56	94.44	**96.67**	**96.67**
Carbon/glass	U_1	0.2, 0.4, 0.6	68.89	64.44	68.89	71.11	**94.44**
		0.8, 1, 1.2, 1.4	**100**	**100**	**100**	**100**	**100**
		1.6, 1.8, 2	**95.56**	83.33	85.56	81.11	71.11
	U_2	0.2, 0.4, 0.6	97.78	82.22	**100**	98.89	**100**
		0.8, 1, 1.2, 1.4	**100**	**100**	**100**	**100**	**100**
		1.6, 1.8, 2	92.22	64.44	**97.78**	95.56	93.33

Author's personal copy

in higher aspect ratios ($\frac{a}{b} = 1.6, 1.8,$ and 2) the situation is different. According to Table 6, the improved QEA obtained the best result in 13 cases, which are equal to or higher than those of other compared algorithms. The GA-Roulette wheel also has suitable performance, but it must be noted that a further parameter setting task was performed to tune its internal parameters while QEA do not have any internal parameter and it can be implemented as a black-box optimizer, so this is another strength feature of this method.

5 Conclusions

The optimal robust arrangements for the stacking sequence of multilayered composites, under different loading conditions, were derived. For the first time, various versions of the QEA were employed for optimization of composite laminates. Moreover, a rank-based dynamical version of QEA was proposed. In order to verify and demonstrate the performance of the proposed algorithm, Roulette wheel, and Tournament selection, as two highly practical mechanisms were implemented in the well-known Genetic algorithm. The studied panels were made of 16-layered carbon-glass, glass-epoxy, and hybrid laminates with carbon-glass and glass-epoxy plies. Two distinct domains of loading conditions were considered as the sources of uncertainty. An anti-optimization process was embedded to find the worst case loading for robust design. The numerical results were examined from different perspectives, including the effect of the utilized materials, plate aspect ratios, and performance of the algorithms. As it can be seen from Figs. 8 and 9, carbon-epoxy plates, especially at lower aspect ratios, have the highest buckling capacity. It was observed in Fig. 11, that circular loading domain resulted in lower buckling loads, especially when the plate is square. According to Table 6, the optimal solutions of near square plates were more accessible than those of other aspect ratios. As provided in Tables 4 and 5, the utilized metaheuristics obtained higher or equal results in comparison with those of Adali et al. (2003). As discussed in Section 4.4, the proposed QEA generally converged faster than other algorithms. In contrary with the GA, the QEA do not have any internal parameter and it can be implemented as a black-box optimizer. Further investigations and sensitivity analyses were provided in Section 4.

Publisher's Note Springer Nature remains neutral with regard to jurisdictional claims in published maps and institutional affiliations.

References

Abrate S (1994) Optimal design of laminated plates and shells. Compos Struct 29:269–286

Adali S, Lene F, Duvaut G, Chiaruttini V (2003) Optimization of laminated composites subject to uncertain buckling loads. Compos Struct 62:261–269

Akmar AI, Kramer O, Rabczuk T (2017) Probabilistic multi-scale optimization of hybrid laminated composites. Compos Struct 184:1111–1125. https://doi.org/10.1016/j.compstruct.2017.10.032

Arora JS (2017) Chapter 17 - nature-inspired search methods. In: Arora JS (ed) Introduction to optimum design, 4th edn. Academic, Boston, pp 739–769. https://doi.org/10.1016/B978-0-12-800806-5.00017-2

Çarbaş S, Saka MP (2012) Optimum topology design of various geometrically nonlinear latticed domes using improved harmony search method. Struct Multidiscip Optim 45:377–399

de Almeida FS (2016) Stacking sequence optimization for maximum buckling load of composite plates using harmony search algorithm. Compos Struct 143:287–299

Elishakoff I, Haftka R, Fang J (1994) Structural design under bounded uncertainty—optimization with anti-optimization. Comput Struct 53:1401–1405

Fang C, Springer GS (1993) Design of composite laminates by a Monte Carlo method. J Compos Mater 27:721–753

Fukunaga H, Sekine H, Sato M, Iino A (1995) Buckling design of symmetrically laminated plates using lamination parameters. Comput Struct 57:643–649. https://doi.org/10.1016/0045-7949(95)00050-Q

Ghiasi H, Pasini D, Lessard L (2009) Optimum stacking sequence design of composite materials part I: constant stiffness design. Compos Struct 90:1–11. https://doi.org/10.1016/j.compstruct.2009.01.006

Ghiasi H, Fayazbakhsh K, Pasini D, Lessard L (2010) Optimum stacking sequence design of composite materials part II: variable stiffness design. Compos Struct 93:1–13

Goldberg DE, Deb K (1991) A comparative analysis of selection schemes used in genetic algorithms. In: Foundations of genetic algorithms, vol 1. Elsevier, New York, pp 69–93

Goldberg DE, Holland JH (1988) Genetic algorithms and machine learning. Mach Learn 3:95–99

Haftka RT, Gürdal Z (2012) Elements of structural optimization. Springer, Dordrecht. https://doi.org/10.1007/978-94-011-2550-5

Han K-H, Kim J-H (2002) Quantum-inspired evolutionary algorithm for a class of combinatorial optimization. IEEE Trans Evol Comput 6: 580–593

Hey T (1999) Quantum computing: an introduction. Comput Control Eng J 10:105–112

Holland JH (1992) Adaptation in natural and artificial systems: an introductory analysis with applications to biology, control, and artificial intelligence, 2nd edn. MIT Press, Cambridge

Huang J, Haftka R (2005) Optimization of fiber orientations near a hole for increased load-carrying capacity of composite laminates. Struct Multidiscip Optim 30:335–341

Hussain K, Salleh MNM, Cheng S, Shi Y (2018) Metaheuristic research: a comprehensive survey. Artif Intell Rev:1–43

Kalantari M, Dong C, Davies IJ (2017) Effect of matrix voids, fibre misalignment and thickness variation on multi-objective robust optimization of carbon/glass fibre-reinforced hybrid composites under flexural loading. Compos Part B 123:136–147

Kaveh A (2017a) Advances in metaheuristic algorithms for optimal design of structures, 2nd edn. Springer International Publishing, Basel

Kaveh A (2017b) Applications of metaheuristic optimization algorithms in civil engineering Springer, Switzerland

Kaveh A, Dadras A (2017) A novel meta-heuristic optimization algorithm: thermal exchange optimization. Adv Eng Softw 110:69–84. https://doi.org/10.1016/j.advengsoft.2017.03.014

Kaveh A, Ilchi Ghazaan M (2015) A comparative study of CBO and ECBO for optimal design of skeletal structures. Comput Struct 153:137–147

Kaveh A, Dadras A, Malek NG (2018) Buckling load of laminated composite plates using three variants of the biogeography-based

Author's personal copy

optimization algorithm. Acta Mech 229:1551–1566. https://doi.org/10.1007/s00707-017-2068-0

Lee D, Morillo C, Oller S, Bugeda G, Oñate E (2013) Robust design optimisation of advance hybrid (fiber–metal) composite structures. Compos Struct 99:181–192

Liu B, Haftka R, Trompette P (2004) Maximization of buckling loads of composite panels using flexural lamination parameters. Struct Multidiscip Optim 26:28–36

Liu D, Toropov VV, Barton DC, Querin OM (2015) Weight and mechanical performance optimization of blended composite wing panels using lamination parameters. Struct Multidiscip Optim 52:549–562

Lombardi M, Haftka RT (1998) Anti-optimization technique for structural design under load uncertainties. Comput Methods Appl Mech Eng 157:19–31

Nemeth MP (1986) Importance of anisotropy on buckling of compression-loaded symmetric composite plates. AIAA J 24: 1831–1835

Reddy JN (2004) Mechanics of laminated composite plates and shells: theory and analysis, 2nd edn. CRC Press, Boca Raton

Reis P, Ferreira J, Antunes F, Costa J (2007) Flexural behaviour of hybrid laminated composites. Compos A Appl Sci Manuf 38:1612–1620

Saka M, Erdal F (2009) Harmony search based algorithm for the optimum design of grillage systems to LRFD-AISC. Struct Multidiscip Optim 38:25–41

Setoodeh S, Abdalla MM, Gürdal Z (2006) Design of variable–stiffness laminates using lamination parameters. Compos Part B 37:301–309

Sivanandam S, Deepa S (2007) Introduction to genetic algorithms. Springer Science & Business Media, Berlin

Sivanandam S, Deepa S (2008) Genetic algorithm optimization problems. In: Introduction to genetic algorithms. Springer, Berlin, pp 165–209

Soremekun G, Gürdal Z, Haftka R, Watson L (2001) Composite laminate design optimization by genetic algorithm with generalized elitist selection. Comput Struct 79:131–143

Tejani GG, Savsani VJ, Patel VK (2016) Adaptive symbiotic organisms search (SOS) algorithm for structural design optimization. J Comput Des Eng 3:226–249

Venkataraman S, Haftka RT (1999) Optimization of composite panels-a review. In: Proc Amer Soc Compos. pp 479–488

Check for updates

JOURNAL OF SANDWICH STRUCTURES & MATERIALS

Original Article

Journal of Sandwich Structures & Materials
0(0) 1–29
© The Author(s) 2018
Reprints and permissions:
sagepub.co.uk/journalsPermissions.nav
DOI: 10.1177/1099636218778998
journals.sagepub.com/home/jsm
SAGE

Effects of the impactor geometrical shape on the non-linear low-velocity impact response of sandwich plate with CNTRC face sheets

A Khalkhali, N Geran Malek and M Bozorgi Nejad

Abstract

In this study, non-linear low-velocity impact response of a simply supported sandwich plate with CNTRC face sheets subjected to the impactors with different geometrical shapes is investigated. It has been assumed that the sandwich plate is made up of two face sheets reinforced with CNTs graded along their thickness as X profile and a homogeneous core. In CNT-reinforced layers, a micromechanical model has been used to obtain the effective material properties and the analysis is performed in the framework of the Reddy's higher order shear deformation theory with regard to thermal effects. An analytical model is proposed to capture the response performance of the three-layer sandwich plates under different thermal environments. Through the proposed analytical study, in order to characterize the contact force between the sandwich plate and the impactors, the modified Hertz contact law is utilized. Rayleigh-Ritz method is applied to the Hamilton principle in order to find the set of equations of motion for the impactor as well as the CNTRC sandwich plate. Afterwards, the solution in the time domain is obtained based on Newmark's numerical time integration scheme. After validating the proposed approach, in order to examine the influences of various involved parameters, different parametric studies are

Automotive Simulation and Optimal Design Research Laboratory, School of Automotive Engineering, Iran University of Science and Technology, Tehran, Iran

Corresponding author:
A Khalkhali, Automotive Simulation and Optimal Design Research Laboratory, School of Automotive Engineering, Iran University of Science and Technology, Tehran 16846-13114, Iran.
Email: ab_khalkhali@iust.ac.ir

conducted. It has been demonstrated that the variation of the initial kinetic energy as one of the parameters under study has a significant effect on the central displacement, contact force, and indentation in both conical and cylindrical impactors and the change in the radius of the cylinder has an insignificant effect on the central displacement. As well, in the case of equal masses, the cylindrical impactor causes more amount of indentation with respect to conical.

Keywords
Impact analysis, impactor shape, nanotube-reinforced composites, thermal environment, sandwich plates

Introduction

Due to the high capability of being tailored to meet the desired applications, composite materials have attracted much attention from scientists. Sandwich structures, owing to their remarkable characteristics, such as high strength to weight and stiffness to weight ratios become one of the most widely used alternatives for crucial structural components [1–4].

Deterioration of mechanical properties with more percent contribution of reinforcement beyond a defined limit, and overcoming the practical problem of sharp discontinuity at the interfaces of laminated composite materials, leads to the use of functionally graded material's (FGM) concept. FGM is a reasonable alternative to traditional fiber-reinforced composite (FRC), because of its capability to being optimized along the thickness in order to meet the desired requirements [5]. Since the discovery of carbon nanotube (CNT) by Iijima [6] in 1991, considerable research has been done on the performance and properties of these distinct types of material. The previous researchers have shown widespread applications of the CNTs due to its outperforming mechanical, electrical and thermal characteristics with respect to many other reinforcements. As a high potential filler, and in the framework of FGM concept, the outstanding features of CNTs become more evident. Several types of researches have been conducted to elucidate vibration [7–9] bending [10–12] buckling and post-buckling [13,14] behavior of FGM. Many previous studies also have pointed out the better performance of X profile distribution of CNTs in the face sheets compared to other distributions such as FG-O, FG-A, and FG-V [5,15,16].

Numerous studies have been conducted on the impact behavior of FGM plate structures using both analytical and numerical methods and most have focused on the spherical impactor as the geometry of indenter. For example, molecular dynamics(MD)-based FEM simulation of single-wall carbon nanotube (SWCNT)

embedded in polymer RVE was investigated by Khalili and Haghbin [17]. They studied the effect of volume fraction, diameter and chirality of single-wall carbon nanotube reinforced composite (SWCNTRC) on impact response for different RVEs. They showed that even with adding a few CNTs, impact behavior is greatly improved. Shariyat and Farzan Nasab [18] studied an eccentrically impact response of a functionally graded plate with fully/partially supported edges in the presence of an elastic foundation based on first-order shear deformation theory(FSDT). In an investigation by Najafi et al. [19], impact response of simply supported FGM doubly curved panels within the framework of Reddy's Higher order shear deformation theory [20], in the presence of elastic foundation was investigated. Such a study was first performed by Shen et al. [21] on nonlinear bending of FG-CNTRC plates under a transverse uniform or sinusoidal loads. Malekzadeh Fard et al. [4] proposed an analytical discrete spring-mass phenomenon for the low-velocity impact of rigid blunted cylinder. Utilizing the minimization of total potential energy, the contact force-indentation rule was presented.

Both in the manufacturing and operating stage conditions, laminated composite plates may be subjected to impacts along with thermal conditions. Little evidence is available for the investigation on the subject of impact in thermal conditions. For instance, thick FGM beam under thermal environment effects with arbitrary edge supports investigated by Kiani et al. [22]. Contact force histories for multiple impacts were derived and also they examined the position of the impact. Shen and Xiang [7] studied the thermal post-buckling behavior of simply supported FG-CNTRC beams by employing two-step perturbation approach, based on third-order shear deformable beam formulation. Thermal environment effects of the low-velocity impact response of FGM plates on simply supported edges was studied by Khalili et al. [23] with the assumption of linearized contact law. Wang et al. [15] investigated the thermal field effects on the low-velocity impact response of CNTRC sandwich plates based on a refined Hertzian contact law. Recently, Golmakani and Zeighami [24] employed dynamic relaxation to solve the bending problem of FG-CNTRC plate.

Compared to all the researches being conducted, little evidence is available for the geometry effect study of indentor with numerical analysis, in the case of sandwich structure and in the presence of thermal filed. Among them, most have focused only on the experimental approach. Recently, Kursun et al. [25] experimentally studied the effect of impactor shape on the performance of aluminum sheets with a polyethylene core sandwich composite plates in the low-velocity impact and showed the absolute dependence of impact response and failure modes on the impactor shape. In regard to hybrid corrugated core sandwich structures with CFRP face sheets, He et al. [13] performed a numerical (simulation) and experimental study and investigate the effect of impactor shape on low-velocity impact behavior. Due to the effect of impactor geometry on the impact response and damage mechanisms of structures, evaluating the effect of impactor shape on low-velocity impact behavior of these structures is necessary [25,26].

Current investigation deals with the effect of impactor geometrical shape on the non-linear low-velocity impact response of FG-CNTRC sandwich plate subjected to three different categories of impactor shape. Spherical, conical, and cylindrical geometries were three different types of geometry that are considered to examine the responses. All four edges of the plate are simply supported. It has been assumed that the sandwich plate, made up of two face sheets reinforced with CNTs which is graded along their thickness as X profile, and a homogeneous core. Displacement field is introduced through the Reddy's higher order shear deformation theory considering the thermal environmental effects. Thermal effects are also taking into account, and the composition of the CNTRC layers of the sandwich panel are assumed to be temperature dependent. Rayleigh-Ritz method applied to the Hamilton principle in order to find the set of equations of motion for the impactor as well as the CNTRC sandwich plate.

Problem statement

In this paper, impact response of a sandwich plate with CNTRC face sheets subjected to the impactors with different geometries, including spherical, conical, and cylindrical geometries is analyzed. The configuration of the investigated sandwich plate is considered according to Wang et al. [15] to be able to verify the results of the current study. The entire derivation is based on linear elasticity and the material behavior is considered as linear elastic. In Figure 1, the configuration of the sandwich plate, the coordinate system, as well as the impactors are shown. The coordinate system is represented in Figure 1(a), where its origin is located at the mid-plane corner of the core and the Z-axis is downward. As shown in Figure 1, the rectangular sandwich plate is composed of two composite face sheets and one homogeneous core. Further, non-uniform FG-X distribution is considered as the profile type of functionally graded nanocomposite face sheets. In such distribution, face sheets are reinforced with CNTs which is graded along their thickness as X profile. In this particular type of distribution, as already shown in Figure 1(a), symmetric distribution of CNTs are applied relative to the mid-plane of the sheets, and it is assumed that the interior and exterior surface layers are CNT-riched. Consequently, the percentage of CNTs in the face sheets is calculated according to equation (1).

$$V_{CNT} = 2\left(\frac{2|z|}{t_f}\right)V^*_{CNT} \tag{1}$$

In which, z is the distance from the center of the plate and V^*_{CNT} is the CNTs volume fraction. The effective FG-CNTRC material properties are evaluated using the extended rule of mixture which can be expressed as follow [27]

$$E_{11} = \eta_1 V_{CNT} E_{11}^{CNT} + V_m E^m \tag{2}$$

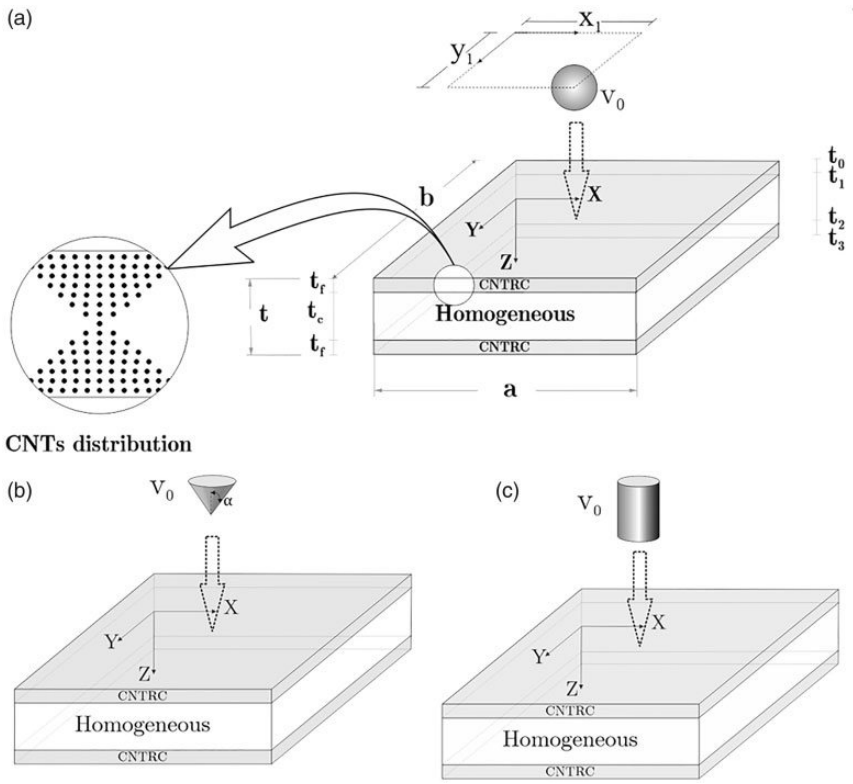

Figure 1. Low-velocity impact of a sandwich plate: (a) Configuration of the plate along with dimensions and coordinate system, subjected to spherical impactor, (b) Conical impactor, (c) Cylindrical impactor.

$$\frac{\eta_2}{E_{22}} = \frac{V_{CNT}}{E_{22}^{CNT}} + \frac{V_m}{E^m} \tag{3}$$

$$\frac{\eta_3}{G_{12}} = \frac{V_{CNT}}{G_{12}^{CNT}} + \frac{V_m}{G^m} \tag{4}$$

$$\rho = V_{CNT}\rho^{CNT} + V_m\rho^m \tag{5}$$

$$\nu_{12} = V_{CNT}^{*}\ \nu^{CNT} + V_m\nu^m \tag{6}$$

where $\eta_j (j = 1, 2, 3)$ are the CNT efficiency parameters. E^m, G^m, E_{11}^{CNT}, E_{22}^{CNT}, and G_{12}^{CNT} are the Young's and shear moduli of the matrix. E_{11}^{CNT}, E_{22}^{CNT}, and G_{12}^{CNT} are the corresponding Young's and shear moduli for the CNTs, respectively.

In addition, V_m and V_{CNT} which satisfy the $V_m + V_{CNT} = 1$ condition, are the volume fractions corresponding to CNT and matrix, respectively. Moreover, ν_{12} and ρ are the effective Poisson's ratio and density, respectively.

In the present study, the sandwich plate with CNTRC face sheets is exposed to various thermal conditions. Longitudinal and transverse thermal expansion coefficients can be expressed as

$$\alpha_{11} = \frac{V_{CNT}E_{11}^{CNT}\alpha_{11}^{CNT} + V_m E^m \alpha^m}{V_{CNT}E_{11}^{CNT} + V_m E^m} \tag{7}$$

$$\alpha_{22} = \left(1 + \nu_{12}^{CNT}\right) V_{CNT}\alpha_{22}^{CNT} + \left(1 + \nu^m\right) V_m \alpha^m - \nu_{12}\alpha_{11} \tag{8}$$

In the above equations, α^m, ν_{12}^{CNT}, α_{11}^{CNT}, and α_{22}^{CNT} denote the thermal expansion coefficient of the matrix, Poisson's ratios of CNT, and the thermal expansion coefficients of CNTs along the longitudinal and transverse directions, respectively. Length and width of the sandwich plate, the thickness of the face sheets, core and the total thickness of the plate are denoted by a, b, t_f, t_c, and t, respectively.

To solve the impact problem, as shown in Figure 1, high-order shear deformation theories [20] are used. Through the proposed analyses, based on Reddy's high-order shear deformation theory, the displacement field components are derived as follows [20]

$$u(x, y, z, t) = u_0(x, y, t) + z\phi_x(x, y, t) - \frac{4z^3}{3h^2}\left(\phi_x + \frac{\partial w_0}{\partial x}\right) \tag{9}$$

$$v(x, y, z, t) = v_0(x, y, t) + z\phi_y(x, y, t) - \frac{4z^3}{3h^2}\left(\phi_y + \frac{\partial w_0}{\partial y}\right) \tag{10}$$

$$w(x, y, z, t) = w_0(x, y, t) \tag{11}$$

where u_0, v_0, and w_0 are the sandwich plate mid-plane displacements along X, Y, and Z directions, respectively. ϕ_x and ϕ_y denote the slopes of a transverse normal at $Z = 0$. Equation (11) suggests that the problem is analyzed as plane strain. While, according to the displacement field components (equations (1) through (3)), strains can be expressed as [20]

$$\begin{Bmatrix} \varepsilon_{xx} \\ \varepsilon_{yy} \\ \gamma_{xy} \end{Bmatrix} = \begin{Bmatrix} \varepsilon_{xx}^{(0)} \\ \varepsilon_{yy}^{(0)} \\ \gamma_{xy}^{(0)} \end{Bmatrix} + z\begin{Bmatrix} \varepsilon_{xx}^{(1)} \\ \varepsilon_{yy}^{(1)} \\ \gamma_{xy}^{(1)} \end{Bmatrix} + z^3\begin{Bmatrix} \varepsilon_{xx}^{(3)} \\ \varepsilon_{yy}^{(3)} \\ \gamma_{xy}^{(3)} \end{Bmatrix} \tag{12}$$

$$\begin{Bmatrix} \gamma_{yz} \\ \gamma_{xz} \end{Bmatrix} = \begin{Bmatrix} \gamma_{yz}^{(0)} \\ \gamma_{xz}^{(0)} \end{Bmatrix} + z^2 \begin{Bmatrix} \gamma_{yz}^{(2)} \\ \gamma_{xz}^{(2)} \end{Bmatrix} \tag{13}$$

$$\begin{Bmatrix} \varepsilon_{xx}^{(0)} \\ \varepsilon_{yy}^{(0)} \\ \gamma_{xy}^{(0)} \end{Bmatrix} = \begin{Bmatrix} \dfrac{\partial u_0}{\partial x} \\ \dfrac{\partial v_0}{\partial y} \\ \dfrac{\partial u_0}{\partial y} + \dfrac{\partial v_0}{\partial x} \end{Bmatrix}, \quad \begin{Bmatrix} \varepsilon_{xx}^{(1)} \\ \varepsilon_{yy}^{(1)} \\ \gamma_{xy}^{(1)} \end{Bmatrix} = \begin{Bmatrix} \dfrac{\partial \phi_x}{\partial x} \\ \dfrac{\partial \phi_y}{\partial y} \\ \dfrac{\partial \phi_x}{\partial y} + \dfrac{\partial \phi_y}{\partial x} \end{Bmatrix} \tag{14}$$

$$\begin{Bmatrix} \varepsilon_{xx}^{(3)} \\ \varepsilon_{yy}^{(3)} \\ \gamma_{xy}^{(3)} \end{Bmatrix} = -c_1 \begin{Bmatrix} \left(\dfrac{\partial \phi_x}{\partial x} + \dfrac{\partial^2 w_0}{\partial x^2} \right) \\ \left(\dfrac{\partial \phi_y}{\partial y} + \dfrac{\partial^2 w_0}{\partial y^2} \right) \\ \left(\dfrac{\partial \phi_x}{\partial y} + \dfrac{\partial \phi_y}{\partial x} + 2\dfrac{\partial^2 w_0}{\partial x \partial y} \right) \end{Bmatrix} \tag{15}$$

$$\begin{Bmatrix} \gamma_{yz}^{(0)} \\ \gamma_{xz}^{(0)} \end{Bmatrix} = \begin{Bmatrix} \phi_y + \dfrac{\partial w_0}{\partial y} \\ \phi_x + \dfrac{\partial w_0}{\partial x} \end{Bmatrix}, \quad \begin{Bmatrix} \gamma_{yz}^{(2)} \\ \gamma_{xz}^{(2)} \end{Bmatrix} = -c_2 \begin{Bmatrix} \left(\phi_y + \dfrac{\partial w_0}{\partial y} \right) \\ \left(\phi_x + \dfrac{\partial w_0}{\partial x} \right) \end{Bmatrix} \tag{16}$$

$$c_1 = \frac{4}{3h^2}, \quad c_2 = 3c_1 = \frac{4}{h^2} \tag{17}$$

Therefore, in-plane and transverse stresses at a point on the sandwich plate can be written as

$$\begin{Bmatrix} \sigma_{xx} \\ \sigma_{yy} \\ \sigma_{xy} \end{Bmatrix} = \begin{bmatrix} Q_{11} & Q_{12} & 0 \\ Q_{12} & Q_{22} & 0 \\ 0 & 0 & Q_{66} \end{bmatrix} \begin{Bmatrix} \varepsilon_{xx} \\ \varepsilon_{yy} \\ \gamma_{xy} \end{Bmatrix} \tag{18}$$

$$\begin{Bmatrix} \sigma_{yz} \\ \sigma_{xz} \end{Bmatrix} = \begin{bmatrix} Q_{44} & 0 \\ 0 & Q_{55} \end{bmatrix} \begin{Bmatrix} \gamma_{yz} \\ \gamma_{xz} \end{Bmatrix} \tag{19}$$

where Q_{ij} are the stiffness coefficients, which can be evaluated by means of the following expressions

$$Q_{11} = \frac{E_1}{1 - \upsilon_{12}\upsilon_{21}} \quad Q_{12} = \frac{\upsilon_{12}E_2}{1 - \upsilon_{12}\upsilon_{21}} \quad Q_{22} = \frac{E_2}{1 - \upsilon_{12}\upsilon_{21}} \tag{20}$$

$$Q_{66} = G_{12} \quad Q_{44} = G_{23} \quad Q_{55} = G_{13}$$

In the above equations, E_1, E_2, and G_{12} are longitudinal Young's modulus, transverse Young's modulus, and shear modulus, and υ_{12} and υ_{21} are Poisson constants of the orthotropic layer, respectively. The equations of motion of the third-order plate theory could be derived using Hamilton's principle, as one of the most powerful energy principles, which is [20]

$$0 = \int (\delta U + \delta V - \delta K)\mathrm{d}t \tag{21}$$

where δU, δV, and δK are virtual strain energy, virtual work done by the applied forces and virtual kinetic energy, respectively. By means of applying Hamilton's principle, Euler-Lagrange equations then can be obtained as [20]

$$\frac{\partial N_{xx}}{\partial x} + \frac{\partial N_{xy}}{\partial y} = I_0\ddot{u}_0 \tag{22}$$

$$\frac{\partial N_{xy}}{\partial x} + \frac{\partial N_{yy}}{\partial y} = I_0\ddot{v}_0 \tag{23}$$

$$\frac{\partial \overline{Q}_x}{\partial x} + \frac{\partial \overline{Q}_y}{\partial y} + c_1\left(\frac{\partial^2 P_{xx}}{\partial x^2} + 2\frac{\partial^2 P_{xy}}{\partial x \partial y} + \frac{\partial^2 P_{yy}}{\partial y^2}\right) + q - kw_0$$

$$= I_0\ddot{w}_0 - c_1^2 I_6\left(\frac{\partial^2 \ddot{w}_0}{\partial x^2} + \frac{\partial^2 \ddot{w}_0}{\partial y^2}\right) + c_1 J_4\left(\frac{\ddot{\phi}_x}{\partial x} + \frac{\ddot{\phi}_y}{\partial y}\right) \tag{24}$$

$$\frac{\partial \overline{M}_{xx}}{\partial x} + \frac{\partial \overline{M}_{xy}}{\partial y} - \overline{Q}_x = K_2\ddot{\phi}_x - c_1 J_4\frac{\partial \ddot{w}_0}{\partial x} \tag{25}$$

$$\frac{\partial \overline{M}_{xy}}{\partial x} + \frac{\partial \overline{M}_{yy}}{\partial y} - \overline{Q}_y = K_2\ddot{\phi}_y - c_1 J_4\frac{\partial \ddot{w}_0}{\partial y} \tag{26}$$

In the above equations, $\overline{M}_{xx}$, $\overline{M}_{xy}$, and $\overline{M}_{xy}$ are average bending moments, $\overline{Q}_x$, and $\overline{Q}_y$ are transformed elastic constants, and N_{xx}, N_{xy}, and N_{yy} are in-plane loading which is caused by mechanical as well as thermal loading. In the thermal environment, the in-plane forces, moments and higher order moments matrices, caused by temperature rising can be defined as follows [21]

$$\begin{bmatrix} N_x^T \\ N_y^T \\ N_{xy}^T \end{bmatrix} = \int_{-\frac{h}{2}}^{\frac{h}{2}} \begin{bmatrix} Q_{11}\alpha_x & Q_{12}\alpha_y & Q_{16}\alpha_{xy} \\ Q_{12}\alpha_x & Q_{22}\alpha_y & Q_{26}\alpha_{xy} \\ Q_{16}\alpha_x & Q_{26}\alpha_y & Q_{66}\alpha_{xy} \end{bmatrix} \Delta T \mathrm{d}z \tag{27}$$

$$\begin{bmatrix} M_x^T \\ M_y^T \\ M_{xy}^T \end{bmatrix} = \int_{-\frac{h}{2}}^{\frac{h}{2}} \begin{bmatrix} Q_{11} & Q_{12} & Q_{16} \\ Q_{12} & Q_{22} & Q_{26} \\ Q_{16} & Q_{26} & Q_{66} \end{bmatrix} \begin{bmatrix} \alpha_x \\ \alpha_y \\ \alpha_{xy} \end{bmatrix} \Delta T \mathrm{d}z \tag{28}$$

$$\begin{bmatrix} P_x^T \\ P_y^T \\ P_{xy}^T \end{bmatrix} = \int_{-\frac{h}{2}}^{\frac{h}{2}} \begin{bmatrix} Q_{11} & Q_{12} & Q_{16} \\ Q_{12} & Q_{22} & Q_{26} \\ Q_{16} & Q_{26} & Q_{66} \end{bmatrix} \begin{bmatrix} \alpha_x \\ \alpha_y \\ \alpha_{xy} \end{bmatrix} z^3 \Delta T \mathrm{d}z \tag{29}$$

Dynamics of the impactors

During the loading phase, local contact indentation ($d(t)$) can be defined according to equation (30)

$$d(t) = \overline{S}(t) - \overline{W}(X, Y, t) \tag{30}$$

where $\overline{S}(t)$ and $\overline{W}(X, Y, t)$ denote the displacement of the impactor and the deflection of the plate at the impact location, respectively. Hence, the equation of motion for the impactor body is expressed as

$$m^i \ddot{\overline{S}}(t) + P_c(t) = 0, \ \overline{S}(0) = 0, \ \dot{\overline{S}}(0) = V_0 \tag{31}$$

where m^i is the mass of the impactor, $P_c(t)$ is the contact force during the unloading phase, and V_0 is its initial velocity. Figure 2 schematically depicts the contact characteristics of an elastic sphere with an elastic half-space. The expressions of normal forces and pressure distributions for the three different geometries are listed in Table 1 [28]. In which, d is the depth of indentation, a is the contact radius, R is the radius of the elastic sphere, E_1 is the elastic modulus

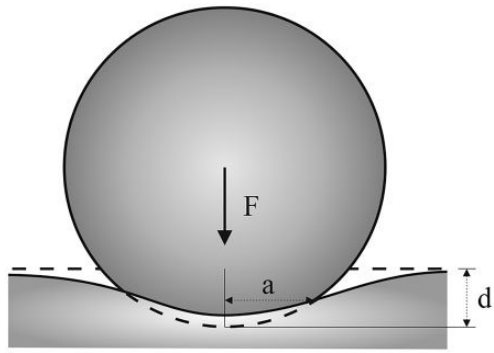

Figure 2. Schematic representation of elastic sphere contacting with an elastic half-space.

Table 1. Pressure distribution and normal force combinations for the three different shapes of impactor.

	Pressure distribution	Normal force	
Sphere	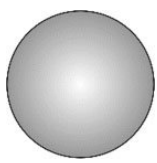	$p(r) = p_0\left(1 - \frac{r^2}{a^2}\right)^{1/2}; p_0 = \frac{3F}{2\pi a^2}$ [28]	$F = \frac{4}{3}E^* R^{1/2} d^{3/2}$; $\frac{1}{E^*} = \frac{(1-\nu_1^2)}{E_1} + \frac{(1-\nu_2^2)}{E_2}$ [29]
Cone	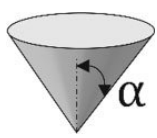	$p(r) = \frac{Ed}{\pi a(1-\nu^2)} \ln \times \left(\frac{a}{r} + \sqrt{\left(\frac{a}{r}\right)^2 - 1}\right) = \frac{Ed}{\pi a(1-\nu^2)} \cosh^{-1}\left(\frac{a}{r}\right)$	$F = \frac{\pi E}{2(1-\nu^2)} a^2 \tan(\theta) = \frac{\pi E}{\pi(1-\nu^2)} \frac{d^2}{\tan(\theta)}$; $\theta = 90 - \alpha$ [32]
Cylinder		$p(r) = p_0\left(1 - \frac{r^2}{a^2}\right)^{-1/2}$	$F = 2aE^* d$; $\frac{1}{E^*} = \frac{(1-\nu_1^2)}{E_1} + \frac{(1-\nu_2^2)}{E_2}$ [30]

of the indenter body, E_2 is the elastic modulus of the half-space, and also υ_1 and υ_2 are Poisson's ratios associated with each of the elastic bodies. For the case of the cylindrical indenter, contact radius, a, is the same as the radius of the elastic cylinder. Moreover, for conical indenter, depth of indentation d and contact radius a are related by the expression $d = a(\pi/2)\tan(\theta)$.

Solution procedure

Implementing Rayleigh-Ritz method leads to obtaining a differential system of equations from the system of partial differential equations as described in equation (32).

$$\begin{bmatrix} [m_1] & [0] & [0] & [0] & [0] \\ [0] & [m_2] & [0] & [0] & [0] \\ [0] & [0] & [m_3] & [m_4] & [m_5] \\ [0] & [0] & [m_6] & [m_7] & [0] \\ [0] & [0] & [m_8] & [0] & [m_9] \end{bmatrix} \begin{bmatrix} [\ddot{u}] \\ [\ddot{v}] \\ [\ddot{w}] \\ [\ddot{\varphi}_x] \\ [\ddot{\varphi}_y] \end{bmatrix} + \begin{bmatrix} [k_1] & [k_2] & [0] & [0] & [0] \\ [k_3] & [k_4] & [0] & [0] & [0] \\ [0] & [0] & [k_5] & [k_6] & [k_7] \\ [0] & [0] & [k_8] & [k_9] & [k_{10}] \\ [0] & [0] & [k_{11}] & [k_{12}] & [k_{13}] \end{bmatrix}$$

$$\times \begin{bmatrix} [wj] \\ [vj] \\ [wj] \\ [\varphi_{xj}] \\ [\varphi_{xj}] \end{bmatrix} = \begin{bmatrix} F_1 \\ F_2 \\ F_3 \\ F_4 \\ F_5 \end{bmatrix} \tag{32}$$

Equation (32) can be written in the matrix form as

$$[M]\{\ddot{X}\} + [K]\{X\} = \{F\} \tag{33}$$

In equation (33), $[M]$, $[K]$, and $[F]$ are completely defined and described in Appendixes 1-3. The solution in the time domain for the time-dependent terms of equation (33) is obtained based on Newmark's numerical time integration scheme.

Results and discussion

The main aim of this study is to investigate the effect of impactor geometrical shape on the non-linear low-velocity impact response of sandwich plate with

Table 2. Material properties of polymethylmethacrylate(PMMA) as the matrix phase ($\Delta T = T - 300$).

$E^m(GPa)$	ν^m	$\rho^m(\mathrm{kg/m^3})$	$\alpha^m(\times 10^{-6}/\mathrm{K})$
$(3.52 - 0.0034(300 + \Delta T))$	*0.34*	*1150*	$45(1 + 0.0005 - \Delta T)$

Table 3. SWCNT material properties in different thermal fields [21].

Temperature (K)	E_{11}^{CNT}(TPa)	E_{22}^{CNT}(TPa)	G_{12}^{CNT}(TPa)	$\alpha_{12}^{CNT}(\times 10^{-6}/\mathrm{K})$	$\alpha_{22}^{CNT}(\times 10^{-6}/\mathrm{K})$
300	5.6466	7.0800	1.9445	3.4584	5.1682
500	5.5308	6.9348	1.9643	4.5361	5.0189
700	5.4744	6.8641	1.9644	4.6677	4.8943

CNTRC face sheets in thermal environments. In this section, to validate the present model, numerical results for the single layer nanotube-reinforced composite plate are first presented and compared with the results [15]. Secondly, results for the sandwich plate with CNTRC face sheets subjected to cylindrical and conical impactors are then presented and fully discussed. Matrix phase of the face sheets is Poly Methyl Methacrylate (PMMA), which its material properties are listed in Table 2. For the rest of the paper, all the impactors are considered made of steel, with the elastic modulus, Poisson's ratio, density, and mass of $E^i = 207$ GPa, $\upsilon^i = 0.3$, $\rho^i = 7960$ kg/m^3, and $m = 0.0085$ kg, respectively.

Titanium Ti-6Al-4V is considered as the homogeneous core material, with the Poisson's ratio (ν_c) and density (ρ_c) of 0.29 and 4429 K/m^3, respectively. Thermal expansion coefficient $\alpha_c = 7.5788 \times (1 + 6.638 \times 10^{-4}T - 3.147 \times 10^{-6}T^2) \times 10^{-6}$K and Young's modulus $E_c = 122.56 \times (1 - 4.586 \times 10^{-4})$ GPa are assumed to be nonlinear functions of temperature [31]. Material properties of SWCNT are depended on size, chirality, and temperature [21]. In this study, the single-wall carbon nanotube with the indexes of (10, 10) was selected as a reinforcing phase for the nanocomposite face sheets. For the computational purpose, elastic moduli and thermal expansion coefficients of SWCNT, which is obtained by MD simulations [21], are represented in Table 3.

The efficiency parameters of CNT, η_i (i = 1, 2, 3), can be obtained by matching the values determined from the extended rule of mixtures with the corresponding values of MD simulations [15]. The values considered in this paper for the efficiency parameters of CNT are represented in Table 4, according to the values reported previously in Shen and Zhang [27]. In addition, it is assumed that $G_{12} = G_{13}$, as well as $G_{23} = 1.2\ G_{12}$ [32].

In order to verify the validity of the present work, nonlinear low-velocity impact analysis of temperature-dependent nanotube-reinforced composite plates subjected to spherical impactor considered by Wang et al. [15] is resolved. Rigid impactor with the diameter of 12.7 mm and density of 7960 kg/m^3, which is striking at the

Table 4. Values of the CNT/matrix efficiency parameters for different volume fractions of CNTs [15].

V^*_{CNT}	η_1	η_2	η_3
0.12	0.137	1.022	0.715
0.17	0.142	1.626	1.138
0.28	0.141	1.585	1.109

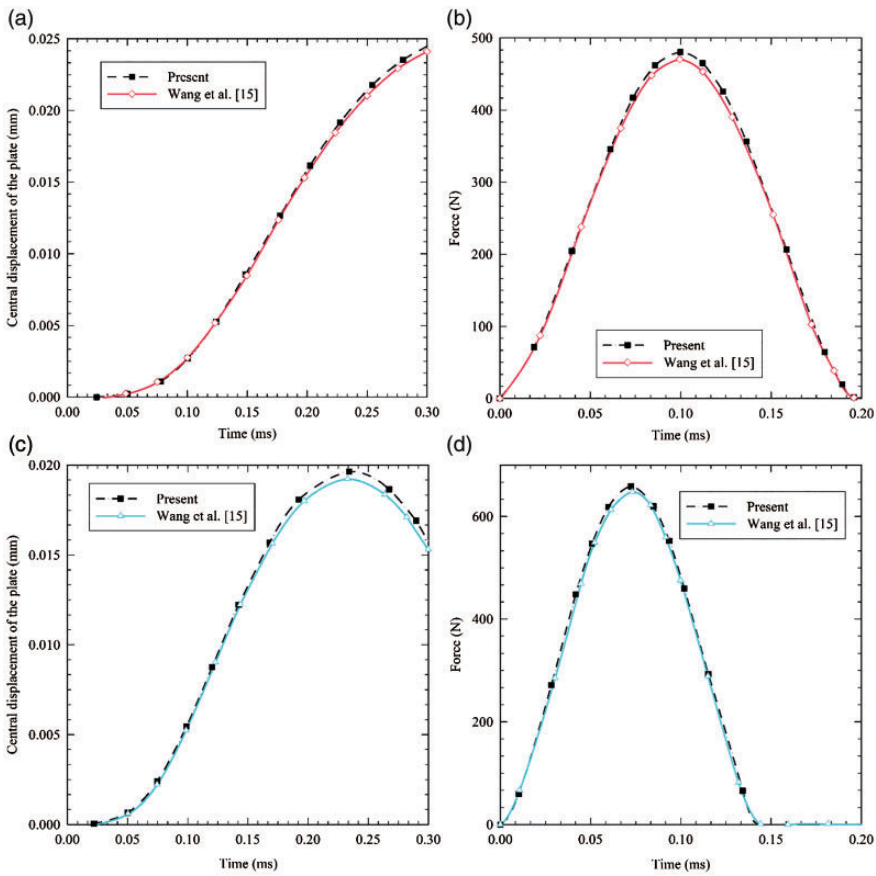

Figure 3. Time histories of the contact force and central displacement of the plate, obtained in the present study along a comparison with Wang et al. [15]: (a) Central displacement of the plate at $T = 700$ K, and $V^*_{CNT} = 0.12$, (b) Contact force of the plate at $T = 700$ K, and $V^*_{CNT} = 0.12$, (c) Central displacement of the plate at $T = 300$ K, and $V^*_{CNT} = 0.12$, and (d) Contact force of the plate at $T = 300$ K, and $V^*_{CNT} = 0.12$.

center of the sandwich plate with CNTRC face sheets are considered. FG-X single-layer plate with the following default parameters and geometric characteristics were selected in this investigation

$$a/b = 1, \quad b/t = 10, \quad T = 300\,\mathrm{K}, \quad V_0 = 3\ \mathrm{m/s}, \quad V^*_{CNT} = 0.12$$

Figure 3 illustrates time histories of the contact force and central displacement for the single layer nanotube-reinforced composite plate subjected to spherical impactor along a comparison with Wang et al. [15]. By comparing the results of these two studies, it could be concluded that the current model is in close agreement with the reference and a small difference observed between the results is due to the theories used in the problem-solving procedure.

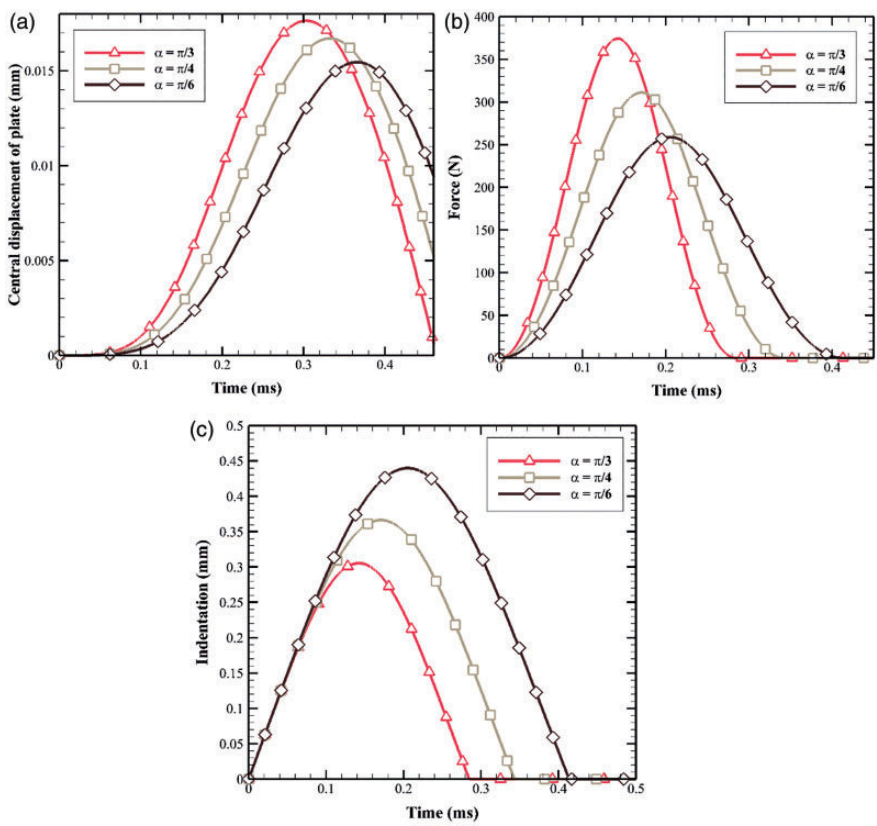

Figure 4. Characteristic geometrical size effect of the cone tip angle on the conical indenter impact response of sandwich plate with CNTRC face sheets: (a) Central displacement of the plate, (b) Contact force, and (c) Indentation.

Impact response of sandwich plate with CNTRC face sheets subjected to the conical impactor

After determining the validity of the solution procedure presented in the previous section, parametric numerical studies of the different variables is performed. In Figures 4 to 7, the effect of temperature rise on the impact dynamic performance of the panel, the geometric effect of cone tip angle variations, the effect of volume percentage of CNTs used in the FG-X CNTRC upper and lower face sheets and the effect of the initial kinetic energy of the impactor on the nonlinear impact response is provided.

The characteristic geometrical size effect of the cone tip angle on the central displacement, contact force and the range of variations in the value of indentation are presented in Figure 4. Indentation is expected to increase for the conical impactors with smaller tip angle. Figure 4(b) and (c) depicts that more indentation with lower force is achieved for smaller tip angles.

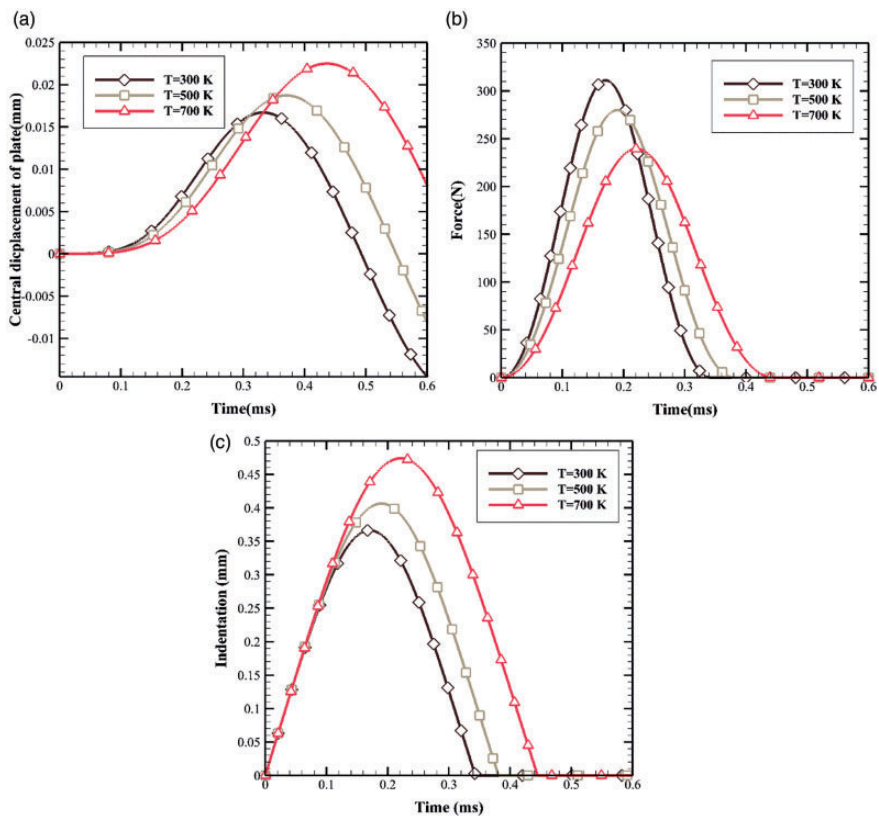

Figure 5. Thermal field effect on the conical impactor response of sandwich plate with CNTRC face sheets: (a) Central displacement of the plate, (b) Contact force, and (c) Indentation.

Figure 5 depicts thermal field effect of the conical impactor response of sandwich plate with CNTRC face sheets. As shown in this figure, the peak time of central displacement, contact force, and indentation curves shifted to the right by raising the temperature. As the material temperature rises, the elasticity modulus of the material decreases accordingly. From this perspective, the matter becomes softer and as this phenomenon occurs to the nature of the body, it takes a lot more time for reaching the maximum displacement compared to lower temperatures. As shown in Figure 5(c), as the temperature rises, the modulus of elasticity decreases, and the indentation increases. Nevertheless, according to Figure 5(b), it could be concluded that the effect of reducing the modulus of elasticity due to the temperature rise is more than the effect of the increase of indentation, further, the maximum amount of applied force is decreased, according to the diagrams.

Figure 6 illustrates the effect of CNT volume fraction V^*_{CNT} on the conical impactor response of sandwich plate with CNTRC face sheets. As shown in the

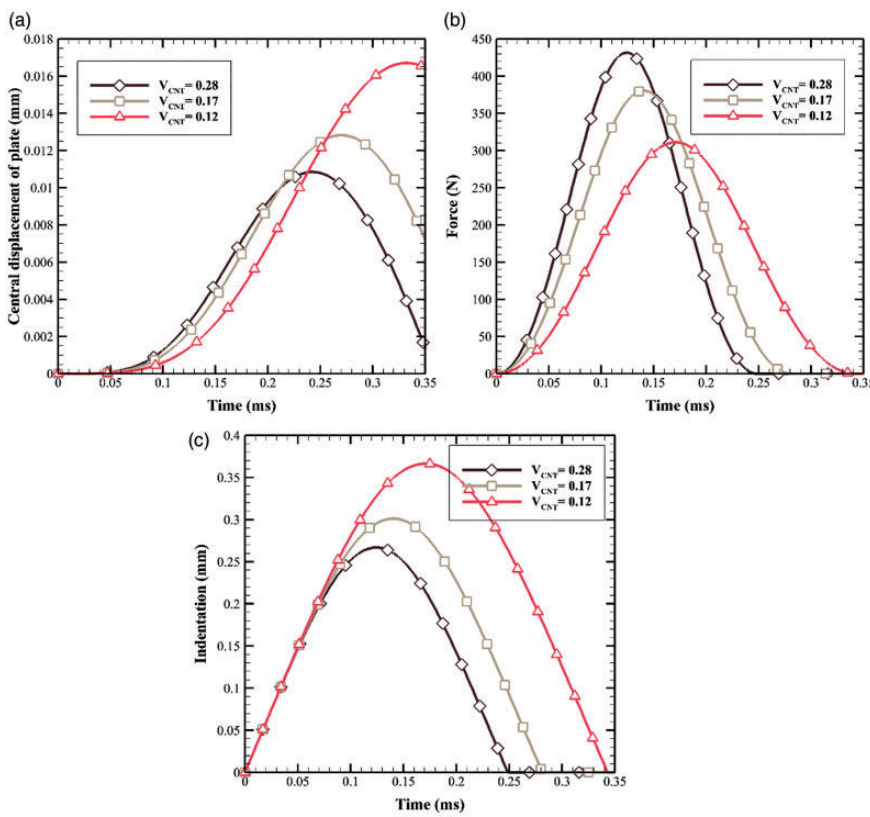

Figure 6. Effect of CNT volume fraction V^*_{CNT} on the conical impactor response of CNTRC sandwich plate: (a) Central displacement of the plate, (b) Contact force, and (c) Indentation.

figure, the peak time of central displacement, contact force, and indentation curves shifted to the right by decreasing the volume percentage of CNTs. The effect of the volume fraction of CNTs on the conical impactor response of sandwich plate with CNTRC face sheets is demonstrated in Figure 6. It can be seen from this figure that both the central displacement and contact time duration decrease with the increase of the volume fraction of CNT. In contrast, the contact force increases when the volume fraction of CNT increases.

Figure 7 presents the displacement-time, force-time and indentation-time curves for the sandwich plate with CNTRC face sheets with three different values of initial velocity to show the initial kinetic energy effect of conical impactor on the nonlinear low-velocity impact performance of the plate. As expected, the peak time of curves shifted to the left and the contact time duration decreases with the increase in the initial kinetic energy of the impactor.

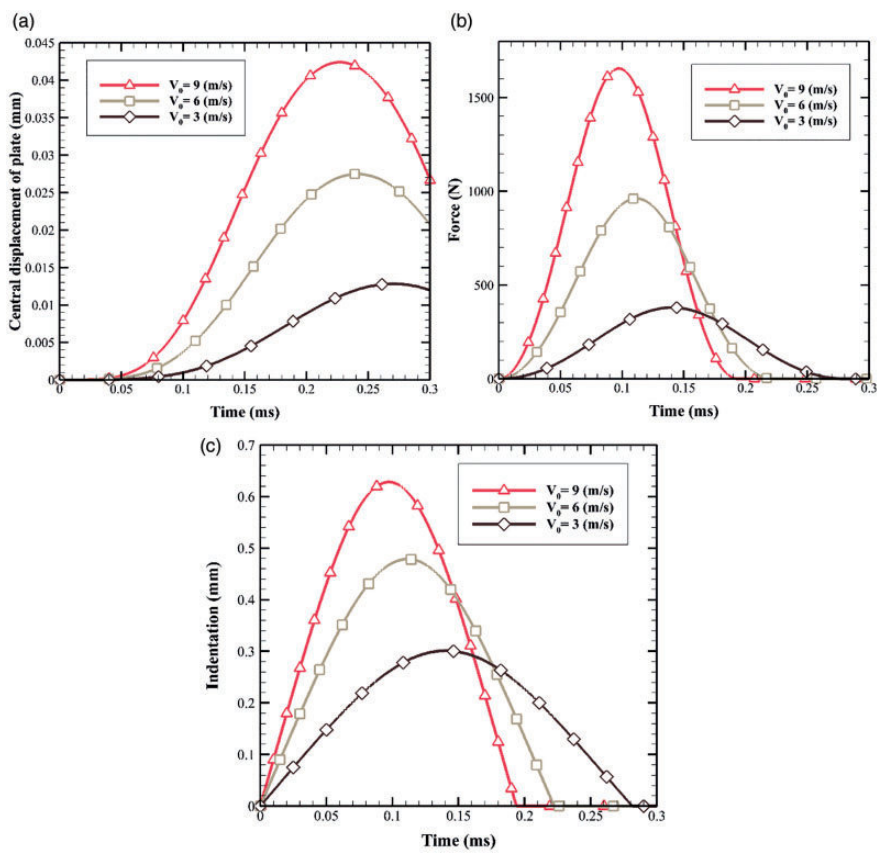

Figure 7. Initial kinetic energy effect on conical impactor response of sandwich plate with CNTRC face sheets: (a) Central displacement of the plate, (b) Contact force, and (c) Indentation.

Impact response of sandwich plate with CNTRC face sheets subjected to the cylindrical impactor

The geometric parameters of the sandwich plate were taken as: $a/b = 1$, $b/t = 10$, $t_f = 1$ mm, and $t_c/t_f = 8$. Similar to the curves shown in Figures 4 through 7 for the conical impactor, these responses for cylindrical impactor are also conducted and presented in this section.

In the present section, the effect of geometrical size effect of cylinder radius (i.e., $R_1 = 6.35$ mm, $R_2 = 2R_1$ and $R_3 = 3R_1$) on the impact behavior of sandwich plate with CNTRC face sheets is studied and its corresponding results are shown in Figure 8. Time histories of central displacement, force, and indentation of the sandwich panels are respectively depicted for different sizes of cylindrical impactor radius in Figure 8. It can be seen from Figure 8(a) that a cylinder with the shortest radius has the lowest central displacement, as well as indentation and shortest time

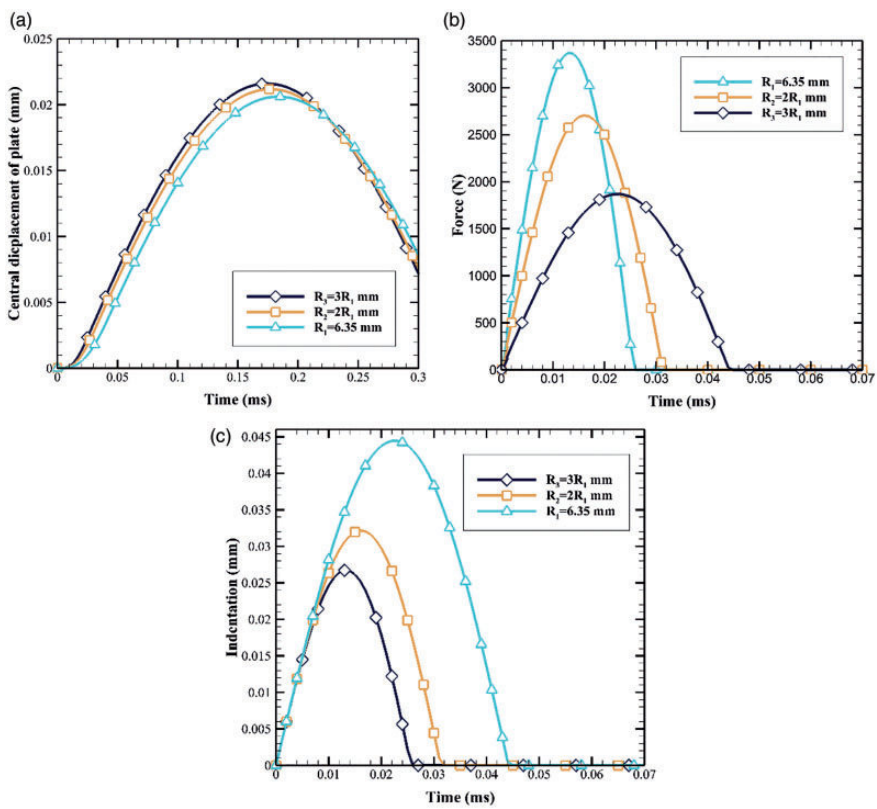

Figure 8. Effect of radius size on the cylindrical impactor response of sandwich plate with CNTRC face sheets: (a) Central displacement of the plate, (b) Contact force, and (c) Indentation.

contact duration. It could be noticed that the change in cylinder radius plays little role in the amount of central displacement.

For a given FG-X CNTRC plate (i.e., $V^*_{CNT} = 0.12$) , Figure 9 presented the influence of temperature variations (i.e., $T = 300$ K, $T = 500$ K, and $T = 700$ K) on the impact behavior. Time histories for the effect of temperature variations on the central displacement, contact force, and indentation of the sandwich plate with CNTRC face sheets are illustrated in Figure 9. For instance, it can be observed from Figure 9 that as the temperature increases, the central displacement of the plate and the contact time duration increase as well, but the contact force decreases. Furthermore, it is clearly seen from Figure 9(c) that the lower the temperature, the lower the amount of indentation at a given time.

For a given temperature (i.e., $T = 300$ K), Figure 10 demonstrated the effect of variation of the CNT volume fraction (i.e., $V_{CNT} = 0.28$, $V_{CNT} = 0.17$, and $V_{CNT} = 0.12$) on the impact behavior of the sandwich panel subjected to cylindrical impactor for a given impactor initial velocity (i.e., $V_0 = 3$ m/s) .

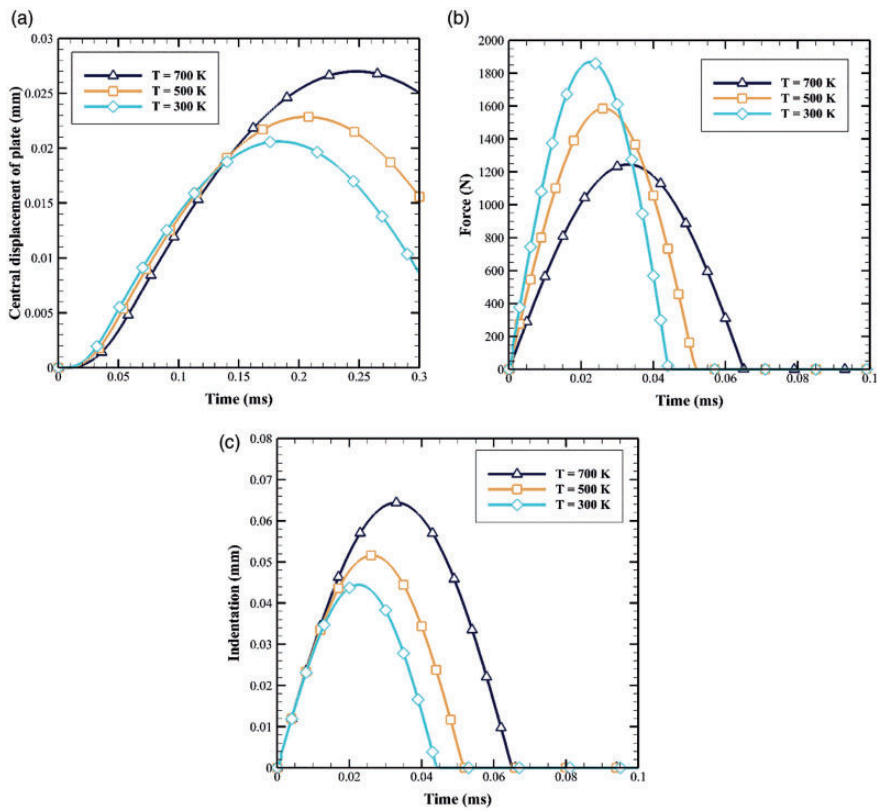

Figure 9. Thermal field effect on cylindrical impactor response of sandwich plate with CNTRC face sheets: (a) Central displacement of the plate, (b) Contact force, and (c) Indentation.

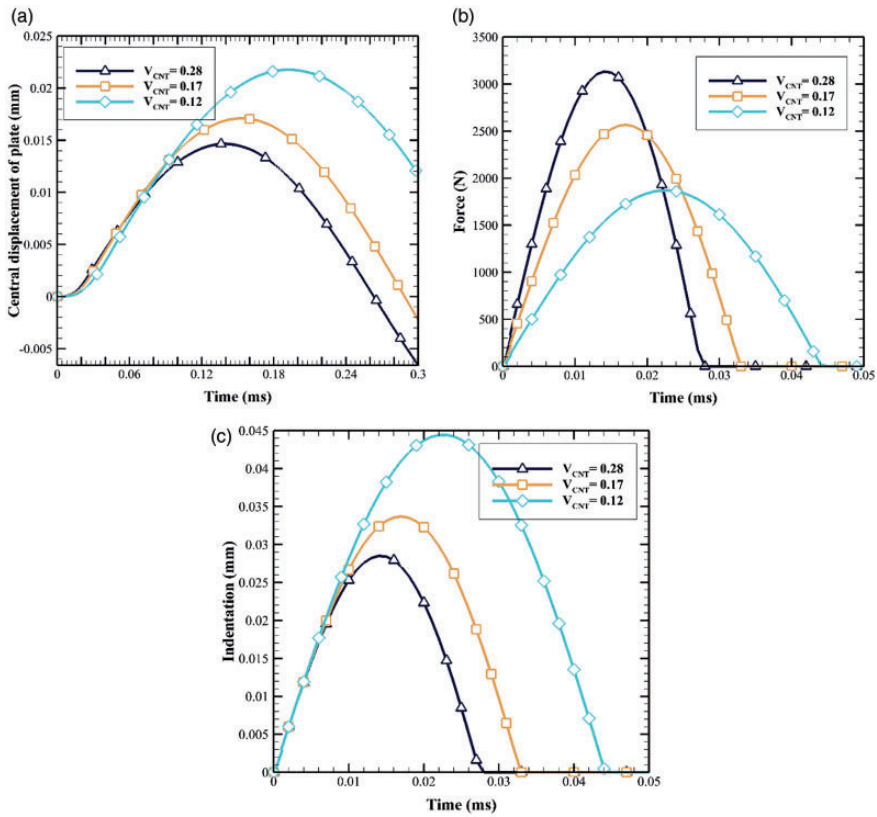

Figure 10. Effect of CNT volume fraction V^*_{CNT} on the cylindrical impactor response of sandwich plate with CNTRC face sheets: (a) Central displacement of the plate, (b) Contact force, and (c) Indentation.

Time history curves for the influence of variation of volume fraction on central displacement, contact force and indentation of the sandwich plate with CNTRC face sheets are depicted in Figure 10(a) to (c), respectively. For instance, the only parameter that increases with the increase in volume fraction is contact force and the rest of the involved parameters, including central displacement, contact time duration, and indentation are all decreases as shown in Figure 10(a) to (c).

In order to show the initial kinetic energy effect, Figure 11 represents the displacement-time, force-time and indentation-time curves of the sandwich plate with CNTRC face sheets with different values of initial velocity (i.e., $V_0 = 3$ m/s, $V_0 = 6$ m/s, and $V_0 = 9$ m/s), for a given FG-X CNTRC plate (i.e., $V^*_{CNT} = 0.28$) and at a constant temperature ($T = 300$ K). For instance, as the velocity increases from 3 m/s *to* 6 m/s the maximum central displacement, the maximum contact force and the maximum indentation increases about 100%

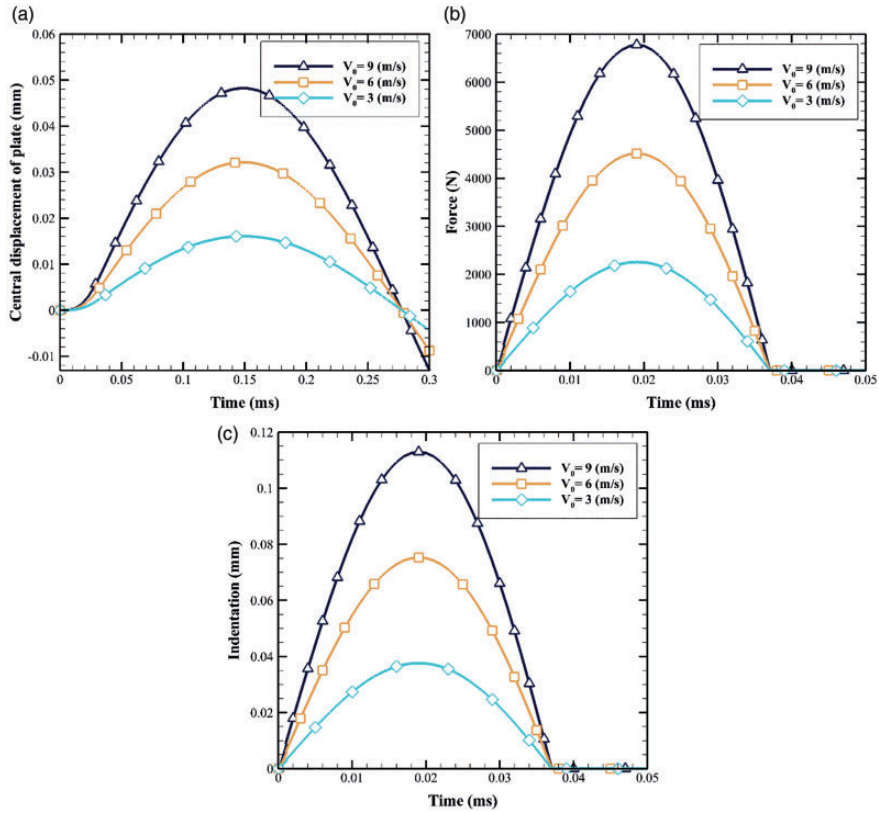

Figure 11. Initial kinetic energy effect on cylindrical impactor response of sandwich plate with CNTRC face sheets: (a) Central displacement of the plate, (b) Contact force, and (c) Indentation.

while there is about 50% as the velocity changes from 6 m/s to 9 m/s. As can be seen, the contact time duration remains constant for all of the impact initial velocities.

Conclusion

In this paper, the nonlinear low-velocity impact response of a sandwich plate, consisting of two CNTRC face sheets and a core, under different thermal environments was investigated for various geometrical shapes of the impactor. In the CNT-reinforced sheets, by means of a micromechanical model, the material properties were obtained. In these layers, the FG-X distribution of CNTs was assumed. Then, this sandwich plate was subjected to three impactors with different geometrical shapes. In the initial stage of the analysis, the displacement field was represented by the Reddy's high-order shear deformation theory [20]. Also, the material

composition of sandwich layers was assumed to be temperature dependent. The CNTRC sandwich plate was analyzed in the framework of the Reddy's higher order shear deformation theory with regard to thermal effects. To find the set of equations of motion for the impactor as well as the CNTRC sandwich plate, Rayleigh-Ritz method was applied to the Hamilton principle. Afterwards, The solution in time domain was obtained based on Newmark's numerical time integration scheme. The conclusions, based on the figures, results, and observations of the previous sections, on the variations of temperature, CNT volume fraction, initial kinetic energy, and geometrical shape of the impactors, are as follows:

- Increasing the amount of CNTs volume fraction in the face sheets will reduce the amount of indentation in this layers, also, at this point, the maximum amount of contact force was applied to the plate.
- With a change in the radius of the cylinder, as well as an increase in the CNT volume fraction, the central displacement of the plates shows lower changes.
- In comparison of the central displacement under two cylindrical and spherical impactor, cylindrical geometry will experience more central displacement.
- Compared to the two cylindrical and conical impactor, the cylindrical impactor causes more amount of indentation, which can be attributed to the equivalence of the mass for the two geometries and the initially involved parameters.
- In the impact of the sphere, cone, and cylinder with the sandwich panel, among the various parametric change of the variables, the variation of the initial kinetic energy, the change in the radius of the cylinder, and the change in velocity result in the larger ratio of the force to displacement, respectively.

Declaration of conflicting interests

The author(s) declared no potential conflicts of interest with respect to the research, authorship, and/or publication of this article.

Funding

The author(s) received no financial support for the research, authorship, and/or publication of this article.

References

1. Schneider C, Kazemahvazi S, Russell BP, et al. Impact response of ductile self-reinforced composite corrugated sandwich beams. *Compos B Eng* 2016; 99: 121–131.
2. Malekzadeh Fard K, Khalili SMR, Forooghy SH, et al. Low velocity transverse impact response of a composite sandwich plate subjected to a rigid blunted cylindrical impactor. *Compos B Eng* 2014; 63: 111–122.
3. Gilioli A, Sbarufatti C, Manes A, et al. Compression after impact test (CAI) on NOMEX^{TM} honeycomb sandwich panels with thin aluminum skins. *Compos B Eng* 2014; 67: 313–325.

4. Xiong J, Ma L, Wu L, et al. Mechanical behavior and failure of composite pyramidal truss core sandwich columns. *Compos B Eng* 2011; 42: 938–945.
5. Fan Y and Wang H. Nonlinear low-velocity impact analysis of matrix cracked hybrid laminated plates containing CNTRC layers resting on visco-Pasternak foundation. *Compos B Eng* 2017; 117: 9–19.
6. Iijima S. Helical microtubules of graphitic carbon. *Nature* 1991; 354: 56.
7. Zhang LW, Lei ZX and Liew KM. Free vibration analysis of functionally graded carbon nanotube-reinforced composite triangular plates using the FSDT and element-free IMLS-Ritz method. *Compos Struct* 2015; 120: 189–199.
8. Şimşek M. Size dependent nonlinear free vibration of an axially functionally graded (AFG) microbeam using He's variational method. *Compos Struct* 2015; 131: 207–214.
9. Neves AMA, Ferreira AJM, Carrera E, et al. A quasi-3D hyperbolic shear deformation theory for the static and free vibration analysis of functionally graded plates. *Compos Struct* 2012; 94: 1814–1825.
10. Zidi M, Tounsi A, Houari MSA, et al. Bending analysis of FGM plates under hygro-thermo-mechanical loading using a four variable refined plate theory. *Aerosp Sci Technol* 2014; 34: 24–34.
11. Tounsi A, Houari MSA, Benyoucef S, et al. A refined trigonometric shear deformation theory for thermoelastic bending of functionally graded sandwich plates. *Aerosp Sci Technol* 2013; 24: 209–220.
12. Abediokhchi J, Shakouri M and Kouchakzadeh MA. Bending analysis of moderately thick functionally graded conical panels with various boundary conditions using GDQ method. *Compos Struct* 2013; 103: 68–74.
13. Lei Z, Liew KM and Yu J. Buckling analysis of functionally graded carbon nanotube-reinforced composite plates using the element-free kp-Ritz method. *Compos Struct* 2013; 98: 160–168.
14. Meziane MAA, Abdelaziz HH and Tounsi A. An efficient and simple refined theory for buckling and free vibration of exponentially graded sandwich plates under various boundary conditions. *J Sandwich StructMater* 2014; 16: 293–318.
15. Wang Z-X, Xu J and Qiao P. Nonlinear low-velocity impact analysis of temperature-dependent nanotube-reinforced composite plates. *Compos Struct* 2014; 108: 423–434.
16. Zarei H, Fallah M, Bisadi H, et al. Multiple impact response of temperature-dependent carbon nanotube-reinforced composite (CNTRC) plates with general boundary conditions. *Compos B Eng* 2017; 113: 206–217.
17. Khalili SMR and Haghbin A. Investigation on design parameters of single-walled carbon nanotube reinforced nanocomposites under impact loads. *Compos Struct* 2013; 98: 253–260.
18. Shariyat M and Farzan Nasab F. Eccentric low-velocity impact analysis of transversely graded plates with Winkler-type elastic foundations and fully or partially supported edges. *Thin-Walled Struct* 2014; 84: 112–122.
19. Najafi F, Shojaeefard MH and Saeidi Googarchin H. Low-velocity impact response of functionally graded doubly curved panels with Winkler–Pasternak elastic foundation: an analytical approach. *Compos Struct* 2017; 162: 351–364.
20. Reddy JN. *Theory and analysis of elastic plates and shells*. Boca Raton: CRC press, 2006.
21. Shen H-S. Nonlinear bending of functionally graded carbon nanotube-reinforced composite plates in thermal environments. *Compos Struct* 2009; 91: 9–19.

22. Kiani Y, Sadighi M, Salami SJ, et al. Low velocity impact response of thick FGM beams with general boundary conditions in thermal field. *Compos Struct* 2013; 104: 293–303.
23. Khalili SMR, Malekzadeh K and Gorgabad AV. Low velocity transverse impact response of functionally graded plates with temperature dependent properties. *Compos Struct* 2013; 96: 64–74.
24. Golmakani M and Zeighami V. Nonlinear thermo-elastic bending of functionally graded carbon nanotube-reinforced composite plates resting on elastic foundations by dynamic relaxation method. *Mech Adv Mater Struct* 2017; 25: 868-880.
25. Kurşun A, Şenel M, Enginsoy HM, et al. Effect of impactor shapes on the low velocity impact damage of sandwich composite plate: experimental study and modelling. *Compos B Eng* 2016; 86: 143–151.
26. Liu J, He W, Xie D, et al. The effect of impactor shape on the low-velocity impact behavior of hybrid corrugated core sandwich structures. *Compos B Eng* 2017; 111: 315–331.
27. Shen H-S and Zhang C-L. Thermal buckling and postbuckling behavior of functionally graded carbon nanotube-reinforced composite plates. *Mater Des* 2010; 31: 3403–3411.
28. Johnson KL and Johnson KL. *Contact mechanics*. Cambridge: Cambridge University Press, 1987.
29. Hanaor DAH, Gan Y and Einav I. Contact mechanics of fractal surfaces by spline assisted discretisation. *Int J Solids Struct* 2015; 59: 121–131.
30. Sneddon IN. The relation between load and penetration in the axisymmetric boussinesq problem for a punch of arbitrary profile. *Int J Eng Sci* 1965; 3: 47–57.
31. Touloukian YS. *Thermophysical properties of high temperature solid materials. Volume 3. Ferrous alloys*. New York, Macmillan: Thermophysical and Electronic Properties Information Analysis Center Lafayette, 1966.
32. Song YS and Youn JR. Modeling of effective elastic properties for polymer based carbon nanotube composites. *Polymer* 2006; 47: 1741–1748.

Appendix 1

$$k_1(i,j) = \int -A_{11}\frac{\partial u}{\partial x}\frac{\partial \delta u}{\partial x}\mathrm{d}A + \int -A_{16}\frac{\partial u}{\partial y}\frac{\partial \delta u}{\partial x}\mathrm{d}A - \int A_{16}\frac{\partial u}{\partial x}\frac{\partial \delta u}{\partial y}\mathrm{d}A - \int A_{66}\frac{\partial u}{\partial y}\frac{\partial \delta u}{\partial y}\mathrm{d}A$$

$$k_2(i,j) = \int -A_{12}\frac{\partial v_0}{\partial x}\frac{\partial \delta u_0}{\partial x}\mathrm{d}A - A_{16}\frac{\partial v}{\partial x}\frac{\partial \delta u_0}{\partial x} - A_{26}\frac{\partial v}{\partial y}\frac{\partial \delta u}{\partial y} - A_{66}\frac{\partial v}{\partial x}\frac{\partial \delta u}{\partial y}\mathrm{d}A$$

$$k_3(i,j) = \int -A_{16}\frac{\partial u}{\partial x}\frac{\partial \delta v}{\partial x}\mathrm{d}A - A_{66}\frac{\partial u}{\partial y}\frac{\partial \delta v}{\partial x} - A_{12}\frac{\partial u}{\partial x}\frac{\partial \delta v}{\partial y} - A_{26}\frac{\partial u}{\partial y}\frac{\partial \delta v}{\partial y}\mathrm{d}A$$

$$k_4(i,j) = \int -A_{26}\frac{\partial v}{\partial y}\frac{\partial \delta v}{\partial x} - A_{66}\frac{\partial v}{\partial x}\frac{\partial \delta v}{\partial x} - A_{22}\frac{\partial v}{\partial y}\frac{\partial \delta v}{\partial y} - A_{26}\frac{\partial v}{\partial x}\frac{\partial \delta v}{\partial y}\mathrm{d}A$$

$$
\begin{aligned}
k_5(i,j) = & \int N_x^T \frac{\partial w}{\partial x}\frac{\partial \delta w}{\partial x}\mathrm{d}A + \int N_y^T \frac{\partial w}{\partial y}\frac{\partial \delta w}{\partial y}\mathrm{d}A \\
& + \int c_1 \frac{\partial^2 \delta w}{\partial x^2}\left(S_{11} \times -c_1 \frac{\partial^2 w}{\partial x^2} + S_{12} \times -c_1 \frac{\partial^2 w}{\partial y^2} + S_{16} \times -c_1 \frac{\partial^2 w}{\partial x \partial y} \times 2\right) \\
& + c_1 \frac{\partial \delta w}{\partial y^2}\left(S_{12} \times -c_1 \frac{\partial^2 w}{\partial x^2} + S_{22} \times -c_1 \frac{\partial^2 w}{\partial y^2} + S_{26} \times -c_1 \times 2 \times \frac{\partial^2 w}{\partial x \partial y}\right) \\
& + 2c_1 \frac{\partial^2 \delta w}{\partial x \partial y}\left(S_{16} \times -c_1 \frac{\partial^2 w}{\partial x^2} + S_{26} \times -c_1 \frac{\partial^2 w}{\partial y^2} + S_{26} \times -c_1 \frac{\partial^2 w}{\partial x^2} + S_{66} \times -c_1 \times 2 \times \frac{\partial^2 w}{\partial x \partial y}\right) \\
& + -\frac{\partial \delta w}{\partial x}\left(g_{55} + g'_{55} \times -c_2\right)\frac{\partial w}{\partial x} + -\frac{\partial \delta w}{\partial y}\left(g_{44} + g'_{44} \times -c_2\right)\frac{\partial w}{\partial y} \\
& + c_2 \frac{\partial \delta w}{\partial x}\left(g'_{55} + r_{55} \times -c_2\right)\frac{\partial w}{\partial x} \quad + c_2 \frac{\partial \delta w}{\partial y}\left(g'_{44} + r_{44} \times -c_2\right)\frac{\partial w}{\partial y}\mathrm{d}A
\end{aligned}
$$

$$
\begin{aligned}
k_6(i,j) = & \int c_1 \frac{\partial^2 \delta w}{\partial x^2}\left(H_{11}\frac{\partial \varphi_x}{\partial x} + H_{16}\frac{\partial \varphi_y}{\partial y} + S_{11} \times -c_1 \frac{\partial \varphi_x}{\partial x} S_{16} \times -c_1 \frac{\partial \varphi_x}{\partial y}\right) \\
& + c_1 \frac{\partial^2 \delta w}{\partial y^2}\left(\frac{\partial \varphi_x}{\partial x}(H_{11} + S_{12} \times -c_1) + \frac{\partial \varphi_x}{\partial y}(H_{16} + S_{26} \times -c_1)\right) \\
& + 2c_1 \frac{\partial^2 \delta w}{\partial x \partial y}\left(\frac{\partial \varphi_x}{\partial x}(H_{16} + S_{16} \times -c_1) + \frac{\partial \varphi_x}{\partial y}(H_{66} + S_{66} \times -c_1)\right) \\
& + -\frac{\partial \delta w}{\partial x}\varphi_x\left(g_{55} + g'_{55} \times -c_2\right) + c_2 \frac{\partial \delta w}{\partial x}\left(g'_{55} + r_{55} \times -c_2\right)\varphi_x \mathrm{d}A
\end{aligned}
$$

$$
\begin{aligned}
k_7(i,j) = & \int c_1 \frac{\partial^2 \delta w}{\partial x^2}\left(\frac{\partial \varphi_y}{\partial y}(H_{12} + S_{12} \times -c_1) + \frac{\partial \varphi_y}{\partial x}(H_{16} + S_{16} \times -c_1)\right) \\
& + c_1 \frac{\partial^2 \delta w}{\partial y^2}\left(\frac{\partial \varphi_y}{\partial y}(H_{22} + S_{22} \times -c_1) + \frac{\partial \varphi_y}{\partial y}(H_{26} + S_{26} \times -c_1)\right) \\
& + 2c_1 \frac{\partial^2 \delta w}{\partial x \partial y}\left(\frac{\partial \varphi_y}{\partial y}(H_{26} + S_{26} \times -c_1) + \frac{\partial \varphi_y}{\partial x}(H_{66} + S_{66} \times -c_1)\right) \\
& + -\frac{\partial \delta w}{\partial y}\varphi_y\left(g_{44} + g'_{44} \times -c_2\right) + c_2 \frac{\partial \delta w}{\partial y}\varphi_y\left(g'_{44} + r_{44} \times -c_2\right)\mathrm{d}A
\end{aligned}
$$

$$
\begin{aligned}
k_7(i,j) = & \int c_1 \frac{\partial^2 \delta w}{\partial x^2}\left(\frac{\partial \varphi_y}{\partial y}(H_{12} + S_{12} \times -c_1) + \frac{\partial \varphi_y}{\partial x}(H_{16} + S_{16} \times -c_1)\right) \\
& + c_1 \frac{\partial^2 \delta w}{\partial y^2}\left(\frac{\partial \varphi_y}{\partial y}(H_{22} + S_{22} \times -c_1) + \frac{\partial \varphi_y}{\partial y}(H_{26} + S_{26} \times -c_1)\right)
\end{aligned}
$$

$$+ 2c_1 \frac{\partial^2 \delta w}{\partial x \partial y}\left(\frac{\partial \varphi_y}{\partial y}(H_{26} + S_{26} \times -c_1) + \frac{\partial \varphi_y}{\partial x}(H_{66} + S_{66} \times -c_1)\right)$$
$$+ -\frac{\partial \delta w}{\partial y}\varphi_y\left(g_{44} + g'_{44} \times -c_2\right) + c_2 \frac{\partial \delta w}{\partial y}\varphi_y\left(g'_{44} + r_{44} \times -c_2\right)\mathrm{d}A$$

$$k_8(i,j) = \int -\frac{\partial \delta \varphi_x}{\partial x}\left(\frac{\partial^2 w}{\partial x^2}(H_{11} \times -c_1) + \frac{\partial^2 w}{\partial y^2}(H_{12} \times -c_1) + \frac{\partial^2 \delta w}{\partial x \partial y}(2H_{16} \times -c_1)\right)$$
$$-\frac{\partial \delta \varphi_x}{\partial y}\left((H_{16} \times -c_1)\frac{\partial^2 w}{\partial x^2} + \frac{\partial^2 w}{\partial y^2}(H_{26} \times -c_1) + \frac{\partial^2 w}{\partial x \partial y}(2H_{66} \times -c_1)\right)$$
$$+ c_1 \frac{\partial \delta \varphi_x}{\partial y}\left(\frac{\partial^2 w}{\partial x^2}(S_{11} \times -c_1) + \frac{\partial^2 w}{\partial y^2}(S_{12} \times -c_1) + \frac{\partial^2 w}{\partial x \partial y}(2S_{16} \times -c_1)\right)$$
$$+ c_1 \frac{\partial \delta \varphi_x}{\partial y}\left(\frac{\partial^2 w}{\partial x^2}(S_{16} \times -c_1) + \frac{\partial^2 w}{\partial y^2}(S_{12} \times -c_1) + \frac{\partial^2 w}{\partial x \partial y}(2S_{16} \times -c_1)\right)$$
$$- \delta \varphi_x\left(\frac{\partial w}{\partial x}\left(g_{55} + g'_{55} \times -c_2\right)\right) + c_2 \delta \varphi_x\left(\frac{\partial w}{\partial y}\left(g'_{55} + r_{55} \times -c_2\right)\right)\mathrm{d}A$$

$$k_9(i,j) = \int -\frac{\partial \delta w}{\partial x}\left(\frac{\partial \varphi_x}{\partial x}(F_{11} + H_{11} \times -c_1) + \frac{\partial \varphi_y}{\partial y}(F_{16} + H_{16} \times -c_1)\right)$$
$$-\frac{\partial \delta \varphi_x}{\partial y}\left(\frac{\partial \varphi_x}{\partial x}(F_{16} + H_{16} \times -c_1) + \frac{\partial \varphi_x}{\partial y}(F_{66} + H_{66} \times -c_1)\right)$$
$$+ c_1 \frac{\partial \delta \varphi_x}{\partial x}\left(\frac{\partial \varphi_x}{\partial x}(H_{11} + S_{11} \times -c_1) + \frac{\partial \varphi_x}{\partial y}(S_{16} + H_{16} \times -c_1)\right)$$
$$+ c_1 \frac{\partial \delta \varphi_x}{\partial y}\left(\frac{\partial \varphi_x}{\partial x}(H_{16} + S_{16} \times -c_1) + \frac{\partial \varphi_x}{\partial y}(S_{16} + H_{66} \times -c_1)\right)$$
$$- \delta \varphi_x \varphi_x(g_{55} + g'_{55} \times -c_2) + c_2 \delta \varphi_x \varphi_x(g'_{55} + r_{55} \times -c_2)\mathrm{d}A$$

$$k_{10}(i,j) = \int -\frac{\partial \delta \varphi_x}{\partial x}\left(\frac{\partial \varphi_y}{\partial x}(F_{16} + H_{16} \times -c_1) + \frac{\partial \varphi_y}{\partial y}(F_{12} + H_{12} \times -c_1)\right)$$
$$-\frac{\partial \delta \varphi_x}{\partial y}\left(\frac{\partial \varphi_y}{\partial x}(F_{66} + H_{66} \times -c_1) + \frac{\partial \varphi_y}{\partial y}(F_{26} + H_{26} \times -c_1)\right)$$
$$+ c_1 \frac{\partial \delta \varphi_x}{\partial x}\left(\frac{\partial \varphi_y}{\partial x}(H_{16} + S_{16} \times -c_1) + \frac{\partial \varphi_y}{\partial y}(H_{12} + S_{12} + -c_1)\right)$$

$$+ c_1 \frac{\partial \delta\varphi_x}{\partial y}\left(\frac{\partial \varphi_y}{\partial x}(H_{66} + S_{16} \times -c_1) + \frac{\partial \varphi_y}{\partial y}(H_{26} + S_{26} \times -c_1)\right)\mathrm{d}A$$

$$\begin{aligned}
k_{11}(i,j) = \int & -\frac{\partial \delta\varphi_y}{\partial x}\left(\frac{\partial^2 w}{\partial x^2}(H_{16} \times -c_1) + \frac{\partial^2 w}{\partial y^2}(H_{26} \times -c_1) + \frac{\partial^2 w}{\partial x \partial y}(2H_{66} \times -c_1)\right) \\
& - \frac{\partial \delta\varphi_y}{\partial y}\left(\frac{\partial^2 w}{\partial x^2}(H_{12} \times -c_1) + \frac{\partial^2 w}{\partial y^2}(H_{22} \times -c_1) + \frac{\partial^2 w}{\partial x \partial y}(2H_{26} \times -c_1)\right) \\
& + c_1 \frac{\partial \varphi_y}{\partial y}\left(\frac{\partial^2 w}{\partial x^2}(S_{12} \times -c_1) + \frac{\partial^2 w}{\partial y^2}(S_{22} \times -c_1) + \frac{\partial^2 w}{\partial x \partial y}(2S_{26} \times -c_1)\right) \\
& + c_1 \frac{\partial \varphi_y}{\partial x}\left(\frac{\partial^2 w}{\partial x^2}(S_{16} \times -c_1) + \frac{\partial^2 w}{\partial y^2}(S_{26} \times -c_1) + \frac{\partial^2 w}{\partial x \partial y}(2S_{66} \times -c_1)\right) \\
& - \delta\varphi_y \frac{\partial w}{\partial y}\left(-g_{44} + 2g'_{44} \times c_2 + r_{44} \times -c_2\right)\mathrm{d}A
\end{aligned}$$

$$\begin{aligned}
k_{12}(i,j) = \int & -\frac{\partial \delta\varphi_y}{\partial x}\left(\frac{\partial \varphi_x}{\partial x}(F_{16} + H_{16} \times -c_1) + \frac{\partial \varphi_x}{\partial y}(F_{66} + H_{66} \times -c_1)\right) \\
& - \frac{\partial \delta\varphi_y}{\partial y}\left(\frac{\partial \varphi_x}{\partial x}(F_{12} + H_{12} \times -c_1) + \frac{\partial \varphi_y}{\partial y}(F_{26} + H_{26} \times -c_1)\right) \\
& + c_1 \frac{\partial \delta\varphi_y}{\partial y}\left(\frac{\partial \varphi_x}{\partial x}(H_{12} + S_{12} \times -c_1) + \frac{\partial \varphi_x}{\partial y}(H_{26} + S_{26} + -c_1)\right) \\
& + c_1 \frac{\partial \delta\varphi_y}{\partial x}\left(\frac{\partial \varphi_x}{\partial x}(H_{16} + S_{16} \times -c_1) + \frac{\partial \varphi_x}{\partial y}(H_{66} + S_{66} \times -c_1)\right)\mathrm{d}A
\end{aligned}$$

$$\begin{aligned}
k_{13}(i,j) = \int & -\frac{\partial \delta\varphi_y}{\partial x}\left(\frac{\partial \varphi_y}{\partial x}(F_{66} + H_{66} \times -c_1) + \frac{\partial \varphi_y}{\partial y}(F_{26} + H_{26} \times -c_1)\right) \\
& - \frac{\partial \delta\varphi_y}{\partial y}\left(\frac{\partial \varphi_y}{\partial x}(F_{26} + H_{26} \times -c_1) + \frac{\partial \varphi_y}{\partial y}(F_{22} + H_{22} \times -c_1)\right) \\
& + c_1 \frac{\partial \delta\varphi_y}{\partial y}\left(\frac{\partial \varphi_y}{\partial x}(H_{26} + S_{26} \times -c_1) + \frac{\partial \varphi_y}{\partial y}(H_{22} + S_{22} + -c_1)\right) \\
& + c_1 \frac{\partial \delta\varphi_y}{\partial x}\left(\frac{\partial \varphi_y}{\partial x}(H_{66} + S_{66} \times -c_1) + \frac{\partial \varphi_y}{\partial y}(H_{26} + S_{26} \times -c_1)\right) \\
& + \delta\varphi_y \varphi_y\left(-g_{44} + 2g'_{44} \times c_2 + r_{44} \times -c_2^2\right)\mathrm{d}A
\end{aligned}$$

In the above equations, we have the following terms

$$(A_{ij}, B_{ij}, E_{ij}) = \int_{-\frac{h}{2}}^{\frac{h}{2}} \varphi_{ij}\left(1, z, z^3\right)\mathrm{d}z$$

$$(S_{ij}) = \int_{-\frac{h}{2}}^{\frac{h}{2}} \varphi_{ij}(z^6)\mathrm{d}z$$

$$(B_{ij}, F_{ij}, H_{ij}) = \int_{-\frac{h}{2}}^{\frac{h}{2}} \varphi_{ij}\left(z, z^2, z^4\right)\mathrm{d}z$$

$$(g_{44}, g_{55}) = \int_{-\frac{h}{2}}^{\frac{h}{2}} (Q_{44}, Q_{55})\mathrm{d}z$$

$$\left(g'_{44}, g'_{55}\right) = \int_{-\frac{h}{2}}^{\frac{h}{2}} (Q_{44}, Q_{55})z^2\mathrm{d}z$$

Appendix 2

$$m_1(i,j) = \int I_0 u \delta u_0 \mathrm{d}A$$

$$m_2(i,j) = \int I_0 v \delta v_0 \mathrm{d}A$$

$$m_3(i,j) = \int I_0 w \delta w_0 + c_1 I_6 \left(\frac{\partial w}{\partial x}\frac{\partial \delta w}{\partial x} + \frac{\partial w}{\partial y}\frac{\partial \delta w}{\partial y}\right)\mathrm{d}A$$

$$m_4(i,j) = \int -c_1[I_4 - c_1 I_6]\varphi_x \frac{\partial \delta w}{\partial x}\mathrm{d}A$$

$$m_5(i,j) = \int -c_1[I_4 - c_1 I_6]\varphi_y \frac{\partial \delta w}{\partial y}\mathrm{d}A$$

$$m_6(i,j) = \int -[c_1 I_6 - c_1 I_4]\frac{\partial w}{\partial x}\delta\varphi_x \mathrm{d}A$$

$$m_7(i,j) = \int [I_2 - 2c_1 I_4 + c_1 I_6]\varphi_x \delta\varphi_x \mathrm{d}A$$

$$m_8(i,j) = \int [c_1 \mathrm{I}_6 - c_1 I_4] \frac{\partial w}{\partial y} \delta\varphi_y \mathrm{d}A$$

$$m_9(i,j) = \int [I_2 - 2c_1 I_4 + c_1 I_6] \varphi_y \delta\varphi_y \mathrm{d}A$$

Appendix 3

$$F_1(i) = \int N_x^T \frac{\partial \delta u}{\partial x} + N_{xy}^T \frac{\partial \delta u}{\partial y} \mathrm{d}A$$

$$F_2(i) = \int N_{xy}^T \frac{\partial \delta v}{\partial x} + N_y^T \frac{\partial \delta v}{\partial y} \mathrm{d}A$$

$$F_3(i) = \int c_1 \frac{\partial^2 \delta w}{\partial x^2} \times -p_x^T + c_1 \frac{\partial^2 \delta w}{\partial y^2} \times -p_y^T + c_1 \frac{\partial^2 \delta w}{\partial x \partial y} \times -p_{xy}^T + q\delta w \mathrm{d}A$$

$$F_4(i) = \int \frac{\partial \delta\varphi_x}{\partial x} M_x^T + \frac{\partial \delta\varphi_x}{\partial y} M_{xy}^T - c_1 \frac{\partial \delta\varphi_x}{\partial x} p_x^T - c_1 \frac{\partial \delta\varphi_x}{\partial y} p_{xy}^T \mathrm{d}A$$

$$F_5(i) = \int \frac{\partial \delta\varphi_y}{\partial x} M_{xy}^T + \frac{\partial \delta\varphi_y}{\partial y} M_y^T - c_1 \frac{\partial \delta\varphi_y}{\partial y} p_y^T - c_1 \frac{\partial \delta\varphi_y}{\partial x} p_{xy}^T \mathrm{d}A$$

Check for updates

Article

JOURNAL OF COMPOSITE MATERIALS

Journal of Composite Materials
0(0) 1–14
© The Author(s) 2019
Article reuse guidelines:
sagepub.com/journals-permissions
DOI: 10.1177/0021998319853034
journals.sagepub.com/home/jcm
SAGE

Electrical properties of stretchable and skin–mountable PDMS/MWCNT hybrid composite films for flexible strain sensors

M Nankali[1], NM Nouri[1], N Geran Malek[1] and MA Sanjari Shahrezaei[2]

Abstract

Flexible strain sensors based on carbon nanofillers have great potential in the application of skin-adhesive sensors, wearable sensors, and tactile sensors, due to their superior electrical properties. Herein, the electrical properties of highly sensitive PDMS/MWCNT strain sensors made by vacuum filtration method were investigated. In order to obtain the electrical percolation curve of the flexible conductive films, first different samples were made with the same surface area but with different wt. % of CNTs. Then, depending on CNT content, the obtained conductive films exhibited initial electrical resistance in the range of 12.5 KΩ to 22.8 MΩ. The piezoresistive films with the CNT concentration of 1.4 to 2.9 mg/mm^2 had shown superior resistance drop, so this interval was determined as the percolation threshold region. According to the SEM images, the nanocomposite layer thickness of the flexible strain sensors in this region was 790 nm to 1210 nm. Afterward, the percolation curve was obtained using curve fitting to the experimental data and the exact value of the percolation threshold was defined as $\phi_c = 2.14$ mg/mm^2. Finally, in order to determine the minimum gauge factor (GF_{min}) of the sensors in percolation region, a flexible strain sensor in the upper limit of this region was selected and the piezoresistive properties of the selected sample were investigated.

Keywords

Flexible strain sensors, electrical percolation curve, vacuum filtration, polydimethylsiloxane

Introduction

Conductive polymer nanocomposites play an important role in stretchable electronics, health monitoring, tactile sensors, biosensors, soft actuators, and flexible sensing elements as well as strain and pressure sensors.[1,2] Nanocomposite sensing elements convert mechanical stimuli to electrical signals by three main mechanisms including piezoresistivity, capacitance, and piezoelectricity.[3] These mechanisms are highly dependent on the type of nanofillers used in the nanocomposite. There are a wide variety of nanofillers with different geometrical shape, electrical,[4] optical[5] and magnetic[6] properties. From the geometrical aspect, the nanofillers have at least one dimension less than 100 nm, and divided into three main groups including two- and three-dimensional (e.g. graphene and box-shaped graphene[7–9]), one-dimensional (e.g. nanowires and nanotubes[7,10,11]), and zero-dimensional (e.g. carbon black nanoparticles[7,12]). CNTs and nanowires have an extreme surface area-to-volume ratio and are one of the best candidates for manufacturing piezoresistive sensing elements.

As one of the most popular solution-based coating method, vacuum filtration can be used in the preparation of CNT transparent conducting films on flexible substrates.[13] Wang et al.[14] fabricated highly transparent ultrathin films of SWCNT using vacuum filtration process. They peeled off SWCNT ultrathin films from the filtration membrane by the surface tension of deionized water, and then transferred that onto polyethylene terephthalate (PET) substrates to make highly

[1]School of Mechanical Engineering, Iran University of Science and Technology, Iran
[2]Department of Polymer Engineering, Amirkabir University of Technology, Iran

Corresponding author:
NM Nouri, Iran University of Science and Technology, Tehran 16844, Iran.
Email: mnouri@iust.ac.ir

sensitive flexible chemiresistive sensors. Xu et al.[15] prepared the flexible conductive films of silver nanowires-PET (AgNW-PET) for high-performance flexible electronics and photovoltaic devices by applying a facile method including vacuum filtration and mold transferring. The effect of silver nanowire weight density on the electrical properties of films, as well as the electrical percolation, was investigated. The resulting typical AgNW-PET film exhibited a high figure of merit with a low sheet resistance and high transparency.

Wang et al.[16] fabricated reduced graphene oxide ultrathin films using vacuum filtration by a reproducible exfoliation method at the liquid/air interface, and developed a flexible relative humidity sensing matrix with high transparency, tunable sheet resistance, uniform electric conductivity, and structural homogeneity over a large area. Hyun et al.[17] used vacuum filtration method to disperse graphene suspension on the surface of a hydrophobic polytetrafluoroethylene (PTFE) membrane filter (pore size: 0.2 μm), and develop foldable paper-based electronic circuits. The shapes of circuits were drawn on the back of the membrane filter with a pen, and the filtered graphene was transferred onto the paper, while the graphene in the other parts remained on the filter. The graphene circuits had shown a small change in conductance under various folding angles and maintain an electronic path on paper substrates after repetition of folding and unfolding. Jiang et al.[18] manufactured foldable and stretchable graphene-based resistors using vacuum filtration method for portable and multifunctional devices and investigated the electrical stability of the films under bending and tension. They showed that nanocomposite resistors made using this method have unique characteristics and some advantages such as mechanical and thermal stability, rapid prototyping, flexibility, and stretchability over the traditional resistors.

In the present study, stretchable and skin-mountable PDMS/MWCNT hybrid composite films for flexible strain sensors were made using the vacuum filtration process. Afterward, the electrical properties of the flexible strain sensors containing different %wt of MWCNTs were evaluated and the electrical percolation region of the stretchable sensors made by this manufacturing method was obtained. Additionally, in order to determine the exact value of the percolation threshold, the percolation curve was obtained through curve fitting using the Gompertz growth numerical model.

Experimental study

Probably, compared with the other methods, the vacuum filtration technique is one of the best methods for the fabrication of ultrathin, electrically conducting films. In this process, surfactant-based suspension of MWCNTs

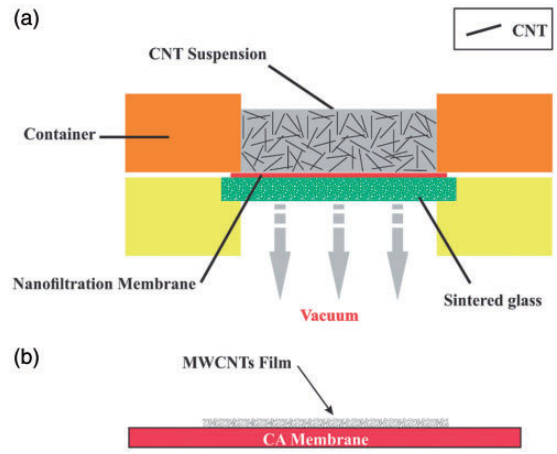

Figure 1. Schematic representation of vacuum filtration process: (a) filtration of the MWCNT suspension, (b) ultrathin film of randomly oriented MWCNTs on a nanofiltration membrane.

Figure 2. Ultrasonic probe, BANDELIN HD 3200 with the probe type VS-70T.

was poured into filtration funnel and due to the differential pressure across the nanofiltration membrane, a homogeneous wafer-scale film of randomly oriented MWCNTs was formed on the filtration membrane.[19] Then, the surfactant was washed away with purified water and the ultrathin layer of MWCNTs was used to prepare flexible strain sensor (see Figure 5).

In this method, the electrical conductivity and mechanical integrity of the resulted film are maximized, because under vacuum, the nanotubes tend to lie straight, gaining maximum overlap and interpenetration with each other. According to Figure 1(a), homogeneity of the MWCNT films is guaranteed since by accumulation of the nanotubes the local permeation rate decreases and the deposition rate will be tuned automatically. Moreover, the CNT nanoparticles in the MWCNT film have a random distribution which results in nanocomposite film with uniform

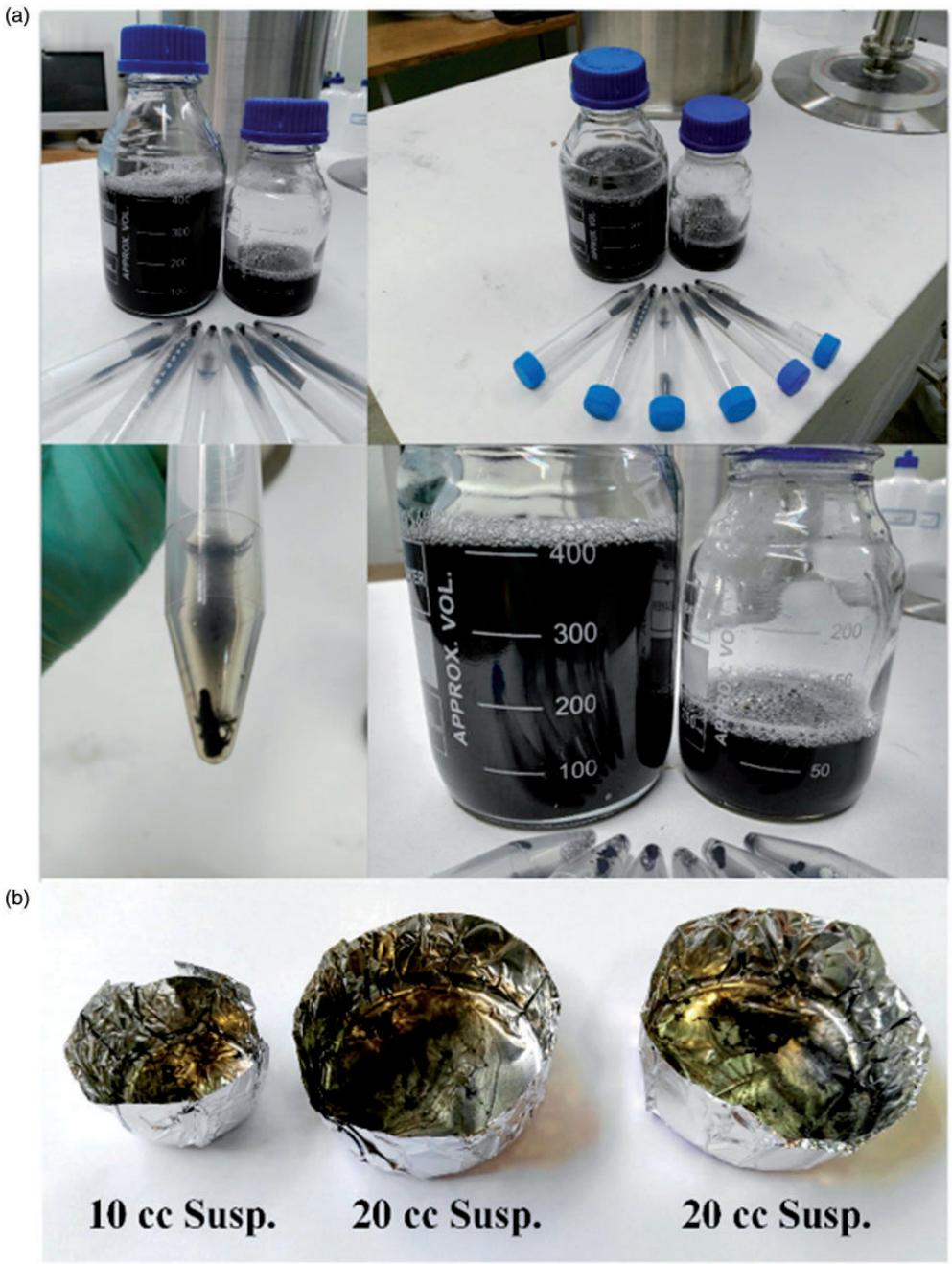

Figure 3. (a) Final CNT suspension after centrifuging. Agglomerated CNTs deposited in centrifuge tube and the final suspension is free from any agglomeration. (b) Aluminum foil container after evaporation of deionized water.

piezoresistive behavior in different directions. Additionally, it is possible to control the MWCNT film thickness with nanoscale precision by adjusting the suspension volume and nanotube concentration.[20]

Materials

To fabricate nanocomposite sensing elements, Sylgard 184 from Dow Corning was used as a matrix and MWCNT as a filler of nanocomposite. Sylgard 184 is the commercial PDMS with desirable properties such as facile polymerization, simple molding and prototyping, long gel time, biocompatibility, transparency, and desirable mechanical and dielectric properties. This elastomer mainly used in stretchable sensors, soft actuators and microfluidics. Schneider et al.[21] measured the rheological, mechanical and optical properties of Sylgard 184 for optical MEMS and showed that

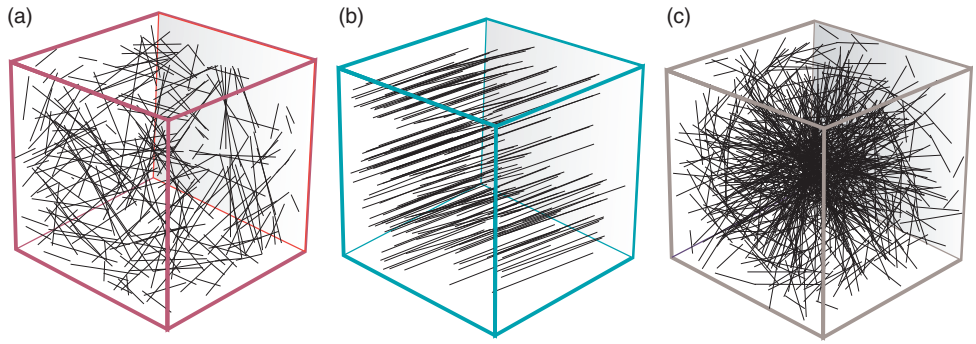

Figure 4. Schematic illustration of (a) uniformly distributed, (b) aligned and (c) agglomerated CNTs of different lengths.

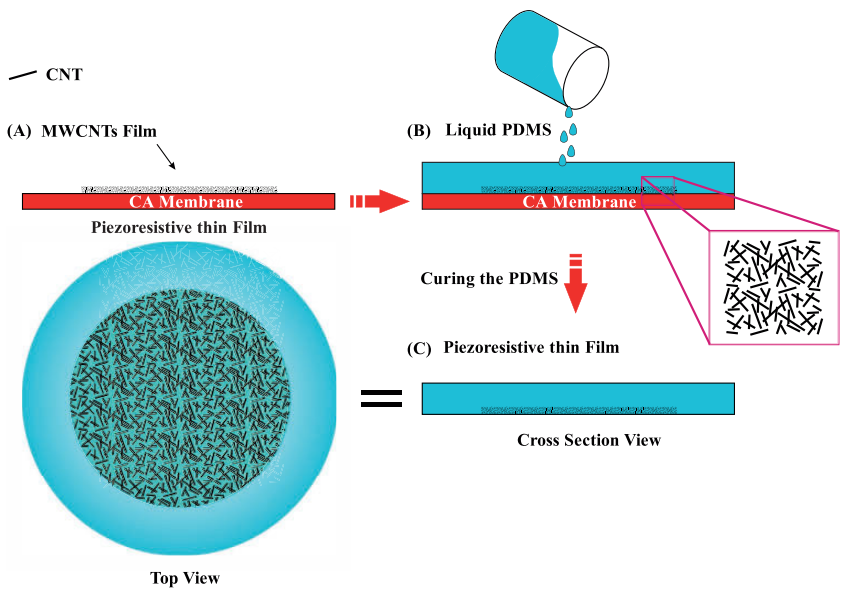

Figure 5. Schematic representation of experimental procedure.

Table 1. Properties of final CNT suspension after centrifuging process (see containers in Figure 3(b)).

Container	Container weight (g)	Suspension volume (mL)	Container weight after evaporation (g)	Difference weight (g)	CNT weight (g)	CNT Concentration (mg/mL)	wt.% of CNTs
A	0.5175	20	0.5636	0.0461	0.00192	0.0960	0.00972
B	0.5160	20	0.5618	0.0458	0.00191	0.0954	0.00962
C	0.2859	10	0.3083	0.0224	0.00093	0.0933	0.00952
Average						0.0949	0.0096

Sylgard 184 can endure strains up to 115%. This elastomer can be cured at different temperatures. In this paper, PDMS/MWCNT nanocomposites were cured at 70 °C for 2 h.

In addition, a suspension of MWCNTs was used as a nanocomposite filler because of its appropriate properties.[22] MWCNTs have desirable geometrical characteristics and physical properties.[23] The electrical conductivity of MWCNTs and their aspect ratio are the most important factors to create piezoresistive behavior in PDMS matrix. For instance, carbon nanotubes (CNT) possess high aspect ratios (length-to-diameter ratio) of up to 10,000[24] and also electrical conductivity of 103 to 104 S/cm.[25]

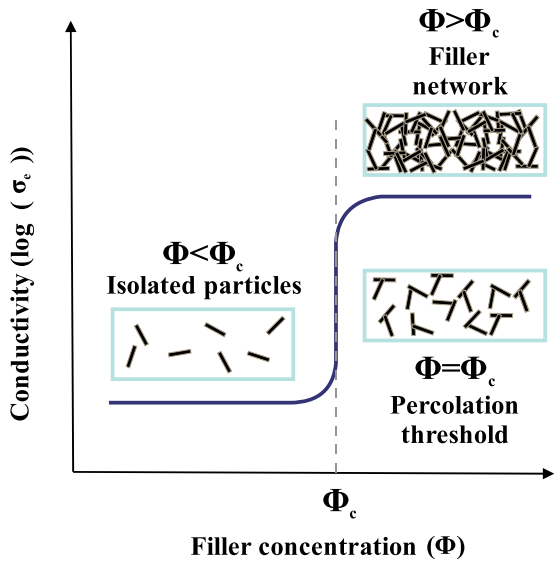

Figure 6. Schematic illustrations of the percolation curve of fillers in conductive FCFs.

Preparation of CNT suspension

In order to disperse MWCNTs in deionized water, the sodium dodecyl sulfate (SDS) was used as a surfactant material. Each SDS molecule has a polar and non-polar head which helps to disperse MWCNTs (non-polar) in deionized water (polar) and creates a stable suspension. At the beginning, CNT was mixed with SDS by the weight ratio of 1:23 in 1 L of deionized water. This value is an optimum quantity for the weight ratio of nanoparticle to surfactant. For this ratio, nanoparticle's surface is completely occupied by surfactant's molecules. Higher amount of surfactant affected the conductivity of CNTs. In lower ratios, the nanoparticles will not be stable.

The critical micelle concentration (CMC) in pure water at 25 °C is 8.2 mM. According to the molar mass of SDS (288.372 g/mol), the CMC in 1 L pure water is formed in the presence of 23 g SDS. We used 1 g CNT to make 1 L CNT suspension, and therefore the weight ratio of CNT:SDS was set to 1:23 in the 1 L of deionized water.[26]

In order to create CNT suspension, the materials were prepared and stirred for 15 min, then uniformly dispersed in deionized water with sonication process. According to Figure 2, the sonication process was done with BANDELIN-HD 3200 with the probe model VS-70T. The pulse duration and power were set to 1 s on/off and 70 W, respectively.

To ensure that the suspension does not contain any agglomerated CNTs, the final step should be done. In this step, all the suspension was centrifuged at 4500 r/min for 15 min in Universal-320 centrifuge machine. After this process, any agglomerated CNTs were deposited in the centrifuge tubes and a well-dispersed CNT suspension was obtained (Figure 3(a)).

Although the centrifuging process separates agglomerated CNTs from suspension (Figure 4(c)), however, this changes wt.% of CNTs in suspension. In order to obtain an exact wt.% of CNTs in the suspension, it is necessary to measure wt.% of CNTs again.

For this, some containers were made from an aluminum foil, then the specific amount of CNT suspension poured inside each container (Figure 3(b)) and all of the containers were weighted. To evaporate deionized water, containers were kept in the oven for 24 h at 65 °C. After 24 h, containers were weighted again.

In Table 1, the difference weight shows the weight of both CNT and SDS. As the CNT/SDS weight ratio was fixed at 1:23 in the primary suspension (before centrifuging), the concentration of MWCNTs in the final CNT suspension can be calculated. According to Table 1, the average concentration of MWCNTs is about 0.1 mg/ml.

Nanocomposite fabrication

The first step in the fabrication of piezoresistive nanocomposite is applying CNT film on CA membrane through vacuum filtration method. In order to implement this technique, preparation of CNT suspension and membrane with porosity smaller than the size of nanoparticles is necessary. These requisites are two important inputs of this process.

To achieve the best piezoresistive properties, it is necessary to have a suspension without any agglomeration of CNTs and use a membrane type (hydrophilic or hydrophobic) that has a proper conformity with suspension. In this study, a colloidal water-based suspension was used so the hydrophilic membranes like CA, Ny, MCE, PE, NC H-PTFE, PES, and H-PVDF were proper for using in vacuum filtration. In this study, CA membrane with pore size of 220 nm and Millipore setup was used in vacuum filtration process.

Different volume fractions of MWCNT suspension were used from 1 to 10 mL to create ultrathin films of MWCNT on CA membrane with Millipore setup. As surfactant material (SDS) reduces the electrical conductivity of CNT nanoparticles, to achieve the maximum electrical conductivity in MWCNTs, it is better to deterge surfactant from nanoparticles. For this purpose, after the filtration process, the CNT layer on CA membrane was washed with deionized water.

Next step is applying PDMS on a CNT-coated CA membrane and curing the PDMS to obtain piezoresistive PDMS/CNT nanocomposite. In this step, a PDMS film with a thickness of 500 μm was applied on CA membrane (Figure 5(b)), and then a liquid PDMS was cured at 70°C for 2 h.

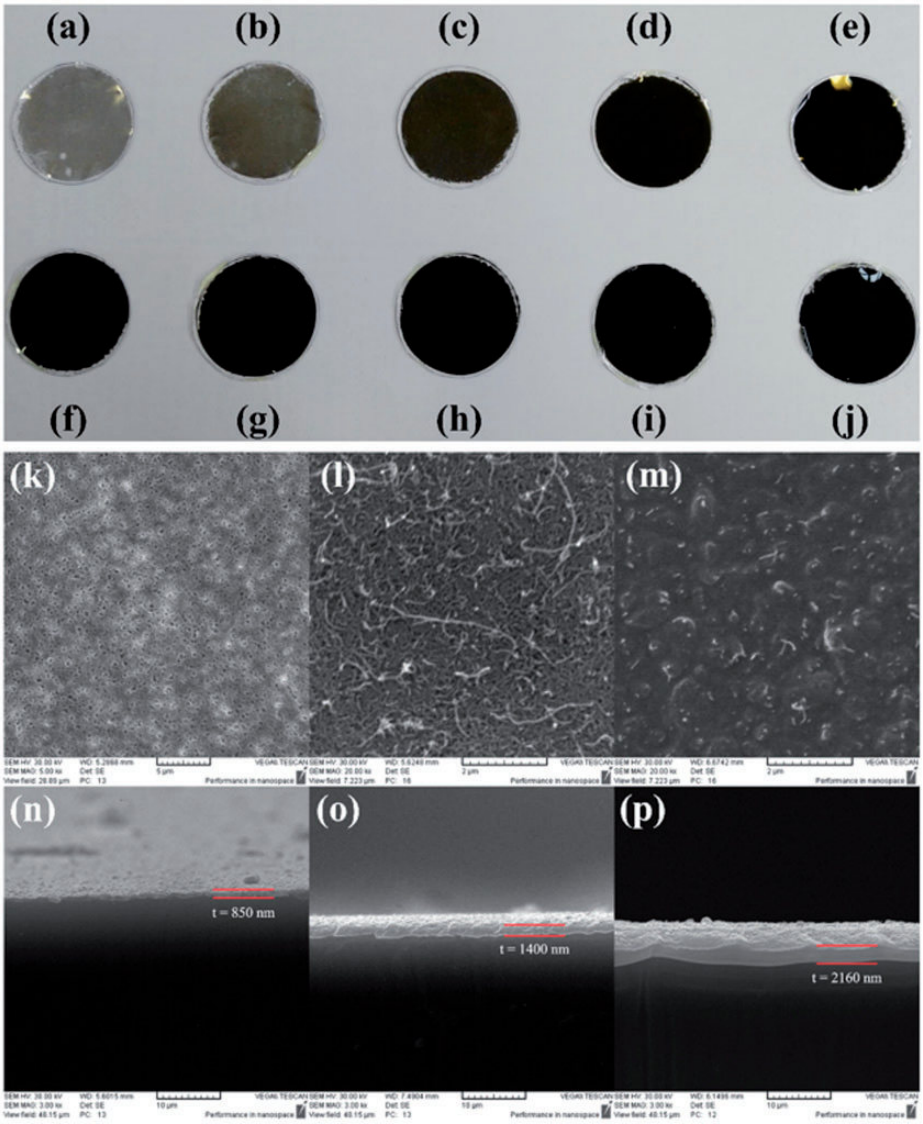

Figure 7. (a–j) Piezoresistive PDMS/ MWCNT nanocomposites with different CNT content made by 1 to 10 mL of CNT suspension, respectively. (k) SEM image of cellulose acetate membrane with pore size of 220 nm. (l) Uniform distribution of MWCNTs on the CA membrane surface. (m) Nanocomposite surface. (n–p) Cross-section of (c), (e) and (i) piezoresistive films with the nanocomposite thickness of 850 nm, 1400 nm, and 2160 nm, respectively.

After curing PDMS, CA membrane was peeled off from PDMS/MWCNT piezoresistive nanocomposite (Figure 5(c)).

Results and discussion

Electrical property

According to the traditional percolation theory,[27] the electrical conductivity of conductive composites can be predicted by

$$\sigma = \sigma_0(\Phi - \Phi_c)^t; \quad \Phi > \Phi_c \tag{1}$$

where σ is the electrical conductivity of FCFs, Φ is the volume fraction of the filler, Φ_c is the percolation threshold, σ_0 is a parameter basically depending on the electrical conductivity of the filler and t is the critical exponent universally related to the dimensionality of the conductive network. According to the S-shaped conductance curve of nanocomposites (Figure 6), the transition from nonconductive to conductive state occurs at some critical volume fraction, known as percolation threshold.

After passing through the percolation threshold ($\Phi = \Phi_c$), the dependence of the electrical conductivity of the nanocomposite on the filler reduces and eventually reaches a saturation point and adding more

conductive nanoparticles will no longer improve the electrical conductivity of the nanocomposite.[28] The highest piezoresistive sensitivity is achieved when the volume fraction of nanotubes is near to the percolation threshold. Given the above description, in order to achieve the maximum sensitivity, it is necessary to find the percolation threshold and manufacture the sensing element with optimum weight percentage of conductive nanofillers.

According to Figure 7, sensing elements with the same size but different CNT contents are made using the manufacturing process illustrated in Figure 5. The sensing elements are hybrid films containing 0.7 to 7.2 mg of CNT nanofillers per square millimeter. Table 2 shows the values of initial resistance (R_0) and the PDMS/MWCNT nanocomposite layer thickness on pure PDMS substrate for different strain sensors made by 1 to 10 mL of CNT suspension. Figure 8 demonstrates the variation of nanocomposite layer thickness with CNT concentration for different strain sensors.

According to Figure 9, with increasing the CNT amount, the initial resistance of the strain sensors decreases exponentially. The decrease of the initial resistance is impressive in the strain sensors with the CNT concentration values lower than 2.9 mg/mm^2.

There is a transition from nonconductive to conductive state in the strain sensors made of 2 to 4 ml of CNT suspension. The suspension used in this study had a concentration of 0.1 mg/ml, and the surface area of all sensors was about 1385 mm^2. It means that the nonconductive to conductive transition is achieved with 1.4 to 2.9 mg/mm^2 of MWCNTs concentration (see Table 2). According to Figure 10, this optimum range is the percolation range of the strain sensors made by

Table 2. Initial resistance versus nanocomposite layer thickness of strain sensors made of 1 to 10 ml CNT suspension.

Suspension value (mL)	Initial resistance (kΩ)	Nanocomposite thickness (*nm*)	CNT concentration $\left(\frac{mg}{(mm^2)}\right)$
1	22,800	480	0.7
2	12,700	790	1.4
3	781	850	2.2
4	74.9	1210	2.9
5	39.6	1400	3.6
6	30.2	1450	4.3
7	21.8	1790	5
8	14.3	2075	5.8
9	13.4	2160	6.5
10	12.55	2540	7.2

Table 3. Constant parameters of the electrical conductivity curve of strain sensors.

Parameter	Value
A	0.039769427
B	3.176950293
C	6.477276124
D	0.589179378

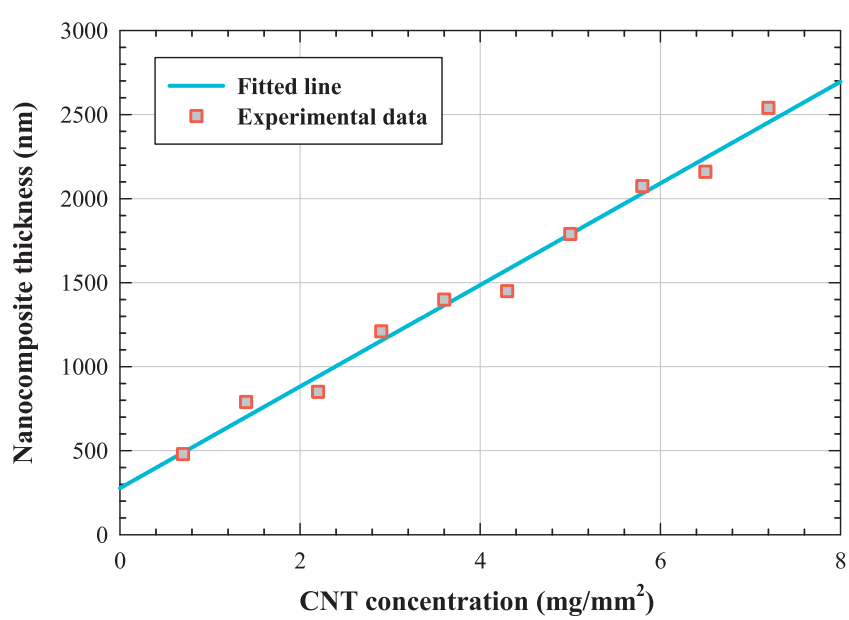

Figure 8. Variation of nanocomposite layer thickness with CNT concentration for different strain sensors.

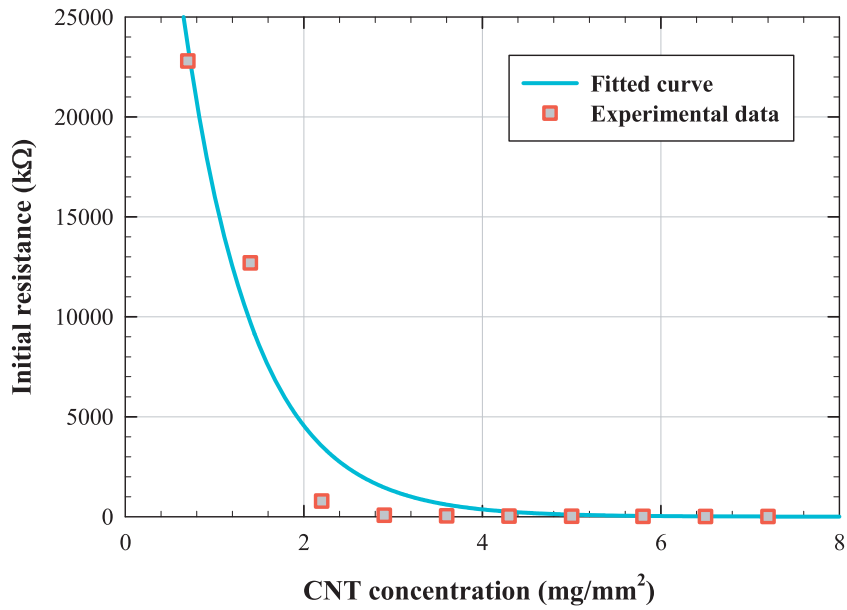

Figure 9. Initial resistance versus CNT concentration for strain sensors.

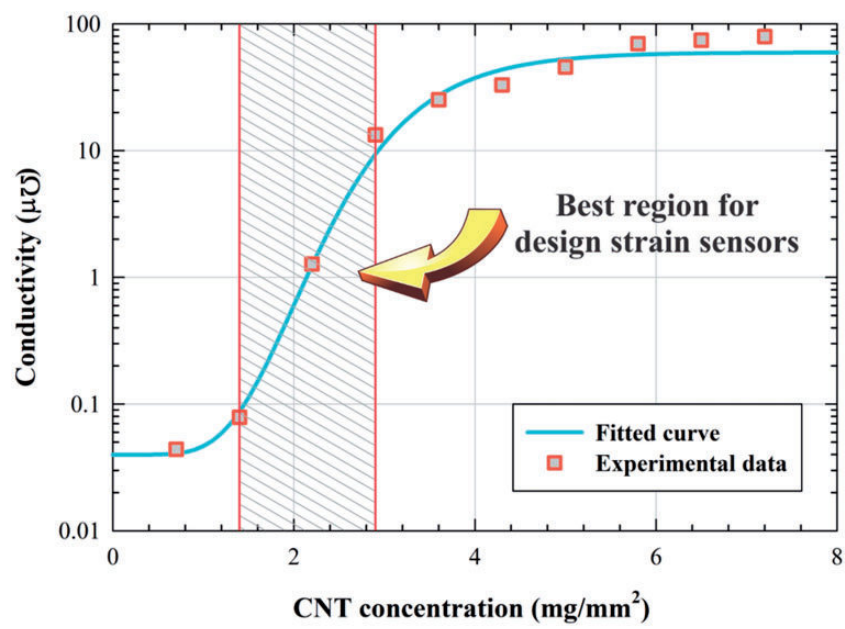

Figure 10. Electrical conductivity versus CNT concentration for strain sensors.

vacuum filtration method and can be used for manufacturing flexible strain sensors with maximum sensitivity.

Numerical fitting

In order to find the exact value of percolation threshold ($\phi = \phi_c$) and predict the electrical conductivity of strain sensors in desired CNT concentration value, an equation was defined using Gompertz growth curve in the form of equation (2). This equation was used in curve fitting and was fitted to the experimental data

$$Conductivity = \mathrm{a} \times 10^{(b \times 10^{(-c \times 10^{(-d \times x)})})} \quad (2)$$

According to equation (2), the electrical conductivity curve of the strain sensors was defined by determining the constant parameters a, b, c and d through nonlinear least-squares best fit.

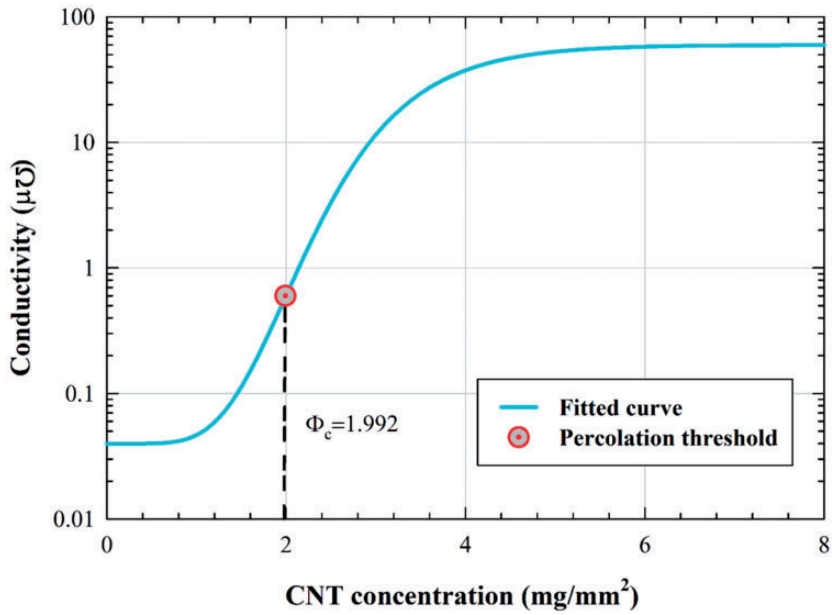

Figure 11. Exact value of percolation threshold for PDMS/MWCNT flexible strain sensors.

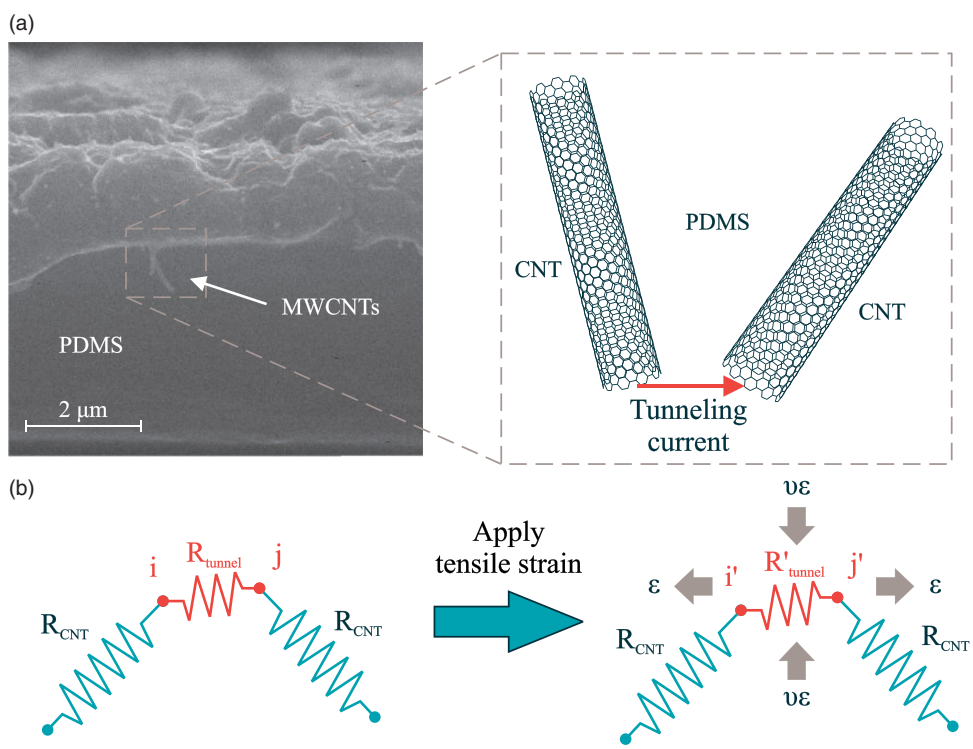

Figure 12. (a) SEM image of possible tunneling effect among neighboring CNTs (b) Variation of tunneling resistance among neighboring CNTs by applying tensile strain to nanocomposite.

The electrical conductivity curve of flexible strain sensors is achieved by replacing the constant parameters a, b, c and d in equation (2). The exact value of percolation threshold ($\phi = \phi_c$) was determined by calculating the inflection point of electrical conductivity curve. For this purpose, the second derivation of the conductivity curve was calculated using numerical derivation method and the percolation value was determined as illustrated in Figure 11.

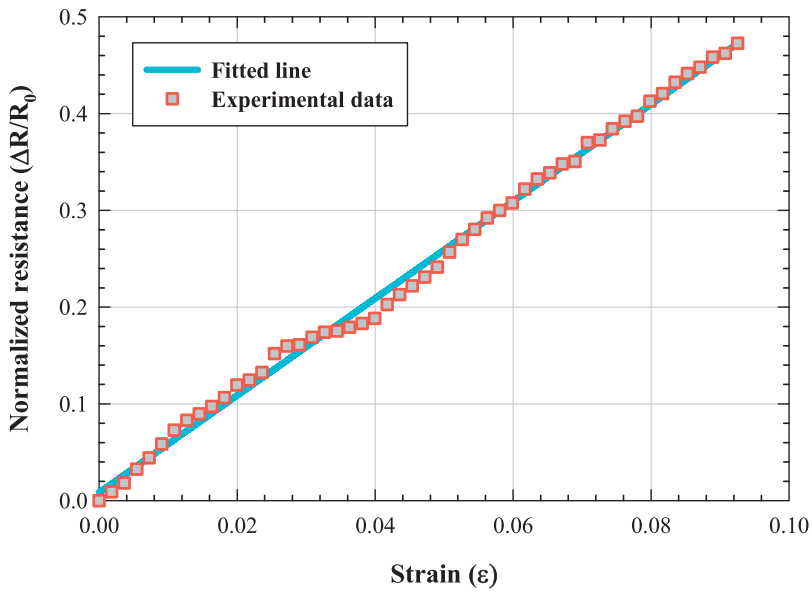

Figure 13. Strain versus normalized resistance change of the strain sensor.

According to Figure 11, in order to manufacture the flexible strain sensors with maximum sensitivity, it is suggested to adjust the CNT concentration of the strain sensor to the value of 1.99 mg/mm^2. By determining the concentration of CNT suspension (mg/ml) and also the surface area of CNT deposition on filtration membrane (mm^2), it is possible to find the exact CNT suspension volume to use in the vacuum filtration method and manufacture a flexible strain sensor which is in the percolation threshold ($\phi = \phi_c$) and has the maximum sensitivity.

Piezoresistive property

As for the working mechanisms in the piezoresistive nanocomposite strain sensors, from the accumulated knowledge until now, the piezoresistivity observed in this kind of strain sensors can be mainly attributed to the following three aspects; (a) significant variation of conductive networks formed by CNTs, e.g. loss of contact among CNTs. (b) Tunneling resistance change in neighboring CNTs due to the distance change. (c) piezoresistivity of CNTs themselves due to their deformation.[29] In the 3D resistor network of polymer nanocomposites, tunneling resistance has a major role in piezoresistivity. For instance, Fang et al.[30] enhanced conductivity of the Ag-NW/PI-PANI composite films by reducing the tunneling resistance between Ag-NWs. The tunneling resistance between two neighboring CNTs as shown in Figure 12, can be approximately estimated as follows[31]

$$R_{tunneling} = \frac{V}{AJ} = \frac{h^2 d}{Ae^2\sqrt{2m\lambda}} \exp\left(\frac{4\pi d}{h}\sqrt{2m\lambda}\right) \quad (3)$$

where J is the tunneling current density (Figure 12), V is the electrical potential difference, e is the quantum of electricity, m is the mass of the electron, h is Planck's constant, d is the distance between CNTs, λ is the height of the barrier (for epoxy, 0.5 to 2.5 eV), and A is the cross-sectional area of the tunnel.[32]

The strain sensor shown in Figure 7(d) was selected and its piezoresistive properties were evaluated. This specimen has total thickness of about 540 μm in which 1.2 μm of its thickness is an ultrathin layer of PDMS/MWCNT nanocomposite. The nanocomposite layer (see Figure 7(n) to (p)) is made of 4 ml CNT suspension and has a CNT concentration of 2.9 mg/mm^2. According to Figure 10, this strain sensor is the upper limit of the suggested region for design strain sensors and has the minimum gauge factor (GF_{min}) of the sensors in this region. By evaluation of the piezoresistive properties of this sensor, GF_{min} was determined.

The strain versus normalized resistance changes of this specimen is shown in Figure 13. The most important parameter of the strain sensor to determine its sensitivity is the gauge factor (GF). This parameter can be calculated as follows

$$GF = \frac{\Delta R/R_0}{\Delta L/L_0} = \frac{\Delta R}{R_0 \times \varepsilon} \quad (4)$$

According to Figure 13, a fitted line has an average slope of 5 and so the average gauge factor of this sensing element is equal to five. We can conclude that the minimum gauge factor (GF_{min}) of the strain sensors in the design region (illustrated in Figure 10) is about 5. Figure 14 shows the gauge factor variation of this sensor in different strains.

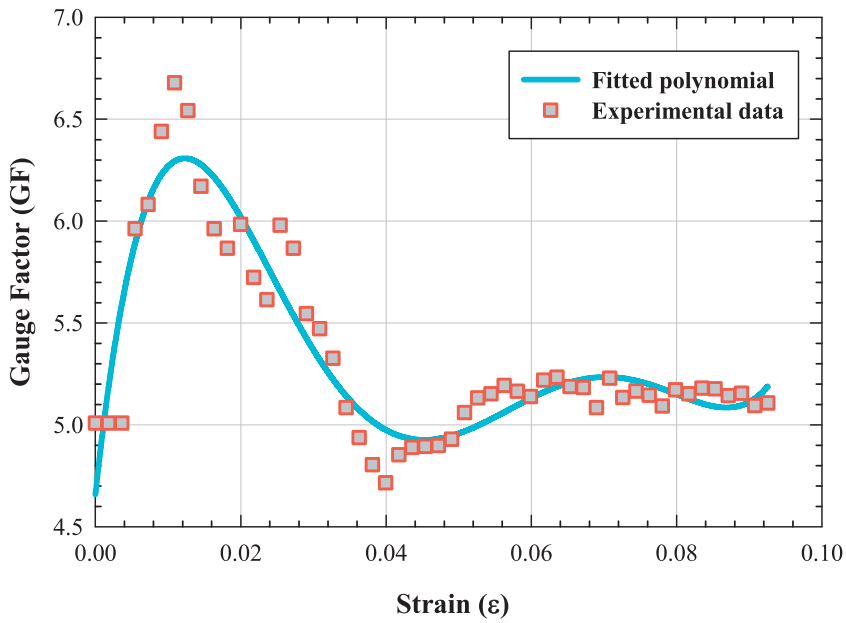

Figure 14. Variation of gauge factor with strain for strain sensor containing 2.9 mg/mm^2 of CNT nanofillers.

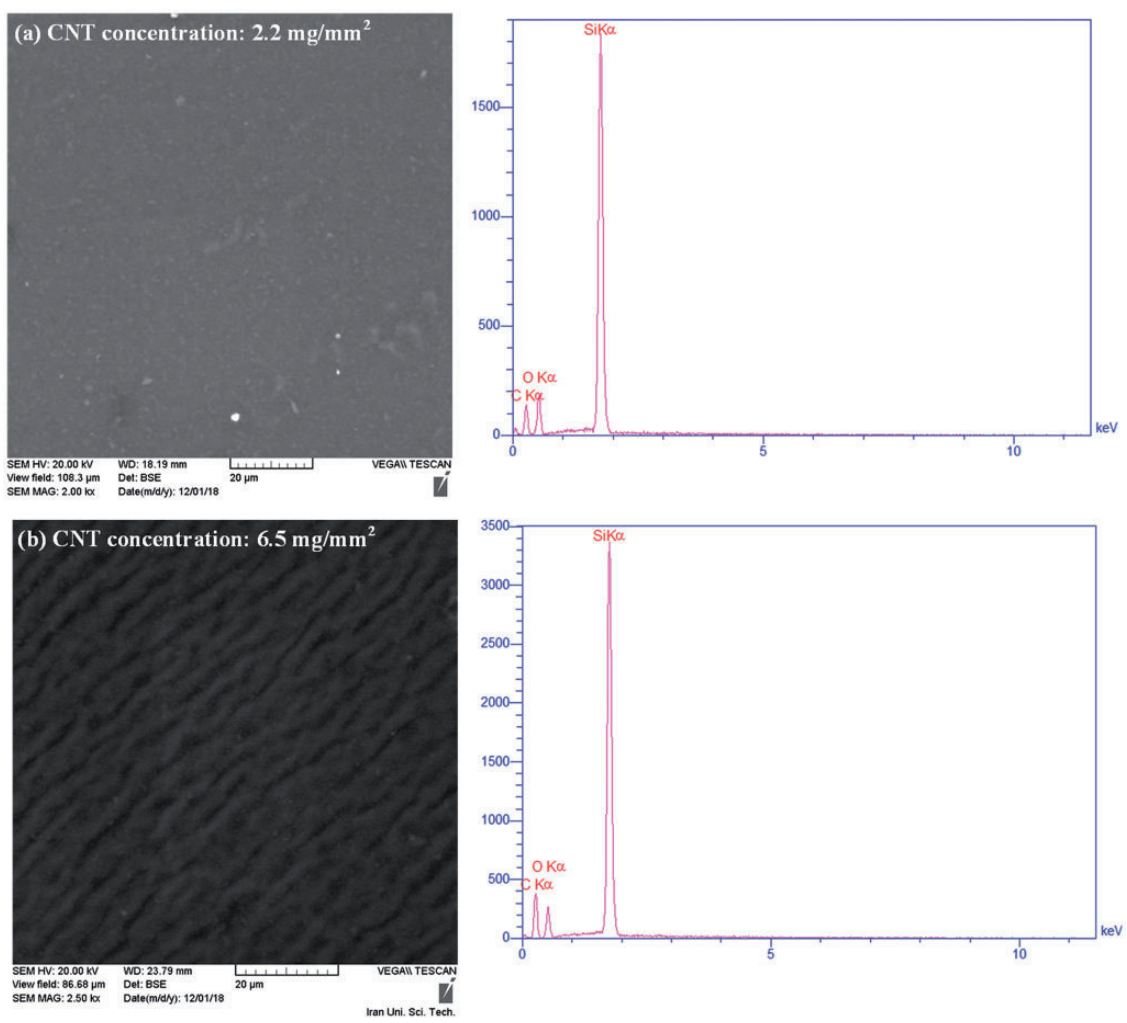

Figure 15. EDS spectrum of the flexible strain sensors with (a) 2.2 and (b) 6.5 mg/mm^2 MWCNT concentration.

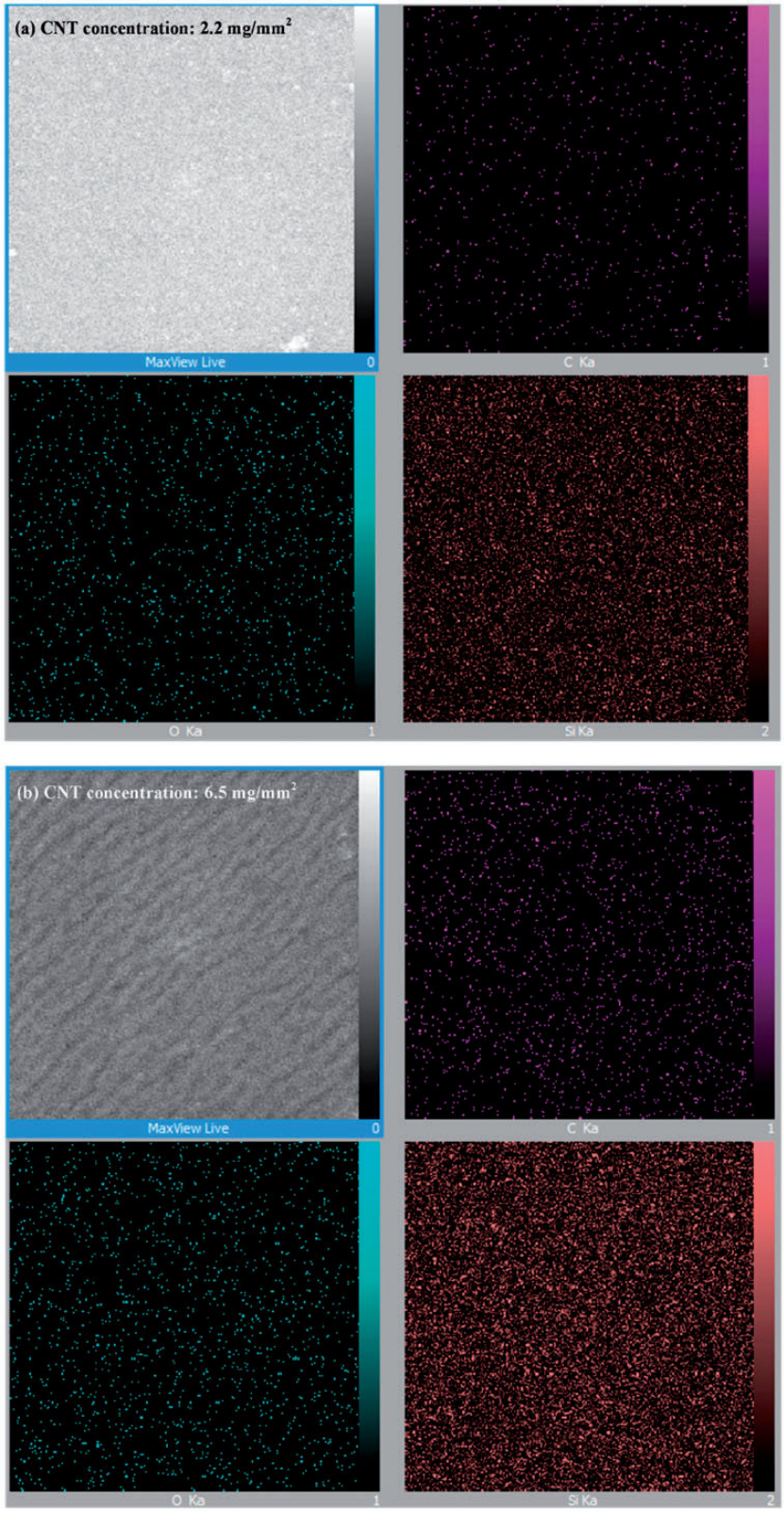

Figure 16. Distribution of the main elements in the flexible strain sensor containing (a) 2.2 mg/mm^2 and (b) 6.5 mg/mm^2 MWCNTs made by SEM scanning.

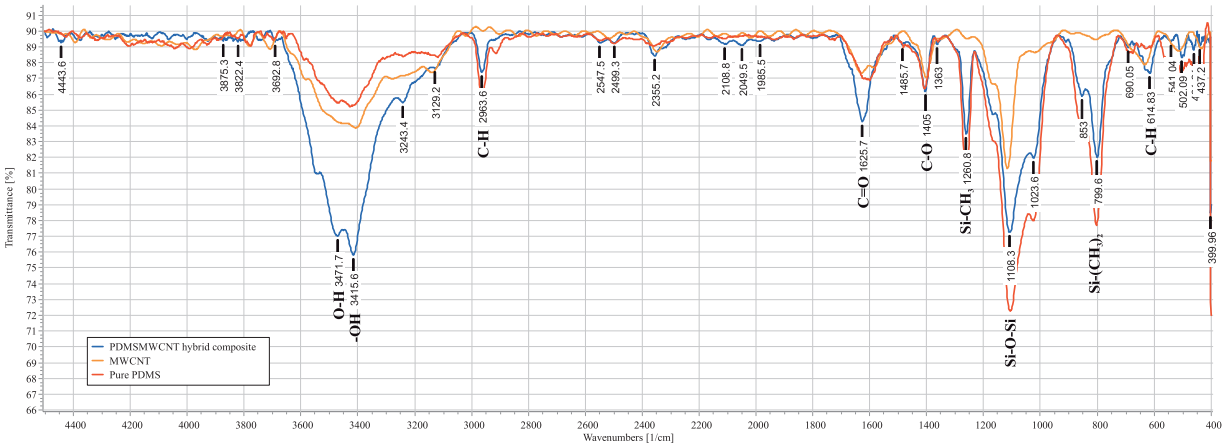

Figure 17. Results of FTIR analysis.

Interaction between components

In addition, in order to determine the contribution of the main elements, two different specimens were selected and tested using energy-dispersive X-ray spectroscopy (EDS) and SEM scanning. EDS is an analytical technique used for the elemental analysis or chemical characterization of a sample which can show both the percentage and distribution of the main elements if accompanied by SEM scanning. EDS spectrum of the flexible strain sensors containing 2.2 and 6.5 mg/mm^2 MWCNT concentration is illustrated in Figure 15(a) and (b), respectively.

Moreover, the distribution of the main elements in the aforementioned specimens extracted by SEM scanning is presented in Figure 16(a) and 16(b), respectively.

Moreover, the interaction between components was analyzed with FTIR method and the final results are shown in Figure 17.

Conclusion

In this study, piezoresistive hybrid films contain an ultrathin layer of PDMS/MWCNT nanocomposite with different wt.% of MWCNTs which were made by vacuum filtration method and their electrical and piezoresistive properties were discussed. First, the initial resistance of each strain sensor was measured, and then the percolation curve and best region for design flexible strain sensors were defined. It was shown that the percolation threshold of the strain sensors is achieved with the CNT concentration of 1.4 to 2.9 mg/mm^2. Afterward, the piezoresistive specimen with the CNT concentration of 2.9 mg/mm^2 and nanocomposite thickness of 1.2 μm was selected and its piezoresistive properties were evaluated. Finally, the distribution of the main elements and the interaction between components for two strain sensors with different CNT concentration were discussed.

Acknowledgments

The authors would like to thank the Iran Polymer and Petrochemical Institute (IPPI) and the members of the Institute of Applied Hydrodynamics and marine technology of Iran University of Science and Technology (IUST) for their help in the work.

Declaration of Conflicting Interests

The author(s) declared no potential conflicts of interest with respect to the research, authorship, and/or publication of this article.

Funding

The author(s) disclosed receipt of the following financial support for the research, authorship, and/or publication of this article: This work was partially supported by the Iran Nanotechnology Initiative Council (INIC).

ORCID iD

M Nankali https://orcid.org/0000-0002-0781-802X
N Geran Malek https://orcid.org/0000-0003-3725-738X

References

1. Zheng Y, Li Y, Dai K, et al. A highly stretchable and stable strain sensor based on hybrid carbon nanofillers/polydimethylsiloxane conductive composites for large human motions monitoring. *Compos Sci Technol* 2018; 156: 276–286.
2. Lu S, Tian C, Wang X, et al. Strain sensing behaviors of GnPs/epoxy sensor and health monitoring for composite materials under monotonic tensile and cyclic deformation. *Compos Sci Technol* 2018; 158: 94–100.
3. Zang Y, Zhang F, Di C-A, et al. Advances of flexible pressure sensors toward artificial intelligence and health care applications. *Mater Horizons* 2015; 2: 140–156.

4. Bandaru PR. Electrical properties and applications of carbon nanotube structures. *J Nanosci Nanotechnol* 2007; 7: 1239–1267.
5. Shi J, Zhu Y, Zhang X, et al. Recent developments in nanomaterial optical sensors. *Trends Analyt Chem* 2004; 23: 351–360.
6. Lu Y, Yin Y, Mayers BT, et al. Modifying the surface properties of superparamagnetic iron oxide nanoparticles through a sol−gel approach. *Nano Lett* 2002; 2: 183–186.
7. Tiwari JN, Tiwari RN and Kim KS. Zero-dimensional, one-dimensional, two-dimensional and three-dimensional nanostructured materials for advanced electrochemical energy devices. *Progr Mater Sci* 2012; 57: 724–803.
8. Rao CN, Sood AK, Subrahmanyam KS, et al. Graphene: the new two-dimensional nanomaterial. *Angew Chem Int Ed Engl* 2009; 48: 7752–7777.
9. Lapshin RV. STM observation of a box-shaped graphene nanostructure appeared after mechanical cleavage of pyrolytic graphite. *Appl Surf Sci* 2016; 360: 451–460.
10. Cui Y, Zhong Z, Wang D, et al. High performance silicon nanowire field effect transistors. *Nano Lett* 2003; 3: 149–152.
11. Iijima S. Helical microtubules of graphitic carbon. *Nature* 1991; 354: 56–58.
12. Suri K, Annapoorni S, Sarkar AK, et al. Gas and humidity sensors based on iron oxide–polypyrrole nanocomposites. *Sensors Actuat B* 2002; 81: 277–282.
13. Yu L, Shearer C and Shapter J. Recent development of carbon nanotube transparent conductive films. *Chem Rev* 2016; 116: 13413–13453.
14. Wang X, Li G, Liu R, et al. Reproducible layer-by-layer exfoliation for free-standing ultrathin films of single-walled carbon nanotubes. *J Mater Chem* 2012; 22: 21824–21827.
15. Xu W, Xu Q, Huang Q, et al. Fabrication of flexible transparent conductive films with silver nanowire by vacuum filtration and PET mold transfer. *J Mater Sci Technol* 2016; 32: 158–161.
16. Wang X, Xiong Z, Liu Z, et al. Exfoliation at the liquid/air interface to assemble reduced graphene oxide ultrathin films for a flexible noncontact sensing device. *Adv Mater* 2015; 27: 1370–1375.
17. Hyun WJ, Park OO and Chin BD. Foldable graphene electronic circuits based on paper substrates. *Adv Mater* 2013; 25: 4729–4734.
18. Jiang X, Zhang R, Yang T, et al. Foldable and electrically stable graphene film resistors prepared by vacuum filtration for flexible electronics. *Surf Coat Technol* 2016; 299: 22–28.
19. He X, Gao W, Xie L, et al. Wafer-scale monodomain films of spontaneously aligned single-walled carbon nanotubes. *Nat Nanotechnol* 2016; 11: 633–638.
20. Yellampalli S. *Vacuum filtration method, carbon nanotubes – synthesis, characterizatiion, applications*. Croatia: Intech, 2011, p.496.
21. Schneider F, Draheim J, Kamberger R, et al. Process and material properties of polydimethylsiloxane (PDMS) for optical MEMS. *Sensors Actuat A* 2009; 151: 95–99.
22. Sengupta R, Bhattacharya M, Bandyopadhyay S, et al. A review on the mechanical and electrical properties of graphite and modified graphite reinforced polymer composites. *Prog Polym Sci* 2011; 36: 638–670.
23. Al-Saleh MH and Sundararaj U. A review of vapor grown carbon nanofiber/polymer conductive composites. *Carbon* 2009; 47: 2–22.
24. Wang X, Jiang Q, Xu W, et al. Effect of carbon nanotube length on thermal, electrical and mechanical properties of CNT/bismaleimide composites. *Carbon* 2013; 53: 145–152.
25. Ma P-C, Siddiqui NA, Marom G, et al. Dispersion and functionalization of carbon nanotubes for polymer-based nanocomposites: a review. *Compos Part A* 2010; 41: 1345–1367.
26. Sanjari Shahrezaei MA, Goharpey F and Foudazi R. Effect of particle–particle and polymer–particle interactions on nanosilica aggregation in polystyrene. *Polym Compos* 2018; 39: 2904–2914.
27. Allen G and Stuart A W (eds).*Percolation, localization, and superconductivity*. Ed. 1. Tel Aviv, Israel: Springer US, 1984, pp.95–113.
28. Cuppoletti J. *Nanocomposites with unique properties in medicine industry*. Rijeka, Croatia: Intech , 2011.
29. Hu N, Fukunaga H, Atobe S, et al. Piezoresistive strain sensors made from carbon nanotubes based polymer nanocomposites. *Sensors* 2011; 11: 10691–10723.
30. Fang F, Huang G-W, Xiao H-M, et al. Largely enhanced electrical conductivity of layer-structured silver nanowire/polyimide composite films by polyaniline. *Compos Sci Technol* 2018; 156: 144–150.
31. Simmons JG. Generalized formula for the electric tunnel effect between similar electrodes separated by a thin insulating film. *J Appl Phys* 1963; 34: 1793–1803.
32. Hu B, Hu N, Li Y, et al. Multi-scale numerical simulations on piezoresistivity of CNT/polymer nanocomposites. *Nanoscale Res Lett* 2012; 7: 402.

Buckling load of laminated composite plates using three variants of the biogeography-based optimization algorithm

A. Kaveh, A. Dadras & N. Geran Malek

Acta Mechanica

ISSN 0001-5970

Acta Mech
DOI 10.1007/s00707-017-2068-0

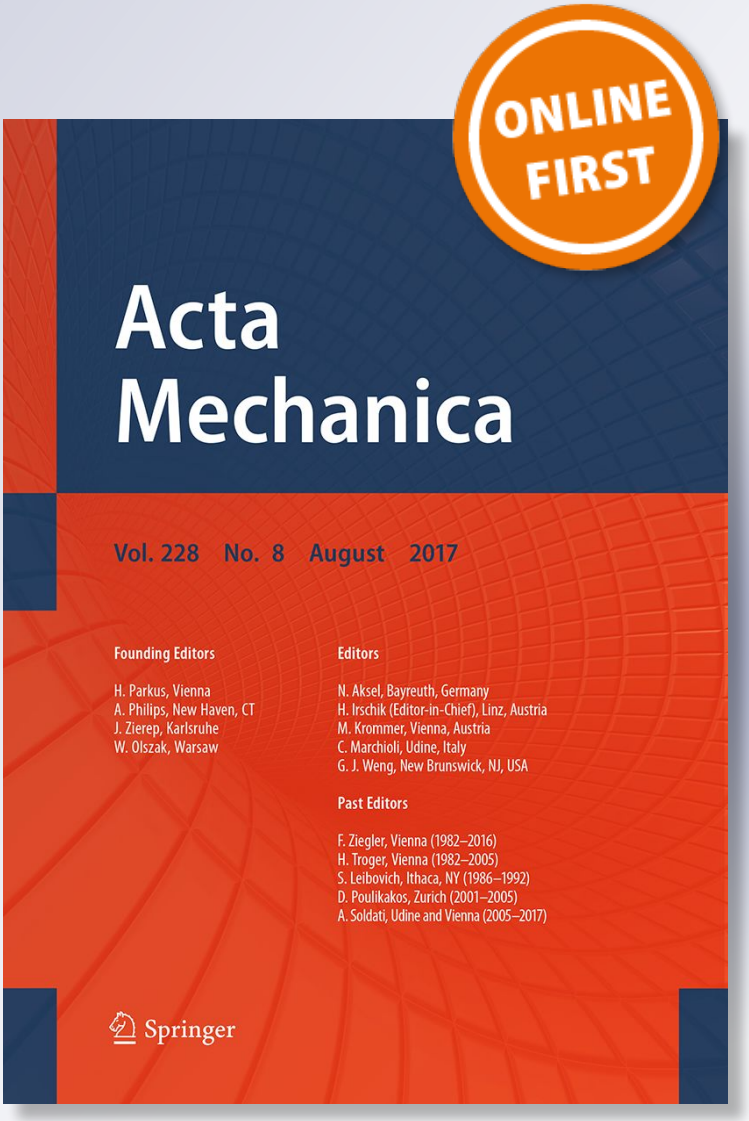

Springer

Your article is protected by copyright and all rights are held exclusively by Springer-Verlag GmbH Austria, part of Springer Nature. This e-offprint is for personal use only and shall not be self-archived in electronic repositories. If you wish to self-archive your article, please use the accepted manuscript version for posting on your own website. You may further deposit the accepted manuscript version in any repository, provided it is only made publicly available 12 months after official publication or later and provided acknowledgement is given to the original source of publication and a link is inserted to the published article on Springer's website. The link must be accompanied by the following text: "The final publication is available at link.springer.com”.

Springer

Author's personal copy

Acta Mech
https://doi.org/10.1007/s00707-017-2068-0

ORIGINAL PAPER

A. Kaveh · A. Dadras · N. Geran Malek

Buckling load of laminated composite plates using three variants of the biogeography-based optimization algorithm

Received: 17 June 2017 / Revised: 12 September 2017
© Springer-Verlag GmbH Austria, part of Springer Nature 2017

Abstract This paper presents the application of the biogeography-based optimization (BBO) and some of its variants in the optimization of stacking sequence of laminated composites. Harmony search is also implemented to compare its results with those of the BBO. The optimization objective is to maximize the buckling load of a symmetric and balanced laminated plate. Four laminated composites with different loadings and dimensions are studied, and the statistical comparison of the obtained configurations and buckling load capacities shows the high capability of the BBO with quadratic migration model in terms of robustness and global search.

1 Introduction

Owing to the superior characteristics of the laminated composites, such as specific strength, stiffness, weight and extreme possibilities, composite structures are extensively used in industries. These structures can be optimized based on parameters such as thickness, fiber orientation, dimension, the number of plies and stacking sequence. Finding the desired mechanical properties of these structures has attracted much attention in recent decades as an optimization task.

Ghiasi et al. [1] in 2009 reviewed the classification of optimization techniques used for optimal layup selection of laminated composite materials provided by Setoodeh et al. [2], in which there were two scenarios for the design of the composite structures: (1) constant stiffness with the goal being to find an optimal stacking sequence for the entire structural material distribution and (2) variable stiffness where the orientation of the fibers might change over the structural domain. Fang and Springer [3] suggested another classification for composite panels, categorizing the design methods into four groups: (1) analytical procedures, (2) enumeration methods, (3) heuristic schemes and (4) nonlinear programming approaches.

As reviewed, different optimization approaches can be employed to optimize the structural performance of the laminated composites against buckling load due to design variables such as the fiber orientations and stacking sequence. Metaheuristics are suitable tools for global search of large and complex problems with affordable computational time and accuracy that are usually inspired by nature. These methods are significantly developed and applied to engineering problems [4–8]. Application of these methods in laminated composite plates is an interesting field, and some of the relevant papers are presented in the following.

Soremekun et al. [9] explored several generalized elitist selections for the design of composite laminates, Ching-Chieh Lin et al. [10] proposed an improved GA which converges much faster than the standard GA. Rao and Arvind [11] in 2005 discussed a scatter search algorithm for the layup sequence optimization of laminate

A. Kaveh (✉) · A. Dadras
Centre of Excellence for Fundamental Studies in Structural Engineering, Iran University of Science and Technology, Tehran, Iran
E-mail: alikaveh@iust.ac.ir

N. G. Malek
School of Automotive Engineering, Iran University of Science and Technology, Narmak, Tehran 16, Iran

Published online: 19 December 2017

Author's personal copy

composite panels and explored the effectiveness of the proposed method. Erdal et al. [12] in 2005 utilized direct simulated annealing (DSA) algorithm for stacking sequence optimization of two-dimensional composite structures. GA with special operators and variables codification associated with the finite element method (FEM) stated by Almeida and Awruch [13] in 2009. Karakaya et al. [14] in 2009 compared GA and GPSA for maximization of buckling capacity of symmetric and balanced laminate panel made up 64 graphite/epoxy plies for several combinations of load cases and plate aspect ratios by varying stacking sequence. Sebaey et al. [15] in 2011 supported the movement of the composite industry toward using dispersed laminates, by the implementation of the ant colony optimization algorithm showing its superiority in terms of stiffness, buckling resistance and strength of laminates subjected to biaxial compression and tension loading cases with respect to conventional laminates. Abachizadeh et al. [16] in 2008 proposed an ant colony optimization algorithm for a multi-objective optimization problem of symmetric hybrid laminates. Maximization of fundamental frequency and minimization of cost were the objective, and the number of surfaces and core layers, and fiber orientations were the design variables. Based on the artificial bee colony (ABC) algorithm, a new version of vector evaluated artificial bee colony (VEABC) algorithm for discrete variables has been discussed by Omkar et al. [17] in 2011 and implemented for the multi-objective minimization of weight and cost. Almeida [18] in 2016 demonstrated the outperforming of the harmony search algorithm (HSA) [19] in stacking sequence optimization problems with respect to other meta-heuristic methods and its low reliability compared to a specially modified genetic algorithm. Vosoughi et al. [20] in 2017 studied the optimum stacking sequences for maximum buckling load of thick laminated composite plates by linking the higher-order shear deformation theory (HSDT) governing equations of the plate FEM solution with a hybrid genetic algorithms (GAs) and particle swarm optimization (PSO) methods. Setoodeh et al. [21] in 2017, by exerting a search-based optimizing method based on the GA on differential equations and the related boundary conditions discretized by differential quadrature method (DQM), studied the buckling of functionally graded carbon nanotube-reinforced laminated composite quadrilateral plates (FG CNTRCQ) with arbitrary straight-sided.

In this study, the biogeography-based optimization (BBO) algorithm is chosen for maximizing the buckling load capacity of the laminated composite structures. Different variants of the BBO are applied to four case studies, and the results are statistically investigated and compared with those of some other well-known metaheuristics.

The rest of the paper is organized as follows. Section 2 outlines a comprehensive description of the BBO and its steps. In Sect. 3, a terse review on the theory of buckling failure in laminated composites and the investigated problem is presented. In Sect. 4, results of various case studies are provided, and finally, the conclusions are presented in Sect. 5.

2 Biogeography-based optimization

2.1 History

Distribution of biological species follows a mathematical pattern. The biogeography is the study of the geographical distribution of biological organisms. In biogeography, the suitability of a habitat to live is called 'habitat suitability index' (HSI), according to this definition the amiable places have high HIS and the unfriendly habitats to live have a low HIS. This index pursues some features, which called 'suitability index variables' (SIVs) [22], for example the land area, topographic diversity, temperature and vegetative diversity. Habitats with low HSI have both a high emigration rate (μ) and a low immigration rate (λ); in contrary, habitats with high HSI have a high λ and a low μ [23].

Nature is a supreme teacher for the human being. Inspiring by the concept stated above, Simons proposed a new population-based algorithm so-called biogeography-based optimization (BBO) algorithm. Suppose a problem is presented with some candidate solutions. A good solution is analogous to a habitat with a high HSI, and a poor solution represents a habitat with a low HSI. High HSI solutions resist changing more than low HSI solutions. Similarly, high HSI solutions tend to share their features with low HSI solutions, while poor solutions accept many new features from the good solutions [8].

Some of the important applications of the BBO are reviewed here: Bhattacharya et al. [24] in 2010 utilized BBO to solve economic load dispatch (ELD) problems of thermal plants, and Wang et al. [25] in 2011 combined the biogeography theory with differential evolution and simplex search to solve parameter estimation of chaotic systems. Roy et al. [26] in 2012 solved multi-constrained optimal reactive power flow and minimized the bus voltage deviation and real power loss. For improving the performance of the krill herd algorithm, a biogeography-based krill herd (BBKH) algorithm was presented for solving complex optimization tasks by

Author's personal copy

Wang et al. [27] in 2014, and a new version of a biogeography-based optimization algorithm with Levy flight distribution (LFBBO) is introduced and used for the optimum design of reinforced concrete cantilever retaining walls by Aydogdu [28]. Aydogdu and Akin also developed computer programs utilizing the BBO algorithm which minimize the cost and the CO_2 emission of the RC retaining walls in [29]. Successful application of BBO for optimal design of steel structures can be found in [30–32]. In 2017, an improved hybrid biogeography-based optimization algorithm for supply chain network design (SCND) problem under uncertainty was utilized by Yang and Liu [33]. Application of different algorithms for domain decomposition of finite element meshes was carried out by Kaveh and Dadras which indicated the efficiency of BBO compared to other well-known algorithms [34]. The application of the BBO to laminated composites in the literature was not found, and in this paper, the BBO algorithm is applied to this field.

2.2 Steps

In all examined cases, the fiber orientations of two-ply stacks are considered 0_2, ± 45, 90_2 as the discrete design variables (where ± 45 denotes fiber orientations of two adjacent stacks with $+45°$ and $-45°$, and 0_2 and 90_2 state the contiguous stacks with 0° and 90°). The steps of discrete BBO are explained in the following:

Step 1 Initialize BBO parameters.

The initial parameters include:

- Maximum habitats count ($H_{\max)}$
- Maximum number of iteration ($\mathrm{Gen}_{\max)}$
- Maximum migration rates (λ and μ)
- Mutation rate (m)
- Elite number (p).

These parameters are initialized in the first step.

Step 2 Initialize habitats.

A set of random solutions with the same number of $H_{\max}$ is initialized.

Step 3 Compute HSI for each habitat.

In this step, the random solutions are evaluated by an objective function described in Sect. 3.2 and sorted according to their values of the cost function in ascending order.

Step 4 Compute λ and μ.

Different models are suggested for migration curve shapes in the BBO algorithm by Simons [35], each of which is described as:

1. *Linear model:*

This model is the preliminary model suggested for BBO. In all models, it is presumed for the simplicity that each one of the habitats has the same species count curve with $E = I$ as illustrated in Fig. 1a. Based on this presumption:

$$\lambda_k = (1 - r_k), \tag{1}$$

$$\mu_k = r_k, \tag{2}$$

where r_k is a ratio which states the rank of the kth habitat among others. This parameter is areal number between 0 and 1 which can be calculated by

$$r_k = \frac{\mathrm{Rank}\ (\mathrm{Habitat}_k)}{H_{\max}}. \tag{3}$$

Author's personal copy

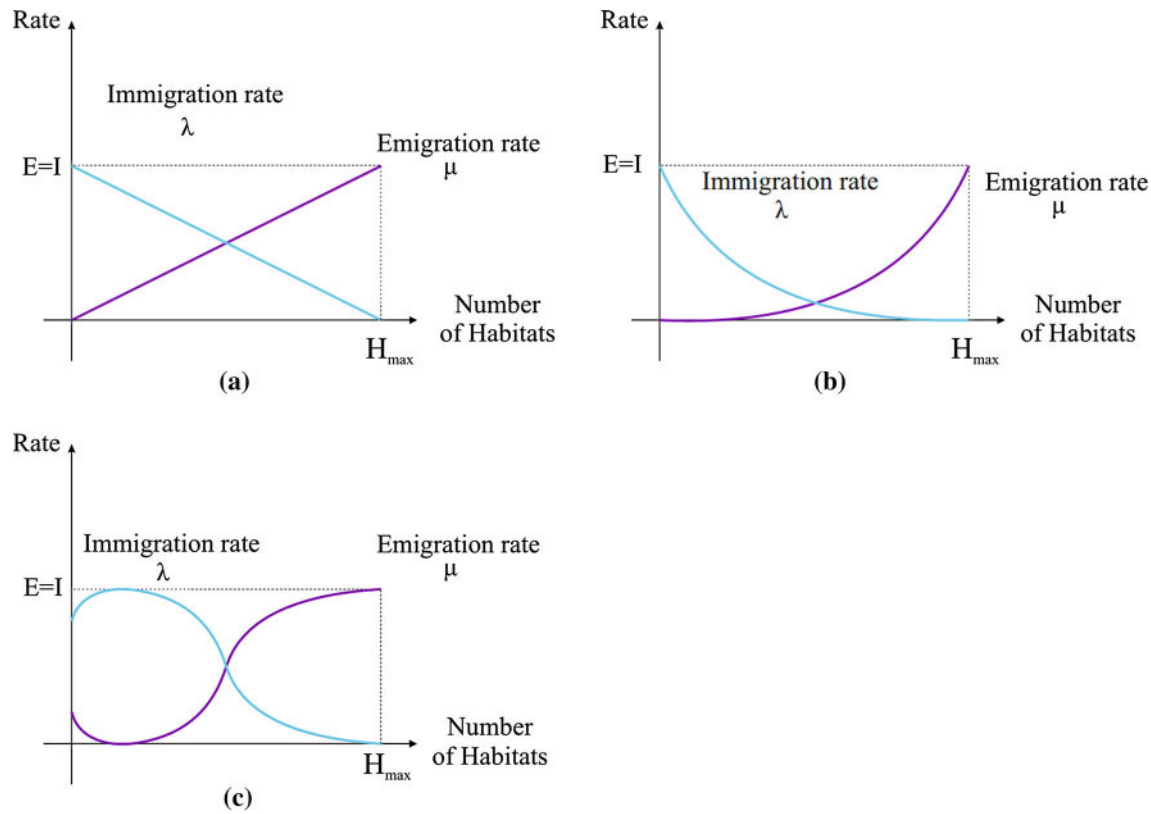

Fig. 1 Various types of migration curves: **a** linear migration curve, **b** quadratic migration curve and **c** generalized sinusoidal migration (it is assumed that in nonlinear models, maximum immigration and maximum emigration rates are both equal to 1)

2. *Quadratic model:*

In this model, λ and μ are concave quadratic functions of solution fitness rank. The quadratic curve model is based on island biogeography. The model is illustrated in Fig. 1b, and the equations are

$$\lambda_k = (1 - r_k)^2 , \tag{4}$$

$$\mu_k = (r_k)^2 . \tag{5}$$

3. *Generalized sinusoidal model:*

In plants, an initial increase in species count results in an initial increase in immigration rate and an initial decrease in emigration rate [36]. Species mobility, the evolution of particular species and population size are taken into consideration at this model. As a result, shapes of the migration curves becomes sinusoids. These migration curves, which are called the generalized sinusoidal migration curves, are depicted in Fig. 1c, and are expressed as:

$$\lambda_k = \frac{1}{2} \left(\cos \left(r_k . \pi + \beta \right) + 1 \right) , \tag{6}$$

$$\mu_k = \frac{1}{2} \left(- \cos \left(r_k . \pi + \beta \right) + 1 \right) . \tag{7}$$

Step 5 Modify the entire ecosystem.

With λ probability of the habitat, each variable is replaced by that of another solution. The selection of source habitat is performed upon μ and utilizing a 'roulette wheel selection' mechanism. Details about this mechanism can be found in [37].

Step 6 Mutate the ecosystem.

With m probability, each variable is replaced by an allowable random value.

Author's personal copy

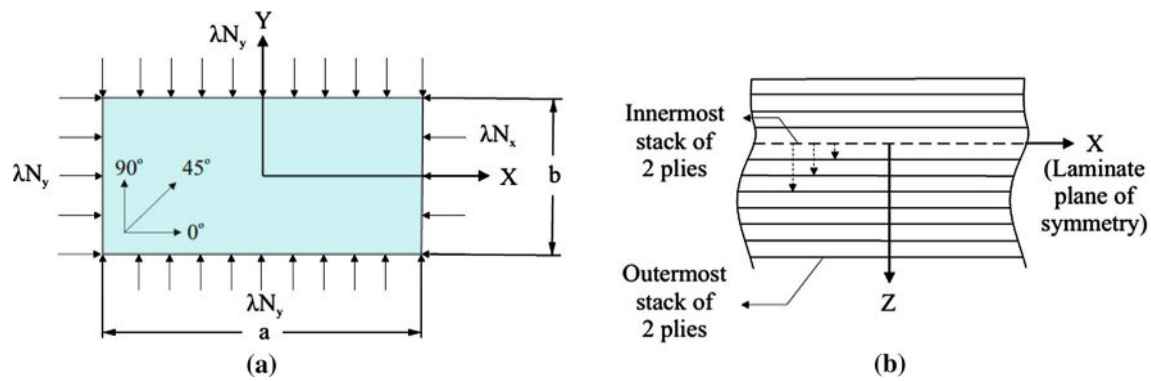

Fig. 2 Schematic of a laminated plate. **a** Laminated plate geometry and applied loads. **b** Ply sequence location

Step 7 Implement elitism.

In this step, the new set of habitats is evaluated by cost function and sorted in ascending order. The first p number of the previous set and first $(H_{\max} - p)$ number of the new set is saved as the candidate solutions.

Step 8 Check the termination condition.

If the termination criterion was met, output the best habitat; otherwise, go to Step 4.

A pseudocode of BBO is represented as follows.

```
Initialize the parameters
Maximum number of iteration⟵ Gen_max ;
Maximum habitats count ⟵ H_max;
Maximum migration rates λ and μ;
Mutation rate ⟵ m
Elite number ⟵ p
Initialize the population
for GenIndex = 1 to Gen_max do
    Applying migration
    for j=1 to H_max do
      Select habitat H_j according to λ_j
      if rand(0,1) < λ_j then
        for e=1 to H_max do
        Select habitat H_e according to μ_e
        Replace the selected SIV of H_j by selected SIV of H_e(using roulette wheel selection)
        end for
      end if
    end for
      Apply mutation
      for j = 1 to H_max do
        if rand(0,1) < m then
        Replace H_j(SIV) with randomly generated SIV
        end if
      end for
      Sort the population according to the increasing order of fitness
      Keep the elite solution
      Stop, if termination criterion is satisfied
end for
```

Author's personal copy

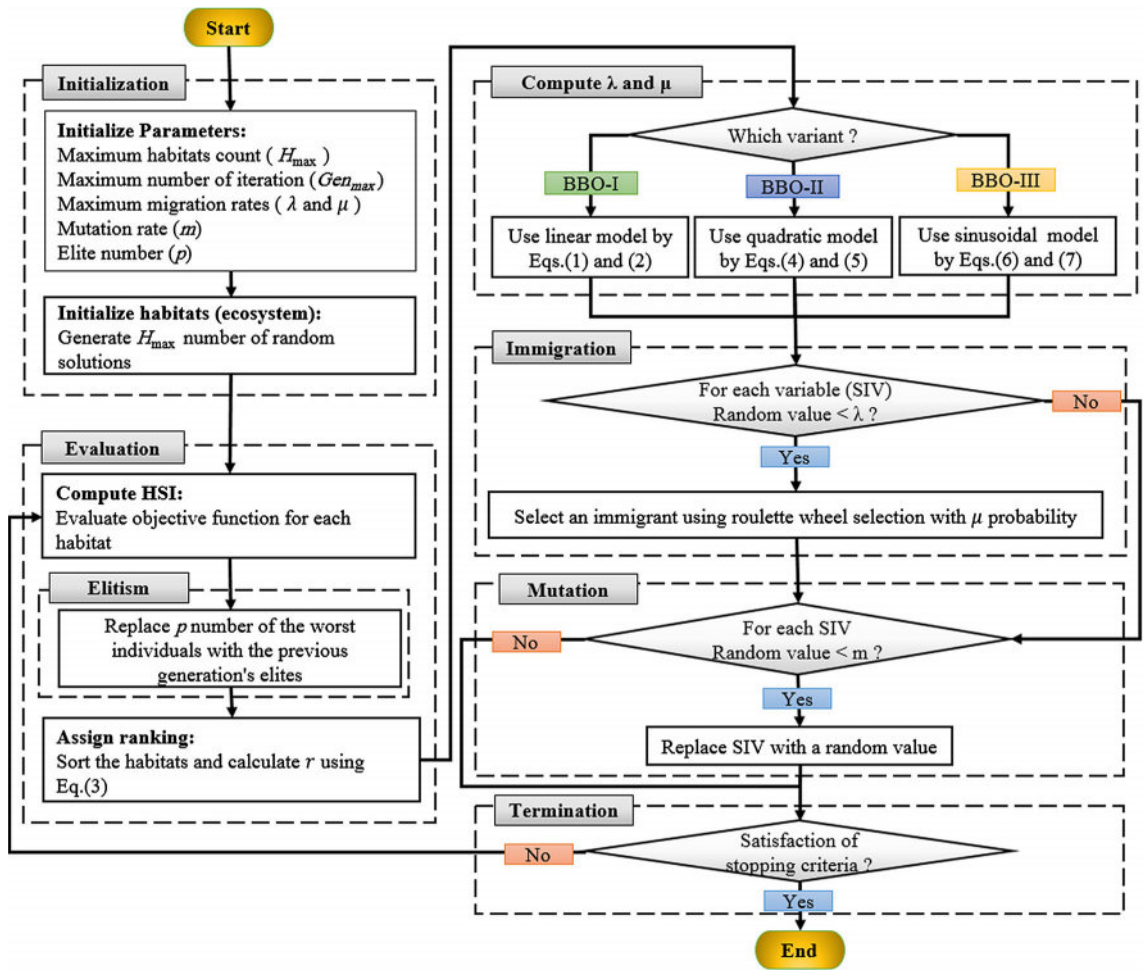

Fig. 3 Flowchart of the variants of the BBO

Table 1 Mechanical properties of graphite/epoxy

Property	Graphite/epoxy
Young's modulus, E_1, GPa (psi)	127.55 (18.5)
Young's modulus, E_2, GPa (psi)	13.03 (1.89)
Shear modulus, G_{12}, GPa (psi)	6.41 (0.93)
Poisson rate, ν_{12}	0.3
Lamina thickness, mm (in)	0.127 (0.005)

3 Formulation and problem statement

3.1 Theory

Considering a symmetric hybrid N layer laminate, the governing equation of motion within the classical laminated plate theory (CLPT) is given by [38]:

$$D_{11}\frac{\partial^4 w}{\partial x^4} + 4D_{16}\frac{\partial^4 w}{\partial x^3 \partial y} + 2\left(D_{12} + 2D_{66}\right)\frac{\partial^4 w}{\partial x^2 \partial y^2} + 4D_{26}\frac{\partial^4 w}{\partial x \partial y^3} + D_{22}\frac{\partial^4 w}{\partial y^4} = \rho h \frac{\partial^2 w}{\partial t^2}, \tag{8}$$

Author's personal copy

Table 2 Properties of the investigated study cases

Case	a (cm)	b (cm)	N_x (N/m)	N_y (N/m)
1	50.8	25.4	1	1
2	50.8	50.8	1	0.5
3	50.8	25.4	1	2
4	50.8	101.6	1	2

Table 3 Initial parameters of the BBO

Parameter	Value
$\text{Gen}_{\max}$	100
$H_{\max}$	50
m	0.15
p	20

Table 4 Statistical results from different methods for Case 1

Method	R_{op} (%)	R_{no} (%)	Average	Best	SD
BBO-I	18	100	695,724.44	695,781.32	63.68
BBO-II	25	100	695,735.17	695,781.32	50.96
BBO-III	2	100	695,475.79	695,781.32	270.68
HS	4	100	695,559.79	695,781.32	203.49

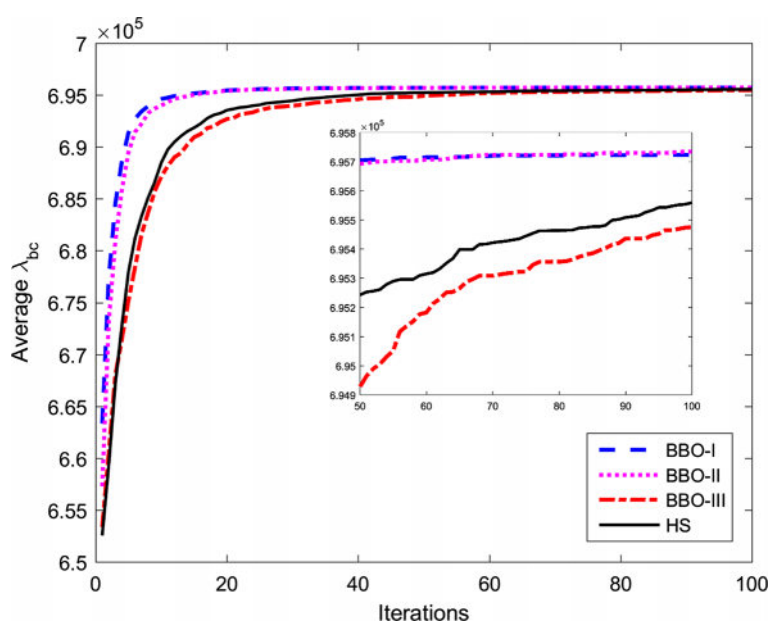

Fig. 4 Convergence curves of average λ_{bc} obtained through 100 iterations for Case 1

where w is the deflection in the z direction, h is the total thickness of the laminate and ρ is the mass density averaged in the thickness direction given by

$$\rho = h^{-1} \int_{-h/2}^{h/2} \rho^{(k)} = \frac{1}{N} \sum_{k=1}^{N} \rho^{(k)}, \tag{9}$$

Author's personal copy

Table 5 Optimal sequence obtained by different algorithms

Solutions		Algorithms							
		BBO-I	BBO-II	BBO-III	HS	GA [9]	SA [12]	SSA [11]	GPSA [14]
2,3,3,3,3,2,3,3, 3,3,3,3,3,3,3,2	$[\pm 45,90_8,\pm 45,90_{18},\pm 45]_s$	–	✓	✓	–	✓	–	✓	✓
2,3,3,3,3,3,2,3, 3,3,3,2,3,3,3,3	$[\pm 45,90_{10},\pm 45,90_8,\pm 45,90_8]_s$	✓	✓	–	–	✓	✓	✓	–
3,2,3,3,3,2,3,3, 3,3,2,3,3,3,3,3	$[90_2,\pm 45,90_6,\pm 45,90_8,\pm 45,90_{10}]_s$	✓	✓	–	–	✓	✓	✓	✓
3,3,2,2,3,3,3,3,3, 3,3,3,2,3,3,3	$[90_4,\pm 45_2, 90_{16},\pm 45,90_6]_s$	✓	✓	–	✓	✓	✓	✓	✓
3,3,3,3,2,3,2,3, 2,3,2,2,2,2,2,2	$[90_8,\pm 45,90_2, \pm 45,90_2,\pm 45, 90_2,\pm 45_6]_s$	✓	✓	✓	✓	–	–	✓	–
3,3,3,3,3,2,2,3,2, 2,2,3,2,2,2,2	$[90_{10},\pm 45_2,90_2, \pm 45_3,90_2\pm 45_4]_s$	✓	✓	–	–	✓	–	✓	✓
3,3,3,3,3,2,3,2,2, 2,2,2,2,2,3,2	$[90_{10},\pm 45,90_2, \pm 45_7,90_2,\pm 45]_s$	✓	✓	–	✓	–	–	✓	-

Table 6 Statistical results from different methods for Case 2

Algorithm	R_{op} (%)	R_{no} (%)	Average	Best	SD
BBO-I	100	100	323,764.13	323,764.13	8.19e−10
BBO-II	100	100	323,764.13	323,764.13	8.19e−10
BBO-III	25	98	323,487.68	323,764.13	382.77
HS	100	100	323,764.13	323,764.13	8.19e−10

where $\rho^{(k)}$ represents the mass density of material in the kth layer. The bending stiffness D_{ij} in Eq. (8) is defined as

$$D_{ij} = \int_{-\frac{h}{2}}^{\frac{h}{2}} \bar{Q}_{ij}\left(z^2\right) dz = \sum_{k=1}^{N} \int_{z_k}^{z_{k+1}} \bar{Q}_{ij}^{(k)}\left(z^2\right) dz = \frac{1}{3} \sum\nolimits_{K=1}^{N} \bar{Q}_{ij}^{(k)}\left(z_{k+1}^3 - z_k^3\right), \tag{10}$$

where $\bar{Q}_{ij}^{(k)}$ is the transformed reduced stiffness of the kth layer which is given by

$$\bar{Q}_{ij}^{(k)} = [T]^{-1}\,[Q]\left([T]^{-1}\right)^T. \tag{11}$$

Here, the coefficients of the reduced stiffness matrix ($[Q]$) are defined as:

$$[Q] = \begin{bmatrix} Q_{11} & Q_{12} & 0 \\ Q_{12} & Q_{22} & 0 \\ 0 & 0 & Q_{66} \end{bmatrix};$$
$$Q_{11} = \frac{E_1}{1-\upsilon_{12}\upsilon_{21}}, \quad Q_{12} = \frac{\upsilon_{12}E_2}{1-\upsilon_{12}\upsilon_{21}} = \frac{\upsilon_{21}E_1}{1-\upsilon_{12}\upsilon_{21}}, \quad Q_{22} = \frac{E_2}{1-\upsilon_{12}\upsilon_{21}}, \quad Q_{66} = G_{12}. \tag{12}$$

In the above equation, E_1, E_2 and G_{12} are longitudinal Young's modulus, transverse Young's modulus and shear modulus, respectively, and υ_{12} and υ_{21} are Poisson constants. Further, the transformation matrix ($[T]$) is expressed as:

$$[T] = \begin{bmatrix} C^2 & S^2 & 2CS \\ S^2 & C^2 & -2CS \\ -CS & CS & C^2 - S^2 \end{bmatrix}; \quad C = \mathrm{Cos}\,(\theta), \quad S = \mathrm{Sin}\,(\theta). \tag{13}$$

Author's personal copy

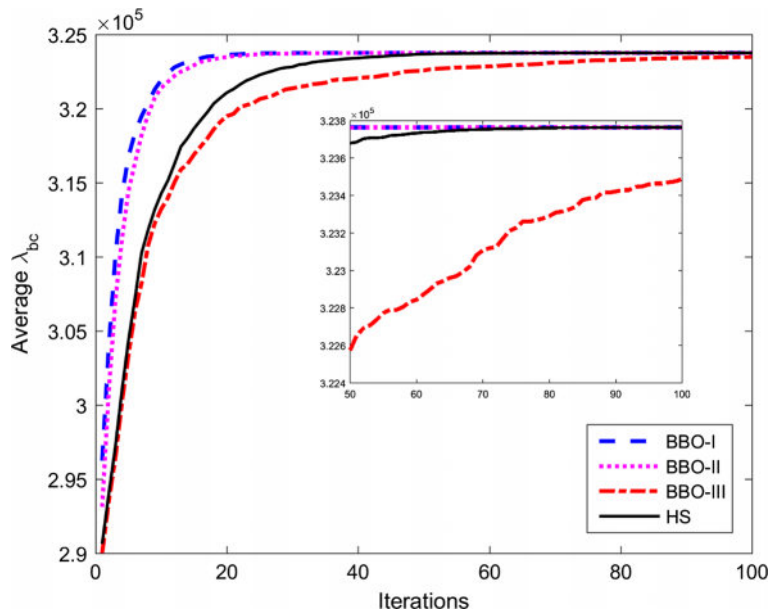

Fig. 5 Convergence curves of average λ_{bc} obtained through 100 iterations for Case 2

Different mode shapes can be obtained by inserting different values of m and n. The boundary conditions for the simply supported plate are given by

$$\omega = 0, \quad M_x = 0 \text{ at } x = 0, a, \tag{14}$$

$$\omega = 0, \quad M_y = 0 \text{ at } y = 0, b, \tag{15}$$

where the moment resultants are defined as:

$$\left(M_x, M_y\right) = \int_{-h/2}^{h/2} \left(\sigma_x, \sigma_y\right) \mathrm{d}z. \tag{16}$$

Taking into account the governing equation (8) and the boundary conditions in Eqs. (14) and (15), a general form of solution for ω in the natural vibration mode (m, n) is presented as

$$\omega\left(x, y, t\right) = \sum\nolimits_{m=1}^{\infty} \sum\nolimits_{n=1}^{\infty} A_{mn} \sin\frac{m\pi x}{a} \sin\frac{n\pi y}{b} e^{i\omega_{mn}t}, \tag{17}$$

where ω_{mn} is the natural frequency of the vibration mode (m, n) and i is the imaginary unit, equal to $\sqrt{-1}$.

Substituting Eq. (17) into Eq. (8) yields the value of the critical buckling load multiplier λ_{cb} of the biaxial compression case:

$$\lambda_b\left(m, n\right) = \pi^2 \left[\frac{m^4 D_{11} + 2\left(D_{12} + D_{66}\right)\left(rmn\right)^2 + \left(rn\right)^4 D_{22}}{\left(am\right)^2 N_x + \left(ran\right)^2 N_y}\right]. \tag{18}$$

D_{16} and D_{26} are zero for 0° and 90° laminas, and are negligible comparing to other D_{ij}'s for a symmetric laminate with a number of laminas with $\pm\theta$ ply angles in sequence; hence, D_{16} and D_{26} do not appear in Eq. (18) [38,39].

3.2 Problem statement

One of the main critical failure modes of laminated composite structures under in-plane compressive loads is buckling, which should be considered in the design process. Figure 2a illustrates the geometry of a simply supported laminated composite, subjected to an in-plane compressive load. It has a total thickness of $t = 8.128$ mm for all load cases and original length of a, and width of b, Ref. [9].

Author's personal copy

Table 7 Statistical results from different methods for Case 3

Algorithm	R_{op} (%)	R_{no} (%)	Average	Best	SD
BBO-I	34	100	412,943.56	412,985.82	47.82
BBO-II	35	100	412,941.36	412,985.82	47.58
BBO-III	2	98	412,567.59	412,985.82	428.47
HS	28	100	412,944.49	412,985.82	42.74

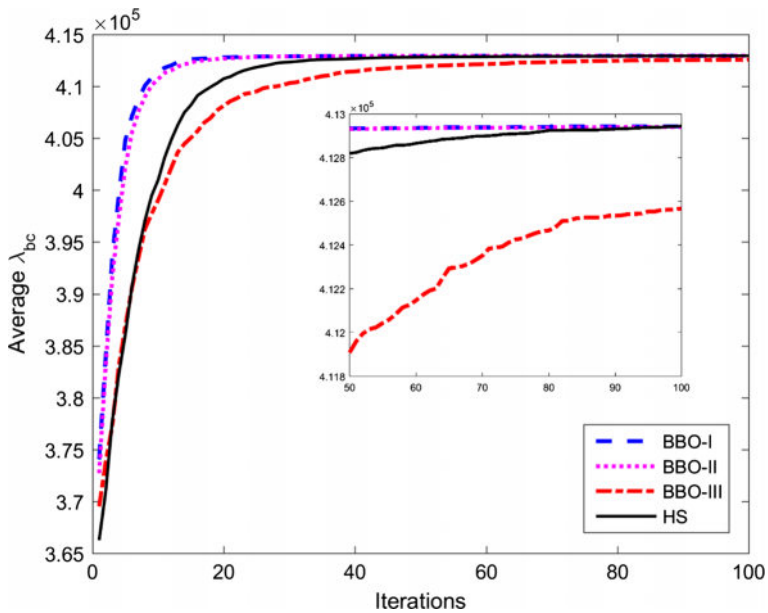

Fig. 6 Convergence curves of the average λ_{bc} obtained through 100 iterations for Case 3

Table 8 Statistical results from different methods for Case 4

Algorithm	R_{op} (%)	R_{no} (%)	Average	Best	SD
BBO-I	68	100	132,236.45	132,243.53	13.84
BBO-II	73	100	132,238.73	132,243.53	10.55
BBO-III	14	100	132,175.28	132,243.53	73.96
HS	17	100	132,198.58	132,243.53	46.92

In this study, the investigated laminate is assumed to be balanced, symmetric and comprised of 64 plies with two-ply stacks 0_2, ± 45 and 90_2. As mentioned before, 0_2 and 90_2 state two contiguous stacks with 0° and 90°, ± 45 is also utilized as contiguous stacks with $+45°$ and $-45°$, so that the balanced conditions are guaranteed. The laminate is symmetric; hence, the number of design variables are reduced from 64 to 16. The objective function to be maximized can be stated as [9]:

$$\text{Maximize:} \quad \lambda_{cb}(\theta) = \pi^2 \left[\frac{m^4 D_{11} + 2\left(D_{12} + D_{66}\right)(rmn)^2 + (rn)^4 D_{22}}{(am)^2 N_x + (ran)^2 N_y} \right], \tag{19}$$

where θ is the vector containing the angles of the laminate stacking sequence and critical buckling load factor λ_{cb} can be found using combinations of m and n that yield lowest buckling load. In the implementation, two-ply stacks with 0_2, ± 45 and 90_2 degrees are replaced by integers 1, 2 and 3, respectively. In addition, the results sequences are in the order of coming from outermost lamina to innermost one (Fig. 2b) and contain 16 variables as described above. The design space consists of 3^{16} different configuration. The original formulation of the BBO is based on continuous variables, so the domains of variables are considered between [0.5, 3.5) and the values are rounded to the nearest integer number. In optimization process, agents may leave the determined intervals. In order to avoid this, the variables which leave their intervals are returned to the nearest bound. The flowchart of the considered variants is shown in Fig. 3.

Author's personal copy

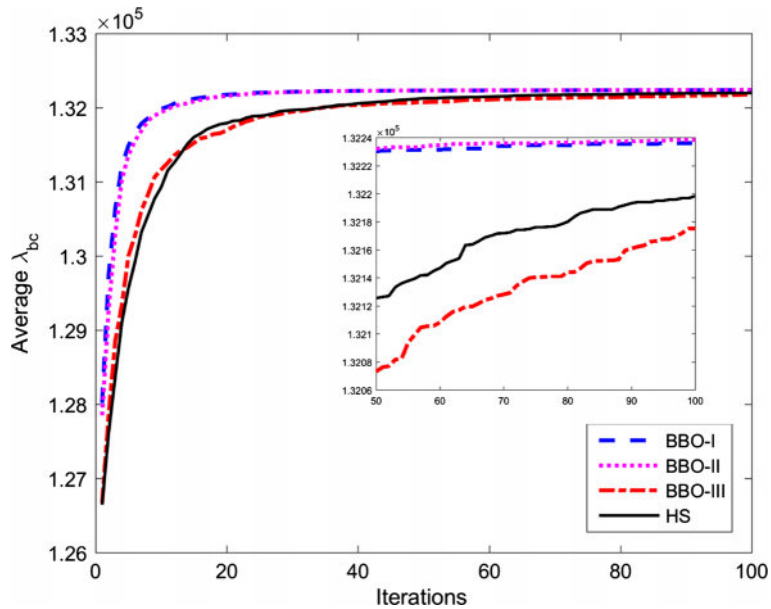

Fig. 7 Convergence curves of average λ_{bc} obtained through 100 iterations for Case 4

4 Parameter setting and numerical results

In this study, the material used for the composite plate is the graphite/epoxy, and its mechanical properties are listed in Table 1. Four combinations of load cases and plate aspect ratios as given in Table 2 are investigated and the critical buckling loads are maximized. The BBO is implemented for each of the cases and rerun 100 times independently. Migration rates are set according to three models described in Sect. 3, and other parameters are assumed according to Table 3. A statistical comparison is carried out among the results of the BBO and some other methods. The number of function evaluations is limited to 5000 by utilizing 100 iterations for both HS and BBO, considering 50 for HMS and $H_{\max}$ for all the examples.

4.1 Parameter tuning for metaheuristics

First, a sensitivity analysis is performed by considering various mutation rates (m) and keeping rates $\left(\frac{p}{H_{\max}}\right)$. These rates are varied from 0.1 to 0.5 with steps of 0.1 for keeping the rate, and for each of them, mutation rate is varied from 0.1 to 0.5 with steps of 0.05. In most cases, the use of 0.1 and 0.15 for performance for keeping rate and mutation rate, respectively, led to the best results. These values are assumed in all the numerical examples.

The harmony search (HS) algorithm is a well-established method, which is recently applied to this problem in Ref. [18], and the results of the cited paper showed that the harmony memory consideration rate (HMCR) and pitch adjusting rate (PAR) equal to 0.99 and 0.2, respectively, resulting in the best performance. In our paper, HS is also implemented for comparison and these suggested values are utilized for HS.

4.2 Test problems and numerical results

Variants of the BBO with linear, quadratic and generalized sinusoidal migration models are denoted by BBO-I, BBO-II and BBO-III, respectively. R_{op} and R_{no} are defined to verify the reliability of methods. R_{op} is the percentage of the independent runs that the applied method found the global optimum and R_{no} is the percentage of the independent runs, which found a near global optimum. As studied in [14], the global optimum results for critical loading factors of cases 1, 2, 3 and 4 are considered as the factors more than 695,781.3, 323,764.0, 412,985.8 and 132,243.5, respectively. Furthermore, the results more than 0.995 of the global optimums are defined as near global optimum for calculating R_{no}.

Author's personal copy

Table 9 Optimal orientation obtained by BBO-I for Case 4

1,1,2,2,1,2,2,2,2,2,1,1,1,1,1,2	$[0_4,\pm 45_2,0_2,\pm 45_5,0_{10},\pm 45]_s$
1,1,2,2,2,1,2,1,2,2,2,2,1,1,1,1	$[0_4,\pm 45_3,0_2,\pm 45,0_2,\pm 45_4,0_8]_s$
1,1,2,2,2,2,1,1,2,2,2,1,1,1,1,2	$[0_4,\pm 45_4,0_4,\pm 45_3,0_8,\pm 45]_s$
1,1,2,2,2,2,1,2,1,2,1,1,2,1,2,1	$[0_4,\pm 45_4,0_2,\pm 45,0_2,\pm 45,0_4,\pm 45,0_2,\pm 45,0_2]_s$
1,2,1,2,1,2,2,2,2,1,1,1,2,1,2,1	$[0_2,\pm 45,0_2,\pm 45,0_2,\pm 45_4,0_6,\pm 45,0_2,\pm 45,0_2]_s$
1,2,1,2,2,1,2,1,2,2,1,2,1,1,2,1	$[0_2,\pm 45,0_2,\pm 45_2,0_2,\pm 45,0_2,\pm 45_2,0_2,\pm 45,0_4,\pm 45,0_2]_s$
1,2,1,2,2,1,2,2,1,2,1,1,1,2,1,2	$[0_2,\pm 45,0_2,\pm 45_2,0_2,\pm 45_2,0_2,\pm 45,0_6,\pm 45,0_2,\pm 45]_s$
1,2,1,2,2,2,1,1,2,1,2,1,2,1,2,1	$[0_2,\pm 45,0_2,\pm 45_3,0_4,\pm 45,0_2,\pm 45,0_2,\pm 45,0_2,\pm 45,0_2]_s$
1,2,2,1,1,2,2,1,2,2,1,1,2,2,1,1	$[0_2,\pm 45_2,0_4,\pm 45_2,0_2,\pm 45_2,0_4,\pm 45_2,0_4]_s$
1,2,2,1,1,2,2,2,1,2,1,1,1,1,2,2	$[0_2,\pm 45_2,0_4,\pm 45_3,0_2,\pm 45,0_8,\pm 45_2]_s$
1,2,2,1,2,1,1,2,2,2,1,1,2,1,2,1	$[0_2,\pm 45_2,0_2,\pm 45,0_4,\pm 45_3,0_4,\pm 45,0_2,\pm 45,0_2]_s$
1,2,2,1,2,1,2,1,1,2,2,2,1,1,2,1	$[0_2,\pm 45_2,0_2,\pm 45,0_2,\pm 45,0_4,\pm 45_3,0_4,\pm 45,0_2]_s$
1,2,2,1,2,2,1,1,1,2,1,2,2,1,1,2	$[0_2,\pm 45_2,0_2,\pm 45_2,0_6,\pm 45,0_2,\pm 45_2,0_4,\pm 45]_s$
1,2,2,1,2,2,1,1,2,1,1,1,2,2,1,2	$[0_2,\pm 45_2,0_2,\pm 45_2,0_4,\pm 45,0_6,\pm 45_2,0_2,\pm 45]_s$
1,2,2,2,1,1,1,1,2,2,2,2,2,1,1,1	$[0_2,\pm 45_3,0_8,\pm 45_5,0_6]_s$
1,2,2,2,1,1,1,2,2,1,1,2,2,1,1,2	$[0_2,\pm 45_3,0_6,\pm 45_2,0_4,\pm 45_2,0_4,\pm 45]_s$
1,2,2,2,1,1,2,1,2,1,1,1,2,1,2,2	$[0_2,\pm 45_3,0_4\pm 45,0_2\pm 45,0_6,\pm 45,0_2,\pm 45_2]_s$
1,2,2,2,1,2,1,1,1,1,2,1,2,2,2,1	$[0_2,\pm 45_3,0_2,\pm 45,0_8,\pm 45,0_2,\pm 45_3,0_2]_s$
2,1,1,2,1,2,1,2,2,2,1,2,2,1,1,1	$[\pm 45,0_4,\pm 45,0_2,\pm 45,0_2,\pm 45_3,02,\pm 45_2,0_6]_s$
2,1,1,2,2,1,1,2,2,1,2,2,1,1,2,1	$[\pm 45,0_4,\pm 45_2,0_4,\pm 45_2,0_2,\pm 45_2,0_4,\pm 45,0_2]_s$
2,1,1,2,2,1,2,1,1,2,2,1,2,2,1,1	$[\pm 45,0_4,\pm 45_2,0_2,\pm 45,0_4,\pm 45_2,0_2,\pm 45_2,0_4]_s$
2,1,1,2,2,1,2,2,1,1,1,1,2,2,1,2	$[\pm 45,0_4,\pm 45_2,0_2,\pm 45_2,0_8,\pm 45_2,0_2,\pm 45]_s$
2,1,1,2,2,2,1,1,1,2,1,2,1,2,2,1	$[\pm 45,0_4,\pm 45_3,0_8\pm 45,0_2\pm 45,0_2,\pm 45_2,02]_s$
2,1,1,2,2,2,1,1,2,1,1,1,2,1,2,2	$[\pm 45,0_4,\pm 45_3,0_4,\pm 45,0_6,\pm 45,0_2,\pm 45_2]_s$
2,1,2,1,1,1,2,2,2,2,1,2,1,2,1,1	$[\pm 45,0_2,\pm 45,0_6,\pm 45_4,0_2,\pm 45,0_2,\pm 45,0_4]_s$
2,1,2,1,1,2,2,2,1,1,1,1,2,1,2,2	$[\pm 45,0_2,\pm 45,0_4,\pm 45_3,0_8,\pm 45,0_2,\pm 45_2]_s$
2,1,2,1,2,1,1,1,2,2,2,2,1,2,1,1	$[\pm 45,0_2,\pm 45,0_2,\pm 45,0_6,\pm 45_4,0_2,\pm 45,0_4]_s$
2,1,2,1,2,1,1,2,2,1,1,2,1,2,1,2	$[\pm 45,0_2,\pm 45,0_2,\pm 45,0_4,\pm 45_2,0_4\pm 45,0_2,\pm 45,0_2,\pm 45]_s$
2,1,2,1,2,1,2,1,1,2,1,2,1,1,2,2	$[\pm 45,0_2,\pm 45,0_2,\pm 45,0_2,\pm 45,0_4,\pm 45,0_2,\pm 45,0_4,\pm 45_2]_s$
2,1,2,1,2,1,2,1,2,1,1,1,1,2,2,2	$[\pm 45,0_2,\pm 45,0_2,\pm 45,0_2,\pm 45,0_2,\pm 45,0_8,\pm 45_3]_s$
2,1,2,2,1,1,1,1,2,2,1,2,2,1,1,2	$[\pm 45,0_2,\pm 45_2,0_8,\pm 45_2,0_2,\pm 45_2,0_4,\pm 45]_s$
2,1,2,2,1,1,1,1,2,2,2,1,1,1,2,2	$[\pm 45,0_2,\pm 45_2,0_8,\pm 45_3,0_6,\pm 45_2]_s$
2,1,2,2,1,1,1,2,1,1,2,2,1,2,2,1	$[\pm 45,0_2,\pm 45_2,0_6,\pm 45,0_4,\pm 45_2,0_2,\pm 45_2,0_2]_s$
2,1,2,2,1,1,2,1,1,1,1,2,2,2,2,1	$[\pm 45,0_2,\pm 45_2,0_4,\pm 45,0_8,\pm 45_4,0_2]_s$
2,1,2,2,1,2,1,1,1,1,1,1,2,2,2,2	$[\pm 45,0_2,\pm 45_2,0_2\pm 45,0_{12},\pm 45_4]_s$
2,2,1,1,1,2,1,1,2,2,2,2,1,1,1,2	$[\pm 45_2,0_6,\pm 45,0_4,\pm 45_4,0_6,\pm 45]_s$
2,2,1,1,2,1,1,1,2,2,1,2,1,2,2,1	$[\pm 45_2,0_4,\pm 45,0_6,\pm 45_2,0_2,\pm 45,0_2,\pm 45_2,0_2]_s$
2,2,2,1,1,1,1,1,1,2,1,2,2,1,2,2	$[\pm 45_3,0_{12},\pm 45,0_2,\pm 45_2,0_2,\pm 45_2]_s$
2,2,2,1,1,1,1,1,2,1,1,1,2,2,2,2	$[\pm 45_3,0_{10}\pm 45,0_6,\pm 45_4]_s$

4.2.1 Case 1

The statistical data on 100 independent runs of this case are given in Table 4. As it can be seen, the BBO-II outperforms other methods in terms of R_{op}, average and SD. The average convergence histories of the methods are depicted in Fig. 4. As it is shown, the convergence rate of the BBO-I and BBO-II is better than other methods.

The optimum solutions obtained by different methods are provided in Table 5. As it can be seen from the table, BBO-II obtained seven distinct optimum solutions similar to genetic algorithm reported in [9], but other reported algorithms have not found these solutions completely. As mentioned above, since the composite plates are assumed to be symmetric, only one side is presented for each solution.

4.2.2 Case 2

The results of this case are given in Table 6. As it can be seen, except BBO-III, all methods have found the global optimum in all runs. The methods have achieved the same values in average, best and standard deviation except BBO-III which led to the weaker result. The average convergence histories are depicted in Fig. 5. Like the previous case, Fig. 5 shows faster convergence for the BBO-I and BBO-II.

The single optimum solution obtained by all methods is $[\pm 45_{32}]_s$. As can be seen, the optimum solution is a composite laminate with ± 45 fiber orientations. The same solution is also reported in [14] for genetic and generalized pattern search algorithms.

Author's personal copy

Table 10 Optimal orientation obtained by BBO-II for Case 4

1,1,2,2,1,2,2,2,2,1,2,1,2,1,1,1	$[0_4,\pm 45_2,0_2,\pm 45_4,0_2,\pm 45,0_2,\pm 45,0_6]_s$
1,1,2,2,1,2,2,2,2,2,1,1,1,1,1,2	$[0_4,\pm 45_2,0_2,\pm 45_5,0_{10},\pm 45]_s$
1,1,2,2,2,1,2,1,2,2,2,2,1,1,1,1	$[0_4,\pm 45_3,0_2,\pm 45,0_2,\pm 45_4,0_8]_s$
1,1,2,2,2,1,2,2,2,1,1,2,1,1,1,2	$[0_4,\pm 45_3,0_2,\pm 45_3,0_4,\pm 45,0_6,\pm 45]_s$
1,1,2,2,2,2,1,1,2,2,2,1,1,1,1,2	$[0_4,\pm 45_4,0_4,\pm 45_3,0_8,\pm 45]_s$
1,1,2,2,2,2,2,1,1,1,2,1,1,2,2,1	$[0_4,\pm 45_5,0_6,\pm 45,0_4,\pm 45_2,0_2]_s$
1,2,1,2,1,2,2,2,2,1,1,1,2,1,2,1	$[0_2,\pm 45,0_2,\pm 45,0_2,\pm 45_4,0_6,\pm 45,0_2,\pm 45,0_2]_s$
1,2,1,2,2,1,2,2,1,1,2,1,2,2,1,1	$[0_2,\pm 45,0_2,\pm 45_2,0_2,\pm 45_2,0_4,\pm 45,0_2,\pm 45_2,0_4]_s$
1,2,1,2,2,1,2,2,1,2,1,1,1,2,1,2	$[0_2,\pm 45,0_2,\pm 45_2,0_2,\pm 45_2,0_2,\pm 45,0_6,\pm 45,0_2,\pm 45]_s$
1,2,1,2,2,2,1,1,2,1,2,1,2,1,2,1	$[0_2,\pm 45,0_2,\pm 45_3,0_4,\pm 45,0_2,\pm 45,0_2,\pm 45,0_2,\pm 45,0_2]_s$
1,2,1,2,2,2,1,1,2,2,1,1,1,1,2,2	$[0_2,\pm 45,0_2,\pm 45_3,0_4,\pm 45_2,0_8,\pm 45_2]_s$
1,2,2,1,1,2,1,2,2,2,2,1,1,2,1,1	$[0_2,\pm 45_2,0_4,\pm 45,0_2,\pm 45_4,0_4,\pm 45,0_4]_s$
1,2,2,1,1,2,2,2,1,1,2,1,2,1,2,1	$[0_2,\pm 45_2,0_4,\pm 45_3,0_4,\pm 45,0_2,\pm 45,0_2,\pm 45,0_2]_s$
1,2,2,1,1,2,2,2,1,2,1,1,1,1,2,2	$[0_2,\pm 45_2,0_4,\pm 45_3,0_2,\pm 45,0_8,\pm 45_2]_s$
1,2,2,1,2,1,1,2,2,1,2,2,1,2,1,1	$[0_2,\pm 45_2,0_2,\pm 45,0_4,\pm 45_2,0_2,\pm 45_2,0_2,\pm 45,0_4]_s$
1,2,2,1,2,1,2,1,1,2,2,2,1,1,2,1	$[0_2,\pm 45_2,0_2,\pm 45,0_2,\pm 45,0_4,\pm 45_3,0_4,\pm 45,0_2]_s$
1,2,2,1,2,1,2,1,2,1,1,2,2,2,1,1	$[0_2,\pm 45_2,0_2,\pm 45,0_2,\pm 45,0_2,\pm 45,0_4,\pm 45_3,0_4]_s$
1,2,2,1,2,2,1,1,2,1,1,1,2,2,1,2	$[0_2,\pm 45_2,0_2,\pm 45_2,0_4,\pm 45,0_6,\pm 45_2,0_2,\pm 45]_s$
1,2,2,2,1,1,1,1,2,2,2,2,2,1,1,1	$[0_2,\pm 45_3,0_8,\pm 45_5,0_6]_s$
1,2,2,2,1,1,2,1,2,1,1,1,2,1,2,2	$[0_2,\pm 45_3,0_4,\pm 45,0_2,\pm 45,0_6,\pm 45,0_2,\pm 45_2]_s$
1,2,2,2,1,2,1,1,1,1,2,1,2,2,2,1	$[0_2,\pm 45_3,0_2,\pm 45,0_8,\pm 45,0_2,\pm 45_3,0_2]_s$
1,2,2,2,2,1,1,1,1,1,1,2,1,2,2,2	$[0_2,\pm 45_4,0_{12},\pm 45,0_2,\pm 45_3]_s$
2,1,1,1,2,2,2,2,2,1,1,1,1,2,2,1	$[\pm 45,0_6,\pm 45_5,0_8,\pm 45_2,0_2]_s$
2,1,1,2,1,2,1,2,2,2,1,2,2,1,1,1	$[\pm 45,0_4,\pm 45,0_2,\pm 45,0_2,\pm 45_3,0_2,\pm 45_2,0_6]_s$
2,1,1,2,1,2,1,2,2,2,2,1,1,1,2,1	$[\pm 45,0_4,\pm 45,0_2,\pm 45,0_2,\pm 45_4,0_6,\pm 45,0_2]_s$
2,1,1,2,2,1,1,2,2,1,2,2,1,1,2,1	$[\pm 45,0_4,\pm 45_2,0_4,\pm 45_2,0_2,\pm 45_2,0_4,\pm 45,0_2]_s$
2,1,1,2,2,1,2,2,1,1,1,1,2,2,1,2	$[\pm 45,0_4,\pm 45_2,0_2,\pm 45_2,0_8,\pm 45_2,0_2,\pm 45]_s$
2,1,1,2,2,2,1,1,1,2,2,1,2,2,1,1	$[\pm 45,0_4,\pm 45_3,0_6,\pm 45,0_2,\pm 45,0_2,\pm 45_2,0_2]_s$
2,1,2,1,1,1,2,2,2,2,1,2,2,1,1,1	$[\pm 45,0_2,\pm 45,0_6,\pm 45_4,0_2,\pm 45,0_2,\pm 45,0_4]_s$
2,1,2,1,1,2,1,2,2,1,2,1,2,2,1,1	$[\pm 45,0_2,\pm 45,0_4,\pm 45,0_2,\pm 45_2,0_2,\pm 45,0_2,\pm 45_2,0_4]_s$
2,1,2,1,1,2,1,2,2,2,1,1,1,2,1,2	$[\pm 45,0_2,\pm 45,0_4,\pm 45_3,0_8,\pm 45,0_2,\pm 45_2]_s$
2,1,2,1,1,2,2,2,1,1,1,1,2,1,2,2	$[\pm 45,0_2,\pm 45,0_2,\pm 45,0_6,\pm 45_4,0_2,\pm 45,0_4]_s$
2,1,2,1,2,1,1,1,2,2,2,2,1,2,1,1	$[\pm 45,0_2,\pm 45,0_2,\pm 45,0_4,\pm 45_2,0_4,\pm 45,0_2,\pm 45,0_2,\pm 45]_s$
2,1,2,1,2,1,1,2,2,1,1,2,1,2,1,2	$[\pm 45,0_2,\pm 45,0_2,\pm 45,0_2,\pm 45,0_2,\pm 45,0_8,\pm 45_3]_s$
2,1,2,1,2,1,2,1,2,1,1,1,1,2,2,2	$[\pm 45,0_2,\pm 45,0_2,\pm 45,0_2,\pm 45,0_2,\pm 45,0_8,\pm 45_3]_s$
2,1,2,2,1,1,1,2,1,1,2,2,1,2,2,1	$[\pm 45,0_2,\pm 45_2,0_6,\pm 45,0_4,\pm 45_2,0_2,\pm 45_2,0_2]_s$
2,1,2,2,1,1,2,1,1,1,1,2,2,2,2,1	$[\pm 45,0_2,\pm 45_2,0_4,\pm 45,0_8,\pm 45_4,0_2]_s$
2,1,2,2,1,2,1,1,1,1,1,1,2,2,2,2	$[\pm 45,0_2,\pm 45_2,0_2,\pm 45,0_{12},\pm 45_4]_s$
2,2,1,1,1,2,1,1,2,2,2,2,1,1,1,2	$[\pm 45_2,0_6,\pm 45,0_4,\pm 45_4,0_6,\pm 45]_s$
2,2,1,1,1,2,1,2,1,2,1,2,2,1,2,1	$[\pm 45_2,0_6,\pm 45,0_2,\pm 45,0_2,\pm 45,0_2,\pm 45_2,0_2,\pm 45,0_2]_s$
2,2,1,1,1,2,1,2,2,1,1,1,2,2,2,1	$[\pm 45_2,0_6,\pm 45,0_2,\pm 45_2,0_6,\pm 45_3,0_2]_s$
2,2,1,1,1,2,2,1,1,1,2,2,1,2,2,1	$[\pm 45_2,0_6,\pm 45_2,0_6,\pm 45_2,0_2,\pm 45_2,0_2]_s$

Table 11 Optimal orientation obtained by BBO-III for Case 4

1,1,2,2,2,1,2,1,2,2,2,2,1,1,1,1	$[0_4,\pm 45_3,0_2,\pm 45,0_2,\pm 45_4,0_8]_s$
1,1,2,2,2,2,1,1,2,2,2,1,1,1,1,2	$[0_4,\pm 45_4,0_4,\pm 45_3,0_8,\pm 45]_s$
1,2,1,2,2,1,2,1,2,2,1,2,1,1,2,1	$[0_2,\pm 45,0_2,\pm 45_2,0_2,\pm 45,0_2,\pm 45_2,0_2,\pm 45,0_4,\pm 45,0_2]_s$
1,2,2,1,1,2,2,2,1,1,2,1,2,1,2,1	$[0_2,\pm 45_2,0_4,\pm 45_3,0_4,\pm 45,0_2,\pm 45,0_2,\pm 45,0_2]_s$
1,2,2,1,2,1,2,2,1,1,1,2,1,1,2,2	$[0_2,\pm 45_2,0_2,\pm 45,0_2,\pm 45_2,0_6,\pm 45,0_4,\pm 45_2]_s$
1,2,2,1,2,2,1,1,2,1,1,1,2,2,1,2	$[0_2,\pm 45_2,0_2,\pm 45_2,0_4,\pm 45,0_6,\pm 45_2,0_2,\pm 45]_s$
1,2,2,2,1,1,1,1,2,2,2,2,2,1,1,1	$[0_2,\pm 45_3,0_8,\pm 45_5,0_6]_s$
2,1,1,2,2,1,2,1,2,1,1,2,2,1,2,1	$[\pm 45,0_4,\pm 45_2,0_2,\pm 45,0_2,\pm 45,0_4,\pm 45_2,0_2,\pm 45,0_2]_s$
2,1,1,2,2,2,1,1,1,2,1,2,2,1,1,2	$[\pm 45,0_4,\pm 45_3,0_6,\pm 45,0_2,\pm 45,0_2,\pm 45_2,0_2]_s$
2,1,2,1,1,2,1,2,2,1,2,1,1,2,2,1	$[\pm 45,0_2,\pm 45_2,0_4,\pm 45,0_2,\pm 45_3,0_6,\pm 45,0_2,\pm 45]_s$
2,1,2,1,2,1,1,2,2,1,1,2,1,2,1,2	$[\pm 45,0_2,\pm 45,0_2,\pm 45,0_4,\pm 45_2,0_4,\pm 45,0_2,\pm 45,0_2,\pm 45]_s$
2,1,2,1,2,1,2,1,2,1,1,2,1,2,1,2	$[\pm 45,0_2,\pm 45,0_2,\pm 45,0_2,\pm 45,0_4,\pm 45,0_2,\pm 45,0_4,\pm 45_2]_s$
2,1,2,2,1,1,2,1,1,2,2,1,2,2,1,1	$[\pm 45,0_2,\pm 45_2,0_6,\pm 45,0_4,\pm 45_2,0_2,\pm 45_2,0_2]_s$
2,1,2,2,1,2,1,1,1,1,1,2,2,2,2,2	$[\pm 45,0_2,\pm 45_2,0_2,\pm 45,0_{12},\pm 45_4]_s$

Author's personal copy

Table 12 Optimal orientation obtained by HS for Case 4

1,1,2,2,1,2,2,2,2,2,1,1,1,1,1,2	$[0_4,\pm 45_2,0_2,\pm 45_5,0_{10},\pm 45]_s$
1,1,2,2,2,2,2,2,1,1,1,1,2,2,2,1,1	$[0_4,\pm 45_5,0_8,\pm 45_3,0_2,0_2]_s$
1,1,2,2,2,2,2,2,1,1,1,2,1,1,2,2,1	$[0_4,\pm 45_5,0_6,\pm 45,0_4,\pm 45_2,0_2]_s$
1,2,1,2,2,1,2,1,2,2,1,2,2,1,2,1,1,2,1	$[0_2,\pm 45,0_2,\pm 45_2,0_2,\pm 45,0_2,\pm 45_2,0_2,\pm 45,0_4,\pm 45,0_2]_s$
1,2,2,1,2,2,1,1,1,2,1,2,2,1,1,2	$[0_2,\pm 45_2,0_2,\pm 45_2,0_6,\pm 45,0_2,\pm 45_2,0_4,\pm 45]_s$
1,2,2,2,1,1,2,1,2,1,1,1,2,1,2,2	$[0_2,\pm 45_3,0_4,\pm 45,0_2,\pm 45,0_6,\pm 45,0_2,\pm 45_2]_s$
2,1,1,2,1,2,2,1,2,2,1,1,2,1,2,1	$[\pm 45,0_4,\pm 45,0_2,\pm 45_2,0_2,\pm 45_2,0_4,\pm 45,0_2,\pm 45,0_2]_s$
2,1,2,1,1,2,1,2,1,2,2,2,2,1,1,1	$[\pm 45,0_2,\pm 45,0_4,\pm 45,0_2,\pm 45,0_2,\pm 45_4,0_6]_s$
2,1,2,1,2,1,1,1,2,2,2,2,1,2,1,1	$[\pm 45,0_2,\pm 45,0_2,\pm 45,0_6,\pm 45_4,0_2,\pm 45,0_4]_s$
2,1,2,1,2,1,2,1,1,2,1,2,1,1,2,2	$[\pm 45,0_2,\pm 45,0_2,\pm 45,0_2,\pm 45,0_4,\pm 45,0_2,\pm 45,0_4,\pm 45_2]_s$
2,1,2,2,1,1,1,1,2,2,1,2,2,1,1,2	$[\pm 45,0_2,\pm 45_2,0_8,\pm 45_2,0_2,\pm 45_2,0_4,\pm 45]_s$
2,1,2,2,1,1,2,1,1,1,1,2,2,2,2,1	$[\pm 45,0_2,\pm 45_2,0_4,\pm 45,0_8,\pm 45_4,0_2]_s$
2,1,2,2,1,2,1,1,1,1,1,1,2,2,2,2	$[\pm 45,0_2,\pm 45_2,0_2,\pm 45,0_{12},\pm 45_3,\pm 45]_s$
2,2,1,1,1,2,1,2,2,1,1,1,2,2,2,1	$[\pm 45_2,0_6,\pm 45,0_2,\pm 45_2,0_6,\pm 45_3,0_2]_s$
2,2,1,1,1,2,2,1,1,1,2,2,1,2,2,1	$[\pm 45_2,0_6,\pm 45_2,0_6,\pm 45_2,0_2,\pm 45_2,0_2]_s$

4.2.3 Case 3

According to statistical results of Table 7, all methods have found the near optimum results in all runs, while BBO-III failed to obtain the near optimum orientations in two runs. BBO-II has found the most number of optimum solutions similar to Case 1. The average result of the HS is about 8e-4% more than that of the BBO-II. According to the convergence curves demonstrated in Fig. 6, the BBO-I and BBO-II have the fastest convergence rate.

Similar to the previous case, different algorithms are led to the identical solution $[90_{16},\pm 45,90_6,\pm 45,90_2,\pm 45,90_2]_s$, as it is also reported in [14].

4.2.4 Case 4

As shown in Table 8, BBO-II has found 73 optimum configurations (distinct or repeated). This variant also outperformed other methods in term of average results. According to the standard deviation column, BBO-II has found more reliable solution compared to other considered methods. Convergence curves of Case 4 are plotted in Fig. 7. Similar to the previous cases, BBO-I and BBO-II have higher convergence rates.

The distinct configurations obtained by generalized pattern search algorithm (GPSA) for this case also are reported in [14], which consist of 32 solutions. Considering the optimum solutions found by the methods reported in Tables 9, 10, 11 and 12, BBO-II has found 42 solutions, which is the most number of distinct configurations reported so far in the literature. According to the tables, none of the obtained optimum orientations include 90_2plies.

5 Conclusions

Three variants of biogeography-based optimization (BBO) as the main optimization algorithm is implemented to optimization of composite panels, which has not been used for the stacking optimization before. Harmony search as a well-known algorithm is also applied to examine the results. Variants of the BBO are considered and comparing the achieved results against other methods showed the good compatibility among the obtained results and those of previous investigations. Four symmetric and balanced laminate panels made up of 64 graphite/epoxy plies with different loading and dimensions are examined as study cases. The critical buckling loading is maximized by varying two-ply stacking sequences and three different fiber orientations of 0_2, ± 45 and 90_2 degrees.

By considering 100 independent runs, in some cases, the algorithms found more than one solution for the same problem. According to the numerical results of the BBO with linear migration model (BBO-I) and quadratic model (BBO-II), they had higher convergence rates in all case studies. As reported in Tables 4, 6, 7 and 8, the BBO-II found either more or equal number of optimal solutions in the same number of trials. According to the reported results, the BBO-II also reached more reliable, endurable and distinct configurations. This algorithm can be considered as a new and powerful tool for optimal stacking sequence of composite structures.

Author's personal copy

References

1. Ghiasi, H., Pasini, D., Lessard, L.: Optimum stacking sequence design of composite materials. Part I: constant stiffness design. Compos. Struct. **90**(1), 1–11 (2009). https://doi.org/10.1016/j.compstruct.2009.01.006
2. Setoodeh, S., Abdalla, M.M., Gürdal, Z.: Design of variable-stiffness laminates using lamination parameters. Compos. Part B Eng. **37**(4), 301–309 (2006)
3. Fang, C., Springer, G.S.: Design of composite laminates by a Monte Carlo method. J. Compos. Mater. **27**(7), 721–753 (1993)
4. Kaveh, A.: Applications of Metaheuristic Optimization Algorithms in Civil Engineering. Springer, Basel (2017)
5. Talbi, E.-G.: Metaheuristics: From Design to Implementation, vol. 74. Wiley, Hoboken (2009)
6. Kaveh, A., Dadras, A.: A novel meta-heuristic optimization algorithm: thermal exchange optimization. Adv. Eng. Softw. **110**(August), 69–84 (2017). https://doi.org/10.1016/j.advengsoft.2017.03.014
7. Kaveh, A., Dadras, A.: Structural damage identification using an enhanced thermal exchange optimization algorithm. Eng. Optim. (2017). https://doi.org/10.1080/0305215X.2017
8. Simon, D.: Biogeography-based optimization. IEEE Trans. Evol. Comput. **12**(6), 702–713 (2008)
9. Soremekun, G., Gürdal, Z., Haftka, R., Watson, L.: Composite laminate design optimization by genetic algorithm with generalized elitist selection. Comput. Struct. **79**(2), 131–143 (2001)
10. Lin, C.-C., Lee, Y.-J.: Stacking sequence optimization of laminated composite structures using genetic algorithm with local improvement. Compos. Struct. **63**(3), 339–345 (2004)
11. Rao, A.R.M., Arvind, N.: A scatter search algorithm for stacking sequence optimisation of laminate composites. Compos. Struct. **70**(4), 383–402 (2005)
12. Erdal, O., Sonmez, F.O.: Optimum design of composite laminates for maximum buckling load capacity using simulated annealing. Compos. Struct. **71**(1), 45–52 (2005)
13. Almeida, F., Awruch, A.: Design optimization of composite laminated structures using genetic algorithms and finite element analysis. Compos. Struct. **88**(3), 443–454 (2009)
14. Karakaya, Ş., Soykasap, Ö.: Buckling optimization of laminated composite plates using genetic algorithm and generalized pattern search algorithm. Struct. Multidiscip. Optim. **39**(5), 477–486 (2009)
15. Sebaey, T., Lopes, C., Blanco, N., Costa, J.: Ant colony optimization for dispersed laminated composite panels under biaxial loading. Compos. Struct. **94**(1), 31–36 (2011)
16. Abachizadeh, M., Tahani, M.: An ant colony optimization approach to multi-objective optimal design of symmetric hybrid laminates for maximum fundamental frequency and minimum cost. Struct. Multidiscip. Optim. **37**(4), 367–376 (2009)
17. Omkar, S., Senthilnath, J., Khandelwal, R., Naik, G.N., Gopalakrishnan, S.: Artificial Bee Colony (ABC) for multi-objective design optimization of composite structures. Appl. Soft Comput. **11**(1), 489–499 (2011)
18. de Almeida, F.S.: Stacking sequence optimization for maximum buckling load of composite plates using harmony search algorithm. Compos. Struct. **143**, 287–299 (2016)
19. Geem, Z.W., Kim, J.H., Loganathan, G.: A new heuristic optimization algorithm: harmony search. Simulation **76**(2), 60–68 (2001)
20. Vosoughi, A., Darabi, A., Forkhorji, H.D.: Optimum stacking sequences of thick laminated composite plates for maximizing buckling load using FE-GAs-PSO. Compos. Struct. **159**, 361–367 (2017)
21. Setoodeh, A., Shojaee, M.: Critical buckling load optimization of functionally graded carbon nanotube-reinforced laminated composite quadrilateral plates. Polym. Compos. (2017). https://doi.org/10.1002/pc.24289
22. Guo, W., Wang, L., Wu, Q.: Numerical comparisons of migration models for multi-objective biogeography-based optimization. Inf. Sci. **328**, 302–320 (2016)
23. Simon, D., Ergezer, M., Du, D., Rarick, R.: Markov models for biogeography-based optimization. IEEE Trans. Syst. Man Cybern. Part B (Cybern.) **41**(1), 299–306 (2011)
24. Bhattacharya, A., Chattopadhyay, P.K.: Biogeography-based optimization for different economic load dispatch problems. IEEE Trans. Power Syst. **25**(2), 1064–1077 (2010)
25. Wang, L., Xu, Y.: An effective hybrid biogeography-based optimization algorithm for parameter estimation of chaotic systems. Expert Syst. Appl. **38**(12), 15103–15109 (2011)
26. Roy, P., Ghoshal, S., Thakur, S.: Optimal var control for improvements in voltage profiles and for real power loss minimization using biogeography based optimization. Int. J. Electr. Power Energy Syst. **43**(1), 830–838 (2012)
27. Wang, G.-G., Gandomi, A.H., Alavi, A.H.: An effective krill herd algorithm with migration operator in biogeography-based optimization. Appl. Math. Model. **38**(9), 2454–2462 (2014)
28. Aydogdu, I.: Cost optimization of reinforced concrete cantilever retaining walls under seismic loading using a biogeography-based optimization algorithm with Levy flights. Eng. Optim. **49**(3), 381–400 (2017)
29. Aydogdu, I., Akin, A.: Biogeography based Co_2 and cost optimization of RC cantilever retaining walls. In: 17th International Conference on Structural Engineering, pp. 1480–1485 (2015)
30. Saka, M., Carbas, S., Aydogdu, I., Akin, A., Geem, Z.: Comparative study on recent metaheuristic algorithms in design optimization of cold-formed steel structures. In: Engineering and Applied Sciences Optimization, pp. 145–173. Springer, Berlin (2015)
31. Jalili, S., Hosseinzadeh, Y., Taghizadieh, N.: A biogeography-based optimization for optimum discrete design of skeletal structures. Eng. Optim. **48**(9), 1491–1514 (2016)
32. Çarbaş, S.: Optimum structural design of spatial steel frames via biogeography-based optimization. Neural Comput. Appl. **28**(6), 1525–1539 (2017)
33. Yang, G., Liu, Y.: Optimizing an equilibrium supply chain network design problem by an improved hybrid biogeography based optimization algorithm. Appl. Soft Comput. **58**, 657–668 (2017)
34. Kaveh, A., Dadras, A.: Optimal decomposition of finite element meshes via k-median methodology and different metaheuristics. Int. J. Optim. Civil Eng. **8**(2), 227–246 (2018)
35. Ma, H., Simon, D.: Evolutionary Computation with Biogeography-Based Optimization. Wiley, Hoboken (2017)
36. Wu, J., Vankat, J.L.: Island biogeography: theory and applications. Encycl. Environ. Biol. **2**, 371–379 (1995)

Author's personal copy

37. Goldberg, D.E.: Genetic Algorithms in Search, Optimization, and Machine Learning, vol. 2. Addison-Wesley, Reading (1989)
38. Reddy, J.N.: Mechanics of Laminated Composite Plates and Shells: Theory and Analysis. CRC Press, Boca Raton (2004)
39. Haftka, R.T., Gürdal, Z.: Elements of Structural Optimization, vol. 11. Springer Science & Business Media, Berlin (2012)

Materials Research Express

PAPER

Comprehensive optimization of friction stir weld parameters of lap joint AA1100 plates using artificial neural networks and modified NSGA-II

To cite this article: Abolfazl Khalkhali *et al* 2018 *Mater. Res. Express* **5** 066508

View the article online for updates and enhancements.

Related content

- Microstructural features of friction stir welded dissimilar Aluminium alloys AA2219-AA7475
  Noor Zaman Khan, Mohammed Ubaid, Arshad Noor Siddiquee et al.
- Effect of tool pin profile and dimensions on mechanical properties and microstructure of friction stir welded armor alloy
  Gyander Ghangas and Sandeep Singhal
- A cellular automaton model for microstructural simulation of friction stir welded AZ91 magnesium alloy
  Mostafa Akbari, Parviz Asadi, MohammadKazem Besharati Givi et al.

IOP ebooks™

Bringing you innovative digital publishing with leading voices to create your essential collection of books in STEM research.

Start exploring the collection - download the first chapter of every title for free.

This content was downloaded from IP address 149.144.220.95 on 03/07/2018 at 08:00

Materials Research Express

CrossMark

RECEIVED
27 February 2018

REVISED
22 April 2018

ACCEPTED FOR PUBLICATION
22 May 2018

PUBLISHED
6 June 2018

PAPER

Comprehensive optimization of friction stir weld parameters of lap joint AA1100 plates using artificial neural networks and modified NSGA-II

Abolfazl Khalkhali[1], **Salman Ebrahimi-Nejad**[2] **and Nima Geran Malek**[1]

[1] Automotive Simulation and Optimal Design Research Laboratory, School of Automotive Engineering, Iran University of Science and Technology, Tehran, Iran

[2] Vehicle Dynamical Systems Research Laboratory, School of Automotive Engineering, Iran University of Science and Technology, Tehran, Iran

E-mail: ab_khalkhali@iust.ac.ir

Keywords: friction stir welding, multi-objective optimization, artificial neural network, Taguchi, NSGA-II, ANOVA

Abstract

Friction stir welding (FSW) process overcomes many difficulties arising in conventional fusion welding processes of aluminum alloys. The current paper presents a comprehensive investigation on the effects of rotational speed, traverse speed, tool tilt angle and tool pin profile on the longitudinal force, axial force, maximum temperature, tensile strength, percent elongation, grain size, micro-hardness of welded zone and welded zone thickness of AA1100 aluminum alloy sheets. Design of experiments (DOE) was applied using the Taguchi approach and subsequently, effects of the input parameter on process outputs were investigated using analysis of variance (ANOVA). A perceptron neural network model was developed to find a correlation between the inputs and outputs. Multi-objective optimization using modified NSGA-II was implemented followed by NIP and TOPSIS approaches to propose optimum points for each of the square, pentagon, hexagon, and circular pin profiles. Results indicate that the optimization process can reach horizontal and vertical forces as low as 1452 N and 2913 N, respectively and a grain size as low as 2 μm. This results in hardness values of up to 57.2 and tensile strength, elongation and joint thickness of 2126 N, 5.9% and 3.7 mm, respectively. The maximum operating temperature can also reach a sufficiently high value of 374 °C to provide adequate material flow.

1. Introduction

Friction stir welding (FSW) introduced by The Welding Institute (TWI) [1, 2], is a low-cost, non-melting weld process. In this approach, welding is performed by creating shear stress and localized plastic deformation for a variety of similar or dissimilar metals and alloys below the melting point, in order to reduce the generated residual stresses. Unlike conventional fusion welding, a rotating tool comprising of a pin and a shoulder, traverses linearly along the adjacent edges of the sheets to be joined. Although the most common configurations of FSW process are butt and overlap, this process can also be applied to other configurations. The FSW tool is subjected to forces in various directions, which are of high importance due to their role in the erosion of the tool as well as the mechanical properties of the joint. Studying the impacts of FSW process parameters on weld joint mechanical properties has been an interesting field for many researchers. This method was originally developed for aluminum and many studies have focused on aluminum alloys [3–7].

Nowadays, FSW is applied on various alloys including magnesium [8–11], copper [12–16], steels [17–19], and also polymers [20, 21]. Forcellese *et al* [10] investigated the effect of process parameters, tool pin geometry and size on friction stir welding of thin sheets of AZ31 magnesium alloy. Friction stir welding of dissimilar Al-Cu joints were conducted by Tan *et al* [15] and the microstructure of FSW joint and its formation mechanism were discussed. Effects of tool deviation on weld quality of DH36 steel was analyzed by Tingey *et al* [19]. Simões and

© 2018 IOP Publishing Ltd

Rodrigues [20] investigated the thermo-mechanical conditions and material flow, during FSW of polymethyl methacrylate (PMMA) polymer.

FSW has been successfully used and studied in aluminum alloys [22–31]. In order to predict the effects of a multitude of process input parameters on weld speed and quality, some researchers have used artificial neural networks (ANNs). Okuyucu *et al* [22] studied butt-welded aluminum plates and developed an artificial neural network to predict weld mechanical properties as a functions of weld speed and tool rotation speed. Fratini *et al* [23] attempted to predict the average grain size values in the FSW process by linking an artificial neural network to a finite element model.

Tansel *et al* [24] designed a genetically optimized neural network for estimation of the optimal operating conditions of FSW process, considering rotational and weld speed as input parameters. Shojaeifard *et al* [25] studied the microstructural and mechanical properties of FSW joints of AA7075-O to AA5083-O alloys. In another research, Shojaeifard *et al* [26] showed the effects of rotational speed and weld speed on welding force, peak temperature and HAZ width in the FSW process on Al5083 alloy, using thermo-mechanically coupled rigid-viscoplastic 3D finite element model (FEM) and employing an ANN. In addition to the aforementioned studies, via Taguchi technique and ANOVA, Khalkhali *et al* [29] examined the best process criteria for lap joint friction stir welding of AA1100 aluminum alloy.

A brief review of the structures of the neural networks used in previous literature is presented in table 1, which shows the limited number of inputs/outputs in previous researches.

To the best knowledge of the authors, a comprehensive study of a variety of input parameters (including rotational speed, weld speed, tilt angle and tool pin geometry) on numerous outputs (i.e., hardness, grain size, elongation, vertical and horizontal forces, tensile strength, and maximum temperature), utilizing appropriate methods of design of experiments, sensitivity analysis, neural networks, and optimization has not been performed yet. This motivated the present study, that is concerned with finding the optimal input parameter values, which is lead to desired outputs. To this end, first, DOE method is employed and 30 experiments to be used in training and testing the ANN, were carried out, separately. Then, NSGA II algorithm, which is fed by the ANN, is implemented, and the results are thoroughly investigated. The topics in the current paper are elaborated through the following sections. Section 2 outlines a thorough description of experimental investigations and the multi-objective optimization approach under study. In section 3, the results of the current study are presented and some two-dimensional mapping planes of 8D Pareto optimal result are provided. Finally, concluding remarks are presented.

2. Methodology

The mechanical properties of FSW welds are highly affected by many input process parameters. Subsequently, determining the best input parameters for this process is difficult, time-consuming and costly. Due to the development of computer and materials sciences, predicting the behavior of materials could be done with the help of materials manufactured in the past. ANNs, through a series of assigned inputs and acquired experimental outputs, are trained through an iterative procedure and then employed to predict this behavior. This training objective is performed by updating network parameters, hence, minimizing the mean square error (MSE). The training process stops, based on the values of MSE or its gradient or when reaching maximum epochs.

Errors between the output values of the neural network and the actual process results could be minimized by modifying the values of weights and biases. The trained neural network can be used to simulate the outputs corresponding to input values that have not been previously tested. The multi-objective optimization problem, is the problem of finding a vector of design variables, which optimizes another vector comprising of objective functions and satisfies the constraints created from variable conditions. In the current investigation, NSGA-II algorithm was employed for finding the Pareto optimal front set, according to the procedure depicted in figure 1.

In this study, each of the input parameters, including rotational speed, weld speed, tool pin geometry and tilt angle, are studied at four levels. Taguchi design of experiments method is utilized for the determination of the optimal levels of the input parameters. Also, by using ANOVA, the percentage contribution of each of the input parameters has been determined. Since there is no explicit correlation for the purpose of estimating the target parameters based on the input parameters, using the results of 30 experimental tests, the target parameters are modeled by a Perceptron's neural network.

After these steps, all of the 1000 samples were placed in the neural network, which was considered as a cost function in the optimization algorithm. The output of cost function for each solution procedure is 8 mean and 8 standard deviations. The mean values, as stated in the deterministic multi-objective optimization, are minimized or maximized and the standard deviation values are minimized. Each of the input parameters is studied in four levels, as shown in table 2. Accordingly, the number of possible scenarios that can be explored is very high (256 modes), which is why using an optimal testing design is critical to save time and cost.

Table 1. A brief review of the neural network structure used in some literature.

Year	Authors	Methods and achievements	Network
2007	Okuyucu *et al* [22]	The hardest samples were obtained in the case in which tool speed was 500 rpm and linear speed was 20 mm min^{-1}.	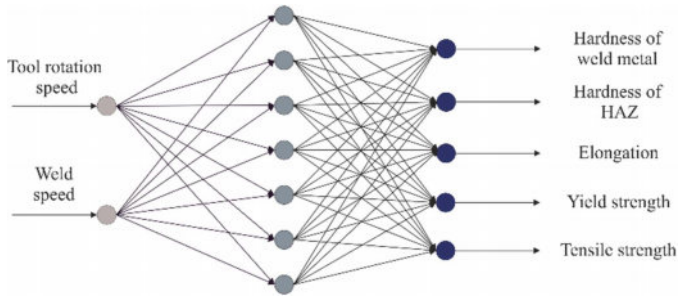
2009	Fratini *et al* [23]	In this research, neural network inputs are obtained through numerical modeling and neural network objectives through experimenting.	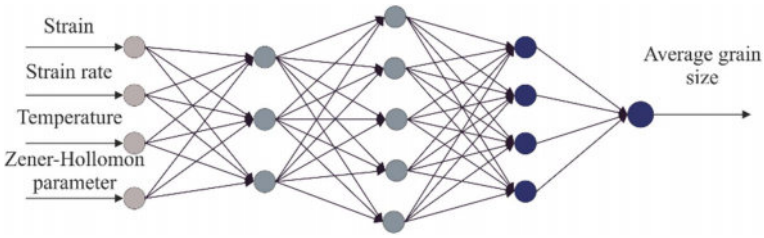
2013	Shojaeefard *et al* [25]	MOPSO and TOPSIS	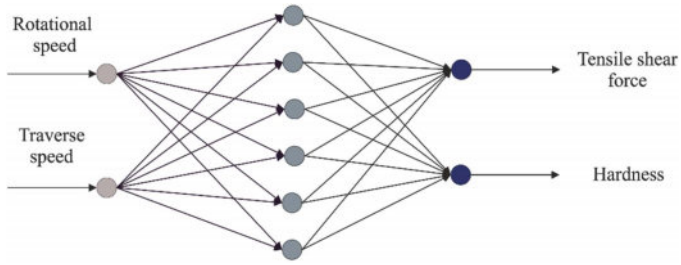
2014	Shojaeefard *et al* [26]	NSGA-II and TOPSIS	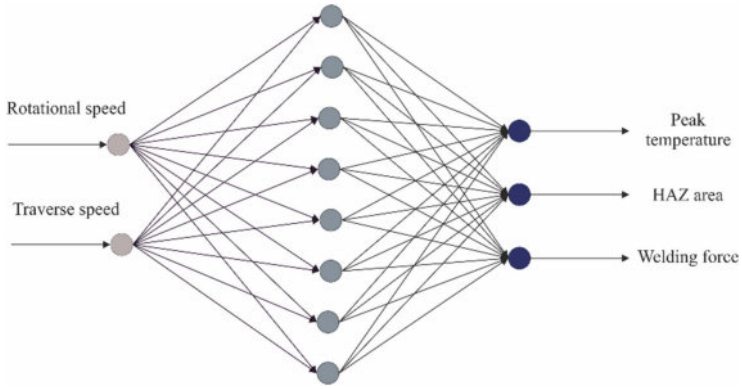
2014	Ghetiya *et al* [27]	ANN	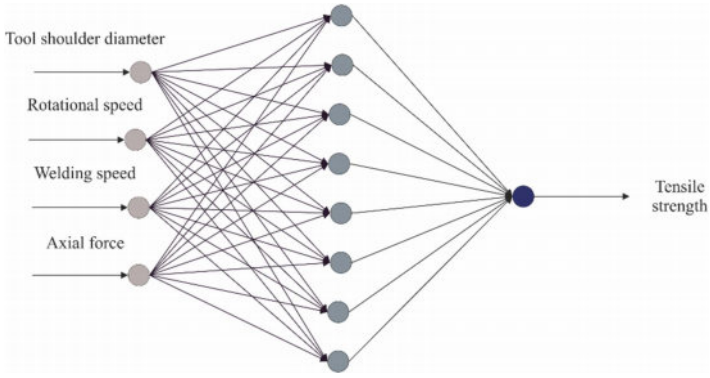

Table 1. (Continued.)

Year	Authors	Methods and achievements	Network
2016	Dehabadi *et al* [28]	ANN for Titanium Alloy (for Triangle Pin Profile Tool)	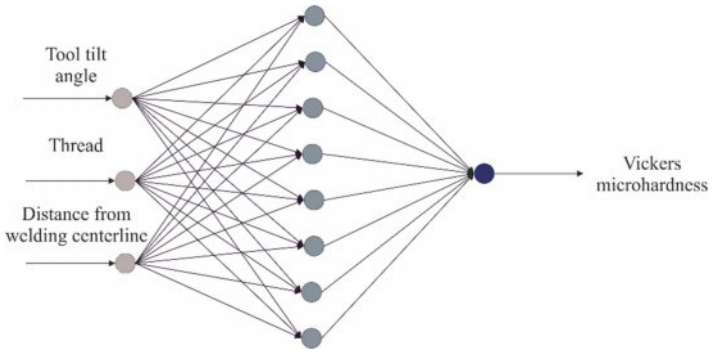

2.1. Parameter selection

Tools used in the FSW process, have two distinct parts including shoulder and pin, which are designed for three different purposes: (I) generating frictional heat to soften the working material; (II) controlling material flow to produce a flawless welded joint; and (III) repletion of the heated material under the shoulder.

Rotational and longitudinal speed of the tool are the most essential parameters in the FSW process. These parameters play a major role in the material flows, mechanical and microstructural properties, welding force and other outputs of FSW process. For this reason, the rotational speed and traverse speed of the tool have been studied in this research. The third parameter studied in this research was the tool tilt angle. This angle can help control the material flow and prevent heat loss. On the other hand, increasing this angle significantly affects the force exerted on the tool. Another adverse effect of tilt angle is the undesirable reduction of the thickness of the bonded surfaces along the weld line. The fourth parameter examined in this study is the geometry of the tool pin (figure 2). Pin geometry is the most significant factor causing material flow and plastic deformation and also the second factor in heat generation in FSW zone. Each of the input parameters investigated in this research were studied at four levels.

2.2. Sensitivity analysis

Using DOE method, the best level for each controllable factor is obtained prior to testing. In this method, initially all the factors in the process are identified and only controllable factors are selected, and the levels for these factors are determined. After this step, the levels of the existing screened controllable factors are optimized. To this end, the Taguchi experimental design method is used to find the best response levels. In addition, the Taguchi method reduces the effect of noise factors accompanying the screened controllable factors, and therefore, the resulting product will be more stable.

In this study, in order to arrange the experimental design table, combination of the Taguchi method and the approach in which the input parameter space is covered with 30 tests are considered for the experimental part of the research. The details of each test, together with the results, are presented in table 2. As shown, the number of experiments proposed by the Taguchi method is 16 out of a total of 30 tests, which are characterized by dark color.

After the friction welding operation, mechanical and microstructural tests were performed on the joints. The mechanical tests in this study are tensile test for measuring joint strength, as well as the percent elongation and micro-hardness test in the center of the welding zone. After these steps, metallographic operations were performed to determine the grain size at the weld center. Finally, the joint thickness along the weld line, which is affected by tool angle, is also calculated analytically.

2.3. Work piece and tool material properties and geometries

Aluminum has become a material of wide-spread use in the automotive industry, because of high formability, desirable mechanical strength, corrosion resistance and fatigue behavior, thermal and electrical conductivity, abundance and recyclability. One of the most important properties of aluminum is its low density and high strength, which makes it a suitable alternative to steel, copper, brass and automotive plastics. In the current study, annealed aluminum 1100 was used as the work piece, the chemical composition of which is listed in table 3, and its material properties are given in table 4. The thickness of the sheet is 2 mm and the parts are

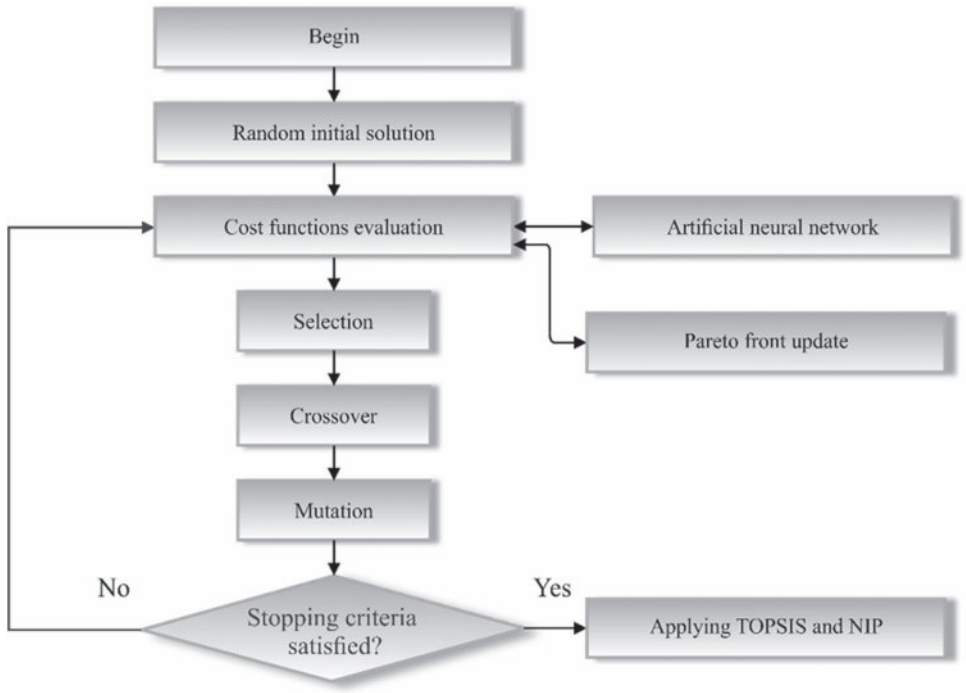

Figure 1. The proposed procedure.

Table 2. Levels and values of FSW design parameters.

Parameter	Level 1	Level 2	Level 3	Level 4
Rotation speed (rpm)	400	800	1250	1600
Weld speed (mm min^{-1})	20	50	80	125
Tool angle (degree)	1	2	3	4
Pin Geometry	Square	Pentagon	Hexagon	Circle

considered as 80 × 80 mm squares. The design configuration of the welded joint considered in this research is lap joint.

Since the temperature during the friction stir welding process is relatively high, in order to create a welded joint in frictional stir welding, it is necessary to have a tool that has the required strength and hardness and can also maintain these properties at high temperatures. Therefore, in this study, hot-work H13 steel is used for the welding tool. The chemical composition of H14 steel is listed in table 3, and its material properties are given in table 4.

After grinding the blank rods to form rods of 20 mm diameter, heat treatment was performed, by placing the work pieces in a furnace at a temperature of 1020 °C for 30 min and then cooling them in oil. After heat treatment, FSW tool pins are manufactured based on the values of shoulder diameter, shoulder angle, and pin height and cross sections. Due to the thickness of the aluminum sheets, shoulder diameter and pin height were designed to be 16 and 3 mm, respectively, and the shoulder angle was 10 degrees. The pins of all four tools fit in a circle of 2.5 mm diameter, and when rotating, all tool pins occupy the same area. The tools were machined using a grinding machine and the final tools are shown in figure 3.

2.4. Friction stir welding (FSW) process

The welding process was carried out according to the design table in 30 experiments, using FP4M milling machine. Overlapping AA1100 aluminum alloy sheets with the dimensions of 80 mm × 80 mm × 2 mm were welded. To measure the vertical forces exerted on the tool during the welding process, two parallel bending load cells were used. The horizontal force applied to the tool was measured using an S-shaped load cell. To this end, a bracing system was designed and constructed according to figure 4, in which the load cells were installed.

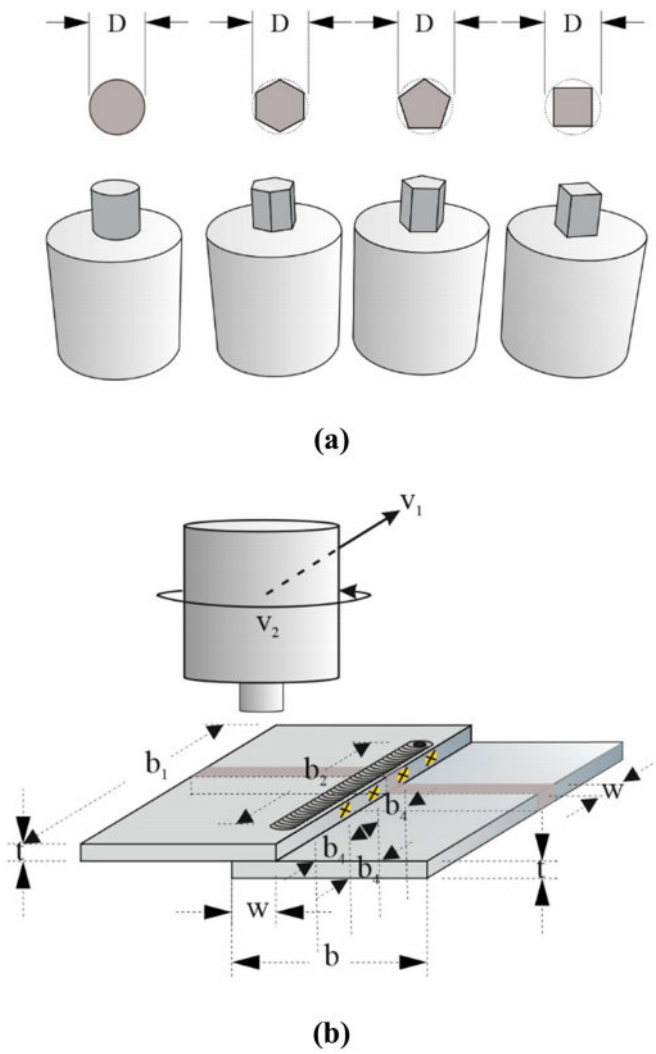

Figure 2. Sketch of the FSW of lap joint: (a) different tool geometries (from left to right: circular, hexagonal, pentagon, and square), (b) configuration of the FSW process, temperature monitoring zones are indicated with yellow crosses and brown shadow illustrates the location of the tensile test specimen.

Another parameter that has been investigated during the friction stir welding process is the process temperature, measured at 10 mm from weld line at four points spaced at 10 mm intervals, using four thermometers. Figure 5 shows the thermometry configuration and the locations of the thermometers on the workpiece. The tool starts to move at a position of 15 mm away from the edge of the sheets and reaches the first thermometer after 20 mm; then it passes the other thermometers every 10 mm.

Several samples of the final welded sheets are presented in figure 6. As shown, the quality of the welds is fairly acceptable.

2.5. Mechanical and microstructural tests

After completing the welding process, microstructure and mechanical tests of the welded samples were investigated. The mechanical tests include tensile test for measuring joint strength, as well as the percent elongation and micro-hardness test for measuring the hardness at the center of the welding region. After these operations, metallographic examinations were performed to determine the grain size at the weld center. Finally, joint thickness along the weld line, which is affected by tool angle, is calculated analytically.

SANTAM-STM150 tensile testing device was used to perform the tensile test. In order to prevent twisting of the lap welded joints in tensile tests, two small fixtures are used.

The initial lengths of the test samples were 60 mm. After completion of the tensile test, small pieces of weld samples were cut from the weld center. These small specimens were mounted in 6 sets of 5 samples. The mounted specimens were polished to perform microhardness test.

Table 3. Chemical composition of aluminum 1100 (work piece) and tool steel (FSW tool).

Aluminum 1100		Tool steel	
Element	Percentage	Element	Percentage
Al	Min 99	Cr	4.80–5.50
Be	Max 0.0008	Mo	1.20–1.50
Cu	0.05–0.2	Si	0.80–1.20
Mn	Max 0.05	V	0.85–1.15
Zn	Max 0.1	C	0.35–0.42
Si+Fe	Max 0.95	Mn	0.25–0.50
Any other element	Max 0.05	S	0–0.005
All other elements	Max 0.15	P	0–0.025

Table 4. Material properties of work piece and tool.

Property	Annealed aluminum 1100	Hot-worked tool steel
Tensile strength (MPa)	89.6	1990
Yield strength (MPa)	34.5	1650
Shear strength (MPa)	62.1	62.1
Fatigue strength (MPa)	34.5	—
Elongation (%)	45	9
Brinell hardness	23	—
Rockwell hardness (C)	—	55
Elastic modulus (GPa)	68.9	210
Shear modulus (GPa)	26	81
Poisson ratio	0.33	0.3
Density (g/cc)	2.71	7.8
Thermal conductivity (W/m.K)	222	24.3
Melting point (°C)	643–657.2	—
Annealing temperature (°C)	343	900–845
Machinability (%)	10	50

The hardness at the weld center is measured by KOOPA-MH3 micro-hardness tester. The amount of force used during the hardening test is 100 grams and the time of applying this force is 10 s. To perform the metallography, the mounted samples were polished electro-etched. Metallography was performed using an optical microscope to detect any existing defect.

Then, average grain size was calculated using metallographic images by determining the number of seeds in a given area and dividing this number by the studied area to obtain the average area of each grain. The average diameter of each grain, which is the common criterion for expressing grain size, is equated from grain area according to the relation $S = \pi D^2/4$. Finally, the relationship in figure 7 is used to measure the welded joint thickness across the weld line.

2.6. Analysis of variance (ANOVA)

After performing the tests related to the Taguchi experimental design and collecting the data, the correlations between each input parameter and the output parameters are studied, by implementing a procedures in MATLAB. From the total 30 available data sets, 16 data sets were investigated according to the DOE method. Then, for each of the output parameters, optimal values for the levels of all input parameters are specified. Using analysis of variance, the percentage of contribution of each input parameter on the output parameters was calculated.

2.7. Design of the artificial neural network (ANN)

MATLAB was used to model an artificial neural network to estimate FSW data. Since there is no explicit correlation for estimating target parameters based on the input parameters, target parameters are modeled by a

Figure 3. Geometries of the designed tools.

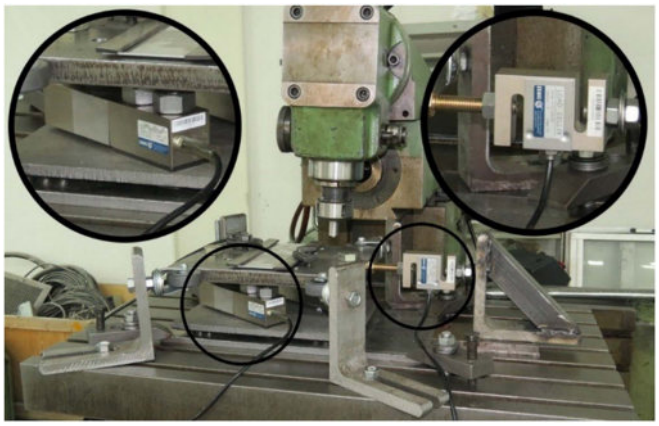

Figure 4. S-shaped load cells and fixture for measuring welding forces.

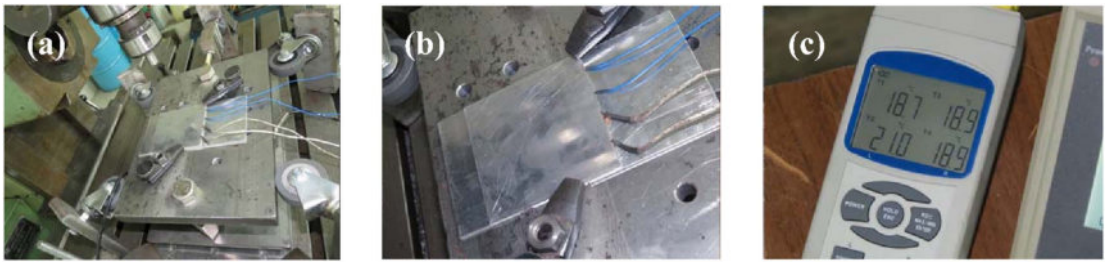

Figure 5. Thermometry configuration used in the friction stir welding process.

three-layer perceptron ANN using data obtained from mechanical and micro-structural experiments. The input layer of this perceprton ANN includes the input parameters. The output layer, also necessarily has 8 neurons, which is the number of output target functions. only the number of intermediate layer(hidden layer) neurons can be changed, which is usually determined by trial and error. The number of data for training the network is 24, and the data sets related to the network test is also considered as 6. To obtain weights and network bias, there exist 24 (number of training data) multiply by 8 (number of target functions) equations. Therefore, the idden layer neurons should be selected in such a way that the number of network unknowns, which are the weights and bias, does not exceed 192. Considering 14 neurons for the hidden layer, the number of neural networks is 180, and this is why this amount is considered for the number of neurons in the intermediate layer. To determine the transfer functions used in the hidden and output layers, by examining all possible scenarios of hidden and output layer transfer functions. both are considered as tansig. In this network, the LM network training

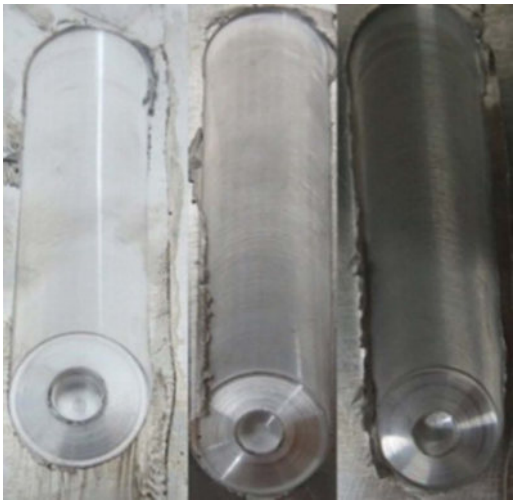

Figure 6. View of AA1100 work piece (80 mm × 80 mm × 2 mm) after FSW process.

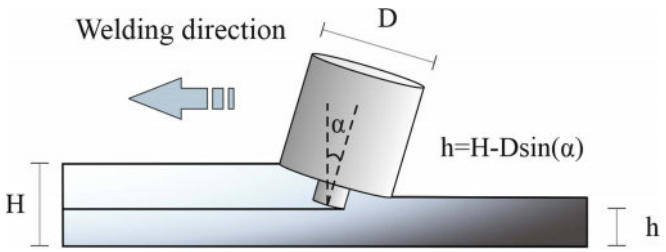

Figure 7. Effect of tool angle on joint thickness in FSW region.

function, as well as the Error Mean Square Error (MSE) for the network error function, is considered. In table 5, some other parameters of this perceptron network are demonstrated.

The schematic arrangement of the neural network architecture and the input and output parameters applied on each layer are demonstrated in figure 8.

2.8. Deterministic multi-objective optimization

After designing a neural network as a simulator for the friction stir welding process, it has been used as a cost function for multi-objective optimization. It should be noted that in this research, the parameters which should be minimized are: the horizontal and vertical force applied to the tool and the grain size. Moreover, reducing the welding forces will reduce the energy consumption and reduce the erosion of the tool, and the smaller the grain size of the welding area, the more favorable mechanical properties will be. All five other parameters should also be maximized. Increasing the inlet heat applied into the workpiece can lead to a softening of the metal in the weld area and better material flow. Increased tensile strength, elongation and stiffness of the joint are also considered desirable in engineering designs. The thickness of the weld is also an important issue, greater value of which is desirable, but since the algorithm is designed to minimize the objective, the inverse of these parameters are minimized.

The algorithm used in this study is the non-dominated sorting genetic algorithm's second version, designated as NSGA-II, programmed in MATLAB. In this study, considering the high number of target functions, the initial population is 1000 and the number of generations is 300. The method used for selecting the parent for the cross-over is the roulette wheel. The probability of cross-over and mutation is considered to be 0.70 and 0.15, respectively, and in the mutation of each chromosome, only one gene changes. The standard form of the optimization problem is as:

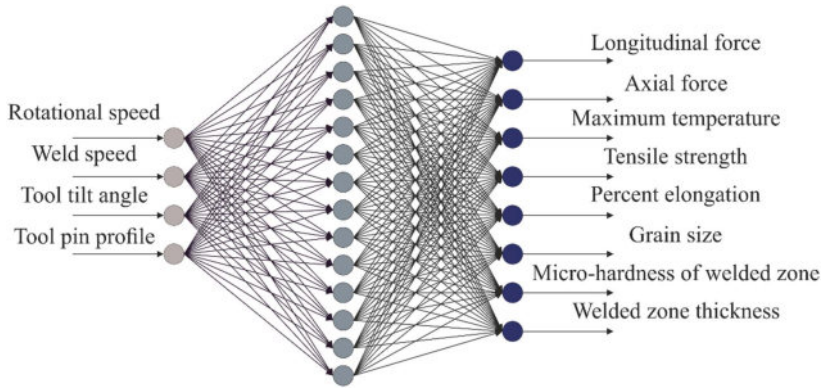

Figure 8. Three-layer structure of the neural network used in the current study.

Table 5. Data of the converged neural network.

Epoch	444 iterations
Time	0:00:07
Performance	5.25e–05
Gradient	0.0001
Mu	1.00e–09
Validation Checks	0

$$\begin{aligned}
&\text{Minimize Horizontal Force}(n, v, \alpha, \beta)\\
&\text{Minimize Vertical Force}(n, v, \alpha, \beta)\\
&\text{Maximize Temperature}(n, v, \alpha, \beta)\\
&\text{Maximize Tensile Strength}(n, v, \alpha, \beta)\\
&\text{Maximize Elongation}(n, v, \alpha, \beta)\\
&\text{Minimize Grain Size}(n, v, \alpha, \beta)\\
&\text{Maximize Hardness}(n, v, \alpha, \beta)\\
&\text{Maximize Thickness}(n, v, \alpha, \beta)\\
&\text{Subject to}\begin{cases} 400 \leqslant n \leqslant 1600 \\ 20 \leqslant v \leqslant 125 \\ 1 \leqslant \alpha \leqslant 4 \\ \beta = 90,\ 108,\ 120,\ \text{or } 180 \end{cases}
\end{aligned} \tag{1}$$

In Relation (1) n, v, α, and β, are the rotation speed in terms of rpm, the weld speed in mm/min, tool angle in terms of degree and tool polygon (internal) angle in degrees, resembling the tool pin profile, respectively. Pin geometry is assumed to be a discrete quantity, because except square, pentagon, hexagon, and circular profiles, no other geometries are considered. Eventually, after the eight-dimensional Pareto front is obtained, for these optimal solutions, nearest to ideal point (NIP) and TOPSIS approaches are employed.

3. Results and discussion

3.1. FSW test results

In this section, first, we study the experimental results of mechanical and microstructural tests, and then the results related to sensitivity analysis and deterministic optimization are thoroughly investigated. As mentioned earlier, the horizontal and vertical forces applied to the tool during the friction stir welding process were measured. The process temperature was also measured by four thermometers, the results of which, were recorded for the first experiment, are shown in figure 9. According to the graph, it can be seen that the maximum

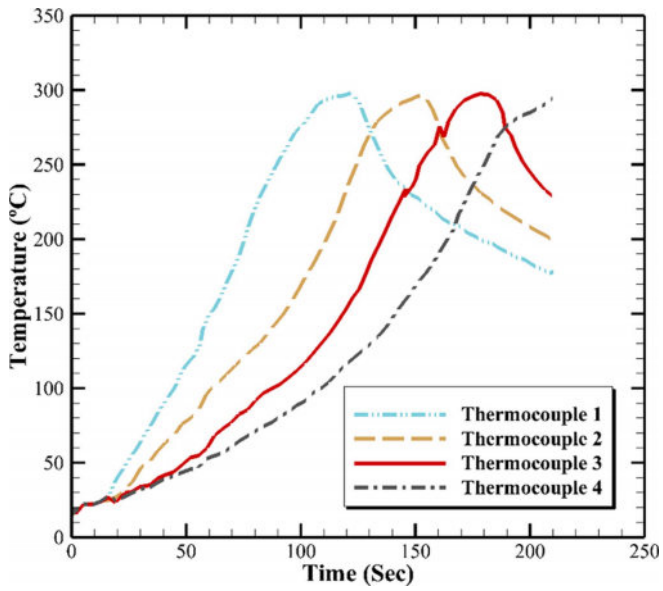

Figure 9. Recorded temperature by four thermometers for test sample number 1.

recorded temperature by each thermometer is related to the time when the tool crosses it. The maximum process temperature is considered as the average value of the maximum temperatures recorded by each thermometer.

The weld joint tensile strength and elongation percentage is considered as the maximum force recorded by the tensile testing device. As an example, the force-displacement diagram for the first sample is shown in figure 10.

Grain size in the center of the weld region was measured after a metallographic operation by an optical microscope. Figure 11 shows selected metallographic images of the microstructure of the weld center region for test samples No. 13, 5 and 15.

The hardness in the center of the weld line is measured using a microhardness testing device. Joint thickness was calculated along the weld line based on the relationship shown in figure 7. This parameter has a value of 3.7, 3.4, 3.1 and 2.9, respectively, for tool angles ranging from 1 to 4 degrees. Therefore, the only factor affecting this parameter is tool angle, by increasing which, joint thickness decreases, which can reduce joint performance. Weld forces, maximum process temperature, tensile strength, elongation percentage, grain size, and microhardness of the FSW samples are listed in table 6 for each of the 30 test samples.

3.2. Analysis of variance (ANOVA)

After performing the tests related to the Taguchi experimental design and data collection, the impact of each input parameter on the output parameters was studied, the results of which are listed in table 7. The percentage of contribution of each input parameter on the output parameters has been reported.

Then, for each of the output parameters, optimal values for the levels of all input parameters are specified. According to the obtained results, it can be seen that the tool rotational speed has the greatest effect for force applied on the tool. Pin shape, weld velocity and tool angle are the most significant factors affecting the horizontal and vertical forces applied to the tool, respectively. The optimal levels related to the horizontal force parameter are predicted as $\alpha_1\beta_2 n_4 v_2$. To achieve the minimum amount of horizontal force applied to the instrument, the angle of the tool, tool angle, pin shape, rotational speed and weld speed should be 1 degree, pentagon, 1600 rpm and 50 mm min^{-1} respectively. In this case, the Taguchi design method predicted the amount of applied horizontal force to 1127 N.

In addition, the optimal levels related to the applied vertical force are predicted as $\alpha_3\beta_1 n_4 v_2$. Moreover, for this case, the Taguchi design method predicted the amount of applied vertical force to 2702 N. Generally, by increasing the ratio of the rotation speed to weld speed, the amount of heat produced in the work piece will increase, which will result in more material softening, and the less force needed to move the tool in the work piece. Also, when tools angle is at its lowest value, the penetration depth of the tool and the intensity of involvement of the tool with the work piece is reduced compared to other states, which will reduce the force applied to the tool. The use of square and pentagon tool profiles also leads to severely localized deformations in the work piece, which is why the heat produced due to plastic deformation is higher in these type of profiles, and as a result, the material is softer and less force is applied to the tool.

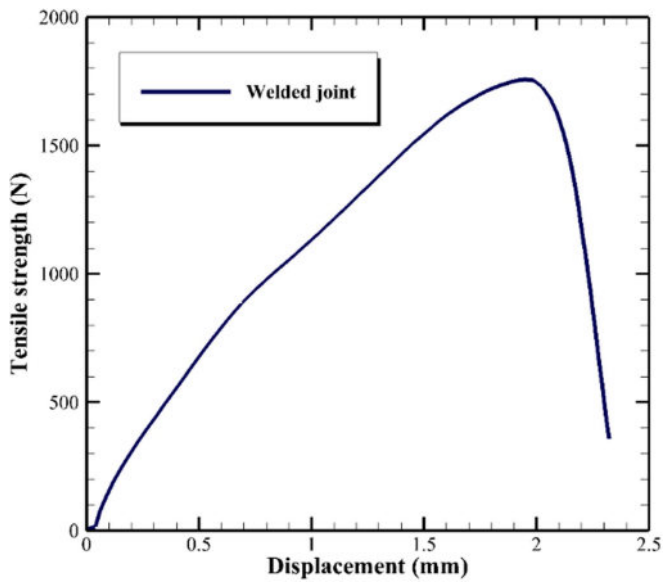

Figure 10. Tensile strength diagram of welded joint in terms of displacement.

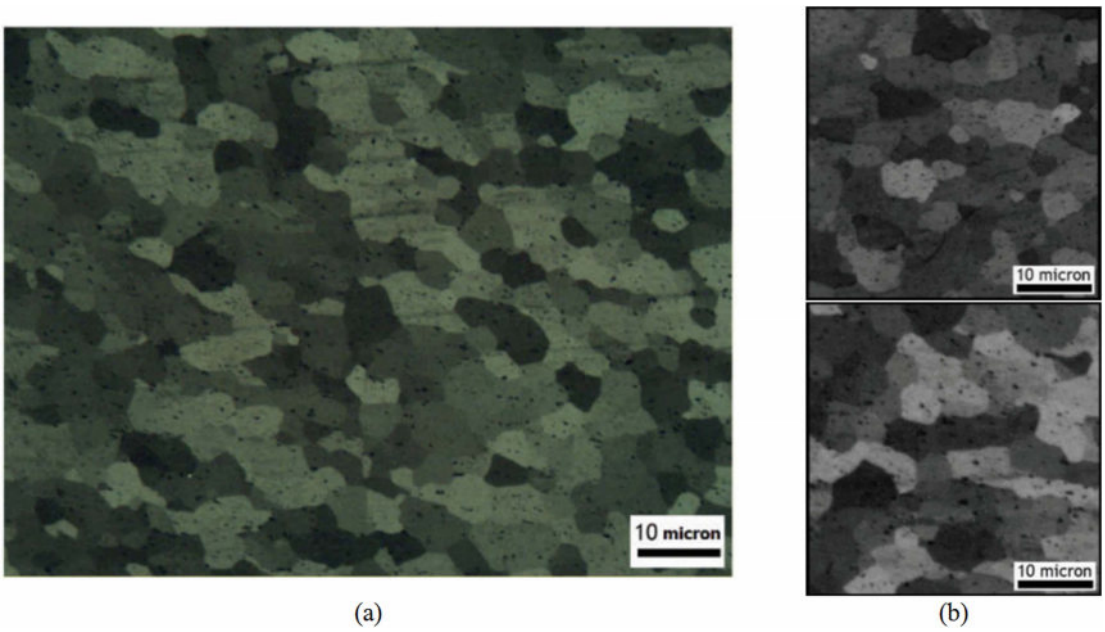

Figure 11. Microstructure images of the weld center for samples No. (a) 13, and (b) 5 (top), and 15 (bottom).

According to the results, the speed of the tool has the greatest effect on the maximum working temperature. Rotational speed, pin shape and tool angle are the most significant factors affecting maximum working temperature, respectively. The optimal levels related to the maximum working temperature parameter are predicted as $\alpha_4\beta_1 n_4 v_1$. In this case, the maximum operating temperature of the friction stir welding process is expected to be 416 °C. Square and pentagon profiles cause more heat in the work piece due to more plastic deformation than other shapes.

The results also show that rotational speed, tool angle, weld speed, and pin shape have the highest effects on joint strength, respectively. The optimal levels related to joint strength are predicted as $\alpha_3\beta_3 n_1 v_4$ for which, the joint strength is predicted as 2129 N. By decreasing the ratio of the rotation speed to weld speed, the amount of heat generation of the work piece decreases, which reduces the width of the heat affected zone. Since the mechanical properties of this area are unfavorable, reducing the heat affected zone can improve weld mechanical properties. On the other hand, polygon pin profile, applies pulsed forces onto the work piece, due to its geometry, leading to breakage and segmentation of the work piece grains in the weld area. Therefore, using these

Table 6. Values of design and output parameters for a combination of L_{16} orthogonal array (rows with dark color) and space covering experiments used in ANN.

Test	Tool angle (°)	Tool pin shape	Rotation speed (rpm)	Weld speed (mm min^{-1})	Average horizontal force (N)	Average vertical force (N)	Maximum temperature (°C)	Tensile strength (N)	Elongation (%)	Grain size (μm)	Hardness (μm)
1	1	Square	400	20	1619	3808	299	1760	3.9	3.6	48.9
2	1	Square	400	125	1890	4127	215	2004	3.0	2.0	57.2
3	1	Square	1600	20	1293	2998	396	1290	4.9	5.2	43.6
4	1	Square	1600	125	1374	3119	273	1538	3.7	3.0	50.8
5	1	Pentagon	800	50	1293	3414	294	1903	1.4	3.7	48.0
6	1	Hexagon	1250	80	1451	3319	292	1813	4.4	3.9	47.2
7	1	Circular	400	20	1934	4193	271	1742	4.9	4.9	44.5
8	1	Circular	400	125	1693	4448	200	1986	3.6	2.8	51.8
9	1	Circular	1600	20	1434	3145	354	1272	5.9	7.7	39.8
10	1	Circular	1600	125	1687	3414	250	1516	4.5	4.3	46.1
11	2	Square	800	80	1729	3545	279	2077	3.5	2.8	51.9
12	2	Pentagon	400	125	1868	4554	217	2127	3.1	2.3	55.0
13	2	Hexagon	1600	20	1379	2913	396	1411	5.4	6.4	41.3
14	2	Circular	1250	50	1543	3501	306	1876	5.1	5.2	43.7
15	3	Square	1250	125	1643	3161	268	1974	3.7	2.8	51.9
16	3	Pentagon	1600	80	1327	2929	330	1626	4.5	4.0	47.1
17	3	Hexagon	400	50	1822	4087	275	2046	3.7	3.2	49.9
18	3	Circular	800	20	1845	3835	315	1846	5.4	6.0	42.0
19	4	Square	400	20	1626	4213	321	1610	4.2	3.5	48.9
20	4	Square	400	125	2097	3792	227	1854	2.8	2.0	57.2
21	4	Square	1600	20	1686	3333	428	1140	5.0	5.2	43.6
22	4	Square	1600	50	1307	2950	382	1305	4.2	4.0	47.0
23	4	Square	1600	125	1597	2993	292	1384	3.6	3.0	50.8
24	4	Pentagon	1250	20	1362	3398	391	1452	5.1	5.6	42.9
25	4	Hexagon	800	125	1664	3792	245	1830	3.6	3.0	50.9
26	4	Circular	400	20	2003	3996	289	1596	4.8	4.9	44.5
27	4	Circular	400	80	1872	4404	239	1804	3.7	3.2	49.9
28	4	Circular	400	125	2118	4408	210	1836	3.6	2.8	51.8
29	4	Circular	1600	20	1574	3118	382	1122	5.7	7.4	39.8
30	4	Circular	1600	125	1581	3373	265	1366	4.4	4.3	46.1

tools can reduce the size of the grain in the weld area. Considering the well-known Hall-Petch relationship ($\sigma = \sigma_0 + \mathrm{Kd}^{-0.5}$ and $\mathrm{H} = \mathrm{H}_0 + \mathrm{Kd}^{-0.5}$) decreasing the grain size will increase the hardness and stiffness of the material. Tool angle also causes the mixing of the materials in the weld region which results in imperfections like cavities and cracks, due to the fact that it reduces the involvement between the tool and work piece and reduces the penetration depth of the pin. Excessive increase in this angle will also reduce joint thickness along the weld line, which will decrease joint strength.

Results also indicate that for each of the three parameters, namely, joint elongation, hardness and grain size, weld speed, rotational speed, pin geometry and tool angle parameters have the most effect, respectively. The optimal levels for these parameters are respectively $\alpha_3\beta_4\mathrm{n}_4\mathrm{v}_1$, $\alpha_2\beta_1\mathrm{n}_1\mathrm{v}_4$ and $\alpha_2\beta_1\mathrm{n}_1\mathrm{v}_4$, and their values in these conditions are expected to be 5.9%, 56.6 Vickers and 1.3 μm, respectively. Generally, increase in weld joint elongation has an adverse effect on the hardness and grain size of the weld. This means that the conditions that lead to an increase in the elongation of the welded joint also leads to the reduction in hardness as well as an increase in the grain size. So far, several analytical models have been presented to calculate the grain size based on the recrystallization phenomenon, one of which is presented in equation (2):

Table 7. ANOVA and Taguchi results.

	Horizontal force on the tool		Vertical force on the tool		Maximum temperature		Tensile strength of welded joint		Elongation		Grain size at the weld center		Hardness at the weld center	
	Effect (%)	Optimal level	Effect (%)	Optimal level	Effect (%)	Optimal level	Effect (%)	Optimal level	Effect (%)	Optimal level	Effect (%)	Optimal level	Effect (%)	Optimal level
Tools angle (°)	8.29	1	2.05	1	4.29	4	22.49	3	1.04	3	1.11	1	0.17	2
Tool Shape	22.81	Pentagon	9.98	Square	5.64	Pentagon	0.09	Square	20.44	Circle	18.78	Square	18.69	Square
Rotational speed (rpm)	47.42	1600	81.05	1600	35.19	1600	61.86	400	36.93	1600	26.96	400	31.27	400
Weld speed (mm min^{-1})	16.15	50	4.31	50	54.67	20	15.55	125	41.51	20	52.92	125	49.85	125

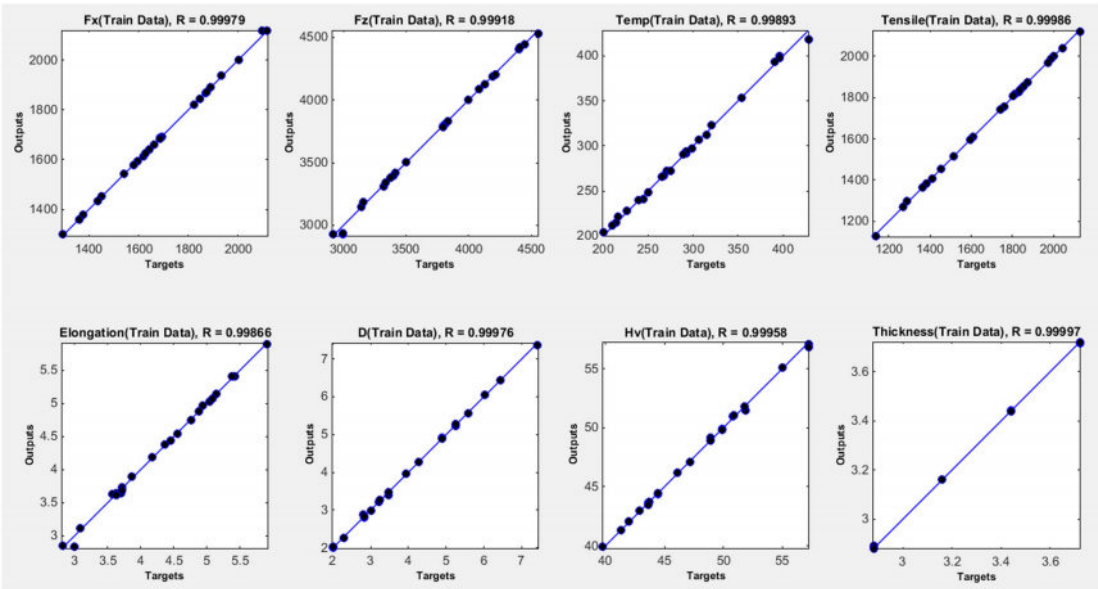

Figure 12. The performance of ANN with training data.

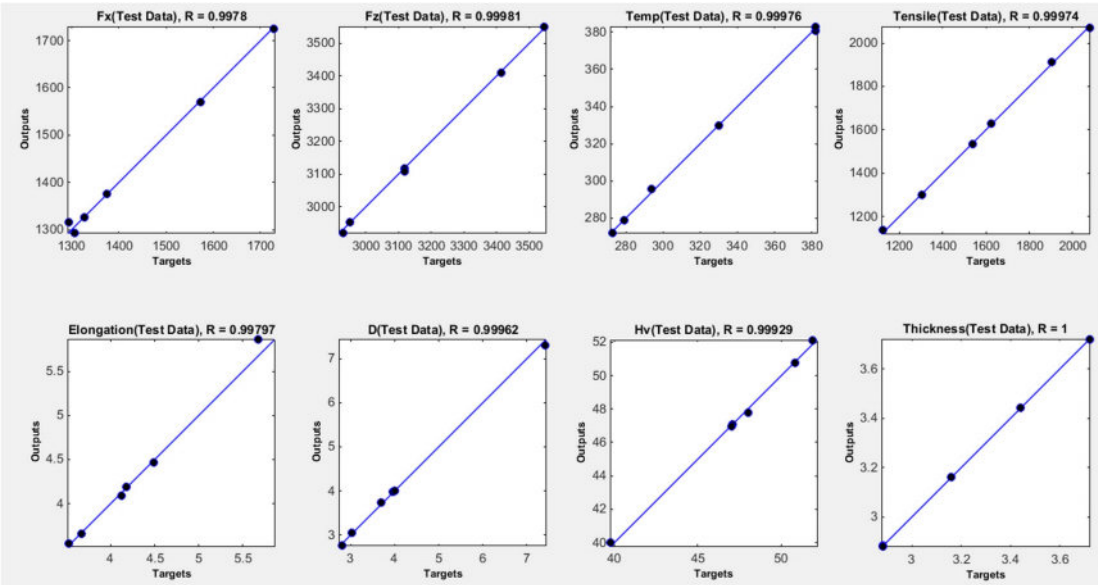

Figure 13. The performance of ANN with test data.

$$D_{CDRX} = C_1\, \varepsilon^{k} \dot{\varepsilon}^{j} D_0^{h} e^{-\left(\frac{Q}{RT}\right)} \tag{2}$$

where D_{CDRX} is the average grain size based on the continuous dynamic recrystallization phenomenon, ε is strain, $\dot{\varepsilon}$ is the strain rate, D_0 is the average initial grain size, Q is the activation energy of continuous recrystallization of the material in Jules, R is the constant of gases per joule per mole on Kelvin and T is the temperature in Kelvin, and the other parameters are material constants. As mentioned before, the heat generated in the work piece decreases with decreasing rotational speed compared to weld speed. In addition, the amount of strain and strain rate in the FSW region will decrease. With respect to relation (1.6), the grain size will be smaller by decreasing temperature, strain and strain rate. In this case, weld hardness will increase in accordance with the Hall-Patch relationship, and the elongation percentage will also decrease as it conflicts with the hardness. The square tool, due to the pulsed forces, mentioned result in finer grains compared to other tools, resulting in higher hardness and also shorter weld length. The optimal tool angle in these parameters is in its mid-range.

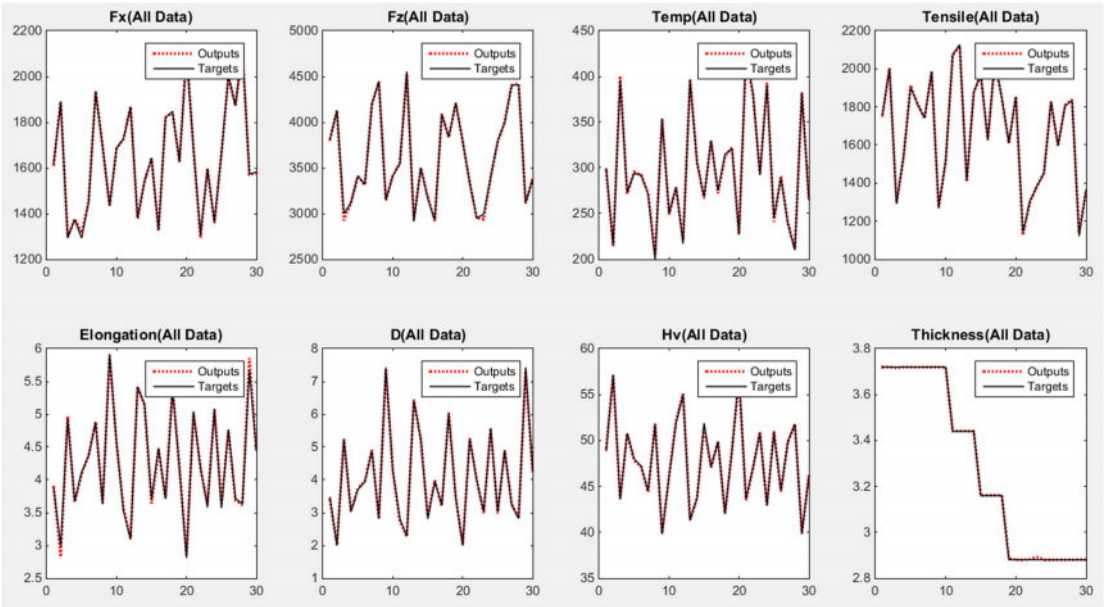

Figure 14. Comparison of ANN prediction with experimental values.

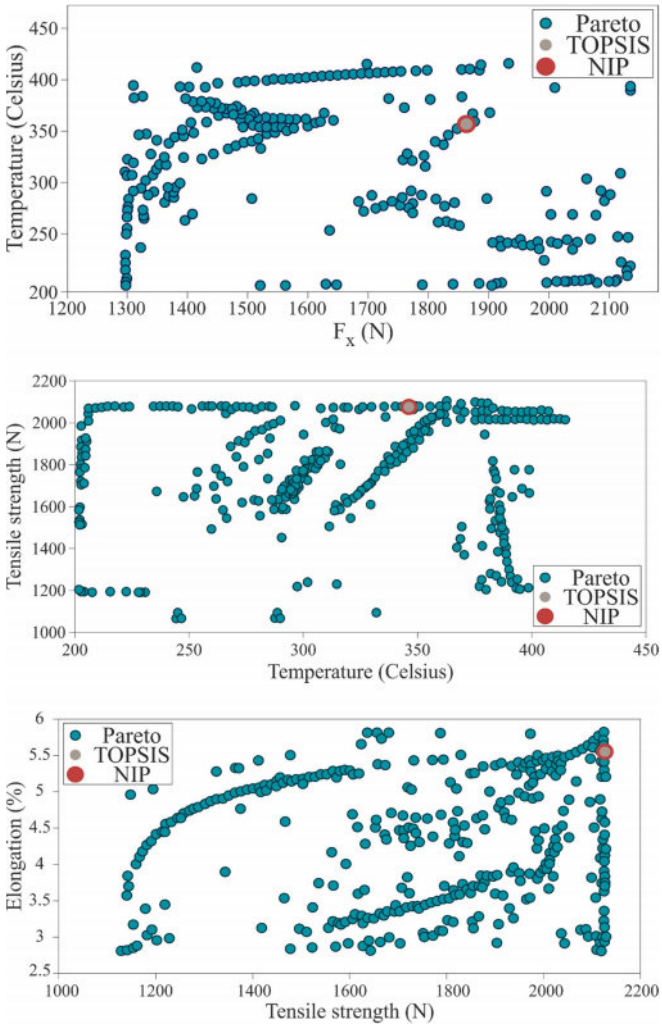

Figure 15. 8D Pareto plots on 2D planes (with pentagon profile) and the proposed points by NIP (red circle) and TOPSIS (blue circle).

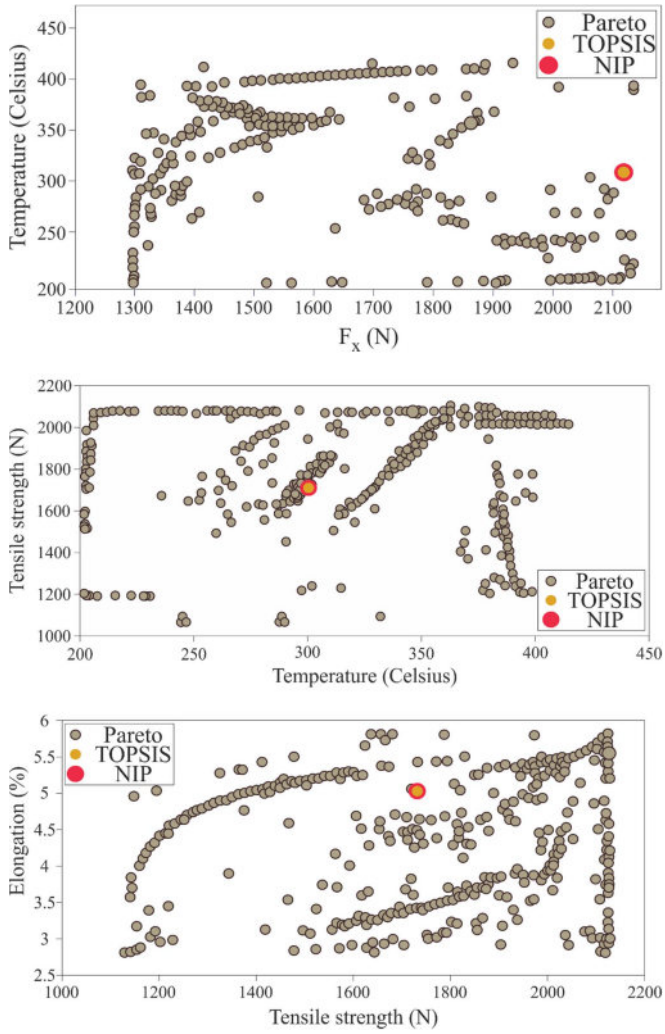

Figure 16. 8D Pareto plot on 2D planes (with circular profile) and points proposed by NIP (red circle) and TOPSIS (blue circle).

Table 8. Summary of the points proposed by NIP and TOPSIS and their respective inputs.

	Tool pin geometry	Square pin		Pentagon pin		Hexagonal pin		Circular pin	
	Method	NIP	TOPSIS	NIP	TOPSIS	NIP	TOPSIS	NIP	TOPSIS
Design variables	Tool angle (degree)	3.41	3.42	2.92	2.92	2.78	1.50	1.42	1.42
	Rotational speed (rpm)	876.34	881.49	970.89	970.89	974.89	411.27	930.38	930.38
	Weld speed (mm min^{-1})	21.43	21.60	44.76	44.76	45.93	121.84	33.05	33.05
Objective function	Horizontal force (N)	1477	1452	1854	1854	1482	2111	2100	2100
	Vertical force (N)	3339	3272	3032	3032	2913	4554	2913	2913
	Max. temperature (°C)	368	374	368	368	362	215	315	315
	Tensile strength (N)	1977	2035	2123	2123	2121	2126	1725	1725
	Elongation (%)	5.0	5.4	5.7	5.7	5.9	4.15	5.1	5.1
	Grain size at weld center (μm)	2.0	2.0	2.0	2.0	7.4	2.0	2.0	2.0
	Hardness at weld center (HV)	57.2	57.2	57.2	57.2	39.8	57.2	57.0	57.0
	Joint thickness (mm)	3.1	3.1	3.2	3.2	3.3	3.6	3.7	3.7

3.3. Artificial neural network training and test

Figures 12 and 13, show the desirable performance of the neural network for training and test data, respectively.

As shown, 24 sets of data are related to the training samples and 6 sets are related to neural network testing data. Additionally, the values predicted by the neural network, as well as the values obtained from practical

experiments and mechanical tests for all the train and test data (30 data sets) are presented in figure 14. As shown, the perceptron neural network designed in this research has been able to provide a very good performance.

3.4. Deterministic multi-objective optimization

After obtaining the eight-dimensional Pareto front, to visualize the results, there is no way other than mapping the Pareto front on two-dimensional planes. The Pareto optimization front on other two-dimensional planes were all studied. Then, NIP and TOPSIS approaches are employed to these optimal solutions, each one offering a solution as an optima.

Afterwards, among each of the square, pentagon, hexagon, and circular profiles, NIP and TOPSIS methods were employed for proposing optimum points. That way, for each tool profile, a proposed optimal point is presented. In figures 15 and 16, the proposed points for selected pentagon and circular profiles are specified, respectively.

The proposed optimum points of the NIP and TOPSIS methods are also indicated in the two-dimensional Pareto front planes. The corresponding values of output parameters for the square, pentagon, hexagonal, and circular profiles and their respective input values are given in table 8.

As shown in table 8, the multi-objective optimization procedure, which was aimed at minimizing horizontal force, vertical force and grain size, and maximizing the operating temperature, tensile strength, elongation, hardness and joint thickness, was performed with complete success. Results indicate that the optimization process can reach horizontal and vertical forces as low as 1452 N and 2913 N, respectively and a grain size as low as 2 μm. This results in hardness values of up to 57.2 and tensile strength, elongation and joint thickness of 2126 N, 5.9% and 3.7 mm, respectively. The maximum operating temperature can also reach a sufficiently high value of 374 °C which can provide adequate material flow.

4. Conclusion

In this study, horizontal and vertical forces applied to the tool during FSW process, temperature, tensile strength, grain size and elongation percentage were recorded. The influence of each input parameter on the outputs was studied. Then, for each of the output parameters, optimal values for the levels of all input parameters, including tool pin profile, tool angle, rotational speed and weld speed, were specified. Moreover, by increasing the ratio of rotation speed to weld speed, the amount of heat produced in the work piece will increase, and also the use of square and pentagon tool profiles leads to severely localized deformations in the work piece, and higher heat and less tool force.

Next, a perceptron artificial neural network was designed, trained and tested which has been able to provide a very good performance. Then, the eight-dimensional Pareto front was obtained and visualized on two-dimensional planes. Finally, NIP and TOPSIS approaches were employed to these optimal solutions, and for each of the square, pentagon, hexagon, and circular profiles, NIP and TOPSIS methods proposed optimum points. The multi-objective optimization procedure which was aimed at minimizing horizontal force, vertical force and grain size, and maximizing the operating temperature, tensile strength, elongation, hardness and joint thickness was performed with complete success.

Results indicate that the optimization process can reach horizontal and vertical forces as low as 1452 N and 2913 N, respectively and a grain size as low as 2 μm. This resulted in hardness values of up to 57.2 and tensile strength, elongation and joint thickness of 2126 N, 5.9% and 3.7 mm, respectively. The maximum operating temperature can also reach a sufficiently high value of 374 °C which can provide adequate material flow.

ORCID iDs

Abolfazl Khalkhali https://orcid.org/0000-0003-1179-1963
Salman Ebrahimi-Nejad https://orcid.org/0000-0002-1591-023X
Nima Geran Malek https://orcid.org/0000-0003-3725-738X

References

[1] Thomas W M, Nicholas E D, Needham J C, Murch M G, Temple-Smith P and Dawes C J 1995 Friction welding *Google Patents*
[2] Dawes C and Thomas W 1995 Friction stir joining of aluminium alloys *TWI Bulletin* **6** 1
[3] Vijayan S, Raju R and Rao S R K 2010 Multiobjective optimization of friction stir welding process parameters on aluminum alloy AA 5083 using taguchi-based grey relation analysis *Mater. Manuf. Process.* **25** 1206–12
[4] Suresha C, Rajaprakash B and Upadhya S 2011 A study of the effect of tool pin profiles on tensile strength of welded joints produced using friction stir welding process *Mater. Manuf. Process.* **26** 1111–6

[5] Cox C D, Gibson B T, Strauss A M and Cook G E 2012 Effect of pin length and rotation rate on the tensile strength of a friction stir spot-welded al alloy: a contribution to automated production *Mater. Manuf. Process.* **27** 472–8
[6] Ganesh P and Kumar V S 2015 Superplastic forming of friction stir welded AA6061-T6 alloy sheet with various tool rotation speed *Mater. Manuf. Process.* **30** 1080–9
[7] Montazerolghaem H, Badrossamay M, Tehrani A F, Rad S Z and Esfahani M S 2015 Dual-rotation speed friction stir welding: experimentation and modeling *Mater. Manuf. Process.* **30** 1109–14
[8] Yang Q, Li X, Chen K and Shi Y 2011 Effect of tool geometry and process condition on static strength of a magnesium friction stir lap linear weld *Materials Science and Engineering:* A **528** 2463–78
[9] Yuan W, Mishra R, Carlson B, Verma R and Mishra R 2012 Material flow and microstructural evolution during friction stir spot welding of AZ31 magnesium alloy *Materials Science and Engineering:* A **543** 200–9
[10] Forcellese A, Gabrielli F and Simoncini M 2012 Mechanical properties and microstructure of joints in AZ31 thin sheets obtained by friction stir welding using 'pin' and 'pinless' tool configurations *Mater. Des.* **34** 219–29
[11] Ni D, Chen D, Yang J and Ma Z 2014 Low cycle fatigue properties of friction stir welded joints of a semi-solid processed AZ91D magnesium alloy *Mater. Des.* **56** 1–8
[12] Kumar A and Raju L S 2012 Influence of tool pin profiles on friction stir welding of copper *Mater. Manuf. Process.* **27** 1414–8
[13] Barekatain H, Kazeminezhad M and Kokabi A 2014 Microstructure and mechanical properties in dissimilar butt friction stir welding of severely plastic deformed aluminum AA 1050 and commercially pure copper sheets *Journal of Materials Science & Technology* **30** 826–34
[14] Firouzdor V and Kou S 2012 Al-to-Cu friction stir lap welding *Metallurgical and Materials Transactions* A **43** 303–15
[15] Tan C, Jiang Z, Li L, Chen Y and Chen X 2013 Microstructural evolution and mechanical properties of dissimilar Al–Cu joints produced by friction stir welding *Mater. Des.* **51** 466–73
[16] Kuang B *et al* 2015 The dissimilar friction stir lap welding of 1A99 Al to pure Cu using Zn as filler metal with 'pinless' tool configuration *Mater. Des.* **68** 54–62
[17] Liu X, Lan S and Ni J 2014 Analysis of process parameters effects on friction stir welding of dissimilar aluminum alloy to advanced high strength steel *Mater. Des.* **59** 50–62
[18] Husain M M, Sarkar R, Pal T, Prabhu N and Ghosh M 2015 Friction stir welding of steel: heat input, microstructure, and mechanical property co-relation *J. Mater. Eng. Perform.* **24** 3673–83
[19] Tingey C, Galloway A, Toumpis A and Cater S 2015 Effect of tool centreline deviation on the mechanical properties of friction stir welded DH36 steel *Mater. Des.* (1980-2015) **65** 896–906
[20] Simões F and Rodrigues D 2014 Material flow and thermo-mechanical conditions during friction stir welding of polymers: literature review, experimental results and empirical analysis *Mater. Des.* **59** 344–51
[21] Huang Y *et al* 2017 Friction stir welding/processing of polymers and polymer matrix composites *Composites Part A: Applied Science and Manufacturing* **105** 235–57
[22] Okuyucu H, Kurt A and Arcaklioglu E 2007 Artificial neural network application to the friction stir welding of aluminum plates *Mater. Des.* **28** 78–84
[23] Fratini L, Buffa G and Palmeri D 2009 Using a neural network for predicting the average grain size in friction stir welding processes *Computers & Structures* **87** 1166–74
[24] Tansel I N, Demetgul M, Okuyucu H and Yapici A 2010 Optimizations of friction stir welding of aluminum alloy by using genetically optimized neural network *The International Journal of Advanced Manufacturing Technology* **48** 95–101
[25] Shojaeefard M H, Behnagh R A, Akbari M, Givi M K B and Farhani F 2013 Modelling and Pareto optimization of mechanical properties of friction stir welded AA7075/AA5083 butt joints using neural network and particle swarm algorithm *Mater. Des.* **44** 190–8
[26] Shojaeefard M H, Akbari M and Asadi P 2014 Multi objective optimization of friction stir welding parameters using FEM and neural network *International journal of precision engineering and manufacturing* **15** 2351–6
[27] Ghetiya N and Patel K 2014 Prediction of tensile strength in friction stir welded aluminium alloy using artificial neural network *Procedia Technology.* **14** 274–81
[28] Dehabadi V M, Ghorbanpour S and Azimi G 2016 Application of artificial neural network to predict Vickers microhardness of AA6061 friction stir welded sheets *Journal of Central South University* **23** 2146–55
[29] Khalkhali A, Sarmadi M and Sarikhani E 2017 Investigation on the best process criteria for lap joint friction stir welding of AA1100 aluminum alloy via Taguchi technique and ANOVA *Proceedings of the Institution of Mechanical Engineers, Part E: Journal of Process Mechanical Engineering* **231** 329–42
[30] Akbari M, Khalkhali A, Keshavarz S M E and Sarikhani E 2016 The effect of in-process cooling conditions on temperature, force, wear resistance, microstructural, and mechanical properties of friction stir processed A356 *Proc. of the Institution of Mechanical Engineers, Part L: Journal of Materials: Design and Applications* **232** 429–37
[31] Akbari M, Khalkhali A, Keshavarz S M E and Sarikhani E 2015 Investigation of the effect of friction stir processing parameters on temperature and forces of Al–Si aluminum alloys *Proceedings of the Institution of Mechanical Engineers, Part L: Journal of Materials: Design and Applications* **232** 213–29

Acta Mech
https://doi.org/10.1007/s00707-020-02648-0

ORIGINAL PAPER

A. Kaveh · A. Dadras Eslamlou · N. Geran Malek · R. Ansari

An open-source computational framework for optimization of laminated composite plates

Received: 24 July 2019 / Revised: 29 January 2020
© Springer-Verlag GmbH Austria, part of Springer Nature 2020

Abstract In the present paper, a flexible framework is developed for the optimization of composite laminate plates. In this framework, an optimization algorithm is employed to find the optimal stacking sequence design of the FE models by interfacing the Abaqus solver with MATLAB through a Python script. The Python script submits dimension, orientation, and diameter of the cutout combinations to Abaqus/CAE. The performance of the codes is validated by applying them to several problems of previous research. Three distinct types of boundary conditions, namely CCCC, SCSC, and SSSS, with different geometries comprising a square and rectangular plates with and without cutouts, are considered as optimal design problems. Besides that, analyses are performed on new symmetrical composites with 16 and 80 plies. The framework is equipped with the GA for optimizing the fiber orientations and maximizing the buckling capacities. The results are comprehensively discussed, showing a reasonable agreement with the literature. This code can easily be used by scientists and industry professionals as an automated tool for optimizing different finite element models and using any arbitrary optimization algorithm.

1 Introduction

Owing to the wide range of applications that fiber-reinforced composite structures have in different industries, and due to their diverse range of design variables, attentions to improving the performance of these structures have been increased greatly [1–5]. Several studies have been conducted in the context of optimization of laminated composites based on an analytical formulation as the objective function, most of which were adopted GA as the optimization algorithm [6,7] and others attempted and showed improved applicability of their proposed algorithms. As an instance, the efficiency of the generalized pattern search algorithm (GPSA) over the genetic algorithm (GA) was discussed by Karakaya and Soykasap [8] for the problem of symmetric simply supported 64 graphite/epoxy plies laminated composite under biaxial buckling loads. The Tabu search algorithm, fractal branch and bound, simulated annealing, and scatter search algorithm were adopted by Pai et al. [9], Matsuzaki and Todoroki [10], Erdal and Sonmez [11], and Rao and Arvind [12], respectively. de Almeida [13] focused on the behavior of the harmony search algorithm and considered the stacking sequence optimization as the case study. Abachizadeh and Tahani [14] adopted the Ant Colony Optimization (ACO) algorithm for the problem of the minimum cost and optimal fundamental frequency of symmetric hybrid composite panels. Additionally, a similar optimization strategy was employed by Sebaey et al. [15] in the case of dispersed orientations for the stacking design.

A. Kaveh (✉) · A. Dadras Eslamlou · N. Geran Malek
School of Civil Engineering, Iran University of Science and Technology, Tehran, Iran
E-mail: alikaveh@iust.ac.ir

R. Ansari
Department of Mechanical Engineering, University of Guilan, Rasht, Iran

For composite plates including two, three, four, and ten layers, Ho-Huu et al. [16] have proposed a modified form of the differential evolution (DE) algorithm in which an elitist selection technique, as well as an adaptive mutation mechanism, take the places of the selection and mutation phases of the DE. Having introduced some adjustments on the memory of the Harmony Search (HS) algorithm, de Almeida [17] compared the performance of the modified HS algorithm with some other metaheuristic algorithms and reported the equal or better performance of the algorithm in the design of laminated composites. Similarly, using simulated annealing (SA) as a mechanism for local search in the particle swarm optimization (PSO) algorithm, Javidrad et al. [18] reported an improvement in the convergence behavior of PSO by defining the fiber orientation angle and layer thickness as discrete variables.

The literature review on buckling load capacity maximization studies shows that many researchers have attempted to design the optimal stacking orientation of plies by solving the governing closed-form equation of laminated composite structures having simplified geometries and boundary conditions appropriate for analytical approaches through metaheuristic optimization algorithms. However, very few researchers have worked on the design of laminated composite plates using an optimization algorithm equipped with FE software capable of dealing with structures having nonlinearity in geometry, or with various types of boundary conditions besides dimensions. In this regard, Marouene et al. [19] designed and optimized composite panels with constant curvature fiber paths under uniaxial compressive buckling load using a Python script and a MATLAB routine. Ouinas and Achour [20] have determined the effect of ply orientation, notch geometry, plate rigidity ratio, and plate thickness on the buckling load of 8-layer $[(\theta/-\theta)]$ square laminated composite plates having an elliptical notch. They pointed out that the optimum buckling loads belong to the smallest values of the geometric defect ratio. Lately, the golden section method equipped with the Abaqus FE package only at the bounds, that is, every 10° increment in the angle θ, has been carried out by Hu and Chen [21] in order to study the effect of the cutout size end, boundary condition, shell length, shell thickness, and shell radius ratio of truncated laminated conical shells under hydrostatic compression. Recently, Shrivastava et al. [22] attempted minimization of torsion box weight using GA. Their study was followed by another article [23] incorporating PD design aspect in order to further improvement in the procedure. Kazemzadeh Azad and Akiş [24] utilized the big bang–big crunch optimizer for automated material selection and thickness optimization of pressurized composite tubes. They minimized the cost and weight of multilayer tube structures only with internal pressure. Recently, they proceeded to investigate the shrink-fitting effect under both external and internal pressure [25]. It was observed that in the cases with a higher ratio of internal pressure to external pressure, considering shrink-fitting can be advantageous.

In our preceding studies, the optimum design of composite structures was investigated in the analytical scheme firstly by using a novel population-based algorithm, the so-called biogeography-based optimization (BBO) [26], and secondly, by implementing four tuning-free parameter-less optimization algorithms [27]. Moreover, a robust design scheme capable of withstanding uncertain loading conditions in the case of hybrid laminates was introduced [28]. As a continuation of the previous studies, the current article employed the finite element method (FEM) to find the optimum orientations for the plies of laminated composites with more complex geometries and boundary conditions by interfacing the Abaqus solver with MATLAB through a Python script-based framework.

This article introduces and makes use of a Python-based framework for the optimal design of laminated composites under buckling loads. Three distinct types of boundary conditions CCCC, SCSC, and SSSS, as well as geometries, namely rectangular, square with cutout, and rectangular with cutout, are considered for the laminated composite.

Primarily, numerical analysis using the finite element method and FE design framework, including the Python script and optimization algorithm implemented in MATLAB, are briefly addressed. By implementing buckling analysis in the Abaqus FE package, the buckling loads of the laminated composites are calculated as the objective function for the optimization algorithm [29]. In this study, the influences of boundary condition, plate aspect ratio, cutout dimension, and layup orientation, in particular, on the maximized buckling load capacity of laminated composite plates are demonstrated. Through implementing a Python script [30] framework, not only can one straightforwardly interface Abaqus with an optimization algorithm, but also they could tailor the dimensions, boundary conditions, and particularly fiber orientations. One of the main advantages of the current FE Python script-based framework over the analytical procedure is that the applied loads could be changed openly to any other type of load cases, that is prescribed for thermal loading, pressures, concentrated forces, and displacements, to name but a few. Since the gradient-based methods are limited to be employed for solving problems with differentiable objective functions and continuous design variables, in stacking sequence design, the metaheuristic algorithms are far preferable [31,32]. It should be mentioned that because of the GA's

popularity, it is chosen as the optimization algorithm. However, the versatile framework is designed in such a way that any other algorithm can be simply replaced with GA. The codes of some efficient algorithms are given in [33].

The remainder of the paper is organized into five sections, as follows. In Sect. 2, numerical simulation of the FE model, as well as the assigned boundary conditions, are provided. Section 3 represents the FEM design framework. This section includes a summary of the fundamental blocks of the Python script code, a brief review of GA as a typical, replaceable optimization algorithm, and MATLAB/Python interface. Section 4 is devoted to showing the suitability of the proposed framework through employing it on laminated composites having a central circular cutout, with various boundary conditions, and dimensions. Finally, some concluding remarks are pointed out in Sect. 5.

2 Numerical analysis using the finite element method

In the current section, various aspects of the laminated composite numerical model followed by the boundary conditions assigned to the FE model are discussed.

2.1 Laminated composite model

Using the commercial software Abaqus, 3D deformable FE models are designed [29]. Analyses have been executed on FE models utilizing "S4R" elements (a four-node doubly curved thin or thick shell, reduced integration, hourglass control, finite membrane strains), in which each node allows six translationsal and rotationsal degrees of freedom ($u_x, u_y, u_z, R_x, R_y, R_z$). In order to simulate the laminated composite, constraint equations are applied to all nodes on the right and top edges. These constraints employ equal displacements in the X- and Y-direction, respectively. The loading is applied in the X-direction and in the form of the "Shell edge load." To import the proposed layup orientations, a routine for calling the Python script along with the optimization algorithm is implemented in MATLAB. The constant value of 0.125 mm is considered as ply thickness. Besides, the nominal load in an eigenvalue analysis is applied to the linear perturbation process. Furthermore, buckling load prediction is performed by evaluating the eigenvalues in the analysis step and multiplying them by the applied loading. In the buckling analysis, the obtained eigenvalue provides the reserve factor for the imposed loads on the structure (Fig. 1).

2.2 Boundary condition

In this section, the values reported by Hu and Lin [34] are used to verify the results of the current framework. The buckling mode shapes along with the critical buckling load (in direction x) ($N_{x,\mathrm{CR}}$) for three typical geometries, which are also reported in Fig. 3 of reference [34], are considered for the verification level. It should be mentioned that, in this reference, the design variables were narrowed down to one ply orientation,

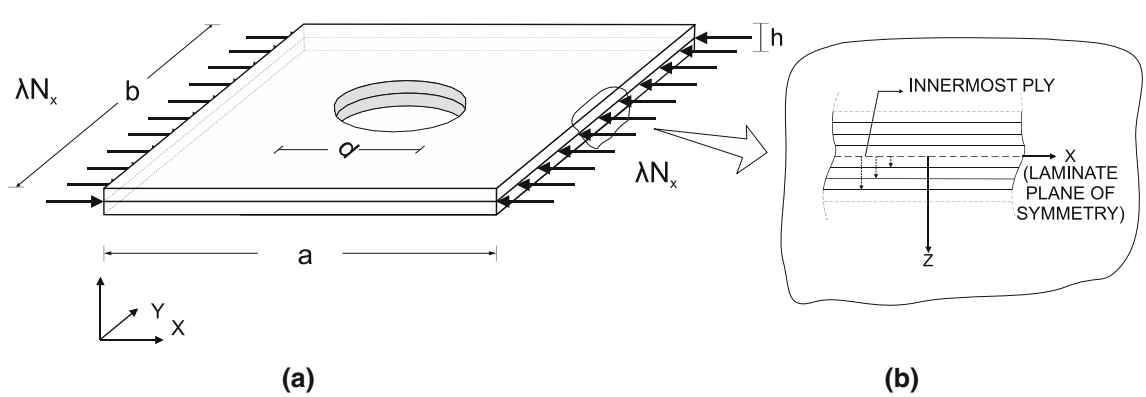

Fig. 1 Configuration of the laminated composite plates: **a** uniaxially compressed laminated composite having a central circular hole along with coordinate system and dimensions, **b** laminate plane of symmetry

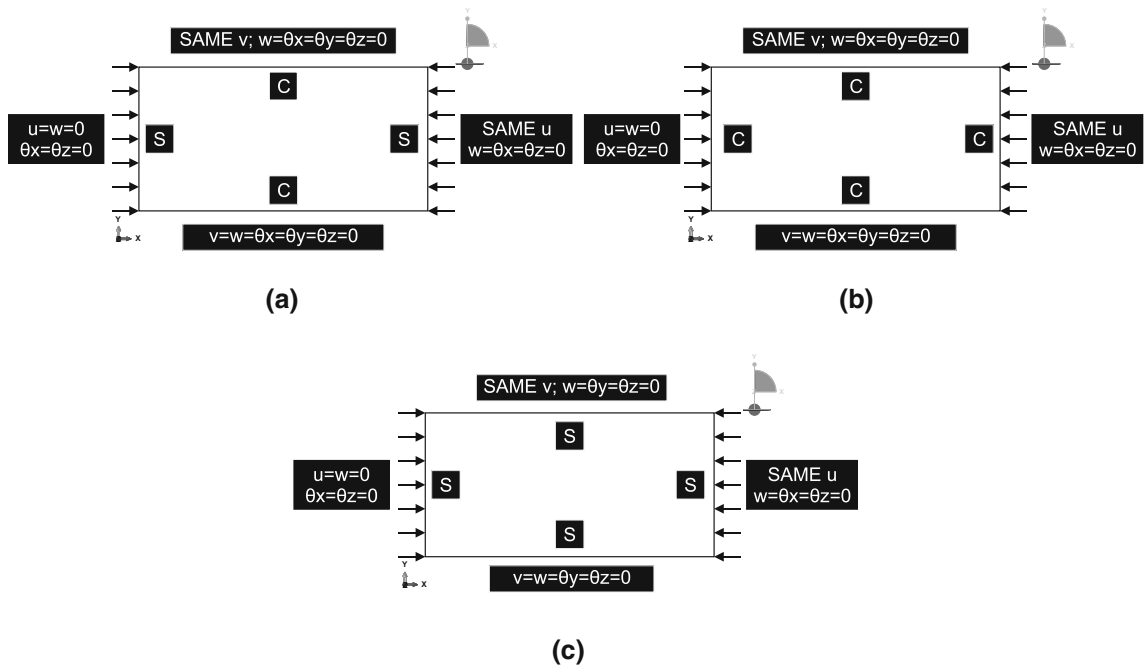

Fig. 2 The boundary condition of rectangular composite plate FE model: **a** laminate with two fix end and two simply supported conditions (SCSC), **b** laminate with four fixed boundary conditions (CCCC), and **c** laminate with four simply supported conditions (SSSS)

however, in the present study four number of design variables are taken into account which also benefits the meeting of manufacturing limitations (i.e., $\pm 45, 90_2, 0_2$). The properties issued in Table 3 are taken as mechanical properties. The FE models are applied to the boundary conditions shown in Fig. 2.

For the present optimization, buckling predictions have been executed using Abaqus/CAE, through which the Lancoz linear eigensolver is used for obtaining the critical buckling mode.

3 FEM design framework

In the present section, the MATLAB/Python interface framework, as well as the Python script's fundamental blocks, are outlined, and the utilized optimization algorithm is reviewed after that. Here, GA is applied to the problem under study as the most commonly used, well-known metaheuristic method. From the framework execution view, this method could be replaced to meet the researchers' needs. The complete codes of the framework with helpful comments are given in the online Appendix and can easily be utilized by the readers.

3.1 Python script

The main task in this study is the combination of the optimization algorithm implemented in MATLAB and the script written in the Python programming language. Throughout the optimization process, the algorithm produces a set of designs to be evaluated by FE analyses.

To shed light on the steps of the Python script, a summary of the fundamental blocks of the code along with their main applications are presented in Table 1. First, the Python script launches the FE solver and then reads the ODB file outputs, and retransfers the results into the algorithm. As depicted by the MATLAB/Python interface of Fig. 3, the Python script acts as a solver for the MATLAB parameters for every analysis of the objective function. In lines 1–12, all the simulation steps, including creating the model, applying loads, creating steps, employing boundary conditions, defining interactions, and meshing the instances, are written inside the Python code, as illustrated by the Python script block of Fig. 3. In line 10, the proposed GA solutions in MATLAB are introduced into Abaqus/CAE. Next, for FE buckling analysis, line number 13 submits the models' job. After waiting for the tob to be completed, the results are written in an ODB file as shown by the output block of

Table 1 Main blocks of the Python script code

1.	*from Abaqus import **	*# Provide access to the Abaqus objects as well as the model's database*
2.	*myModel = mdb.Model(name = 'laminatedPlate')*	*# Create model*
3.	*s = mdb.models['Model-%d'%(jj+1)].ConstrainedSketch(name='__profile__',sheetSize=2)* *g, v, d, c =s.geometry, s.vertices, s.dimensions, s.constraints* *s.sketchOptions.setValues(decimalPlaces=3)* *s.setPrimaryObject(option=STANDALONE)* *s.rectangle(point1=(0.0, 0.0), point2= (a, b))*	*# Create sketch*
4.	*p = mdb.models['laminatedPlate'].Part(name='Part-1',dimensionality=THREE_D,type=DEFORMABLE_BODY)*	*# Create the deformable, three-dimensional part.*
5.	*mdb.models['laminatedPlate'].Material(name='Material_%d'%(l+1))* *mdb.models['laminatedPlate'].materials['Material_%d'%(l+1)].Elastic(type=LAMINA, table=((1.28e+11, 1.1e+10, 0.25, 4.48e+9, 4.48e+9, 1.53e+9),)) #GPa*	*# Import material*
6.	*mdb.models['laminatedPlate'].BuckleStep(name='Buckle', previous='Initial', numEigen=5, vectors=10)* *mdb.models['laminatedPlate'].steps['Buckle'].setValues(maxIterations=10000)*	*# Import step (Buckling)*
7.	*s2.CircleByCenterPerimeter(center=(a/2, b/2), point1=((a/2)+r, 0.05))* *del mdb.models['Model-1'].sketches['__edit__']*	*# Create cutout*
8.	*a.setMeshControls(regions=pickedRegions, elemShape=QUAD, algorithm=MEDIAL_AXIS)* *a = mdb.models['Model-1'].rootAssembly* *partInstances =(a.instances['Part-1-1'],)* *a.generateMesh(regions=partInstances)*	*# Assign mesh controls*
9.	*# Top edge* *a.seedEdgeByNumber(edges=pickedEdges, number=NUM, constraint=FINER)*	*# Meshing (seeding the four edges)*
10.	*for i in range(len(propOrientation)):* *compositeLayup.CompositePly(suppressed=False, plyName='Ply- %d'%(i+1),* *region=region1, material='Material_%d'%(counter+1), thicknessType=SPECIFY_THICKNESS, thickness=0.125E-3, orientationType=SPECIFY_ORIENT, orientationValue= propOrientation[i], additionalRotationType=ROTATION_NONE, additionalRotationField='',* *axis=AXIS_3, angle=0.0, numIntPoints=3)*	*# Composite layup*
11.	*# Right edge* *mdb.models['Model-1'].DisplacementBC(name='BC-%d'%(j), createStepName='Initial', region=region, u1=UNSET, u2=UNSET, u3=0.0, ur1=0, ur2=0, ur3=0, amplitude=UNSET, distributionType=UNIFORM, fieldName='', localCsys=None)*	*# Create boundary condition*
12.	*# Right edge* *mdb.models['Model-1'].ShellEdgeLoad(name='loadBCRight-%d'%(j+1), createStepName=' Buckle', region=region, magnitude=1, distributionType=UNIFORM, field='', localCsys=None)*	*# Import load*
13.	*mdb.jobs['Job-%d'%(jj+1+nFiles)].submit (consistencyChecking =OFF)* *mdb.jobs['Job-%d'%(jj+1+nFiles)].waitForCompletion()*	*# Create and submit the job*
14.	*o3 = session.openOdb('name = .../laminatedPlate.odb')*	*# Start result session*
15.	*odb = session.odbs['.../laminatedPlate.odb']* *a1=odbAccess.openOdb('Job-%d.odb'%(j))*	*# opening the result file and reading the outputs*
16.	*mdb.save(), sys.exit()*	*# Saving and exiting*

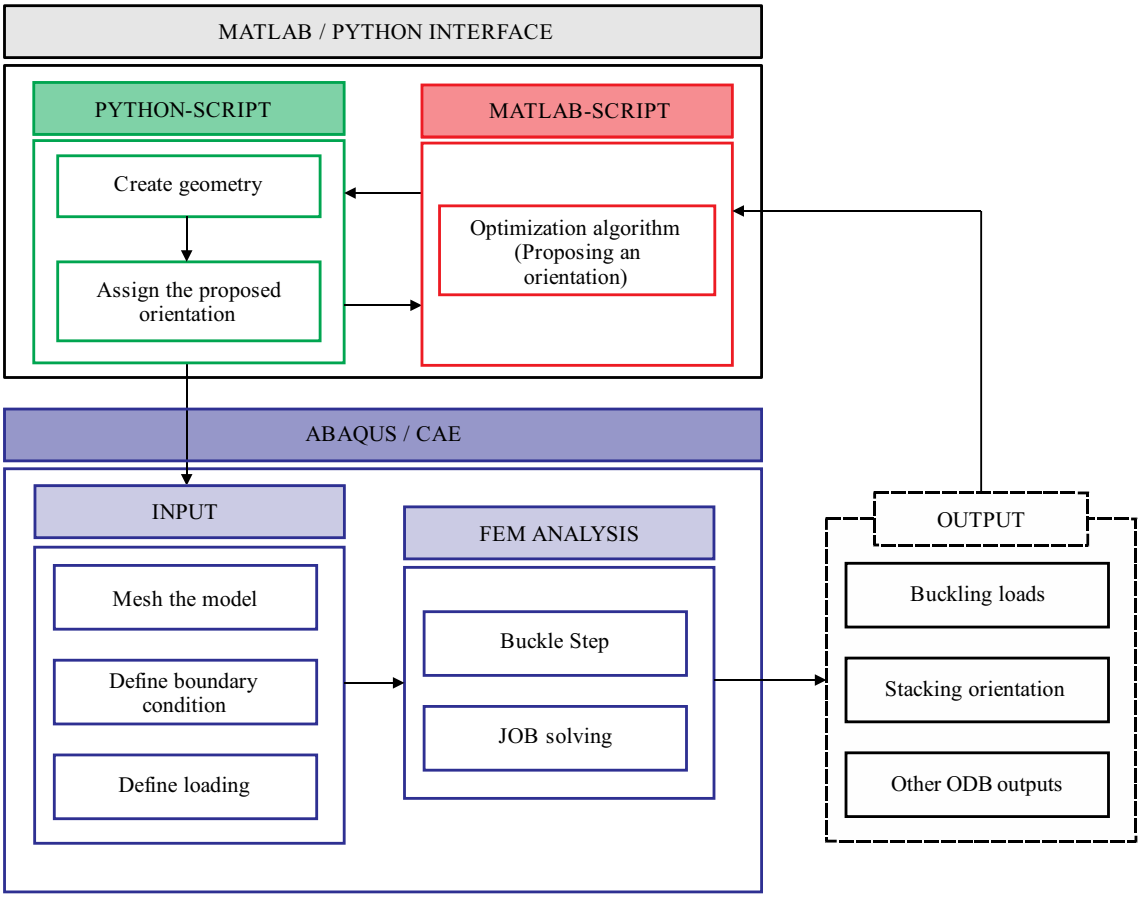

Fig. 3 Flowchart of the finite element Python script-based framework

Fig. 3. Then, all models, along with their outputs produced by the Abaqus Solver, are stored in a folder with the same name as the model number (see Abaqus/CAE block of Fig. 3). After a given number of iterations, in each of these folders, a TXT file containing the optimal fiber angles and the maximum buckling load capacity is created automatically. Afterward, MATLAB reads the fitness values from the output files. This process will continue until the optimization algorithm terminates, as demonstrated by the cyclic arrow diagram of Fig. 3.

3.2 Optimization algorithm

The classical genetic algorithm (GA) is the most common metaheuristic method that is employed for finding the best stacking sequences of the FE models [35–37]. Derived from the theory of Darwin, classical GA is developed by Holland [38]. It mimics the survival of fittest biological individuals. Parent selection, survivor selection, crossover, and mutation are the main genetic operators [39,40]. The major aim of the GA is finding a solution (i.e., child) that has been produced by the preceding solutions (i.e., parents) applying selection mechanisms as well as genetic operators. Genetic algorithms, in general, are categorized as being either continuous (real) or integer (binary). In the current study, regarding the optimization problem, the integer GA is employed, and its steps are outlined in the following [41]. As shown in Fig. 4a, there are seven general steps to take in the execution process of GA: initialization, evaluation, selection, crossover, mutation, elitism, and termination.

In the initialization step, the first generation of chromosomes is initialized randomly. As depicted in Fig. 4b, it should be defined that each chromosome acts as a solution consisting of design variables called genes. Additionally, each design variable comprises a set of binary digits called genomes. Subsequently, in the evaluation phase, the Abaqus FE Package is employed to determine the fitness value of the solutions. This step is performed through interfacing the MATLAB environment with the Python script, as described in Sect. 3.1.

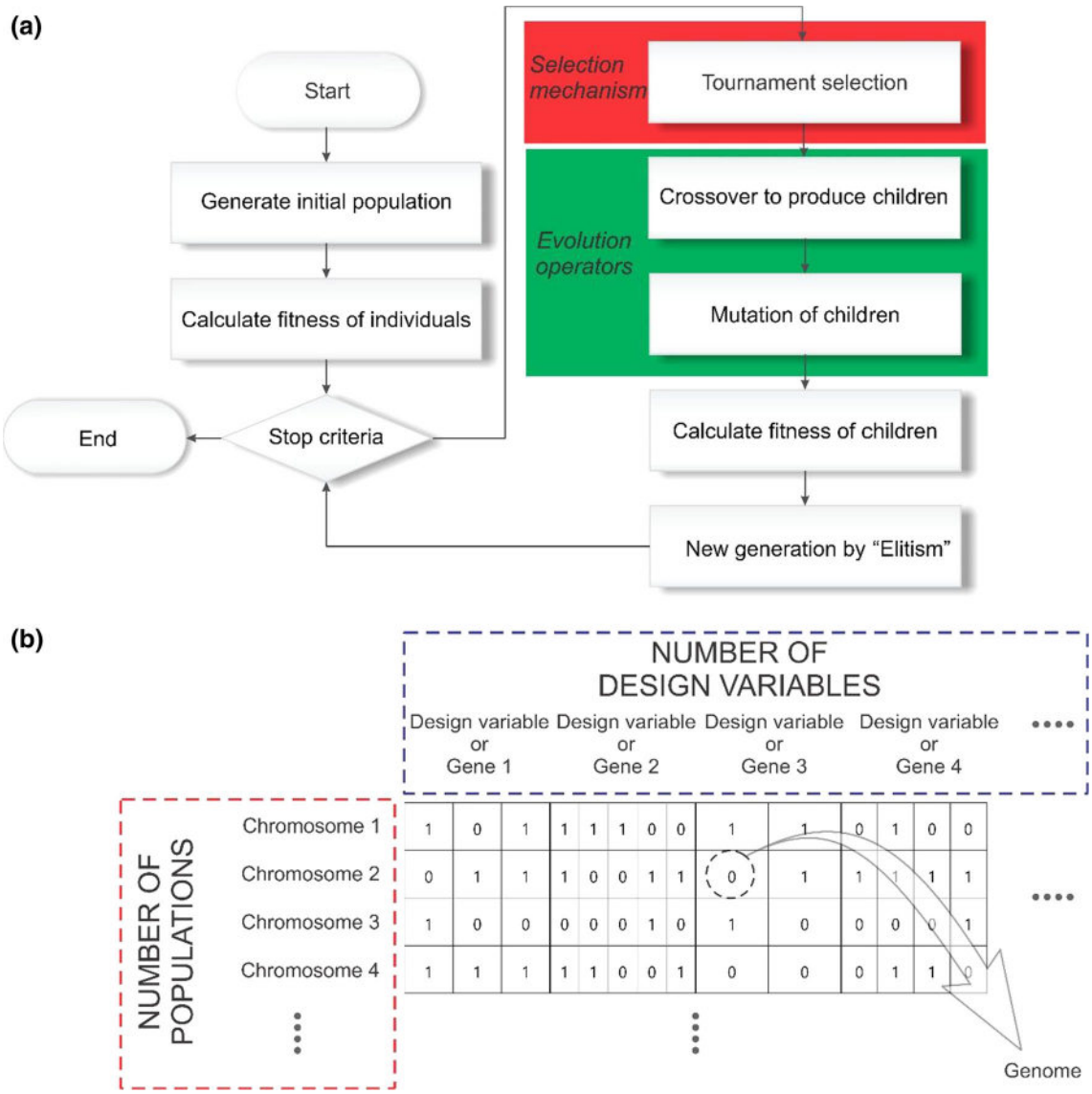

Fig. 4 Classical GA algorithm: **a** flowchart of seven primary steps must take in the execution process **b** the structure of the populations [28]

In order to select the parents of the next generation, tournament selection is utilized. Tournament selection is a method where the champions of head-to-head competitions are determined for the following generation [42,43]. Subsequently, in the crossover evolution operation, two children are reproduced from each of the selected parents. For this purpose, 80% of the populations are made using uniform random, two-points, and one-point crossover operators. Besides, 20% of the populations are being mutated in the mutation step, which mimics a similar mutation in biology to keep the diversity. (The reference to the internal controlling parameters of the GA.) Also, only one of the chromosomes is being subjected to the mutation operation. Then, for the following generation, specific numbers of leading chromosomes, equal to the predefined number of population (*nPop)*, are taken into account. Finally, the algorithm terminates the repetition of the above steps when the number of function evaluations reaches the given stopping number.

Table 2 Buckling load capacity N_x and stacking design of 64-ply rectangular laminated plates with SSSS as the boundary condition

Case	N_x	N_y	a (m)	b (m)	Stacking design		Buckling load (λ)	
					Kaveh et al. [26], Karakaya and Soykasap [8]	Present	Kaveh et al. [26], Karakaya and Soykasap [8]	Present
1	1	1	0.508	0.254	$[90_{10}, \pm 45, 90_2, \pm 45_7, 90_2, \pm 45]_s$	$[90_{10}, \pm 45, 90_2, \pm 45_7, 90_2, \pm 45]_s$	695,781	685,955
2	1	0.5	0.508	0.508	$[\pm 45_{16}]_s$	$[\pm 45_{16}]_s$	323,764	323,081
3	1	2	0.508	0.254	$[90_{16}, \pm 45, 90_6, \pm 45, 90_2, \pm 45, 90_2]_s$	$[90_{16}, \pm 45, 90_6, \pm 45, 90_2, \pm 45, 90_2]_s$	412,985	406,788
4	1	2	0.508	1.016	$[0_4, \pm 45_3, 0_2, \pm 45, 0_2, \pm 45_4, 0_8]_s$	$[0_4, \pm 45_3, 0_2, \pm 45, 0_2, \pm 45_4, 0_8]_s$	132,243	133,793

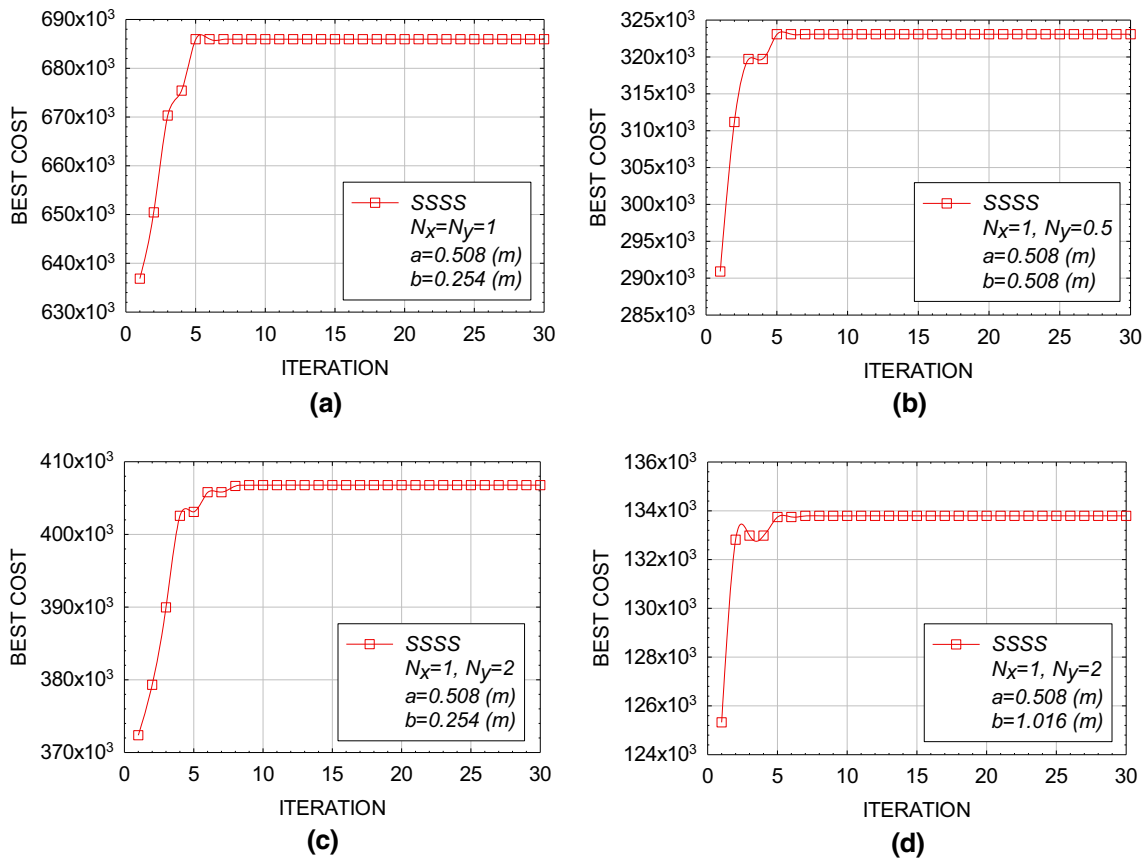

Fig. 5 Convergence diagrams of validation load cases

4 Verification of the framework

The present section aims to validate the application of the framework. Table 2 verifies the current FE approach by reporting the optimum values of buckling resistance along with their associated fiber orientations. The obtained results are compared with the matching values attempted by Kaveh et al. [26] and Karakaya and Soykasap [8] for four different load cases and plate aspect ratios. The mechanical properties can be found in the referred articles. It appears that the FE numerical results have a good match with the analytical approach. The differences possibly originate from neglecting D_{16} and D_{26} from the formulations of the previous works [8,26].

In Table 2, N_x and N_y represent in-plane compressive loads along the x- and y-axis, respectively. A convergence study for these cases is conducted through 30 iterations considering 50 populations and is given in Fig. 5. As can be seen from the curves, these analyses have converged after about 10 iterations. The first mode shapes, as well as the buckling load capacity of the optimized FE models at the last iteration of the algorithm, are also shown in Fig. 6.

5 Numerical results and discussion

Three different categories for the geometry of the laminated composites are examined to further validate the applicability of the current framework. Rectangular and square laminated plates having a central circular cutout and rectangular plates without central circular cutout are considered in that regard and illustrated in Figs. 7a–c, respectively. As shown in these figures, the plates have various circular cutouts and aspect ratios. For the rectangular cases demonstrated in Figs. 7a and c, with constant width $b = 10\,\text{cm}$, the plates' aspect ratio a/b varies between 1 and 4. On the other hand, for the square laminated plates, the size of the cutout, i.e., the ratio d/b, changes from 0.1 to 0.8. Besides these geometric variables, various boundary conditions, as well

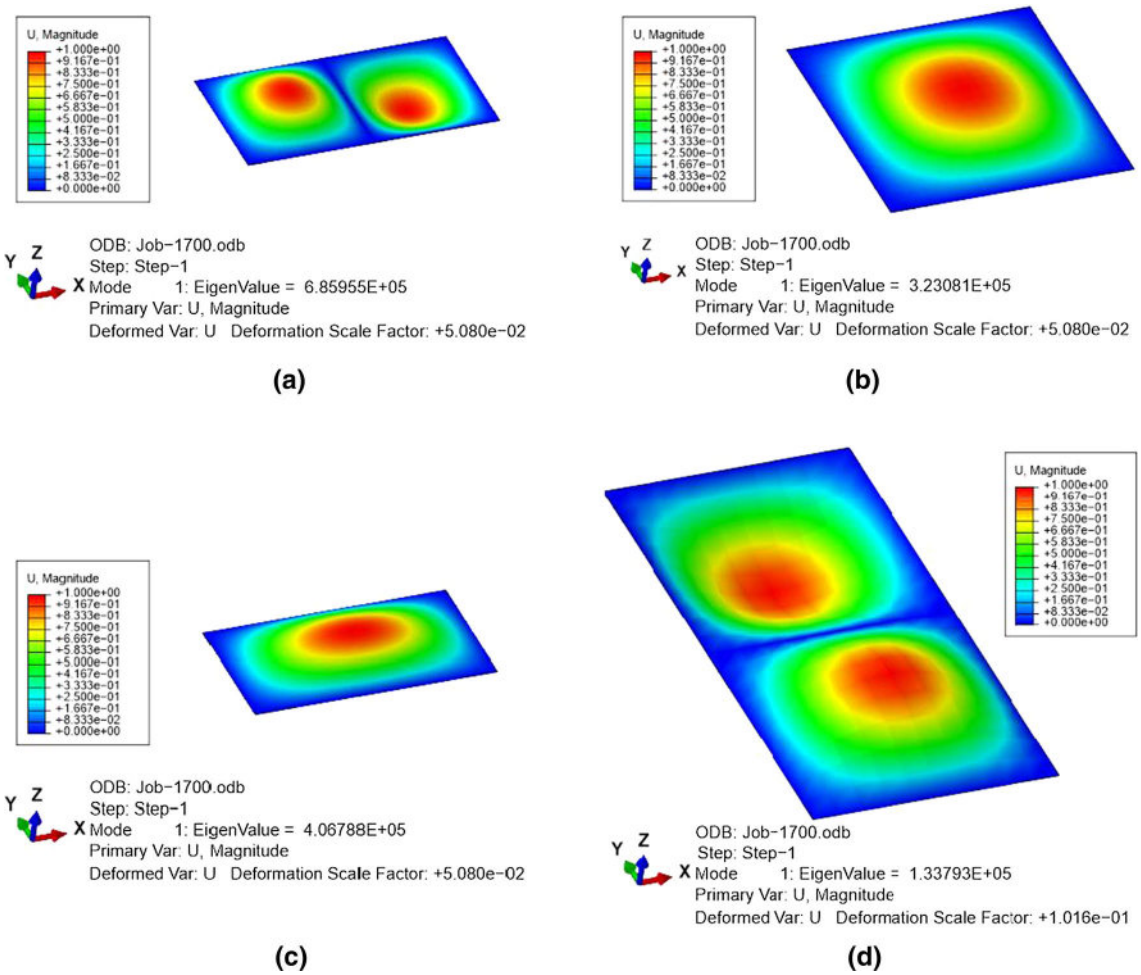

Fig. 6 The first mode shape and the buckling load capacity of the optimized FE models

Table 3 Graphite/epoxy lamina properties (Hu and Lin [34])

Property	Hercules AS/3501-6
E_{11}	128 GPa
E_{22}	11 GPa
G_{12}, G_{13}	4.48 GPa
G_{23}	1.53 GPa
Poisson rate, ν_{12}	0.25
Ply thickness	0.125 (mm)

as plate thickness, which exert a special effect on the optimum buckling resistance and fiber orientations, are also included. In order to study how the solutions are affected by the plate thickness, a symmetric 16-ply-thin plate, as well as an 80-ply-thick plate, are incorporated in the current analysis. Here, each variable can take ± 45, 90_2, or 0_2 as the orientations of fibers. The material constitutive properties of lamina graphite/epoxy (Hercules AS/3501-6), given in Table 3, are introduced into all FE models.

The section also discusses the effect of various boundary conditions and aspect ratios of the composite laminated plates on the optimum design of buckling load factor and fiber orientations.

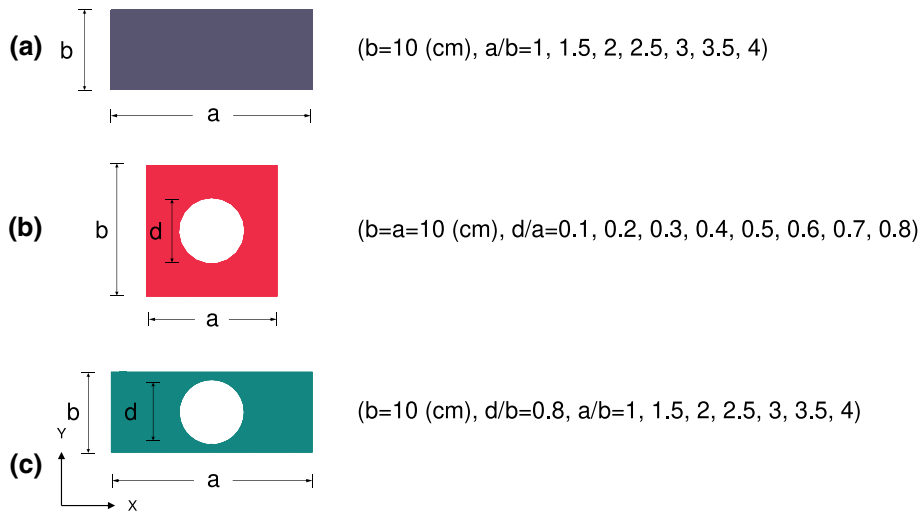

Fig. 7 Various aspect ratios and dimensions considered for the uniaxial compressed composite plates: **a** rectangular laminated plates, **b** square laminated plates having a central circular hole, and **c** rectangular laminated plates having a central circular hole

5.1 Rectangular laminated plates

In this section, buckling optimization under different types of boundary conditions is assessed on rectangular laminated plates with various plate aspect ratios. As shown in Fig. 7a, with constant width b, the plates' aspect ratio a/b varies from 1 to 4.

5.1.1 Finite element verification

The current section confirms the validity of the numerical simulation with the results from Hu and Lin [34]. In Fig. 8a, the critical buckling load of a typical rectangular laminated panel is verified numerically. The plate has SCSC as the boundary condition with the aspect ratio of a/b= 2, moreover, $[\pm 40, 90, 0]_{2s}$ is considered as the stacking layup, in which the subscript "s" and in general terms "ns", denotes n-symmetric lamination. As an example, $[0, \pm 45]_{2s}$ represents the $0, +45, -45, -45, +45, 0, 0, +45, -45, -45, +45, 0$ layup. Then, the obtained buckling load is compared with that obtained in the reference, which is equal to 2.41 kN/cm. As listed in Fig. 8a, the obtained value has an absolute agreement with the reported result. Figure 8b shows the convergence effect of mesh size on the buckling load factor. The predicted load factor with different mesh resolutions is compared with the verified FE result, in Fig. 8b. 300, 800, 1200, 1500, and 1800 are the numbers of $S4R$ elements in the models. These results show almost equal values obtained by both fine and coarse meshing condition.

5.1.2 Buckling load capacity maximization of 16-ply rectangular composite laminated plates

In this section, in order to study the buckling behavior of rectangular laminates with constant width $b = 10$ cm, various lengths for a/b between 1 and 4 are considered. Three types of boundary conditions are taken into account: four edges clamped denoted by CCCC, four edges simply supported indicated by SSSS, and two edges fixed-two edges simply supported denoted by SCSC. These boundary conditions are intended to provide the structure with in-plane displacements u as well as v, yet preventing out of plane translation. Besides, two equations on the right and top edges of the plates are defined in order to enforce equal displacements of all nodes on those edges toward the horizontal and vertical directions, respectively. The constant value of 0.125 mm is considered as ply thickness.

Even though the common genetic algorithm is selected for the optimization, the whole algorithm is functionalized in such a way that the optimization part could be replaced with every other class of algorithms.

Optimal buckling loads $N_{x,\mathrm{CR}}$ are obtained from conducting FEM optimization 16-ply rectangular composite plate aspect ratios a/b, separately. These buckling loads reached by an optimization procedure and their associated fiber stacking configurations are presented in Tables 4 and 5. It should be pointed out from the

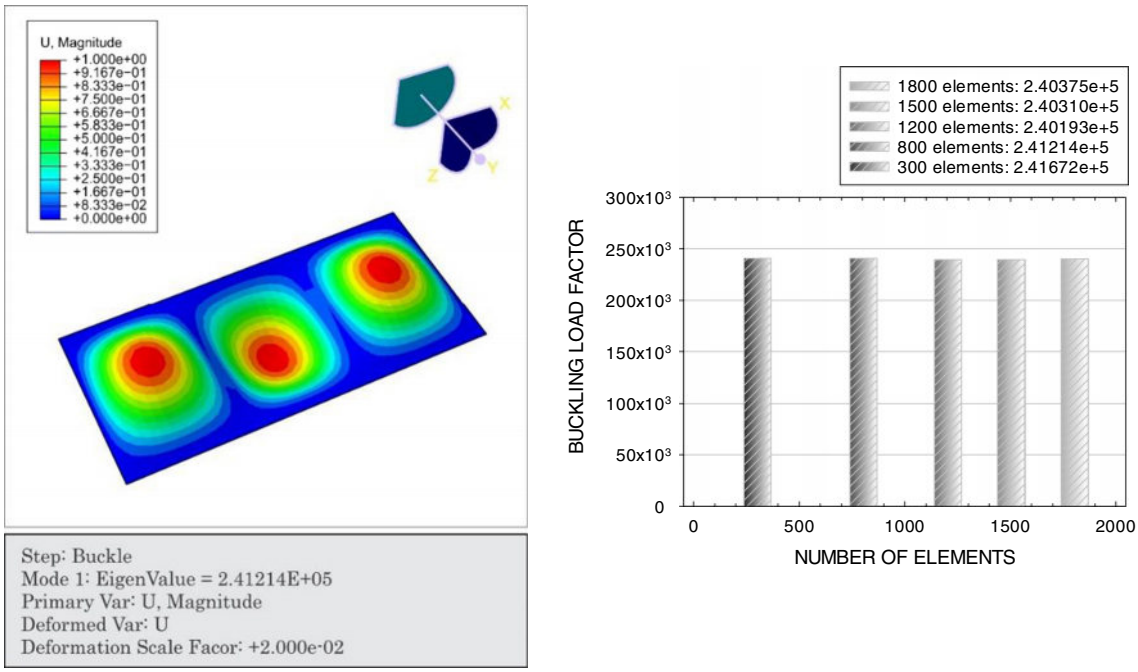

Fig. 8 Critical buckling loads of SCSC rectangular laminated panel: **a** buckling load factor for ($a/b = 2$), $N_{x,\mathrm{CR}} = 2.41214\mathrm{E}+05$ kN/cm (Hu and Lin [34]: 2.41 kN/cm), **b** the comparison of predicted buckling load factor from different meshes with the verified FE result

Table 4 Buckling load capacity N_x of 16-ply rectangular laminated plates

a/b	Boundary condition		
	SCSC	SSSS	CCCC
1	2.80625	1.782	3.74864
1.5	2.63542	1.85316	3.12087
2	2.57132	1.7782	2.81556
2.5	2.56286	1.79146	2.7006
3	2.56724	1.77704	2.65648
3.5	2.56852	1.78876	2.61849
4	2.57065	1.77646	2.61299

Table 5 Designed orientations of 16-ply rectangular laminated plates

a/b	Boundary condition		
	SCSC	SSSS	CCCC
1	$[45, -45, 45, -45, 0, 0, 0, 0]_S$	$[45, -45, 45, -45, 45, -45, 45, -45]_S$	$[0, 0, 0, 0, 0, 0, 0, 0]_S$
1.5	$[45, -45, 45, -45, 45, -45, 90, 90]_S$	$[45, -45, 45, -45, 45, -45, 0, 0]_S$	$[45, -45, 0, 0, 0, 0, 0, 0]_S$
2	$[45, -45, 45, -45, 45, -45, 90, 90]_S$	$[45, -45, 45, -45, 45, -45, 45, -45]_S$	$[45, -45, 45, -45, 0, 0, 0, 0]_S$
2.5	$[45, -45, 45, -45, 45, -45, 90, 90]_S$	$[45, -45, 45, -45, 45, -45, 90, 90]_S$	$[45, -45, 45, -45, 45, -45, 90, 90]_S$
3	$[45, -45, 45, -45, 45, -45, 90, 90]_S$	$[45, -45, 45, -45, 45, -45, 45, -45]_S$	$[45, -45, 45, -45, 45, -45, 90, 90]_S$
3.5	$[45, -45, 45, -45, 45, -45, 45, -45]_S$	$[45, -45, 45, -45, 45, -45, 45, -45]_S$	$[45, -45, 45, -45, 45, -45, 45, -45]_S$
4	$[45, -45, 45, -45, 45, -45, 90, 90]_S$	$[45, -45, 45, -45, 45, -45, 45, -45]_S$	$[45, -45, 45, -45, 45, -45, 90, 90]_S$

optimal fiber orientations of Table 5 that the composite laminates with SCSC and SSSS boundary conditions show less insensitivity to a/b concerning the corresponding laminated plates with CCCC boundary conditions. For the optimum buckling loads presented in Fig. 9, as the aspect ratio decreases, especially for $a/b < 2.5$, the impact of the boundary conditions becomes more effective. At the higher values of a/b, the difference in

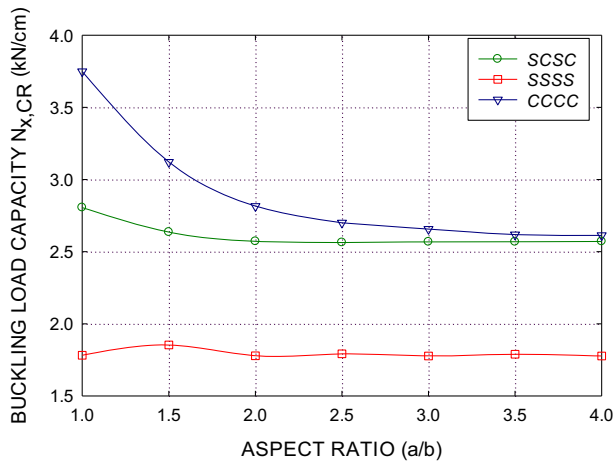

Fig. 9 Maximized buckling load capacity of 16-ply rectangular laminated plates

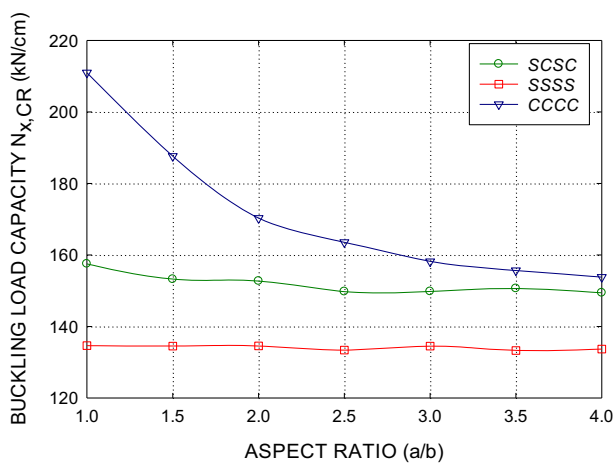

Fig. 10 Maximized buckling load capacity of 80-ply rectangular laminated plates

optimum buckling loads decreases and approaches a constant value; in the same way, it occurs for stacking orientations. Figure 9 shows that the rectangular plates having CCCC boundary conditions exhibit the highest optimal buckling loads, while with the consistent orientations, the rectangular plates with SSSS boundary conditions show the lowest values.

5.1.3 Buckling load capacity maximization of 80-ply rectangular composite laminated plates

Similar to the previous section for 16-ply composite laminates, the optimizations for 80-ply panels are presented in Fig. 10, the values of which are listed in Table 6, and the corresponding fiber stacking designs are reported in Table 7. It is observed from Fig. 10 that the optimal fiber angle for composite laminates with SSSS boundary condition is not highly sensitive to a/b. In general, at lower aspect ratio values the change in optimal buckling loads is more significant than larger ones, and at higher values, the buckling loads tend to become gradually constant. By drawing a comparison between Figs. 9 and 10, it is observed that as the thickness increases, the optimum buckling loads of the rectangular composite plates increases, whereby the great effect of transverse shear deformation on the optimum stacking orientations is represented [34].

5.2 Square laminated plate having a central circular hole

In Sects. 5.2.1 and 5.2.2, buckling performance optimization under different types of boundary conditions is evaluated on square laminated plates, including various cutout dimensions. As illustrated in Fig. 7b, in square

Table 6 Buckling load capacity N_x of 80-ply rectangular laminated plates

a/b	Boundary condition		
	SCSC	SSSS	CCCC
1	157.5	134.63	210.988
1.5	153.206	134.513	187.639
2	152.71	134.552	170.297
2.5	149.731	133.373	163.546
3	149.772	134.51	158.163
3.5	150.621	133.281	155.631
4	149.412	133.665	153.796

Table 7 Designed orientations of 80-ply rectangular laminated plates

a/b	Boundary condition		
	SCSC	*SSSS*	*CCCC*
1	$[45, -45, 45, -45, 0, 0, 0, 0]_{5s}$	$[45, -45, 0, 0, 45, -45, 45, -45]_{5s}$	$[0, 0, 0, 0, 0, 0, 45, -45]_{5s}$
1.5	$[0, 0, 0, 0, 45, -45, 0, 0]_{5s}$	$[0, 0, 45, -45, 45, -45, 45, -45]_{5s}$	$[0, 0, 0, 0, 45, -45, 0, 0]_{5s}$
2	$[0, 0, 0, 0, 45, -45, 45, -45]_{5s}$	$[0, 0, 45, -45, 45, -45, 45, -45]_{5s}$	$[0, 0, 0, 0, 45, -45, 0, 0]_{5s}$
2.5	$[45, -45, 0, 0, 45, -45, 0, 0]_{5s}$	$[0, 0, 45, -45, 45, -45, 45, -45]_{5s}$	$[45, -45, 0, 0, 0, 0, 0, 0]_{5s}$
3	$[0, 0, 45, -45, 0, 0, 45, -45]_{5s}$	$[0, 0, 45, -45, 45, -45, 45, -45]_{5s}$	$[45, -45, 0, 0, 0, 0, 0, 0]_{5s}$
3.5	$[45, -45, 0, 0, 0, 0, 45, -45]_{5s}$	$[0, 0, 45, -45, 45, -45, 45, -45]_{5s}$	$[45, -45, 0, 0, 0, 0, 0, 0]_{5s}$
4	$[0, 0, 45, -45, 0, 0, 45, -45]_{5s}$	$[0, 0, 45, -45, 45, -45, 45, -45]_{5s}$	$[0, 0, 45, -45, 0, 0, 45, -45]_{5s}$

laminated plates, the size of the cutout, i.e., the ratio d/b changes from 0.1 to 0.8. Analogously, a symmetric 16-ply-thin plate, as well as an 80-ply-thick plate are considered in the current analysis in order to study how the buckling results depend on the plate thickness. Similar to the case of a rectangular plate, three types of boundary conditions, CCCC, SCSC, and SSSS, are considered for this analysis.

5.2.1 Finite element verification

The critical buckling load of a typical square laminated panel having a central circular cutout is verified numerically in Fig. 11a. The plate has SCSC as the boundary condition, $[\pm 40, 90, 0]_{2s}$ as the stacking layup, and a cutout size $d/b = 0.5$. The result is compared with the value obtained in [34], which was reported to be 3.36 kN/cm. As shown in Fig. 11a, the value for the composite plate matches with the reported result. Figure 11b is represented as the effect of mesh size on the buckling load factor. In Fig. 11b, the predicted buckling load factor with different mesh resolutions is compared with the verified FE result. 102, 136, 188, 220, and 287 $S4R$ elements were in the models. The results show a slight difference in the values obtained by the fine and the coarse meshing condition. For compatibility of the results, the size of elements is fixed according to [34].

5.2.2 Buckling load capacity maximization of 16-ply square composite laminated plates

In the current section, for constant length $a = 10$ cm, various diameters for cutouts d between 1 and 8 cm are taken into consideration. Buckling loads $N_{x,\mathrm{CR}}$ are optimized after conducting FEM optimization for each of the aspect ratios d/b of the 16-ply square composite plates, separately. These results are presented in Fig. 12 for the associated d/a, the values of which are given in Table 8 and the associated fiber stacking designs are given in Table 9. It should be pointed out from Table 9 that, the optimum fiber angles of hole-possessed square composite laminates with SSSS boundary conditions are less sensitive to d/a compared to the other two types of boundary conditions. According to the optimum fiber orientations reported for the case of square plates having SSSS boundary conditions, these plates show the highest sensitivity for the other two cases. At larger d/a ratios, $[45, -45, 45, -45, 0, 0, 0, 0]_s$ can be considered as the optimal fiber orientations of a plate with SSSS boundary condition. In addition, at smaller d/a ratios, $[0, 0, 0, 0, 0, 0, 0, 0]_s$ can be presumed as the optimal fiber orientations of the square plates with CCCC boundary condition. It can be observed in Fig. 12 that as the size of the cutout increases, the optimum buckling load increases for all the boundary conditions. Figure 12 reveals an upward-trend phenomenon for the behavior of optimal buckling loads against introducing

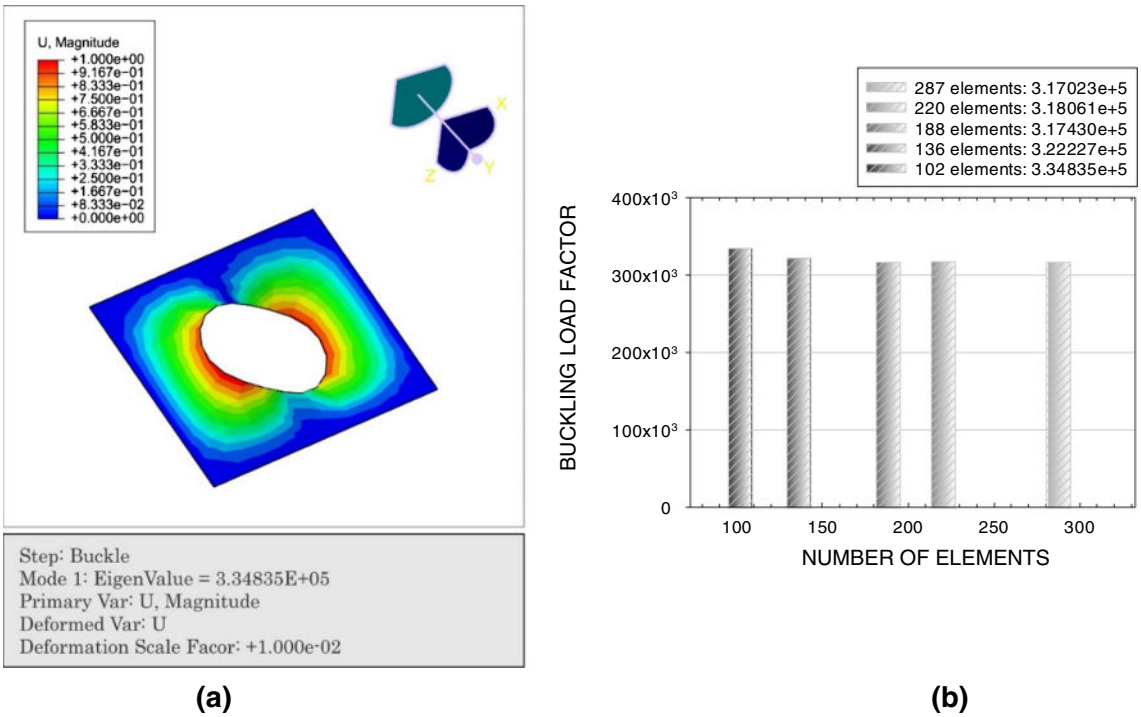

Fig. 11 Critical buckling loads of SCSC square laminated panel having central circular cutout: **a** buckling load factor of square plate with ($d/b = 0.5$), $N_{x,\mathrm{CR}} = 3.34835\mathrm{E}+05$ kN/cm (Hu and Lin [34]: 3.36 kN/cm), **b** comparison of predicted buckling load factor from different meshes with the verified FE result

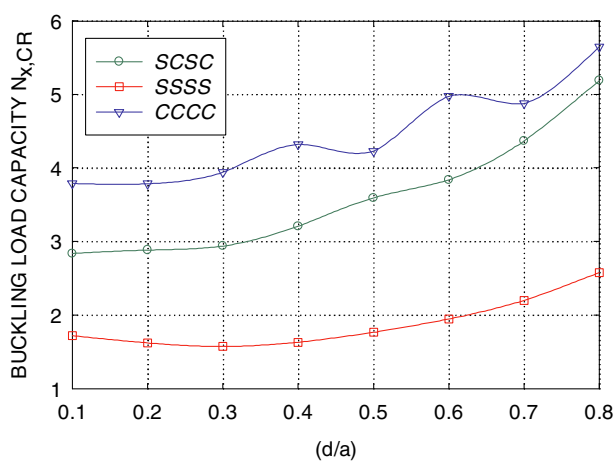

Fig. 12 Maximized buckling load capacity of the 16-ply square laminated plates having a central circular hole

holes, which is utterly different from one's perception, namely reduction in the optimal buckling loads by cutting a hole in a plate. This phenomenon is in accordance with the results reported in [34]. The increase in the optimal buckling loads of plates with SSSS boundary condition has occurred after a slight decrease in $d/a = 0.1$ to 0.3.

5.2.3 Buckling load capacity maximization of 80*-ply square composite laminated plates*

Similar to Sect. 5.2.2, the studies for 80-ply laminae are carried out. Afterward, these results versus associated aspect ratios are given in Fig. 13 and listed in Tables 10 and 11. It can be observed that for a given d/a ratio, similar to the previous case, CCCC, SCSC, and SSSS have the highest capacity of the buckling load, respectively. In addition, as the size of the cutout increases, particularly for $d/a > 0.6$, the difference in

Table 8 Buckling load capacity N_x of 16-ply square laminated plates having a central circular hole

d/a	Boundary condition		
	SCSC	SSSS	CCCC
0.1	2.83558	1.71903	3.78793
0.2	2.88144	1.62008	3.78404
0.3	2.93646	1.57108	3.93866
0.4	3.20619	1.62881	4.32177
0.5	3.58985	1.76294	4.22736
0.6	3.8364	1.94495	4.97361
0.7	4.36632	2.19814	4.87444
0.8	5.18611	2.57688	5.64467

Table 9 Configurations of 16-ply square laminated plates having a central circular hole

d/a	Boundary condition		
	SCSC	SSSS	CCCC
0.1	$[45, -45, 45, -45, 0, 0, 90, 90]_s$	$[45, -45, 45, -45, 45, -45, 0, 0]_s$	$[0, 0, 0, 0, 0, 0, 0, 0]_s$
0.2	$[90, 90, 0, 0, 0, 0, 0, 0]_s$	$[45, -45, 45, -45, 45, -45, 0, 0]_s$	$[0, 0, 0, 0, 0, 0, 0, 0]_s$
0.3	$[45, -45, 90, 90, 0, 0, 0, 0]_s$	$[45, -45, 45, -45, 0, 0, 0, 0]_s$	$[0, 0, 0, 0, 0, 0, 0, 0]_s$
0.4	$[45, -45, 45, -45, 0, 0, 0, 0]_s$	$[45, -45, 45, -45, 0, 0, 0, 0]_s$	$[0, 0, 90, 90, 0, 0, 0, 0]_s$
0.5	$[45, -45, 0, 0, 0, 0, 0, 0]_s$	$[45, -45, 45, -45, 0, 0, 0, 0]_s$	$[0, 0, 0, 0, 90, 90, 0, 0]_s$
0.6	$[90, 90, 0, 0, 0, 0, 0, 0]_s$	$[45, -45, 45, -45, 0, 0, 0, 0]_s$	$[0, 0, 90, 90, 0, 0, 0, 0]_s$
0.7	$[45, -45, 0, 0, 0, 0, 0, 0]_s$	$[45, -45, 45, -45, 0, 0, 0, 0]_s$	$[0, 0, 90, 90, 90, 90, 0, 0]_s$
0.8	$[90, 90, 0, 0, 0, 0, 0, 0]_s$	$[45, -45, 45, -45, 0, 0, 0, 0]_s$	$[0, 0, 90, 90, 0, 0, 0, 0]_s$

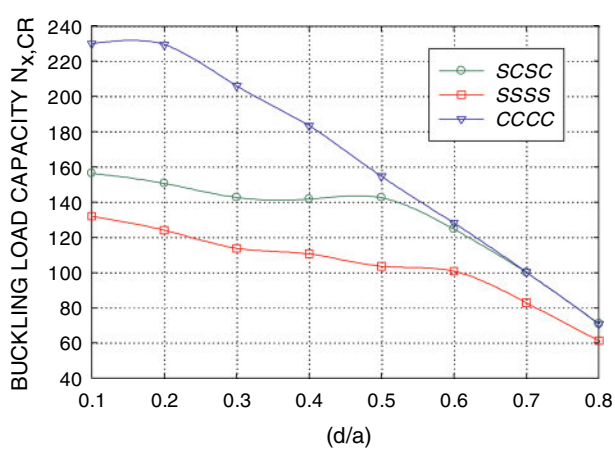

Fig. 13 Maximized buckling load capacity of the 80-ply square laminated plates having a central circular hole

optimum buckling loads disappears gradually. Besides, the optimum buckling loads of the square composite plates decline, irrespective of the type of boundary conditions. A comparison between Figs. 12 and 13 shows that as the thickness increases, the optimum buckling load of square composite plates with cutout increases.

5.3 Rectangular laminated plate having central a circular hole

The buckling performance optimization under different types of boundary conditions is analyzed in the following sections on rectangular laminated plates having a cutout and considering various plate aspect ratios. At constant width b, the plates' aspect ratio a/b varies between 1 and 4, as depicted in Fig. 7c.

Table 10 Buckling load capacity N_x of 80-ply square laminated plates having a central circular hole

d/a	Boundary condition		
	SCSC	SSSS	CCCC
0.1	156.252	131.9	229.933
0.2	150.589	124.051	229.4
0.3	142.599	113.728	206.015
0.4	141.699	110.585	183.429
0.5	142.483	103.541	154.543
0.6	124.661	100.804	128.104
0.7	100.024	82.8591	100.22
0.8	70.8262	61.28670	70.8498

Table 11 Designed orientations of 80-ply square laminated plates having a central circular hole

d/a	Boundary condition		
	SCSC	*SSSS*	*CCCC*
0.1	$[45, -45, 45, -45, 0, 0, 0, 0]_{5s}$	$[45, -45, 0, 0, 45, -45, 45, -45]_{5s}$	$[0, 0, 0, 0, 0, 0, 0, 0]_{5s}$
0.2	$[90, 90, 0, 0, 0, 0, 0, 0]_{5s}$	$[0, 0, 45, -45, 45, -45, 45, -45]_{5s}$	$[0, 0, 0, 0, 0, 0, 0, 0]_{5s}$
0.3	$[0, 0, 45, -45, 0, 0, 0, 0]_{5s}$	$[45, -45, 45, -45, 0, 0, 0, 0]_{5s}$	$[0, 0, 0, 0, 0, 0, 0, 0]_{5s}$
0.4	$[0, 0, 0, 0, 0, 0, 45, -45]_{5s}$	$[0, 0, 45, -45, 0, 0, 45, -45]_{5s}$	$[0, 0, 0, 0, 0, 0, 0, 0]_{5s}$
0.5	$[0, 0, 0, 0, 0, 0, 0, 0]_{5s}$	$[0, 0, 45, -45, 0, 0, 45, -45]_{5s}$	$[0, 0, 0, 0, 0, 0, 0, 0]_{5s}$
0.6	$[0, 0, 0, 0, 0, 0, 0, 0]_{5s}$	$[0, 0, 0, 0, 45, -45, 0, 0]_{5s}$	$[0, 0, 0, 0, 0, 0, 0, 0]_{5s}$
0.7	$[0, 0, 0, 0, 0, 0, 0, 0]_{5s}$	$[0, 0, 0, 0, 0, 0, 45, -45]_{5s}$	$[0, 0, 0, 0, 0, 0, 0, 0]_{5s}$
0.8	$[0, 0, 0, 0, 0, 0, 0, 0]_{5s}$	$[0, 0, 0, 0, 0, 0, 45, -45]_{5s}$	$[0, 0, 0, 0, 0, 0, 0, 0]_{5s}$

5.3.1 Finite element verification

In Fig. 14a, the critical buckling load of a typical rectangular laminated panel having a central circular cutout is verified. The plate has SCSC as the boundary condition, cutout size with $d/b = 0.8$, and an aspect ratio of $a/b = 2$; moreover, $[\pm 40, 90, 0]_{2s}$ is considered as the stacking layup. The result is compared with the value obtained in [34], which was reported equal to 3.30 kN/cm. As given in Fig. 14a, the value for the composite plate has a good match with the reported result. The effect of meshing resolution size on the buckling load factor is depicted in Fig. 14b. The predicted buckling load factors with different mesh resolutions are compared with the verified FE result, in Fig. 14b. 122, 177, 312, 414, and 531 $S4R$ elements were used in the models. These results show a negligible difference in the values obtained by both fine and coarse meshing.

5.3.2 Buckling load capacity maximization of 16-ply rectangular composite laminated plates

In the present section, at constant width, $b = 10$ cm, various lengths a, that is between 5 and 40 cm are taken into consideration in order to capture the buckling behavior of rectangular composite laminates having a circular central cutout. Similar to the case of a rectangular plate without cutout as well as the square laminated plate, three types of boundary conditions, CCCC, SCSC, and SSSS, are considered. Optimal buckling loads $N_{x,\mathrm{CR}}$ are achieved from conducting FEM optimization for each of the aspect ratios a/b of the symmetric 16-ply rectangular laminated plates having a central circular cutout, separately. These results are presented in Fig. 15 with respect to the considered a/b values, which are given in Table 12, and the associated fiber stacking designs are given in Table 13. According to the optimal buckling loads shown in Fig. 15, as a/b increases, the rectangular plate having CCCC and SCSC boundary conditions shows the highest optimal buckling loads, and the SSSS boundary conditions exhibit the lowest values. Also, it is observed that the optimal buckling loads for laminates with SSSS boundary conditions are not highly sensitive to the aspect ratio a/b.

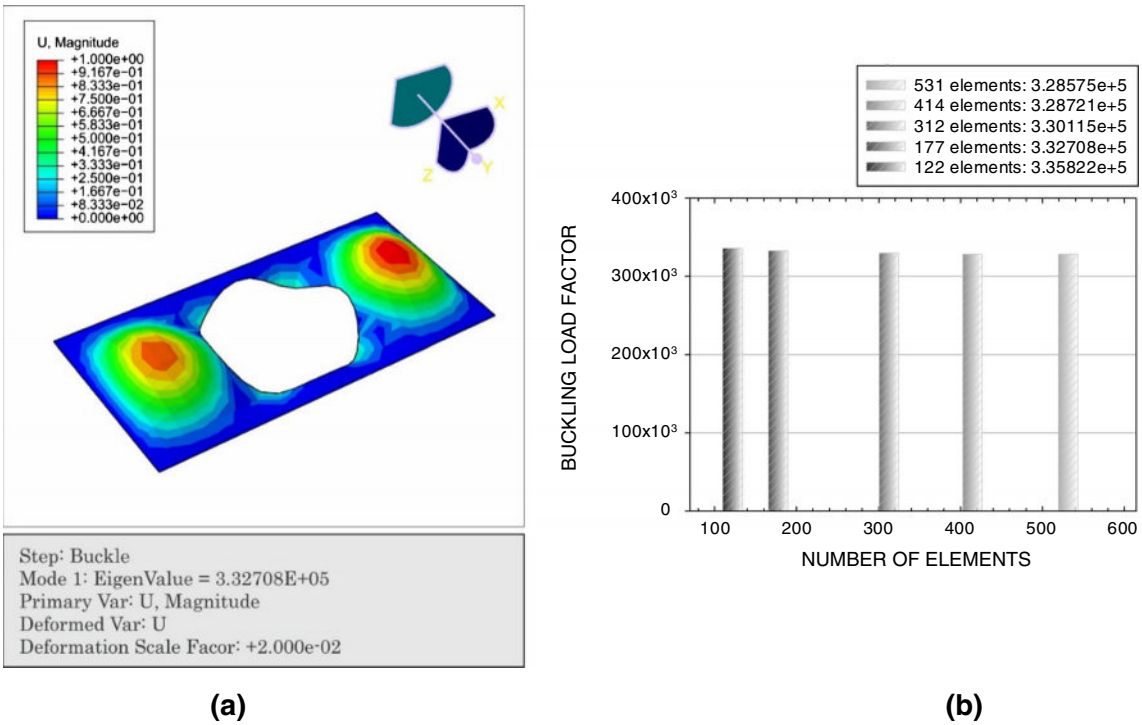

Fig. 14 Critical buckling loads of SCSC rectangular laminated panel having central circular cutout: **a** buckling load factor for ($a/b = 2, d/b = 0.8$), $N_{x,\mathrm{CR}} = 3.32708\mathrm{E} + 05$ kN/cm (Hu and Lin [34]: 3.30 kN/cm), **b** comparison of predicted buckling load factor from different meshes with the verified FE result

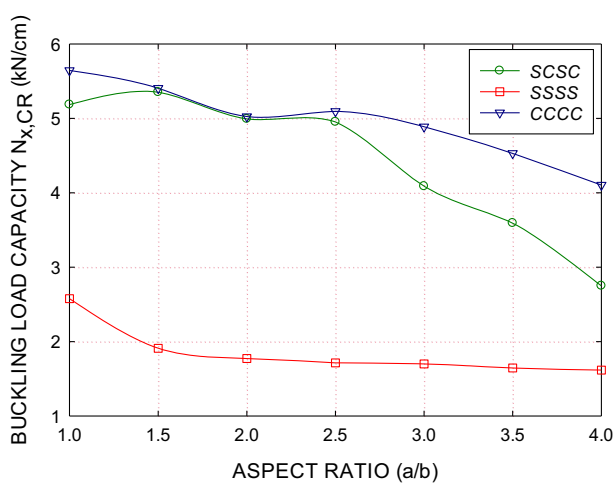

Fig. 15 Maximized buckling load capacity of the 16-ply rectangular laminated plates having a central circular hole

5.3.3 Buckling load capacity maximization of 80-ply rectangular composite laminated plates with a central circular cutout

Analogous to the previous cases, the optimizations for 80-ply panels are provided in the current section. The results are reported in Fig. 16 and Tables 14 and 15. According to Fig. 16, the buckling loads of each boundary condition oscillate in a narrower range than those of the previous 80-ply cases. It is observed that the buckling loads and orientations of all boundary conditions, specifically for CCCC and SCSC, are very close. To compare the optimized buckling loads considering $\pm 45, 90_2, 0_2$ as the feasible values for design variables, with those of Hu and Lin [34], with $[(\pm\theta, 90, 0)]_{10s}$ the bar chart of Fig. 17 is plotted. As can be seen, by considering additional variables the capacity of the plates is enhanced significantly.

Table 12 Buckling load capacity N_x of 16-ply rectangular laminated plates having a central circular hole

a/b	Boundary condition		
	SCSC	SSSS	CCCC
1	5.18611	2.57688	5.64467
1.5	5.35369	1.90987	5.40642
2	4.99326	1.77226	5.02495
2.5	4.95358	1.71419	5.09539
3	4.08895	1.69982	4.88827
3.5	3.59414	1.64472	4.53129
4	2.74887	1.61671	4.10525

Table 13 Designed orientations of 16-ply rectangular laminated plates having a central circular cutout

a/b	Boundary condition		
	SCSC	SSSS	CCCC
1	$[90, 90, 0, 0, 0, 0, 0, 0]_s$	$[45, -45, 45, -45, 0, 0, 0, 0]_s$	$[0, 0, 90, 90, 0, 0, 0, 0]_s$
1.5	$[90, 90, 0, 0, 0, 0, 0, 0]_s$	$[45, -45, 45, -45, 0, 0, 0, 0]_s$	$[90, 90, 0, 0, 0, 0, 0, 0]_s$
2	$[0, 0, 90, 90, 0, 0, 0, 0]_s$	$[45, -45, 90, 90, 0, 0, 0, 0]_s$	$[0, 0, 90, 90, 0, 0, 0, 0]_s$
2.5	$[90, 90, 0, 0, 0, 0, 0, 0]_s$	$[45, -45, 45, -45, 0, 0, 0, 0]_s$	$[0, 0, 90, 90, 0, 0, 0, 0]_s$
3	$[0, 0, 90, 90, 0, 0, 0, 0]_s$	$[45, -45, 45, -45, 0, 0, 0, 0]_s$	$[0, 0, 90, 90, 0, 0, 0, 0]_s$
3.5	$[0, 0, 90, 90, 0, 0, 0, 0]_s$	$[45, -45, 45, -45, 0, 0, 0, 0]_s$	$[0, 0, 90, 90, 0, 0, 0, 0]_s$
4	$[45, -45, 0, 0, 90, 90, 0, 0]_s$	$[45, -45, 45, -45, 0, 0, 0, 0]_s$	$[0, 0, 90, 90, 0, 0, 0, 0]_s$

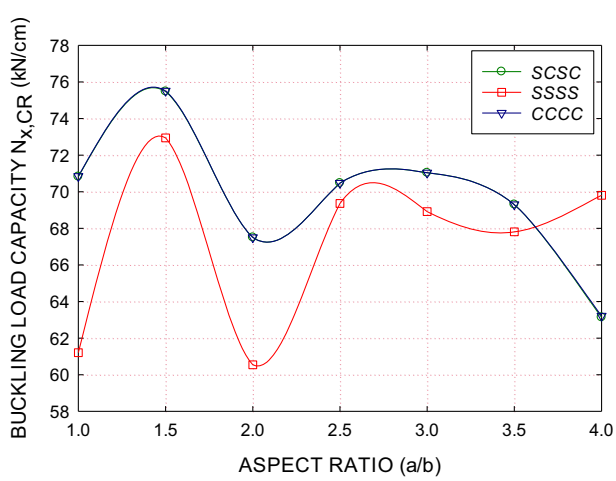

Fig. 16 Maximized buckling load capacity of the 80-ply rectangular laminated plates having a central circular hole

Table 14 Buckling load capacity N_x of 80-ply rectangular laminated plates having a central circular hole

a/b	Boundary condition		
	SCSC	SSSS	CCCC
1	70.8262	61.202	70.8498
1.5	75.4805	72.9454	75.5105
2	67.5061	60.5387	67.5076
2.5	70.476	69.3641	70.476
3	71.035	68.9187	71.0353
3.5	69.3071	67.8115	69.3071
4	63.133	69.8105	63.2112

Table 15 Designed orientations of 80-ply rectangular laminated plates having a central circular hole

a/b	Boundary condition		
	SCSC	SSSS	CCCC
1	$[0, 0, 0, 0, 0, 0, 0, 0]_{5s}$	$[0, 0, 0, 0, 45, -45, 0, 0]_{5s}$	$[0, 0, 0, 0, 0, 0, 0, 0]_{5s}$
1.5	$[0, 0, 0, 0, 0, 0, 0, 0]_{5s}$	$[0, 0, 0, 0,0, 0, 0, 0]_{5s}$	$[0, 0, 0, 0, 0, 0, 0, 0]_{5s}$
2	$[0, 0, 0, 0, 0, 0, 0, 0]_{5s}$	$[0, 0, 0, 0, 0,0, 45, -45]_{5s}$	$[0, 0, 0, 0, 0, 0, 0, 0]_{5s}$
2.5	$[0, 0, 0, 0, 0, 0, 0, 0]_{5s}$	$[0, 0, 0, 0,0, 0, 0, 0]_{5s}$	$[0, 0, 0, 0, 0, 0, 0, 0]_{5s}$
3	$[0, 0, 0, 0, 0, 0, 0, 0]_{5s}$	$[0, 0, 0, 0, 0,0, 0, 0]_{5s}$	$[0, 0, 0, 0, 0, 0, 0, 0]_{5s}$
3.5	$[0, 0, 0, 0, 0, 0, 0, 0]_{5s}$	$[0, 0, 0, 0,0, 0, 0, 0]_{5s}$	$[0, 0, 0, 0, 0, 0, 0, 0]_{5s}$
4	$[0, 0, 0, 0, 45, -45, 0, 0]_{5s}$	$[0, 0, 0, 0,0, 0, 0, 0]_{5s}$	$[0, 0, 0, 0, 0, 0, 45, -45]_{5s}$

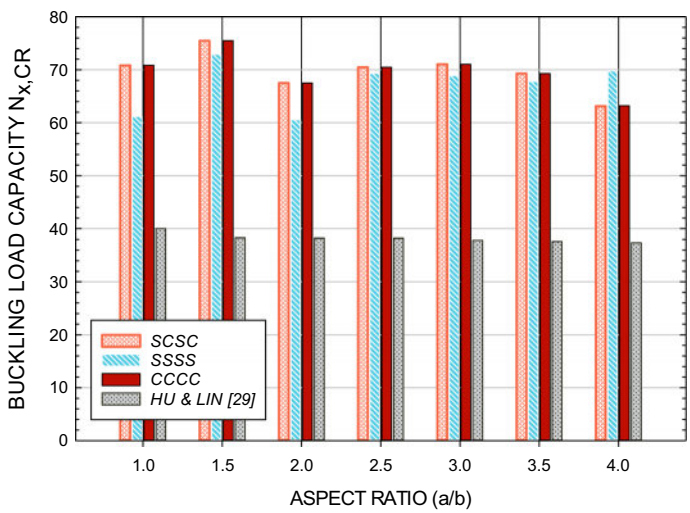

Fig. 17 A comparison of the maximized buckling load capacity of the 80-ply rectangular laminated plates having a central circular hole possessing different types of boundary conditions with the results reported by Hu and Lin [34]

6 Conclusion

This article investigated a Python script-based framework to study the optimization of laminated composites having a central circular cutout, with different boundary conditions and various aspect ratios. A Python script was implemented to let the user submit dimension, orientation, and diameter of the cutout combinations to Abaqus/CAE. Then, a routine for calling the Python script along with the optimization algorithm was implemented in MATLAB. The performance of the algorithm was validated by presenting a good agreement of the results with those of previous researches. Furthermore, three sets of new problems are considered and optimized, introducing additional variables to cases studied by [34].

According to the analysis for rectangular plates, with CCCC boundary conditions, the buckling load is more sensitive to the aspect ratios than for the other boundary conditions. In plain rectangular plates, by increasing the number of layers from 16 to 80, an increase in the buckling load capacity is observed. According to the type of boundary conditions, this increase happens over the range of 58 times to 75 times, the greatest of which is associated with the SSSS boundary condition. In these plates, the SSSS type of boundary condition is of least sensitivity to the change in a/b and the most sensitive one is the CCCC boundary condition. Moreover, in square plates having a central hole, the buckling load increases from an average of 38 times to 58 times as the number of layers increases from 16 to 80 layers. In these plates, for the 16-layer case, when increasing the diameter, the buckling load capacity increases in contrast with what might intuitively be expected to happen. Nevertheless, in the case of 80 layers, this is not true, and the buckling load capacity is reduced by approximately 55–70% [34]. For the third case where there are rectangular plates with a central hole, by increasing the number of layers from 16 to 80 layers, an increase in the buckling load capacity can be noticed. This increase is within the range of 14 to 37 times greater than for the 16-layer plates. In this case, the maximum buckling load capacity of 16-layer plates occurs at $a/b = 1$ and the minimum at $a/b = 4$. However, in 80-layer plates, it occurs at $a/b = 2$. In the 16-layer rectangular plates, the presence of the hole increases the buckling load capacity.

For both of the plates with SCSC and CCCC boundary conditions, this increase is by approximately 70%. However, in the 80-layer plates, the buckling load capacity decreases by 50–60%.

The applicability, simplicity, and accuracy of the introduced framework were shown by investigating different examples. Besides, in the current FE Python script-based framework, the applied loads could be changed easily to any other types of loading, such as thermal loading, pressure, concentrated forces, displacements. Meanwhile, the optimizer, boundary conditions, dimensions, and even the geometry itself could be changed into a desirable one.

References

1. Kaw, A.K.: Mechanics of Composite Materials. CRC Press, Boca Raton (2005)
2. Jones, R.M.: Mechanics of Composite Materials. CRC Press, Boca Raton (1998)
3. Reddy, J.N.: Mechanics of Laminated Composite Plates and Shells: Theory and Analysis. CRC Press, Boca Raton (2004)
4. Khalkhali, A., Geran Malek, N., Bozorgi Nejad, M.: Effects of the impactor geometrical shape on the non-linear low-velocity impact response of sandwich plate with CNTRC face sheets. J. Sandw. Struct. Mater. (2018). https://doi.org/10.1177/1099636218778998
5. Khalkhali, A., Ebrahimi-Nejad, S., Malek, N.G.: Comprehensive optimization of friction stir weld parameters of lap joint AA1100 plates using artificial neural networks and modified NSGA-II. Mater. Res. Express **5**(6), 066508 (2018). https://doi.org/10.1088/2053-1591/aac6f6
6. Sargent, P.M., Ige, D.O., Ball, N.R.: Design of laminate composite layups using genetic algorithms. Eng. Comput. **11**(2), 59–69 (1995). https://doi.org/10.1007/BF01312200
7. McMahon, M.T., Watson, L.T., Soremekun, G.A., Gürdal, Z., Haftka, R.T.: A Fortran 90 genetic algorithm module for composite laminate structure design. Eng. Comput. **14**(3), 260–273 (1998). https://doi.org/10.1007/BF01215979
8. Karakaya, Ş., Soykasap, Ö.: Buckling optimization of laminated composite plates using genetic algorithm and generalized pattern search algorithm. Struct. Multidiscip. Optim. **39**(5), 477–486 (2009)
9. Pai, N., Kaw, A., Weng, M.: Optimization of laminate stacking sequence for failure load maximization using Tabu search. Compos. Part B Eng. **34**(4), 405–413 (2003). https://doi.org/10.1016/S1359-8368(02)00135-X
10. Matsuzaki, R., Todoroki, A.: Stacking-sequence optimization using fractal branch-and-bound method for unsymmetrical laminates. Compos. Struct. **78**(4), 537–550 (2007). https://doi.org/10.1016/j.compstruct.2005.11.015
11. Erdal, O., Sonmez, F.O.: Optimum design of composite laminates for maximum buckling load capacity using simulated annealing. Compos. Struct. **71**(1), 45–52 (2005)
12. Rao, A.R.M., Arvind, N.: A scatter search algorithm for stacking sequence optimisation of laminate composites. Compos. Struct. **70**(4), 383–402 (2005)
13. de Almeida, F.S.: Stacking sequence optimization for maximum buckling load of composite plates using harmony search algorithm. Compos. Struct. **143**, 287–299 (2016)
14. Abachizadeh, M., Tahani, M.: An ant colony optimization approach to multi-objective optimal design of symmetric hybrid laminates for maximum fundamental frequency and minimum cost. Struct. Multidiscip. Optim. **37**(4), 367–376 (2009). https://doi.org/10.1007/s00158-008-0235-6
15. Sebaey, T., Lopes, C., Blanco, N., Costa, J.: Ant colony optimization for dispersed laminated composite panels under biaxial loading. Compos. Struct. **94**(1), 31–36 (2011). https://doi.org/10.1016/j.compstruct.2011.07.021
16. Ho-Huu, V., Do-Thi, T., Dang-Trung, H., Vo-Duy, T., Nguyen-Thoi, T.: Optimization of laminated composite plates for maximizing buckling load using improved differential evolution and smoothed finite element method. Compos. Struct. **146**, 132–147 (2016). https://doi.org/10.1016/j.compstruct.2016.03.016
17. de Almeida, F.S.: Optimization of laminated composite structures using harmony search algorithm. Compos. Struct. (2019). https://doi.org/10.1016/j.compstruct.2019.04.024
18. Javidrad, F., Nazari, M., Javidrad, H.: Optimum stacking sequence design of laminates using a hybrid PSO-SA method. Compos. Struct. **185**, 607–618 (2018). https://doi.org/10.1016/j.compstruct.2017.11.074
19. Marouene, A., Boukhili, R., Chen, J., Yousefpour, A.: Effects of gaps and overlaps on the buckling behavior of an optimally designed variable-stiffness composite laminates—a numerical and experimental study. Compos. Struct. **140**, 556–566 (2016). https://doi.org/10.1016/j.compstruct.2016.01.012
20. Ouinas, D., Achour, B.: Buckling analysis of laminated composite plates $[(\theta/-\theta)]$ containing an elliptical notch. Compos. Part B Eng. **55**, 575–579 (2013). https://doi.org/10.1016/j.compositesb.2013.07.011
21. Hu, H.-T., Chen, H.-C.: Buckling optimization of laminated truncated conical shells subjected to external hydrostatic compression. Compos. Part B Eng. **135**, 95–109 (2018). https://doi.org/10.1016/j.compositesb.2017.09.065
22. Shrivastava, S., Mohite, P., Yadav, T., Malagaudanavar, A.: Multi-objective multi-laminate design and optimization of a carbon fibre composite wing torsion box using evolutionary algorithm. Compos. Struct. **185**, 132–147 (2018). https://doi.org/10.1016/j.compstruct.2017.10.041
23. Shrivastava, S., Mohite, P.M., Limaye, M.D.: Optimal design of fighter aircraft wing panels laminates under multi-load case environment by ply-drop and ply-migrations. Compos. Struct. **207**, 909–922 (2019). https://doi.org/10.1016/j.compstruct.2018.09.004
24. Kazemzadeh Azad, S., Akış, T.: Automated selection of optimal material for pressurized multi-layer composite tubes based on an evolutionary approach. Neural Comput. Appl. **29**(7), 405–416 (2018). https://doi.org/10.1007/s00521-016-2563-6
25. Kazemzadeh Azad, S., Akış, T.: A study of shrink-fitting for optimal design of multi-layer composite tubes subjected to internal and external pressure. Iran. J. Sci. Technol. Trans. Mech. Eng. **43**(1), 451–467 (2019). https://doi.org/10.1007/s40997-018-0170-0

26. Kaveh, A., Dadras, A., Malek, N.G.: Buckling load of laminated composite plates using three variants of the biogeography-based optimization algorithm. Acta Mech. **229**(4), 1551–1566 (2018). https://doi.org/10.1007/s00707-017-2068-0
27. Kaveh, A., Dadras, A., Geran Malek, N.: Optimum stacking sequence design of composite laminates for maximum buckling load capacity using parameter-less optimization algorithms. Eng. Comput. (2018). https://doi.org/10.1007/s00366-018-0634-2
28. Kaveh, A., Dadras, A., Geran Malek, N.: Robust design optimization of laminated plates under uncertain bounded buckling loads. Struct. Multidiscip. Optim. **59**(3), 877–891 (2019). https://doi.org/10.1007/s00158-018-2106-0
29. Systèmes, D.: Abaqus 6.10: Analysis User's Manual. Dassault Systèmes Simulia Corp, Providence (2010)
30. Van Rossum, G.: Python programming language. In: USENIX Annual Technical Conference, p. 36 (2007)
31. Kaveh, A.: Advances in Metaheuristic Algorithms for Optimal Design of Structures, 2nd edn. Springer, Berlin (2017)
32. Kaveh, A.: Applications of Metaheuristic Optimization Algorithms in Civil Engineering, vol. PUBDB-2017-153072. Springer, Berlin (2017)
33. Kaveh, A., Bakhshpoori, T.: Metaheuristics: Outlines, MATLAB Codes and Examples. Springer, Berlin (2019)
34. Hu, H.-T., Lin, B.-H.: Buckling optimization of symmetrically laminated plates with various geometries and end conditions. Compos. Sci. Technol. **55**(3), 277–285 (1995). https://doi.org/10.1016/0266-3538(95)00105-0
35. Kaveh, A., Kalatjari, V.: Genetic algorithm for discrete-sizing optimal design of trusses using the force method. Int. J. Numer. Methods Eng. **55**(1), 55–72 (2002). https://doi.org/10.1002/nme.483
36. Kaveh, A., Rahami, H.: Analysis, design and optimization of structures using force method and genetic algorithm. Int. J. Numer. Methods Eng. **65**(10), 1570–1584 (2006). https://doi.org/10.1002/nme.1506
37. Kaveh, A., Kalatjari, V.: Topology optimization of trusses using genetic algorithm, force method and graph theory. Int. J. Numer. Methods Eng. **58**(5), 771–791 (2003). https://doi.org/10.1002/nme.800
38. Holland, J.H.: Adaptation in Natural and Artificial Systems: An Introductory Analysis with Applications to Biology, Control, and Artificial Intelligence. MIT press, Cambridge (1992)
39. Sivanandam, S., Deepa, S.: Introduction to Genetic Algorithms. Springer, Berlin (2007)
40. Kaveh, A., Ilchi Ghazaan, M.: A comparative study of CBO and ECBO for optimal design of skeletal structures. Comput. Struct. **153**, 137–147 (2015)
41. Arora, J.: Introduction to Optimum Design. Elsevier Science, Amsterdam (2011)
42. Goldberg, D.E., Deb, K.: A comparative analysis of selection schemes used in genetic algorithms. In: Rawlins, G.J.E. (ed.) Foundations of Genetic Algorithms, vol. 1, pp. 69–93. Elsevier, Amsterdam (1991)
43. Sivaraj, R., Ravichandran, T.: A review of selection methods in genetic algorithm. Int. J. Eng. Sci. Technol. **3**(5), 3792–3797 (2011)

Publisher's Note Springer Nature remains neutral with regard to jurisdictional claims in published maps and institutional affiliations.

Acta Mech 232, 921–931 (2021)
https://doi.org/10.1007/s00707-020-02878-2

ORIGINAL PAPER

A. Kaveh · A. Dadras Eslamlou · S. M. Javadi · N. Geran Malek

Machine learning regression approaches for predicting the ultimate buckling load of variable-stiffness composite cylinders

Received: 9 October 2020 / Accepted: 30 October 2020 / Published online: 3 January 2021
© Springer-Verlag GmbH Austria, part of Springer Nature 2021

Abstract Due to the high computational cost of finite element analyses, particularly in optimization tasks, establishing a high-fidelity surrogate model is of immense importance to engineers. Analyses of fiber steering composite cylinders are costly and often involve high nonlinearity. Among different metamodeling approaches, machine learning techniques provide effective models that can capture high nonlinearity. Therefore, in this study, different machine learning techniques are employed to establish a relationship between the fiber angle and buckling capacity of the cylinders under bending-induced loads. The utilized data set contains a total of 11,000 cases, including seven attributes (i.e., fiber angles) for 11 different aspect ratios (L/R). The numerical results demonstrate that compared with the Random Forest Regressor, Decision Tree algorithm, and Multiple Linear Regression, the Deep Learning model obtains stable results with smaller errors and higher generalization.

1 Introduction

Variable-stiffness (VS) composites enable designers to get the most out of the directional properties of composite structures thanks to the automated fiber placement (AFP) technology. AFP produces continuously variable fiber orientation plies and enables the engineers to exploit the design space fully. Therefore, the design space is extended beyond the constant-stiffness structure case with the same weight but more efficient load paths to be explored [1, 2]. Along with the variation of fiber angles in constant-stiffness structures or fiber paths in VSs, composite laminates may be designed based on other factors, such as dimensions, weight, robustness, and the number of plies [3–5].

After it was first studied by Tatting [6], optimization of variable-stiffness composite cylinders subjected to buckling moment became the focus of other researchers, considering cylindrical [7, 8] or elliptical [9, 10] cross-sections. Ghiasi et al. [11] have reviewed the study of the optimization algorithms used to design variable-stiffness composites. The transient response of the variable-stiffness composite plates placed on an elastic foundation and subjected to a time-dependent load was investigated by Heydarpour and Aghdam [12]. Farsadi et al. [13] studied the dynamics of instability and the post-flutter performance of a variable-stiffness wing-like composite plate. The purpose of the paper was to exploit the ideal fiber paths corresponding to enhanced aeroelastic flutter and post-flutter performance of the plate.

Surrogate modeling [14] is a common approach for the analysis of VS composite structures to overcome the computational costs and involved complexity, particularly for variable-stiffness composites having higher aspect ratios. Especially, as the design optimization of these structures requires an iterative scheme, inexpensive function evaluations become crucial. Metamodel-based design optimization (MBDO) is an optimization strategy in which simple analytical functions, so-called metamodels, that predict a high-fidelity model can

A. Kaveh (✉) · A. Dadras Eslamlou · S. M. Javadi · N. Geran Malek
Centre of Excellence for Fundamental Studies in Structural Engineering, Iran University of Science and Technology, Tehran, Iran
e-mail: alikaveh@iust.ac.ir

be adopted as surrogate alternatives for expensive functions [15]. There is an increasing demand, for designers in manufacturing industries, for prediction-based optimization strategies by which low-cost, high-quality products could be designed more quickly. Performance, robustness, and accuracy of some surrogate-based techniques, including Multivariate Adaptive Regression Splines (MARS), Kriging (KRG), Radial Basis Functions (RBF), and Response Surface Method (RSM), are compared in several reviews [15–17]. This procedure is highly effective when facing a wide variety of engineering design problems, say energy absorption [18] or crashworthiness design [19], for which intensive computational efforts are demanded.

This study is in the continuation of the authors' previous research on developing a metamodeling framework for laminated constant-stiffness planar and variable-stiffness cylindrical composite structures [20, 21]. Metamodels are mainly classified into three groups: heuristic models such as Neural Networks (NN), Support Vector Machines (SVM), frequency domain approaches; stochastic models like Kriging models and Radial Basis Functions (RBFs); and Geometric Models such as Response Surface Models (RSMs) or Non-Uniform Rational B-splines (NURBs) [22]. Considering that the metamodel is problem-dependent, at first, a key challenge is to examine and select the best surrogate model. There are available some investigations examining various surrogate-based optimization approaches. For example, Rikards et al. [23] examined the performance of the RSM metamodeling approach for the post-buckling design of stiffened composite shells. An advanced Kriging model (AKM) was used by Haeri and Fadaee [24], showing that the running time is reduced in comparison with the previous ANN-based surrogate method conducted by Lopes et al. [25]. Arian Nik et al. [26] adopted second-order polynomial regression (PR) for the optimization of a composite laminate with curvilinear fibers, where the fitting of the parameters was performed using the least square method. Rouhi et al. developed a multi-step design approach based on the radial basis functions (RBF) for improving the buckling behavior of laminated composite cylinders subjected to simple [27, 28] and bi-directional bending moment [29]; elliptical cylinders subjected to compressive axial force [10]; and bending moment [30]. Arian Nik et al. [31] reviewed the performance of various metamodeling methods, including Support Vector Regression, Kriging, Radial Basis Functions, and Polynomial Regression, in the design of VS composite. In that study, Kriging and Radial Basis Functions (RBF) were announced as the most sustainable and accurate metamodels in the design process of variable-stiffness composite structures. Using a metamodeling approach based on the Kriging model, Luersen et al. [32] reduced the costly computations in the design problem of a VS composite cylinder. Ye et al. [33] analyzed the performance of the support vector regression approach in the design of VS composite planar structure subjected to compressive load and VS cylindrical structure under bending moment.

The sample size and the number of design variables are two of the main factors that influence the approximated metamodel accuracy. From the Deep Learning (DL) perspective, the performance of the metamodeling approach increases by raising the sample points. Simultaneously, though, there must be a compromise between the sample size and the computational cost.

In this study, predicting the ultimate buckling load of variable-stiffness composite cylinders using data-driven modeling as well as Machine Learning regression approaches, including Multiple Linear Regression (MLR), Regression Decision Tree (RDT), Random Forest (RF) regressor, and DL are investigated.

The rest of the paper is organized as follows. Section 2 is devoted to the statement of the problem. Section 3 presents the descriptions of Machine Learning (ML) approaches. The results and discussion of the predicting models are presented in Sect. 4. Finally, the conclusions are drawn in Sect. 5.

2 Numerical analysis using the finite element method

In the current study, the software Abaqus [34] is used for the finite element analysis of the variable-stiffness composite cylinders and generating labels—ultimate buckling load—of data samples. Figure 1a illustrates the dimensions, length L and radius R, and the applied moment loads on the cylinders. As shown in Fig. 1b, from the numerical modeling point of view, the cylinders must be partitioned such that the variability in the direction of the fibers can be achieved. For each of these partitioned sections, 16-ply symmetric layups of $\left[0^\circ, \theta^\circ, 90^\circ, -\theta^\circ, -\theta^\circ, 90^\circ, \theta^\circ, 0^\circ\right]s$ are considered, where the plies having θ° are to be fiber-steered. The spatial position of each narrow section is determined by the angle α, whose value starts from the symmetry plane ZT in the circumferential direction of the cylinder. On both sides of the ZT-plane, fibers have equal angles but in the opposite direction ($\theta(-\alpha) = -\theta(\alpha)$).

Seven narrow sections are considered as the main sections for fiber optimization, and a linear expression is used to gradually link the remaining angles between two consecutive ones. These seven sections have fibers whose values are denoted by $T_i\ s$ ($i = 1, 2, \ldots, 7$), which make up the seven design variables of the present

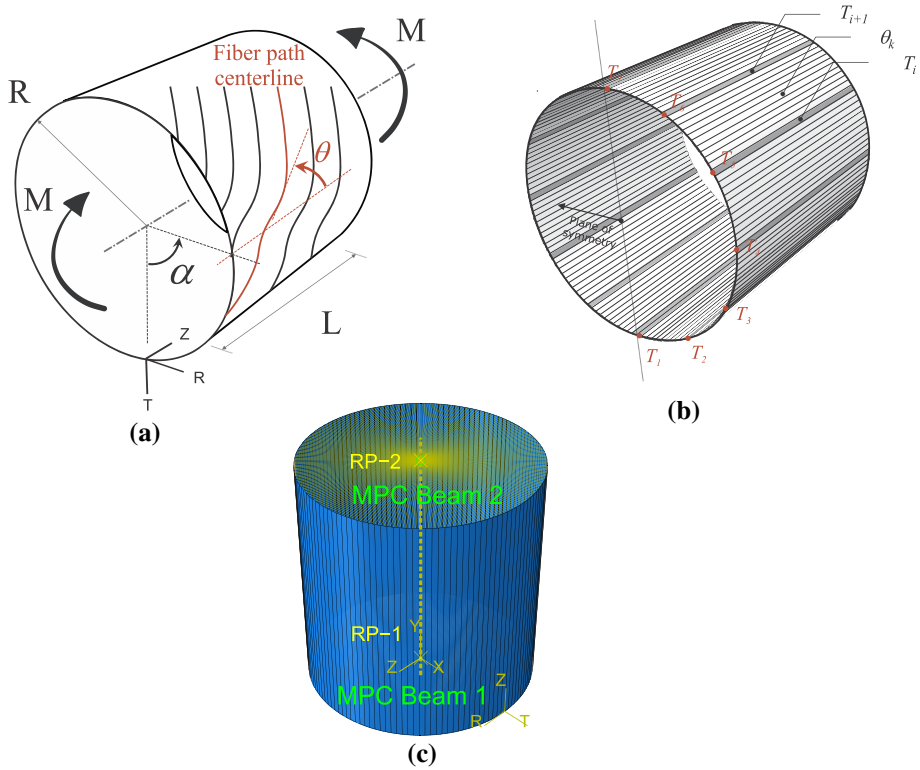

Fig. 1 Variable-stiffness composite cylinder: **a** configuration of the cylinder along with dimensions and coordinate system, subjected to bending-induced buckling moment, **b** piece-wise constant orientation angle narrow section

structure. Angles of the rest of the sections θ_k are obtained according to their spatial location α_k and the values of the successive T_i-s, as given in Eq. (1):

$$\theta_k = T_i + \frac{\alpha_k - \alpha_i}{\alpha_{i+1} - \alpha_i}(T_{i+1} - T_i); \quad i = 1, \ldots m, \text{ and } k = 1, \ldots, n, \tag{1}$$

where n and m are the number of narrow sections between each subsequent section having T_i and the number of design variables (here $m = 7$), respectively. Buckling eigenvalues and mode shapes are obtained by employing the Lanczos eigensolver.

Since the narrow sections are turned around the cylinder's circumference, to define the fibers' direction, the orientation of the material must be assigned. As shown in Fig. 1a, RTZ is the reference cylindrical coordinate system to which the material orientations are specified. For each of the narrow section, a datum coordinate system is defined. While revolving around the circumference of the cylinder, material orientations are assigned according to the associated coordinate system of the narrow section.

The finite element models are meshed using the "S8R5" type element, which has eight nodes and five degrees of freedom for each node. The size of the elements is obtained according to a mesh convergence study conducted on the FE models. By doing so, the FE model has meshed with 5762 quadrilateral quadratic elements, such that, in each of the top and bottom edges of the narrow sections, only one seed, with the global size of 10.6, is assigned. Also, beam-type multi-point constraint (MPC) is applied on both sides of the cylinders to guarantee that their circular geometry preserves under deformation (see Fig. 1c). MPC constraints tie both circular edges to their central point's counterparts. The cylinders are then subjected to a pure bending moment.

3 Machine learning approaches

3.1 Preparing data set

Data set preparation is one of the crucial tasks in ML and involves data collection, data exploration, data cleaning, preprocessing, feature engineering, labeling, and finally, splitting data into training and testing sets. In this study, the Latin Hypercube Sampling (LHS) is used for generating the involved parameters in the problem. LHS was first introduced by McKay et al. [35] and then developed further by other researchers for different purposes [36, 37]. A square 2-dimensional matrix is called Latin square if and only if in each row and column, there appears only one sample. The generalization of this 2D square in higher dimensions is called Latin Hypercube. Using these features, the LHS approach can allocate n design points in an m-dimensional design space such that those points do not overlap when mapped onto each dimension [26]. The main advantages of using LHS are providing the flexibility to take the number of sample points under control, achieving a uniform distribution of sample points, avoiding the overlapping in sample points, and, therefore, dramatically reducing the required number of samples.

Herein, the LHS is used to generate parameters (fiber angles) of 1000 samples with 11 aspect ratios ($L/R=$ 0.1, 0.2, 0.3, 0.4, 0.5, 0.6, 0.7, 0.8, 0.9, 1.0, and 2). Therefore, the data set for each of 11 aspect ratios (L/R) includes a table with 1000 rows and eight columns containing fiber angles and corresponding buckling load. The buckling loads are calculated using the computational framework developed in [21]. Figure 2a depicts box plots for each of the variables in the composite cylinder's data set of the aspect ratio at $L/R = 1$. In addition, as seen in Fig. 2b, it can be seen that the variables are well distributed throughout the parameter space. The corresponding heat map for this data set is illustrated in Fig. 3a. From this figure, it can be inferred that T_7 and the buckling load are relatively correlated. Besides, the relationship between the seven input variables (i.e., fiber angles) and the buckling loads in the composite cylinder's data set for $L/R = 1$ are presented in Fig. 3b.

3.2 Linear regression

The aim of the linear regression method is to minimize the residual sum of squares between the observed responses in the data set and the targets predicted by a linear approximation. Multiple Linear Regression (MLR) models are based on the linear correlation. A regression model consisting of multiple variables can be represented as

$$y = b_0 + m_1 b_1 + m_2 b_2 + \cdots + m_n b_n, \tag{2}$$

where y is the output, b_1 to b_n represent the influence parameters, and m_1 to m_n are the coefficients for the corresponding influence parameters.

3.3 Regression decision tree

A decision tree as a powerful supervised ML algorithm is used extensively in both classification and regression problems [38, 39]. MLR models use a global predictive formula holding the entire data-space while the decision tree sub-divides the space into controllable smaller regions [40].

The process of solving regression problems with a decision tree is similar to decision tree classification; however, decision tree regressor typically uses mean square error (MSE), the mean absolute error (MAE), or similar criteria, such as Gini impurity, instead of classification metrics to determine splits. In the Regression Decision Tree (RDT) method, the function to measure the quality of a split is MSE which is equal to variance reduction as a feature selection criterion. The strategy is used to choose the split at each node, and the nodes are expanded until all leaves become pure. Figure 4 shows the schematic and details of the first three levels of the RDT (test size = 0.3) for the composite cylinder's data set generated for $L/R = 1$.

3.4 Random forests

A Random Forest (RF) regressor is an ensemble model that relies on aggregating the results of an ensemble of simpler estimators. In this supervised ML algorithm, each tree in a random forest is trained on the subset of

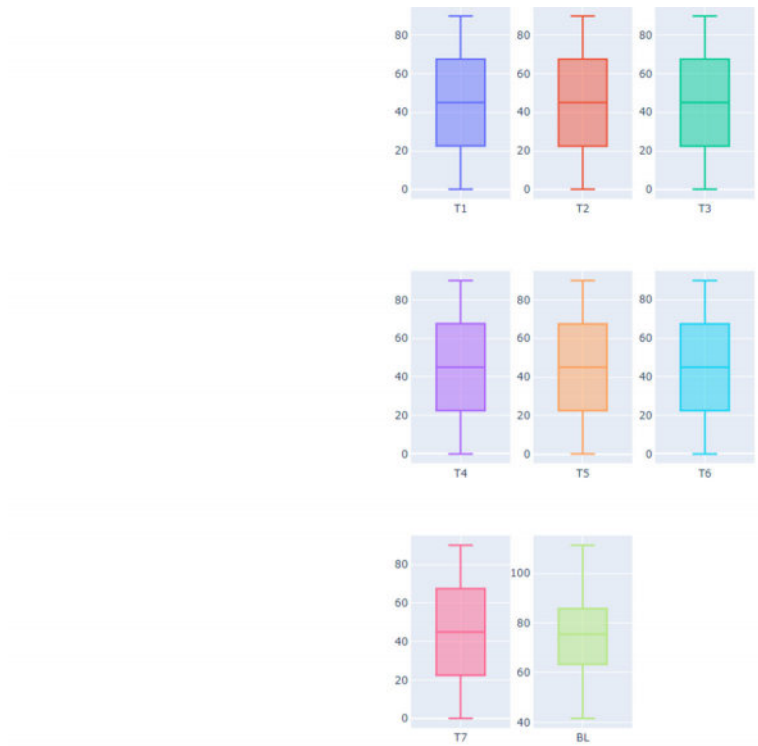

(a) Box plot for each of the variables

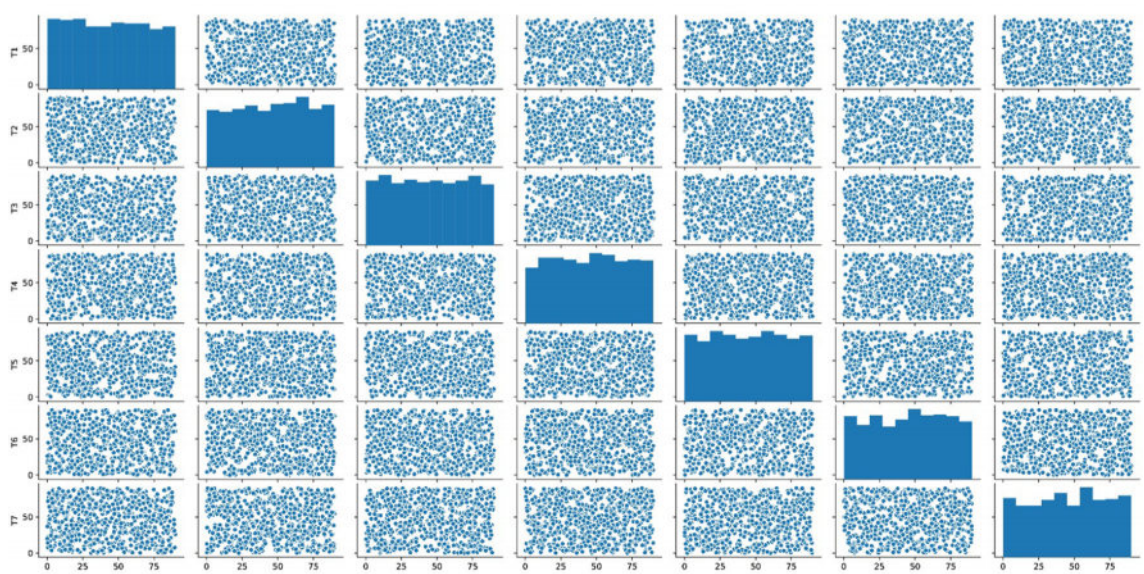

(b) Scatter plot matrix

Fig. 2 The examination of generated fiber angles as composite cylinder's input data set

the provided data and the output of multiple randomly created decision trees that are combined to generate the final output. The RF algorithm is not biased and works well even when data have missing values or they have not been scaled well. In addition, it improves the predictive accuracy and controls over-fitting. The pseudocode of this algorithm is illustrated in Algorithm 1. Figure 5 shows the schematic of a tree in the random forest for a composite cylinder's training data set for $L/R = 1$. Herein, the number of trees in the forest is set to 100. Further details about the feature's importance for a composite cylinder's training data set for $L/R = 1$

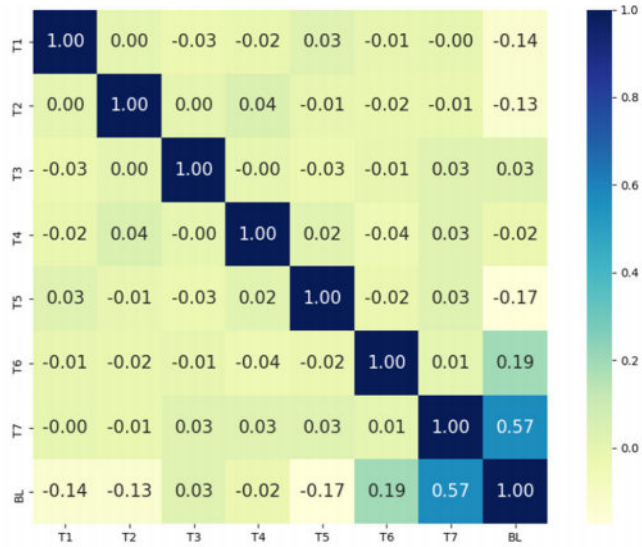

(a) Heat-map for the composite cylinder's data set of the aspect ratio at L/R = 1

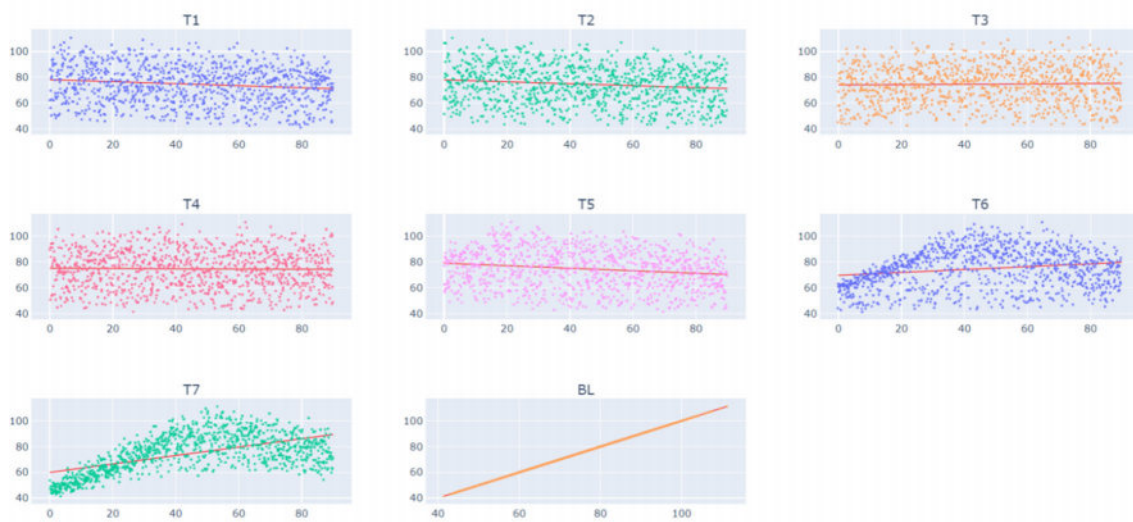

(b) The relationship between the seven input variables and the buckling load

Fig. 3 Investigating the correlation between fiber angles and buckling load in the composite cylinder's data set for aspect ratios $L/R = 1$

is depicted in Fig. 6. As can be seen, using this technique we can assign a score to input features based on how useful selected parameters are at predicting a target variable. In this example, T_7, T_6, and T_5 have more weight in comparison with other parameters.

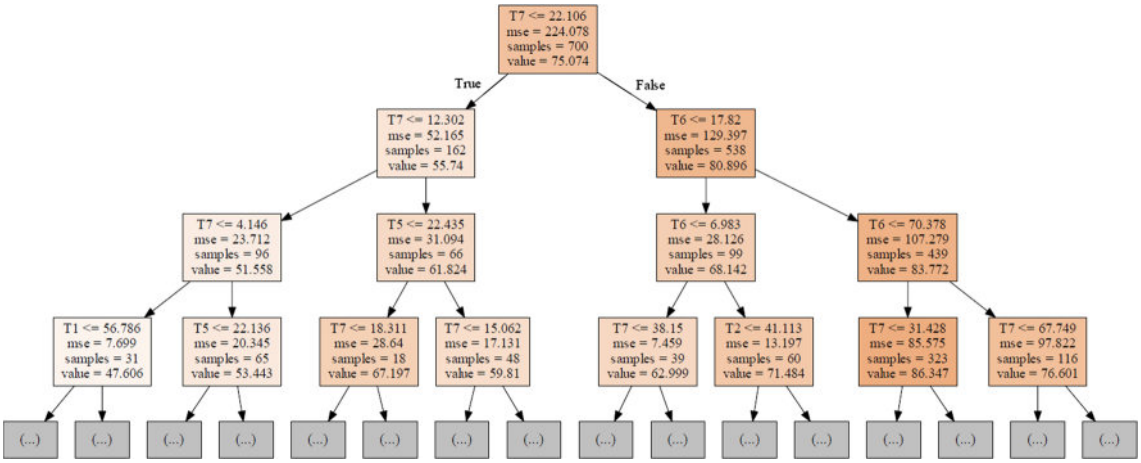

Fig. 4 The first three levels of regression decision tree for a composite cylinder's data set ($L/R = 1$)

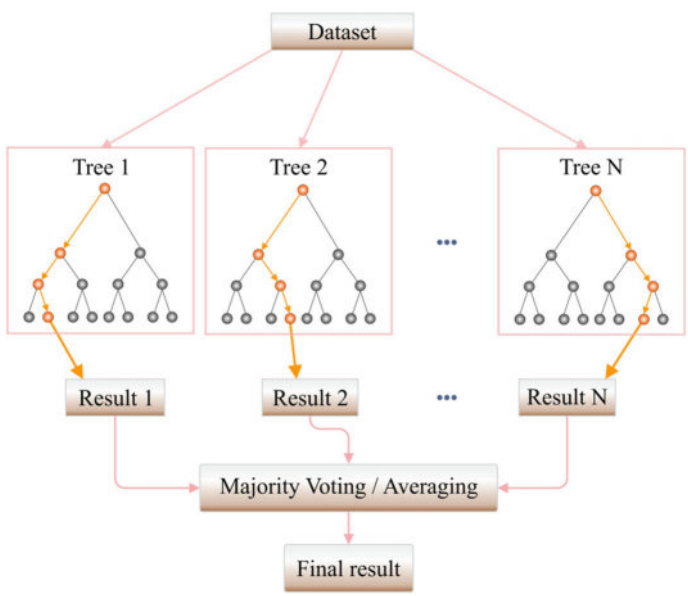

Fig. 5 A schematic of random forest tree regressor

Algorithm 1. Random Forest

```
function RandomForest (G, F)            # G: Training set; F: Features
    H ← ∅
    for i ∈ 1, ..., N
        G^i ← A bootstrap sample from G
        h_i ← RandomizedTree (G^i, F)
        H ← H ∪ {h_i}
    end for
end function
function RandomizedTree (G, F)
    At each node:
        f ← very small subset of F
        Split on best feature in f
    return The Learned Tree
end function
```

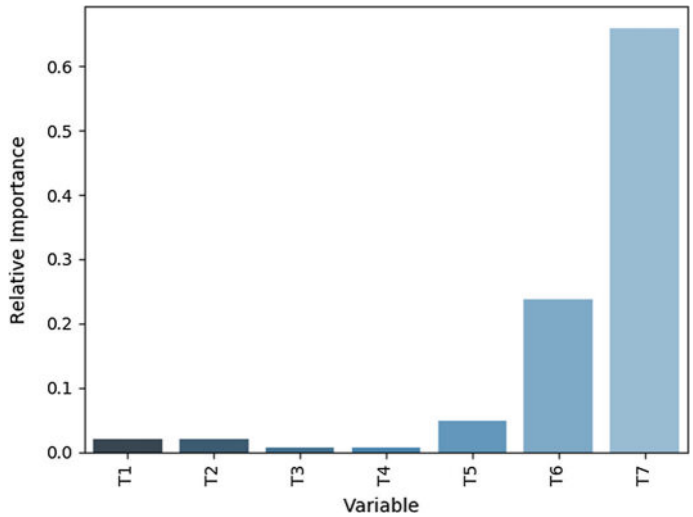

Fig. 6 The random forest's features importance for a composite cylinder's data set ($L/R = 1$)

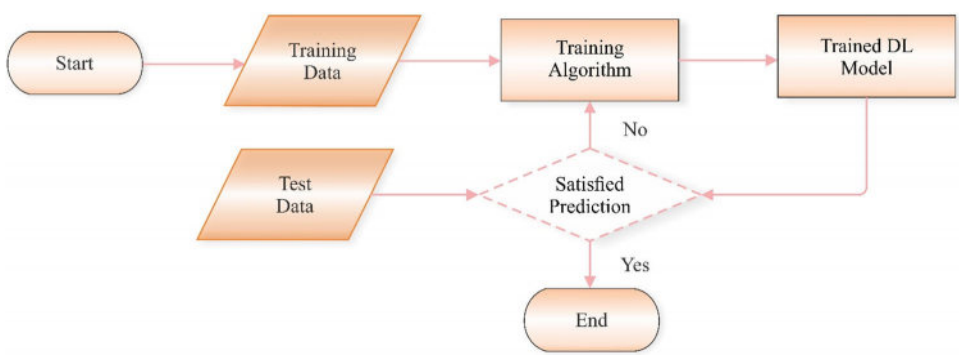

Fig. 7 Deep learning algorithm process

3.5 Deep learning

Deep Learning (DL) is a new area of ML research, which has been inspired by the mechanism of brain recognition. It allows computational models composed of multiple processing layers to learn representations of data with multiple levels of abstraction [41] and can be used in a supervised manner to develop accurate prediction models with given inputs and outputs. The flowchart illustrated in Fig. 7 represents the process of a (deep) neural network learning algorithm.

The schematic of a deep neural network architecture diagrams for a composite cylinder's data set using four fully connected layers is depicted in Fig. 8.

4 Results and discussion

In this paper, criteria involving MSE and MAE are used to evaluate the performance of the algorithms. The equations of these performance measures are as follows:

$$\mathrm{MSE} = \frac{1}{n}\sum_{i=1}^{n}\left(Y_i - \hat{Y}_i\right)^2, \tag{3}$$

$$\mathrm{MAE} = \frac{\sum_{i=1}^{n}\left|Y_i - \hat{Y}_i\right|}{n} = \frac{\sum_{i=1}^{n}|e_i|}{n}, \tag{4}$$

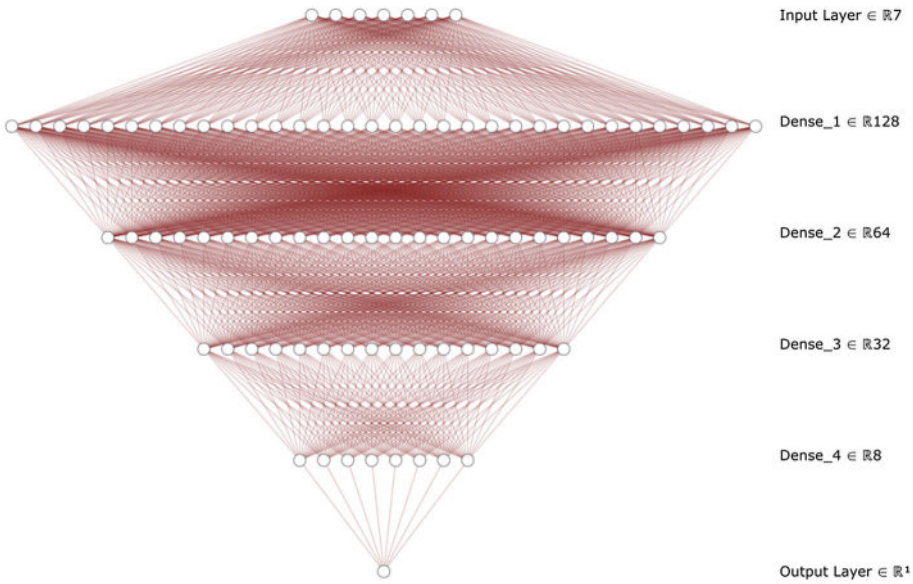

Fig. 8 Schematic of deep learning network architecture diagrams for a composite cylinder's data set

Table 1 Comparing the accuracy of different ML models trained for predicting buckling loads of composite cylinders

L/*R* ratio	Cost function	Multiple linear regression (MLR)	Regression decision tree (RDT)	Random forest (RF)	Deep learning (DL)
0.1	MSE	901.3962	643.0680	271.4959	101.4804
	MAE	25.0948	19.1160	13.4574	8.0374
0.2	MSE	97.3296	98.1023	47.6514	20.6507
	MAE	8.1993	7.4109	5.4918	3.4662
0.3	MSE	89.3885	47.6909	20.3716	8.7401
	MAE	7.6263	5.3485	3.5404	2.1514
0.4	MSE	108.0726	35.0119	16.3071	15.2123
	MAE	8.3965	4.6140	3.1210	3.0121
0.5	MSE	107.3713	35.7441	15.5056	14.1155
	MAE	8.3983	4.7057	3.0319	2.7656
0.6	MSE	107.3713	36.6218	14.6670	19.7918
	MAE	8.3984	4.7280	2.9467	3.2256
0.7	MSE	103.0849	29.1974	12.5686	7.3189
	MAE	8.2672	4.1517	2.7799	1.9247
0.8	MSE	104.6747	28.6885	12.4642	11.7946
	MAE	8.3484	4.0807	2.7608	2.4931
0.9	MSE	106.3005	30.9268	12.8439	7.5431
	MAE	8.4308	4.3105	2.7769	2.1223
1	MSE	107.4442	30.0477	12.8613	8.6533
	MAE	8.4788	4.1663	2.7992	2.2060
2	MSE	114.4586	32.7845	12.8608	8.6268
	MAE	8.7780	4.3127	2.8177	2.2071

where Y is the vector of observed values of the variable being predicted, with $\hat{Y}_i$ as the predicted values. Model predictions of the buckling load of composite cylinders made by fiber steering using four ML approaches are listed in Table 1.

The results demonstrate that the DL method can significantly improve the prediction accuracy of the buckling load of composite cylinders made by fiber steering compared to MLR, RDT, and RF. Figure 9 illustrates the history diagram of the DL method for the composite cylinder's data set for $L/R = 1$.

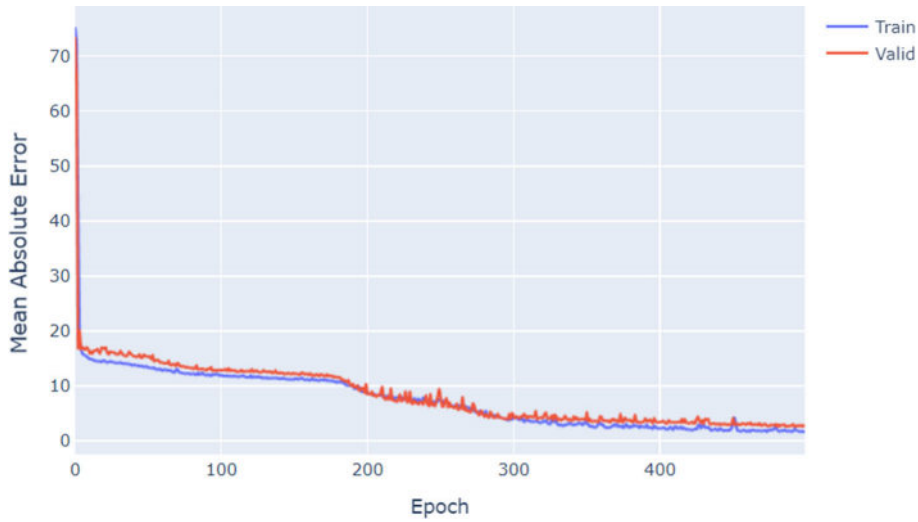

Fig. 9 The history diagram of the DL method for the composite cylinder's data at $L/R = 1$

5 Conclusion

This paper presented a comparative study and analysis between various regression techniques in ML for predicting the ultimate buckling load of variable-stiffness composite cylinders using data-driven metamodeling. In this study, Latin hypercube sampling (LHS) is used to generate parameters (fiber angles) of 1000 samples and 11 aspect ratios. To investigate the prediction models, the performance of Multiple Linear Regression, Decision Tree, Random Forest, and the DL model as supervised learning algorithms have been compared in terms of MSE and MAE. Among these methods, the proposed DL algorithm achieved the best MSE on most of the test problems. Also, the DL appeared to be more reliable and robust in terms of MAE. It is worth noting that the advantage of the DL can be further revealed with a more extensive data set.

Compliance with ethical standards

Conflict of interest The authors have no conflict of interest.

References

1. Gürdal, Z., Tatting, B.F., Wu, C.K.: Variable stiffness composite panels: effects of stiffness variation on the in-plane and buckling response. Compos. A Appl. Sci. Manuf. **39**(5), 911–922 (2008). https://doi.org/10.1016/j.compositesa.2007.11.015
2. Setoodeh, S., Abdalla, M.M., Ijsselmuiden, S.T., Gürdal, Z.: Design of variable-stiffness composite panels for maximum buckling load. Compos. Struct. **87**(1), 109–117 (2009). https://doi.org/10.1016/j.compstruct.2008.01.008
3. Kaveh, A., Dadras Eslamlou, A., Geran Malek, N.: Buckling load of laminated composite plates using three variants of the biogeography-based optimization algorithm. Acta Mech. **229**(4), 1551–1566 (2018). https://doi.org/10.1007/s00707-017-2068-0
4. Kaveh, A., Dadras Eslamlou, A., Geran Malek, N.: Optimum stacking sequence design of composite laminates for maximum buckling load capacity using parameter-less optimization algorithms. Eng. Comput. **35**(3), 813–832 (2019). https://doi.org/10.1007/s00366-018-0634-2
5. Kaveh, A., Dadras Eslamlou, A., Geran Malek, N.: Robust design optimization of laminated plates under uncertain bounded buckling loads. Struct. Multidiscip. Optim. **59**(3), 877–891 (2019). https://doi.org/10.1007/s00158-018-2106-0
6. Tatting, B.F.: Analysis and Design of Variable Stiffness Composite Cylinders. Virginia Tech, Tehran (1998)
7. Blom, A.W., Stickler, P.B., Gürdal, Z.: Optimization of a composite cylinder under bending by tailoring stiffness properties in circumferential direction. Compos. B Eng. **41**(2), 157–165 (2010). https://doi.org/10.1016/j.compositesb.2009.10.004
8. Khani, A., Abdalla, M.M., Gürdal, Z.: Circumferential stiffness tailoring of general cross section cylinders for maximum buckling load with strength constraints. Compos. Struct. **94**(9), 2851–2860 (2012). https://doi.org/10.1016/j.compstruct.2012.04.018
9. Sun, M., Hyer, M.W.: Use of material tailoring to improve buckling capacity of elliptical composite cylinders. AIAA J. **46**(3), 770–782 (2008). https://doi.org/10.2514/1.32495

10. Rouhi, M., Ghayoor, H., Hoa, S.V., Hojjati, M., Weaver, P.M.: Stiffness tailoring of elliptical composite cylinders for axial buckling performance. Compos. Struct. **150**, 115–123 (2016). https://doi.org/10.1016/j.compstruct.2016.05.007
11. Ghiasi, H., Fayazbakhsh, K., Pasini, D., Lessard, L.: Optimum stacking sequence design of composite materials part II: variable stiffness design. Compos. Struct. **93**(1), 1–13 (2010). https://doi.org/10.1016/j.compstruct.2010.06.001
12. Heydarpour, Y., Aghdam, M.M.: A coupled integral–differential quadrature and B-spline-based multi-step technique for transient analysis of VSCL plates. Acta Mech. **228**(9), 2965–2986 (2017). https://doi.org/10.1007/s00707-017-1850-3
13. Farsadi, T., Asadi, D., Kurtaran, H.: Nonlinear flutter response of a composite plate applying curvilinear fiber paths. Acta Mech. **231**(2), 715–731 (2020). https://doi.org/10.1007/s00707-019-02564-y
14. Forrester, A.I.J., Sóbester, A., Keane, A.J.: Multi-fidelity optimization via surrogate modelling. Proc. R. Soc. A: Math., Phys. Eng. Sci. **463**(2088), 3251–3269 (2007). https://doi.org/10.1098/rspa.2007.1900
15. Wang, G.G., Shan, S.: Review of metamodeling techniques in support of engineering design optimization. J. Mech. Des. **129**(4), 370–380 (2007)
16. Younis, A., Dong, Z.: Trends, features, and tests of common and recently introduced global optimization methods. Eng. Optim. **42**(8), 691–718 (2010). https://doi.org/10.1080/03052150903386674
17. Jin, R., Chen, W., Simpson, T.W.: Comparative studies of metamodelling techniques under multiple modelling criteria. Struct. Multidiscip. Optim. **23**(1), 1–13 (2001). https://doi.org/10.1007/s00158-001-0160-4
18. Rouhi, M., Rais-Rohani, M., Najafi, A.: Probabilistic analysis and optimization of energy absorbing components made of nanofiber enhanced composite materials. Compos. Struct. **100**, 144–153 (2013). https://doi.org/10.1016/j.compstruct.2012.12.037
19. Fang, H., Rais-Rohani, M., Liu, Z., Horstemeyer, M.F.: A comparative study of metamodeling methods for multiobjective crashworthiness optimization. Comput. Struct. **83**(25), 2121–2136 (2005). https://doi.org/10.1016/j.compstruc.2005.02.025
20. Kaveh, A., Dadras Eslamlou, A., Geran Malek, N., Ansari, R.: An open-source computational framework for optimization of laminated composite plates. Acta Mech. **231**(6), 2629–2650 (2020). https://doi.org/10.1007/s00707-020-02648-0
21. Kaveh, A., Geran Malek, N., Dadras Eslamlou, A., Azimi, M.: An open-source framework for the FE modelling and optimal design of fiber-steered variable-stiffness composite cylinders using water strider algorithm. Mechanics Based Design of Structures and Machines 1–18 (2020). (Accepted for publication)
22. Steuben, J., Michopoulos, J., Iliopoulos, A., Turner, C.: Inverse characterization of composite materials via surrogate modeling. Compos. Struct. **132**, 694–708 (2015). https://doi.org/10.1016/j.compstruct.2015.05.029
23. Rikards, R., Abramovich, H., Auzins, J., Korjakins, A., Ozolinsh, O., Kalnins, K., Green, T.: Surrogate models for optimum design of stiffened composite shells. Compos. Struct. **63**(2), 243–251 (2004). https://doi.org/10.1016/S0263-8223(03)00171-5
24. Haeri, A., Fadaee, M.J.: Efficient reliability analysis of laminated composites using advanced Kriging surrogate model. Compos. Struct. **149**, 26–32 (2016). https://doi.org/10.1016/j.compstruct.2016.04.013
25. Lopes, P.A.M., Gomes, H.M., Awruch, A.M.: Reliability analysis of laminated composite structures using finite elements and neural networks. Compos. Struct. **92**(7), 1603–1613 (2010). https://doi.org/10.1016/j.compstruct.2009.11.023
26. Arian Nik, M., Fayazbakhsh, K., Pasini, D., Lessard, L.: Surrogate-based multi-objective optimization of a composite laminate with curvilinear fibers. Compos. Struct. **94**(8), 2306–2313 (2012). https://doi.org/10.1016/j.compstruct.2012.03.021
27. Rouhi, M., Ghayoor, H., Hoa, S.V., Hojjati, M.: Effect of structural parameters on design of variable-stiffness composite cylinders made by fiber steering. Compos. Struct. **118**, 472–481 (2014). https://doi.org/10.1016/j.compstruct.2014.08.021
28. Rouhi, M., Ghayoor, H., Hoa, S.V., Hojjati, M.: Computational efficiency and accuracy of multi-step design optimization method for variable stiffness composite structures. Thin Walled Struct. **113**, 136–143 (2017). https://doi.org/10.1016/j.tws.2017.01.019
29. Rouhi, M., Ghayoor, H., Hoa, S.V., Hojjati, M.: Multi-objective design optimization of variable stiffness composite cylinders. Compos. B Eng. **69**, 249–255 (2015). https://doi.org/10.1016/j.compositesb.2014.10.011
30. Ghayoor, H., Rouhi, M., Hoa, S.V., Hojjati, M.: Use of curvilinear fibers for improved bending-induced buckling capacity of elliptical composite cylinders. Int. J. Solids Struct. **109**, 112–122 (2017). https://doi.org/10.1016/j.ijsolstr.2017.01.012
31. Arian Nik, M., Fayazbakhsh, K., Pasini, D., Lessard, L.: A comparative study of metamodeling methods for the design optimization of variable stiffness composites. Compos. Struct. **107**, 494–501 (2014). https://doi.org/10.1016/j.compstruct.2013.08.023
32. Luersen, M.A., Steeves, C.A., Nair, P.B.: Curved fiber paths optimization of a composite cylindrical shell via Kriging-based approach. J. Compos. Mater. **49**(29), 3583–3597 (2015). https://doi.org/10.1177/0021998314568168
33. Ye, F., Wang, H., Li, G.: Variable stiffness composite material design by using support vector regression assisted efficient global optimization method. Struct. Multidiscip. Optim. **56**(1), 203–219 (2017). https://doi.org/10.1007/s00158-017-1658-8
34. Systèmes, D.: Abaqus 6.10: Analysis User's Manual. Dassault Systèmes Simulia Corp, Providence (2010)
35. McKay, M.D., Beckman, R.J., Conover, W.J.: A comparison of three methods for selecting values of input variables in the analysis of output from a computer code. Technometrics **21**(2), 239–245 (1979)
36. Iman, R.L., Conover, W.J.: A distribution-free approach to inducing rank correlation among input variables. Commun. Stat. Simul. Comput. **11**(3), 311–334 (1982). https://doi.org/10.1080/03610918208812265
37. Stein, M.: Large sample properties of simulations using latin hypercube sampling. Technometrics **29**(2), 143–151 (1987). https://doi.org/10.1080/00401706.1987.10488205
38. Breiman, L., Friedman, J., Stone, C.J., Olshen, R.A.: Classification and Regression Trees. CRC Press, Boca Raton (1984)
39. Breiman, L., Friedman, J., Olshen, R.: Classification and Regression Trees. Routledge, Abingdon (2017)
40. Yildiz, B., Bilbao, J.I., Sproul, A.B.: A review and analysis of regression and machine learning models on commercial building electricity load forecasting. Renew. Sustain. Energy Rev. **73**, 1104–1122 (2017). https://doi.org/10.1016/j.rser.2017.02.023
41. LeCun, Y., Bengio, Y., Hinton, G.: Deep learning. Nature **521**(7553), 436–444 (2015). https://doi.org/10.1038/nature14539

Publisher's Note Springer Nature remains neutral with regard to jurisdictional claims in published maps and institutional affiliations.

Optimum stacking sequence design of composite laminates for maximum buckling load capacity using parameter-less optimization algorithms

A. Kaveh, A. Dadras & N. Geran Malek

Engineering with Computers
An International Journal for Simulation-Based Engineering

ISSN 0177-0667

Engineering with Computers
DOI 10.1007/s00366-018-0634-2

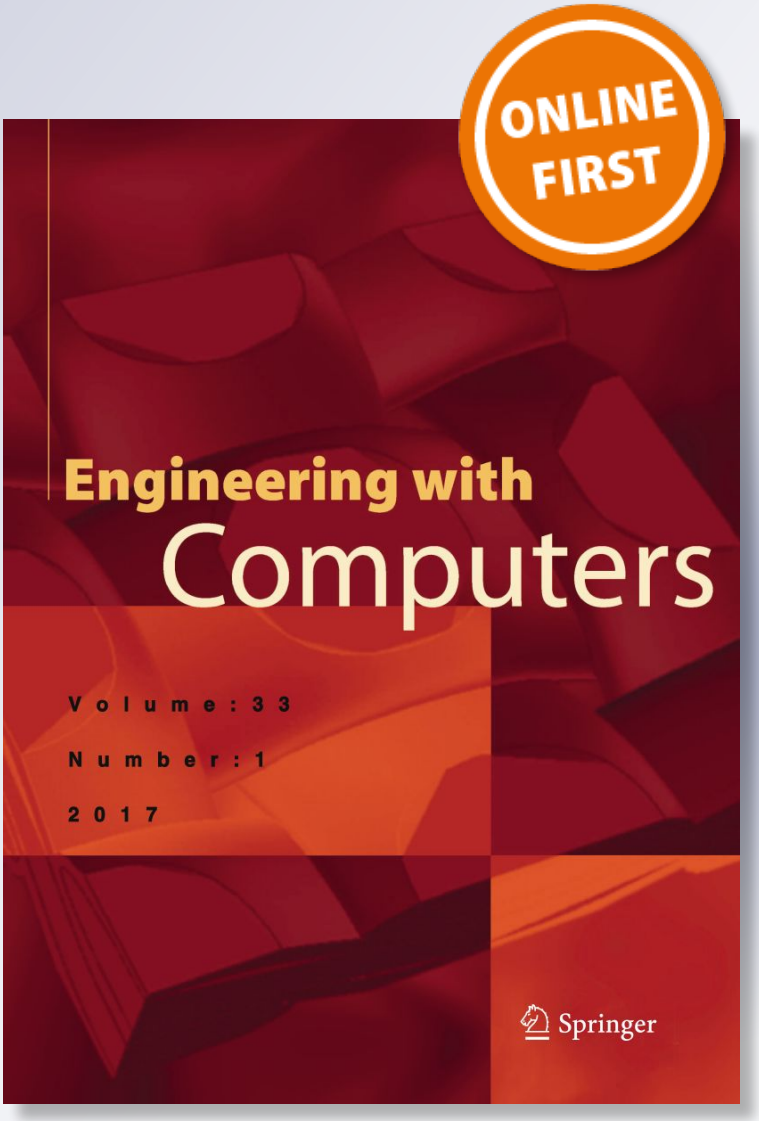

Springer

Your article is protected by copyright and all rights are held exclusively by Springer-Verlag London Ltd., part of Springer Nature. This e-offprint is for personal use only and shall not be self-archived in electronic repositories. If you wish to self-archive your article, please use the accepted manuscript version for posting on your own website. You may further deposit the accepted manuscript version in any repository, provided it is only made publicly available 12 months after official publication or later and provided acknowledgement is given to the original source of publication and a link is inserted to the published article on Springer's website. The link must be accompanied by the following text: "The final publication is available at link.springer.com”.

Springer

Author's personal copy

Engineering with Computers
https://doi.org/10.1007/s00366-018-0634-2

ORIGINAL ARTICLE

Optimum stacking sequence design of composite laminates for maximum buckling load capacity using parameter-less optimization algorithms

A. Kaveh[1] · A. Dadras[1] · N. Geran Malek[1]

Received: 4 June 2018 / Accepted: 10 August 2018
© Springer-Verlag London Ltd., part of Springer Nature 2018

Abstract
This paper presents a comparative study of the application of parameter-less meta-heuristic algorithms in optimum stacking sequence design of com of composite laminates for maximum buckling load capacity. Here, JAYA algorithm, along with Salp Swarm Algorithm, Colliding Bodies Optimization, Grey Wolf Optimizer, and Genetic Algorithm with standard setting and self-adaptive version are implemented to the problem of composite laminates with 64 graphite/epoxy plies with conventional ply angles, under several bi-axial cases and panel aspect ratios. Optimization objective is to maximize the buckling load of symmetric and balanced laminated plate. Statistical analysis are performed for six cases and the results are compared in terms of mean, standard deviation, the coefficient of variation, best and worst solutions, accompanied by the percentage of the independent runs that found the global optimum (R_{op}) and near global optimum (R_{no}). The Kruskal–Wallis nonparametric test is also utilized to make further confidence in the examinations. Numerical results show the high capability of the JAYA algorithm for maximizing the buckling capacity of composite plates.

Keywords Optimum stacking sequence design · Composite laminates · Maximum buckling load capacity · JAYA algorithm · Colliding bodies optimization · Grey wolf optimizer

1 Introduction

The increasingly structural applications of laminated composites are inevitable due to their outstanding properties such as high specific strength, stiffness, and lightweight. On the other hand, there exist some crucial parameters, such as laminate configurations including thickness, number of plies, fiber orientations, and aspect ratio, which may considerably affect the behavior of such substructures under different circumstances. Design and optimization of laminated composites to achieve the desired mechanical performance has attracted a great attention of researchers [25, 33, 50].

In the field of stacking sequence design optimization of laminated composites, earlier works were based on classical gradient-based methods with considering the design variables as continuous [19, 24]. Since the manufacturing process restricted the imposed continuous variables to be discrete, such classical methods resulted in limited success [27]. In addition, the stacking sequence design optimization involves multimodal search spaces, which may converge gradient-based methods into local optimal regions [4, 56]. The drawbacks of these gradient-based methods can be avoided using meta-heuristics stochastic search methods [10, 27, 28, 56, 57, 60]. Simple concept, derivation-free mechanism, the flexibility of employing for different problems, and global search ability of stochastic optimization algorithms, make them well-suited for solving most of the complex optimization problems with affordable computational time and accuracy [27, 28]. In the following, some of the significant works, which applied these meta-heuristics to the engineering problems of optimization of composite structures, are presented.

In the past few decades, a considerable amount of research has been carried out on the optimization of composite

Electronic supplementary material The online version of this article (https://doi.org/10.1007/s00366-018-0634-2) contains supplementary material, which is available to authorized users.

✉ A. Kaveh
alikaveh@iust.ac.ir

[1] Centre of Excellence for Fundamental Studies in Structural Engineering, Iran University of Science and Technology, Tehran, Iran

Published online: 16 August 2018

Author's personal copy

structures. The comprehensive reviews on the classification and comparison of optimization methods used for optimal lay-up selection of laminated composite structures are presented in [14, 15]. In these reviews, various classifications were suggested, including the four classifications described as follows: (1) An approach suggested by Venkataraman and Haftka [58], in which they categorized the procedure as two single laminate and stiffened plate design. (2) Abrate [3] classified the problems according to the objective functions. (3) Fang and Springer [11] used four categories for the designing approach, i.e., analytical methods, enumeration procedures, heuristic approaches, and nonlinear programming. (4) Setoodeh et al. [55] considered two approaches for the design of a composite structure, i.e., constant stiffness that the aim is to obtain an optimum stacking sequence for the entire structure material distribution and variable stiffness which fiber orientation might change over the domain of the structure.

Specialized genetic algorithms have been developed by Haftka and his coworkers to solve the problem of stacking sequence design optimization of composite structures for buckling load maximization [34, 35, 37, 56]. Lin and Lee [36] showed that replacing real calculations of the standard GA with a precise regression model affects the convergence rate of the solution. Almeida and Awruch [4] employed genetic algorithms with special operators associated with finite element analysis to evaluate the buckling strength of the structure, for the multi-objective minimization of the deflection and weight of laminated plates. Recently, buckling optimization of functionally graded carbon nanotube-reinforced laminated composite (FG-CNTRC) quadrilateral plates with different patterns of CNT distributions was conducted by Setoodeh and Shojaee [54]. Optimization of critical buckling loads was performed with the design parameter being fiber orientations.

In most of the studies GA was adopted as the optimization tools [40, 52], nevertheless a few other meta-heuristics have also been applied to the problem of laminated composite design optimization. For instance, scatter search algorithm was adopted by Rao and Arvind [47], direct simulated annealing by Erdal and Sonmez [10], Fractal Branch and Bound by Matsuzaki and Todoroki [39]. Pai et al. [46], treated the problem with Tabu Search algorithm. Karakaya and Soykasap [26] compared the performance of the genetic algorithm (GA) and generalized pattern search algorithm (GPSA) on the problem of maximum buckling load of simply supported symmetric and balanced laminated plate consists of 64 graphite/epoxy plies for several bi-axial load cases and panel aspect ratios. In [43–45] the Vector Evaluated Particle Swarm Optimization (VEPSO), Quantum behaved Particle Swarm Optimization (QPSO), and Vector Evaluated Artificial Bee Colony (VEABC), based on PSO and ABC, respectively, were adopted for the multi-objective optimization of composite structures. Attaran et al. [5] discussed the optimization of stacking sequence with the application to flutter speed of a cantilevered laminated composites plate. de Almeida [7], has been recently explored the performance of the harmony search algorithm (HSA) in the optimization of the stacking sequence of laminated composites. Sebaey et al. [53] conducted a study about using the dispersed laminates over conventional, 0°, ±45° and 90°, orientations, through the Ant Colony Optimization algorithm (ACO). In addition, the same method was adopted by Abachizadeh and Tahani [1] to find the maximum fundamental frequency and minimum cost of symmetric hybrid laminates. Vosoughi et al. [59], maximized the buckling load of thick laminated composites through coupling finite element method (FE), genetic algorithms (GAs) and particle swarm optimization (PSO). The thick laminated composite plate was analyzed in the framework of higher order shear deformation theory. Abhishek et al. [2] made a comparison between the performance of different optimization algorithms for multi-response optimization route for selection of optimal process parameter setting during the machining of CFRP by integrating nonlinear regression modeling, and fuzzy inference system. Recently, Kaveh et al. [29] applied Biogeographic Based Optimization (BBO) algorithm for buckling load capacity optimization of laminated composite plates, different variants of BBO were applied to four load cases and the results were statistically investigated and compared with those of some other well-established meta-heuristics.

The performance of the Jaya algorithm has been examined in the recent studies conducted by some of the researchers. Among these studies, one can refer to the study of extending the Jaya algorithm by Du et al. [9] for solving the optimization-based damage identification problems. Rao and Waghmare [49] examined the performance of Jaya algorithm on a class of constrained design optimization problems. Ghavidel et al. [13] have proposed a hybrid enhanced Jaya algorithm for reliability–redundancy problems.

One of the challenges in solving the optimization problems with evolutionary and swarm intelligence-based algorithms is the difficulty in the determination of their ideal controlling parameters, such as population size, crossover and mutation rates in GA, inertia weight, social and cognitive parameters in PSO. Finding the ideal parameters is itself an optimization task and sometimes the inappropriate parameter setting may distract the users from the main problem and disturb the performance of algorithms. For instance, de Almeida [7] demonstrated that the harmony memory size (HMS), harmony memory consideration rate (HMCR) and pitch adjusting rate (PAR) have an apparent effect on the reliability of the algorithm on the optimization of laminated composites. From this point of view, the parameter-less algorithms are at an advantage. In this regard, this paper

Author's personal copy

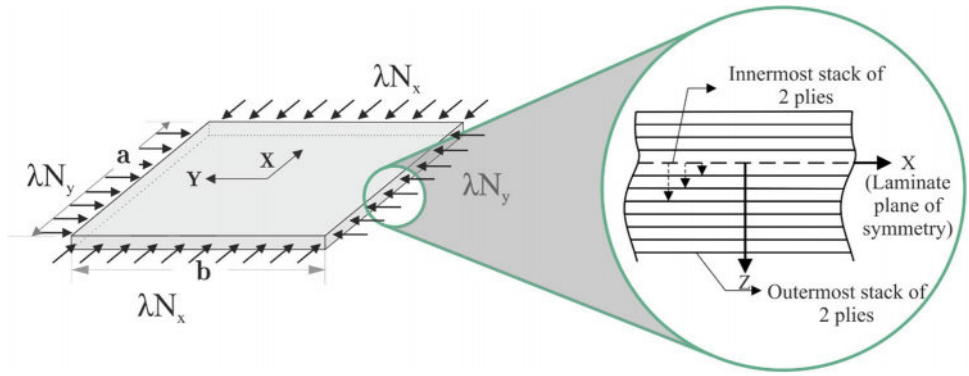

Fig. 1 Schematic representation of symmetric laminated composite

presents the application of four parameter-less algorithms, i.e. JAYA Algorithm [48], Salp Swarm Algorithm (SSA) [41], Colliding Bodies Optimization (CBO) [32], Grey Wolf Optimizer (GWO) [42], and Genetic algorithms with standard setting and self-adaptive version [8, 22] on the problem of stacking sequence optimization for maximum buckling load of laminated composites. Moreover, in some cases, the related results are also reported from the literature and are compared. Herein, the composite structures are made up of 64 graphite/epoxy plies with conventional ply angles, for several bi-axial loading and panel aspect ratios.

The remainder of this paper is organized as follows: The mathematical formulations of the composite laminates and objective function are described in Sect. 2. In Sect. 3, a comprehensive description of the applied algorithms is provided. In Sect. 4, the numerical experiments are investigated and different comparisons are conducted. Since solutions for some cases are massive, they are appended in Appendix A and Appendix B. The conclusions are derived in the last section.

Table 1 Properties of the investigated numerical examples

Case	a (cm)	b (cm)	N_x (N/m)	N_y (N/m)
1	50.8	25.4	1	0.5
2	50.8	25.4	1	1
3	50.8	25.4	1	2
4	50.8	101.6	1	0.5
5	50.8	101.6	1	1
6	50.8	101.6	1	2

Table 2 Mechanical properties of graphite/epoxy

Property	Graphite/epoxy
Young's modulus, E_1, GPa (psi)	127.55 (18.5)
Young's modulus, E_2, GPa (psi)	13.03 (1.89)
Shear modulus, G_{12}, GPa (psi)	6.41 (0.93)
Poisson rate, ν_{12}	0.3
Lamina thickness, mm (in)	0.127 (0.005)

2 Problem statement

Buckling failure is one of the main critical failure modes in laminated composite structures under in-plane compressive loads, hence, the studying of the buckling performance of these structures is crucial. The schematic diagram of the geometry of a simply supported composite laminate, subjected to an in-plane compressive load, is shown in Fig. 1. It has a total thickness of $t = 8.128$ mm for all cases and The geometry and loading of each case are affected by six combinations of a, b, N_x and N_y, as listed in Table 1, according to [26].

The investigated laminated composite is assumed balanced, symmetric and comprised of 64 plies made of graphite/epoxy, with two-ply stacks 0_2, ± 45 and 90_2. In Table 2, the mechanical properties of graphite/epoxy are given.

As aforesaid, 0_2 and 90_2 state two contiguous stacks with 0° and 90°, ± 45 is also utilized as contiguous stacks with $+45°$ and $-45°$, so that the balanced conditions are guaranteed [21]. The laminate is symmetric; hence, the number of design variables is reduced from 64 to 16. The objective function is the maximization of the critical buckling load factor λ_{cb} and can be stated by the following equation [20, 50]::

$$\text{Maximize} \ : \ \lambda_{cb} = \pi^2 \left[\frac{m^4 D_{11} + 2\left(D_{12} + D_{66}\right)(\text{rmn})^2 + (\text{rn})^4 D_{22}}{(\text{am})^2 N_x + (\text{bn})^2 N_y} \right], \tag{1}$$

where a and b are the plate length and width, respectively; $r = a/b$ is the aspect ratio. N_x and N_y stand for the loads in the x and y directions, repectively. The buckling loads can be obtained by inserting different values of m and n, which are the number of half waves in the x and y directions, respectively. Here, the smallest of $\lambda_b(1,1)$, $\lambda_b(1,2)$, $\lambda_b(2,1)$ and $\lambda_b(2,2)$ is taken as the critical buckling load. In Eq. [1], the bending stiffness coefficients D_{16} and D_{26} are neglected because of the laminates formed by plies with angles $\pm\theta$ in sequence [26]. λ_{cb} can be found using combinations of m and

Author's personal copy

n that yield the lowest buckling load. In the implementation of the real-coded algorithms (JAYA, CBO, GWO, and SSA), two-ply stacks with 0_2, ± 45 and 90_2 degrees are replaced by integers 1, 2 and 3, respectively. For other algorithms (standard and self-adaptive GA), the binary encoding of these integers (01, 10 and 11) are utilized. Additionally, the results sequences are in the order of coming from the outermost lamina to the innermost one (Fig. 1). The design space consisted of 3^{16} different configuration.

3 Optimization algorithms

The details of the utilized meta-heuristics are presented in the following sections. Except for GA, other algorithms are parameter-less, which only require the definition of population size and the number of iterations. To avoid the complexities of parameter tuning which is one of the priorities of the present paper, the population size and number of iterations are set as 50 and 100, respectively, as suggested in [7, 29].

3.1 JAYA algorithm

The new global search population-based algorithm (JAYA) is proposed by Rao [48]. Simplicity and high efficiency of this method were shown by implementing on various constrained and unconstrained benchmark problems [48]. The concept of this method is exploring the best solution while avoiding the worst one, hence it is named as a Sanskrit word meaning victory, i.e., JAYA. One of the significant features of this algorithm is that JAYA needs no algorithm-specific parameter. Consequently, population size and the number of iterations are the only two required standard controlling parameters.

The solution updating of JAYA algorithm is performed by the following equation:

$$X'_{j,k,i} = X_{j,k,i} + r_{1,j,i}\left(X_{j,\text{best},i} - \left|X_{j,k,i}\right|\right) - r_{2,j,i}\left(X_{j,\text{worst},i} - \left|X_{j,k,i}\right|\right) \tag{2}$$

In the above equation, $X'_{j,k,i}$ is the updated value of the $X_{j,k,i}$. Here, $r_{1,j,i}$ and $r_{2,j,i}$ are two random numbers ranged from 0 to 1, during the ith iteration, to ensure the better exploration in the search space. Number of design variables and population size, are indicated by 'm' ($j = 1, 2, \ldots, m$), and 'n' ($k = 1, 2, \ldots, n$), respectively. Moreover, $X_{j,\text{best},i}$, and $X_{j,\text{worst},i}$ denoted the best and worst solution, out of all candidate solutions in that iteration. In Eq. [2], the terms "$r_{1,j,i}\left(X_{j,\text{best},i} - \left|X_{j,k,i}\right|\right)$" and "$-r_{2,j,i}\left(X_{j,\text{worst},i} - \left|X_{j,k,i}\right|\right)$", respectively represent that the solution attempts to move towards the best solution and avoid the worst one. The presentation of Eq. [2] in 2D space can be seen in Fig. 2.

At the end of each iteration, if the value of the objective function improves, the updated position ($X'_{j,k,i}$) participates in the next iteration. The aforementioned procedure continues until the termination conditions are met. The maximum number of iterations is considered as the termination condition. A flowchart of the JAYA algorithm is presented in Fig. 3.

The pseudo code of JAYA algorithm is as follows:

```
Randomly initialize the population
Calculate the fitness of each search agent
Sort Population
Find the best and worst solutions
while (i<Max number of iterations)
        for each search agent
                Update the position by Eq. (2)
                Calculate the fitness of search agent
        end for
    Sort Population
    Update the best and worst solutions
    i=i+1
end While
Return the best solution
```

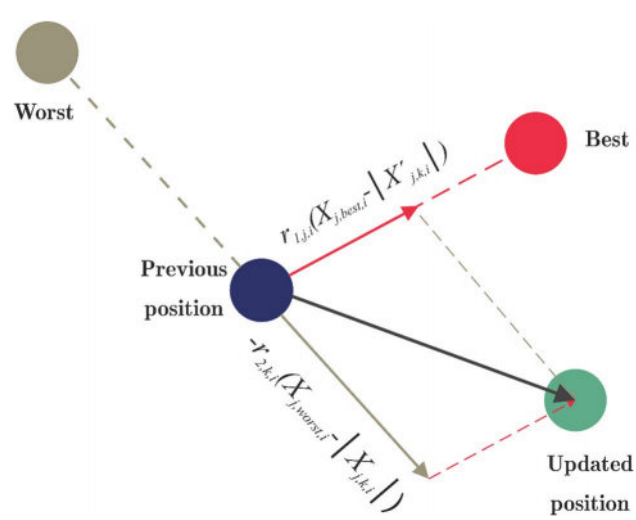

Fig. 2 A schematic of position updating in JAYA algorithm

Author's personal copy

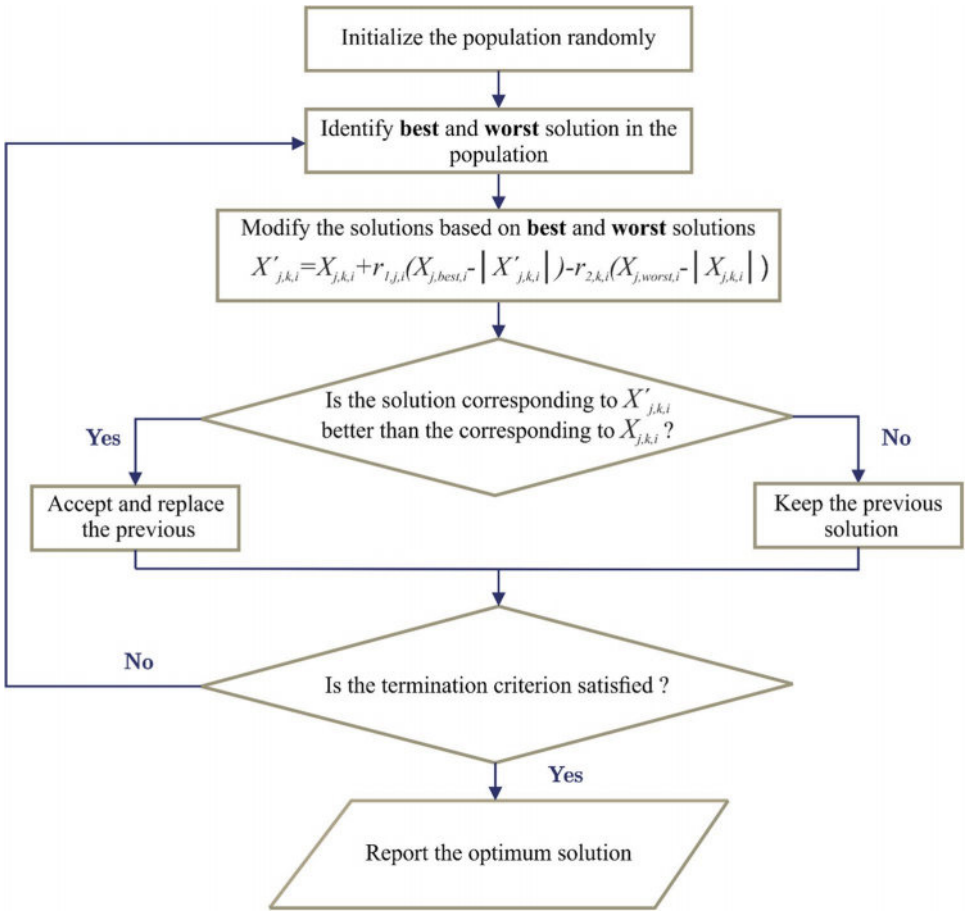

Fig. 3 Flowchart of the JAYA algorithm

3.2 Grey wolf optimizer

One of the impressive aspects of the social life of wolves is their hierarchy structure at group hunting. Grey Wolf Optimizer (GWO) [42] inspired by the leadership hierarchy and hunting behavior of them in nature. Social hierarchy, tracking (exploration) the prey, encircling it, and attacking (exploitation) is the main four sections of the GWO algorithm. Herein, all the wolves are categorized as alpha (α), beta (β), delta (δ), and omega (ω), which respectively, represent the first, second, third, and other remaining candidate solutions. The roles and the status of each of them in the hierarchy are illustrated in Fig. 4.

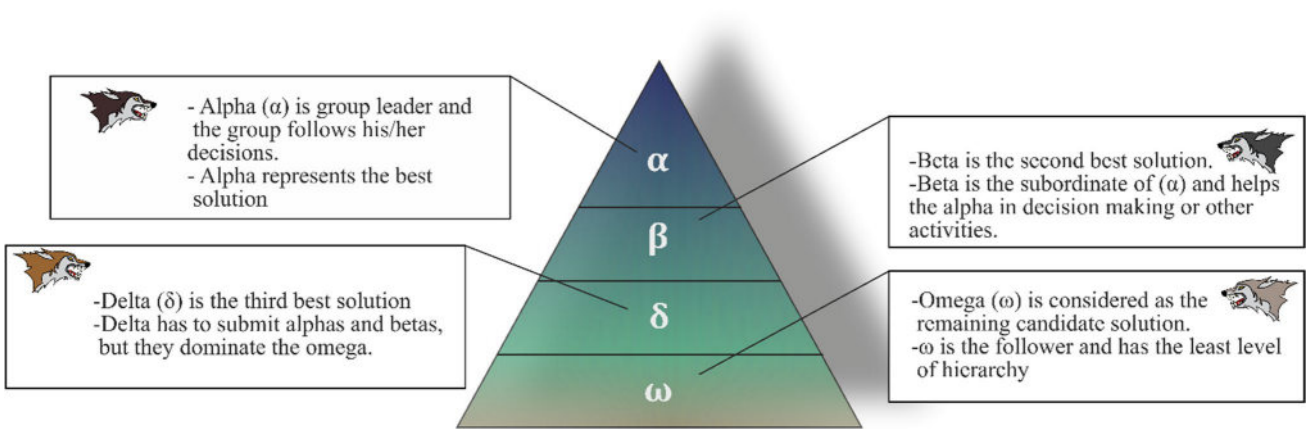

Fig. 4 The social hierarchy of a pack of grey wolves

Author's personal copy

By considering that alpha, beta, and delta have better knowledge about the potential location of prey and the other wolves follow them, the following equation shows the updated position of each wolf at $(t+1)$th iteration:

$$X^{t+1} = \frac{1}{3}\left(X_1^t + X_2^t + X_3^t\right) \tag{3}$$

where X_1^t, X_2^t, and X_3^t are calculated by Eqs. (4, 5, 6), respectively.

$$X_1^t = X_\alpha^t - A_1.D_\alpha \tag{4}$$

$$X_2^t = X_\beta^t - A_2.D_\beta \tag{5}$$

$$X_3^t = X_\delta^t - A_3.D_\delta \tag{6}$$

Here, X_α^t, X_β^t, and X_δ^t are the positions of the three best solutions. A_i is a random vector in the interval [-2a, 2a], where a is linearly decreased from 2 to 0 over the cycles of optimization. The D vectors mathematically simulate the encircling behavior by the following equations:

$$D_\alpha = \left|C_1.X_\alpha^t - X^t\right| \tag{7}$$

$$D_\beta = \left|C_2.X_\beta^t - X^t\right| \tag{8}$$

$$D_\delta = \left|C_3.X_\delta^t - X^t\right| \tag{9}$$

where C_i is a random vector whose arrays are between 0 and 2.

The pseudo code of the GWO algorithm is provided as follows:

Initialize the grey wolf population $X_i (i = 1,2,\ldots,n)$
Calculate the fitness of each search agent
Identify X_α, X_β, *and* X_δ
While *(t<Max number of iterations)*
    for *each search agent*
        Update the position of the current search agent by Eq. (3)
    end for
    Update a, A, and C
    Calculate the fitness of all search agents
    Update X_α, X_β, *and* X_δ
    t=t+1
end while
Return X_α

The flowchart of GWO is demonstrated in Fig. 5.

3.3 Colliding bodies optimization

Colliding bodies optimization (CBO) algorithm [30–32], is a new method inspired by the conservation of linear momentum and kinetic energies. The algorithm includes some CBs colliding with each other for exploration in the search space. The mass of each CB is defined according to the following equation:

$$m_k = \frac{\frac{1}{fit(k)}}{\frac{1}{\sum_{i=1}^{n}\frac{1}{fit(i)}}}, \quad k = 1,\ 2,\ \ldots,\ n \tag{10}$$

In the Eq. [10], fit(i) represents the value of the objective function for the ith CB and n is the number of CBs. After sorting the CBs according to the associated masses in

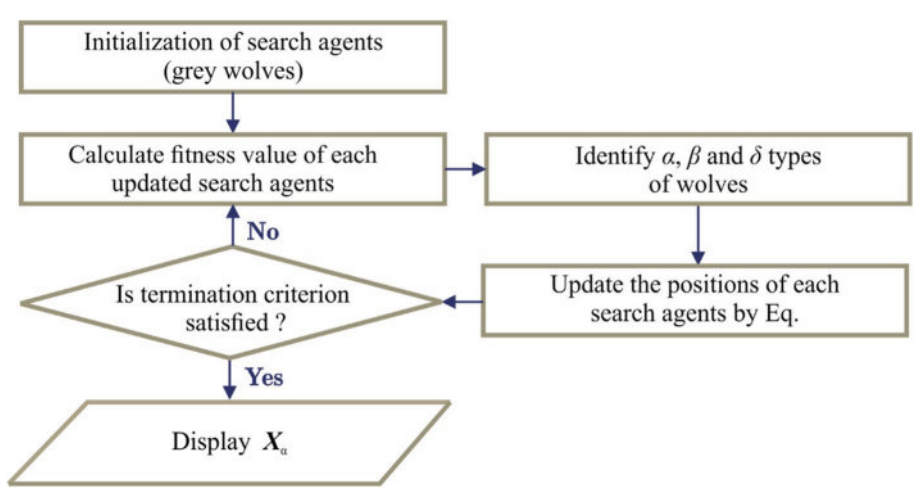

Fig. 5 Flowchart of the GWO

Author's personal copy

an ascending order, (1) stationary, and (2) moving groups are created. Moving objects, by colliding to the stationary objects, bring them to the new positions. Following expressions represent the velocities of the stationary and moving CBs before (v_i) and after the collision (v_i'), respectively:

$$\boldsymbol{v}_i = 0, \quad i = 1,\ 2,\ \ldots,\ \frac{n}{2} \tag{11}$$

$$\boldsymbol{v}_i = \boldsymbol{x}_{i-\frac{n}{2}} - \boldsymbol{x}_i, \quad i = \frac{n}{2}+1,\ \frac{n}{2}+2,\ \ldots,\ n \tag{12}$$

$$\boldsymbol{v}_i' = \frac{\left(m_{i+\frac{n}{2}} + \varepsilon m_{i+\frac{n}{2}}\right)\boldsymbol{v}_{i+\frac{n}{2}}}{m_i + m_{i+\frac{n}{2}}}, \quad i = 1,\ 2,\ \ldots,\ \frac{n}{2} \tag{13}$$

$$\boldsymbol{v}_i' = \frac{\left(m_i - \varepsilon m_{i-\frac{n}{2}}\right)\boldsymbol{v}_i}{m_i + m_{i-\frac{n}{2}}}, \quad i = \frac{n}{2}+1,\ \frac{n}{2}+2,\ \ldots,\ n \tag{14}$$

$$\varepsilon = 1 - \frac{\text{iter}}{\text{iter}_{\max}}, \tag{15}$$

where $\boldsymbol{x}_i$ is a vector representing the position of the ith colliding body. ε is the Coefficient of Restitution (COR), iter is the current iteration number and $\text{iter}_{\max}$ is the total number of iterations. New position vectors of each group are calculated by:

$$\boldsymbol{x}_i^{\text{new}} = \boldsymbol{x}_i + \text{rand}\circ\boldsymbol{v}_i', \quad i = 1,\ 2,\ \ldots,\ \frac{n}{2} \tag{16}$$

$$\boldsymbol{x}_i^{\text{new}} = \boldsymbol{x}_{i-\frac{n}{2}} + \text{rand}\circ\boldsymbol{v}_i', \quad i = \frac{n}{2}+1,\ \frac{n}{2}+2,\ \ldots,\ n \tag{17}$$

where $\boldsymbol{x}_i^{\text{new}}$ is the new position vector of the ith colliding body. In addition, rand generates a uniformly distributed random vector between 0 and 1. While, the symbol "$\circ$" represents the element-by-element multiplication between two vectors. The flowchart of the CBO is shown in Fig. 6.

The pseudo code of the CBO algorithm is:

The pseudo code of the CBO algorithm is

Randomly initialize the positions of $N(=2n)$ number of CBs

while *(t<the maximum number of iterations)*

  Evaluate the objective function and the masses of the new position (X)

  Sort CBs in an ascending order

  Calculate the coefficient of restitution (ε) by Eq. (15)

  for *j=1 to n*

    Calculate the velocity of the stationary body pair before collision by Eq. (11)

    Calculate the velocity of moving body pair before collision by Eq. (12)

    Evaluate the velocity of the stationary body pair after the collision by Eq. (13)

    Evaluate the velocity of moving body pair after the collision by Eq. (14)

    Evaluate the position of the stationary body after the collision by Eq. (16)

    Evaluate the position of moving body after the collision by Eq. (17)

  end for

  t=t+1

end while

Return the heaviest CB

Author's personal copy

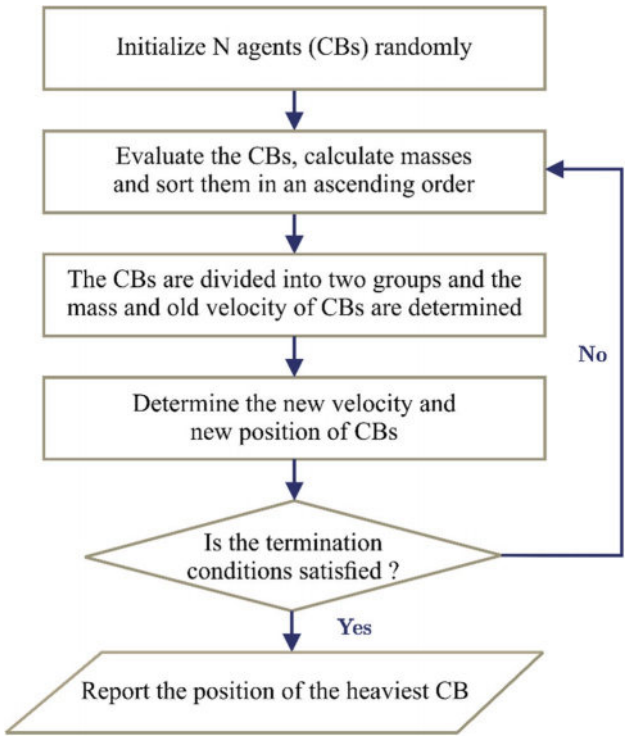

Fig. 6 Flowchart of the CBO algorithm

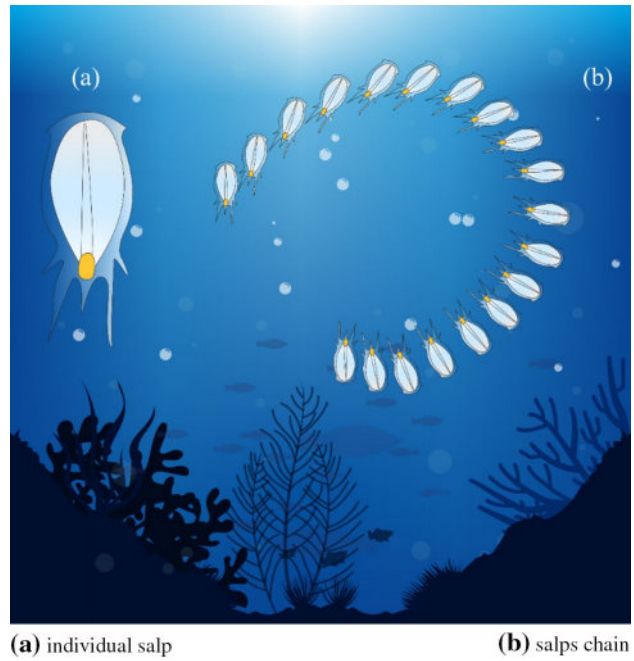

Fig. 7 The swarming behavior of salps

3.4 Salp swarm algorithm

Recently, another nature-inspired algorithm is proposed by Mirjalili et al. [41], which mimics the behavior of salps. According to researchers, salps made swarms together to achieve effective locomotion, rapid coordinated changes, and foraging. An individual of salp and salps chain are schematically illustrated in Fig. 7. This behavior was imitated in mathematical form in Salp Swarm Algorithm (SSA).

This algorithm updates the position of the salps by the following equations:

$$x_j^1 = \begin{cases} F_j + c_1\left(\left(ub_j - lb_j\right)c_2 + lb_j\right) & c_3 \geq 0 \\ F_j - c_1\left(\left(ub_j - lb_j\right)c_2 + lb_j\right) & c_3 < 0 \end{cases} \tag{18}$$

$$x_j^i = \frac{1}{2}\left(x_j^i + x_j^{i-1}\right), \tag{19}$$

where F_j is the position of the food source in the jth dimension, ub_j and lb_j show the upper and lower bound of the jth dimension, respectively. c_2 and c_3 are random numbers, while c_1 is calculated by:

$$c_1 = 2\mathrm{e}^{-\left(\frac{4l}{L}\right)^2}, \tag{20}$$

where l is the number of current iteration and L is the maximum number of iterations.

The pseudo code of the SSA algorithm is mentioned in the following:

Author's personal copy


```
Randomly initialize the salp population
while (l<Max number of iterations(L))
Calculate the fitness of each search agents (salps)
Sort and label the search agents in increasing order
Set the best search agent as F
Update c1 by Eq. (20)
    for each salp (xi)
        if (i==1)
            Update the position of the leading salp by Eq. (18)
        else
            Update the position of the follower salp by Eq. (19)
        end if
    end for
    l=l+1
end while
Return F
```

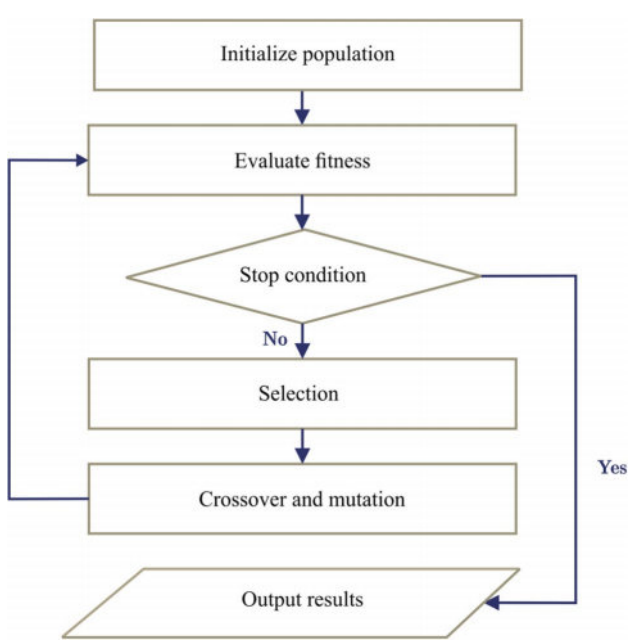

Fig. 8 Flowchart of the GA

3.5 Genetic algorithm

Genetic algorithm (GA) is a well-known search method based on the rules of Darwin's theory of evolution [16, 18]. In GA, the new solutions are generated by crossover and mutation operators. Crossover is a process in which the parent solutions reproduce one or more child solutions through the combination of their chromosomes. The parent selection is usually a probabilistic process that the probability of selection decreases with the cost of the individual. The mutation operator mimics the biological mutation by altering some of the gene values in a chromosome. Thus here, unlike the previous algorithms, the GA is surrounded by parameters and probabilities which must be regulated. Several researchers attempted to address this issue [8, 22, 38]. For instance, De Jong [8] examined the various combination of parameters on different functions and concluded that a specific parameter setting can be considered as the standard setting, also, Harik and Lobo [22] introduced a self-adaptive version to get rid of the parameters of the GA. These algorithms are implemented and their results are investigated and compared with other parameter-less algorithms. In the next subsections, both the "standard" and "self-adaptive" GAs are described in detail.

Author's personal copy

3.5.1 Standard GA

In this algorithm, the binary encoding is conducted for representation of the discrete variables. After random initialization of the population, the objective function for each chromosome is evaluated. While the termination condition is not met, the selection, crossover and mutation operators are repeated to update the generations. The roulette wheel selection is considered as the selection operator [17]. The reproduction is performed using one-point crossover operator [6]. In the next step, one of the gene values of each individual is randomly selected and replaced with an allowable random value for the mutation of the population.

Table 3 Statistical results of different methods for case 1

	Mean	Best	Worst	STD	$R_{no}(\%)$	$R_{op}(\%)$
JAYA	**1057882.119**	**1057948.319**	**1057288.046**	**112.1585**	**100**	**64**
GWO	1056228.152	**1057948.319**	1045596.214	2566.9284	91	23
SSA	1053510.039	**1057948.319**	1029836.755	5414.4933	73	3
CBO	1057742.557	**1057948.319**	1055873.175	357.6208	**100**	44
Standard GA	1057591.975	**1057948.319**	1055212.902	491.4215	**100**	31
Self-adaptive GA	1057780.553	**1057948.319**	1056636.387	252.8838	**100**	44

The best results are in bold

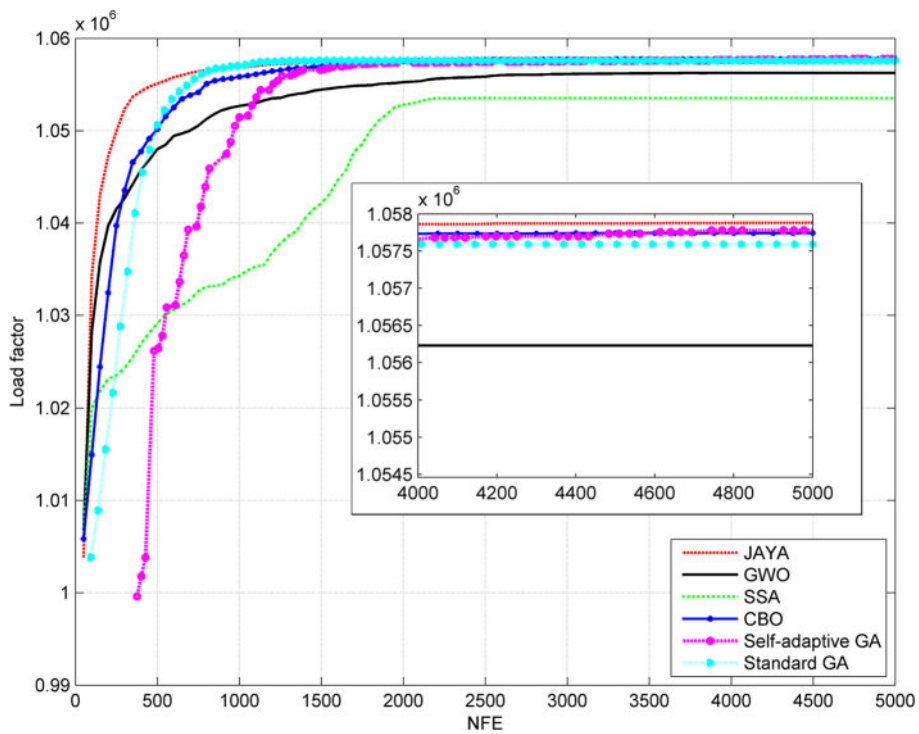

Fig. 9 Mean of the convergence histories for Case 1

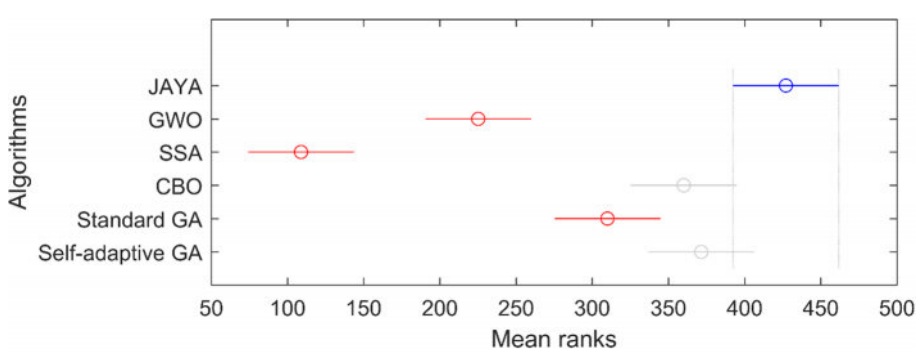

Fig. 10 The visualization of Kruskal–Wallis nonparametric test for Case 1

Author's personal copy

According to [22], the population size, crossover probability, and mutation probability are considered as 50, 0.6 and 0.001, respectively. The flowchart of this algorithm can be seen in Fig. 8.

3.5.2 Self-adaptive GA

For the sake of brevity, only the differences of this algorithm with standard GA are discussed. This version of GA is based on establishing a race among multiple populations with different population sizes [8]. Three groups containing n, $2n$ and $4n$ number of populations are randomly initialized. If the iteration number is devisable by 16, the algorithm runs with the largest population, if the iteration number is devisable by 4, it runs the population with $2n$ individuals, otherwise, the low population group is ran. After generating three groups, the average of cost values of each group is calculated. If the average of cost values of a small population is higher than the larger population, individuals of the small group will be removed and it will adopt the population of the larger group, otherwise, the new iteration will be performed. In this version, the mutation is ignored and the crossover probability and selection rate are equal to 0.5 and 4, respectively.

4 Results and discussions

In this section, λ_{cb} is optimized for six numerical examples using the proposed algorithms. The algorithms are implemented for each case and executed 100 times, independently. To assess the efficiency of the proposed algorithms, the statistical results are compared in terms of mean, standard deviation, the coefficient of variation, the best and worst solutions accompanied by the non-parametric test. In addition,

Table 4 Statistical results of different methods for case 2

	Mean	Best	Worst	STD	$R_{no}(\%)$	$R_{op}(\%)$
JAYA	**695745.4362**	**695781.3202**	**695509.7023**	**51.0602**	**100**	**31**
GWO	695000.5769	**695781.3202**	687687.8223	1458.7457	96	12
SSA	694190.4493	**695781.3202**	686838.8998	1984.3597	87	4
CBO	695692.7269	**695781.3202**	694513.77	146.8093	**100**	12
Standard GA	695446.3614	**695781.3202**	693231.4561	501.1979	**100**	7
Self-adaptive GA	695553.8902	**695781.3202**	693879.9949	303.8557	**100**	4
BBO [29]	695724.44	**695781.32**	–	63.68	**100**	18
HS [29]	695559.79	**695781.32**	–	203.49	**100**	4

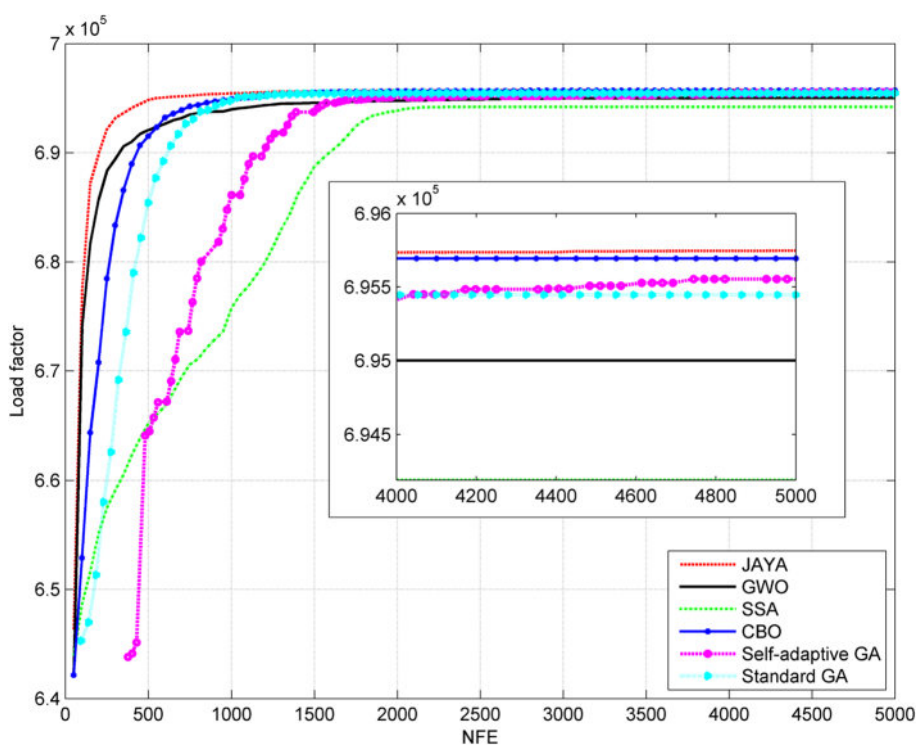

Fig. 11 Mean of the convergence histories for case 2

Author's personal copy

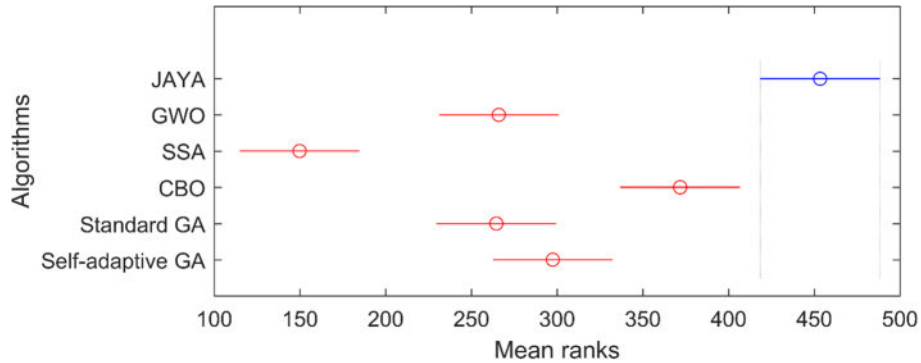

Fig. 12 The visualization of Kruskal–Wallis nonparametric test for case 2

the percentage of the independent runs that successfully ended up in the global optimum (R_{op}) and near global optimum $\left(R_{no}\right)$, out of all 100 runs, are also reported. Those results higher than 0.995 of the global optimum is defined as the near global optimum for calculating R_{no}. Moreover, the convergence histories of the average of load factors are provided for all cases. The number of populations and iterations are considered as 50 and 100, respectively. In other words, the Number of Function Evaluations (NFEs) is limited to 5000 for all the considered algorithms. It should be mentioned that, the saving all designs and objective values requires a considerable memory, hence all designs are evaluated separately, including repeated and non-repeated ones.

The Kruskal–Wallis nonparametric one-way analysis is also performed to test null hypothesis [12, 23, 51]. It uses the ranks of the data, rather than numeric values, to compute the test statistics. The Kruskal–Wallis test is a nonparametric version of the classical one-way ANOVA, and an extension of the Wilcoxon rank sum test to more than two groups. The F-statistic used in classical one-way ANOVA is replaced by a Chi-square statistic, and the p value measures the significance of the Chi-square statistic.

4.1 Case 1

The results of the statistical analysis conducted on Case 1 are shown in Table 3. As seen, the maximum mean, worst, R_{no}, R_{op} and minimum standard deviation are found by JAYA. In this case, JAYA, CBO, and GAs have found the near-optimal solutions in all of the independent runs. The convergence histories of the algorithms are depicted in Fig. 9. As shown in this figure, the convergence rate of the JAYA is better than other methods. Besides, it is obvious from the figure that SSA is trapped to the local minimum. Since self-adaptive GA requires the evaluation of three groups of population, thus it starts with higher NFE. A lucid visualization of Kruskal–Wallis analysis is depicted in Fig. 10, that shows JAYA algorithm (blue line) has significantly (with the p value less than 0.05) different mean ranks from GWO, SSA and standard GA (red lines). Optimum configurations found by each method are provided in Appendix A. Considering the optimum results found by the algorithms, none of the obtained configurations includes 0_2 plies. According to Appendix A, the number of unique solutions for JAYA, CBO, GWO, SSA, standard and self-adaptive GAs are equal to 38, 32, 17, 3, 26 and 34, respectively.

4.2 Case 2

The statistical results obtained from 100 independent runs of this case are listed in Table 4. From Table 4, it is obvious that the identical best solution is obtained by all the methods and JAYA has the best mean solution, worst solution, $R_{no}(\%)$, and $R_{op}(\%)$. Like the previous case, JAYA, CBO, and GAs have found the near optimal solution in all independent runs, but JAYA has the lowest standard deviation. As reported from [29], BBO is in the second place in terms of the mean and standard deviation. SSA, Self-adaptive GA and HS have the lowest R_{op}. Convergence histories of load factors, for the proposed methods, are presented in Fig. 11. The figure shows the fast convergence of the JAYA algorithm with respect to other meta-heuristics. As shown in Fig. 12, JAYA algorithm significantly outperformed other algorithms by considering the mean ranks of 100 independent results. The optimum orientation angles obtained by different methods are presented in Table 5. It can be seen, that JAYA algorithm has found all optimal solutions similar to the Scatter Search Algorithm (SSA) [47], GA algorithm [26], and Harmony Search algorithm (HSA) with NFE = 6750 [7]; but other reported algorithms, namely GWO, SSA, GA [56], SA [10], GPSA [26], Standard GA, and Self-adaptive GA have not found these solutions completely. It should be mentioned that, since laminated plates have a symmetry of stacking sequence about the mid-plane surface, only one side of the composite plates are presented.

Author's personal copy

Table 5 Optimum configurations obtained by different algorithms for case 2

Configurations	Algorithms											
	JAYA	GWO	SSA	CBO	GA [56]	SA [10]	Scatter Search Algorithm [47]	GPSA [26]	GA [26]	HSA [7]	Standard GA	Self-adaptive GA
2,3,3,3,3,2,3,3,3,3,3,3,3,3,2	[±45,90_8,±45,90_{18},±45]s	✓	✓	–	✓	✓	–	✓	✓	✓	✓	–
2,3,3,3,3,3,2,3,3,3,3,2,3,3,3	[±45,90_{10},±45,90_8,±45,90_8]s	✓	✓	–	✓	✓	✓	–	✓	✓	–	✓
3,2,3,3,3,2,3,3,3,3,3,2,3,3,3	[90_2,±45,90_6,±45,90_8,±45,90_{10}]s	✓	✓	✓	✓	✓	✓	✓	✓	✓	–	–
3,3,2,2,3,3,3,3,3,3,3,2,3,3,3	[90_4,±45,90_{16},±45,90_6]s	✓	✓	✓	✓	✓	✓	✓	✓	✓	✓	–
3,3,3,3,2,3,2,3,2,3,2,2,2,2,2	[90_8,±45,90_2,±45,90_2,±45,90_2,±45,90_2,±45,90_6]s	✓	✓	✓	✓	–	✓	–	✓	✓	✓	✓
3,3,3,3,3,2,2,3,2,2,3,2,2,2,2	[90_{10},±45,90_2,90_2,±45,90_3,90_2,±45,90_4]s	✓	–	–	✓	–	✓	✓	✓	✓	✓	✓
3,3,3,3,3,2,3,2,2,2,2,2,2,3,2	[90_{10},±45,90_2,±45,90_7,90_2,±45]s	✓	–	–	✓	–	✓	–	✓	✓	✓	✓

4.3 Case 3

Table 6, shows the statistical results obtained from 100 independent runs for the Case 3. Similar to the first case, the best mean solution, worst solution, $R_{no}(\%)$, and $R_{op}(\%)$ belong to JAYA algorithm. The results reported from [29] show that BBO and HS are respectively in the second and third place for standard deviation and R_{op}. They also reached to near optimal solutions in all runs. Average convergence histories of load factors, for the proposed algorithms are presented in Fig. 13. Results show that, like the previous case, the convergence rate of the JAYA and GWO are better than those of other utilized methods. The result of the nonparametric test shown in Fig. 14 confirms the efficiency of the JAYA algorithm. The best solution found by each of the proposed algorithms is identical, i.e., $[90_{16}, \pm 45, 90_6, \pm 45, 90_2, \pm 45, 90_2]_s$. The same configuration has been reported by Karakaya and Soykasap [26].

4.4 Case 4

Similarly, the statistical results obtained from 100 independent runs of the Case 4, are presented in Table 7. From this table, it can be seen that JAYA outperformed other methods in terms of the best mean solution, worst solution, standard deviation, $R_{no}(\%)$ and $R_{op}(\%)$. The only unique optimum solution for this case is $[0_{16}, \pm 45, 0_6, \pm 45, 0_2, \pm 45, 0_2]_s$. By comparing the result which was reported by Karakaya and Soykasap [26], the same optimal configuration had been obtained by GPSA algorithm. Besides, convergence histories of load factor, for the proposed methods are presented in Fig. 15, which shows the higher convergence rate of both JAYA and GWO algorithms. The result of the nonparametric test depicted in Fig. 16, shows the meaningful superiority of JAYA against SSA and both versions of GA.

4.5 Case 5

Table 8 listed the statistical results obtained from 100 independent runs for the Case 5. By comparing the worst and mean solutions, it can be found that not only worst solution found by JAYA is more stable than others but also this solution is more stable than the mean of the results obtained by SSA. In this case, SSA has achieved the optimal orientations in only 85% of the runs. Further, in only one percent of runs, it has achieved the optimal solution. Table 9 shows that seven distinct optimal solutions of this case are obtained by JAYA and GA with standard setting, while SSA just found one of them. It can also be seen that GWO and CBO obtained the distinct solutions excluding the first configuration. Figure 17 shows

Author's personal copy

Table 6 Statistical results of different methods for Case 3

	Mean	Best	Worst	STD	$R_{no}(\%)$	$R_{op}(\%)$
JAYA	**412954.33**	**412985.8223**	**412860.056**	**39.4395**	**100**	**44**
GWO	412478.8875	**412985.8223**	406210.8605	1032.574	97	15
SSA	411899.8371	**412985.8223**	406192.2121	1427.4559	80	5
CBO	412936.0016	**412985.8223**	412828.6144	51.0408	100	34
Standard GA	411267.5604	**412985.8223**	392391.5905	3416.0874	79	8
Self-adaptive GA	412173.1138	**412985.8223**	405062.5453	1285.0146	89	5
BBO [29]	412943.56	**412985.82**	–	47.82	**100**	34
HS [29]	412944.49	**412985.82**	–	42.74	**100**	28

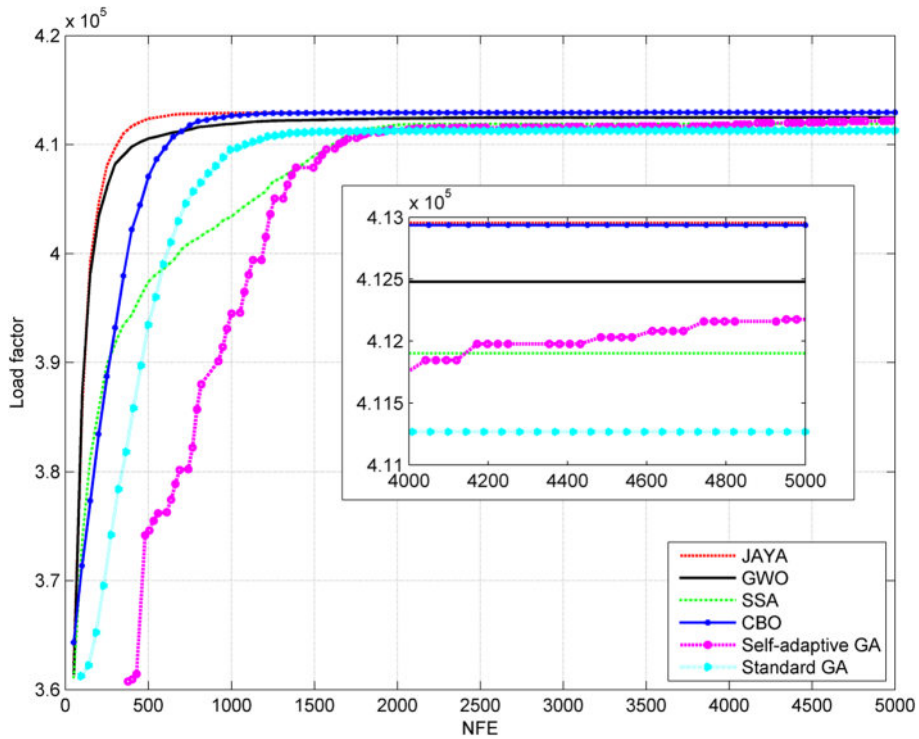

Fig. 13 Mean of the convergence histories for Case 3

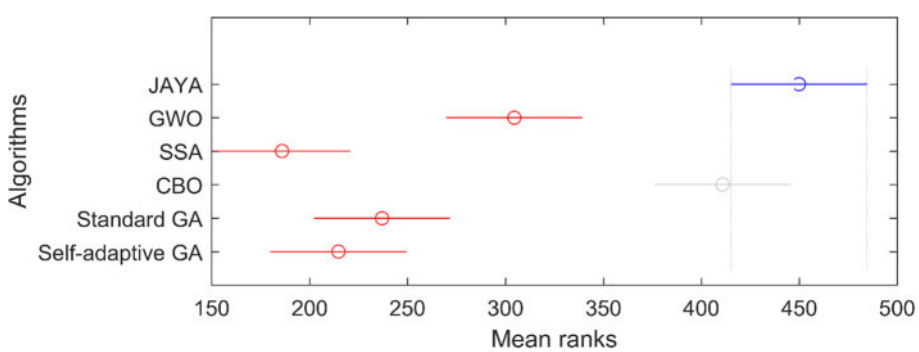

Fig. 14 The visualization of Kruskal–Wallis nonparametric test for Case 3

the high convergence rate of JAYA and GWO. According to Fig. 18, except the GWO, other algorithms are significantly outperformed by JAYA.

The optimal orientation angles are reported in Table 9, where JAYA has obtained the most number of unique solutions.

Author's personal copy

Table 7 Statistical results of different methods for case 4

	Mean	Best	Worst	STD	$R_{no}(\%)$	$R_{op}(\%)$
JAYA	**206475.9682**	**206492.9111**	**206430.028**	**21.7927**	**100**	**46**
GWO	206461.5866	**206492.9111**	206395.0247	29.4209	**100**	32
SSA	206026.2023	**206492.9111**	202703.7345	631.7293	83	5
CBO	206459.5515	**206492.9111**	206225.6577	42.7441	**100**	24
Standard GA	206417.9331	**206492.9111**	202468.3895	400.9985	99	32
Self-adaptive GA	206227.6033	**206492.9111**	204041.0029	372.6237	95	4

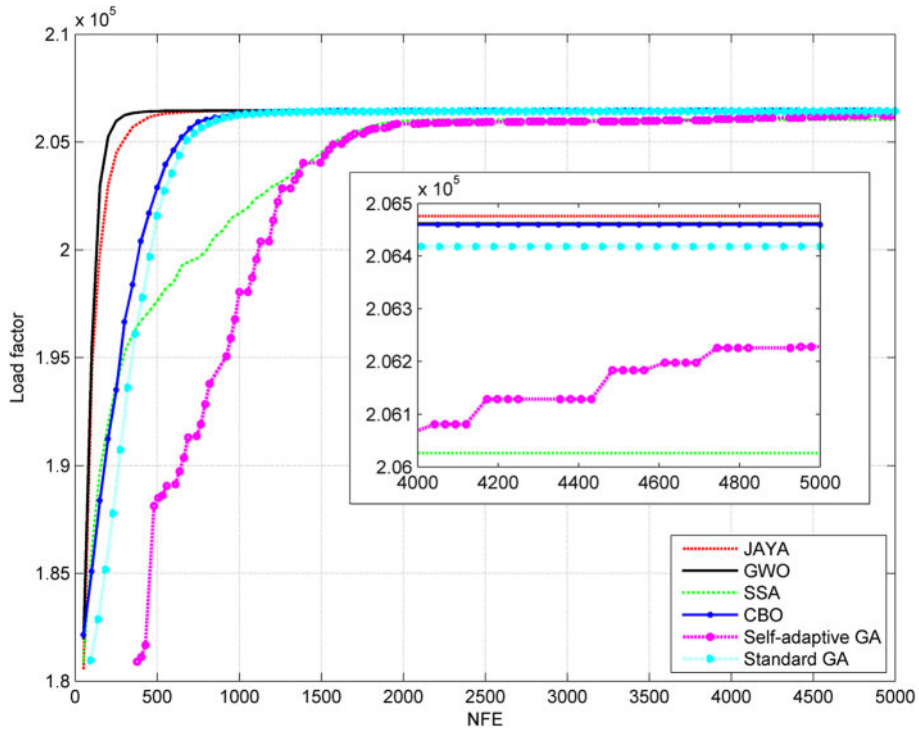

Fig. 15 Mean of the convergence histories for case 4

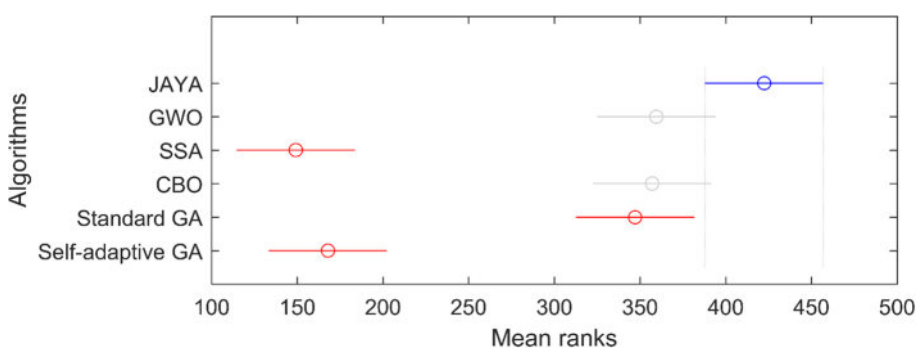

Fig. 16 The visualization of Kruskal–Wallis nonparametric test for case 4

4.6 Case 6

The statistical results for Case 6 are provided in Table 10. As the previous cases, JAYA has found the best mean and worst. Here, according to the reported results in [29], BBO algorithm has found the highest R_{op} and the lowest standard deviation, but it must be taken into account that a great effort has been gone into tuning the internal parameters of BBO, while JAYA has directly implemented and it has found the competitive results. According to the statistical results in Table 10, all the algorithms have found the near optimum results in all runs, except SSA, which failed to obtain the near optimum orientations in 37 runs. Optimum configurations found by these methods are listed in

Author's personal copy

Table 8 Statistical results of different methods for case 5

	Mean	Best	Worst	STD	R_{no}(%)	R_{op}(%)
JAYA	**173934.9832**	**173945.3301**	**173877.4256**	**14.6509**	**100**	**29**
GWO	173929.0795	**173945.3301**	173704.0279	40.5637	**100**	28
SSA	173512.5856	**173945.3301**	168964.2104	731.7784	85	1
CBO	173920.7429	**173945.3301**	173786.8863	29.4792	**100**	15
Standard GA	173923.7793	**173945.3301**	173435.2024	61.5184	**100**	19
Self-adaptive GA	173898.2305	**173945.3301**	173311.5549	81.2366	**100**	8

Table 9 Optimum configurations obtained by different algorithms for case 5

Configurations		Algorithms					
		JAYA	GWO	SSA	CBO	Standard GA	Self-adaptive GA
1 1 1 1 1 2 1 2 2 2 2 2 2 2 1 2	$[0_{10},\pm45,0_2,\pm45_7,0_2,\pm45]$s	✓	–	–	–	✓	✓
1 1 1 1 1 2 2 1 2 2 2 1 2 2 2 2	$[0_{10},\pm45_2,0_2,\pm45_3,0_2,\pm45_4]$s	✓	✓	–	✓	✓	✓
1 1 1 1 2 1 2 1 2 1 2 2 2 2 2 2	$[0_8,\pm45,0_2,\pm45,0_2,\pm45,0_2,\pm45_6]$s	✓	✓	–	✓	✓	–
1 1 2 2 1 1 1 1 1 1 1 1 2 1 1 1	$[0_4,\pm45_2,0_{16},\pm45,0_6]$s	✓	✓	✓	✓	✓	✓
1 2 1 1 1 2 1 1 1 1 2 1 1 1 1 1	$[0_2,\pm45,0_6,\pm45,0_8,\pm45,0_{10}]$s	✓	✓	–	✓	✓	✓
2 1 1 1 1 1 2 1 1 1 1 2 1 1 1 1	$[\pm45,0_{10},\pm45,0_8,\pm45,0_8]$s	✓	✓	–	✓	✓	✓
2 1 1 1 1 2 1 1 1 1 1 1 1 1 1 2	$[\pm45,0_8,\pm45,0_{18},\pm45]$s	✓	✓	–	✓	✓	–

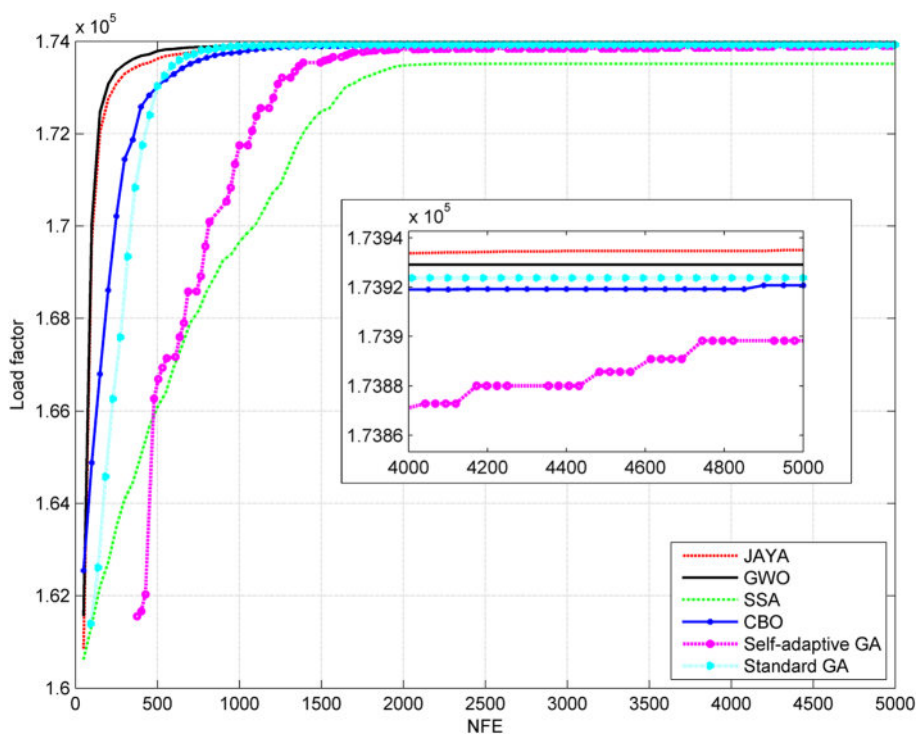

Fig. 17 Mean of the convergence histories for case 5

Appendix B, where JAYA, CBO, standard GA, self-adaptive GA, GWO, and SSA, respectively have the highest number of distinct optimal solutions. Additionally, considering the optimum results found by the algorithms, which are listed, none of the obtained configurations includes any 90_2 plies. According to the convergence curves given in Fig. 19, it can be seen that the SSA could not found the globally optimum solution and has been trapped in the

Author's personal copy

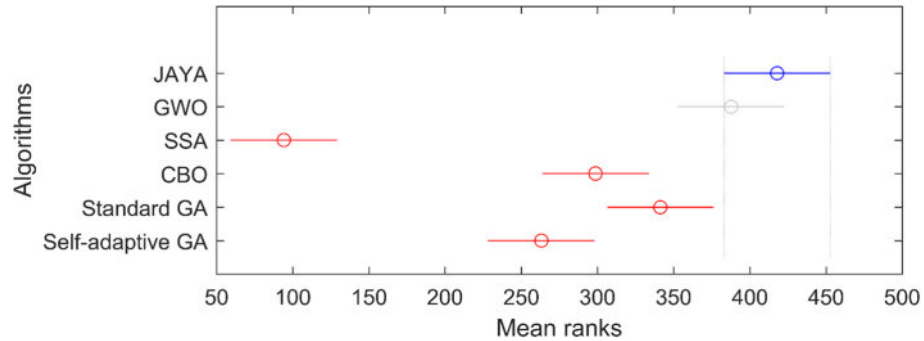

Fig. 18 The visualization of Kruskal–Wallis nonparametric test for case 5

Table 10 Statistical results of different methods for case 6

	Mean	Best	Worst	STD	$R_{no}(\%)$	$R_{op}(\%)$
JAYA	132234.3513	**132243.5399**	**132139.9079**	18.0947	**100**	66
GWO	132219.7549	**132243.5399**	132124.8181	24.7805	**100**	28
SSA	131531.9473	**132243.5399**	128911.2006	810.343	63	3
CBO	132215.9018	**132243.5399**	132103.0024	37.1923	**100**	46
Standard GA	132224.1764	**132243.5399**	131842.6598	50.796	**100**	58
Self-adaptive GA	132220.6924	**132243.5399**	132034.2787	40.2526	**100**	47
BBO [29]	132236.45	**132243.53**	–	**13.84**	**100**	**68**
HS [29]	132198.58	**132243.53**	–	46.92	**100**	17

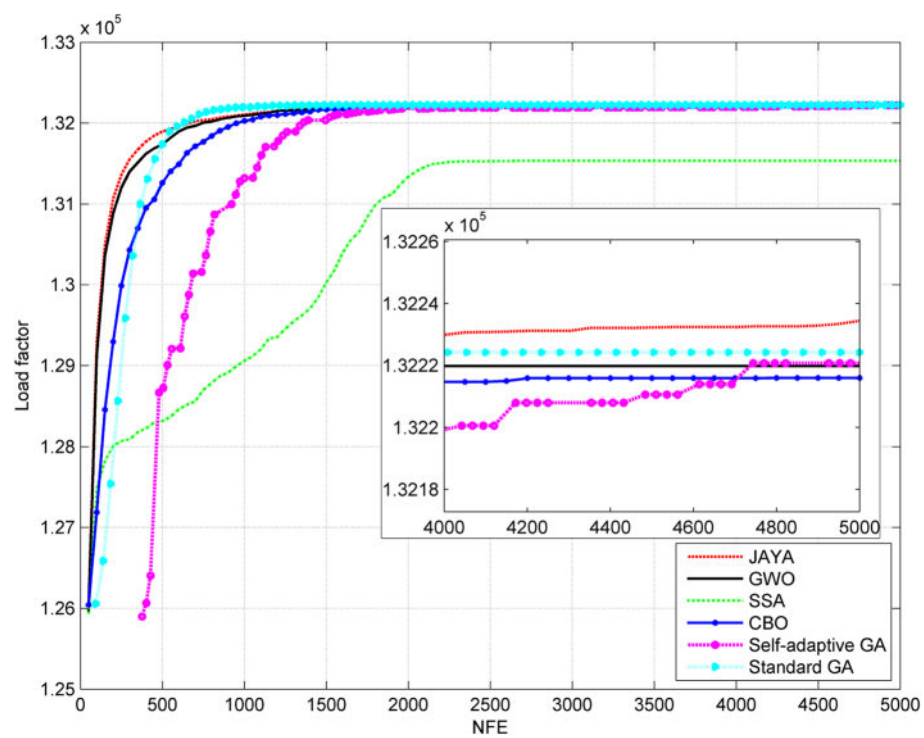

Fig. 19 Mean of the convergence histories for case 6

local minima. Figure 20, shows the significant superiority of the JAYA in comparison with GWO, CBO and SSA algorithms.

5 Concluding remarks

In the present study, some of the meta-heuristic optimization algorithms have been applied to the composite

Author's personal copy

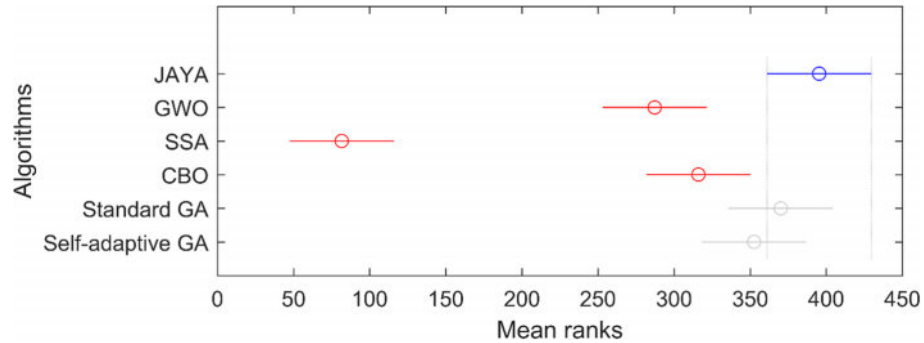

Fig. 20 The visualization of Kruskal–Wallis nonparametric test for case 6

Table 11 The coefficient of variation in percentage

	JAYA	GWO	SSA	CBO	Standard-GA	Self-adaptive GA
Case 1	**0.0106**	0.243	0.5139	0.0338	0.0465	0.0239
Case 2	**0.0073**	0.2099	0.2859	0.0211	0.0721	0.0437
Case 3	**0.0096**	0.2503	0.3466	0.0124	0.8306	0.3118
Case 4	**0.0106**	0.0143	0.3066	0.0207	0.1943	0.1807
Case 5	**0.0084**	0.0233	0.4217	0.0169	0.0354	0.0467
Case 6	**0.0137**	0.0187	0.6161	0.0281	0.0384	0.0304
Average	**0.0016**	0.1078	0.1021	0.0059	0.2092	0.0934

laminates for maximization of buckling load capacity. Since the parameter-less algorithms do not need specific parameters for tuning, are at an advantage against other algorithms. They just need the number of populations and iterations to start the optimization process. Here, for the first time, JAYA, GWO, SSA and CBO algorithms have been implemented for this problem. Two version of GA algorithm, with standard setting and self-adaptive version, have been also implemented for comparison. Six numerical case studies with symmetric and balanced laminate panels made up 64 graphite/epoxy plies with different loading and dimensions have been selected and 100 times have been executed for each case to assess the algorithms. The critical buckling load has been maximized by varying two-ply stacking sequences and 3 different fiber orientations of 0_2, ± 45 and 90_2 degrees. According to the results, all the algorithms have found the optimal solution at least one trial, while JAYA algorithm has outperformed other algorithms in terms of mean, worst and standard deviation. In most cases, the number of optimal orientations that has been found by JAYA, are higher than those of others; also it has found the near-optimal results in all trials. One of the important criteria for assessing the algorithms is the number of distinct optimal solutions found by them, where JAYA also showed an effective performance there. The mean convergence histories have been demonstrated for all the considered cases. In most cases, the GWO and JAYA algorithms converged faster than other compared algorithms, but GWO commonly tended to converge to a premature local optimum. An enhanced method for exploring mechanism of GWO may prevent the trapping of this algorithm. The Kruskal–Wallis nonparametric one-way analysis was also been performed in all cases. The results showed the superiority of JAYA against other algorithms, although this superiority was not significant in a few cases. Table 11 represents the coefficient of variation for all cases. As can be seen, the JAYA algorithm averagely has 0.0016% coefficient of variation that is 73% less than the best average of the CBO (the best among other algorithms). This shows the low degree of variation and high reliability of the JAYA algorithm.

References

1. Abachizadeh M, Tahani M (2009) An ant colony optimization approach to multi-objective optimal design of symmetric hybrid laminates for maximum fundamental frequency and minimum cost. Struct Multidiscip Optim 37:367–376
2. Abhishek K, Kumar VR, Datta S, Mahapatra SS (2017) Application of JAYA algorithm for the optimization of machining performance characteristics during the turning of CFRP (epoxy) composites: comparison with TLBO, GA and ICA. Eng Comput 33:457–475
3. Abrate S (1994) Optimal design of laminated plates and shells. Compos Struct 29:269–286
4. Almeida F, Awruch A (2009) Design optimization of composite laminated structures using genetic algorithms and finite element analysis. Compos Struct 88:443–454
5. Attaran A, Majid DL, Basri S, Mohd Rafie AS, Abdullah EJ (2008) Structural optimization of an aeroelastically tailored

Author's personal copy

composite flat plate made of woven fiberglass/epoxy. Acta Mech 196:161–173. https://doi.org/10.1007/s00707-007-0488-y
6. Bäck T, Fogel DB, Michalewicz Z (2000) Evolutionary computation 1: Basic algorithms and operators. vol 1. CRC press, Boca Raton
7. de Almeida FS (2016) Stacking sequence optimization for maximum buckling load of composite plates using harmony search algorithm. Compos Struct 143:287–299
8. De Jong KA (1975) Analysis of the behavior of a class of genetic adaptive systems. Ph.D. Thesis, University of Michigan, USA
9. Du D-C, Vinh H-H, Trung V-D, Hong Quyen N-T, Trung N-T (2017) Efficiency of Jaya algorithm for solving the optimization-based structural damage identification problem based on a hybrid objective function. Eng Optim 50:1–19
10. Erdal O, Sonmez FO (2005) Optimum design of composite laminates for maximum buckling load capacity using simulated annealing. Compos Struct 71:45–52
11. Fang C, Springer GS (1993) Design of composite laminates by a Monte Carlo method. J Compos Mater 27:721–753
12. García S, Molina D, Lozano M, Herrera F (2009) A study on the use of non-parametric tests for analyzing the evolutionary algorithms' behaviour: a case study on the CEC'2005 special session on real parameter optimization. J Heuristics 15:617
13. Ghavidel S, Azizivahed A, Li L (2018) A hybrid Jaya algorithm for reliability–redundancy. allocation problems. Eng Optim 50:698–715
14. Ghiasi H, Fayazbakhsh K, Pasini D, Lessard L (2010) Optimum stacking sequence design of composite materials Part II: variable stiffness design. Compos Struct 93:1–13
15. Ghiasi H, Pasini D, Lessard L (2009) Optimum stacking sequence design of composite materials Part I: constant stiffness design. Compos Struct 90:1–11. https://doi.org/10.1016/j.compstruct.2009.01.006
16. Goldberg DE (2006) Genetic algorithms. Pearson Education India, Noida
17. Goldberg DE, Deb K (1991) A comparative analysis of selection schemes used in genetic algorithms. In: Foundations of genetic algorithms, vol 1. Elsevier, Amsterdam, pp 69–93
18. Goldberg DE, Holland JH (1988) Genetic algorithms and machine learning 3:95–99
19. Gürdal Z, Haftka RT (1993) Optimization of composite laminates. In: Rozvany GIN (ed) Optimization of large structural systems. Springer Netherlands, Dordrecht, pp 623–648. https://doi.org/10.1007/978-94-010-9577-8_31
20. Haftka RT, Gürdal Z (2012) Elements of structural optimization, vol 11. Springer Science & Business Media, Dordrecht
21. Haftka RT, Walsh JL (1992) Stacking-sequence optimization for buckling of laminated plates by integer programming. AIAA J 30:814–819
22. Harik GR, Lobo FG (1999) A parameter-less genetic algorithm. In: Proceedings of the 1st Annual conference on genetic and evolutionary computation, Vol. 1. Morgan Kaufmann Publishers Inc., pp 258–265
23. Hollander M, Wolfe A, Chicken DE (2014) Nonparametric statistical methods. 3edn. John Wiley, New York, USA
24. Jacoby SL, Kowalik J, Pizzo JT (1972) Iterative methods for nonlinear optimization problems, Prentice Hall series in automatic computation
25. Jones RM (1998) Mechanics of composite materials. CRC press, Boca Raton
26. Karakaya Ş, Soykasap Ö (2009) Buckling optimization of laminated composite plates using genetic algorithm and generalized pattern search algorithm. Struct Multidiscip Optim 39:477–486
27. Kaveh A (2017) Advances in metaheuristic algorithms for optimal design of structures. 2 edn. Springer, Berlin. https://doi.org/10.1007/978-3-319-46173-1
28. Kaveh A (2017) Applications of metaheuristic optimization algorithms in civil engineering. Springer, Berlin
29. Kaveh A, Dadras A, Malek NG (2018) Buckling load of laminated composite plates using three variants of the biogeography-based optimization algorithm. Acta Mech 229:1551–1566
30. Kaveh A, Ilchi Ghazaan M (2015) A comparative study of CBO and ECBO for optimal design of skeletal structures. Comput Struct 153:137–147
31. Kaveh A, Mahdavi VR (2014) Colliding bodies optimization method for optimum design of truss structures with continuous variables. Adv Eng Softw 70:1–12
32. Kaveh A, Mahdavi VR (2014) Colliding bodies optimization: a novel meta-heuristic method. Comput Struct 139:18–27
33. Kaw AK (2005) Mechanics of composite materials. CRC press, Boca Raton
34. Kogiso N, Watson LT, Gürdal Z, Haftka RT (1994) Genetic algorithms with local improvement for composite laminate design. Struct Multidiscip Optim 7:207–218
35. Le Riche R, Haftka RT (1993) Optimization of laminate stacking sequence for buckling load maximization by genetic algorithm. AIAA J 31:951–956
36. Lin C-C, Lee Y-J (2004) Stacking sequence optimization of laminated composite structures using genetic algorithm with local improvement. Compos Struct 63:339–345
37. Liu B, Haftka RT, Akgün MA, Todoroki A (2000) Permutation genetic algorithm for stacking sequence design of composite laminates. Comput Methods Appl Mech Eng 186:357–372
38. Lobo FG, Goldberg DE (2004) The parameter-less genetic algorithm in practice. Inf Sci 167:217–232
39. Matsuzaki R, Todoroki A (2007) Stacking-sequence optimization using fractal branch-and-bound method for unsymmetrical laminates. Compos Struct 78:537–550. https://doi.org/10.1016/j.compstruct.2005.11.015
40. McMahon MT, Watson LT, Soremekun GA, Gürdal Z, Haftka RT (1998) A Fortran 90 genetic algorithm module for composite laminate structure design. Eng with Comput 14:260–273
41. Mirjalili S, Gandomi AH, Mirjalili SZ, Saremi S, Faris H, Mirjalili SM (2017) Salp Swarm algorithm: a bio-inspired optimizer for engineering design problems. Adv Eng Softw
42. Mirjalili S, Mirjalili SM, Lewis A (2014) Grey wolf optimizer. Adv Eng Softw 69:46–61
43. Omkar S, Senthilnath J, Khandelwal R, Naik GN, Gopalakrishnan S (2011) Artificial Bee Colony (ABC) for multi-objective design optimization of composite structures. Appl Soft Comput 11:489–499
44. Omkar SN, Khandelwal R, Ananth TVS, Narayana Naik G, Gopalakrishnan S (2009) Quantum behaved Particle Swarm Optimization (QPSO) for multi-objective design optimization of composite structures. Expert Syst Appl 36:11312–11322. https://doi.org/10.1016/j.eswa.2009.03.006
45. Omkar SN, Mudigere D, Naik GN, Gopalakrishnan S (2008) Vector evaluated particle swarm optimization (VEPSO) for multi-objective design optimization of composite structures. Comput Struct 86:1–14. https://doi.org/10.1016/j.compstruc.2007.06.004
46. Pai N, Kaw A, Weng M (2003) Optimization of laminate stacking sequence for failure load maximization using. Tabu Search Compos Part B Eng 34:405–413. https://doi.org/10.1016/S1359-8368(02)00135-X
47. Rao ARM, Arvind N (2005) A scatter search algorithm for stacking sequence optimisation of laminate composites. Compos Struct 70:383–402
48. Rao R (2016) Jaya: A simple and new optimization algorithm for solving constrained and unconstrained optimization problems. Int J Ind Eng Comput 7:19–34

Author's personal copy

49. Rao RV, Waghmare G (2017) A new optimization algorithm for solving complex constrained design optimization problems. Eng Optim 49:60–83
50. Reddy JN (2004) Mechanics of laminated composite plates and shells: theory and analysis. CRC press, Boca raton
51. Rnndles RH (1986) Nonparametric statistical inference. Taylor & Francis, Routledge
52. Sargent PM, Ige DO, Ball NR (1995) Design of laminate composite layups using genetic algorithms. Eng Comput 11:59–69
53. Sebaey T, Lopes C, Blanco N, Costa J (2011) Ant colony optimization for dispersed laminated composite panels under biaxial loading. Compos Struct 94:31–36
54. Setoodeh A, Shojaee M (2017) Critical buckling load optimization of functionally graded carbon nanotube-reinforced laminated composite quadrilateral plates. Polym Compos 39:853–868
55. Setoodeh S, Abdalla MM, Gürdal Z (2006) Design of variable–stiffness laminates using lamination Parameters. Compos Part B Eng 37:301–309
56. Soremekun G, Gürdal Z, Haftka R, Watson L (2001) Composite laminate design optimization by genetic algorithm with generalized elitist selection. Comput struct 79:131–143
57. Talbi E-G (2009) Metaheuristics: from design to implementation vol 74. Wiley, Hoboken
58. Venkataraman S, Haftka RT (1999) Optimization of composite panels—a review. Proc Am Soc Compos 195:479–488
59. Vosoughi A, Darabi A, Forkhorji HD (2017) Optimum stacking sequences of thick laminated composite plates for maximizing buckling load using FE-GAs-. PSO Compos Struct 159:361–367
60. Yang X-S (2010) Nature-inspired metaheuristic algorithms. Luniver press

Publisher's Note Springer Nature remains neutral with regard to jurisdictional claims in published maps and institutional affiliations.

Investigation on the Size of reinforcement in AZ31/Al_2O_3 Nanocomposite with Array Distribution

A. Khalkhali[1], **B. Anbarlooie**[2], **N. Geran Malek** [3], **M. Nankali** [4]

[1]School of Automotive Engineering, Iran University of Science and Technology; ab_khalkhali@iust.ac.ir

[2]School of Aerospace Engineering, Amirkabir University of Technology; anbarlooie@gmail.com

[3]School of Automotive Engineering, Iran University of Science and Technology; nima_geran@auto.iust.ac.ir

[4]School of Mechanical Engineering, Iran University of Science and Technology; m_nankali@mecheng.iust.ac.ir

Abstract

Light metals and alloys such as magnesium, due to its intrinsic characteristics of low density, good machinability and availability in the global market are in close attention. However, the relatively low strength, poor room temperature ductility, and toughness limit the range of magnesium applications. Alloying with Al, Zn, Mn, Ca and other elements is a conventional way to improve properties of magnesium. In this investigation, AL_2O_3/AZ31 nanocomposites with cohesive interactions along interfaces were simulated and the mechanical behavior was investigated. Fracture or delamination along an interface between phases plays a major role in limiting the toughness and the ductility of the multi-phase materials. Finite element method is widely employed to track fracture process and evaluate material toughness. Cohesive finite element method (CFEM) has shown its effectiveness in these issues, such as modeling the matrix fracture and phase interface failure in reinforced composites. In this paper, a cohesive finite element method is proposed on array distribution of AL_2O_3 nanoparticles in the AZ31 matrix to characterize reinforcement/matrix interface and debonding phenomena occurring. A statistical investigation was done for models with 50 different size of nanoparticles with 10 circular particles array dispersed, to obtain the optimum mechanical behavior. The stress-strain curves for different radius dimensions depict that the most smaller particle size has higher offset yield stress and have smaller stress at the same strain.

Keywords: MMC Nanocomposite, Debonding, Finite element analysis (FEA), Cohesive Zone Modeling, Abaqus, Python, Matlab.

Introduction

Development of new structural materials with higher strength-to-weight ratios is one of the biggest challenges in the transportation industry to reduce fuel consumption and to reduce greenhouse gas emissions. Accordingly, close attention is paid to light metals and alloys such as magnesium, due to its intrinsic characteristics of low density, good machineability, and availability in the global market. However, the relatively low strength, poor room temperature ductility, and toughness limit the range of magnesium applications. Alloying with Al, Zn, Mn, Ca and other elements is a conventional way to improve properties of magnesium. The enhancement in mechanical properties of the obtained alloys, however, might not be as high as those obtained by composite reinforcements. Since composite materials have several advantages over pure metals and alloys, numerous studies have been conducted on the addition of discontinuous particles in the micro to nano-scale and their effects on the achieved properties during the last two decades. Selection of reinforcements is typically governed by cost, availability, and compatibility with matrix [1].

AZ31 is a very commonly used Al-containing (or Zr-free) Mg alloy and is characterized by (a) low cost; (b) ease of handling; (c) good strength and ductility; and (d) resistance to atmospheric corrosion. AZ31 has recently been surface-reinforced with SiC microparticulates[2], C60 molecules [3], and multi-walled carbon nanotubes [4], using the friction stir processing technique.

The intense stress field at the tip of a crack generates a fracture process zone: a plastic zone in ductile solids, a zone of micro-cracking in ceramics, a zone of delamination, debonding and fiber pull-out in composites. Linear elastic fracture mechanics (LEFM) is only applicable when the size of the fracture process zone (FPZ) at the crack tip is small compared to the size of the crack and the size of the specimen [5]. Other models must be used to take into account the FPZ. The cohesive crack model is one of such models. In a cohesive crack, the propagation is governed by a traction–displacement relation across the crack faces near the tip [6]. This model was introduced in the early sixties for metals by Dugdale [7] and Barenblatt [8]. In the late seventies, Hillerborg et al. [9] introduced the concept of fracture energy into the cohesive crack model and proposed a number of traction–displacement relationships for concrete.

Fracture or delamination along an interface between phases plays a major role in limiting the toughness and the ductility of the multi-phase materials. Finite element method is widely employed to track fracture process and evaluate material toughness. Cohesive finite element method (CFEM) has shown its effectiveness in these issues, such as modeling the matrix fracture and phase interface failure in reinforced composites.

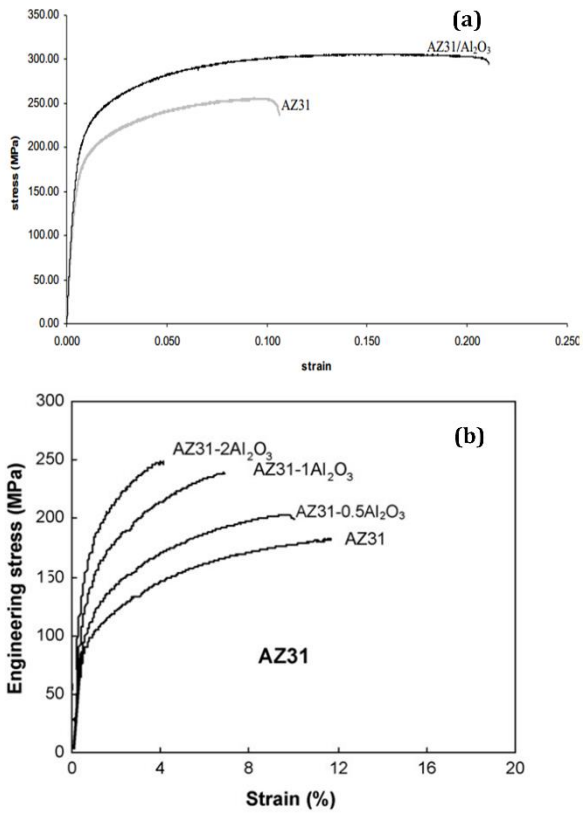

Figure 1. Stress-strain curves of the wrought materials: (a) Mg-based and (b) AZ31-base.The representative tensile stress-strain curve of monolithic AZ31 and AZ31/AL_2O_3 nanocomposite [1].

Some analytical models have been developed to study interfacial debonding between reinforcements and matrix, cracking in the matrix, plastic yielding of nanovoids (created by debonded nanoparticles) and matrix shear banding develop from the early stage of deformation under monotonic or cyclic loads [10, 11]. Interfacial debonding in polymer/nanoparticle composites was studied in [12] by means of Eshelby's equivalent inclusion method combined with an energy-derived debonding criterion stating a relationship between the interfacial adhesion strength and the work of adhesion of the components. Boutaleb et al. [13] proposed a micromechanical analytical model, in order to address the problem of stiffness and yield stress prediction in the case of nanocomposites consisting of silica nanoparticles embedded in a polymer matrix. In nanocomposites, a variety of damage modes such as fracture of reinforcements, interfacial debonding between reinforcements and matrix, cracking in the matrix, plastic yielding of nanovoids (created by debonded nanoparticles) and matrix shear banding develop from the early stage of deformation under monotonic or cyclic loads. These

damage modes mainly affect the mechanical performance of the nanocomposites. Therefore to extend the application of the nanocomposites and to develop even a new composite, thorough understanding of the micromechanics of damage process is essential. Lauke [14] and Williams [15] analyzed the energy dissipation phenomena by considering, besides particle debonding, voiding and subsequent yielding of the polymer. Salviot et al. [16] developed a hierarchical multi-scale model to assess the fracture toughness improvements due to the debonding of nanoparticles and the plastic yielding of nanovoids. The same authors have recently proposed a multiscale analytical model to quantify the toughness improvement due to the shear banding around nanoparticles [10]. They also proved that nanocomposite toughening is strongly affected by the size of nanoparticles and by surface treatments. Hsieh et al. [9] experimentally observed two dominant mechanisms responsible of toughening improvements: localized shear banding of the matrix and particle debonding followed by subsequent plastic void growth.

Cohesive zone models (CZMs) have been widely used in the continuum study of interface debonding and sliding in composites. A CZM assumes a relation between the normal (and shear adhesion of the components. Boutaleb et al. [12] proposed a micromechanical analytical model, in order to address the problem of stiffness and yield stress prediction in the case of nanocomposites consisting of silica nanoparticles embedded in a polymer matrix. In nanocomposites, a variety of damage modes such as fracture of reinforcements, interfacial debonding between reinforcements and matrix, cracking in matrix, plastic yielding of nanovoids (created by debonded nanoparticles) and matrix shear banding develop from the early stage of deformation under monotonic or traction(s)) and the opening (and sliding) displacement(s). When implemented in the finite element method (FEM), the CZM is capable of simulating interface debonding and sliding. The existing cohesive models are all phenomenological because it is difficult to obtain directly the cohesive laws for interfaces. However, CZM is a phenomenological model instead of an exact physical representation of material behavior in the debonding zone. In commonly adopted CZMs, simple cohesive laws are employed and the cohesive parameters are treated as case-independent constants which can be determined by fitting the simulation results to a set of experimental data or micromechanical results [16,17]. FE model with cohesive interface has been rarely employed in the simulation of nanocomposites. Needleman et al. [18], in a finite element study, investigated the effects of interphase thickness and interfacial strength between the carbon nanotube and polymer on the stiffness and strength of the nanocomposite. They modeled interface between the polymer and the CNT by a phenomenological cohesive relation. Liu et al. [19] investigated the interface analysis in CNT array composite based on cohesive finite element approach. They applied a micromechanics-based bilinear cohesive law in cohesive finite element model to characterize CNT/matrix interface.

Modeling

Cohesive zone model

Cohesive damage-debonding processes use a traction–displacement relationship to describe the cohesive element model by applying the model forms (bilinear, trapezoidal, exponential and so on) [17-19]. In the CZM, the fracture process zone is simplified as being an initially zero-thickness zone, composed of two coinciding cohesive surfaces. Under loading, the two surfaces separate and the traction between them varies in accordance with a specified traction–separation law. The interface element constitutive model which is used in present work is the exponential softening law proposed by Xu and Needleman [19].

Fig. 2 shows the concept of traction-separation law in cohesive elements.

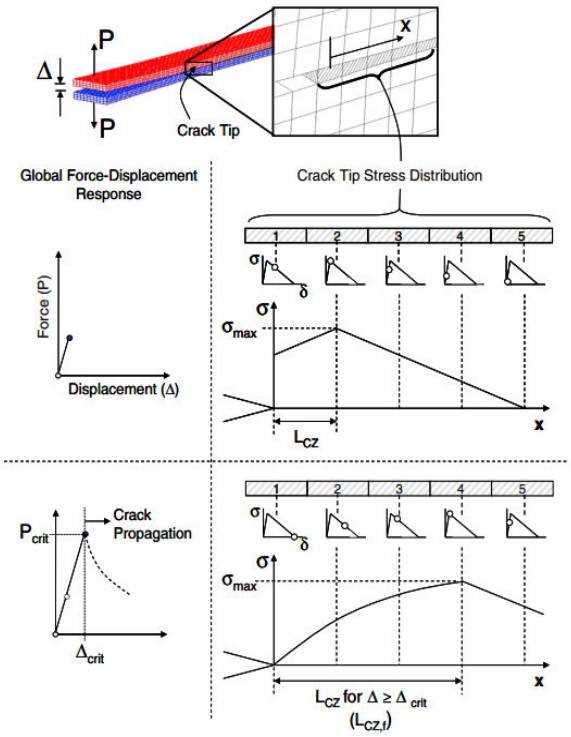

Figure 2. Development of the numerical cohesive zone [20].

An exponential cohesive zone model based on the universal binding energy curve from the atomistic consideration has found frequent usage in simulating crack growth in ductile metals. The exponential

softening law model is represented in Eq. (1) which uses a surface potential as follows:

$$\gamma_c(\delta) = eT_c\bar{\delta}_n[1-(1+\Delta_n)e^{-\Delta_n}e^{-\Delta_t^2}] \qquad (1)$$

Where, $\gamma_c(\delta)$ is the specific interface cohesive energy $e = 2.7182818$, T_c is the cohesive strength, $\Delta_n = \frac{\delta_n}{\bar{\delta}_n}$ and $\Delta_t = \frac{\delta_t}{\bar{\delta}_t}$. δ_n , δ_t are respectively normal and shear separation and $\bar{\delta}_n$ is the normal separation across the interface where the maximum normal traction is attained with $\delta_t = 0$, $\bar{\delta}_n$ is the shear separation where the maximum shear traction is attained at $\delta_t = \frac{\sqrt{2}}{2}\bar{\delta}_t$. The cohesive traction–separation relation is plotted in Fig. 3.

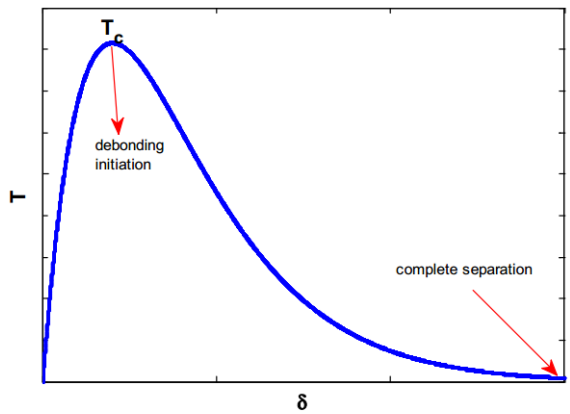

Figure 3. Traction-separation law for modeling cohesive failure[21]

Dastgerdi et al. [21] proposed a cohesive method to characterize interface debonding occurring in the particulate-reinforced nanocomposite. According to their results, adhesive energy and cohesive strength for AZ31/Al_2O_3 nanocomposite were 0.005J/m^2 and 163.27MPa respectively and the material properties of the composite constituents (Al_2O_3 nanoparticles, AZ31) are presented in Table 1.

Table 1. Material parameter of the composite constituents [21, 22]

Material	E(GPa)	ν	$\sigma_{YS}\ (MPa)$
AZ31	45	0.35	172 ± 15
Al_2O_3	379	0.17	-

In order to gain a deeper understanding of the mechanical performance of particulate-reinforced nanocomposites and into debonding phenomena occurring at the nanoscale, a modeling approach closely related to the real microstructure of nanocomposites was presented. The CZM was adopted to capture the nanofillers deboning. When implemented in the FEM, the CZM is capable of simulating interface debonding and sliding. In fact, in their work, a computational tool able to map a composite microstructure onto a finite element mesh was adopted in order to construct models which accurately reproduce the composite microstructure and characteristics.

According to their research, In the composite medium, the matrix undergoes elastic–plastic deformation and the reinforcement deforms elastically. AZ31 matrix and the Al_2O_3 nanoparticles are considered to behave as elastoplastic and linear elastic materials, respectively. Fig. 4 shows a real TEM image of AZ31/Al_2O_3 nanocomposite microstructure and its binarized image.

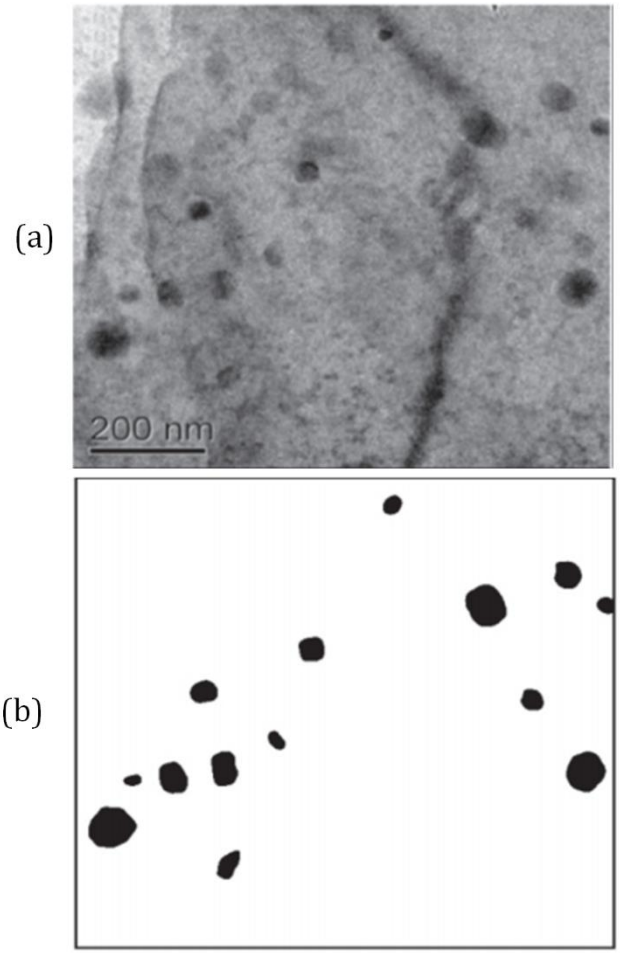

Figure 4. Selected RVE from real microstructure: (a) TEM image [20] and (b) binarized microstructure.

Results and Discussion

In this study, the deformation pattern and stress–strain behavior of particulate-reinforced nanocomposite (Al_2O_3–AZ31) were predicted based on the present numerical approach. This was done in ABAQUS CAE software with modeling of cohesive interactions and use of PYTHON codes.

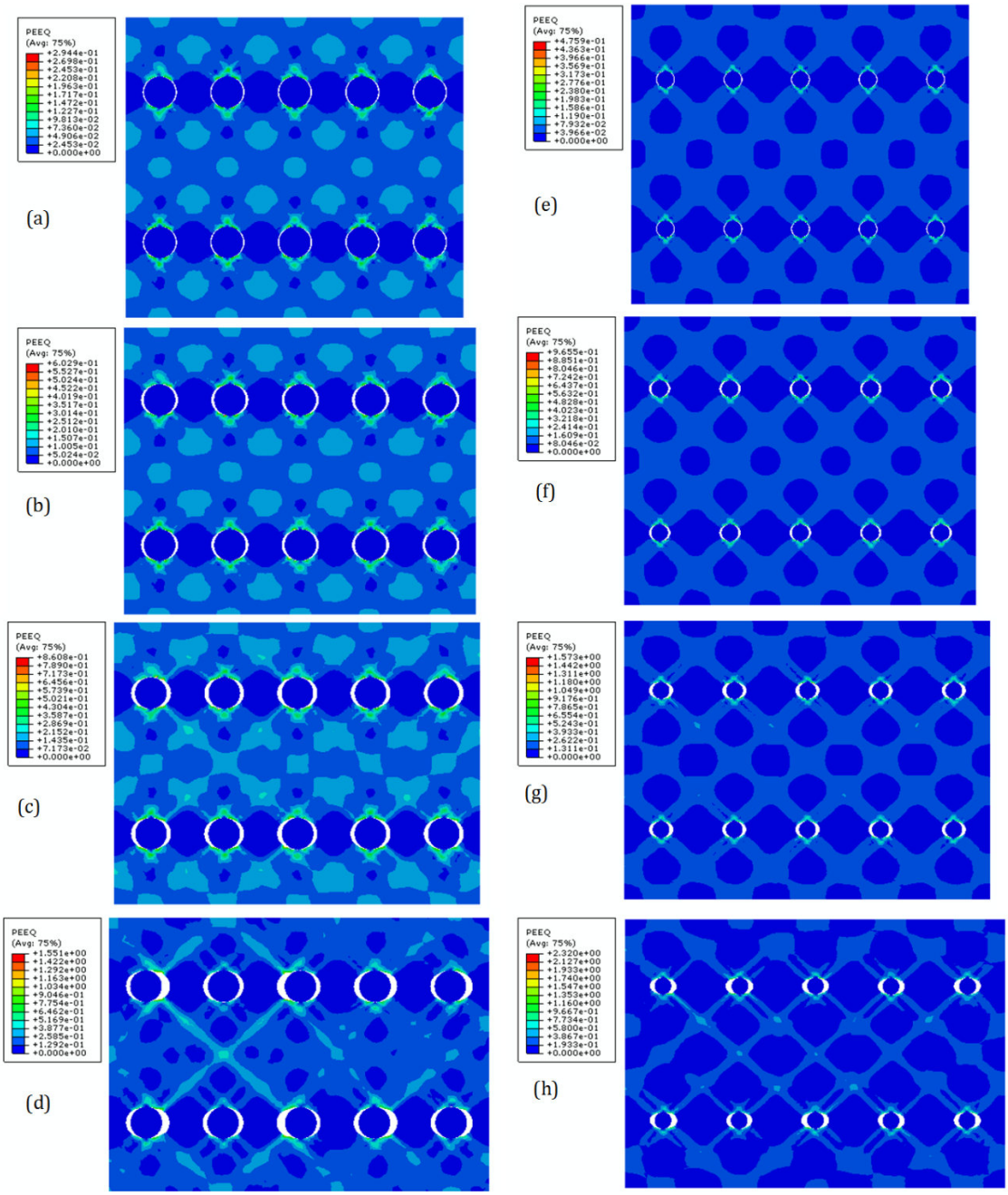

Figure 5. Distribution of equivalent plastic strain at various loading values of (a,e) 25%, (b,f) 50%, (c,g) 75% and (d,h) 100% for (a-d) nanocomposite with maximum radius(56.14 nm) (e-h) nanocomposite with minimum radius(29.85 nm)

Primarily, 50 models were created. Then a normal distribution of nanoparticles radius with a mean radius of 45nm and standard deviation of 5nm was created by the aim of PYTHON Programming Language. According to Fig. 6 as the radius of nanoparticles decreases, the stress in same strain increases. Fig. 5 depicts the equivalent plastic strain at various loading values for two different sizes of nanoparticles. The first case is the nanocomposite with maximum radius and the second case with a minimum radius of spherical nanoparticles with the same size and array distribution in the matrix. it is clear that strain localization zone (shear band) can be considered as a zone which is highly potential sites for void initiation.

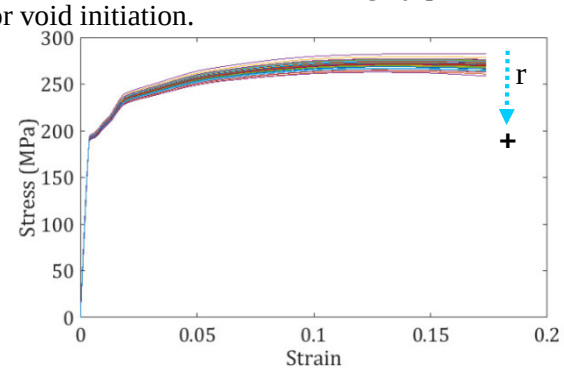

Figure 6. Stress-strain Curves for 50 Different Particle Sizes.

Fig. 7 shows offset yield stress of nanocomposites with different nanoparticle radiuses. According to this figure, the radius of nanoparticles between 40 to 50 nm is more than regions, because of the normal distribution of particle radius sizes.

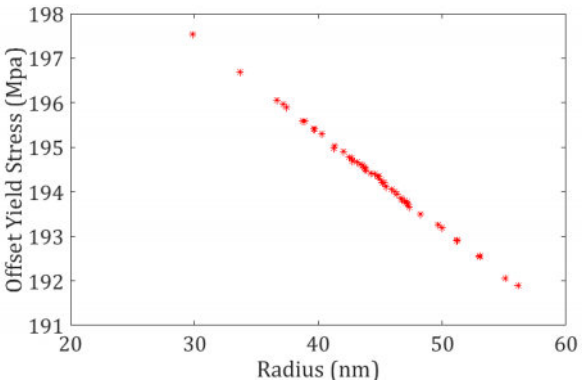

Figure 7. Stress-strain Curve for Different Particle Sizes

Conclusion

In this investigation, AL_2O_3/AZ31 nanocomposite with cohesive interactions along interfaces were simulated and the mechanical behavior was investigate. variations of radius sizes for array distribution of nanoparticles shows that the less the radius size of nanoparticles the more the yield stress in nanocomposite.

References

[1] M. Habibnejad-Korayem, R. Mahmudi, and W. Poole, "Enhanced properties of Mg-based nano-composites reinforced with Al 2 O 3 nano-particles," *Materials Science and Engineering: A*, vol. 519, pp. 198-203, 2009.

[2] Y. Morisada, H. Fujii, T. Nagaoka, and M. Fukusumi, "Effect of friction stir processing with SiC particles on microstructure and hardness of AZ31," *Materials Science and Engineering: A*, vol. 433, pp. 50-54, 2006.

[3] Y. Morisada, H. Fujii, T. Nagaoka, and M. Fukusumi, "Nanocrystallized magnesium alloy–uniform dispersion of C 60 molecules," *Scripta Materialia*, vol. 55, pp. 1067-1070, 2006.

[4] Y. Morisada, H. Fujii, T. Nagaoka, and M. Fukusumi, "MWCNTs/AZ31 surface composites fabricated by friction stir processing," *Materials science and engineering: A*, vol. 419, pp. 344-348, 2006.

[5] M. F. Ashby, H. Shercliff, and D. Cebon, *Materials: engineering, science, processing and design*: Butterworth-Heinemann, 2013.

[6] N. Moës and T. Belytschko, "Extended finite element method for cohesive crack growth," *Engineering fracture mechanics*, vol. 69, pp. 813-833, 2002.

[7] D. S. Dugdale, "Yielding of steel sheets containing slits," *Journal of the Mechanics and Physics of Solids*, vol. 8, pp. 100-104, 1960.

[8] G. I. Barenblatt, "The mathematical theory of equilibrium cracks in brittle fracture," *Advances in applied mechanics*, vol. 7, pp. 55-129, 1962.

[9] A. Hillerborg, M. Modéer, and P.-E. Petersson, "Analysis of crack formation and crack growth in concrete by means of fracture mechanics and finite elements," *Cement and concrete research*, vol. 6, pp. 773-781, 1976.

[10] M. Salviato, M. Zappalorto, and M. Quaresimin, "Plastic shear bands and fracture toughness improvements of nanoparticle filled polymers: a multiscale analytical model," *Composites Part A: Applied Science and Manufacturing*, vol. 48, pp. 144-152, 2013.

[11] T. Hui and Y.-H. Chen, "Surface effect and size dependence on the energy release due to a nano inas inclusion expansion in a gaas matrix material," *A A*, vol. 1, p. 1, 2010.

[12] J.-k. Chen, G.-T. Wang, Z.-Z. Yu, Z. Huang, and Y.-W. Mai, "Critical particle size for interfacial debonding in polymer/nanoparticle composites," *Composites Science and Technology*, vol. 70, pp. 861-872, 2010.

[13] S. Boutaleb, F. Zaïri, A. Mesbah, M. Naït-Abdelaziz, J.-M. Gloaguen, T. Boukharouba, *et al.*, "Micromechanics-based modelling of stiffness and yield stress for silica/polymer nanocomposites," *International Journal*

of Solids and Structures, vol. 46, pp. 1716-1726, 2009.

[14] B. Lauke, "On the effect of particle size on fracture toughness of polymer composites," *Composites Science and Technology,* vol. 68, pp. 3365-3372, 2008.

[15] J. Williams, "Particle toughening of polymers by plastic void growth," *Composites science and technology,* vol. 70, pp. 885-891, 2010.

[16] M. Zappalorto, M. Salviato, and M. Quaresimin, "A multiscale model to describe nanocomposite fracture toughness enhancement by the plastic yielding of nanovoids," *Composites Science and Technology,* vol. 72, pp. 1683-1691, 2012.

[17] J. Segurado and J. LLorca, "Computational micromechanics of composites: the effect of particle spatial distribution," *Mechanics of materials,* vol. 38, pp. 873-883, 2006.

[18] L. Sun, J. Ju, and H. Liu, "Elastoplastic modeling of metal matrix composites with evolutionary particle debonding," *Mechanics of Materials,* vol. 35, pp. 559-569, 2003.

[19] X.-P. Xu and A. Needleman, "Numerical simulations of fast crack growth in brittle solids," *Journal of the Mechanics and Physics of Solids,* vol. 42, pp. 1397-1434, 1994.

[20] P. W. Harper and S. R. Hallett, "Cohesive zone length in numerical simulations of composite delamination," *Engineering Fracture Mechanics,* vol. 75, pp. 4774-4792, 2008.

[21] J. N. Dastgerdi, G. Marquis, and M. Salimi, "Micromechanical modeling of nanocomposites considering debonding and waviness of reinforcements," *Composite Structures,* vol. 110, pp. 1-6, 2014.

[22] M. Paramsothy, J. Chan, R. Kwok, and M. Gupta, "Al2O3 nanoparticle addition to commercial magnesium alloys: multiple beneficial effects," *Nanomaterials,* vol. 2, pp. 147-162, 2012.

محاسبه‌ی خواص مکانیکی نانوکامپوزیت‌های نانولوله‌ی کربنی و بررسی اثر تعداد لایه های فاز میانی با استفاده از روش المان حجمی نمونه

ابوالفضل خلخالی[۱] محمد جواد سرانجام[۲] نیما گران ملک[۳] حامد رضوان پور[۴]

ایران، تهران، دانشگاه علم و صنعت ایران، دانشکده خودرو، آزمایشگاه تحقیقاتی شبیه سازی و طراحی بهینه خودرو

ab_khalkhali@iust.ac.ir

چکیده

به دلیل بهبود خواص مکانیکی و الکتریکی در نانوکامپوزیت‌ها، این دسته از مواد توجه بسیاری از محققین در سال‌های اخیر را به سمت خود جلب کرده‌اند. با این حال، هندسه بسیار پیچیده نانوکامپوزیت‌ها سبب شده است که محققین این عرصه از روش‌های عددی، اجزا محدود و دینامیک مولکولی برای بدست آوردن خواص آن‌ها استفاده کنند. در این مقاله مدل المان حجمی نمونه (RVE) نانوکامپوزیت تقویت شده با نانولوله کربنی در نرم افزار اجزا محدود آباکوس (ABAQUS) مدل شده و با استفاده از ترکیب کد نرم افزار اجزا محدود و کد متلب (MATLAB)، مدول الاستیسیته ماده زمینه تغییر کرده تا مدول الاستیسیته نانوکامپوزیت محاسبه شود. در ادامه، نتایج بدست آمده با نتایج تخمین زده شده از قانون ترکیب تعمیم یافته مقایسه می‌شود تا از صحت آن‌ها اطمینان حاصل شود. سپس با جایگذاری خواص حاصل از روش المان حجمی در معادلات قانون ترکیب تعمیم یافته، ضرایب نانولوله کربنی در تمامی حالات محاسبه شده و فرض خطی یا نمایی بودن ویژگی‌های مکانیکی فاز میانی و تاثیر آن بر روی دقت مدل بررسی می‌شود. در نهایت تعداد لایه‌های فاز میانی افزایش داده شده تا دقت مدل المان حجمی نمونه افزایش یابد؛ و نشان داده می‌شود که ایجاد هشت لایه در فاز میانی بهترین پاسخ‌ها را به همراه دارد.

واژه‌های کلیدی: نانوکامپوزیت – المان حجمی نمونه – روش اجزا محدود – ABAQUS

مقدمــه

کاهش مصرف سوخت چالش پیش روی شرکت‌های خودروسازی است که سعی می‌کنند با کاهش وزن محصول نهایی و جایگزینی موادی که نسبت استحکام به وزن بالاتری دارند، میزان مصرف سوخت را بهبود بخشند. نانولوله‌های کربنی با توجه به وزن بسیار کم خود به عنوان سفت‌ترین و مستحکم‌ترین ماده ساخته دست بشر شناخته می‌شوند. به شکلی که، نسبت سطح به حجم بالای آن‌ها باعث می‌شود که مقادیر بسیار کمی از این مواد، خواص کامپوزیت‌های پلیمری سبک را به مقدار زیادی تحت تاثیر قرار دهند. از این رو، استفاده از نانولوله های کربنی در صنعت خودرو رو به گسترش است. مواد مرکب به دلیل تغییر درصد وزنی عناصر تشکیل دهنده و هنچنین شکل هندسی این عناصر و نحوه ترکیب آن‌ها، خاصیت‌های مکانیکی ثابتی ندارند و این موضوع برای نانوکامپوزیت‌ها به مراتب پیچیده‌تر است. پیدا کردن روشی برای محاسبه خاصیت الاستیک نانوکامپوزیت‌ها ما را یاری می‌کند تا با تغییر هر یک از پارامترهای ذکر شده، بتوانیم خواص نهایی ماده جدید را محاسبه کنیم.

در سال‌های اخیر، محققان تلاش‌های فراوانی برای محاسبه خاصیت‌های مکانیکی نانوکامپوزیت‌ها انجام داده‌اند. چن‌لی ژانگ (Chen-Li Zhang) و همکارانش [۱] در سال ۲۰۰۶، خاصیت الاستیک نانوکامپوزیت‌های نانولوله کربنی تک‌دیواره‌ای را تحت ضرایب حجمی مختلف نانولوله و با استفاده از روش دینامیک مولکولی بدست آوردند. همچنین، دکتر آیت اللهی و

۱- استادیار و عضو هیئت علمی دانشکده مهندسی خودرو، ۰۹۱۲۲۰۸۹۶۰۳، ab_khalkhali@iust.ac.ir
۲- دانشجوی دکتری تخصصی مهندسی خودرو
۳و۴- دانشجوی کارشناسی ارشد مهندسی خودرو

همکارانش [۲] در ساال ۲۰۱۱ به بررسی تاثیر پارامترهای مختلفی از جمله جهت‌گیری و طول نانولوله‌های کربنی بر خواص مکانیکی کامپوزیت پرداختند. آن‌ها در تحقیقاتشان از روش المان حجمی نمونه استفاده کرده و فاز میانی را نیز در نظر گرفتند. پس از محاسبه‌ی خواص الاستیک موثر ماده‌ی نانوکامپوزیتی، نوبت به تحلیل‌های ماکروسکوپیک می‌رسد، که برای این منظور از نرم افزار اجزا محدود مانند آباکوس استفاده شده است. به عنوان مثال، پینگ ژو (Ping Zhu) و همکارانش [۳] در سال ۲۰۱۲ یک صفحه نانوکامپوزیت را مورد تحلیل استاتیک و دینامیک قرار دادند. علاوه بر این، در سال ۲۰۱۲، شن (Shen) [۴]، به تحلیل کمانش حرارتی یک نانوکامپوزیت نانولوله‌کربنی استوانه‌ای شکل، تحت آرایش‌های مختلف نانولوله‌ها پرداخت.

در مسائل مربوط به نانوکامپوزیت‌ها که در آن فاز تقویت کننده به صورت تابعی توزیع شده باشد، برای شبیه‌سازی ماده بایستی آن را به لایه‌های مختلفی تقسیم‌بندی کرده و خواص مکانیکی هر لایه به طور مجزا اعمال شود. برای محاسبه خواص مکانیکی نانو کامپوزیت‌ها علاوه بر روش‌های آزمایشگاهی و تجربی، چهار روش پرکاربرد عددی شامل روش دینامیک مولکولی، المان حجمی نمونه، قانون ترکیب تعمیم یافته و روش سلول واحد مورد استفاده قرار می‌گیرد.

در روش دینامیک مولکولی پیوند بین اتم‌های ماده در نرم افزاز مدل شده و خاصیت‌های مکانیکی آن‌ها استخراج می‌شود؛ در روش المان حجمی نمونه برای تخمین خاصیت‌های مکانیکی نانو کامپوزیت در جهات مختلف، یک المان سه بعدی استوانه‌ای شکل تحت بارگزاری‌های مختلف قرار گرفته و خاصیت‌های مکانیکی المان حجمی نمونه محاسبه می‌شود و در روش قانون ترکیب تعمیم یافته نیز می‌توان با استفاده از قانون ترکیب کلی کامپوزیتها و اضافه کردن ضرایب، خواص مکانیکی نانوکامپوزیت‌های نانوتیوب کربنی را با دقت بالایی محاسبه نمود. محاسبه خواص مکانیکی به روش سلول واحد تقریبا مشابه روش المان حجمی نمونه است با این تفاوت که در این روش یک سلول کروی شکل بزرگ‌تر در نظر گرفته می‌شود که شامل چندین عدد تقویت کننده می‌باشد.

در این مقاله ابتدا با استفاده از روش المان حجمی نمونه و بارگذاری های کششی، فشار شعاعی و پیچش و برای مقادیر مختلف مدول یانگ ماده زمینه خاصیت های الاستیک نانوکامپوزیت محاسبه شده و بعد از با استفاده از قانون ترکیب تعمیم یافته و خواص الاستیک نانوکامپوزیت نانولوله کربنی با استفاده از قانون ترکیب تعمیم یافته محاسبه شده است.در آخر، با استفاده از تغییر تعداد لایه های فاز میانی و با استفاده از دو رابطه تغییرات لگاریتمی و خطی برای محاسبه مدول یانگ فاز میانی، تعداد لایه های مناسب برای افزایش دقت مدل المان حجمی نمونه مشخص شده است.

مدل سازی عددی نانوکامپوزیت نانوتیوب کربنی

روش المان حجمی نمونه

به منظور بیان اثرات میکروسکوپیک میکروساختار به صورت ناحیه ماکروسکوپیک پیوسته، حجم کوچک V در ابعاد مزو، پیرامون نقطه‌ای مادی از جسم B مطابق شکل ۱ در نظر گرفته می‌شود. فرض شده است که ماده‌ی ناپیوسته‌ی موجود در حجم V، از لحاظ آماری همگن بوده و نیز حالت مکانیکی ماده موجود در حجم V بتواند توسط میانگین آماری متغیرهای مکانیکی موجود در حجم V بیان شود. اگر این المان حجمی V، کوچکترین حجمی باشد که این شرط را برقرار کند، به V، المان حجمی نمونه گفته می‌شود.

در ابتدا برای مدل سازی اجزا محدود، مدول یانگ نانولوله کربنی برابر با مقدار متداول (Tpa) ۱ در نظر گرفته شده است. برای ماده زمینه نیز مقدار مدول یانگ را متغیر و به صورت (Gpa) ۱، ۲، ۳، ۴، ۵، ۱۰، ۱۵، ۲۵، ۵۰، ۸۰ و ۱۰۰ در نظر گرفته تا طیف گسترده‌ای از مواد را شامل شود. همچنین تغییرات مدول یانگ برای فاز میانی به دو صورت لگاریتمی و خطی در نظر گرفته شده است (معادلات ۱ و ۲). در هر دو حالت، مدول یانگ با افزایش فاصله از مرکز استوانه کاهش می‌یابد. همچنین در سطح تماس لایه میانی با نانولوله و با ماده زمینه، مقدار مدول یانگ به ترتیب برابر با مدول یانگ نانولوله و ماده زمینه است.

$$(E_k)_{Linear} = E_t - (\frac{E_t - E_m}{t_i})\Delta t_k \qquad (۱)$$

$$(E_k)_{\exp} = E_t e^{-(\frac{1}{t_i}\ln\frac{E_t}{E_m})} \Delta t_k \qquad (۲)$$

در روابط فوق، Δt_k فاصله نقطه میانی k امین قسمت، تا سطح خارجی نانولوله کربنی می‌باشد.

به منظور محاسبه خواص الاستیک نانوکامپوزیت، المان حجمی نمونه در نرم افزار اجزاء محدود آباکوس تحت سه نوع بارگذاری کششی، فشار شعاعی و پیچش قرار گرفته و نتایج هر بخش استخراج شده است. پس از انجام محاسبات لازم بر روی نتایج این سه بارگذاری، خواص الاستیک ماده استخراج می‌شود. از انجام این سه بارگذاری که در شکل ۲ نشان داده شده است، مقدار چهار پارامتر اصلی تغییر طول در بارگذاری ب (ΔL)، تغییر شعاع المان در بارگذاری ب (ΔR_I)، تغییر شعاع المان در بارگذاری الف (ΔR_{II}) و زاویه پیچش المان در بارگذاری پ (α) بدست آمده است. سپس با استفاده از روابط هرناندز (Hernandez) خواص الاستیک نانوکامپوزیت محاسبه شده است [۵]. نتایج حاصل از شبیه‌سازی المان محدود و جایگذاری آن‌ها در روابط هرناندز در جدول ۱ آورده شده است.

جدول ۱ مقادیر بدست آمده از جایگذاری نتایج شبیه سازی المان محدود در روابط هرناندز

	گرادیان نمایی					گرادیان خطی				
E_m	E_z	E_r	$G_{r\theta}$	$\nu_{r\theta}$	ν_{zr}	E_z	E_r	$G_{r\theta}$	$\nu_{r\theta}$	ν_{zr}
۱	۳۷,۹۰	۲,۰۳	۱,۰۳	-۰,۰۲	۰,۳۱۴۳	۲۵,۲۰	۱,۶۰	۰,۶۷	۰,۱۹	۰,۳۱۴۲۸۲
۲	۳۸,۹۴	۳,۳۰	۱,۴۱	۰,۱۷	۰,۳۱۴۴	۲۶,۷۷	۲,۷۶	۱,۰۷	۰,۲۹	۰,۳۱۴۳۲۹
۳	۳۹,۹۷	۴,۴۷	۱,۸۰	۰,۲۴	۰,۳۱۴۴	۲۸,۱۷	۳,۸۸	۱,۴۶	۰,۳۳	۰,۳۱۴۳۷۴
۴	۴۱,۰۰	۵,۵۹	۲,۱۸	۰,۲۸	۰,۳۱۴۴	۲۹,۴۹	۴,۹۸	۱,۸۵	۰,۳۵	۰,۳۱۴۴۱۲
۵	۴۲,۰۴	۶,۷۰	۲,۵۶	۰,۳۱	۰,۳۱۴۴	۳۰,۷۶	۶,۰۷	۲,۲۴	۰,۳۶	۰,۳۱۴۴۴۸
۱۰	۴۷,۲۰	۱۲,۰۹	۴,۴۷	۰,۳۵	۰,۳۱۴۵	۳۶,۷۸	۱۱,۴۲	۴,۱۷	۰,۳۷	۰,۳۱۴۵۹۴
۱۵	۵۲,۳۶	۱۷,۳۸	۶,۳۸	۰,۳۶	۰,۳۱۴۶	۴۲,۵۴	۱۶,۶۷	۶,۱۰	۰,۳۷	۰,۳۱۴۷۲۵
۲۰	۵۷,۵۲	۲۲,۶۰	۸,۲۹	۰,۳۶	۰,۳۱۴۷	۴۸,۱۷	۲۱,۸۷	۸,۰۲	۰,۳۶	۰,۳۱۴۸۲۳
۵۰	۸۸,۴۵	۵۳,۲۸	۱۹,۷۶	۰,۳۵	۰,۳۱۵۲	۸۰,۹۱	۵۲,۴۴	۱۹,۵۴	۰,۳۴	۰,۳۱۵۳۰۷
۸۰	۱۱۹,۳۴	۸۳,۴۳	۳۱,۲۳	۰,۳۴	۰,۳۱۵۵	۱۱۲,۹۳	۸۲,۵۸	۳۱,۰۴	۰,۳۳	۰,۳۱۵۶۰۵
۱۰۰	۱۳۹,۹۱	۱۰۳,۴۰	۳۸,۸۷	۰,۳۳	۰,۳۱۵۷	۱۳۴,۰۹	۱۰۲,۵۴	۳۸,۷۰	۰,۳۲	۰,۳۱۵۷۶۹

روش قانون ترکیب تعمیم یافته

خواص مواد میانگین نانوکامپوزیت دوفازی حاوی تقویت‌کننده نانولوله‌های کربنی دارای آرایش تابعی در جهت ضخامت و ماده زمینه پلیمر همسانگرد را می‌توان به یکی از دو روش موری ـ تانکانا و یا قانون ترکیب تعمیم‌یافته تخمین زد. به منظور سادگی و راحتی، در این تحقیق از قانون ترکیب تعمیم‌یافته، که حاوی ترم‌های ضرایب موثر نانولوله‌های کربنی و ترم‌های خواص مواد نانوکامپوزیت می‌باشد، استفاده شده است. ، که می‌تواند به صورت زیر بیان گردد:

$$E_{11} = \eta_1 V_{CNT} E_{11}^{CNT} + V_m E^m \qquad (۳)$$

$$\frac{\eta_2}{E_{22}} = \frac{V_{CNT}}{E_{22}^{CNT}} + \frac{V_m}{E^m} \qquad (۴)$$

$$\frac{\eta_3}{G_{12}} = \frac{V_{CNT}}{G_{12}^{CNT}} + \frac{V_m}{G^m} \qquad (۵)$$

ضرایب η_1، η_2 و η_3 نیز که ضرایب تاثیر نانوله کربنی نامیده می‌شود، مستقل از درصد حجمی فاز تقویت کننده، به شرط عدم تغییر طول نانولوله‌های کربنی هستند. لذا، این ضرایب تاثیر را می‌توان از جایگذاری مدول‌های الاستیکی که برای نانوکامپوزیت، توسط یکی از روش‌های آزمایشگاهی، دینامیک مولکولی و یا المان حجمی نمونه، تحت یک درصد حجمی ثابت برای نانولوله‌های کربنی و طولی معین برای آن‌ها بدست می‌آید، در رابطه قانون ترکیب تعمیم‌یافته بدست آورد. از قانون ترکیب حاصل می‌توان برای درصد حجمی‌های دیگر نانوله‌های کربنی استفاده کرد، به شرطی که از همان طول معین نانولوله‌های کربنی در فاز تقویت کننده استفاده شود. بنابر این قانون ترکیب تعمیم یافته برای محاسبه خواص الاستیک نانوکمپوزیت نانولوله کربنی کار گرفته شده‌اند. اگر در این معادلات η_1 الی η_3 را برابر با یک قرار دهیم، به معادلات قانون ترکیب مقاومت مصالحی خواهیم رسید. برای محاسبه خواص الاستیک ماده، مقدار مدول یانگ هر دو فاز فیلر و ماتریس را در دو جهت اصلی برابر فرض کرده و مدول برشی برای هر دو فاز از معادله زیر محاسبه شده و در جدول ۲ نشان داده شده است:

$$G_{r\theta} = \frac{E_z}{2(1+\nu)} \qquad (۶)$$

جدول ۲ نتایج حاصل از قانون ترکیب تعمیم یافته

E_m	E_z	E_r	$G_{r\theta}$
1	20.98	1.02039	0.39246
2	10.98	1.02037	0.39245
3	7.65	1.02035	0.39244
4	5.98	1.02032	0.39243
5	4.98	1.02030	0.39242
10	2.98	1.02020	0.39238
15	2.31	1.02010	0.39234
20	1.98	1.01999	0.39230
50	1.38	1.01937	0.39206
80	1.23	1.01874	0.39182
100	1.18	1.01833	0.39167

اثر افزایش تعداد لایه‌های فاز میانی

دانشمندان در سالهای اخیر به منظور افزایش دقت مدل المان حجمی نمونه به منظور محاسبه خاصیت‌های مکانیکی نانوکانپوزیت‌ها، لایه‌ای به نام فاز میانی را مدل اضافه کرده‌اند. فاز میانی در واقع فازی مجازی است که نشان دهنده تاثیر قدرت پیوند بین اتم‌های ماده زمینه و ماده تقویت‌کننده می‌باشد. مدول الاستیسیته که برای این فاز در نظر گرفته می‌شود در راستای شعاع متغییر بوده و در دو حالت مختلف خطی و لگاریتمی تغییر می‌کند.

آزمایشهایی که در این زمینه انجام شده نشان می دهند که تغییر مدول الاستیسیته در حالت لگاریتمی دقت بهتری را ارایه می‌دهد. با توجه به اینکه بیشتر تحلیل‌های انجام شده به ازای ۵ لایه میانی می‌باشد ممکن است پاسخ‌هایی که بدست آمده مطلوب نبوده و دارای خطا باشد. به همین دلیل با تکیه بر نرم افزارهای حل عددی و اجزاء محدود سعی بر بدست آوردن تعداد مطلوب لایه‌های فاز میانی شده است که دقت مطلوبی را ارائه دهد.

برای بررسی اثر تعداد لایه‌های فاز میانی بر روی میزان دقت محاسبه خواص الاستیک نانوکامپوزیت، مرحله به مرحله تعداد این لایه‌ها را افزایش داده و پس از هر افزایش با استفاده از مدلسازی المان حجمی نمونه، خواص الاستیک نانوکامپوزیت محاسبه شده است. مشاهده می‌شود که پس از افزودن هر لایه و انجام محاسبات، دقت افزایش پیدا کرده و پس از افزودن

هشتمین لایه، مقادیر بدست آمده برای خواص الاستیک نانو کامپوزیت از دقت خوبی برخوردار است. نمودارهای شبیه‌سازی تعداد لایه‌های فاز میانی در حالتی که مدول یانگ ماده زمینه برابر با ۱و۱۰ در نظر گرفته شده به ترتیب در شکل ۳ و ۴ نشان داده شده است.

شکل ۳ نشان‌دهنده تغییرات مدول محوری بی بعد Ez/Em نسبت به افزایش تعداد لایه‌های فاز میانی هنگامی که مدول یانگ ماده زمینه برابر با ۱۰ در نظر گرفته شده است. شکل ۴ نشان‌دهنده همان تغییرات در زمانی است که مدول یانگ ماده زمینه برابر با ۱ در نظر گرفته شده است. و نمودار شماره ۳ نشان‌دهنده تغییرات مدول شعاعی بی‌بعد Er/Em برای مدول یانگ ماده زمینه برابر با ۱۰ است. با توجه به نتایج بدست آمده مشخص می شود که نمودار تخمین زده شده پس از هشت لایه برای فاز میانی به هم پوشانی مناسبی با خواص الاستیک ماده نانوکامپوزیت اصلی رسیده است.

نتیجه‌گیری

پژوهش‌های حاضر به منظور محاسبه خواص الاستیسیته نانوکامپوزیتهای نانولوله کربنی و همچنین بدست آوردن تعداد لایه‌های فاز میانی مناسب برای محاسبه این خواص انجام گرفت. نتایج نشان می دهد که اگر تغییرات مدول الاستیسیته فاز میانی به صورت نمایی در نظر گرفته شود، نتایج بدست آمده دقت بهتری را ارئه خواهند کرد. علاوه بر این مشخص می‌شود که اگر در هنگام شبیه‌سازی اثر فاز میانی برای محاسبه خواص الاستیسیته، اگر تعداد لایه‌های موثر فاز میانی به جای پنج لایه هشت لایه در نظر گرفته شود، دقت کار بالا رفته و نتایج به واقعیت نزدیکتر خواهند شد. البته پس از محاسبه خواص مکانیکی نانو کامپوزیت، همسویی کامل نتایج بدست آمده با پژوهش‌های پیشین مشاهده می‌شود و می توان با بهبود تعداد لایه های فاز میانی، در بهبود نتایج گام موثری برداشت.

شکل‌ها و نمودارها

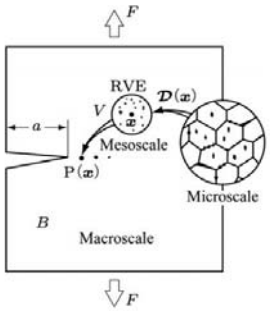

شکل ۱ مدل المان حجمی نمونه

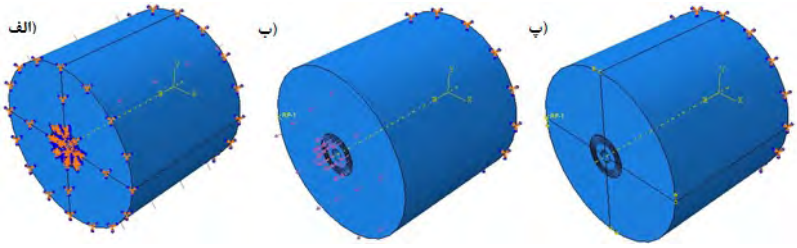

شکل ۲ مدل اجزاء محدود المان حجمی نمونه الف) بارگذاری فشار شعاعی، ب) بارگذاری کششی و پ) بارگذاری پیچشی

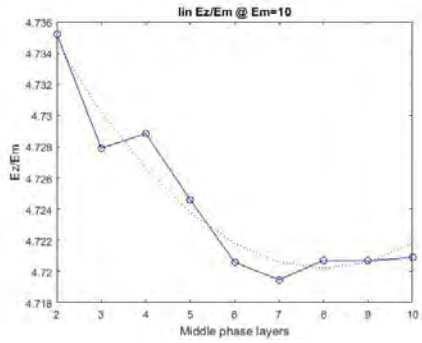

شکل ۳ تغییرات مدول محوری بی بعد Ez/Em نسبت به افزایش تعداد لایه‌های فاز میانی برای Em= ۱۰

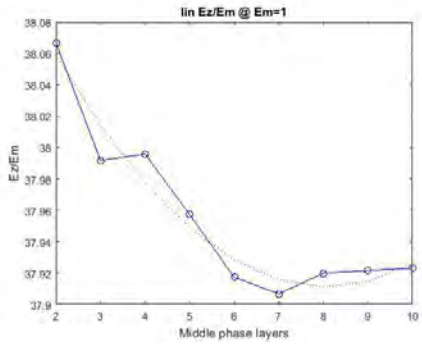

شکل ۴ تغییرات مدول محوری بی بعد Ez/Em نسبت به افزایش تعداد لایه‌های فاز میانی برای Em= ۱

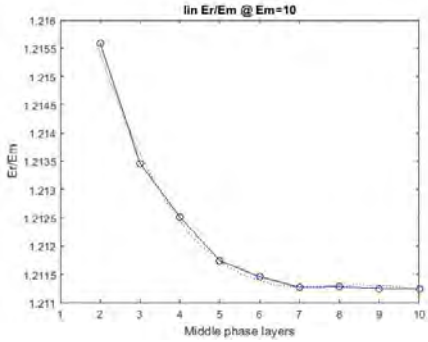

شکل ۵ تغییرات مدول محوری بی بعد Er/Em نسبت به افزایش تعداد لایه‌های فاز میانی برای Em= ۱۰

مراجع

1- Zhang, Chen-Li, and Hui-Shen Shen. "Temperature-dependent elastic properties of single-walled carbon nanotubes: prediction from molecular dynamics simulation." Applied Physics Letters 89.8 (2006): 081904.
2- Ayatollahi, M. R., S. Shadlou, and M. M. Shokrieh. "Multiscale modeling for mechanical properties of carbon nanotube reinforced nanocomposites subjected to different types of loading." Composite Structures 93.9 (2011): 2250-2259.
3- P. Zhu, Z. X. Lei, and K. M. Liew, "Static and free vibration analyses of carbon nanotube-reinforced composite plates using finite element method with first order shear deformation plate theory," Composite Structures, vol. 94, pp. 1450-1460, 3// 2012.
4- Shen, Hui-Shen. "Thermal buckling and postbuckling behavior of functionally graded carbon nanotube-reinforced composite cylindrical shells." Composites Part B: Engineering 43.3 (2012): 1030-1038.
5- Hernández-Pérez, A., and F. Avilés. "Modeling the influence of interphase on the elastic properties of carbon nanotube composites." *Computational Materials Science* 47.4 (2010): 926-933.

Piezoresistive Behavior of PDMS/CNT Nanocomposites Made by Vacuum Filtration Method

M. Nankali[1], **N. Geran Malek**[2], **N. M. Nouri**[3], **M. Navidbakhsh**

[1]School of Mechanical Engineering, Iran University of Science and Technology; m_nankali@mecheng.iust.ac.ir

[2]School of Automotive Engineering, Iran University of Science and Technology; nima_geran@auto.iust.ac.ir

[3]School of Mechanical Engineering, Iran University of Science and Technology; mnouri@iust.ac.ir

[4]School of Mechanical Engineering, Iran University of Science and Technology; mnavid@iust.ac.ir

Abstract

In this study, the conductive polymer nanocomposites (CPNCs) of PDMS/CNT flexible films were prepared by layer-by-layer (LBL) production method. This was done by vacuum filtration and doctor-blading deposition method to manufacture sandwich-structured nanocomposites and then the piezoresistive properties of PDMS/CNT thin films were discussed. Nanocomposite samples were made in different %wt of CNT but on the same membrane. For this, we used CA membranes in Millipore setup. In order to apply this technique, a suspension of CNT particles was prepared. To do this, known amount of CNT particles were dispersed in deionized water by the aim of surfactant material and sonication then the suspension was centrifuged to remove any agglomerated CNT particles. Afterward, to ensure the amount of CNT content in suspension, the %wt of CNT was measured again. Depend on CNT content, the obtained CPNC films exhibited initial electrical resistance in the range of 12.5 KΩ to 22.8 MΩ and a great piezoresistive behavior under strain. The effect of CNT weight density on electrical and piezoresistive properties of CPNC films, as well as the electrical percolation, initial resistance, and variation of electrical resistance by applying strain, was investigated. These nanocomposites have a great potential in the application of flexible and stretchable electronics as well as sensing elements strain and pressure sensors, biosensors, actuators, tactile sensors, supercapacitors and etc.

Keywords : Piezoresistive effect, Polydimethylsiloxane (PDMS), PDMS/CNT Nanocomposites, Vacuum Filtration, Cellulose Acetate (CA) Membrane

1. Introduction

Conductive polymer nanocomposites (CPNCs) are one of the most important subgroups of advanced materials. they play an important role in stretchable electronics, industrial monitoring and medical instruments and have wide applications in personal electronic devices, actuators, supercapacitors, flexible sensing elements like pressure sensors, strain sensors, tactile sensors, biosensors, and etc. for example in the sensors and actuators family there are various mechanisms, including pieziresistivity, capacitance, piezoelectricity and etc. that convert stimuli to electrical signals. Each of these three important mechanisms are presented below:

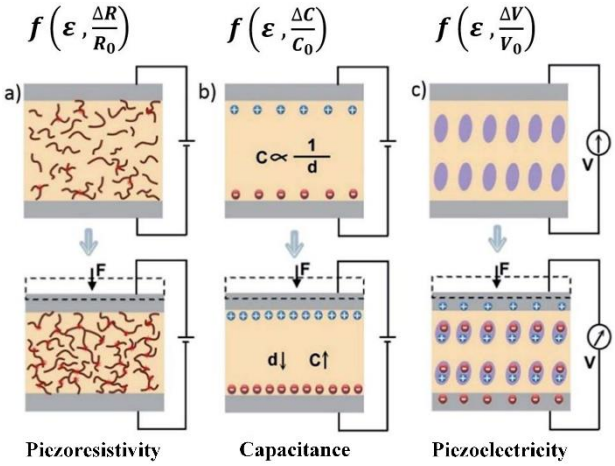

Figure 1. The schematic images of transduction methods: (a) piezoresistivity, (b) capacitance and (c) piezoelectricity [1].

In this study we considered the piezoresistive behavior of PDMS/CNT nanocomposites made by vacuum filtration method. Wang et al. [2] developed a facile fabrication method for highly transparent free-standing SWCNT ultrathin films. they demonstrated SWCNT ultrathin films can be reproducibly exfoliated from the dense SWCNT film on the filtration membrane by surface tension of deionized water, which were easily transferred onto PET substrates. They used SWCNT ultrathin films to make highly sensitive flexible chemiresistive sensors. The fabrication process for a free standing SWCNT ultrathin film used in the research is shown in the Fig. 1.

In their next study, they fabricated reduced graphene oxide ultrathin films by a reproducible exfoliation method at the liquid/air interface, and they showed high transparency, tunable sheet resistance, uniform electric conductivity, and structural homogeneity over a large area. A flexible relative humidity sensing matrix was demonstrated and it was shown to be excellent for close proximity sensing without touching it [3].

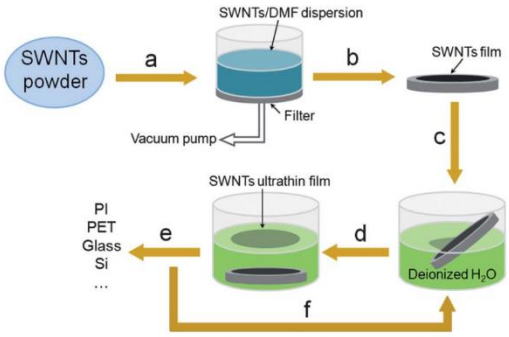

Figure 2. Schematic of the fabrication process for free-standing SWNT ultrathin films used by Wang et al. [2]

Xu et al. [4] prepared the flexible transparent conductive films (FTCFs) of silver nanowire-polyethylene terephthalate (Ag NW-PET) by a facile method including vacuum filtration and mold transferring. The effect of silver nanowire weight density on the optical and electrical properties of films, as well as the electrical percolation were investigated. The obtained typical Ag NW-PET film exhibited high figure of merit of 31.3 × 10-3 Ω-1 with low sheet resistance of 4.95 Ω sq-1 and high transparency at 550 nm of 83.0% (excluding PET substrate). The resulting FTCFs based on PET substrate with high transmittance and low sheet resistance have a great potential in the application of high-performance flexible electronics and photovoltaic devices.

Hyun et al. [5] developed Graphene electronic circuits on paper substrates by using graphene nanoplates and applied to foldable paper-based electronics. The graphene circuits had shown a small change in conductance under various folding angles and maintain an electronic path on paper substrates after repetition of folding and unfolding with excellent stability. fabrication started with vacuum filtration (Fig. 3a) of the graphene dispersion by using a hydrophobic polytetrafluoroethylene (PTFE) membrane filter (pore size: 0.2 μm). Then, the graphene nanoplates were uniformly deposited on the filter. The membrane filter with the filtered graphene was moved onto a paper substrate by turning the graphene side down to contact the filtered graphene with the paper (Fig. 3b). After drawing the shapes of circuits on the back of the membrane filter with a pen, the filter was separated from the substrate (Fig. 3c). Thus, the filtered graphene was transferred onto the paper where the shapes of the circuits were drawn on the back of the filter, while the graphene in the other parts remained on the filter.

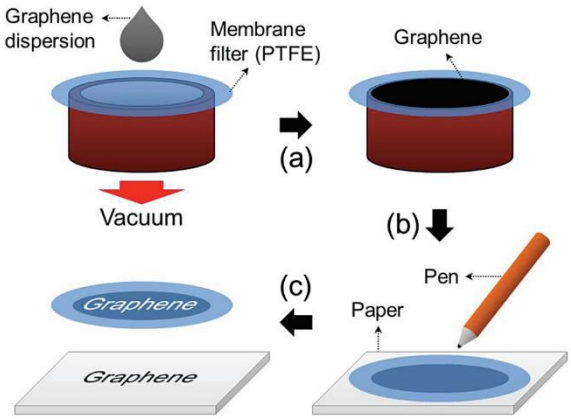

Figure 3. preparation of a graphene circuit on a paper substrate via vacuum filtration of a dispersion of graphene nanoplates and a selective transfer process with a pen [5].

The graphene circuits have been prepared by vacuum filtration of a graphene dispersion and a selective transfer process with a pen.

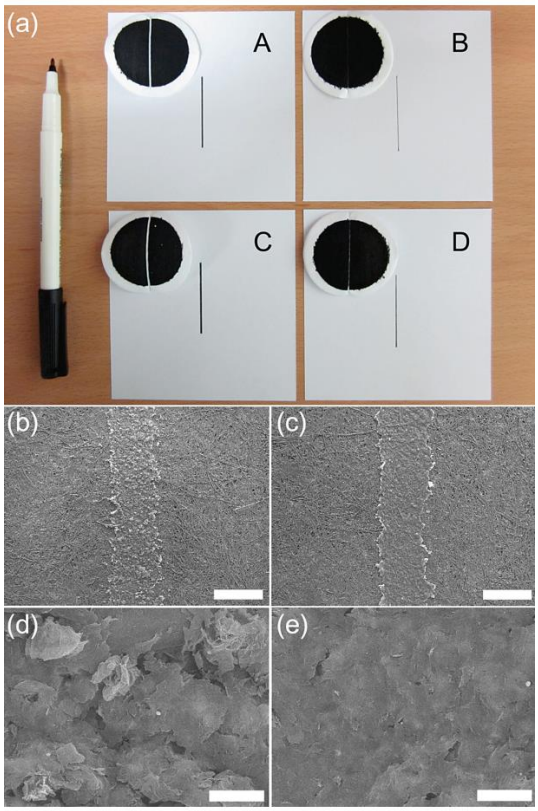

Figure 4. Photograph of filtered graphene on membrane filters ofSample A to D and graphene transferred onto the paper substrates by a felt tip pen from the membrane filters. b, c) Low- and d, e) high-magnification SEM images of graphene circuits obtained from the Sample A and the Sample C. Scale bars are 500 μm for b and c and 10 μm for d and e [5].

Employing the graphene circuits, finally, they demonstrated foldable circuit boards based on paper substrates for operating LED chips under various kinds of deformation.

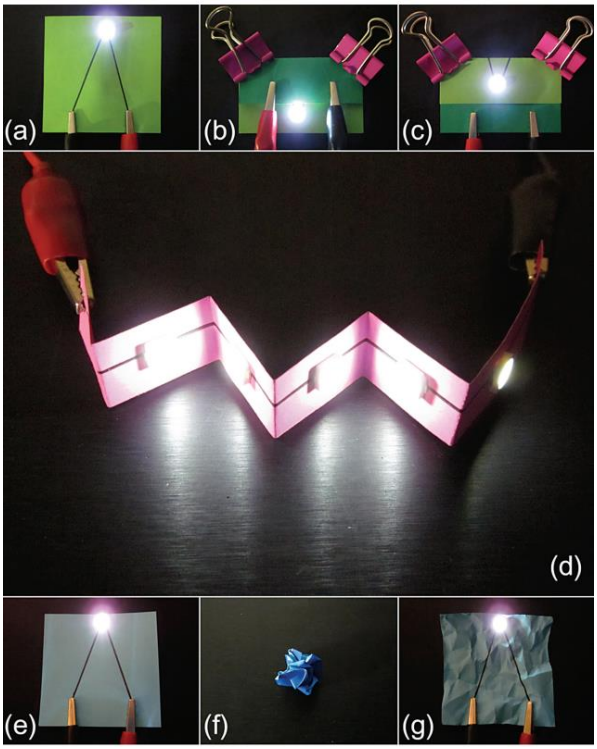

Figure 5. Photographs of applications. a,b,c) Operation of a LED chip with graphene circuits on a paper substrate under −180° folding and 180° folding. d) An array of LED chips on a three-dimensional circuit board including negative and positive angle folding. e,f,g) Operation of a LED chip on the paper-based circuit board before and after crumpling [5].

Jiang et al. [6] demonstrated a shortcut fabrication strategy, vacuum filtration, and cutting, to construct foldable and electrically stable graphene-based film resistors. Through investigation of resistor behavior under different stress conditions, it was found that micro-cracks appeared on the surface was correlated to curvature and percolation theories. The effects of ionic cellulose ethers on the contact state of graphene layers under tension and bending were investigated, which efficiently prevent the surface crack from happening. This rapid fabrication method to carry out individual customization may further realize other environmental friendly, portable and multifunctional devices.

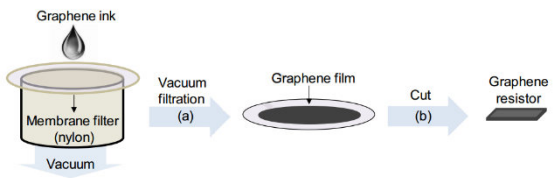

Figure 6. Schematic diagram of the preparation process of foldable graphene resistor. (a)Graphene ink filtered by Nylon membrane filter. (b)Graphene resistor cut off from graphene film by scissors [6].

2. Experimental

2.1. Material

In this study we used Sylgard 184 from Dow Corning-USA, that is the commercial PDMS and often used in microfluidics, MEMS, stretchable sensors and actuators. This elastomer was used as a nanocomposite matrix Due to facile polymerization, simple molding and prototyping, long gel time, biocompatibility, transparency and desirable mechanical and dielectric properties. Schneider et al. [7] measured the rheological, mechanical and optical properties of Sylgard 184 for optical MEMS. As shown in Fig. 7, Sylgard 184 can endure strains up to 115% .

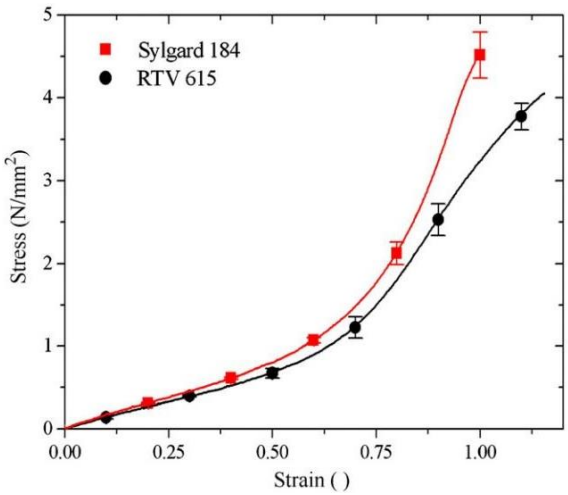

Figure 7. Stress–strain diagram of RTV 615 and Sylgard 184. Continuous measurement with exemplarily shown error bars [7].

From the manufacturer catalogue, Sylgard 184 can be cured in different temperatures. Table 1 contains curing time and temperature of Sylgard 184.

Table 1. Curing time and temperature of Sylgard 184 [8]

Curing Temperature	Time
Curing at 25ºC	48 hours
Heat Curing at 75ºC	120 minutes
Heat Curing at 100ºC	35 minutes
Heat Curing at 125ºC	20 minutes
Heat Curing at 150ºC	10 minutes

Also a suspension of MWCNTs was used as a nanocomposite filler because its appropriate properties. Table 2. Contains some important properties of SWCNTs and MWCNTs. According to the Table 2. Electrical conductivity of MWCNTs and their aspect ratio are the most important factors to create piezoresistive behavior in PDMS matrix.

Table 2. Geometrical characteristics and physical properties of SWCNT and MWCNT [9] [10] [11].

property	SWCNT	MWCNT
Thickness (nm)	0.6-1.8	5-50
Length (µm)	0.2-6	0.2-5
Aspect ratio	100-10000	100-10000
Density (gr/cm^3)	1.3	1.75
Thermal conductivity (W/mK)	3000-6000	3000-6000
Electrical conductivity (S/cm)	10^3 - 10^4	2×10^3 - 10^4
Tensile strength (GPa)	5-500	10-60

2.2. Preparation of CNT suspension

In order to disperse MWCNTs in deionized water we used sodium dodecyl sulfate (SDS) as a surfactant material. Each SDS molecule has a polar and non-polar head and because of this, this surfactant can disperse MWCNTs (non-polar) in deionized water (polar). The %wt of materials used in suspension is mentioned Table 4.

Figure 8. BANDELIN Ultrasonic probe, HD 3200 model and VS-70T probe.

At first, the materials were prepared (Table 4), then stirred for 15 minutes and after that uniformly dispersed in deionized water with sonication process. To do sonication, there was used from BANDELIN-HD 3200 with the probe model VS-70T, the pulse duration of 1sec on/off and power of 70 Watt .

Table 3. Suspenstion properties

Data	Petri-a	Petri-b	Petri-c	Petri-d	Petri-e	Petri-f
10 cc suspension (gr)	10.45	10.11	10.35	10.39	10.41	10.43
Powder Weight (gr)	0.021	0.025	0.023	0.022	0.023	0.023
CNT Weight (gr)	8.75e-4	10.41e-4	9.58e-4	9.17e-4	9.58e-4	9.58e-4
SDS Weight (gr)	2.01e-2	2.39e-2	2.20e-2	2.11e-2	2.20e-2	2.20e-2
CNT weight fraction (%wt)	0.0083	0.0103	0.0093	0.0088	0.0092	0.0092
Average %wt of CNT in susp.	0.0092					
Average %wt of SDS in susp.	0.211					
Average %wt of water in susp.	99.779					

To ensure that the suspension doesn't contain any agglomerated CNTs, final step should be done. In this step, all the suspension was centrifuged in 4500 rpm for 15 minutes in Universal-320 centrifuger and agglomerated CNTs were deposited in centrifuge tubes consequently.

Figure 9. Photograph of (a) segregating the agglomerated MWCNTs by centrifuging machine and, (b) Evaporation of deionized water from CTN suspension in oven (c) Calculation of CNT fraction in final suspension [12].

After centrifuging step, %wt MWCNTs in suspension may be change a little. because of this, at the end of the centrifuging step %wt MWCNTs was measured again by the aim of six petri-dishes each petri-dish containes 10 mL suspension.

As you can see in Table 3, petri-dishes were placed in oven to evaporate deionized water then for each petri-dish the powder weight and subsequently the CNT weight fraction was measured. Finally, the average %wt of MWCNTs in suspension was achieved. The average %wt of CNT was about 0.01.

Table 4. Materials in CNT suspension

Materials	Value
MWCNT	0.1 gr
SDS surfactant	2.3 gr
Deionized Water	1 Liter

2.3. Applying CNT film on CA membrane

Applying CNT film on CA membrane was done by vacuum filtration method. In order to implement this technique, preparation of nanoparticle dispersed suspension and membranes with porosity smaller than the size of nanoparticles is necessary. this two requisites, are two important inputs of this process.

To achieve the best piezoresistive properties it is necessary to have a suspension without any agglomeration of CNTs and also use a membrane type (hydrophilic or hydrophobic) that has a proper conformity with suspension type. In this study, a colloidal water-based suspension was used so the hydrophilic membranes like CA, Ny, MCE, PE, NC H-PTFE, PES and H-PVDF were proper for using in vacuum filtration.

Probably, compared with the other methods, the vacuum-filtering method is regarded as the simplest process for the fabrication of ultrathin, transparent, optically homogeneous, electrically conducting films composed of pure CNTs. This process is quite simple, containing three steps: vacuum filtering a dilute, surfactant-based suspension of purified nanotubes onto a filtration membrane to form a homogeneous film on the membrane, then washing away the surfactant with purified water to allow film formation of pure CNT, followed by dissolving the filtration membrane in the solvent [13].

From the above, this filtration method has several advantages: (i) as the nanotubes accumulate, the generated filter cake acts to impede the permeation rate, which can tune the local permeation rate and associated deposition rate automatically. Therefore, homogeneity of the films is guaranteed. (ii) Under vacuum, the nanotubes tend to lie straight, gaining maximum overlap and interpenetration within the film as they accumulate. This yields maximum electrical conductivity and mechanical integrity throughout the films. (iii) The film thickness is

controlled, with nanoscale precision, by the nanotube concentration and volume of the suspension filtered [13]. In spite of three advantages above, in this method the CNT nanoparticles have random distribution that cause to better piezoresistive behavior in nanocomposite film.

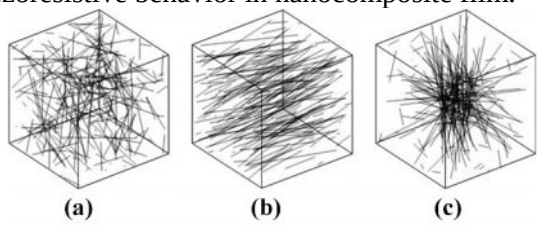

Figure 10. Schematics of (a) uniformly distributed, (b) aligned and (c) agglomerated CNTs of different lengths in a cuboid with assumed periodic boundary [12].

Vaccum filtration process is commonly executed by a filtration setup known as Millipore, so the process was done by Millipore setup. a layer of MWCNTs were deposited on the CA membrane with pore size of 0.22µm.

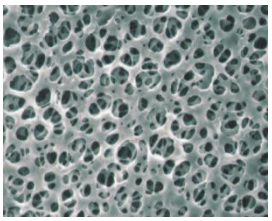

Figure 11. SEM image of Cellulose Acetate membrane with pore size of 0.22 µm [14].

Different volume fractions of MWCNT suspension was used from 1 to 10 mL to create thin films of MWCNT on CA membrane in Millipore setup. According to the Table 5, different thickness of CNT layers were created on ten CA membranes with different suspension values. as the area of CA membranes and %wt CNT in suspension (Table 3) are known and also from the Table 2 we know the density of MWCNT, we can calculate the thickness of MWCNT layer on the CA membrane.

Table 5. Thickness of CNT layer for different suspension values.

suspension value (mL)	Thickness of CNT layer (µm)
1	1.58
2	3.17
3	4.75
4	6.33
5	7.92
6	9.50
7	11.10
8	12.70
9	14.30
10	15.80

As surfactant material (SDS) reduces the electrical conductivity of CNT nanoparticles, to achieve the maximum electrical conductivity in MWCNTs it is better to deterge surfactant from nanoparticles. To do this, after filtration process the CNT layer on CA membrane was washed with deionized water. CA membranes coated with 1 to 10mL of CNT suspension are shown in (Fig. 12).

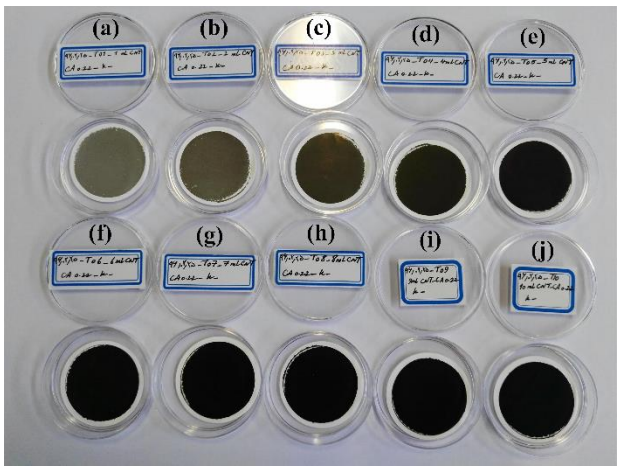

Figure 12. CA membranes coated with CNT by vaccum filtration method. Membranes (a) to (j) coated with 1 to 10mL of CNT respectively.

2.4. Applying PDMS and curing

Previously, a CNT film was applied on CA membrane. In this step a PDMS film with a thickness of 600µm was applied on CA membrane with doctor-blading deposition method (see Fig. 14). Then, a liquid PDMS was cured in 100 $°C$ for 35 minutes (see Table 1). curing process was done by radiative oven which was calibrated by Lutron YK-2005RH real time digital thermometer with a precision of ± 0.1 ℃. After curing PDMS, a CA membrane/piezoresistive PDMS composite film was created and CA membrane was peeled off from piezoresistive PDMS. So the final thin film nanocomposite with piezoresistive behavior was made.

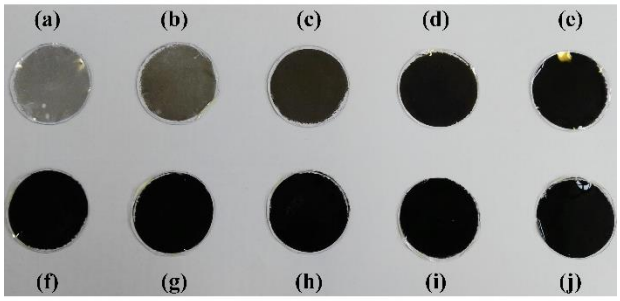

Figure 13. Piezoresistive PDMS/CNT nanocomposites. Specimens (a) to (j) have 1 to 10mL of CNT suspension respectively.

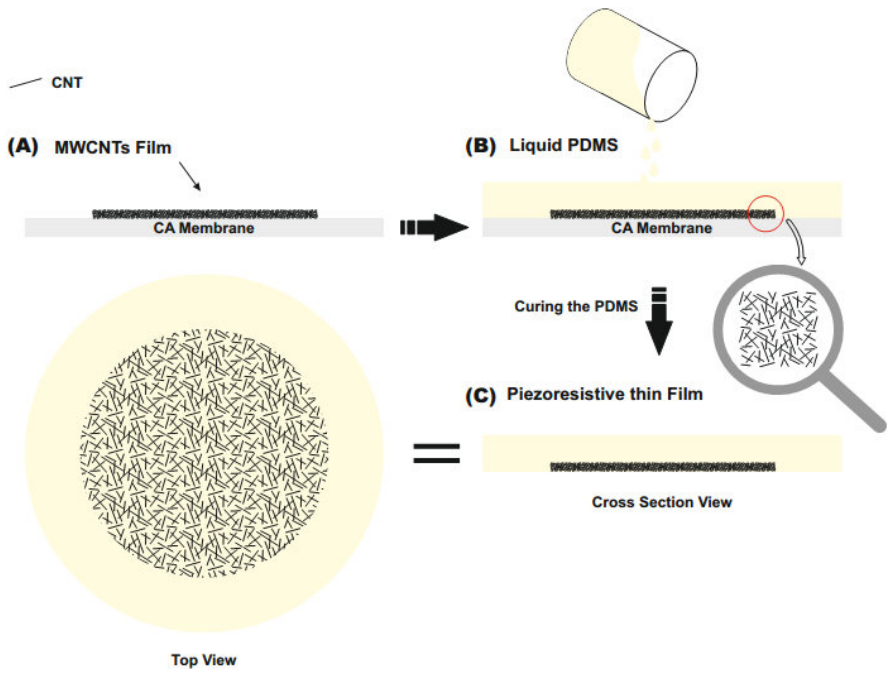

Figure 14. Schematic representation of experimental procedure

2.5. Characterization and measurement

The electrical conductivity and piezoresisitive behavior of PDMS/CNT nanocomposite films was measured by Fluke 179 True RMS Digital Multimeter and tensile test.

3. Results and Discussion

3.1. Electrical property

According to the traditional percolation theory [15], the electrical conductivity of conductive composites can be predicted by :

$$\sigma = \sigma_0 (\phi - \phi_c)^t \quad \text{for} \quad \phi > \phi_c \qquad (1)$$

Where σ is electrical conductivity of CPNCs, ϕ is the volume fraction of the filler, ϕ_c is the percolation threshold, σ_0 is a parameter basically depending on the electrical conductivity of the filler and t is the critical exponent universally related to the dimensionality of the conductive network formed in CPNCs.

As it clear in S-shaped conductance curve of nanocomposites (Fig. 15), The transition from nonconductive to conductive state occurs at some critical volume fraction, known as percolation threshold. After passing through the percolation threshold ($\phi = \phi_c$) dependence of the electrical conductivity of the nanocomposite on the filler reduces and eventually reaches a saturation point and adding more conductive nanoparticles will no longer improves the electrical conductivity of nanocomposite. the highest piezoresistive sensitivity is achieved when the volume fraction of nanotubes is near to percolation threshold.

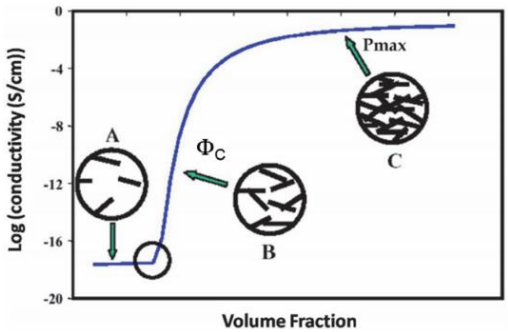

Figure 15. Schematic illustrations of the percolation curve of fillers in conductive CPNCs [16].

Given the above description, for finding the best piezoresistive properties of nanocomposite, it is necessary to control the weight percentage of conductive nano-fillers in nanocomposites. Fig. 16 shows the maximum R_0 values for the Piezoresistive PDMS/CNT nanocomposite Specimens (see Fig. 13) have 1 to 10mL of CNT suspension.

Table 5. Initial Resistance versus Suspension volume for PDMS/CNT piezoresistive nanocomposite specimens

Suspension value (mL)	Initial resistance (R_0)
1	22800
2	12700
3	781
4	74.9

5	39.6
6	30.2
7	21.8
8	14.3
9	13.4
10	12.55

It is clear that initial resistance of specimens with suspension values lower than 4mL

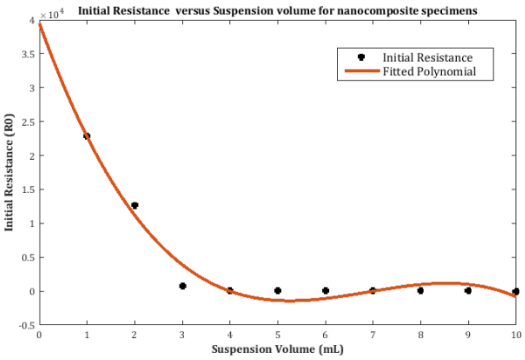

Figure 16. Initial Resistance versus Suspension volume for PDMS/CNT piezoresistive nanocomposite specimens

3.2. Piezoresistive property

As for the working mechanisms in the piezoresistive nanocomposite strain sensors, from the accumulated knowledge until now, the piezoresistivity observed in this kind of piezoresistivite CNT/polymer nanocomposites can be mainly attributed to the following three aspects; (a) significant variation of conductive networks formed by CNTs, e.g., loss of contact among CNTs. (b) tunneling resistance change in neighboring CNTs due to the distance change. (c) piezoresistivity of CNTs themselves due to their deformation [17].

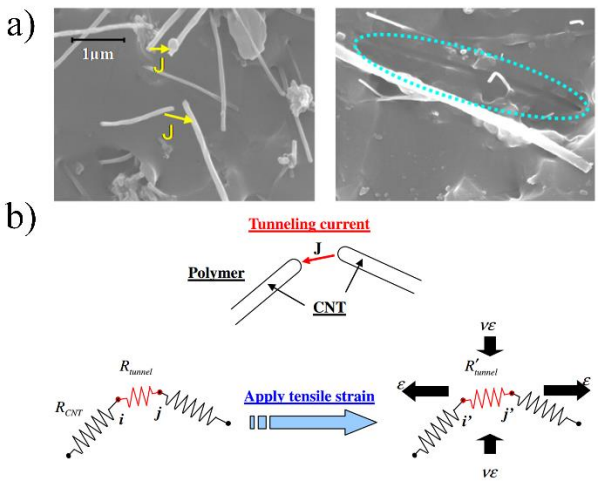

Figure 17. (a)SEM image of possible tunneling effect among neighboring CNTs and evident of weak interface between polymer and CNTs in nanocomposites [17]. (b) tunneling effect among neighboring CNTs [18].

From three aspects above, in the 3D resistor network of PDMS/CNT, tunneling resistance has a major role in piezoresistivity of nanocomposites. The tunneling resistance between two neighboring CNTs can be approximately estimated as follows [19]:

$$R_{tunneling} = \frac{V}{AJ} = \frac{h^2 d}{Ae^2\sqrt{2m\lambda}} \exp\left(\frac{4\pi d}{h}\sqrt{2m\lambda}\right) \qquad (2)$$

Where J is tunneling current density (see Fig. 17), V is the electrical potential difference, e is the quantum of electricity, m is the mass of the electron, h is Planck's constant, d is the distance between CNTs, λ is the height of the barrier (for epoxy, 0.5 to 2.5 eV), and A is the cross sectional area of the tunnel [18].

Should be use and deleted ----->>> As shown in Fig. 2, the normalized resistance change of the four prepared samples displays similar monotonic increase with strain. At higher R0, the strain-normalized resistance change is linear (at strain range 0–2.5 %), with calculated gauge factors of 20 (R0-462 kΩ) and 32 (R0-380 kΩ). During 2.6–14 %, strain nonlinearity appeared, and upon strain release, the resistances of these two sensors were immediately restored to 420 and 590 kΩ, and after 4 h to 390 and 450 kΩ. This indicates that the sensing process does not permanently deform/damage the micro lines. The patternable PDMS/MWCNT sensors possess additional advantages of larger working range (>10 %) and mechanical flexibility compared to the conventional metal foil sensors and find applications in tissues, microfluidic systems, as well as flexible 3D microsystems. when the gage factor parameter for a semiconductor material is higher, sensitivity to small strain is higher. according to Fig. 2, samples having lower initial resistance, have higher sensitivity to strain and also higher gage factor [20].

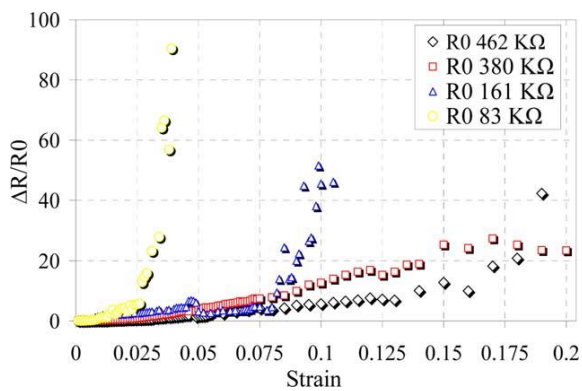

Figure 16. Strain versus normalized resistance change of the MWCNT/PDMS sensors with different initial resistances(R_0) [20].

In this study,….

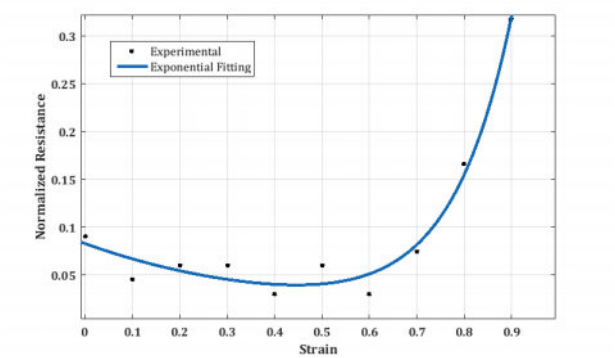

Figure 18. Strain versus normalized resistance change of the Piezoresistive PDMS/MWCNT nanocomposite specimen contain 5mL CNT suspension.

4. Conclusion

In this study,….

Acknowledgments

We thank the financial support from Professors N. M. Nouri and M. Navidbakhsh and also the supports from Laboratory of applied hydrodynamics.

Nomenclatures

CPNC	Conductive polymer nanocomposite
FTCF	Flexible transparent conductive films
PDMS	Polydimethylsiloxane
MWCNT	Multi-wall carbon nanotube
AgNw	Ag nanowire
SDS	Sodium dodecyl sulfate
CA	Cellulose acetate
NC	Cellulose nitrate
MCE	Cellulose mixed esters
H – PTFE	Hydrophilized polytetrafluoroethylene
H – PVDF	Hydrophilized polyvinylidene difluoride
PES	Polyethersulfon
PE	Polyester

References

[1] Y. Zang, F. Zhang, C.-a. Di, and D. Zhu, "Advances of flexible pressure sensors toward artificial intelligence and health care applications," *Materials Horizons*, vol. 2, pp. 140-156, 2015.

[2] X. Wang, G. Li, R. Liu, H. Ding, and T. Zhang, "Reproducible layer-by-layer exfoliation for free-standing ultrathin films of single-walled carbon nanotubes," *Journal of Materials Chemistry*, vol. 22, pp. 21824-21827, 2012.

[3] X. Wang, Z. Xiong, Z. Liu, and T. Zhang, "Exfoliation at the liquid/air interface to assemble reduced graphene oxide ultrathin films for a flexible noncontact sensing device," *Advanced Materials*, vol. 27, pp. 1370-1375, 2015.

[4] W. Xu, Q. Xu, Q. Huang, R. Tan, W. Shen, and W. Song, "Fabrication of Flexible Transparent Conductive Films with Silver Nanowire by Vacuum Filtration and PET Mold Transfer," *Journal of Materials Science & Technology*, vol. 32, pp. 158-161, 2016.

[5] W. J. Hyun, O. O. Park, and B. D. Chin, "Foldable graphene electronic circuits based on paper substrates," *Advanced Materials*, vol. 25, pp. 4729-4734, 2013.

[6] X. Jiang, R. Zhang, T. Yang, S. Lin, Q. Chen, Z. Zhen, *et al.*, "Foldable and electrically stable graphene film resistors prepared by vacuum filtration for flexible electronics," *Surface and Coatings Technology*, vol. 299, pp. 22-28, 2016.

[7] F. Schneider, J. Draheim, R. Kamberger, and U. Wallrabe, "Process and material properties of polydimethylsiloxane (PDMS) for Optical MEMS," *Sensors and Actuators A: Physical*, vol. 151, pp. 95-99, 2009.

[8] (2017). *SYLGARD® 184 SILICONE ELASTOMER KIT*. Available: http://www.dowcorning.com/applications/search/products/Details.aspx?prod=01064291

[9] R. Sengupta, M. Bhattacharya, S. Bandyopadhyay, and A. K. Bhowmick, "A review on the mechanical and

electrical properties of graphite and modified graphite reinforced polymer composites," *Progress in polymer science*, vol. 36, pp. 638-670, 2011.

[10] M. H. Al-Saleh and U. Sundararaj, "A review of vapor grown carbon nanofiber/polymer conductive composites," *Carbon*, vol. 47, pp. 2-22, 2009.

[11] P.-C. Ma, N. A. Siddiqui, G. Marom, and J.-K. Kim, "Dispersion and functionalization of carbon nanotubes for polymer-based nanocomposites: a review," *Composites Part A: Applied Science and Manufacturing*, vol. 41, pp. 1345-1367, 2010.

[12] W. Bao, S. Meguid, Z. Zhu, Y. Pan, and G. Weng, "A novel approach to predict the electrical conductivity of multifunctional nanocomposites," *Mechanics of Materials*, vol. 46, pp. 129-138, 2012.

[13] S. Yellampalli, "Vacuum filtration method," in *Carbon Nanotubes - Synthesis, Characterizatiion, Applications*, ed Croatia: Intech, 2011, p. 496.

[14] A. m. INC. (2017, 1 1). Membrane Filters. Available: http://www.advantecmfs.com/catalog/filt/membrane.pdf

[15] A. M. G. A. J. Leggett (auth.), Stuart A. Wolf (eds.), "PERCOLATION AND SUPERCONDUCTIVITY," in *Percolation, Localization, and Superconductivity (Edition 1)*, ed Tel Aviv , Israel: Springer US, 1984, pp. 95-113.

[16] J. Cuppoletti, *Nanocomposites With Unique Properties in Medicine, Industry*. Rijeka, Croatia: Intech 2011.

[17] N. Hu, H. Fukunaga, S. Atobe, Y. Liu, and J. Li, "Piezoresistive strain sensors made from carbon nanotubes based polymer nanocomposites," *Sensors*, vol. 11, pp. 10691-10723, 2011.

[18] B. Hu, N. Hu, Y. Li, K. Akagi, W. Yuan, T. Watanabe, *et al.*, "Multi-scale numerical simulations on piezoresistivity of CNT/polymer nanocomposites," *Nanoscale research letters*, vol. 7, p. 402, 2012.

[19] J. G. Simmons, "Generalized formula for the electric tunnel effect between similar electrodes separated by a thin insulating film," *Journal of applied physics*, vol. 34, pp. 1793-1803, 1963.

[20] D. Ponnamma, K. K. Sadasivuni, C. Wan, S. Thomas, and M. A.-A. AlMa'adeed, "Flexible and stretchable electronic composites," *Springer series on polymer and composite materials*, 2016.

IUST

The Biennial International Conference on Experimental Solid Mechanics
(X-Mech 2018)
13-14 Feb., 2018, Tehran, Iran

Center of Excellence in Experimental Solid Mechanics and Dynamics,
School of Mechanical Engineering, Iran University of Science and Technology

Evaluation of non-linear Effects in Piezoresistive PDMS/MWCNT Sensing Elements

[1] Nankali, M., [2*]Nouri, N. M., and [3] Geran Malek, N.
[1] Postgraduate Student, Department of Mechanical Engineering, Iran University of Science and Technology, Tehran, 16846-13114, Iran
[2] Professor, Department of Mechanical Engineering, Iran University of Science and Technology, Tehran, 16846-13114, Iran
[3] Postgraduate Student, Department of Automotive Engineering, Iran University of Science and Technology, Tehran, 16846-13114, Iran

*(Corresponding author: mnouri@iust.ac.ir)

***Abstract*- In this study, the non-linear effects of piezoresistive PDMS/MWCNT sensing element were evaluated. The sensing element is a sandwich-structured film containing an ultrathin layer of piezoresistive nanocomposite and is a type of conductive polymer nanocomposite (CPNCs). In order to manufacturing sensing element, first, a CNT suspension was prepared and then the piezoresistive film was made using vacuum filtration method. Finally, non-linear effects of the piezoresistive sensing element such as voltage drop, which is mainly due to creep and hysteresis, were evaluated and the results were discussed.**

Keywords - Piezoresistive effect, Sensing Element, Non-linear effects, Vacuum Filtration, Polydimethylsiloxane (PDMS)

I. INTRODUCTION

II. PIEZORESISTIVE PROPERTIES

Piezoresistive test procedure

The piezoresistive properties of the hybrid film were evaluated according to the procedure of Figure 1. For this, specific strain values were applied to the piezoresistive hybrid film and the variation of electrical resistance was recorded at the frequency of $1\ \mathrm{kHz}$ using data acquisition system.

Figure 1. Data processing procedure. (A) Voltage source (B) Wheatstone bridge circuit (C) Data acquisition device (D) Analogue-to-digital converter (E) desktop computer.

Initially, several tests were performed according to the Figure 1. In each test, a cyclic loading/unloading was applied to the piezoresistive hybrid film and the data acquisition system recorded the variation of electrical resistance at the

frequency of $1\ \mathrm{kHz}$. According to the Figure 2, each loading cycle is about 600 seconds and contains 10 equal increments. In each increment, the hybrid film was subjected to an elongation of $300\ \mu\mathrm{m}$ and was rested for 60 sec so the interval between two consecutive increments was 60 seconds. Given that the initial length (L_0) of the piezoresistive hybrid film was $26.15\ \mathrm{mm}$, so the strain values in each increment is $\varepsilon = 0.0115$. The maximum strain was occurred in the final increment due to an elongation of $\Delta L = 3\ \mathrm{mm}$ and its value was $\varepsilon_{Max} = 0.115$. In the loading cycle by increasing the strain, the electrical resistance of the hybrid film was increased to a maximum value (see Figure 2) then the strain values were decreased up to zero in the unloading cycle and the electrical resistance was decreased consequently. This loading/unloading state is repeated three times in the red signal and once for the blue signal.

Figure 3. Electrical resistance signals, (a) Noisy and (b) Filtered signals. The distance between the two consecutive increments (peak points) is about $\mathbf{60}$ seconds.

According to the Figure 2a, red and blue signals have 6 and 2 branches, respectively. These signals are denoised by the butterworth lowpass filter with the $F_{pass} = 1\ \mathrm{Hz}$ and $F_{stop} = 2\ \mathrm{Hz}$. Each branch represents a complete loading or unloading cycle. The branches in which the electrical resistance is increasing are related to loading cycles and the branches in which the electrical resistance is decreasing are related to unloading cycles.

III. NON-LINEAR EFFECTS

Linear and repeatable behaviour are two important parameters in a piezoresistive sensing element. In order to use this hybrid film as a piezoresistive sensing element, we should consider these issues. There are some phenomena such as stress relaxation, creep and hysteresis in the piezoresistive sensing elements that reduce the linear behaviour and repeatability of the sensing element. In order to evaluate the nonlinear behaviour of the hybrid film, the blue signal from Figure 2 was selected to evaluate the linear behaviour and repeatability of the piezoresistive hybrid film. This signal is generated by data acquisition system at a sampling frequency of $1\ \mathrm{kHz}$.

Figure 2. Peak points of the electrical resistance signal numbered based on values.

In the Figure 3, the peak points of the electrical resistance signal are numbered according to their values, in which that the lowest and highest peaks are numbered with 1 and 21, respectively. By comparing the corresponding points in the loading and unloading cycles (such as points 19 and 17), hysteresis behaviour can be seen the in the hybrid film. On the other hand, after peak points, despite the fact that the piezoresistive film has been rested for 60 seconds without any elongation, the electrical resistance has been dropped. This phenomenon is also due to creep and stress relaxation.

For further investigation of these phenomena, the middle regions of the adjacent peaks (regions A to J in Figure 3) were extracted and plotted in Figure 24. Ideally, these areas should be in the form of horizontal lines, while in Figure 4 the electrical resistance of the aforementioned areas (A to J) is slightly reduced and the areas are not perfectly horizontal.

Figure 4. The peak-to-peak regions of Figure 3. Ideally, these regions should be in the form of horizontal lines.

According to the Figure 4, any electrical resistance drop is due to the nonlinear behaviour of the piezoresistive element. The more decrease in the nonlinear behaviour of the piezoresistive element, the more increase in the potential of using it as the primary material in the sensing elements.

The lower the nonlinear behaviour of the piezoresistive element, the potential of using it as the primary material in the sensing elements is increasing.

In order to evaluate the electrical resistance drop in a closer view, the vertical axis of Figure 4, is plotted on a smaller

scale shown in Figure 5. According to the Figure 5, the hybrid film has had the highest and lowest electrical resistance drop in the regions “E” and “J”, respectively. It should be noticed that hybrid film was made of an ultrathin PDMS/CNT nanocomposite layer with the 14 vol% and 21 wt. % of CNT nanoparticles. Also, the highest and lowest electrical resistance drop in the regions “E” and “J” has been 1.8622 kΩ and 1.1341 kΩ, respectively.

Figure 5. The peak-to-peak regions of Figure 4 in a closer view.

According to the values of electrical resistance in the regions A to J, the piezoresistive hybrid film has had a 1.58% drop in electrical resistance. These small imperfections are the piezoresistive hybrid film defects, and it is suggested to resolve them in the future research as much as possible. This can be done by the modification of the materials and the manufacturing methods. As the number of imperfections in the piezoresistive hybrid film approaches zero, the ability to use this piezoresistive material as commercial product increases.

IV. CONCLUSIONS

REFERENCES